



Design, synthesis and study of coordination complexes for quantum computing

David Aguilà Avilés

ADVERTIMENT. La consulta d'aquesta tesi queda condicionada a l'acceptació de les següents condicions d'ús: La difusió d'aquesta tesi per mitjà del servei TDX (www.tdx.cat) i a través del Dipòsit Digital de la UB (diposit.ub.edu) ha estat autoritzada pels titulars dels drets de propietat intel·lectual únicament per a usos privats emmarcats en activitats d'investigació i docència. No s'autoritza la seva reproducció amb finalitats de lucre ni la seva difusió i posada a disposició des d'un lloc aliè al servei TDX ni al Dipòsit Digital de la UB. No s'autoritza la presentació del seu contingut en una finestra o marc aliè a TDX o al Dipòsit Digital de la UB (framing). Aquesta reserva de drets afecta tant al resum de presentació de la tesi com als seus continguts. En la utilització o cita de parts de la tesi és obligat indicar el nom de la persona autora.

ADVERTENCIA. La consulta de esta tesis queda condicionada a la aceptación de las siguientes condiciones de uso: La difusión de esta tesis por medio del servicio TDR (www.tdx.cat) y a través del Repositorio Digital de la UB (diposit.ub.edu) ha sido autorizada por los titulares de los derechos de propiedad intelectual únicamente para usos privados enmarcados en actividades de investigación y docencia. No se autoriza su reproducción con finalidades de lucro ni su difusión y puesta a disposición desde un sitio ajeno al servicio TDR o al Repositorio Digital de la UB. No se autoriza la presentación de su contenido en una ventana o marco ajeno a TDR o al Repositorio Digital de la UB (framing). Esta reserva de derechos afecta tanto al resumen de presentación de la tesis como a sus contenidos. En la utilización o cita de partes de la tesis es obligado indicar el nombre de la persona autora.

WARNING. On having consulted this thesis you're accepting the following use conditions: Spreading this thesis by the TDX (www.tdx.cat) service and by the UB Digital Repository (diposit.ub.edu) has been authorized by the titular of the intellectual property rights only for private uses placed in investigation and teaching activities. Reproduction with lucrative aims is not authorized nor its spreading and availability from a site foreign to the TDX service or to the UB Digital Repository. Introducing its content in a window or frame foreign to the TDX service or to the UB Digital Repository is not authorized (framing). Those rights affect to the presentation summary of the thesis as well as to its contents. In the using or citation of parts of the thesis it's obliged to indicate the name of the author.

DESIGN, SYNTHESIS AND STUDY OF COORDINATION COMPLEXES FOR QUANTUM COMPUTING

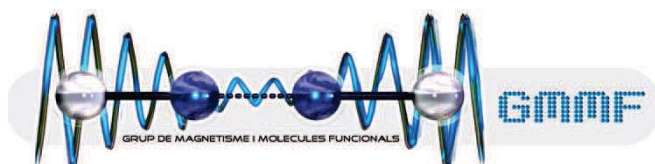
Universitat de Barcelona

Facultat de Química

Departament de Química Inorgànica

Programa de Doctorat: Química Inorgànica Molecular

Grup de Magnetisme i Molècules Funcionals



David Aguilà Avilés

Director: Dr. Guillem Aromí Bedmar, Departament de Química Inorgànica

Tutor: Dr. Albert Escuer Fité, Departament de Química Inorgànica

Guillem Aromí Bedmar, Professor del Departament de Química Inorgànica de la Facultat de Química de la Universitat de Barcelona,

CERTIFICA: que el treball titulat *Design, synthesis and study of coordination complexes for quantum computing* que presenta el David Aguilà Avilés per optar al grau de Doctor per la Universitat de Barcelona, ha estat realitzat sota la seva direcció al Departament de Química Inorgànica d'aquesta Facultat.

Barcelona, abril de 2013

Dr. Guillem Aromí Bedmar

Albert Escuer Fité, Catedràtic del Departament de Química Inorgànica de la Facultat de Química de la Universitat de Barcelona,

CERTIFICA: que ha estat el tutor responsable dels estudis de Doctorat realitzats dins del programa de Doctorat de Química Inorgànica Molecular pel David Aguilà Avilés.

Barcelona, abril de 2013

Dr. Albert Escuer Fité

Als meus pares i al meu germà

CONTENTS

CHAPTER I. INTRODUCCION

1. Molecular Magnetism: General aspects	3
2. Quantum Computing	8
2.1. From classical to quantum computing: Exploring a new world	8
2.2. Potential candidates for the quantum “hardware”	13
2.3. Electronic spin in coordination magnetic molecules	20
2.4. DiVincenzo criteria in coordination magnetic molecules	27
2.5. Qubits and SMM's: Differences and similarities	29
3. Current coordination chemistry proposals of 2-qubit QGs	30
4. Our proposal: Design of multidentate β -diketone ligands to access qubits	38

CHAPTER II. DESIGN, SYNTHESIS AND CHARACTERIZATION OF β -DIKETONE LIGANDS TO ACCESS FUNCTIONAL COORDINATION COMPLEXES

1. Introduction	45
2. Description, synthesis and characterization of H ₄ L1: 1,3-bis-(3-oxo-3-(2-hydroxyphenyl)propionyl)benzene	47
3. Description, synthesis and characterization of H ₄ L2: 1,3-bis-(3-oxo-3-(2-hydroxyphenyl)propionyl)pyridine	49
4. Description, synthesis and characterization of H ₂ L3: 1,3-bis-(3-oxo-3-(2-pyridyl)propionyl)pyridine	52
5. Description, synthesis and characterization of H ₃ L4: 6-(3-oxo-3-(2-hydroxyphenyl)propionyl)-2-pyridinecarboxylic acid	55
6. Experimental	58

CHAPTER III. TRIPLE- AND QUADRUPLE-STRANDED HELICATES

1. Introduction	65
2. Triple-stranded helicates with Fe ^{III} and Ga ^{III}	68
2.1. Description of the structure of [Fe ₂ (H ₂ L1) ₃] and [Ga ₂ (H ₂ L1) ₃]	70
3. Quadruple-stranded helicate with U ^{IV}	75
3.1. Description of the structure of [U ₂ (H ₂ L1) ₄ (X) ₂]	76
3.2. Infrared spectroscopy and study of the redox activity of [U ₂ (H ₂ L1) ₄ (X) ₂]	80
4. Experimental	82

CHAPTER IV. MOLECULAR PAIR OF CLUSTERS: COMPLEXES CONTAINING TWO WEAKLY COUPLED METALLOAGGREGATES

1. Introduction	89
2. Homometallic tetranuclear [MM'···MM'] clusters	91
2.1. Synthesis and study of the crystal structures	91
2.2. Study of the redox activity	99
2.3. Study of the magnetic behavior	101
3. Site-selective heterometallic [MM'···M'M'] clusters	106
3.1. Synthesis and structural study of [CuNi···NiCu] and [CuCo···CoCu]	107
3.2. Study of the metal composition of [CuNi···NiCu]	112
3.3. Study of the redox activity of [CuNi···NiCu]	114
3.4. Study of the magnetic properties of [CuNi···NiCu]	115
4. Linear metal chain assembly using bifunctional ligands	118
4.1. Synthesis and structural study of a rhombohedral cobalt(II)/cobalt(III) cluster	118
4.2. Pairs of clusters using a tetranuclear linear cobalt(II) complex	121
4.2.1. Synthesis and structural study	121
4.2.2. Characterization of tetranuclear linear cobalt(II) complexes	125

4.2.3. Electrochemical behavior of $[\text{Co}_4(\text{L3})_2(\text{H}_2\text{O})_8](\text{NO}_3)_4$	128
4.2.4. Magnetic behavior of $[\text{Co}_4(\text{L3})_2(\text{H}_2\text{O})_8](\text{NO}_3)_4$	129
4.2.5. Linking chemically $[\text{Co}^{\text{II}}_4]$ complexes: Synthesis and structural study of $[\text{Co}^{\text{II}}_4](\text{bpy})_4-[\text{Co}^{\text{II}}_4]$	131
4.2.6. Electrochemical behavior of $[\text{Co}_4(\text{L3})_2](\text{bpy})_4-[\text{Co}_4(\text{L3})_2]$	138
4.2.7. Magnetic behavior of $[\text{Co}_4(\text{L3})_2](\text{bpy})_4-[\text{Co}_4(\text{L3})_2]$	141
5. Experimental	143

CHAPTER V. DINUCLEAR LANTHANIDE COMPLEXES AS PROTOYPES FOR 2-QUBIT QUANTUM GATES

1. Introduction	151
2. A comprehensive family of dinuclear homometallic lanthanide complexes	153
2.1. Study of the crystal structures	154
2.2. Analysis of the lanthanide contraction	157
2.3. Continuous-shape measures of the coordination polyhedra in $[\text{Ln}_2(\text{HL4})_2(\text{H}_2\text{L4})(\text{NO}_3)(\text{H}_2\text{O})(\text{py})]$	165
2.4. Mass spectrometry of the $[\text{Ln}_2(\text{HL4})_2(\text{H}_2\text{L4})(\text{NO}_3)(\text{H}_2\text{O})(\text{py})]$ series	168
2.5. Magnetic behavior of complexes $[\text{Ln}_2(\text{HL4})_2(\text{H}_2\text{L4})(\text{NO}_3)(\text{H}_2\text{O})(\text{py})]$	170
2.6. Photoluminescent properties of complexes $[\text{Ln}_2(\text{HL4})_2(\text{H}_2\text{L4})(\text{NO}_3)(\text{H}_2\text{O})(\text{py})]$	174
3. Exchanging the anion in the series: $[\text{Ln}_2(\text{HL4})_2(\text{H}_2\text{L4})\text{Cl}(\text{py})\text{L}]$ complexes	178
3.1. Study of the crystal structures	179
3.2. Magnetic properties of complexes $[\text{Ln}_2(\text{HL4})_2(\text{H}_2\text{L4})\text{Cl}(\text{py})\text{L}]$	183
4. Dinuclear terbium(III) cluster as molecular prototype for spin-based CNOT and $\sqrt{\text{SWAP}}$ quantum gates	185
5. Extending the family: Asymmetric heterometallic dinuclear lanthanide complexes	194
5.1. Crystal structure of $[\text{LnLn}'(\text{HL4})_2(\text{H}_2\text{L4})(\text{NO}_3)(\text{py})(\text{H}_2\text{O})]$	197
5.2. Study of the $[\text{LnPr}(\text{HL4})_2(\text{H}_2\text{L4})(\text{NO}_3)(\text{py})(\text{H}_2\text{O})]$ series	198

6. Study of [CeEr(HL4) ₂ (H ₂ L4)(NO ₃)(py)(H ₂ O)] as a molecular 2-qubit quantum gate	203
6.1. Defining Ce ^{III} and Er ^{III} as quantum bits	206
6.2. Heterometallic [CeEr] complex as a molecular quantum processor	216
7. Experimental	222
CHAPTER VI. CONCLUSIONS AND FUTURE PRESPECTIVES	239
APPENDIX	247
LIST OF PUBLICATIONS	327

CHAPTER I

INTRODUCTION

INTRODUCTION

The synthesis and study of coordination complexes has an enormous interest in the scientific community due to the physical properties that arise from these molecular entities. By exploiting the functionalities provided by such molecular properties, these materials can constitute the required tools for the development and implementation of new technological devices at the nanometric scale. Along these lines, in the last ten years the magnetic properties of coordination clusters have been proposed as an exceptional resource for the future information processing technologies such as quantum computing.^[1] The application of magnetic molecules as the possible hardware of quantum computation is turning from an utopic idea into a strong possibility, in view of the promising results demonstrated in this research line.^[2, 3] The versatility of magnetic coordination complexes ensues from the design of ligands for the assembly of paramagnetic metal ions into molecules with the desired topology and properties. Following such approach, the aim of this work is the deliberate preparation of magnetic coordination complexes for their application in quantum information processing by using multidentate ligands based on the β -diketonate unit. Throughout this manuscript, the design, synthesis and study of these molecular materials will be described, focusing on the comprehension of their magnetic properties and its suitability for the implementation of quantum information processing.

1. Molecular Magnetism: General aspects^[4, 5]

The design of coordination magnetic complexes for their application in quantum computation is grounded on their magnetic molecular properties, which arise from the open-shell moieties of such molecules. Macroscopically, when a sample of a magnetic complex is placed within a homogenous external magnetic field H , it acquires a magnetization, M , that can be also expressed as magnetic susceptibility, $\chi = \delta M / \delta H$. The magnetization can be related with the energy variation of the sample, according to classical mechanics, as follows, $M = - \delta E / \delta H$. In quantum mechanics, the microscopic magnetization or magnetic moment, μ , of a polyelectronic system (e.g., a coordination magnetic complex) is originated from its total orbital angular momentum (L) and its

total spin angular momentum (S). Depending on the energetic terms generated from the ligand field effect, the system can have the orbital contribution quenched,^[4] presenting only spin angular momentum or, on the contrary, exhibit both contributions, leading to an interaction between both angular momenta known as first order spin-orbit interaction.^[4] For the former case, the magnetic moment μ is defined as:

$$\mu^S = g_s \beta [S(S + 1)]^{1/2} \quad (1) \qquad \mu_z^S = -g_s \beta M_s \quad (2)$$

where β is the Bohr factor, μ_z^S is the z-component of the magnetic moment, and M_s is the spin quantum number associated with S_z that varies by an integer value from $-S$ to $+S$ generating different degenerate states. The degeneration of these states is split by the interaction with an external magnetic field (a phenomenon known as *Zeeman effect*). This splitting is governed by the gyromagnetic factor g_s , which slightly differs from the g -factor of a free electron $g_e = 2.0023$ (also known as *Landé factor*) due to the coupling between the ground-state and the excited states of the same spin multiplicity (second-order spin-orbit coupling). The Hamiltonian that describes the energy of this interaction is known as *spin Hamiltonian*:

$$\mathbf{H} = \beta S g H \quad (3)$$

Depending on the symmetry of the magnetic complex, the value of the g -factor has to be calculated in a different manner. For isotropic mono- or polyelectronic systems, the g value is orientation independent, and is described as $g = g_e - n\lambda/\Delta$, n being a constant, λ the spin-orbit coupling parameter, and Δ the energy gap between the ground and the excited states. For a monoelectronic anisotropic system, the g value does depend on the direction of the applied magnetic field, leading to different n_u constant values ($u = x, y$ or z) depending on each axis: $g_u = g_e - n_u\lambda/\Delta$. Finally, for an anisotropic multielectronic system, an additional term known as *zero-field splitting* (ZFS) is included in the spin Hamiltonian. This splitting breaks the zero field degeneracy of the different quantized orientations of the total spin angular momentum:

$$\mathbf{H} = g_u \beta S_u H_u + D \left[S_z^2 - \frac{S(S + 1)}{3} \right] + E(S_x^2 - S_y^2) \quad (4)$$

where u denotes the orthogonal direction (x, y, z), and D and E are the axial and rhombic zero-field splitting parameters, respectively. This approach involves, for example, coordination complexes embedding $3d$ elements with A or E terms, where the crystal field effect from the ligands has an important contribution. In contrast, when the spin-orbit coupling has a bigger influence than the crystal field (first-order coupling), like in $4f$ elements or $3d$ with T terms, the orbital angular momentum L must be taken into account. The coupling of the spin and orbital angular momenta leads to a total angular momenta J . In this case, the magnetic moment is defined as:

$$\mu^J = g_J \beta [J(J + 1)]^{1/2} \quad (5) \quad \mu_z^J = -g_J \beta M_J \quad (6)$$

where μ_z^J is the z -component of the magnetic moment, M_J is the angular momentum quantum number associated with J_z , generating different states that vary from $-J$ to $+J$ by an integer value. Each $\pm M_J$ pair has a different energy due to the crystal-field effect. The degeneracy of these $\pm M_J$ levels is further removed by the effect of the applied magnetic field (*Zeeman effect*) depending on the corresponding gyromagnetic g -factor. The value of such g -factor can be calculated according the following equation:

$$g = g_J = \frac{3}{2} + \frac{S(S + 1) - (L + 1)}{2J(J + 1)} \quad (7)$$

However, the Hamiltonian describing the magnetic energy in this kind of systems can be described by treating separately the orbital and the spin contributions to the angular momentum, thus not including the orbital influence in the g -factor. Following such procedure, one can include the spin-orbit coupling term, $\mathbf{H} = \lambda LS$, in the final Hamiltonian:

$$\mathbf{H} = \lambda LS + \beta(L + g_e S)H \quad (8)$$

In general terms, the energy of the interaction between the microscopic magnetic moment μ and the external magnetic field applied in the z principal axis is defined as $E = -\mu H = -\mu_z H$. Moreover, since in the presence of a magnetic field H each molecule displays a quantized energy spectrum E_n ($n = 1, 2, \dots$), the microscopic magnetization of each state, μ_n can be defined as $\mu_n = -\delta E_n / \delta H$. Consequently, the macroscopic magnetization M becomes the sum of the different microscopic magnetizations (μ_n) of

the molecules of the sample, considering the population of each state (P_n) according to the Boltzmann distribution law:

$$M = N \sum_n \mu_n P_n = \frac{N \sum_n \left(-\frac{\delta E_n}{\delta H} \right) \exp\left(-\frac{E_n}{kT}\right)}{\sum_n \exp\left(-\frac{E_n}{kT}\right)} \quad (9)$$

where T is the temperature, k the Boltzmann constant and N Avogadro's constant. However, the application of this expression is complicated since it requires to know the $E_n = f(H)$ for all the thermally populated states of the molecule. In 1932, Van Vleck proposed a simplification following a perturbation method, decomposing the energy of each state: $E_n = E_n^{(0)} + E_n^{(1)}H + E_n^{(2)}H^2 + \dots$, where $E_n^{(0)}$ is the energy of level n in zero field, while $E^{(i)}$ is the i^{th} order Zeeman coefficient.^[6] Applying the definition of the magnetic susceptibility, $\chi = \delta M / \delta H$, the Van Vleck formula up to 2nd order is then defined as

$$\chi = \frac{N \sum_n \left(\frac{E_n^{(1)2}}{kT} - 2E_n^{(2)} \right) \exp\left(-\frac{E_n^{(0)}}{kT}\right)}{\sum_n \exp\left(-\frac{E_n^{(0)}}{kT}\right)} \quad (10)$$

The application of the formula just requires knowledge of $E_n^{(0)}$, $E_n^{(1)}$ and $E_n^{(2)}$, which can be calculated when the eigenvalues $E_n^{(0)}$ and eigenfunctions $|n\rangle$ of the Hamiltonian in zero-field associated with the molecule studied are known. The formula can be simplified when the external magnetic fields and temperatures are sufficiently small, and can be used to develop an analytical expression of the molar magnetic susceptibility χ_M versus temperature.

$$\chi_M = \frac{Ng^2\beta^2}{3k_B T} \frac{\sum_n S(S+1)(2S+1) \exp\left[\frac{-E_n^{(0)}}{k_B T}\right]}{\sum_n (2S+1) \exp\left[\frac{-E_n^{(0)}}{k_B T}\right]} \quad (11)$$

For a system of only one paramagnetic center or with the ground-state well-separated from the excited states, the molar magnetic susceptibility versus temperature follows the equation:

$$\chi_M = \frac{Ng^2\beta^2}{3k_B T} S(S+1) \quad (12)$$

from where $\chi_M = ct/T$. Thus, the $\chi_M T$ product has a constant value along the temperature range. This expression is known as the *Curie law*. This behavior can be only ascribed to complexes without first-order spin-orbit coupling. However, for the cases where the influence of the latter is feeble, the magnetic behavior can be described by the modified *Curie-Weiss law*, $\chi_M = ct/(T-\theta)$, within some defined temperature range.

With the above mathematical expressions, any multielectronic system of a molecular entity can be defined. In this context, the use of coordination magnetic complexes for quantum computing is grounded on the versatility of multinuclear molecular magnetic systems and the possibility of tuning the interactions between the different metal ions contained in such systems. Thus, the magnetic properties of a coordination complex arise not only from the isolated ions in a cluster, but also from the interaction between them, as well as from the diamagnetic contribution of the ligands in the molecule. The interaction between spin magnetic moments can be quantified phenomenologically with the constant J , and the energy of this interaction is described by the Heisenberg-Dirac-Van Vleck (HDVV) Hamiltonian. In the simplest example of a dinuclear coordination magnetic complex with A and B being paramagnetic metal ions, the Hamiltonian derived is:

$$\mathbf{H} = -JS_A S_B \quad (13)$$

where S_A and S_B are the spin operators of each ion. If the interaction between both centers is antiferromagnetic (i.e. both spin moments align against each other), then J is negative. If, by contrast, the spin moments align in the same direction, then the interaction is ferromagnetic and the J value is positive. In addition, two different conventions have been used to define the HDVV Hamiltonian by the scientific community, thus using $H = -JS_A S_B$ or $H = -2JS_A S_B$, both accepted and applied along this thesis. The application of HDVV Hamiltonian in the Van Vleck equation allows the quantification of the magnetic interaction J through magnetic susceptibility measurements. The coupling within the magnetic coordination complexes in Chapter

IV will be studied following such procedure. It is worth noting that the magnetic interaction can be also studied by magnetic heat capacity measurements. The splitting of the energy levels (provided by the magnetic coupling) produces a characteristic heat capacity behavior, known as the Schottky anomaly, and the temperature where such anomaly takes place can be used to determine the value of J . In Chapter V, some of the complexes will be studied by magnetic heat capacity measurements for obtaining the value of the magnetic interaction within them.

2. Quantum computing

2.1. From classical to quantum computing: Exploring a new world

During the last years, computer science has been evolving continuously due to the breakthrough on the design of new computational systems and new technological advances. Conventional computers process information as bits, which are the basic element of information and are embodied in macrostates of a bistable physical system. Its material realization relies on a system with two well defined states, such as small magnetic domains (employing the magnetization up or down), the charge state of a capacitor (charged or not charged), or a transistor element (switched off or on).^[7] Thus, the bit can be in one macrostate or in the other, i.e., 0 or 1. The information stored as bits can be then manipulated performing logical operations, using the so-called logic gates, which can be composed by one or more bits. An interesting question arises from considering the application of the information processing technology using a quantum system. Storing, transmitting and processing information encoded in systems of quantum nature represents an exciting but ambitious project.^[8-10] This challenge has motivated the search of suitable physical materials for the use of the laws of quantum mechanics to perform tasks of information processing, termed as **Quantum Computing (QC)**. The process information units in QC, named **Quantum bits** or **Qubits** (the quantum counterpart of the classical bits) are quantum systems with two quantum microstates. These systems can have the values like in the classical bits, $|1\rangle$ or $|0\rangle$, but also any combination of these two, known as quantum superpositions: $|\varphi\rangle = \alpha|1\rangle + \beta|0\rangle$, where α and β are complex numbers with $|\alpha|^2 + |\beta|^2 = 1$. The

different possibilities for a superposition state are well represented by the Bloch sphere (Figure I.1, left).^[2, 11] The qubit can be in the north and south poles, representing the states $|1\rangle$ and $|0\rangle$ respectively, but also on all the other points, representing the superposition states as a combination of these two. The feature of such superposition is one of the key points in QC, being one of the main reasons for its high potential (see below). The study of the binary logic of these quantum two-level systems is called **Quantum Information Processing (QIP)**. The quantum logic (much richer than the classical one) allows the implementation of algorithms to solve problems in fewer steps than with classical logic. In fact, quantum information is expected to provide important improvements over its classical counterpart, with a potential that can lead to still not imaginable capacity. One example is the possibility of developing the Shor's quantum algorithm for factoring large numbers, which would be able to solve the specific problem of encryption of data. Another interesting features are the quantum communication, that enables the sharing of secrets with security guaranteed by the laws of physics (see below), or the quantum metrology, that provides higher precision on time or distance measurements.^[9]

The operations on a quantum computer are performed by logic **Quantum Gates** or **Qugates (QGs)**, the quantum counterpart of the classical logic gates) that can be also build by one single qubit (one-qubit gate) or by more qubits. These quantum gates operate over the qubits in an initial state (input), returning them in a final state (output). The simplest operation is the NOT qugate, a single-qubit unitary rotation (one-qubit gate) from an initial state $|\varphi_i\rangle = |0\rangle$ to a final superposed state $|\varphi_f\rangle = \alpha|1\rangle + \beta|0\rangle$. However, the most famous logic gates are the so-called *Universal Quantum Gates*, since any complex logic operation can be carried out by a combination of few of these elementary operations. Moreover, it has been accepted that any algorithm can be realized as a sequence of unitary rotations and universal quantum gates.^[11] The two more important universal quantum gates are the controlled-NOT (CNOT) gate and the $\sqrt{\text{SWAP}}$ gate (Figure I.1, right)^[2], both composed by two qubits. The CNOT quantum gate inverts the state of one qubit (named target qubit) depending on the state of the second qubit (named control qubit). Thus, if the control qubit is in the state $|1\rangle$, the target qubit switches from $|1\rangle$ to $|0\rangle$ (or vice versa). However, if the value of the state

of the control qubit is $|0\rangle$, the state of the target qubit remains undisturbed. The $\sqrt{\text{SWAP}}$ gate turns an initial $|a,b\rangle$ state into a superposition $(|a,b\rangle + i|b,a\rangle)/(1+i)$. One of the most important features of these quantum operations is that the nature of the final two-qubit state (the output) may be impossible to be expressed as a product of states of each of the qubits embodying the Qugate, i.e., each individual qubit would not be fully described without considering the other. This occurs naturally with the $\sqrt{\text{SWAP}}$ qugate and happens upon application of a CNOT to an input containing a superimposed qubit (see below). In such cases, the two-qubit output state is known as an entangled state.^[3] Entanglement is a natural occurrence of quantum systems that are correlated by some weak interaction, and it is essential for the implementation of some QC algorithms.

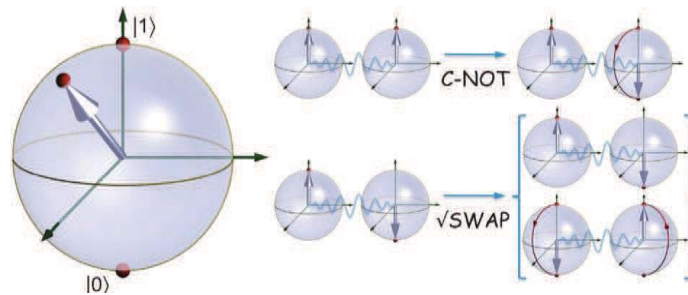
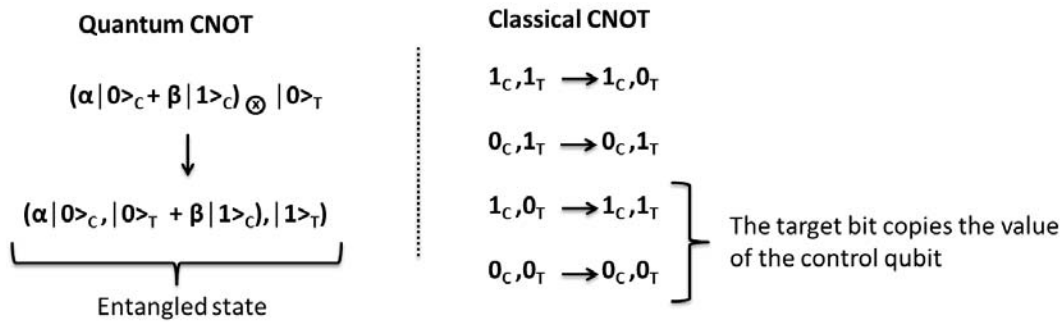


Figure 1.1.^[2] (Left) Schematic representation of the Bloch sphere, exhibiting all the possible states for a quantum superposition $|\varphi\rangle = \alpha|1\rangle + \beta|0\rangle$. (Right) Representation of CNOT and $\sqrt{\text{SWAP}}$ gate operations (only $|1,1\rangle \rightarrow |1,0\rangle$ for CNOT and $|1,0\rangle \rightarrow (|1,0\rangle + i|0,1\rangle)/(1+i)$ for $\sqrt{\text{SWAP}}$ operations are shown).

The importance of quantum superpositions and entanglement in quantum computation is evidenced when comparing the application of NOT or CNOT logical operations in classical and quantum machines.^[11] The NOT operation in a classical computer simply switches the state of a bit, from 0 to 1, or vice versa. However, as shown before, the same logical NOT operation acting on a qubit with initial state $|\varphi_i\rangle = |0\rangle$ produces a final state $|\varphi_f\rangle = \alpha|1\rangle + \beta|0\rangle$, which is a superposition of the initial $|0\rangle$ state and the switched state $|1\rangle$. For the CNOT operation, the classical gate switches the target bit if the control bit is in state 1. Following this procedure, one can do for example a COPY operation of the control qubit, just establishing the target bit of the input in the 0 state (Scheme I.2). In contrast, the quantum CNOT logic gate forbids the COPY operation if the control qubit lies in a superposition state, since it produces a

final entangled state that cannot be written as a product of the states of each qubit. Thus, an arbitrary quantum bit cannot be copied (allowing a securer information processing).



Scheme I.2. Classical and quantum CNOT operations. The classical operation allows copying the value of the control qubit, while the quantum counterpart produces an entangled state that prevents the control qubit to be copied.

As shown in the Scheme I.2, the inputs of the Quantum CNOT can be expressed in a product state, this is, separating the control qubit $(\alpha|0\rangle_c + \beta|1\rangle_c)$ from the target one $|0\rangle_T$. However, the operation leads to a final output state which cannot be expressed as a product state (entangled state). The entanglement is considered the key feature that provides to quantum algorithms the advantage over the classical algorithms.

Another important issue that must be considered in quantum computation is that a qubit, which is in a superposition of its two states $|1\rangle$ and $|0\rangle$, represents a quantum oscillator. Thus, the information of a qubit is encoded in the amplitudes and phases within the complex numbers α and β that describe the superposition state $|\varphi\rangle = \alpha|1\rangle + \beta|0\rangle$.^[7] The integrity of this information must be maintained during the running time of the computer, which means that the state of this quantum superposition has to be unaltered during the gate operation. This implies that the different components of the quantum oscillator, that show an interference and thus a coherence, must not be lost while a qubit is changing from one state to another. The process of losing the interference between the quantum mechanical waves of the quantum oscillator is known as decoherence (since their phases do not longer cohere) and it is quantified by the decoherence time τ_d .^[3] This time must be, thus, as long as possible to ensure the

quantum gate operation without losing the information stored in its qubits. In fact, the important parameter is given not by the absolute value of τ_d , but by the ratio between τ_d and the characteristic timescale of the operation, i.e., the duration of the quantum gate, τ_g . It is considered that this ratio, known as figure of merit (Q), must be $\tau_g / \tau_d \leq 10^{-4}$ for a fault-tolerant computation (the property of the computer to be able to continue operating even in the failure of some of its components). The coupling of the quantum components with the environment of the system tends to break the coherent character of it, leading the system to decohere by two different mechanisms.^[3] The first one is related to excitation/relaxation processes, produced by transitions between different states of the quantum system induced by the interaction with the environment. This process brings the system to a thermal equilibrium on a timescale T_1 known as longitudinal relaxation time constant. On the other hand, the interactions with the environment can cause also a loss of phase coherence between the components of the linear superposition (dephasing of the oscillators), making the initial state of the quantum system to evolve into a statistical mixture of states. The process is characterized by the transverse relaxation time constant T_2 . Both processes exhibit exponential dependence on time, but since $T_1 \gg T_2$, it is considered that the elements of the quantum computer must operate much faster than T_2 to allow the previous mentioned fault-tolerance. The figure of merit Q can be therefore expressed as $\tau_g / T_2 \leq 10^{-4}$, since the decoherence time τ_d will be governed by T_2 . The coherent transitions can be probed experimentally by the observation of Rabi oscillations between two quantum states. These transitions can be observed by driving a coherent beam of electromagnetic radiation, or by free rotations like a spin precessing in a static magnetic field.

An interesting comparison exposed by Ladd et al. between QC and another quantum technology, the laser, can be helpful to understand the potential behind the quantum computation.^[9] Before the existence of the laser, there were different technologies for making light, like the fire, lanterns or the light bulb. For all this sources, the light created is incoherent, with many electromagnetic waves generated at completely random times with respect each other. In contrast, the quantum mechanically effects in the laser technology lead the waves to be generated in phase, providing a different

light source (coherent light). However, this kind of light has different applications when compared to the incoherent one, like in eye surgery, barcode readers, or in weapons, but cannot replace the light bulbs. Thus, the authors consider that the quantum computer would maybe not be a faster, smaller version of an ordinary computer, but just a different kind of computer that can control the coherent quantum mechanical waves for different applications. This is, without a doubt, a consideration that should be kept in mind.

2.2. Potential candidates for the quantum “hardware”

After evaluating the capabilities and the potential of quantum computation, the first question that arises is which kind of material is the most appropriate for the implementation of such technology. Nowadays, several research groups around the world are working towards the goal of building a quantum computer, and so many materials are under study to build the necessary quantum bits. The first proposal that was designed for a CNOT quantum gate with a physical system was exposed by Cirac and Zoller, based on ions confined in a trap and cooled by laser beams, in which the two internal states of each ion define the qubit states.^[12] The coupling of two or more qubits was proposed through an excitation of the centre of mass motion of the ions. Following this scheme, the first experimental demonstration of the gate was carried out shortly after the theoretical proposal.^[13] Few years later, another approach based on nuclear magnetic resonance was proposed by Chuang et al., which was also experimentally demonstrated.^[14, 15] The authors used the ^1H and ^{13}C nuclear spins as an input and output respectively, in a solution of CHCl_3 molecules, using the highly difference of their gyromagnetic ratios, which leads to a different Zeeman splitting under an homogeneous magnetic field. Thus, it is possible to rotate either one or the other with the appropriate frequency of an electromagnetic pulse. Even both nuclear spin and cold ions approaches are very well isolated from the environment, and provide long coherence times, they present some inconvenient for scaling up the proposal into complex structures. Despite the fact that their coherence times are not so favorable, the use of solid-state devices for qubit realizations, like superconducting

devices, can easily be implemented and scaled. These devices have been therefore identified as potential qubits, and their coherence times have been improved during the last years.^[16] Additionally, it is relatively easy to engineer superconductivity circuits and couple two such qubits to build quantum gates. In the following sections, an introduction to these and other materials that are currently being studied and proposed as prototypes of qubits for the development of a quantum computer is presented.^[9]

· *Photons:*

The proposal is based on the realization of a qubit by the polarization state of a photon, the elemental particle from an electromagnetic radiation. One of the best advantages of this approach is that photons are relatively free of decoherence, which is comparatively larger in other quantum systems. The polarization rotations can be thus used as qubits, and are easily produced by using “waveplates” made of a birefringent material. The inconvenient comes with the control of universal multi-qubit gates, since the interactions required need optical nonlinearities stronger than the ones obtained with the available technology. However, a considerable advance was made on 2001 by Knill, Laflamme and Milburn, who showed that a scalable quantum computer was possible using only single-photons sources and detectors, and linear optical circuits,^[17] an scheme that was implemented some years later.^[18] Nowadays, efforts are focused on developing highly-efficient single-photon detectors and sources, and devices that can enable the interaction between different photons. As an example, silicon single-photon detectors operating at room temperature can achieve a 70 % of efficiency. Using superconducting detectors as sensitive thermometers allows an efficiency of 95 %, but these only operate at very low temperatures and very slowly. One approach to a highly-efficient single-photon source is based on multiplex nonlinear optical sources, which are currently used to emit pairs of photons spontaneously. Nevertheless, these advantages do not withstand the problem of photon loss, which still remains a significant challenge. Such energy loss can be viewed as the T_2 decoherence time that is calculated in matter-based qubits.

· *Trapped neutral or ionic atoms:*

Maybe the most important characteristic of using neutral atoms or ions as qubits is that they present very high T_2 time scales due to the excellent coherence properties of certain energy levels within them. Therefore, the energy levels in trapped atoms or ions are very reliable qubits, with T_2 times in the range of seconds or even longer. In addition, entanglement within quantum gates can be brought about by designing the appropriate interactions between atoms. The atomic qubits can be initialized by optical pumping, i.e., by application of light to arrange the electrons from lower energy states in the atom to higher ones. In addition, the measurement can be carried out using state-dependent optical fluorescence detection, with an efficiency of almost 100%. The proposal for the use of trapped ions as qubits contemplates the use of the electronic states of each ion, which are confined and suspended in free space using electromagnetic fields, to define the qubit itself. Thus, using an appropriate electric field from nearby electrodes, individual atomic ions can be introduced in free space with a nanometric precision. The consequent quantum gates can be then produced by multiple trapped ion qubits, which are in turn entangled through laser-induced coupling of their spins, mediated by collective mode of harmonic motion in the trap. The formation of quantum gates through this method of entanglement was proposed by Cirac and Zoller, and demonstrated the same year.^[19] This approach to obtain entangled trapped ion qubits has been extended by using optical spin-dependent forces, which do not require neither individual optical addressing of the ions nor the preparation of the harmonic motion for the preparation of the quantum states. Using such approach, up to eight trapped ion qubits have been entangled satisfactorily.^[20] However, scaling trapped ions as quantum gates is difficult when a large number of ions participate in the collective motion, where the laser-cooling becomes inefficient. Consequently, the participating ions become more susceptible to noisy electric fields and the motion density can degrade the quantum gates through undesired motions or nonlinearities, thus increasing the decoherence of the system. An alternative approach for scaling the quantum gates of trapped ion qubits is to use photonic interactions to couple small collections of ions, which gives a communication channel that can traverse large distances.

Similar to the trapped ions, trapped neutral atoms can be also used as qubits. An array of cold neutral atoms can be confined in free space using crossed laser beams, forming an optical lattice. The dimensionality, form, depth and position of such optical lattice can be precisely controlled through the geometry, polarization and intensity of the laser beams. Thus, the challenges emerge from the controlled initialization, interaction and measurement of the atomic qubits using optical lattices. The interaction between the atomic qubits within the lattice usually comes from adjacent atoms, bound with appropriate laser forces, while the entanglement arises from contact interactions. Like trapped ions, coherence times of this kind of physical realization of qubits are much higher than the time needed for controlling or measuring the system. However, the scale of these qubits into more complex architectures is a problematic issue that researchers are still facing.

· *Spin-based systems: Quantum dots and dopants in solids*

One of the main difficulties when defining single atoms in vacuum as qubits is the need of cooling and trapping them. In contrast, arrays of such qubits may be easier to assemble and cool if they are integrated into a solid-state host, like quantum dots or single dopants in solids. Using such impurities or small semiconductor nanostructures, one can create “artificial atoms” by confining electrons or holes in a localized potential with discrete E levels. A quantum dot can be defined in two different groups depending on the method to create the confinement. Electrostatically defined quantum dots obtain the confinement by controlled voltages on lithographically defined metallic gates, operate at low temperatures ($< 1\text{K}$) and are controlled electrically. In contrast, the so-called self-assembled quantum dots create the potential for confining electrons or holes by a random semiconductor growth process, operate at higher temperatures (around 4 K) and are controlled optically.

The first proposals were established by Loss and DiVincenzo, considering arrays of electrostatically defined quantum dots containing a single electron (the two spin-states providing the qubit definition). The quantum logic was achieved by changing voltages on the electrostatic gates, thus moving the electrons closer and further (activating/deactivating the exchange interaction respectively).^[21] The measurement of

the qubits has been demonstrated by using a single-electron transistor, which allows the change from spin to charge and the measurement of their conductance (sensitive to the charge of an electron in a quantum dot). The control of the spins was demonstrated by a direct generation of microwave magnetic and electric fields that enable also the measurement of T_2 time constants by spin-echo techniques (defined in Section 2.3). Maybe the most critical problem of this proposal is the presence of nuclear spins in the semiconductor substrate, which causes an inhomogeneous magnetic field that represents a source of decoherence for the electron spin, limiting the T_2 time constant to around a few microseconds. One possible way to solve this problem is the use of zero-nuclear-spin semiconductors (group IV, silicon or germanium). Another important factor to keep in mind is the short range of the exchange interaction that appears when using electrostatically defined quantum dots or impurities for quantum computing. However, it can be improved with photonic connections. On the other hand, using self-assembled quantum dots as qubits appears to be more difficult, due to the random nature of these materials. Since they are formed in random locations, the optical characteristics vary from dot to dot, and thus an effort on engineered fabrication techniques for determining the placement of dots must be carried out.

Using optically active solid-state dopants has been also proposed as a prototype to embody a quantum bit, like a negatively charged nitrogen-vacancy center in diamond.^[22] The nitrogen atom, disposed at a lattice site neighboring a missing carbon atom, forms a triplet state system. Under optical illumination, it can be brought optically to a single spin state, and represents a fast initialization of the spin qubit. Moreover, it can be coherently manipulated with resonant microwave fields,^[23] and detected via spin-dependent fluorescence with optical microscopes. Since the carbon lattice is nearly a nuclear-spin-free system, the quantum bits present longer spin coherence times than GaAs quantum dots. Furthermore, this time scales can be increased by working with isotopically enriched ^{12}C . Finally, for both quantum dots and dopant spins approaches, magnetic interactions can allow local couplings. However, scaling a system of coupled spins remains a challenge. Even microsecond T_2 times are

long compared with 1-100 ps control times or 1-10 ns measurement and initialization times, a large-scale will require an improved connectivity and homogeneity.

· *Nuclear Magnetic Resonance: Nuclear Spins*

Using nuclear magnetic resonance techniques for quantum computation has been proposed and experimentally demonstrated with nuclear spins in molecules as qubits within liquid solutions. This approach has shown good coherence since the spin orientation of the nuclei is maintained for T_2 times of some seconds.^[14] Additionally, the high experience in nuclear magnetic resonance technology provides the necessary tools for the development of this approach for quantum computation. In a strong magnetic field, different nuclear spins can be identified because of their different Larmor frequency. In a molecule, this nuclear Larmor frequency varies from atom to atom according to their chemical shift. Thus, irradiating systems with resonant radio-frequency pulses allows the manipulation of nuclei with a determinate frequency, providing a prototype of one-qubit gate. Two-qubit interactions can be then achieved by indirect coupling mediated through molecular electrons. By observing the induced current in a coil that surrounds the array of qubits, one can measure and determine the state of the qubit. Following this procedure, the liquid-state nuclear magnetic resonance has allowed the manipulation of quantum processors with up to twelve qubits^[24] and the implementation of certain algorithms.^[25] However, experiments on NMR-based quantum computers have lead to difficulties for the detection of the output signal, since they are performed at temperatures where thermal energy exceeds the nuclear Zeeman energy and complicates the initialization of qubits.^[26] A proposal using pseudo-pure-state techniques to isolate the signal of an initialized pure state against a high-entropy background has been used to achieve such initialization. By contrast, no scalability was allowed. The limitation of the scalability can be addressed by using solid-state nuclear magnetic resonance, supported by the different dynamic nuclear polarization techniques that exist nowadays. In spite of the progress in the development of such technology, no sufficient initialization or measurement capabilities have been achieved using nuclear magnetic resonance. In addition, despite the good coherence shown by the nuclear spin, T_2 time scales are still short in comparison to initialization and measurement times, and have to be improved.

· Superconductors:

At very low temperature, electrons in superconductors are bound into pairs (known as Cooper pairs) that condense into a state with zero-resistance current and a well-defined phase. The potential of a Cooper pair can be changed controlling the inductance (L) and capacitance (C) of the circuit of the superconductor, providing the formation of a qubit. The superconducting qubits are therefore defined in LC-resonator circuits, which provide a quantum harmonic oscillator. The position and momentum of a single quantum particle are thus provided by the magnetic flux across the inductor (Φ) and the charge on capacitor plate (Q) of the circuit, respectively. The thin insulating layer of the superconductors (known as Josephson junction) allows an anharmonicity to the system. Two of the quantized levels in the resulting anharmonic potential allow the definition of the qubit. Using superconducting qubits, a single-qubit gate can be implemented with resonant pulses of 1 to 10 ns of duration applied on the qubit. The neighboring qubits, which are coupled either capacitively or inductively, allow low dimension quantum logic gates (few qubits). For larger systems, the coupling with microwave photons is being studied. This proposal has allowed two-qubit gate operations within few tens of nanoseconds, and has been used to implement some algorithms.^[27] However, the qubit readout schemes are still under development. The two qubit states can be discriminated using the switching behavior of the Josephson junction at its critical current,^[28] or with state-dependent phase shift of an electromagnetic wave in a transmission line.^[29] One of the greatest characteristics of superconducting qubits is their scalability at the macroscopic level. In fact, a large number of conduction electrons (around 10^{10}) can be confined in quite small devices (100 μm of size). However, the states created from these devices, with a more “macroscopic” character, are expected to show faster decoherence than the studied “microscopic” systems. Although some early experiments have shown considerably long T_2 values, decreasing decoherence is still an important challenge in superconducting qubits, and an effort on material engineering on microscopic scale is needed.

From the different techniques described in this section, one could study and compare each physical system for the implementation of the qubit, and decided which type of

hardware is the most promising. If we consider T_2 constant value as the limiting factor for a successful quantum computation realization, using trapped ions as qubits may win this race. However, coherence properties will improve for the different proposals with the development of each technology. More important, each T_2 value must be compared with timescales involving the control, initialization and measurement of the qubit, and thus each figure of merit must be considered. Additionally, beyond the fact that imperfection in the coherent control of the qubit seems to be the limiting factor for the quantum computing realization, one must consider also constraints for connectivity between qubits, specific noise-processes for that hardware, and speed of qubit-to-qubit communication. From an industrial point of view, the cost of the architectures needed for each algorithm will be also an important factor that must be contemplated.

The assessment of the most suitable technique could also be done focusing on their scalability. From this point of view, superconducting qubits seem to be the best positioned, since they can arrange a large number of qubits on a macroscopic scale (see above). Nevertheless, the loss of coherence related to the superpositions of these larger, more “macroscopic” states can be also a limiting factor. In this respect, a very promising approach that has emerged during the last years is the use of coordination magnetic molecules as the carriers of the quantum bit, since macroscopic arrays of identical molecules are naturally accessible. The great advantage in terms of scalability of these molecular materials has led them to be considered as potential candidates to embody the elementary register of quantum computation.

2.3. Electronic spin in coordination magnetic molecules

The chemical design of magnetic complexes has become an attractive route for realizing qubits.^[1] Around a decade ago, it was proposed that the qubit states might be encoded using the different molecular spin orientations and their quantum superpositions.^[1, 30, 31] This proposal encouraged some experimental groups to focus their attention on engineering molecules containing open-shell moieties in optimal conditions for their use as qubits. The electronic spin embedded in a consistent

designed molecule thus turned into a very interesting candidate to become the qubit of the future quantum computers, since it may be a true two-level system that can define the two states of a qubit. Considering a monoelectronic $S = \frac{1}{2}$ spin system, the implementation of the qubits is based on the spin-up state, $|\uparrow\rangle = |S = \frac{1}{2}, m = \frac{1}{2}\rangle$, and spin-down state, $|\downarrow\rangle = |S = \frac{1}{2}, m = -\frac{1}{2}\rangle$, that can be related to $|1\rangle$ and $|0\rangle$. This pair of spin states can be coherently occupied and driven from one to another via application of electromagnetic radiation pulse with enough long spin decoherence time (Figure I.3). In contrast to the NMR-based quantum computers, the electron Zeeman energy can exceed the thermal energy with conventional magnetic fields and laboratory accessible temperatures, providing an easy way of initialization of the qubit. Furthermore, there are some other important advantages in comparison with some of the physical materials previously discussed. Firstly, all molecules are identical, which represents, as previously introduced, an important characteristic in terms of scalability. Secondly, the structure of a magnetic coordination complex can be easily modified through chemical methods, which provides a high flexibility for the design of a suitable magnetic coordination complex as a qubit. Additionally, its behavior is governed purely by quantum mechanics.

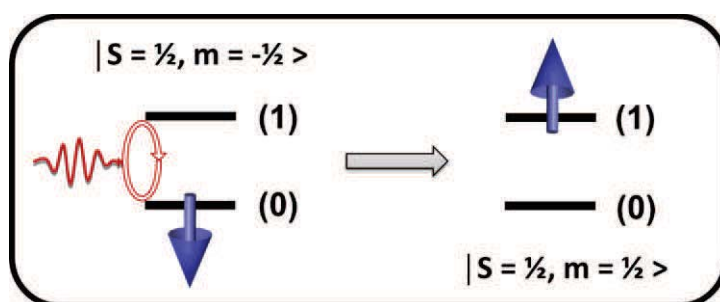


Figure I.3. Two-level $S = \frac{1}{2}$ system exhibiting the two states of a qubit. Spin-up and spin-down states are coherently occupied through electromagnetic radiation pulse.

Interestingly, electronic spin-based qubits have not strictly to consist in monoelectronic $S = \frac{1}{2}$ spin systems. In fact, the two state levels may be embodied by any spin system that in a certain regime exhibits two states (known as “effective” $S = \frac{1}{2}$), for example an isolated ground-state of antiferromagnetically coupled spin

moments,^[32] or a highly anisotropic lanthanide ion with a two-level ground-state system.^[33] However, the ground state must be well-isolated from the possible excited states. The possible leakage from $|1\rangle$ and $|0\rangle$ ground-state to such excited states represents a possible source of error that should be avoided. An undesired population of excited states might result from thermal distribution (if temperature is not low enough compared with the energy splitting between ground and excited states), or from unintentional transitions that can occur during the manipulation of the qubit, induced by electromagnetic pulses. Nevertheless, the excited states can also be seen as auxiliary levels for specific computational sequences, thus as an additional information resource. One example is the use of the auxiliary states for switching on and off the coupling between two molecular magnets when it is not possible by switching the physical interaction.^[34] Another alternative resource of the excited states might be their use as auxiliary qubits, thus reducing the number of qubits and simplifying the implementation of the quantum logic gate.^[35] One disadvantage that should be also considered for high-spin ground state molecular clusters is that the dipolar interaction can be increased, as compared with the reduced one in $S = \frac{1}{2}$ qubit spins. In addition, the possible preferential orientation provided by the anisotropy in a high-spin ground state system can play also a role when studying their possibilities as quantum bits. The strong dependence of the transition energies on the orientation of the molecule with respect the external magnetic field should be considered if one studies a particular transition in an ensemble of identical molecules, which might be then orientationally ordered.

One of the most important benefits of using magnetic molecules for quantum computation is that some molecular structures may embody several weakly coupled qubits, than can be consequently used as quantum gates.^[2] Coordination chemistry gives the tools for the assembly of two (or more) paramagnetic ions or group of strongly coupled open-shell metals within a molecule, and provides the way of connecting such ions/groups through convenient and switchable interactions. However, the design of a robust single molecule embodying several qubits is a challenge for chemists, since many times the synthesis is governed by a serendipitous self-assembly. Thus, the necessity of designing or selecting a convenient multidentate

ligand becomes the core of the rational design of this approach to quantum computing. These molecular architectures allow thus not only the study of the coherence of this type of qubits but also the entanglement between them through the coupling between the paramagnetic ions or metal aggregates.

· *Entanglement within magnetic complexes for quantum information processing*

As has been previously exposed, the entanglement is probably the most peculiar feature of quantum-mechanical systems, providing a fundamental resource in quantum information processing.^[3] In a hypothetical case of a magnetic complex with two qubits 1 and 2, the two spins S_1 and S_2 are entangled if the two-spin states $|\varphi\rangle$ cannot be written as a product of single-spin states $|\varphi\rangle \neq |\Phi_1\rangle \times |\Phi_2\rangle$ for any $|\Phi_1\rangle$ and $|\Phi_2\rangle$. Therefore, the state of each subsystem (Φ_1 and Φ_2) cannot be described independently of the state of the other one. For a study of the entanglement, the physical system should consist of a collection of well-defined and (weakly) coupled subsystems, i.e., a collection of paramagnetic ions or metal aggregates encapsulated and bridged by a multifunctional ligand. However, it should be noticed that coupling and entanglement are different concepts. While coupling is a phenomenological property related to the system and to its Hamiltonian, the entanglement is a property of the quantum state. The generation of entangled states in a magnetic coordination complex can be established in three steps. In a first term, the subsystems must be coupled to create a ground state of a Hamiltonian that coincides with the entangled state. Secondly, the system should be cooled down in order to approach this ground state and initialize such defined state. Finally, if the system is rotated by a pulsed external field into the final output state, such state is known to be entangled. The entanglement can be then quantified experimentally, addressing selectively the subsystems and measuring the correlations between their observables. Detecting entanglement within two subsystems, thus distinguishing the system between an entangled state from a separable one, can be carried out using the so-called “entanglement witnesses”. This “witness” is an observable with positive expectation value if the two subsystems can be factorizable ($|\varphi\rangle = |\Phi_1\rangle \times |\Phi_2\rangle$) and negative for entangled states. The main advantage of using an “entanglement witness” is that there is no necessity of knowing neither the system state nor its Hamiltonian. In molecular

magnetism, magnetic susceptibility can play this role for a system of N spins S as long as the system is isotropic, i.e., the Hamiltonian is the same under any arbitrary rotation of the total spin. In this case, a threshold is defined where if $\chi \geq cN_S/K_B T$ (c being a dimensional constant), the system is factorizable and consequently not entangled. This procedure has been used to evaluate the entanglement between Ho^{III} ions in a magnetic salt,^[36] or between two weakly coupled antiferromagnetic molecular rings.^[37] In this last case, the entanglement is more difficult to observe due to the higher complexity of the system. A non-trivial requirement is that the two coupled nanomagnets (the two subsystems Φ_1 and Φ_2) must preserve their own individual properties substantially unaffected while being chemically and magnetically coupled. Thus, the coupling between both moieties must be large with respect to the working temperatures, but small enough to maintain the effective two-level system of each of them.

· Decoherence in magnetic complexes for quantum information processing

For realistic quantum information processing, the evolution of the initial state of a quantum system (qubit) to its final state must be based on a coherent progression. Such coherence can be lost through the coupling with the environment, which tends to break the coherent character of the system. In magnetic coordination complexes, decoherence of the electronic spin arises from the coupling to phonons and nuclear spins, as well as from dipolar interactions in the case of an ensemble of such molecular nanomagnets. While coupling to phonons and dipolar interactions depend on the arrangement of the magnetic complexes in the sample, and thus can be reduced by modifying such arrangement, the coupling between electron and nuclear spins within each molecule is an intrinsic source of decoherence. This implies that hyperfine interactions represent the fundamental source of decoherence when studying magnetic complexes, and can even produce an electron-nuclear entanglement. It has been demonstrated that polarizing the nuclear spins can reduce the effects of the interaction between the electron and nuclear spins, thus providing a source for disentangling both spins.^[38, 39] It is also important to notice that quantum computing and quantum information processing relies on linear superpositions of multi-qubit states, i.e., weakly coupled magnetic molecules that can act as quantum gates. The

state of such multi-qubit systems can decohere as well and thus the study of the decoherence cannot be reduced only to that of a single qubit. For the case of a two-qubit system like $S_A = \frac{1}{2} \cdots S_B = \frac{1}{2}$, the state of each individual qubit can be '1' or '0' (or any superposition of these two), which can be represented as the spin up $|\uparrow\rangle$ or spin down $|\downarrow\rangle$ projections respectively. The final entangled state of the whole system can be represented by different combinations depending on the operation performed ($|\uparrow, \uparrow\rangle, |\uparrow, \downarrow\rangle, |\downarrow, \uparrow\rangle, |\downarrow, \downarrow\rangle$) but both spin projections of each qubit will be still affecting the nuclear dynamics and thus the entangled system will also decohere under the effect of hyperfine interactions.

It seems then of utmost importance to identify T_1 and T_2 time scales to evaluate the decoherence and thus the suitability of a molecular magnet for embodying a qubit. Experimentally, this study can be carried out using pulsed EPR measurements.^[7] In order to obtain enough signal, however, the experiments must be performed on an ensemble of molecules. This represents a problem, because the magnetic environments of the molecules are slightly different due to inhomogeneities of the magnetic field, and brings each molecule to precess at a different rate. After some time, the molecules start precessing out of phase of each other, and implies another source of decoherence not from the intrinsic individual spin of the individual molecules but from an unbalanced spin moment of the whole ensemble. The goal can be then achieved by using a Hahn echo sequence in the pulsed EPR measurement (see Figure I.4), which allows calculating the T_2 time avoiding the effect of dephasing caused by inhomogeneities of the magnetic field.

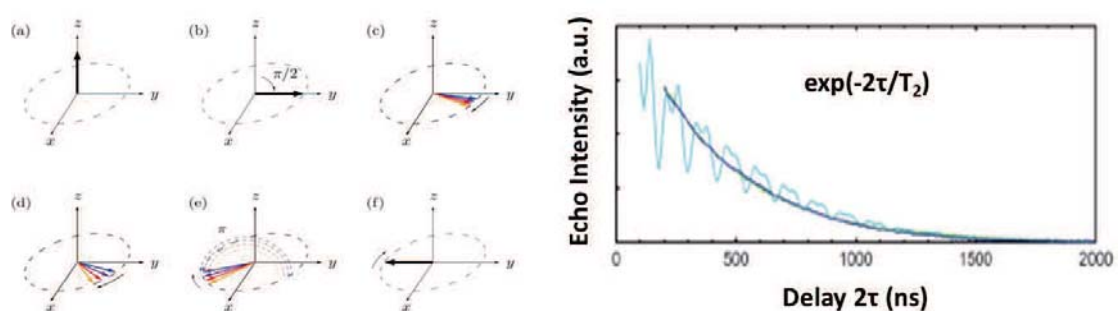


Figure I.4.^[7] (Left) Hahn echo sequence. (a) Spin polarization along z axis. (b) Microwave $\pi/2$ pulse along x axis to rotate spins into xy plane. (c, d) Different precession of spins due to inhomogeneities. (e) Microwave π pulse reverses the order of the spins at time τ . (f) At time 2τ the spins are back together (refocusing). (Right) Echo signal exponential decay in a heterometallic Cr_7Ni complex.

In a first term, a static magnetic field along the z axis is applied to polarize the spins of the molecules along this direction (a). At a time $t = 0$, a microwave $\pi/2$ pulse is applied along the x axis forcing the spins to rotate into the xy plane (b). Due to inhomogeneities, the spins of the different molecules start to precess at different rates in the xy plane (c), spreading out more and more as they evolve with the time (d). The decay of the macroscopic magnetization produced by this effect is known as free induction decay. After a time τ , a π pulse along x axis is applied, rotating the spins by π around x axis, reversing the order of the spins. Thus, the slower precessing spins (blue) overtake the faster ones (yellow) (e). After exactly a time 2τ , the spins come back together producing the echo signal, a process that is known as refocusing (f). The magnetization at this point (echo signal) decreases exponentially when the delay time τ is increased, meaning that the coherence of the system is being vanished. In Figure I.4, right, the echo signal exponential decay in a heterometallic Cr_7Ni complex^[32] is shown as example. Thus, one can identify the decoherence time T_2 performing several Hahn echoes experiments with different τ times, and representing the echo signal in front of the 2τ delay time. When T_2 becomes comparable to τ , some members of the ensemble lose their phase information, they cannot do the echo, and their signal starts to decrease exponentially (blue line). The value of the T_2 timescale can be then calculated by fitting the decay with an exponential function (echo signal = $\exp(-2\tau/T_2)$). When the nuclear and the electron spins are coupled, the “refocusing” π pulse can flip also the nuclear spin. This involves that the electron population branches, with the ones suffering a nuclear-flip and the ones that do not. The former have a different precession when comparing the first and the second evolution ((d) and (e) cases in Figure I.4), and create an echo at different place in the xy plane compared with the ones that have not suffered a nuclear spin flip. The two echoes thus give place to constructive and destructive interferences successively, causing an oscillation in the Echo amplitude (cyan line). This phenomenon is known as Electron Spin-Echo Envelope Modulation (ESEEM), and the study of the oscillation can give strong indication of the gyromagnetic ratio of the nuclei involved.

The measurement of T_1 can be also carried out using spin-echo measurements, using an inversion-recovery sequence. This involves starting the sequence with a π pulse at

the beginning, establishing a highly non-equilibrium magnetization. In that point, the magnetization can be probed by applying a $\pi/2$ pulse and studying the free induction decay, or by using a short Hahn echo sequence.

2.4. DiVincenzo criteria in coordination magnetic molecules

At a theoretical level, the potential of treating extremely complex problems using quantum computation has been well established.^[8, 10] After evaluating the different proposals for the quantum hardware, it seems clear that the requirements that such materials must fulfill are not straightforward. The basic conditions that any physical system needs to satisfy in order to act as hardware in quantum computation were defined by DiVincenzo more than one decade ago,^[40] and can be also applied for magnetic molecular complexes. The five criteria (DiVincenzo criteria) that constitute those basic conditions are the following:

i) Properly defined and scalable qubits: Each spin qubit must be sufficiently isolated within the molecule to exhibit a proper two-level qubit basis $|1\rangle$ and $|0\rangle$ ($|\uparrow\rangle$ and $|\downarrow\rangle$) to encode quantum information, and well separated from possible excited states. Some examples can be found in a true spin $\frac{1}{2}$ moiety like Cu^{II} ion isolated within a complex molecule,^[31] a metallic aggregate with well isolated two-level ground state,^[41] or lanthanide ions with strong crystal field.^[42] The scalability involves the possibility of engaging many identical qubits, which is a key factor to build realistic quantum computers and very important for quantum error correction.^[40] Spin-based qubits on magnetic complexes provide a great advantage in this point due to the easy production of macroscopic arrays of identical molecules. However, the disposition of reliable identical molecules within a device, like a surface, is not straightforward, since it can result in some misalignment or molecular isomerism due to interactions with the substrate. A possible solution might be an externally functionalization of the molecules for grafting them on surfaces. Some authors have proposed the use of SMM's not to define a single qubit but to carried out quantum information processes through the multiple states (M_s) accessible within a high-spin ground-state.^[1] This approach allows the implementation of an algorithm using the different states of the

SMM. Nevertheless, the approach limits the scalability of the system, since they rely only on a single multilevel system.^[43]

ii) Easy and efficient initialization: Each qubit must be easily set in a well-defined initial state at any time and in an efficient way. For electronic molecular spin, this can be easily satisfied by cooling the molecules under external magnetic fields to bring them into their ground state.

iii) Long decoherence times: As it has been exposed, the decoherence time τ_d is related to the time during which the quantum information stored in a qubit is maintained before it is lost due interaction with the surroundings. Thus, for a system to perform QC operations, it is necessary that the coherence is kept much longer than the gating time (Figure of Merit $Q = \tau_g/\tau_d \leq 10^{-4}$). For the electron-spin based qubits, the operations are based on the precession of a spin $S = \frac{1}{2}$ (true or effective), which is switched from one initial input state to a final output state. Experimentally, a magnetic pulse of 10 Oe to an electronic spin $S = \frac{1}{2}$ with g-factor $g = 2$ provides a switching time of around 10 ns, that represents thus the τ_g gate time for such approach.^[44] To preserve the quantic nature of the system, an electron spin-based qubit must then have a coherence time longer enough compared with this switching time.

iv) Implementing universal quantum gates: The magnetic molecules embodying spin-based qubits might provide attractive prototypes for universal qugates, like CNOT or $\sqrt{\text{SWAP}}$ operations. For the CNOT gate, the energy difference between the two states defined in each qubit must be much higher than the interaction between these qubits. This goal can be achieved by using strong axially anisotropic spins, or designing the conditions for a weak coupling between them. Additionally, control and target qubits must be different to be defined and addressed specifically. This required dissymmetry might be provided by the structure of the molecule. On the other part, the $\sqrt{\text{SWAP}}$ quantum gate requires that both spins exhibit a weak antiferromagnetic Heisenberg-type coupling. During a desired period of time (τ_g), this interaction must be able to be modified by an external stimuli for the system to evolve to the desired final state. For the achievement of these operations, it is necessary that the qubits of the gate can

exhibit entangled states, which can be consequently observed by an entanglement witness (see above).

v) Readout of the qubits: After an operation, the state of the target qubit (the output of the operation) has to be determined. Thus, any qubit, including the ones inside the gate, must be addressable selectively to be measured, whether spatially, spectrally, magnetically or by any other means.

2.5. Qubits and SMM's: Differences and similarities

One of the main resources for the synthetic chemists to build up molecular spin-based quantum bits is the use of single-molecule magnets (SMM's) as the qubit carrier. Single-molecule magnets are characterized by exhibiting slow relaxation of the magnetization at low temperatures and by magnetic hysteresis on account of the properties of the molecule itself. Usually, these compounds present a high-spin ground state S and a negative anisotropy D , creating a potential-energy barrier between the generated "spin-up" and "spin-down" m_s sublevels. The spin reversal is then required to take some energy to reorient the spin. Thus, below the blocking T_B temperature, when the applied magnetic field is removed, the relaxation of the magnetization becomes a slow process and is therefore conserved. The magnetic behavior of such molecules can be then useful for its application in quantum computing. In fact, single-molecule magnets fulfill some of the DiVincenzo requirements to embody a qubit. The required anisotropy for a SMM provides a well-defined two-level ground state that can be easily initialized by cooling down the system. In addition, the scalability at the molecular level is still one of the main advantages of such approach. However, the magnetic orientation of a single-molecule magnet just describes a classical bit, i.e, 1 or 0. For a SMM to be regarded as a qubit, one must pay attention to the arbitrary superposition between both quantum states.^[45] Moreover, the different states must be able to be rotated one into each other. Thus, a qubit can be embodied in a single-molecule magnet, but a molecule behaving as SMM does not strictly imply to be a prototype of a quantum bit. The hyperfine interaction from the nuclear spin, the electron-phonon coupling or the interaction with neighboring spins are some of the

additional aspects that one must consider for regarding a single-molecule magnet as a quantum bit.

On the other hand, it should be also noticed that a coordination complex can fulfill the DiVincenzo criteria to embody a quantum bit without satisfying the requirements of a single-molecule magnet. In a molecular quantum bit, the magnetic orientation of a cluster has not to be maintained after the magnetic field is removed (as it occurs with SMM's). In contrast, it must be able to rotate coherently from one initial (superimposed) state to a final one within a quantum gate operation, with the requirement of the readout of such final state after the gate time. Thus, the differences between these two concepts, which are sometimes merged when studying magnetic coordination molecules as the bearers of the quantum bits, should be kept in mind for a better comprehension of the spin-based quantum computation.

3. Current coordination chemistry proposals of 2-qubit QGs

To date, very few coordination molecular systems have been proposed as possible hardware in QIP. The conditions that such molecules must fulfill to realize quantum universal gates, like magnetic asymmetry for CNOT gates, or switchability of magnetic interactions for $\sqrt{\text{SWAP}}$ operations, are difficult to achieve. In this section, some of the most representative molecular spin-based 2-qubit quantum gates are briefly detailed.

· *Linking heterometallic rings [Cr₇M]:*

Probably the most studied molecular system for its application in quantum computing comprises heterometallic rings of chromium and a divalent metal synthesized by Winpenny et al., that can be linked by supramolecular or covalent bonds for the development of a 2-qubit gate. Each ring has a general formula $(\text{NH}_2\text{R}_2)[\text{Cr}_7\text{MF}_8(\text{O}_2\text{CR}')_8]$ ($\text{M}^{\text{II}} = \text{Mn, Fe, Co, Ni, Cd}$; $\text{R, R}' = \text{various}$) that is simplified by $[\text{Cr}_7\text{M}]$.^[32, 46] The versatility of this system allows studying of the coherence depending on the spin ground state of a ring. Thus, an exhaustive work for measuring T_1 and T_2 decoherence timescales was carried out by Ardavan and Blundell based on individual $[\text{Cr}_7\text{Ni}]$ or $[\text{Cr}_7\text{Mn}]$ rings, with $S = \frac{1}{2}$ and $S = 1$ respectively.^[7] With these two systems,

the effects of the orientation in an anisotropic system can be evaluated, since $[\text{Cr}_7\text{Ni}]$ has no anisotropy, while $[\text{Cr}_7\text{Mn}]$ has a zero-field splitting contribution. The samples were dissolved in toluene progressively until the results do not depend on the dilution, indicating that the dipolar interactions have been vanished. A Hahn echo sequence on the $[\text{Cr}_7\text{Ni}]$ solution was carried out using two different pulses; when a long pulse (64 ns $\pi/2$ pulse, 128 ns π pulse) is used, a simple exponential decay is observed, obtaining a value of $T_2 = 379$ ns at 4.5 K (Figure I.4, right, blue line). In contrast, when a shorter broadband pulse is used (16 ns $\pi/2$ pulse, 32 ns π pulse), an oscillatory decay is obtained due to the ESEEM effect, since the short pulse has a broader frequency content which can flip both nuclear and electron spins (Figure I.4, right, cyan line). The results of the ESEEM effect indicate that the coupling to nuclei comes from the protons of the ring. Thus, when the experiment was repeated in a deuterated sample, the T_2 timescale increased up to 3 μs at 2 K. Interestingly, when the values of T_1 and T_2 timescales from $[\text{Cr}_7\text{Ni}]$ and $[\text{Cr}_7\text{Mn}]$ were compared, no significant differences were found. Such behavior demonstrates that no anisotropy effects are governing the longitudinal relaxation (T_1), which might come from some thermal process like the coupling with phonons. Regarding the T_2 constant value, this experiment shows that the influence of the nuclei for the phase decoherence dominates over the effect of the anisotropy. The values obtained are many times longer than the duration of the qubit manipulation, thus supporting the candidature of this system as a qubit prototype. Moreover, the rings can be successfully grafted on different substrates including gold and graphite, experiencing only minor changes on the low lying levels.^[47]

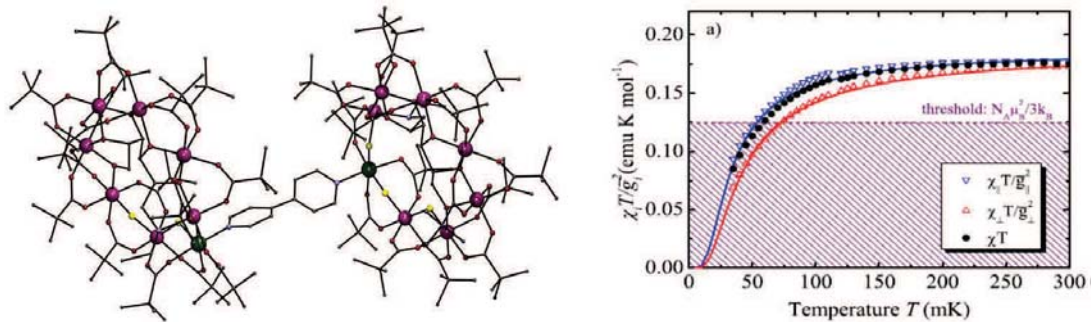


Figure I.5. (Left) Representation of the double ring assembly with formula $[(\text{Cr}_7\text{NiF}_3(\text{Etglu})(\text{O}_2\text{C}^t\text{Bu})_{15})_2(\text{bipy})]$. Purple, Cr; green, Ni; red, O; cyan, N; yellow, F; rest, C. H atoms excluded. (Right)^[37] Temperature dependence of the dc χM for the perpendicular (red) and parallel (blue) contributions, as well as the average (black) for the compound $(\text{Cr}_7\text{Ni})_2\text{-bipy}$, compared with the threshold $N_A \mu_B^2 / 3k_B$ (shaded area).

To build 2-qubit quantum gates, the rings can be linked in three different ways. The first strategy is based on exploiting a combination of coulombic and H-bonding interactions between rings (anionic) and diammonium long linkers. This procedure can lead to systems with and without additional paramagnetic metals (ex: Cu^{II}) between the rings, depending on the linker used. However, the magnetic coupling between the rings seems to be almost negligible. A second approach is based on the replacement of a carboxylate unit from the ring by a carboxylate linker unit. These linkers can coordinate free Cu^{II} ions that can mediate the interaction and link the rings. The interaction can be thus turned off by including two strongly antiferromagnetically coupled Cu^{II} ions. The third strategy suggests the use of ring derivatives with one labile coordination site to facilitate the linkage between them (Figure I.5, left). This versatile approach allows several ways of tuning the magnetic exchange between the rings, since different bidentate bridging ligands can be applied within the system. In addition, the entanglement between the two heterometallic ring spins has been experimentally demonstrated by low-temperature susceptibility and theoretically quantified by microscopic modeling of the ring dimer.^[37] The antiferromagnetic inter-ring coupling between two $[\text{Cr}_7\text{Ni}]$ rings at low temperature is small enough to preserve the magnetic properties of each ring, but large enough to dominate over the dipolar interactions and to induce an entanglement between both rings. A single ring was magnetically characterized by low-temperature specific heat, obtaining a Schottky

anomaly at 4 K due to the splitting on the ground state. When the $[\text{Cr}_7\text{Ni}]$ -bipy- $[\text{Cr}_7\text{Ni}]$ (bipy = 4,4'-bipyridine) complex was studied, an additional rise at 0.5 K due to the splitting between the antiferromagnetic and the ferromagnetic states was obtained, allowing the estimation of the magnitude of the weak interaction between both rings ($J = -0.11 \text{ cm}^{-1}$). The $\chi_{\text{M}}T$ curve of a single crystal measurement at very low temperature shows a decrease of their value below 0.2 K, demonstrating also the presence of the antiferromagnetic coupling. The molar magnetic susceptibility χ_{M} was then used as an entanglement witness following the inequality $\chi_{\text{M}}T \leq N_{\text{A}}\mu^2/K_{\text{B}}$. For this system, it is shown that under $T = 50 \text{ mK}$, the threshold is reached, meaning that the effective spins of the two rings are non-factorizable and thus entangled (Figure I.5, right).

· *Polyoxometalate* $[\text{PMo}_{14}\text{O}_{40}(\text{VO})_2]^{q-}$

A very interesting proposal to realize $\sqrt{\text{SWAP}}$ operations by Loss et al. is based on the use of the polyoxometalate (POM) $[\text{PMo}_{12}\text{O}_{40}(\text{VO})_2]^{q-}$.^[48, 49] This molecule has two localized spins $S = \frac{1}{2}$ that can be coupled through electrons on the central core, which can change its charge by means of electrical manipulation of the molecular redox potential, and therefore modify the total charge q of the compound. The structure features a central mixed-valence core based on a $[\text{PMo}_{12}\text{O}_{40}]$ unit, capped at both ends by two vanadyl groups containing two localized $S = \frac{1}{2}$ spins (Figure I.6, left). The core of the cage can change the number of electrons, which are delocalized over the Mo(V/VI) ions. The antiferromagnetic coupling between both $(\text{VO})^+$ units can be then switched on and off, providing the fundamentals for a two-qubit $\sqrt{\text{SWAP}}$ gate $|\uparrow, \downarrow\rangle \rightarrow (|\uparrow, \downarrow\rangle + i|\downarrow, \uparrow\rangle)/(1 + i)$. If the number of electrons of the cage is even, the central spin is zero and the vanadyl units interact weakly antiferromagnetically. The number of electrons can be manipulated to an odd number by changing the applied voltage, obtaining a central spin of $S = \frac{1}{2}$. The initial state $|\uparrow, \downarrow\rangle$ is thus changed to $|\downarrow, \uparrow\rangle$ through the coupling of the three $S = \frac{1}{2}$ spins during gate time τ_{gate} (Figure I.6, right). The goal is achieved by adjusting first the voltage in a way that the central core has a stable configuration of even number electrons ($S = 0$). The voltage is then changed such that an electron enters to the core ($S = \frac{1}{2}$) and after the τ_{gate} , the initial voltage is switched back. The readout of the quantum gate is based on the measurement of the quantum number of the two outer spins. This can be carried out by measuring the

current through the central block of the molecule, that depends on the global spin state S_T of the molecule (which is different depending on the value of the central $S_{\text{core}} = 0$ or $\frac{1}{2}$). Some additional considerations should be pointed out. Firstly, the orientation of the molecules may be difficult to control. Nevertheless, it does not seem crucial since the versatile change of the charge affects the central core $\text{Mo}_{12}\text{O}_{40}$ and not the vanadyl groups. The alteration of the symmetry and, thus, the electronic structure upon deposition on a surface can also affect the proposal. However, such change is expected to be minimal since an insulating thin layer may separate the molecule from the metallic substrate. Another issue comes from the cations that compensate the $[\text{PMo}_{12}\text{O}_{40}(\text{VO})_2]^{9-}$ anion charge, which can influence in the electronic structure as well. This problem can be solved by using electro spray techniques that have demonstrated the ability of separating the polyoxometalate anions by choosing the appropriate mass/charge ratio.^[50]

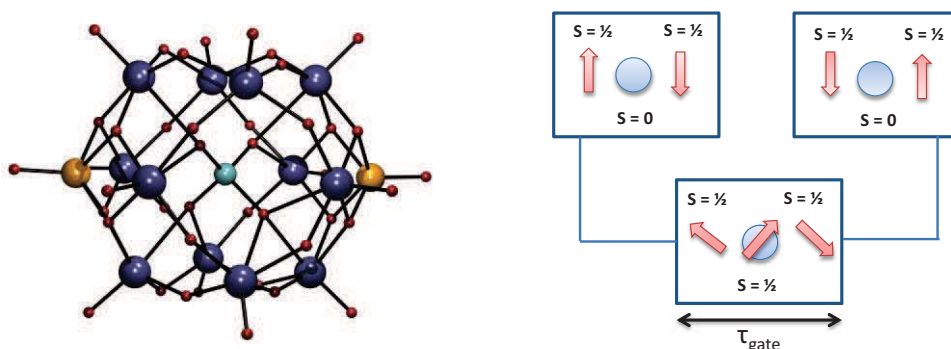


Figure I.6. (Left) Representation of the molecular structure of the polyoxometalate $[\text{PMo}_{12}\text{O}_{40}(\text{VO})_2]^{9-}$. Dark blue, Mo; orange, V; cadet blue, P; red, O. (Right) Turn on-off scheme of the three spin system for the switching of the antiferromagnetic interaction.

This approach for the design of a spin-based molecular prototype of vSWAP gate can be extended to other systems that can reversibly lose or gain one electron. Tetrathiofulvalene derivatives, polypyrrole, porphyrins/phtalocyanines, fullerene and single-walled nanotubes are some of the multiple examples that organic chemistry can provide as systems that can lose or gain electrons to be applied as the central building block of a molecular vSWAP gate.^[49]

· *Triple-stranded metallo-helicates:*

A different approach of molecular electron spin qubits for implementing scalable quantum computers proposed by Takui and coworkers is based on an electron spin-qubit version of a Lloyd $(ABC)_n$ model,^[51, 52] which is based on spatial alignment of open-shell entities with non-equivalent g -tensors. A designed triple-stranded dinuclear metallo-helicate with Mn^{II} or Zn^{II} cations and four-membered oligoimidazole ligands has been used as a prototype of such model, providing the required g -tensor molecular engineering (Figure I.7, left). In general terms, each open-shell metal carrying an electron-spin qubit is magnetically inequivalent because of the twisted helical structure. However, to achieve selective spin excitation for QIP under pulse microwave technology, there are further conditions that must be fulfilled. The periodic model needs intrahelicate weak exchange coupling between the spin-bearing cations, and no interhelicate interactions. As has been exposed previously, the first condition is related to quantum operations, while the second one contemplates the suppression of decoherence of the system. Thus, the distance between metals within the helicate must be long enough for weakening the exchange interactions. To vanish the undesired intermolecular interactions one can synthesize magnetically diluted single crystals, where paramagnetic helicates are embedded in diamagnetic host crystal lattices. Following such procedure, the studies were carried out on a magnetically diluted mixed single crystals of $[Mn_2]$ helicate/ $[Zn_2]$ helicate. The ligand chosen features four 4,4'-biimidazole moieties (Qim), and the four positive charges of each molecule is compensated with nitrate anions. The metal ions within the helicate are relatively long separated ($> 5 \text{ \AA}$), with nonequivalent g -tensors and weak exchange coupling. In the crystal, the related metals of the two isomers (left-handed and right-handed isomers) are magnetically equivalent by inversion and translation symmetry operations. Thus, magnetically, only one kind of helicate exists in the unit cell; therefore two addressable electron spins with different g -tensors are obtained, defining the two-qubit quantum gate. Such spin addressability of the Mn^{II} cations as spin qubits have been demonstrated by ESR Q-band, showing that these helicates are good candidates to embody a quantum gate. The different g -tensor of both metals, as well as the desired weak exchange interaction between the cations, demonstrates the success of the

targeted *g*-engineering. As shown in the spectra (Figure I.7, right), the electron spin is altered by hyperfine coupling of Mn^{II} ($I = 5/2$), exhibiting a six-line hyperfine structure split in two series due to the differences of the two Mn^{II} in the structure. In addition, the differences in the different *g* values concerning the three axes are also evidenced.

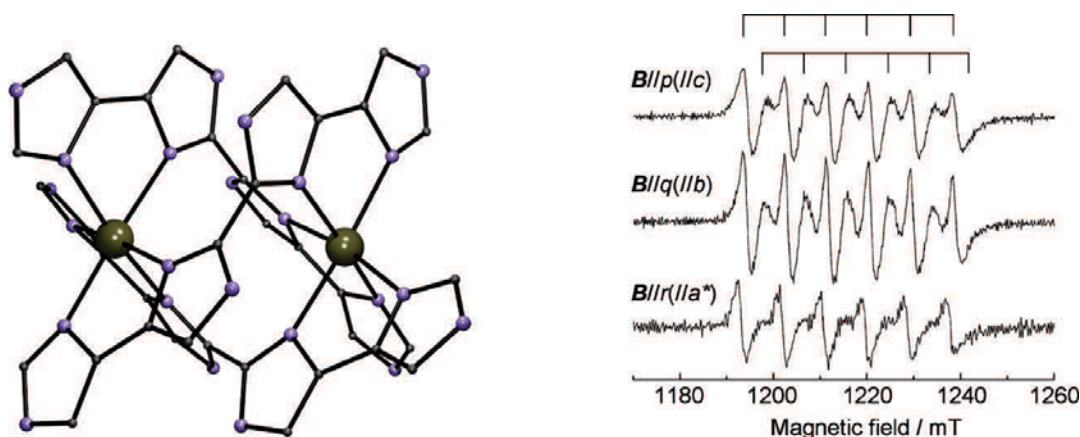


Figure I.7. (Left) Representation of the molecular structure of the helicate $[\text{Mn}_2(\text{Qim})_3]^{4+}$. Dark green, Mn; violet, N; rest, C. (Right)^[52] Q-band ESR spectra of the magnetically diluted crystal of $[\text{Mn}_2(\text{Qim})_3](\text{NO}_3)_4/[\text{Zn}_2(\text{Qim})_3](\text{NO}_3)_4$.

Magnetic susceptibility measurements were carried out to demonstrate a weak but detectable interaction between both metal ions within the helicate. The study by quantum chemical calculations of the *g* anisotropy was used to support the experimental results, demonstrating the suitability of this approach for implementing QC. The possibility of linking such spin qubits with phonon qubits due to the helicate chirality of such complexes has been also proposed and should be also noticed.

· Pair of $[\text{Mn}_4\text{O}_3\text{Cl}_4(\text{O}_2\text{CET})_3(\text{py})_3]$ SMM's

The quantum superposition of the spin wave functions of a pair of SMM's has been demonstrated by Hill and coworkers studying the dimer of $\text{Mn}^{\text{III}}/\text{Mn}^{\text{IV}}$ clusters, $[\text{Mn}_4\text{O}_3\text{Cl}_4(\text{O}_2\text{CET})_3(\text{py})_3]_2 \cdot \text{C}_6\text{H}_{14}$, simplified as $[\text{Mn}_4]_2$ (Figure I.8, left).^[53] The well-defined spin-ground state $S = 9/2$ of both SMM's, acting as qubits, are coupled through a magnetic interaction, and its coherence has been shown by EPR measurements. The $[\text{Mn}_4] \cdots [\text{Mn}_4]$ system is held by C-H \cdots Cl hydrogen bonds, that provides a weak antiferromagnetic superexchange coupling between both units ($J \approx -0.08 \text{ cm}^{-1}$). The

magnetic studies performed on the monomer $[\text{Mn}_4]$ exhibits quantum tunneling at zero-field. However, the same measurements on the dimer $[\text{Mn}_4] \cdots [\text{Mn}_4]$ reveals a bias in the field where such magnetic tunneling occurs, as a result of the exchange field that each SMM experiences due to its pair. This influence between both molecules in the dimer is shown in the EPR results on a single crystal. The monomer (Figure I.8, right, inset) exhibits an easy typical spaced resonance pattern. However, the spectrum of the dimer is considerably complex owing to the different transition between the different states of the two-SMM complex (Figure I.8, right). Resonance is observed over a low-field region (< 0.7 T), where the $|\pm(9/2), \pm(9/2)\rangle$ is the ground-state of the dimer.

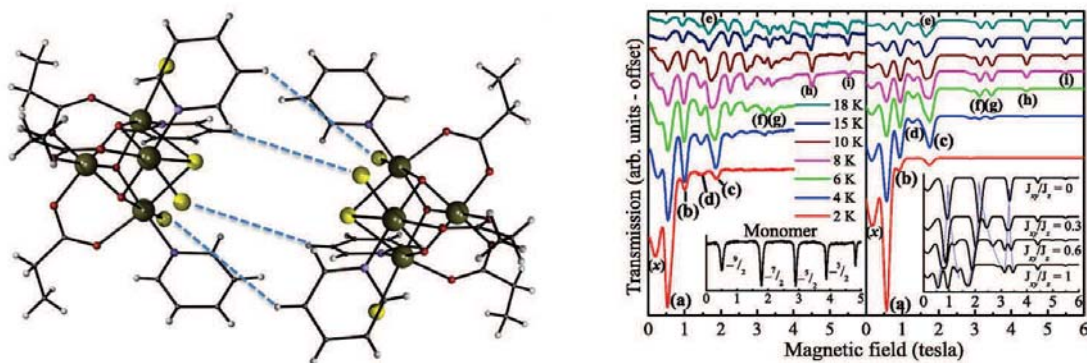


Figure I.8. (Left) Schematic representation of the molecular structure of the dimer $[\text{Mn}_4\text{O}_3\text{Cl}_4(\text{O}_2\text{CET})_3(\text{py})_3]_2$ featuring the hydrogen bonding $\text{CH} \cdots \text{Cl}$. Dark green, Mn; violet, N; red, O; yellow, Cl; Light grey, hydrogen; rest, C. (Right)^[52] Temperature-dependent easy-axis data of high-frequency EPR of the dimer (left part) and of the monomer (left part, inset), and simulation of the dimer data (right part).

The authors suggest that if the phase decoheres, one would expect broad EPR peaks because of transitions between bands of incoherent states. The EPR, by contrast, shows narrow resonances, and decoherence time on the order of 1 ns can be extracted from such spectra. To determine the T_2 timescale, however, pulsed EPR experiments should be carried out.

4. Our proposal: Design of multidentate β -diketone ligands to access qubits

The different examples studied in the previous section show the difficulties of designing a molecular complex with the requirements to be used as two-qubit quantum gates. The interaction between two well defined molecular entities might be sufficiently robust to allow the entanglement of the states defined for each qubit, but small enough to let each qubit exhibit the proper two-level qubit basis. The serendipity showed in most of the studied molecular spin-based quantum gates reflects the complexity of a designed synthesis of this kind of systems. One possible strategy to achieve this goal is the preparation of ligands featuring the required coordination pockets for a predefined distribution of the metal ions within the complex. This approach towards the preparation of potential qubit systems can be carried out focusing on the synthesis of ligands with β -diketone coordination units, which are very versatile for the design of metallocluster assemblies.^[54] One of the main advantages of using this kind of ligands is that they can be easily prepared through simple Claisen condensation, providing different combinations and possibilities for the addition of big variety of donor atoms and pockets. The description of the general synthesis, as well as the detailed synthesis of the four ligands used along this thesis is exposed in Chapter II (Figure I.9). Each ligand has been designed for the preparation of predefined magnetic coordination complexes that can fulfill the conditions of a two-qubit molecular quantum gate. The different complexes synthesized within this thesis can be defined in two different categories: Molecular pairs of well-defined and weakly coupled metal clusters, and complexes of two dissimilar and weakly coupled anisotropic metal ions. In addition, the use of the designed ligands for the preparation of metallo-helicates has been also carried out. The description and study of their helicoidal structure is shown in Chapter III, using the ligand H₄L1 with trivalent and tetravalent metal ions like Fe^{III}, Ga^{III} or U^{IV}.

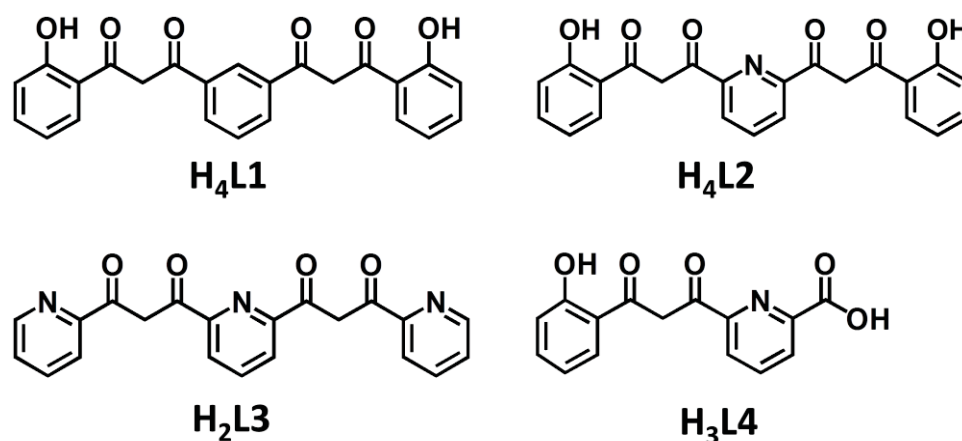


Figure I.9. Schematic representation of the ligands employed for the design of magnetic coordination complexes.

· Molecules featuring two weakly coupled clusters:

The approach is based on the design of molecules featuring two well defined coordination clusters that could represent ideal systems for realizing two-qubit quantum gates, as long as each cluster exhibits the appropriate spin properties. Two different ligand-based strategies have been followed for the preparation of such molecular pairs of well-defined metal clusters. The first one is based on the design of poly- β -diketone ligands exhibiting two groups of coordination pockets, which serve to aggregate metals in close proximity. Following this approach, the ligand is responsible for having metals grouped into two clusters, as well as for keeping each metal group together within each subsystem (Figure I.10, left). The structural characteristics of H₄L1 (Figure I.9) provides the requirements for the construction of this kind of clusters, since it might align and separate metals into two dimetallic entities. The goal has been achieved by using the deprotonated ligand that organizes the metals in two groups within molecular linear arrays, saturating the equatorial positions. Compounds with Ni^{II}, Cu^{II} and Co^{II} metal ions are described and studied in Chapter IV. The second strategy is based on the preparation of poly- β -diketone ligands with an additional X donor atom in the middle for acting as a “template” for the aggregation of metals into linear clusters, further linked as molecular pairs by auxiliary ligands (Figure I.10, middle). Organic ligands like H₄L2 or H₂L3 fulfill the requirements to aggregate closely

spaced metals, which can be then used as building blocks to be linked into molecular pairs by other bifunctional external ligands (Figure I.9). An example using Co^{II} is described and studied in Chapter IV.

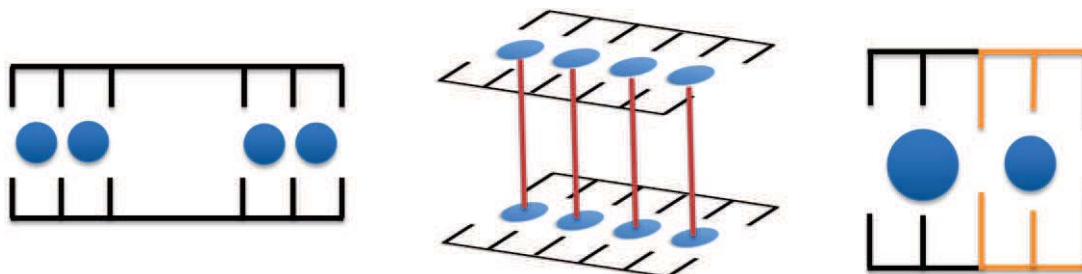


Figure I.10. Schematic representation of the three different ligand-based strategies followed for the design of spin-based molecular 2-qubit gates. (Left) Bis- β -diketone ligands (black) hold together each metal aggregate and link them within the molecule. (Middle) Bis- β -diketone ligands (black) hold together each metal cluster, and these are linked through external ligands (red). (Right): β -diketone asymmetric ligand (black and orange) coordinates two anisotropic ions in a different environment.

· *Dinuclear complexes of anisotropic metal ions:*

The synthesis of complexes of two dissimilar and weakly coupled lanthanides has been used as approach for the construction of molecular prototypes of CNOT quantum gates. The ligand-based strategy considers the design of non-symmetric ligands as a possible way of having two inequivalent lanthanide qubits within a molecule (Figure I.10, right). The ligand $\text{H}_3\text{L4}$ exhibits a collection of donor groups disposed to favor the aggregation of two metals in different coordination environments (Figure I.9). The use of lanthanide ions are good candidates for encoding quantum information following such approach, since they can exhibit strong anisotropy and very well isolated ground state doublets $\pm m_J$ (effective $S = \frac{1}{2}$). In addition, lanthanide ions have been proved to have spin states with long decoherence, with T_2 timescales that can reach values up to $7 \mu\text{s}$.^[41] In Chapter V, a detailed study of a vast number of dinuclear homo- and heterometallic lanthanide coordination complexes is exposed, including an exhaustive study for some of them to prove their possibilities as CNOT and $\sqrt{\text{SWAP}}$ quantum gates.

-
- [1] M. N. Leuenberger, D. Loss, *Nature* **2001**, *410*, 789.
- [2] G. Aromí, D. Aguilà, P. Gamez, F. Luis, O. Roubeau, *Chemical Society Reviews* **2012**, *41*, 537.
- [3] F. Troiani, M. Affronte, *Chemical Society Reviews* **2011**, *40*, 3119.
- [4] O. Khan, *Molecular Magnetism*, VCH Publishers, New York, **1993**.
- [5] J. Ribas, *Coordination Chemistry*, Wiley-VCH Verlag GmbH & Co. KGaA, Weinheim **2008**.
- [6] J. H. Van Vleck, *The theory of electric and magnetic susceptibilities*, Oxford University Press, Oxford, **1932**.
- [7] A. Ardavan, S. J. Blundell, *Journal of Materials Chemistry* **2009**, *19*, 1754.
- [8] M. A. Nielsen, I. L. Chuang, *Quantum Computation and Quantum Information*, Cambridge University Press, Cambridge, **2000**.
- [9] T. D. Ladd, F. Jelezko, R. Laflamme, Y. Nakamura, C. Monroe, J. L. O'Brien, *Nature* **2010**, *464*, 45.
- [10] R. P. Feynman, *Found. Phys.* **1986**, *16*, 507.
- [11] F. Luis, O. Roubeau, G. Aromí, *Artificial Molecular Nanomagnets as Spin-Based Quantum Logic Gates*, in *Architecture and Design of Molecule Logic Gates and Atom Circuits*, (Eds.: N. Lorente, C. Joachim), Springer Berlin Heidelberg, Berlin, **2013**
- [12] J. I. Cirac, P. Zoller, *Physical Review Letters* **1995**, *74*, 4091.
- [13] C. Monroe, D. M. Meekhof, B. E. King, W. M. Itano, D. J. Wineland, *Physical Review Letters* **1995**, *75*, 4714.
- [14] N. A. Gershenfeld, I. L. Chuang, *Science* **1997**, *275*, 350.
- [15] I. L. Chuang, L. M. K. Vandersypen, X. Zhou, D. W. Leung, S. Lloyd, *Nature* **1998**, *393*, 143.
- [16] J. Clarke, F. K. Wilhelm, *Nature* **2008**, *453*, 1031.
- [17] E. Knill, R. Laflamme, G. J. Milburn, *Nature* **2001**, *409*, 46.
- [18] A. Politi, J. C. F. Matthews, J. L. O'Brien, *Science*, **2009**, *325*, 1221.
- [19] D. J. Wineland, W. M. Itano, D. Leibfried, B. E. King, D. M. Meekhof, *Journal of Research of the National Institute of Standards and Technology* **1998**, *103*, 259.
- [20] R. Blatt, D. Wineland, *Nature* **2008**, *453*, 1008.
- [21] R. Hanson, L. P. Kouwenhoven, J. R. Petta, S. Tarucha, L. M. K. Vandersypen, *Reviews of Modern Physics* **2007**, *79*, 1217.
- [22] J. Harrison, M. J. Sellars, N. B. Manson, *Diamond and Related Materials* **2006**, *15*, 586.
- [23] M. V. G. Dutt, L. Childress, L. Jiang, E. Togan, J. Maze, F. Jelezko, A. S. Zibrov, P. R. Hemmer, M. D. Lukin, *Science* **2007**, *316*, 1312.
- [24] C. Negrevergne, T. S. Mahesh, C. A. Ryan, M. Ditty, F. Cyr-Racine, W. Power, N. Boulant, T. Havel, D. G. Cory, R. Laflamme, *Physical Review Letters* **2006**, *96*, 170501.
- [25] L. M. K. Vandersypen, M. Steffen, G. Breyta, C. S. Yannoni, M. H. Sherwood, I. L. Chuang, *Nature* **2001**, *414*, 883.
- [26] W. S. Warren, *Science* **1997**, *277*, 1688.
- [27] L. DiCarlo, J. M. Chow, J. M. Gambetta, L. S. Bishop, B. R. Johnson, D. I. Schuster, J. Majer, A. Blais, L. Frunzio, S. M. Girvin, R. J. Schoelkopf, *Nature* **2009**, *460*, 240.
- [28] M. Ansmann, H. Wang, R. C. Bialczak, M. Hofheinz, E. Lucero, M. Neeley, A. D. O'Connell, D. Sank, M. Weides, J. Wenner, A. N. Cleland, J. M. Martinis, *Nature* **2009**, *461*, 504.
- [29] A. Lupascu, S. Saito, T. Picot, P. C. de Groot, C. J. P. M. Harmans, J. E. Mooij, *Nat Phys* **2007**, *3*, 119.
- [30] J. Tejada, E. M. Chudnovsky, E. del Barco. J. M. Hernandez. T. P. Spiller, *Nanotechnology* **2001**, *12*, 181.
- [31] F. Meier, J. Levy, D. Loss, *Physical Review Letters* **2003**, *90*, 047901.
- [32] M. Affronte, S. Carretta, G. A. Timco, R. E. P. Winpenny, *Chemical Communications* **2007**, 1789.

- [33] F. Luis, A. Repollés, M. J. Martínez-Pérez, D. Aguilà, O. Roubeau, D. Zueco, P. J. Alonso, M. Evangelisti, A. Camón, J. Sesé, L. A. Barrios, G. Aromí, *Physical Review Letters* **2011**, *107*, 117203.
- [34] F. Troiani, M. Affronte, S. Carretta, P. Santini, G. Amoretti, *Physical Review Letters* **2005**, *94*, 190501.
- [35] S. Carretta, P. Santini, G. Amoretti, F. Troiani, M. Affronte, *Physical Review B* **2007**, *76*, 024408.
- [36] S. Ghosh, T. F. Rosenbaum, G. Aeppli, S. N. Coppersmith, *Nature* **2003**, *425*, 48.
- [37] A. Candini, G. Lorusso, F. Troiani, A. Ghirri, S. Carretta, P. Santini, G. Amoretti, C. Murn, F. Tuna, G. Timco, E. J. L. McInnes, R. E. P. Winpenny, W. Wernsdorfer, M. Affronte, *Physical Review Letters* **2010**, *104*, 037203.
- [38] W. A. Coish, D. Loss, *Physical Review B* **2004**, *70*, 195340.
- [39] W. Yao, R.-B. Liu, L. J. Sham, *Physical Review Letters* **2007**, *98*, 077602.
- [40] D. P. DiVincenzo, *Fortschritte der Physik* **2000**, *48*, 771.
- [41] S. Bertaina, S. Gambarelli, T. Mitra, B. Tsukerblat, A. Muller, B. Barbara, *Nature* **2008**, *453*, 203.
- [42] S. Bertaina, S. Gambarelli, A. Tkachuk, I. N. Kurkin, B. Malkin, A. Stepanov, B. Barbara, *Nat Nano* **2007**, *2*, 39.
- [43] V. Cerletti, W. A. Coish, O. Gywat, D. Loss, *Nanotechnology* **2005**, *16*, R27.
- [44] M. Affronte, *Journal of Materials Chemistry* **2009**, *19*, 1731.
- [45] J. J. Baldoví, S. Cardona-Serra, J. M. Clemente-Juan, E. Coronado, A. Gaita-Ariño, A. Palií, *Inorganic Chemistry*, *51*, 12565.
- [46] G. A. Timco, T. B. Faust, F. Tuna, R. E. P. Winpenny, *Chemical Society Reviews* **2011**, *40*, 3067.
- [47] V. Corradini, F. Moro, R. Biagi, V. De Renzi, U. del Pennino, V. Bellini, S. Carretta, P. Santini, V. A. Milway, G. Timco, R. E. P. Winpenny, M. Affronte, *Physical Review B* **2009**, *79*, 144419.
- [48] Q. Chen, C. L. Hill, *Inorganic Chemistry* **1996**, *35*, 2403.
- [49] J. Lehmann, A. Gaita-Ariño, E. Coronado, D. Loss, *Nat Nano* **2007**, *2*, 312.
- [50] M. Bonchio, O. Bortolini, V. Conte, A. Sartorel, *European Journal of Inorganic Chemistry* **2003**, *2003*, 699.
- [51] S. Lloyd, *Scientific American* **1995**, *73*, 140.
- [52] Y. Morita, Y. Yakiyama, S. Nakazawa, T. Murata, T. Ise, D. Hashizume, D. Shiomi, K. Sato, M. Kitagawa, K. Nakasuji, T. Takui, *Journal of the American Chemical Society* **2010**, *132*, 6944.
- [53] S. Hill, R. S. Edwards, N. Aliaga-Alcalde, G. Christou, *Vol. 302*, **2003**, pp. 1015.
- [54] G. Aromí, P. Gamez, J. Reedijk, *Coordination Chemistry Reviews* **2008**, *252*, 964.

CHAPTER II

DESIGN, SYNTHESIS AND CHARACTERIZATION OF β - DIKETONE LIGANDS TO ACCESS FUNCTIONAL COORDINATION COMPLEXES

1. Introduction

The design and implementation of molecular devices as quantum gates (QGs) depend on the synthesis of systems with a determined topology. We are interested on the proposal that such QGs could be achieved by molecules containing two well-defined qubits with an interaction between them. Thus, the design of new ligands able to control such topology represents the first challenge towards this goal.^[1]

Our synthetic approach towards the preparation of these ligands involves the exploitation of the β -diketone unit. This chelating moiety has been used intensely in coordination chemistry since more than one century ago, when Claisen prepared the acetylacetonate ligand, also known as *Hacac* or 2,4-pentanedione. The synthesis was carried out by condensing acetone and ethyl acetate, a process that would become well-known as the Claisen condensation.^[2] The use of a suitable ester and a ketone as starting materials allows multiple possibilities for the design of linear ligands with one or more β -diketone units. The addition of different functional groups in these poly- β -diketone ligands affords a wide variety of coordination pockets for the assembly of metal ions. In that respect, the imagination and creativity when designing these ligands have permitted the synthesis of a wide group of systems in coordination chemistry, like metallocycles, metallohelicates, linear arrays of metals, polynuclear cage complexes, coordination polymers, or their use as spacers.^[3] This versatility, as provided by the poly β -diketone ligands, is an exquisite tool that can be well-spent for the assembly of molecules that fulfill the requirements of a 2-qubit QG. The ligands presented in this work can be divided in two categories. The first group is composed by bis- β -diketone ligands with the goal of designing molecular pairs of well-defined, weakly coupled metal clusters. For its achievement, the ligands are designed either featuring two groups of coordination pockets to allow two clusters within the ligand itself (like H₄L1), or containing a collection of donor groups to synthesize chains of metals that can be further linked by additional ligands (like H₄L2 and H₂L3). The general procedure for the preparation of these poly β -diketone ligands is sketched in Figure II.1.

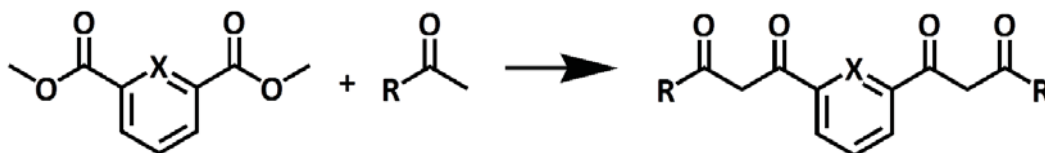


Figure II.1. General procedure for the preparation of the poly β -diketone ligands H_4L1 , H_4L2 and H_2L3 through the Claisen condensation. X = C or N, while R = phenolyl or pyridyl.

The second group involves the asymmetric ligand H_3L4 , which has been designed for a new category of qubits. In this second case, the aim is to synthesize dinuclear complexes of anisotropic metal ions, generating dinuclear asymmetric complexes.

The characterization of the ligands has been carried out by using the common techniques for this type of compounds. Whereas the infrared spectrum has been used as an easy way for detecting the ligand when synthesizing coordination complexes, the 1H NMR allows the full assignment of the protons in the organic molecule, and so its identity and purity. One difficulty that sometimes can emerge in the characterization of β -diketone ligands using this technique relates to the keto-enol conversion that they can exhibit because of the possible tautomers (Figure II.2).^[4]

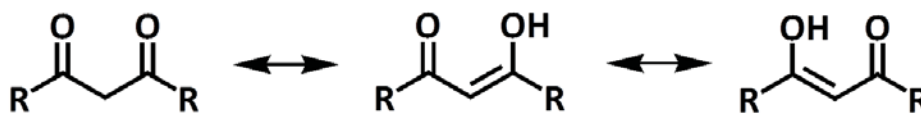


Figure II.2. Keto-enol equilibrium of a β -diketone unit.

This phenomenon can generate confusion when interpreting the NMR 1H spectrum, but can be easily solved by removing one of the protons of the β -diketone group (see below). For a complete examination of these organic molecules, mass spectrometry can provide a definitive proof of the existence of the ligand. In the following, the description and synthesis of each ligand, as well as its characterization, is described.

2. Description, synthesis and characterization of H_4L1 : 1,3-bis-(3-oxo-3-(2-hydroxyphenyl)propionyl)benzene

The ligand H_4L1 was previously synthesized in the group,^[5] and it can be considered as the father of the different ligands designed and synthesized in this work. This organic molecule consists in a benzene group bonded in the meta position to two β -diketone units and featuring two phenol groups in both sides (Figure II.3). The topology of this ligand affords two pockets to gather closely spaced paramagnetic metals within a complex in a linear manner.

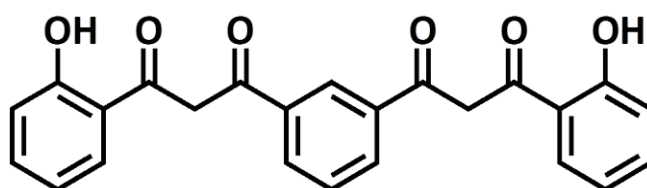


Figure II.3. Schematic representation of the ligand H_4L1 .

The synthesis of the ligand follows the general procedure sketched in Figure II.1. The reaction of one equivalent of dimethyl isophthalate with two equivalents of 2-hydroxyacetophenone in the presence of six equivalents of sodium hydride leads to the sodium salt of the ligand, which is finally obtained by acidifying the reaction mixture with aqueous hydrochloric acid (Figure II.4).

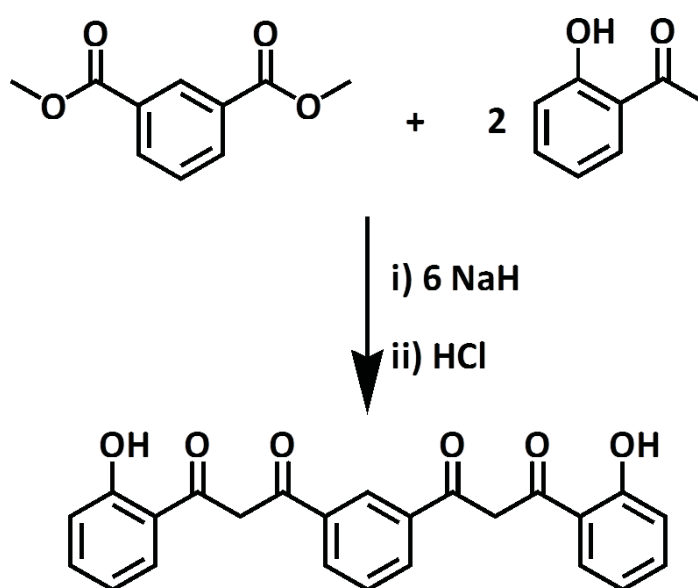


Figure II.4. Schematic representation of the synthesis of the ligand H_4L1 .

An important feature of H_4L1 is that the ionisable protons of the phenol and the β -diketone group have a remarkably different acidity. Previous work revealed that the use of the acetate salt of divalent metals in front of this ligand provided a base capable of deprotonating the β -diketone groups, but was not strong enough to remove the protons of the phenol units.^[5] A series of dinuclear clusters with Mn^{II} , Co^{II} , Ni^{II} and Cu^{II} were obtained and characterized, the ligand exhibiting the coordination mode shown in Figure II.5 (top). Thus, it seems reasonable that by increasing the basicity of the reaction media, the targeted tetranuclear clusters could be prepared by engaging the oxygen donor atoms from the deprotonated phenol groups (Figure II.5, bottom). The realization of these new tetranuclear clusters would provide systems belonging to the two well-defined pairs of clusters category proposed to develop molecular prototypes of two-qubit QG's.

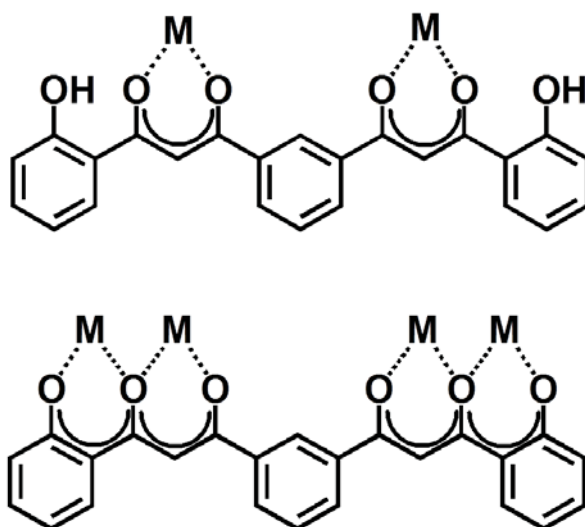


Figure II.5. Representation of the coordination mode for μ_2 - H_2L1^{2-} (top) and for μ_4 - $L1^{4-}$ (bottom).

The versatility of these different coordination modes allows not only imparting the linear topology of the clusters but also controlling their nuclearity. Thus, by choosing the appropriate base, the system can be prepared as dinuclear clusters or as the expected $[M-M \cdots M-M]$ moiety.

The characterization of H_4L1 was carried out by infrared spectroscopy and 1H NMR in $CDCl_3$. This last technique shows unequivocally the identity and purity of the enolic

form of this organic molecule. In Figure II.6, the assigned spectrum of the aromatic region is detailed.

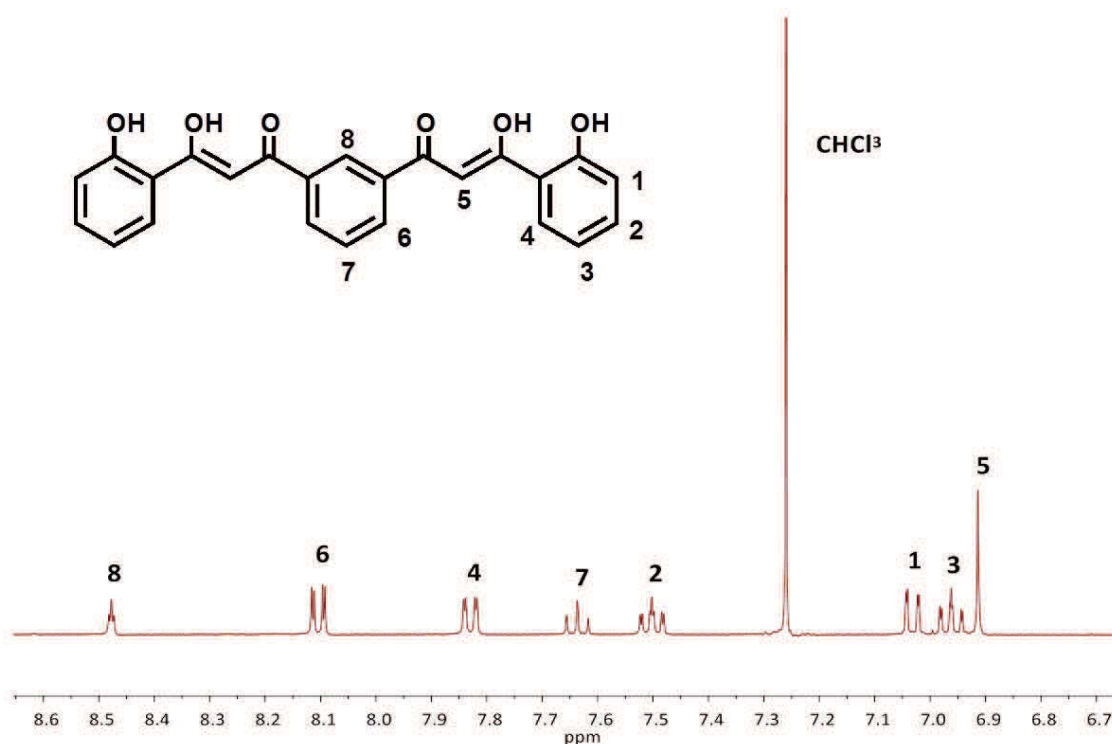


Figure II.6. ^1H NMR spectrum (aromatic region) of $\text{H}_4\text{L1}$, featuring the enolic form.

3. Description, synthesis and characterization of $\text{H}_4\text{L2}$: 1,3-bis-(3-oxo-3-(2-hydroxyphenyl)propionyl)pyridine

The versatility of the Claisen condensation provides a broad range of variations for the design of these ligands just by changing the starting materials. For the new ligand $\text{H}_4\text{L2}$ (Figure II.7), the addition of a nitrogen donor atom in the center benzene ring brings in a new coordination pocket.

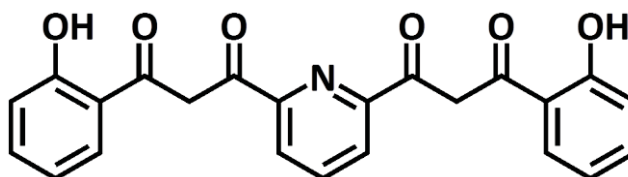


Figure II.7. Schematic representation of $\text{H}_4\text{L2}$.

The pyridyl group adds new geometric and electronic characteristics to the coordination modes of the ligand, providing an additional donor in addition to the β -diketone and phenol groups. This new 'ONO' central moiety, also known as dipicolinate-like group, has been successfully employed by others for the preparation of complexes involving heterometallic systems of 3d ions together with lanthanides,^[6, 7] or in combination with alkaline and earth-alkaline metals.^[8, 9] The combination of the donor groups of this new ligand could be used for the assembly of pairs of clusters as expected for the previous ligand, but with the addition of a new metal with bigger radius in the center, like a 4f ion (Figure II.8).

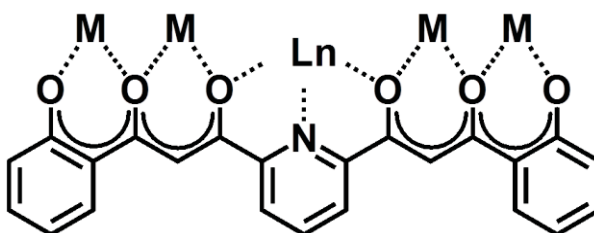


Figure II.8. Representation of the suggested coordination mode for μ_5 -L2⁴⁻.

Thus, the possibility of adding a new center in the middle of the pair of clusters allows the desired synthesis of linear chain of metals ions. As described in Chapter 1, one of the approaches to build 2-qubit QGs is to synthesize arrays of paramagnetic ions as possible molecular qubits, which should then be further linked to each other by bifunctional ligands.

For the synthesis of H₄L2, the same procedure as for H₄L1 was followed, now choosing diethyl 2,6-pyridinedicarboxylate as the ester. This starting material can be easily prepared by esterification of 2,6-pyridinedicarboxylic acid in ethanol using thionyl chloride. The Claisen condensation between this ester and 2-hydroxyacetophenone using sodium hydride as a source of base produces the sodium salt of the ligand. A further acidification with acetic acid allows the full protonation of the ligand (Figure II.9).

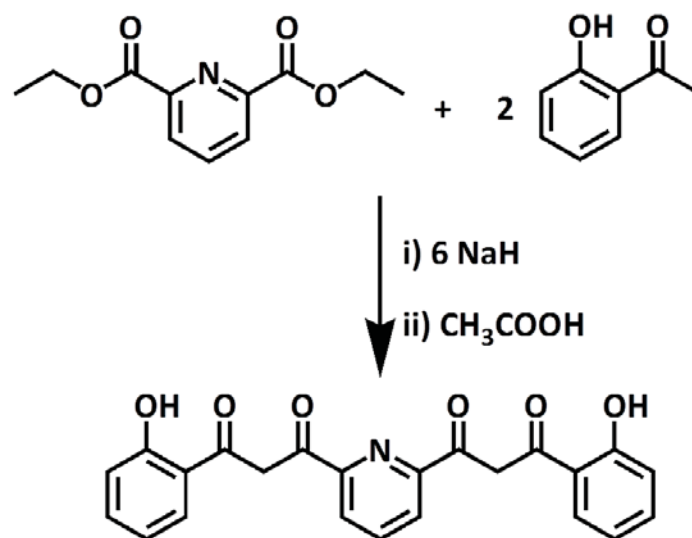


Figure II.9. Schematic representation of the synthesis of the ligand H_4L_2 .

As for the previous ligand, H_4L_2 was characterized by infrared spectroscopy and 1H NMR in $CDCl_3$. In this case, it is not trivial to assign each proton in the NMR spectrum, since both ketonic and enolic forms were present in solution (Figure II.10).

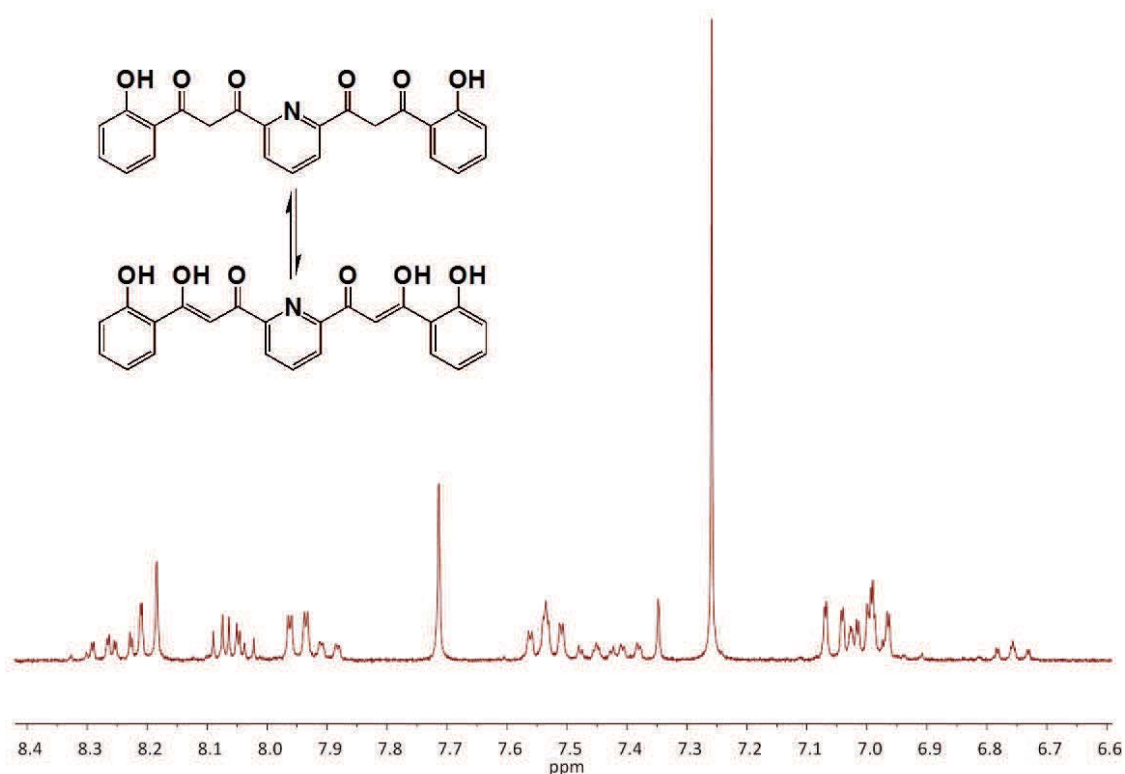


Figure II.10. 1H NMR spectrum (aromatic region) of H_4L_2 , featuring the keto-enol equilibrium.

One strategy to avoid this equilibrium and simplify the spectrum is to synthesize the dinuclear sodium salt of the ligand, $[\text{Na}_2(\text{H}_2\text{L}_2)]$, removing the β -diketonic protons and thus the tautomerism. The ligand H_4L_2 was dissolved in THF and treated with the stoichiometric amount of NaHCO_3 . The by-products of the reaction (H_2O and CO_2) allow a clean synthesis of the sodium salt of the ligand. Once the reaction is complete and the solvent is removed, the product obtained can be analyzed by NMR ^1H in deuterated DMSO. Figure II.11 shows the spectrum with the assignment of the signals in the aromatic region, which demonstrates the purity of the ligand.

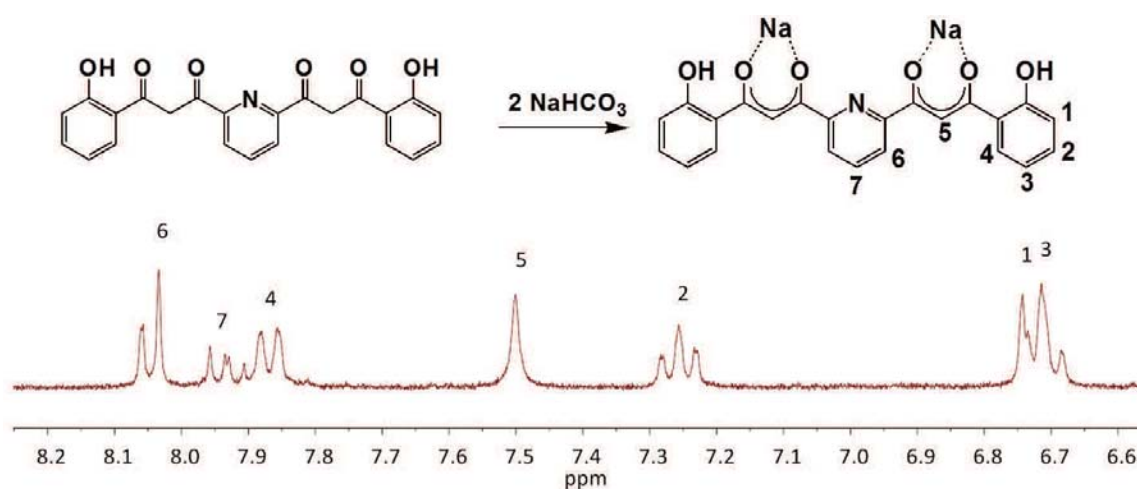


Figure II.11. Schematic synthesis and ^1H NMR spectrum (aromatic region) of $[\text{Na}_2(\text{H}_2\text{L}_2)]$.

4. Description, synthesis and characterization of H_2L_3 : 1,3-bis-(3-oxo-3-(2-pyridyl)propionyl)pyridine

The synthesis of this tris-pyridyl/bis- β -diketone was developed in order to access other molecular strings of paramagnetic ions. As seen for the previous ligand, pyridyl/bis- β -diketone donors that contain the central part of these ligands have been used for the preparation of heterometallic complexes, which suggests that H_2L_3 could favour the formation of longer heterometallic molecular chains (Figure II.12).

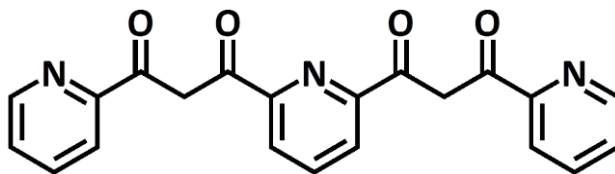


Figure II.12. Schematic representation of H₂L3.

Although this molecule has been briefly described as an intermediate during the synthesis of the corresponding bis-pyrimidinyl derivate,^[10] its modified synthesis has been carried out following the procedure shown in the previous ligands. Thus, the Claisen condensation between one equivalent of diethyl 2,6-pyridinedicarboxylate and two equivalents of 2-acetylpyridine using NaH was carried out to generate the sodic salt of the ligand, which was finally isolated by acidifying with acetic acid (Figure II.13).

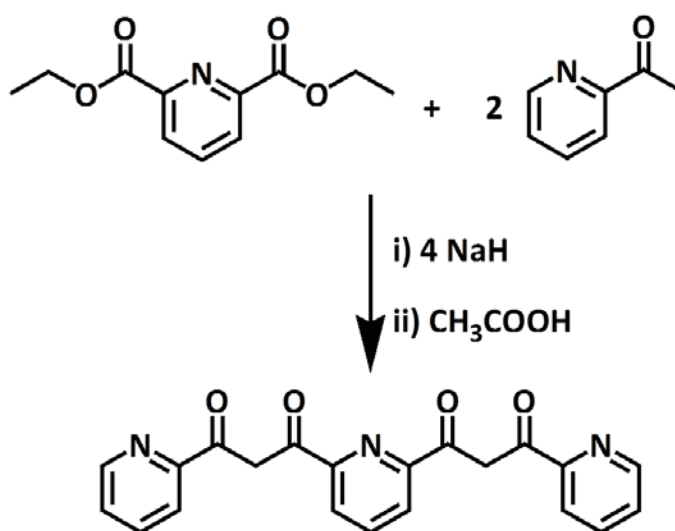


Figure II.13. Schematic representation of the synthesis of the ligand H₂L3.

The different functionalities of this ligand should allow the preparation of heterometallic chain-like molecular clusters (3d and 4f ions simultaneously) by benefiting from the different types and sizes of the coordination pockets present on it. In this respect, a possible coordination mode of H₂L3 is represented in Figure II.14.

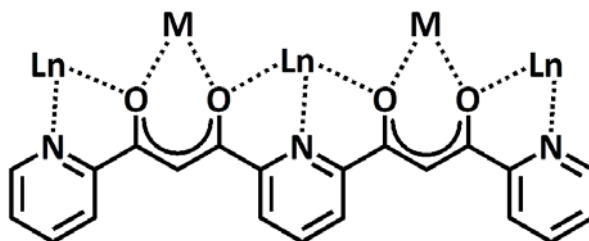


Figure II.14. Representation of the suggested coordination mode for μ_6 - L_3^{2-} .

H_2L_3 was characterized by infrared spectroscopy and NMR. In chloroform, the presence of different isomers of H_2L_3 was found by 1H NMR when varying the history of the sample, which suggests that in this medium and at room temperature, the equilibrium is not reached. An example is shown in Figure II.15, where in this case the ligand exhibits its enolic form.

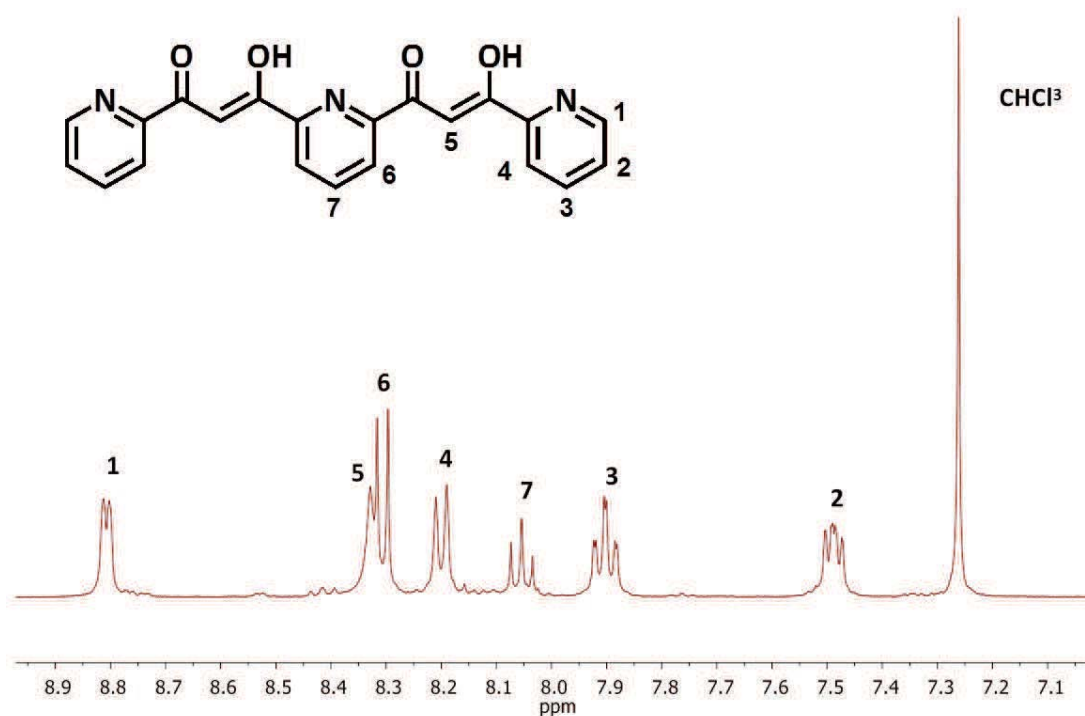


Figure II.15. 1H NMR spectrum (aromatic region) of H_2L_3 , featuring the enolic form.

The ligand was further characterized by positive ion electrospray ionization (ESI $^+$) using $CHCl_3$ as a solvent. Some fragments that involved the ligand were confirmed by exact

mass. In addition of the $[M+H]^+$, the peaks corresponding to $[M+Na]^+$ and $[M_2+Na]^+$ were also identified (Figure II.A1, Appendix).

5. Description, synthesis and characterization of H_3L4 : 6-(3-oxo-3-(2-hydroxyphenyl)propionyl)-2-pyridinecarboxylic acid

As discussed in Chapter 1, some operations in quantum computing require dissimilar qubits exhibiting a weak interaction. It seems then reasonable to focus on the design of a new category of asymmetric ligands in order to introduce the necessary inequivalence between the spin carriers of the assembly. In this respect, the new ligand H_3L4 (Figure II.16) was designed with the donor groups disposed in a way to favor the aggregation of metals in different coordination environments.

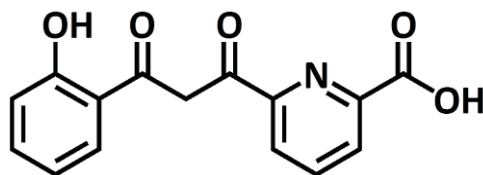


Figure II.16. Schematic representation of H_3L4 .

The asymmetry of this ligand is reached because of the different substituents featuring in the meta position of the pyridine group. While a carboxylic acid group is bonded in one position, a β -diketone and phenol units are positioned in the other side. With this topology, different coordination modes of the ligand would lead the metals in a different environment, developing possible asymmetric complexes (Figure II.17).

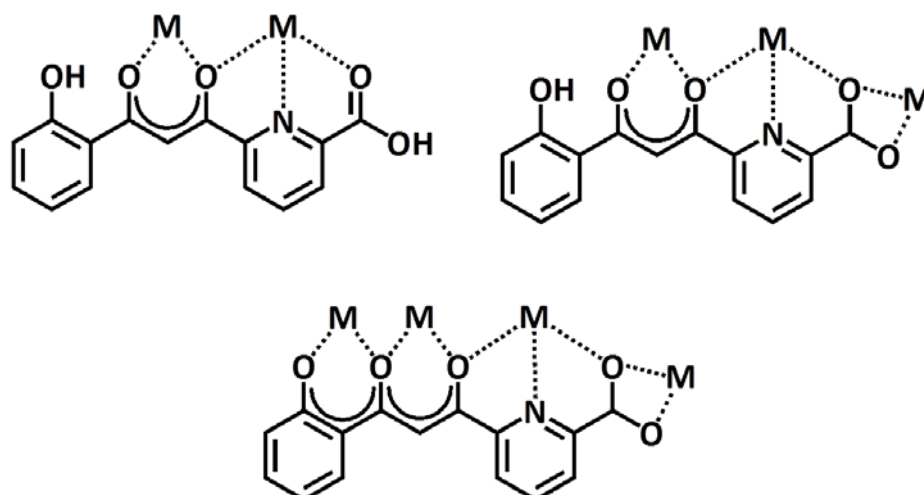


Figure II.17. Scheme of the suggested coordination modes for μ_2 -H₂L₄⁻ (top, left), μ_3 -HL₄²⁻ (top, right) and μ_4 -L₄³⁻ (bottom).

The asymmetry of the ligand was introduced in the synthesis before the Claisen condensation step, when synthesizing the corresponding ester. As for H₄L₂ and H₂L₃, the diester (in this case, dimethyl 2,6-pyridinedicarboxylate) was firstly obtained from the esterification of the 2,6-pyridinedicarboxylic acid using thionyl chloride in methanol. This diester was hydrolyzed on only one side using potassium hydroxide at 0 °C, according to a literature method.^[11] The half acid 6-(methoxycarbonyl)pyridine-2-carboxylic acid obtained was used in the Claisen condensation with 2-hydroxyacetophenone (in this case, one equivalent for each mol of starting material) employing sodium hydride as a base, and acetic acid as a proton source to finally obtain H₃L₄. The scheme of the whole synthesis is shown in Figure II.18.

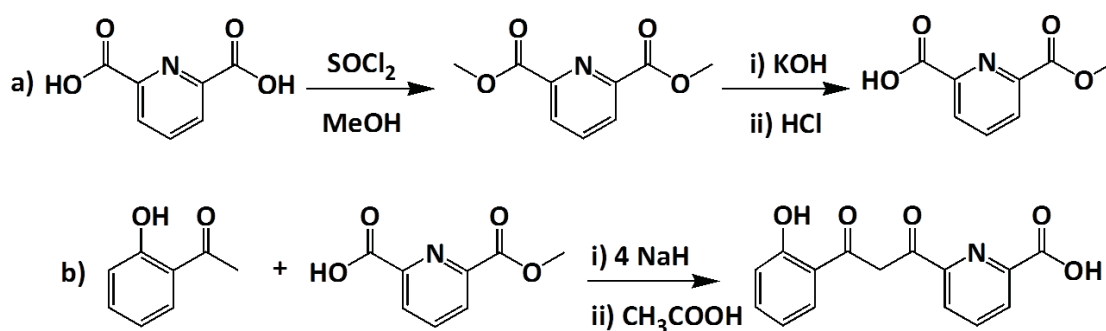


Figure II.18. Schematic representation of the synthesis of a) the half acid and b) the ligand H₃L₄.

The characterization of this asymmetric organic molecule was carried out using infrared spectroscopy, ^1H NMR, and also mass spectrometry. As for the first ligand presented, mostly the enolic form was found when analyzing $\text{H}_3\text{L4}$ by ^1H NMR in chloroform. Low intense peaks from the ketonic form appears next to each proton signal. The assignment of the signals in the aromatic region is shown in Figure II.19.

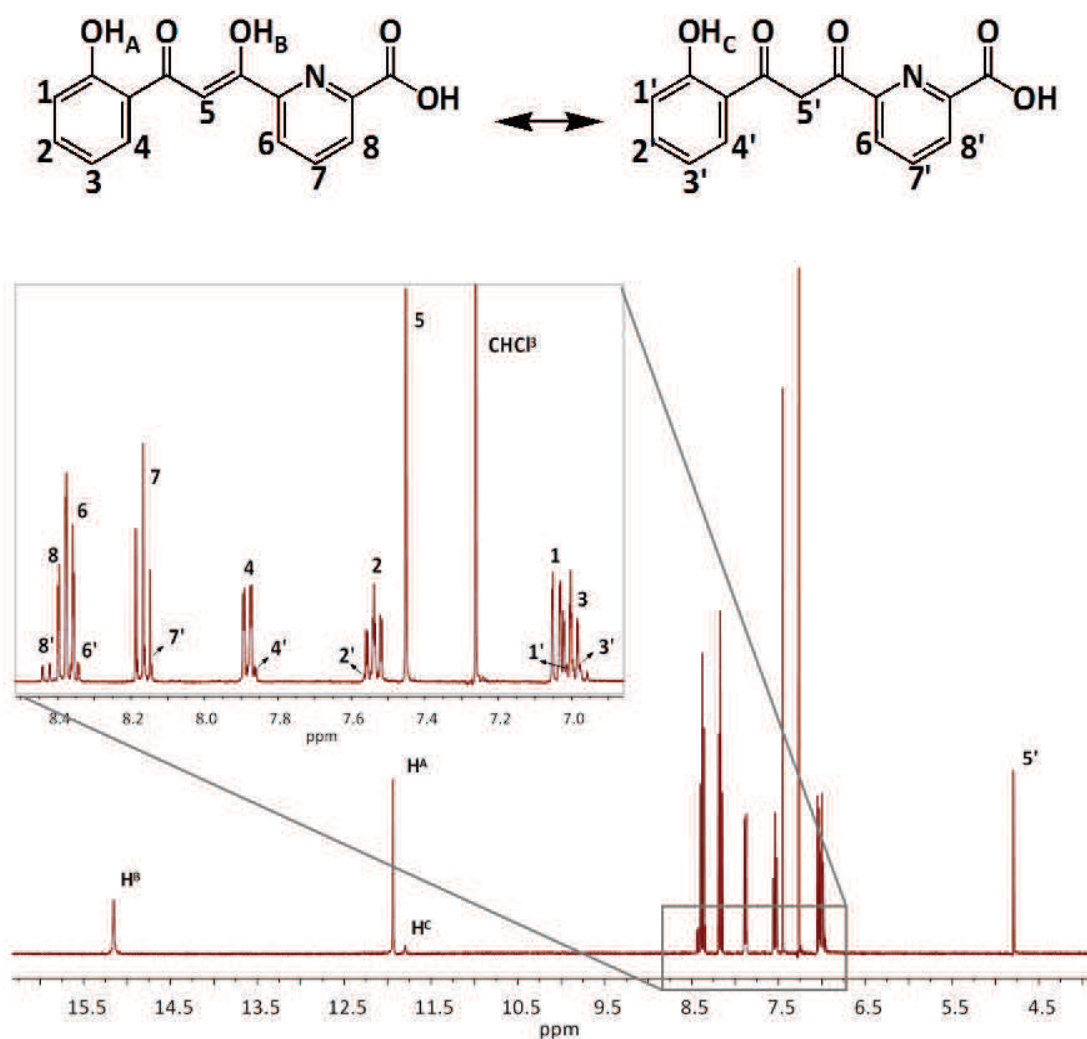


Figure II.19. ^1H NMR spectrum (zoom in aromatic region) of $\text{H}_3\text{L4}$, featuring both keto and enolic forms.

For an additional characterization of the ligand, a sample of $\text{H}_3\text{L4}$ was dissolved in MeOH and examined by positive ion electrospray ionization (ESI^+). Some fragments that involved the ligand were confirmed by exact mass; In addition of the $[\text{M}+\text{H}]^+$, the peaks corresponding to $[\text{M}+\text{Na}]^+$ and $[\text{M}-\text{OH}]^+$ were also identified (Figure II.A2, Appendix).

6. Experimental

1,3-bis-(3-oxo-3(2-hydroxyphenyl)propionyl)benzene, H₄L1. A white suspension of NaH (8.24 g, 206 mmol) in DME (50 ml) was added dropwise, under nitrogen atmosphere, into a colourless solution of dimethyl isophthalate (5.0 g, 25.7 mmol) and 2-hydroxyacetophenone (6.14 ml, 51.5 mmol) in DME (290 ml) leading to a yellow suspension. Once the addition was complete, the mixture was brought to reflux for two hours, while it gradually turned brown. After the suspension was allowed to cool to room temperature, the excess of NaH was quenched by adding EtOH (20 ml). The brown solid was collected by filtration and suspended into CH₂Cl₂/HCl 0.1 M (400 ml, 1:1 v/v), followed by the addition of hydrochloric acid (5 ml). The resulting brown mixture was left stirring for 15 hours, and the system gradually turned light yellow. A light yellow solid was separated by filtration, washed with water and then with Et₂O. On the other part, the two phases formed in the filtrate were separated and the aqueous part was extracted with CH₂Cl₂ (2x50 ml). The combined organic layers were dried over Na₂SO₄, filtered and rotaevaporated. The remaining residue was redissolved in refluxing EtOH. Upon cooling, a yellow-greenish solid obtained was washed with water and then with Et₂O. Considering both fractions of the ligand, the yield was 60 %. ¹H NMR (300 MHz, CDCl₃): δ (ppm) = 8.48 (s, 1H, C_{aro}H), 8.10 (d, 2H, C_{aro}H), 7.83 (d, 2H, C_{aro}H), 7.64 (t, 1H, C_{aro}H), 7.50 (t, 2H, C_{aro}H), 7.04 (d, 2H, C_{aro}H), 6.96 (t, 2H, C_{aro}H), 6.92 (s, 2H, CH). IR (KBr pellet, cm⁻¹): 3407 mb, 1609 m, 1578 s, 1563 s, 1545 s, 1517 s, 1457 s, 1384 s, 1318 m, 1294 m, 1257 w, 1224 w, 1170 w, 1077 w, 1049 w, 1017 w, 944 w, 810 w, 748 m, 709 m, 658 w, 636 w, 517 w.

Diethyl 2,6-pyridinedicarboxylate. A solution of 2,6-pyridinedicarboxylic (5 g, 30.0 mmol) and thionyl chloride (4.38 ml, 60.0 mmol) in EtOH (200 ml) was brought to reflux for two hours. The resulting colourless solution was allowed to cool to room temperature and was rotaevaporated, obtaining a white solid in 91 % yield. ¹H NMR (300 MHz, CDCl₃): δ (ppm) = 8.29 (d, 2H, C_{aro}H), 8.01 (t, 1H, C_{aro}H), 4.50 (q, 4H, CH₂), 1.47 (t, 6H, CH₃).

1,3-bis-(3-oxo-3(2-hydroxyphenyl)propionyl)pyridine, H₄L2. A white suspension of NaH (7.20 g, 180 mmol) in DME (50 ml) was added dropwise, under nitrogen atmosphere, into a colourless solution of diethyl 2,6-pyridinedicarboxylate (5.0 g, 22.4 mmol) and 2-hydroxyacetophenone (5.40 ml ml, 44.8 mmol) in DME (150 ml) obtaining a dark yellow suspension. Once the addition was complete, the mixture was brought to reflux for 15 hours, while it gradually turned darker. After the suspension was allowed to cool to room temperature, the excess of NaH was quenched by adding EtOH (20 ml). The dark yellow solid was collected by filtration and suspended into Et₂O/AcOH 0.1 M (400 ml, 1:1 v/v). The mixture was left stirring for 20 minutes. A yellow solid was separated by filtration, washed with water and then with Et₂O. On the other part, a mixture of CH₂Cl₂ (50 ml) and HCl (4 ml) was added to the filtrate. The two parts formed were separated and the organic layer was dried over Na₂SO₄, filtered and rotaevaporated. The yellow solid obtained was redissolved in CH₂Cl₂ (200 ml) and AcOH 0.1 M (200 ml). The organic layer was separated, dried over Na₂SO₄, filtered and rotaevaporated, obtaining a yellow solid. Considering both fractions of the ligand, the yield was 76 %. IR (KBr pellet, cm⁻¹): 1636 s, 1623 s, 1568 s, 1486 s, 1444 m, 1412 m, 1337 m, 1306 m, 1273 s, 1196 s, 1158 m, 1107 m, 1094 m, 1033 m, 996 w, 862 w, 836 w, 806 s, 743 s, 681 w, 626 m, 564 w, 527 w.

[Na₂(H₂L2)]. An aqueous solution (2 ml) of NaHCO₃ (41.7 mg, 0.496 mmols) was added on a solution of H₄L2 (100 mg, 0.248 mmol) in THF (10 ml). The mixture was brought to reflux for 30 minutes, and allowed to cool to room temperature. The yellow solution was rotaevaporated, obtaining a yellow solid of [Na₂(H₂L2)]. ¹H NMR (300 MHz, CDCl₃): δ (ppm) = 8.04 (d, 2H, C_{aro}H), 7.95 (t, 1H, C_{aro}H), 7.87 (d, 2H, C_{aro}H), 7.50 (s, 2H, CH), 7.25 (t, 2H, C_{aro}H), 6.72 (d, 2H, C_{aro}H), 6.70 (t, 2H, C_{aro}H).

1,3-bis-(3-oxo-3(2-pyridil)propionyl)pyridine, H₂L3. A white suspension of NaH (3.34 g, 139 mmol) in DME (30 ml) was added dropwise, under nitrogen atmosphere, into a light yellow solution of diethyl 2,6-pyridinedicarboxylate (6.52 g, 29 mmol) and 2-acetylpyridine (14.1 ml, 115 mmol) in DME (200 ml), obtaining a light brown suspension. Once the addition was complete, the mixture was brought to reflux for 20 hours, while it gradually turned light brown. After the suspension was allowed to cool to room temperature, the excess of NaH was quenched by adding EtOH (6 ml). A

brown solid was collected by filtration and suspended in AcOH/H₂O (150 ml, 2:1 v/v), and the mixture was stirred for 15 minutes. A beige/yellow crude product was separated by filtration and suspended in THF (75 ml). To this mixture was added a saturated solution of NaHCO₃ (1.57 g, 19 mmol). The mixture was brought to reflux for 10 minutes, while it gradually turned yellow. After the suspension was allowed to cool to room temperature, a yellow solid was filtrated and suspended in AcOH/H₂O (100 ml, 1:1 v/v). The solution was left stirring for 15 minutes. The resulting beige solid was separated by filtration, washed with water and then with Et₂O. The yield was 14 %. ¹H NMR (300 MHz, CDCl₃): δ (ppm) = 8.81 (d, 2H, C_{aro}H), 8.33 (s, 2H, C_{aro}H), 8.31 (d, 2H, C_{aro}H), 8.20 (d, 2H, CH), 8.06 (t, 1H, C_{aro}H), 7.90 (t, 2H, C_{aro}H), 7.49 (t, 2H, C_{aro}H). ESI MS: $m/z = 374 [M + H]^+$. Anal Calcd (Found) for H₂L3·0.5H₂O: C 65.96 (65.97), H 4.22 (4.41), N 10.99 (10.88). IR (KBr pellet, cm⁻¹): 3431 mb, 1614 s, 1578 s, 1563 s, 1437 m, 1291 m, 1275 m, 1243 m, 1227 w, 1084 m, 1075 m, 993 m, 826 w, 791 s, 746 m, 625 w, 617 m.

Dimethyl 2,6-pyridinedicarboxylate. A solution of 2,6-pyridinedicarboxylic (5 g, 30.0 mmol) and thionyl chloride (5.40 ml, 74.0 mmol) in MeOH (200 ml) was brought to reflux for two hours. The resulting colourless solution was allowed to cool to room temperature and was rotaevaporated, obtaining a white solid in 90 % yield. ¹H NMR (300 MHz, CDCl₃): δ (ppm) = 8.32 (d, 2H, C_{aro}H), 8.03 (t, 1H, C_{aro}H), 4.04 (s, 6H, CH₃).

6-(methoxycarbonyl)pyridine-2-carboxylic acid. To a suspension of dimethyl 2,6-pyridinedicarboxylate (5.9 g, 30.0 mmol) in MeOH (300 ml) at 0 °C was added KOH as pellets (2 g, 30.0 mmol) and was left stirring for 2 hours. The resulting colourless solution was brought to room temperature and rotaevaporated. The white solid obtained was suspended in ethyl acetate (150 ml) and stirred for 30 minutes. A white solid was collected by filtration, and dissolved in water (300 ml). Using hydrochloric acid, the solution was brought to pH = 2, and left stirring for 30 minutes. The aqueous solution was extracted with CHCl₃ (3x100 ml), and the combined organic layers were dried over Na₂SO₄, filtered and rotaevaporated. The white solid obtained was washed with cold 2-propanol (5 ml). The yield was 41 %. ¹H NMR (300 MHz, CDCl₃): δ (ppm) = 8.42 (d, 1H, C_{aro}H), 8.37 (d, 1H, C_{aro}H), 8.13 (t, 1H, C_{aro}H), 4.04 (s, 3H, CH₃).

6-(3-oxo-3-(2-hydroxyphenyl)propionyl)-2-pyridinecarboxylic acid, H₃L4. A white suspension of NaH (1.2 g, 50 mmol) in DME (20 ml) was added dropwise, under nitrogen atmosphere, into a colourless solution of 6-(methoxycarbonyl)pyridine-2-carboxylic acid (2.25 g, 12 mmol) and 2-hydroxyacetophenone (1.5 ml, 12 mmol) in DME (200 ml), obtaining a yellow suspension. Once the addition was complete, the mixture was brought to reflux, while it gradually turned brown. After 20 hours, the suspension was allowed to cool to room temperature, and the excess of NaH was quenched by adding EtOH (1 ml). A light brown solid was collected by filtration and suspended into Et₂O/H₂O (200 ml, 1:1 v/v), followed by the addition of AcOH (7 ml). The resulting brown mixture was left under stirring for 2 hours, and the system gradually turned light yellow. A yellow solid was separated by filtration, washed with water, and then with Et₂O. The yield was 28 %. ¹H NMR (300 MHz, CDCl₃): δ (ppm) = 15.17 (s, 1H, C_{eno}OH), 11.93 (s, 1H, C_{aro}OH), 8.39 (d, 1H, C_{aro}H), 8.37 (d, 1H, C_{aro}H), 8.17 (t, 1H, C_{aro}H), 7.89 (d, 1H, C_{aro}H), 7.54 (t, 1H, C_{aro}H), 7.45 (s, 1H, CH), 7.04 (d, 1H, C_{aro}H), 7.01 (t, 1H, C_{aro}H). ESI MS: m/z = 286.07 [M + H]⁺. Anal Calcd (Found) for H₃L4·0.7H₂O: C 60.48 (60.47), H 4.20 (3.88), N 4.70 (4.52). IR (KBr pellet, cm⁻¹): 3359 mb, 1743 m, 1622 s, 1576 s, 1493 m, 1455 m, 1399 w, 1344 m, 1302 s, 1246 m, 1205 m, 1177 w, 1165 m, 1101 m, 997 w, 873 w, 821 m, 756 m, 736 m, 697 w, 680 w, 655 w, 628 m, 564 w.

- [1] G. Aromí, D. Aguilà, P. Gamez, F. Luis, O. Roubeau, *Chemical Society Reviews* **2012**, *41*, 537.
- [2] L. Claisen, E. F. Ergardt, *Chemische Berichte* **1889**, *22*, 1009.
- [3] G. Aromí, P. Gamez, J. Reedijk, *Coordination Chemistry Reviews* **2008**, *252*, 964.
- [4] G. Aromí, P. Gamez, C. Boldron, H. Kooijman, A. L. Spek, J. Reedijk, *European Journal of Inorganic Chemistry* **2006**, *2006*, 1940.
- [5] G. Aromí, C. Boldron, P. Gamez, O. Roubeau, H. Kooijman, A. L. Spek, H. Stoeckli-Evans, J. Ribas, J. Reedijk, *Dalton Transactions* **2004**, 3586.
- [6] T. Shiga, N. Ito, A. Hidaka, H. Ökawa, S. Kitagawa, M. Ohba, *Inorganic Chemistry* **2007**, *46*, 3492.
- [7] T. Shiga, M. Ohba, H. Ökawa, *Inorganic Chemistry* **2004**, *43*, 4435.
- [8] T. Shiga, T. Nakanishi, M. Ohba, H. Ökawa, *Polyhedron* **2005**, *24*, 2732.
- [9] R. W. Saalfrank, A. Dresel, V. Seitz, S. Trummer, F. Hampel, M. Teichert, D. Stalke, C. Stadler, J. Daub, V. Schünemann, A. X. Trautwein, *Chemistry – A European Journal* **1997**, *3*, 2058.
- [10] I. G. Phillips, P. J. Steel, *Inorganica Chimica Acta* **1996**, *244*, 3.
- [11] K. G. Hull, M. Visnick, W. Tautz, A. Sheffron, *Tetrahedron* **1997**, *53*, 12405.

CHAPTER III

TRIPLE- AND QUADRUPLE-STRANDED HELICATES

1. Introduction

Metallohelicates are one of the standard architectures in coordination chemistry, and their importance is related not only to the study of recognition and self-assembly processes in supramolecular chemistry, but to the search for new supramolecular functional devices.^[1] The formation of such structures is based on the nature of the ligands and the electrochemical properties of the metals, and sometimes also to additional information that can be introduced by templates or reaction conditions.^[2] The term *helicate* was first introduced by Lehn and coworkers for the description of a polymetallic helical double-stranded complex, being consequently generalized for metal complexes containing one or more ligand strands and two or more ion centers.^[3] One such structure is thus a discrete helical supramolecular complex when one or more organic strands wrap and coordinate a series of ions (in general cations) defining a helical axis. In addition to this axis, a helicate can be characterized by the screw sense (which evokes the chirality of the complex) and the pitch L , a rate that relates axially linear to angular properties through the following equation,

$$L = d/(\omega_1/360) \quad (14)$$

where d is the distance (Å) between two points of the helical axis, and ω_1 the twist angle (in degrees) between them. For a helicate to be ideal, this rate pitch should be constant for the entire compound, leading to a palindromic helicate. The screw sense is related to the motion along and around the axis, that may be right-handed (plus, P) or left-handed (minus, M) depending if the rotation is clockwise or anticlockwise respectively.

The reaction between the ligand strands and the metal ions has been defined as strict self-assembly, where the final helicate belongs to the most thermodynamically stable product.^[4] These ligands should have several binding units along the strand to carry out the recognition and coordination of the metal ions, and some spacers between these units, rigid (or short) enough to allow linear topology of the metal ions, but flexible enough to undergo the helication and wrap those centers. The ligand's design thus plays a crucial role, since without complying with these criteria, both arms of one ligand could for example coordinate the same metal, thus losing the helicoidal

architecture of the complex. Depending on the nature of the ligands, the helicate can be classified in different groups.^[2] Helicates where all the strands are identical are considered *homostranded helicates*, while different strand ligands inside the complex lead to *heterostranded helicates*. Furthermore, ligands with the same binding units along the strand lead to *homotopic helicates*, while complexes with ligands having different binding units are termed *heterotopic helicates*. These helicates can present different isomeric forms, depending on the orientation of the strands (head-to-head, HH, or head-to-tail, HT, if considering two strands). An additional classification can be carried out depending on the coordination sphere of the metal ions. While *saturated helicates* fulfill their coordination spheres by the donor atoms of the strands, *unsaturated helicates* need of supplementary ligands to achieve their required coordination number.

Another important issue to consider when studying multi-stranded complexes is the possible formation of mesocates (side-by-side complex, or mesohelicate), where no helical wrapping of the ligand-strands occurs. Considering a dinuclear triple-stranded M_2L_3 complex of octahedral metals as example (in fact, the most common metal-ligand ratio), the formation of a helicoidal structure affords two possible chiral architectures, where the two metal centers exhibit the same configuration ($\Delta\Delta$ or $\Lambda\Lambda$). On the contrary, if the ligands are disposed in a non-helical manner, the achiral mesocate is obtained and the two metals exhibit different configuration ($\Delta\Lambda$). The generation of a racemic mixture of the helicates is usually more favored than the mesocate architecture, and rarely the two types of isomers can be found in the same reaction.^[5]

Before the concept of helicate was established,^[6, 7] some examples of helical double- and triple-stranded^[8, 9] dinuclear complexes were already known. Even if most of the examples come from N-based polynucleating ligands, some examples can be found involving oxygen donor ligands. The first structurally characterized helicate of this last category, featuring ligands with hydroxamic acid oxygen donors, was published by Raymond and coworkers in 1985.^[9] Since then, a broad group of oxygen-donor ligands has been designed and synthesized, where bis- β -diketone ligands have become an excellent candidate for wrapping and coordinating metals to generate helicates.^[10-12]

While most of the examples that exist in the literature are neutral dinuclear triple-stranded helicates, which concerns trivalent metals ($[M_2L_3]$),^[10, 13-15] very few examples of dinuclear quadruple-stranded helicates have been published until present,^[16] and even fewer with ligands featuring chelating groups like the β -diketone.^[17]

One of the major parts of the research involving metallohelicates is related to the design of new molecular architectures in supramolecular chemistry. Indeed, these molecular entities have been studied as materials for applications associated with their fascinating helical structure. Some examples are the use of helicates as building block to construct helical macromolecular structures with new nonlinear properties, transferring helical chirality to larger supramolecular edifices,^[18] the use of the packing of helicates for the formation of helical columns of stacked complexes,^[19] or taking advantage of the cavity inside the helical bodies for the study of selective host-guest recognition processes.^[20, 21] These helicoidal structures have been studied also for the molecular recognition of the DNA,^[22] as potential sensors for cations,^[23] or as light-converting devices when introducing lanthanide ions in the helicate.^[24] More recently, Takui et al have presented a proposal for using helicates as a molecule-based scalable electron-spin qubits array.^[25] In that sense, the properties of a helicate complex can allow its application in QC when fulfilling the following requirements: structural robustness through multi-bonding coordination, toleration for having a wide selection of metal cationic spin-qubits inside the helicate, the existence of H-bonding sites to control the packing by changing counter anions or solvent, and the possibility of tuning the synthetic strategy of the ligand by inserting functional spacers. Moreover, the helical chirality can also be used as an additional photon qubit in combination with the spin-qubits. Following this proposal, a magnetically diluted dinuclear triple-stranded manganese/zinc helicate featuring different g-tensors between the metal ions has been proposed as a molecular carrier of qubits (see Chapter I, Section 3.3).^[26]

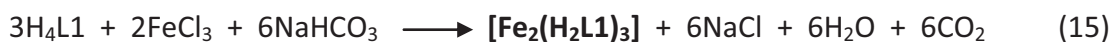
The twisting of metallohelicates depends on the flexibility of the strands, which is directly related to the topology of the ligand. The ligands presented in Chapter II, as seen before for related ligands,^[10] offer all the requirements to act as strands and to wrap metal ions for the design of clusters with helicoidal topologies. The rigid aromatic backbone featuring in the center of these organic molecules (which holds the chelating

units) should prevent them to assemble to a single metal. In the following sections, three different helicates using H₄L1 are presented, focusing on their structural properties.

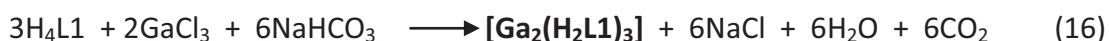
2. Tripled-stranded helicates with Fe^{III} and Ga^{III}

The aim of looking for metallohelicates with H₄L1 was initially in search of triple-stranded tetranuclear helicates of trivalent cations like Fe^{III} and Ga^{III}, featuring a [MM...MM] helicoidal topology. The use of trivalent metals requires three bidentate chelating groups in each of these ions to satisfy an octahedral geometry, involving thus three equivalents of H₄L1 for obtaining [M₄(L1)₃] species. In this environment, each M^{III} should be encapsulated by six ketone-oxygen donors (two from each ligand), leading to neutral species. While iron(III) is a paramagnetic cation that can stimulate the synthesis of complexes featuring interesting magnetic properties, the diamagnetic gallium(III) cation can offer a similar behavior in a synthetic point of view (see below), but a very different one when studying the physical properties.

As a first attempt to achieve this goal, four equivalents of FeCl₃ were employed together with three equivalents of H₄L1 using NaHCO₃ as a base and THF as solvent. Even not using a strong base, the coordination of Fe^{III} to the ligand increases its acidity, and the by-products formed (H₂O and CO₂) would afford a very clean reaction. When layering the resulting reaction solution with ether, red small needles were obtained. The crystal structure was determined by X-ray diffraction using synchrotron radiation, showing that only two metals have been encapsulated in the helicate, with a formula [Fe₂(H₂L1)₃] (**1**). In this compound, two Fe^{III} are coordinated through the β-diketone oxygen atoms, while the phenol units are still protonated. This evidence demonstrates that NaHCO₃ is a base not strong enough to deprotonate this groups in such conditions. For a direct synthesis of compound **1**, the same conditions but following the stoichiometry in Equation 14 were employed:



One of the possibilities when employing the cation Fe^{III} is designing analogous compounds with no unpaired electrons. In the literature there are some examples where Ga^{III} plays the same role as Fe^{III} in polynuclear complexes.^[27, 28] In this regard, the same synthesis carried out for compound **1** was followed using the corresponding gallium(III) salt. Thus, two equivalents of GaCl_3 were treated with $\text{H}_4\text{L1}$ and NaHCO_3 in THF to obtain the analogous helicate $[\text{Ga}_2(\text{H}_2\text{L1})_3]$ (**2**) as yellow crystals after layering the solution with ether. The reaction is described in Equation 15:



Both compounds were characterized by infrared spectroscopy, as well as by X-ray diffraction. The diamagnetic behavior of compound **2** allowed also examining the cluster in solution using ^1H NMR. In chloroform, the spectrum shows that the three ligands are equivalent, where each proton has been assigned, demonstrating the integrity of the metallohelicate in solution.

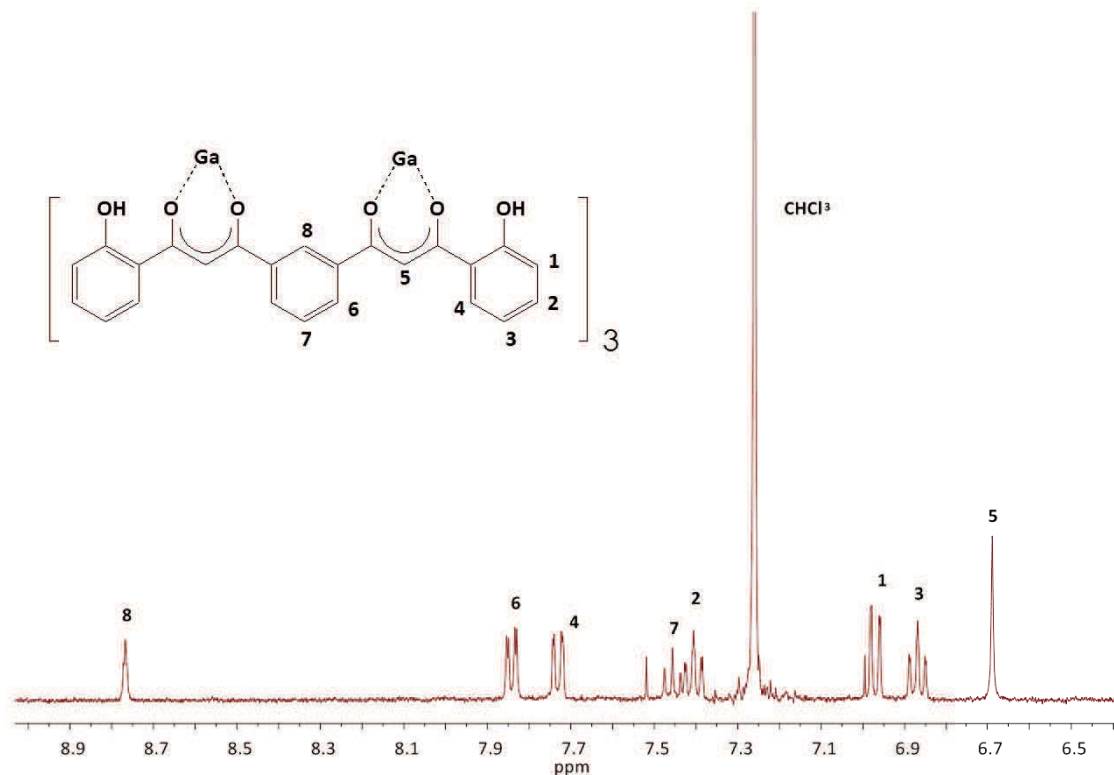


Figure III.1. ^1H NMR spectrum featuring the aromatic region of compound **2**.

Figure III.1 shows the NMR spectrum of compound **2**. Upon complexation to gallium, the signals assigned to protons 1 to 7 are slightly downfield shifted when compared to the free ligand, in contrast to the singlet 8 assigned to the central aromatic proton of the ligand, which is shifted slightly upfield. The same behavior has been detected in similar helicates with a related ligand.^[12] In the literature, different NMR spectral properties between Λ -Ga and Δ -Ga mononuclear compounds have been detected if chiral groups are introduced to the ligand.^[29] However, since no chirality is present in H₄L1, both Λ, Λ - and Δ, Δ - (possible chiral helicates) configurations are not expected to generate distinct sets of NMR resonances. As predicted, only one set of resonances can be detected in the NMR spectra of compound **2**. However, it is well known that helicates show interconversion of both configurations in solution, and while indistinguishable in the NMR ¹H spectra, both $\Lambda\Lambda$ - and $\Delta\Delta$ -Ga₂(H₂L1)₃ racemates should be present in solution.

2.1. Description of the structure of [Fe₂(H₂L1)₃] and [Ga₂(H₂L1)₃]

The molecular structures of [Fe₂(H₂L1)₃] and [Ga₂(H₂L1)₃] were determined by single-crystal X-ray diffraction using synchrotron radiation, providing a final proof of the homochiral helical configurations derived from the NMR spectra. Crystallographic details are provided in the Appendix (Table III.A1). Metallohelicates **1** and **2** crystallize as racemic mixtures in the monoclinic P₂₁/*n* and P₂₁/*c* space group, respectively, featuring both left-handed $\Lambda\Lambda$ -M₂(H₂L1)₃ and right-handed $\Delta\Delta$ -M₂(H₂L1)₃ configurations. Three main molecules constitute the asymmetric unit of compound **1**. In contrast, in the present refinement status of the structure for compound **2**, only one molecule appears in the asymmetric unit. Clusters **1** and **2** are isostructural, exhibiting two metal ions encapsulated by three molecules of the ligand (Figure III.2). These three partially deprotonated ligands bridge and wrap the two trivalent metal centers, saturating all their octahedral coordination sites and compensating the six total positive charge.

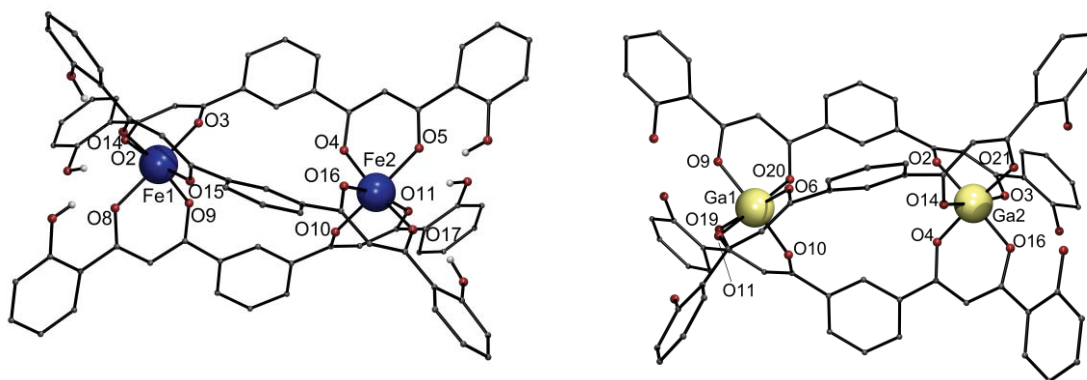


Figure III.2. Representation of the molecular structure of compounds $[\text{Fe}_2(\text{H}_2\text{L1})_3]$ (**1**) and $[\text{Ga}_2(\text{H}_2\text{L1})_3]$ (**2**). Blue, Fe; yellow, Ga; red, O; rest, C. Only hydrogen atoms bound to O are shown.

Each cation is coordinated to six oxygen donor atoms from the β -diketone group, featuring a distorted octahedral geometry, separated by 7.1772(11) Å and 7.240 Å for compound **1** and **2** respectively. In that sense, these helicates can be classified as saturated, homostranded and homotopic. As demonstrated in Figure III.2, the long $\text{M}\cdots\text{M}$ distance prompts considerable room inside the helicoidal architectures. The average of the distance between M^{III} and the oxygen atoms from the β -diketone reaches values of 1.985 Å for compound **1**, and of 1.947 Å for compound **2**. A complete list of bond distances and angles for compound **1** and **2** is shown in Tables III.1 and III.2, respectively. In the present refinement status of the structure of compound **2**, it is not possible to observe the proton of the phenol groups of the ligand. However, by analogy with the structure of **1**, these phenol groups are expected to be also protonated. In addition, the average of the distances between the oxygen of the phenol unit and the one belonging to the adjacent C-O group are 2.522 Å for compound **1**, and 2.537 Å for compound **2**, which indicates the probable hydrogen bonding between this two oxygen atoms and therefore the existence of the proton in the phenol unit. This feature has been seen before in related compounds using the ligand $\text{H}_4\text{L1}$,^[30] and entails a factor of stability to the dinuclear species obtained in front of the desired tetranuclear helicates. In addition to the main molecule, THF solvent molecules are observed inside the crystal lattice.

Table III.1. Selected interatomic distances [Å] and angles [°] for [Fe₂(H₂L1)₃] (1)

Fe1-O3	1.951(3)	O15-Fe1-O14	85.05(11)
Fe1-O15	1.954(3)	O9-Fe1-O14	170.42(13)
Fe1-O9	1.955(3)	O8-Fe1-O14	86.50(12)
Fe1-O8	1.994(3)	O3-Fe1-O2	85.47(11)
Fe1-O14	2.006(3)	O15-Fe1-O2	168.23(12)
Fe1-O2	2.008(3)	O9-Fe1-O2	98.49(12)
Fe2-O16	1.947(3)	O8-Fe1-O2	86.96(12)
Fe2-O10	1.963(3)	O14-Fe1-O2	85.67(12)
Fe2-O4	1.974(3)	O16-Fe2-O10	90.78(14)
Fe2-O11	2.005(3)	O16-Fe2-O4	88.01(12)
Fe2-O5	2.014(4)	O10-Fe2-O4	88.67(13)
Fe2-O17	2.018(3)	O16-Fe2-O11	170.55(14)
O3-Fe1-O15	88.85(12)	O10-Fe2-O11	84.51(13)
O3-Fe1-O9	89.91(12)	O4-Fe2-O11	100.03(13)
O15-Fe1-O9	91.79(12)	O16-Fe2-O5	99.63(14)
O3-Fe1-O8	170.24(12)	O10-Fe2-O5	167.45(14)
O15-Fe1-O8	99.68(12)	O4-Fe2-O5	84.74(12)
O9-Fe1-O8	85.12(12)	O11-Fe2-O5	86.14(14)
O3-Fe1-O14	99.04(12)	O16-Fe2-O17	85.40(12)
O10-Fe2-O17	100.98(14)	O4-Fe2-O17	168.36(14)
O11-Fe2-O17	87.46(13)	O5-Fe2-O17	86.91(14)

Table III.2. Selected interatomic distances [Å] and angles [°] for [Ga₂(H₂L1)₃] (2)

Ga1-O6	1.9336	O10-Ga1-O11	97.25
Ga1-O9	1.9689	O10-Ga1-O19	90.24
Ga1-O10	1.9383	O10-Ga1-O20	87.88
Ga1-O11	1.9599	O11-Ga1-O19	85.09
Ga1-O19	1.9470	O11-Ga1-O20	174.76
Ga1-O20	1.9172	O19-Ga1-O20	96.03
Ga2-O2	1.9412	O2-Ga2-O3	87.51
Ga2-O3	1.9676	O2-Ga2-O4	87.81
Ga2-O4	1.9353	O2-Ga2-O14	91.36
Ga2-O14	1.9332	O2-Ga2-O16	172.20
Ga2-O16	1.9538	O2-Ga2-O21	93.95
Ga2-O21	1.9669	O3-Ga2-O4	97.41
O6-Ga1-O9	93.13	O3-Ga2-O14	174.46
O6-Ga1-O10	88.06	O3-Ga2-O16	85.23
O6-Ga1-O11	88.02	O3-Ga2-O21	85.45
O6-Ga1-O19	172.63	O4-Ga2-O14	87.96
O6-Ga1-O20	91.08	O4-Ga2-O16	90.31
O9-Ga1-O10	177.08	O4-Ga2-O21	176.71

O9-Ga1-O11	85.46	O14-Ga2-O16	96.14
O9-Ga1-O19	88.91	O14-Ga2-O21	89.22
O9-Ga1-O20	89.44	O16-Ga2-O21	88.31

The study of their crystal structure allows quantifying the helicoidal arrangement of these compounds, which reflects the torsion experienced by the ligands in accommodating the distorted octahedral twist at the Fe^{III} and Ga^{III} centers. The total pitch L_T of both compounds is defined, together with the pitch related to the environment of each metal of the helicate (L_1 and L_2), as described in Figure III.3.

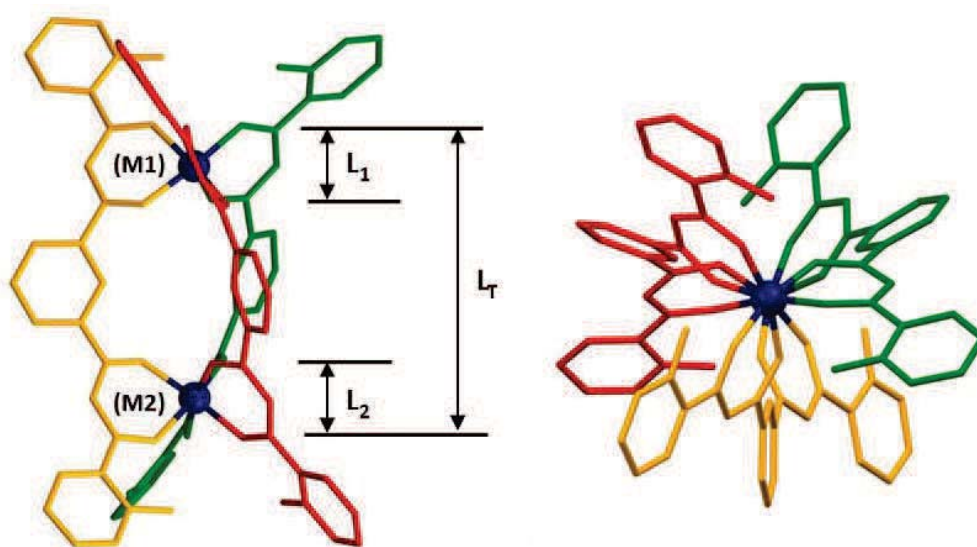


Figure III.3. Frame-and-sphere representation of compound **1** (as example for both compounds) as viewed perpendicular (left) and down (right) to the helical axis, exhibiting the subpitches L_1 , L_2 and the total pitch L_T .

For the total pitch L_T , the distance between the centroids of the outer triangular faces of the octahedral environment of the two metal ions has been considered (d_T). The twist angle ($\omega_{1(T)}$) is calculated as the average of the torsion angles O-M1-M2-O of each ligand (considering the outer oxygen donors of the two β -diketone units of the ligand). The two subpitches L_1 and L_2 are referred to the twist inside the polyhedra around M1 and M2, respectively. The distance between the centroids of the outer and the inner triangular faces of each octahedral environment define d_1 and d_2 . For the study of the

angles $\omega_{1(1)}$ and $\omega_{1(2)}$, the twist between the two triangular faces with respect to each other has been considered (Figure III.4). The values of d , ω_1 , and L for each case of compounds **1** and **2** are presented in Table III.3.

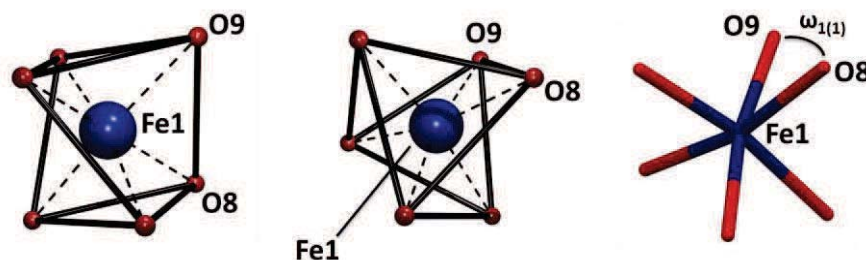


Figure III.4. Representation of the coordination geometry of Fe1 of **1** (as example for the two metals of both compounds) defining the twist angle $\omega_{1(1)}$. (left) View of the polyhedron perpendicular to the helical axis. (middle) Polyhedron along the helical axis. (right) View along the helical axis, defining the twist angle $\omega_{1(1)}$ of one of the three ligands (O8 and O9).

Table III.3: Distances, twist angles and helical pitches in 1 and 2	[Fe ₂ (H ₂ L1) ₃] (1)	[Ga ₂ (H ₂ L1) ₃] (2)
d₁: Height upper octahedra M1 (Å)	2.37	2.33
ω₁₍₁₎: Twist angle upper octahedra M1 (°) (average)	48.9 – 45.0 – 46.4 (47.8)	56.0 – 55.7 – 51.5 (54.4)
L₁: Pitch of upper octahedra M1 (Å)	17.9	15.4
d₂: Height octahedra M2 (Å)	2.35	2.34
ω₁₍₂₎: Twist angles bottom octahedra M2 (°) (average)	46.2 – 46.9 – 43.7 (45.6)	50.5 – 55.5 – 55.6 (53.8)
L₂: Pitch of bottom octahedra M2 (Å)	17.8	15.6
d_T: Distance between outer faces M1 and M2 (Å)	9.63	9.64
ω_{1(T)}: Total twist angles (°) (average)	75.3 – 74.2 – 75.6 (75.0)	83.3 – 83.4 – 83.2 (83.3)
L_T: Total pitch (Å)	45.7	41.7

The analysis of the helical motif of compounds **1** and **2** reveals some minor differences in their molecular structures. The three ligands of the Fe^{III} helicate exhibit a lower degree of twisting, the values of their twist angles being smaller than in compound **2** (75.0° and 83.3° in average, respectively). This demonstrates a better “wrapping”

capacity of the ligand in the gallium(III) compound than in the iron(III) helicate. For both compounds, the ligands present slightly different twist angles when compared with each other. Within the polyhedra (L_1 and L_2), one of the ligands presents a lower twist angle value (see for example the angle 50.5° versus the angles 55.5° and 55.6° when defining $\omega_{1(2)}$ in compound **2**). In contrast, the three twist angles that define the total pitch have more similar values.

3. Quadruple-stranded helicate with U^{IV}

The interest on actinide ions has increased exponentially during the last years based on the exceptional properties that result from the unpaired electrons in 5f orbitals.^[31] Their ability to combine the properties from the spin-orbit coupling together with strong magnetic interactions provided by the increased radial extension of 5f orbitals makes actinide-containing complexes a very interesting tool to exploit their magnetic properties. In this respect, the construction of new functional molecules incorporating paramagnetic uranium centers opens a new approach for this project. All the chemistry related to actinide compounds was carried out during a three month stay in the Long Group of UC Berkeley (California, Berkeley, USA) under the supervision of Prof. Jeffrey R. Long.

The study of the previous complexes in Section 2 has demonstrated that H₄L1 can act as a good precursor for synthesizing helicates with trivalent ions. Uranium(III) ion has been shown to be an ideal metallic center for molecules acting as molecular magnets, and the structural characteristics of complexes **1** and **2** suggest the possibility of having two U^{III} ions inside a helicate structure, which could constitute a potential molecular nanomagnet.^[32, 33] Thus, different reactions were carried out using different solvents and starting materials, working in an air-free atmosphere due to the extremely sensitivity of uranium(III) ion towards oxidation. The reaction of one equivalent of [U(OTf)₃(MeCN)₃] (synthesized as previously reported)^[34] with two equivalents of H₄L1 in acetonitrile affords an orange/brown suspension. The orange solid obtained was dissolved in DMF and layered with MeCN to obtain small red crystals suitable for X-ray diffraction. The crystal structure reveals a quadruple-stranded helicate with four equivalents of the ligand and two equivalents of uranium; [U₂(H₂L1)₄(X)₂] (**3**).

The poor quality of the crystal did not allow elucidating the nature of the molecules of X, but they may be reasonably ascribed to DMF molecules, coming from the solvent used in the last step. Being a neutral entity, and supposing four diprotonated molecules of the ligand, both uranium ions seem oxidized to U^{IV}. This hypothesis has been supported from studying the bond distances in the molecular structure (see below). It is known that U^{III} can be easily oxidized to higher forms that can be stabilized within the final complex. This would explain the new oxidation state of both uranium centers.^[35, 36] Besides single crystal X-ray diffraction experiments, the compound was characterized by infrared spectroscopy and cyclic voltammetry (see below).

3.1. Description of the structure of [U₂(H₂L1)₄(X)₂]

The molecular structure of compound **3** shows two U^{IV} ions wrapped by four ligands H₂L1²⁻ through the β-diketone units, featuring a quadruple-helicate (Figure III.5). As mentioned before, this kind of helicoidal structure with four strands is very rare in the literature. In addition, to the best of our knowledge, no uranium helicate structure has been published previously, which makes this compound really unique. This metallohelicate crystallizes as racemic mixture in the triclinic P-1 space group, featuring both configurations (left- and right-handed) in the unit cell. The helical motif arranges the metals with a separation of 7.41 Å, each of them being nine-coordinate. Crystallographic details are provided in the Appendix (Table III.A1), while selected structural parameters are shown in Table III.4. Each U^{IV} ion is encapsulated by four β-diketone groups, and one more atom, that could belong to a molecule of DMF from the solvent. This metallohelicate can be thus classified as unsaturated, homotopic and homostranded. From all the different possible geometries belonging to coordination number nine, the trigonal prism (D_{3h}) and capped square antiprism (C_{4v}) are known to be the most stable ones; The small energetic difference between them in [M(bidentate)₄(monodentate)] systems has been predicted by repulsion energy calculations.^[37] In compound **3**, the coordination geometry of both metals was quantified by means of continuous-shape measures (CShMS).^[38] This measurement compares the coordination polyhedra of a metal ion with different ideal polyhedra existing for its respective coordination number. For compound **3**, the shape of these

ions is best described as a capped square antiprism. The different values obtained from the measurement are shown in Table III.A2 (Appendix).

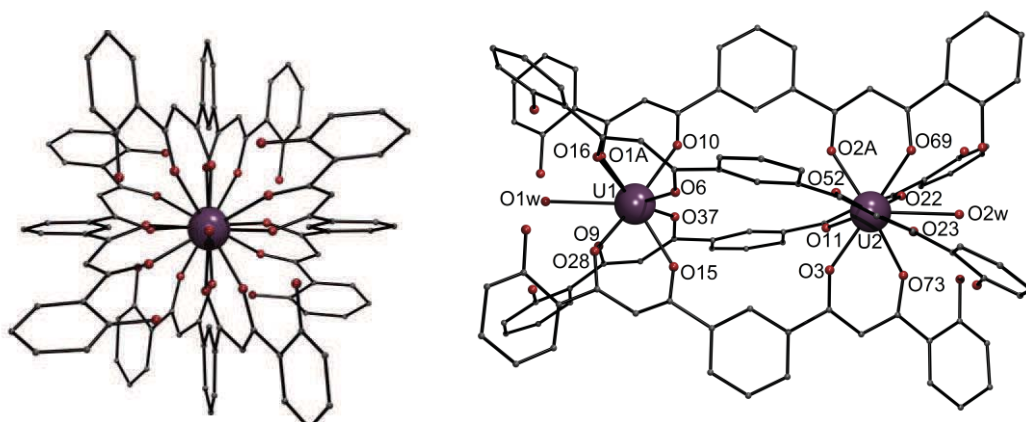


Figure III.5. Representation of the molecular structure of compound $[U_4(H_2L1)_4(X)_2]$ as viewed perpendicular (right) and down (left) the helical axis. Purple, U; red, O; rest, C. H atoms excluded

Table III.4. Selected interatomic distances [\AA] and angles [$^\circ$] for $[U_2(H_2L1)_4] (3)$

U1-O6	2.3211	O16-U1-O37	152.36
U1-O9	2.3518	O16-U1-O1A	76.15
U1-O10	2.3093	O16-U1-O1w	60.61
U1-O15	2.3343	O28-U1-O37	69.37
U1-O16	2.3551	O28-U1-O1A	75.62
U1-O28	2.3353	O28-U1-O1w	60.18
U1-O37	2.3140	O37-U1-O1A	82.68
U1-O1A	2.3557	O37-U1-O1w	122.66
U1-O1w	2.8001	O1A-U1-O1w	60.71
U2-O3	2.3179	O3-U2-O11	72.59
U2-O11	2.3103	O3-U2-O22	131.51
U2-O22	2.3375	O3-U2-O23	83.12
U2-O23	2.3306	O3-U2-O52	72.49
U2-O52	2.3157	O3-U2-O69	151.86
U2-O69	2.3457	O3-U2-O73	69.71
U2-O73	2.3623	O3-U2-O2A	114.25
U2-O2A	2.3349	O3-U2-O2w	123.35
U2-O2w	2.8042	O11-U2-O22	69.96
O6-U1-O9	83.43	O11-U2-O23	151.81
O6-U1-O10	72.15	O11-U2-O52	114.61
O6-U1-O15	73.63	O11-U2-O69	131.77
O6-U1-O16	69.09	O11-U2-O73	82.78
O6-U1-O28	153.25	O11-U2-O2A	73.44

O6-U1-O37	114.45	O11-U2-O2w	122.98
O6-U1-O1A	130.51	O22-U2-O23	120.19
O6-U1-O1w	122.89	O22-U2-O52	152.60
O9-U1-O10	152.36	O22-U2-O69	76.00
O9-U1-O15	69.84	O22-U2-O73	76.00
O9-U1-O16	75.88	O22-U2-O2A	83.07
O9-U1-O28	76.09	O22-U2-O2w	60.14
O9-U1-O37	131.09	O23-U2-O52	69.55
O9-U1-O1A	121.07	O23-U2-O69	75.70
O9-U1-O1w	60.36	O23-U2-O73	75.39
O10-U1-O15	113.64	O23-U2-O2A	131.31
O10-U1-O16	83.29	O23-U2-O2w	60.06
O10-U1-O28	130.99	O52-U2-O69	82.75
O10-U1-O37	72.72	O52-U2-O73	130.61
O10-U1-O1A	69.74	O52-U2-O2A	73.28
O10-U1-O1w	123.42	O52-U2-O2w	122.41
O15-U1-O16	131.40	O69-U2-O73	120.92
O15-U1-O28	83.17	O69-U2-O2A	69.38
O15-U1-O37	72.57	O69-U2-O2w	60.18
O15-U1-O1A	151.88	O73-U2-O2A	152.59
O15-U1-O1w	122.94	O73-U2-O2w	60.74
O16-U1-O28	120.79	O2A-U2-O2w	122.40

In contrast to the observed in similar structures, the oxygen donor atoms featuring the uncapped face (uf) of the polyhedra experience slightly less repulsion than those forming the capped face (cf).^[17, 37] This effect can be evaluated when comparing the average of the bond distances of U-O_{cf} (2.35 Å) and U-O_{uf} (2.32 Å). Nevertheless, it must be considered that the distances of this preliminary structure are an approximation of the refined final one. All the U-O distances confirm the oxidation state IV of the uranium ions in the structure (previously predicted by the charge balance) since are in range of the values reported in other oxo U^{IV} clusters,^[34, 39, 40] and smaller than the expected distances for U^{III}-O bonds (≈ 2.5 Å).^[34, 40] The average of the distances between the oxygen of the phenol unit and the one belonging to the adjacent C-O group is 2.54 Å, indicating the probable hydrogen bonding between this two oxygen atoms and therefore the existence of the proton in the phenol unit.^[30]

As for compounds **1** and **2**, the three pitches L_1 , L_2 and L_T can be defined within the structure of [U₂(H₂L1)₄(X)₂], (Figure III.6, left). L_1 and L_2 are referred to the twist inside

both capped square antiprisms. The distance between the centroids of the outer and inner square faces of their polyhedra define d_1 and d_2 . For the study of the angles $\omega_{1(1)}$ and $\omega_{1(2)}$, the twist between the two square faces has been considered. For the total pitch L_T , d_T is determined by the distance between the centroids of the outer faces of the capped square antiprism of each U^IV . The twist angle ($\omega_{1(T)}$) have been defined as the average of the torsion angles O-U1-U2-O of each ligand (considering the outer oxygen donors of the two β -diketone units of the ligand). The values of d , ω_1 , and L for each case are presented in Table III.5.

Table III.5: Distances, twist angles and helical pitches in 3	
d_1 : Height square antiprism U1 (Å)	2.42
$\omega_{1(1)}$: Twist angle square antiprism U1 (°)	32.5 – 32.3 – 32.3 – 32.7
(average)	(32.4)
L_1 : Pitch of square antiprism U1 (Å)	26.9
d_2 : Height square antiprism U2 (Å)	2.42
$\omega_{1(2)}$: Twist angle square antiprism U2 (°)	32.1 – 32.6 – 31.3 – 32.4
(average)	(32.1)
L_2 : Pitch of square antiprism U2 (Å)	27.2
d_T : Distance between outer faces U1 and U2 (Å)	9.73
$\omega_{1(T)}$: Total twist angle (°) (average)	59.5 – 58.8 – 58.9 – 59.3
	(58.4)
L_T : Total pitch (Å)	60.0

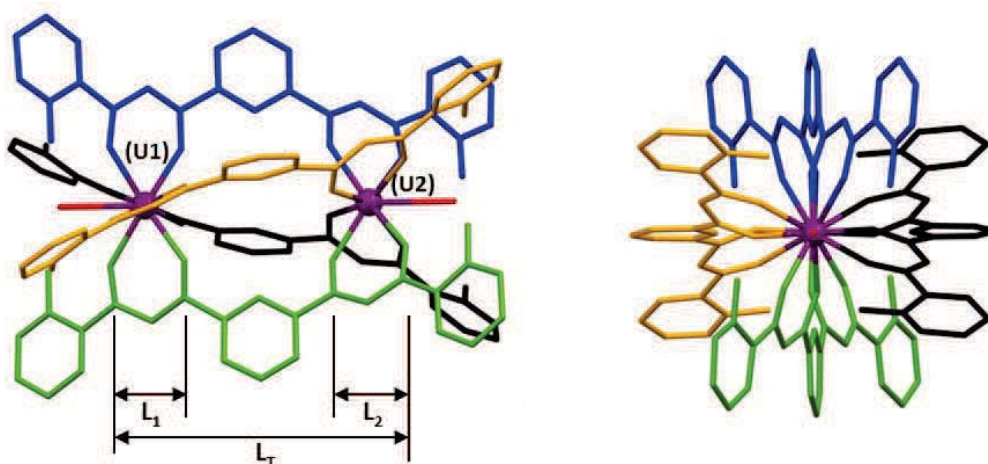


Figure III.6. Frame-and-sphere representation featuring the subpitches L_1 , L_2 and the total pitch L_T of compound **3** as viewed down (right) and perpendicular (left) to the helical axis.

The study of the helicoidal structure reflects the high similar behavior of the four strands of the helicate, since the value of the twist angles are all very close (see Table III.5). These angles also reflect the small twist of the strands, which shows the low degree of helicity in this cluster (Figure III.6, right).

3.2. Infrared spectroscopy and study of the redox activity of $[U_2(H_2L1)_4(X)_2]$

For a further characterization, the infrared spectrum of **3** was studied and compared with the spectra of the free ligand and DMF. The spectrum shows the shifted bands of the ligand and additional peaks that match the bands from the DMF molecule, confirming the nature of the molecule coordinated (X) to complete the coordination environment of the uranium ions (see section 4, Experimental part). The frequencies from the experimental IR spectra belonging to the coordinated DMF molecules for compound **3** and the theoretical IR spectra for DMF are presented in Table III.6.^[41]

Table III.6. Frequencies for DMF in complex 3 and as free molecule. ν , δ and ρ are stretching, bending and swinging vibrations respectively.

Assignment	$[U_2(H_2L1)_4(X)_2]$ (cm^{-1})	DMF (cm^{-1})
$\nu C=O$	1657	1671
	1447	1440
$\delta_{as}C'H_3 + \delta_{as}C''H_3$	1411	1411
$\rho C'H_3 + \nu CN$	1095	1092
$\nu_s (NC' + NC'')$	868	865
$\delta C=O + \nu NC'$	664	661

As shown in the table, there is not a significant shift of the bands except for the 1657-1671 cm^{-1} pair. The major shift in that band, which belongs to the stretching vibration of the carbonyl group of the DMF molecule, suggests the coordination through the oxygen donor atom of the solvent ligand.

For $5f^2 U^{IV}$ complexes, the coupling of the orbital angular momentum to the spin angular momentum, together with the ligand field effect gives rise to some degree of

spin pairing that diminishes considerably the magnetic response of the paramagnetic ion.^[42, 43] On the other hand, complexes featuring U^{III} ions reveal interesting magnetic properties, and have been found as interesting single-molecule magnets.^[32, 33] Thus, the reduction of the uranium centers from **3** into U^{III} seems an interesting approach for the synthesis of a new complex with more interesting magnetic properties. Following this proposal, the redox activity of compound **3** was investigated through preliminary cyclic voltammetry experiments. All measurements were carried out in DMF at room temperature, using TBA.PF₆ as supporting electrolyte in air-free conditions. A conventional three-electrode setup consisting of one platinum wire as the auxiliary electrode, one silver wire as reference electrode, and a working glassy carbon (GC) electrode (3 mm diameter) was used. Figure III.7 shows the voltammogram of compound **3** at 100 mV/s, exhibiting three irreversible reduction processes.

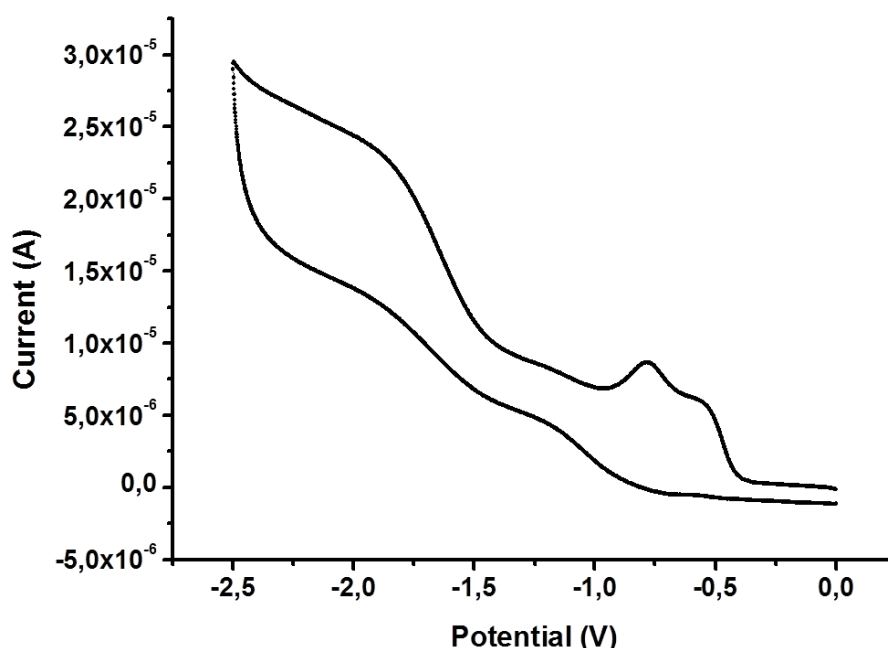


Figure III.7. Cyclic voltammogram at 100 mV/s for compound **3** in DMF at a glassy carbon electrode and TBA.PF₆ as a supporting electrolyte.

Since the first reduction process at 0.544 V is irreversible even studying only this first peak, it seems clear that adding one electron to this helicate imposes a rearrangement of the structure that makes the process not reversible. However, looking for the reduction of the compound at this potential through bulk electrolysis could lead to a new material with the uranium ion in more interesting lower oxidation state. On the

other hand, no oxidation processes have been detected in the potential window allowed by the DMF.

4. Experimental

[Fe₂(H₂L1)₃] (1). A solution of H₄L1 (50 mg, 0.12 mmol) and NaHCO₃ (20.8 mg, 0.25 mmol) in THF (30 ml) was added dropwise onto a solution of FeCl₃ (13.4 mg, 0.083 mmol) in THF (20 ml). The resulting red solution was stirred under reflux for 45 minutes and then cooled down to room temperature. The red solution was layered with Et₂O, and red crystals were obtained after two days in 12 % yield. IR (KBr pellet, cm⁻¹): 3437 mb, 1619 m, 1583 m, 1507 s, 1477 s, 1457 s, 1376 m, 1339 m, 1298 m, 1243 w, 1198 m, 1133 w, 1102 w, 1054 w, 1033 w, 798 w, 750 w, 725 w, 668 w, 633 w, 564 w.

[Ga₂(H₂L1)₃] (2). A solution of H₄L1 (66.6 mg, 0.17 mmol) and NaHCO₃ (55.9 mg, 0.67 mmol) in THF (60 ml) was added dropwise onto a solution of GaCl₃ (22.1 mg, 0.126 mmol) in THF (40 ml). The resulting yellow solution was stirred under reflux for 45 minutes and then cooled down to room temperature. The yellow solution was layered with Et₂O, and orange crystals were obtained after two days in 7 % yield. ¹H NMR (CDCl₃, 300 MHz): 8,77 (s, 1 H, C_{aro}H), 7,84 (d, 2 H, C_{aro}H), 7,73 (d, 2 H, C_{aro}H), 7,46 (t, 1 H, C_{aro}H), 7,41 (t, 2 H, C_{aro}H), 6,97 (d, 2 H, C_{aro}H), 6,87 (t, 2 H, C_{aro}H), 6,69 (s, 2 H, CH). IR (KBr pellet, cm⁻¹): 3448 mb, 1615 m, 1559 m, 1507 s, 1473 s, 1457 s, 1399 m, 1339 m, 1303 m, 1137 w, 1101 w, 1048 w, 1029 w, 1001 m, 836 m, 696 s, 667 w, 657 w, 564 w.

[U(OTf)₃(MeCN)₃]. An acetonitrile solution (10 ml) of K(OTf) (183 mg, 0.97 mmol) was added dropwise in an air-free atmosphere onto a solution of U₁₃ (200 mg, 0.33 mmol) in MeCN (10 ml). The resulting dark green reaction was left stirring for 20 hours. The green solid precipitated was isolated by removing the MeCN, and dried under vacuum. ¹⁹F NMR (CD₃CN, 400 MHz): -79.22.

[U₂(H₂L1)₄(X)₂] (3). A suspension of H₄L1 (39.8 mg, 0.1 mmol) in MeCN (5 ml) was added dropwise onto an acetonitrile solution (3 ml) of [U(OTf)₃(MeCN)₃] (40 mg, 0.05 mmol) in an air-free atmosphere. The final orange suspension was left stirring for 24

hours. A brown solid was isolated by removing the MeCN and dissolved in DMF (4 ml). The solution was left undisturbed for 24 hours at 3 °C, after which time a white solid had precipitated from the reaction mixture. The solid was removed by filtration, and the resulting orange solution was layered with MeCN. After four days, few red crystals of **3** were obtained. IR (KBr pellet, cm^{-1}): 3050 mb, 1657 w, 1615 m, 1580 m, 1504 s, 1471 s, 1447 s, 1411 m, 1371 m, 1333 m, 1282 m, 1236 m, 1192 m, 1162 m, 1128 s, 1095 m, 1050 m, 1032 m, 796 w, 747 w, 720 w, 664 w, 618 w, 564 w.

- [1] M. Albrecht, *Chemical Reviews* **2001**, *101*, 3457.
- [2] C. Piguet, G. Bernardinelli, G. Hopfgartner, *Chemical Reviews* **1997**, *97*, 2005.
- [3] J.-M. Lehn, A. Rigault, J. Siegel, J. Harrowfield, B. Chevrier, D. Moras, *Proceedings of the National Academy of Sciences of the United States of America* **1987**, *84*, 5.
- [4] J. S. Lindsey, *New Journal of Chemistry* **1991**, *15*, 28.
- [5] Z. Zhang, D. Dolphin, *Chemical Communications* **2009**, 6931.
- [6] G. Struckmeier, U. Thewalt, J. H. Fuhrhop, *Journal of the American Chemical Society* **1976**, *98*, 278.
- [7] G. C. van Stein, H. van der Poel, G. van Koten, A. L. Spek, A. J. M. Duisenberg, P. S. Pregosin, *Journal of the Chemical Society, Chemical Communications* **1980**, 1016.
- [8] C. M. Harris, E. D. McKenzie, *Journal of the Chemical Society A: Inorganic, Physical, Theoretical* **1969**, 746.
- [9] R. C. Scarrow, D. L. White, K. N. Raymond, *Journal of the American Chemical Society* **1985**, *107*, 6540.
- [10] V. A. Grillo, E. J. Seddon, C. M. Grant, G. Aromí, J. C. Bollinger, K. Folting, G. Christou, *Chemical Communications* **1997**, 1561.
- [11] R. W. Saalfrank, A. Dresel, V. Seitz, S. Trummer, F. Hampel, M. Teichert, D. Stalke, C. Stadler, J. Daub, V. Schünemann, A. X. Trautwein, *Chemistry – A European Journal* **1997**, *3*, 2058.
- [12] A. P. Bassett, S. W. Magennis, P. B. Glover, D. J. Lewis, N. Spencer, S. Parsons, R. M. Williams, L. De Cola, Z. Pikramenou, *Journal of the American Chemical Society* **2004**, *126*, 9413.
- [13] R. L. Lintvedt, G. Ranger, C. Ceccarelli, *Inorganic Chemistry* **1985**, *24*, 1819.
- [14] J. K. Clegg, L. F. Lindoy, J. C. McMurtrie, D. Schilter, *Dalton Transactions* **2005**, 857.
- [15] H.-F. Li, P.-F. Yan, P. Chen, Y. Wang, H. Xu, G.-M. Li, *Dalton Transactions* **2012**, *41*, 900.
- [16] H. S. Sahoo, D. K. Chand, *Dalton Transactions* **2010**, *39*, 7223.
- [17] J. Xu, K. N. Raymond, *Angewandte Chemie International Edition* **2006**, *45*, 6480.
- [18] T. Gulik-Krzywicki, C. Fouquey, J. Lehn, *Proceedings of the National Academy of Sciences* **1993**, *90*, 163.
- [19] R. F. Carina, G. Bernardinelli, A. F. Williams, *Angewandte Chemie International Edition in English* **1993**, *32*, 1463.
- [20] S. Goetz, P. E. Kruger, *Dalton Transactions* **2006**, 1277.
- [21] A. Bilyk, M. M. Harding, *Journal of the Chemical Society, Chemical Communications* **1995**, 1697.
- [22] A. Oleksi, A. G. Blanco, R. Boer, I. Usón, J. Aymamí, A. Rodger, M. J. Hannon, M. Coll, *Angewandte Chemie International Edition* **2006**, *45*, 1227.
- [23] G. Bokolinis, T. Riis-Johannessen, L. P. Harding, J. C. Jeffery, N. McLay, C. R. Rice, *Chemical Communications* **2006**, 1980.
- [24] N. Martin, J.-C. G. Bünzli, V. McKee, C. Piguet, G. Hopfgartner, *Inorganic Chemistry* **1998**, *37*, 577.
- [25] K. Sato, S. Nakazawa, R. Rahimi, T. Ise, S. Nishida, T. Yoshino, N. Mori, K. Toyota, D. Shiomi, Y. Yakiyama, Y. Morita, M. Kitagawa, K. Nakasuji, M. Nakahara, H. Hara, P. Carl, P. Hofer, T. Takui, *Journal of Materials Chemistry* **2009**, *19*, 3739.
- [26] Y. Morita, Y. Yakiyama, S. Nakazawa, T. Murata, T. Ise, D. Hashizume, D. Shiomi, K. Sato, M. Kitagawa, K. Nakasuji, T. Takui, *Journal of the American Chemical Society* **2010**, *132*, 6944.
- [27] P. King, T. C. Stamatatos, K. A. Abboud, G. Christou, *Angewandte Chemie International Edition* **2006**, *45*, 7379.
- [28] B. Kersting, M. Meyer, R. E. Powers, K. N. Raymond, *Journal of the American Chemical Society* **1996**, *118*, 7221.
- [29] T. B. Karpishin, T. D. P. Stack, K. N. Raymond, *Journal of the American Chemical Society* **1993**, *115*, 6115.

- [30] G. Aromí, C. Boldron, P. Gamez, O. Roubeau, H. Kooijman, A. L. Spek, H. Stoeckli-Evans, J. Ribas, J. Reedijk, *Dalton Transactions* **2004**, 3586.
- [31] J. D. Rinehart, T. D. Harris, S. A. Kozimor, B. M. Bartlett, J. R. Long, *Inorganic Chemistry* **2009**, *48*, 3382.
- [32] J. D. Rinehart, J. R. Long, *Journal of the American Chemical Society* **2009**, *131*, 12558.
- [33] J. D. Rinehart, K. R. Meihaus, J. R. Long, *Journal of the American Chemical Society* **2010**, *132*, 7572.
- [34] L. Natrajan, M. Mazzanti, J.-P. Bezombes, J. Pécaut, *Inorganic Chemistry* **2005**, *44*, 6115.
- [35] P. Roussel, R. Boaretto, A. J. Kingsley, N. W. Alcock, P. Scott, *Journal of the Chemical Society, Dalton Transactions* **2002**, 1423.
- [36] L. R. Avens, D. M. Barnhart, C. J. Burns, S. D. McKee, W. H. Smith, *Inorganic Chemistry* **1994**, *33*, 4245.
- [37] T. Hambley, D. Kepert, C. Raston, A. White, *Australian Journal of Chemistry* **1978**, *31*, 2635.
- [38] A. Ruiz-Martínez, D. Casanova, S. Alvarez, *Chemistry – A European Journal* **2008**, *14*, 1291.
- [39] J.-C. Berthet, P. Thuéry, M. Ephritikhine, *Inorganic Chemistry* **2010**, *49*, 8173.
- [40] J.-C. Berthet, M. Nierlich, Y. Miquel, C. Madic, M. Ephritikhine, *Dalton Transactions* **2005**, 369.
- [41] M. Shundalau, A. Komyak, A. Zazhugin, D. Umreiko, *Journal of Applied Spectroscopy* **2012**, *79*, 22.
- [42] J. P. Day, L. M. Venanzi, *Journal of the Chemical Society A: Inorganic, Physical, Theoretical* **1966**, 197.
- [43] J. D. Rinehart, B. M. Bartlett, S. A. Kozimor, J. R. Long, *Inorganica Chimica Acta* **2008**, *361*, 3534.

CHAPTER IV

**MOLECULAR PAIR OF CLUSTERS: COMPLEXES
CONTAINING TWO WEAKLY COUPLED
METALLOAGGREGATES**

1. Introduction

The advantages of using the electron spin as the carrier of a quantum bit convert it into one of the most promising ones to become the hardware in QIP. However, as exposed in the first chapter, finding molecular systems that fulfill the conditions to realize universal quantum gates is not straightforward. Therefore, one of the main challenges for the synthetic chemists is the design and synthesis of molecules with predetermined functions and physicochemical properties. This strategy has been successfully carried out by different groups for various purposes, for example to deliberately obtain ferromagnetically exchanged clusters,^[1] or to prepare magnetically active molecules in the form of grids.^[2,3] One strategy to possibly reach a molecular 2-qubit quantum gate is the development of molecular systems featuring two well-defined coordination clusters with the appropriate spin properties and a weak interaction between them. This approach has been used to develop systems with two weakly coupled clusters and their magnetic properties have been tested to fulfill the requirements for quantum computation (see Chapter I, Section 3). One of the most representative examples is the molecular assembly of two heterometallic rings of transition metals developed by Winpenny and coworkers, a versatile system that can be modulated by modifying the groundstate of each cluster or the linker between them.^[4]

In this chapter, new candidates of molecular pairs of clusters systems are described and their magnetic properties are investigated. Polydentate ligands presented in Chapter II, capable of gathering paramagnetic centers within molecular clusters with a predetermined nuclearity and topology, are shown to be suitable for addressing this challenge. In that sense, the characteristics of the ligand H₄L1 can be exploited to achieve new architectures that belong to the above definition (Figure IV.1, top), since it contains two separated groups of coordination pockets (Sections 1 and 2 of this chapter). The main goal for using this ligand is the synthesis of new assemblies of linear chains of paramagnetic metals disposed as two separated dimers, and the study of the magnetic properties of these targeted systems. Previous work carried out in the group revealed that the use of acetates as metal salts was enough for removing only the protons from the β -diketone units. Thus, when using the acetate of Mn^{II}, Co^{II}, Ni^{II}

or Cu^{II} , dinuclear entities were obtained and characterized (Figure IV.1, bottom, left).^[5] It seems clear then that in order to prepare the targeted tetranuclear clusters, a stronger base in the media is needed. If such tetranuclear architectures can be achieved, the disposition of the metallic centers would exhibit a pair of dimers, and it would open the possibility of exploiting each well-defined cluster as a potential qubit (Figure IV.1, bottom, right).

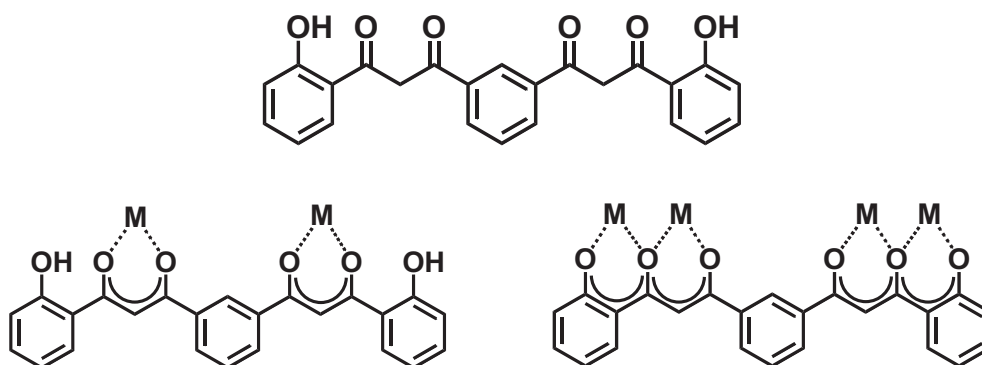


Figure IV.1. Schematic representation of ligand $\text{H}_4\text{L1}$ and possible coordination modes.

On the other hand, $\text{H}_4\text{L2}$ and $\text{H}_2\text{L3}$ are multidentate ligands that alternate three phenol and/or pyridyl donors with two β -diketone groups, affording a linear array of donor atoms. This linear topology, together with some heterometallic linear clusters obtained with similar pyridyl/ β -diketone ligands,^[6-8] suggests the formation of longer heterometallic molecular chains combining lanthanide ions and transition metal centres (Figure IV.2).

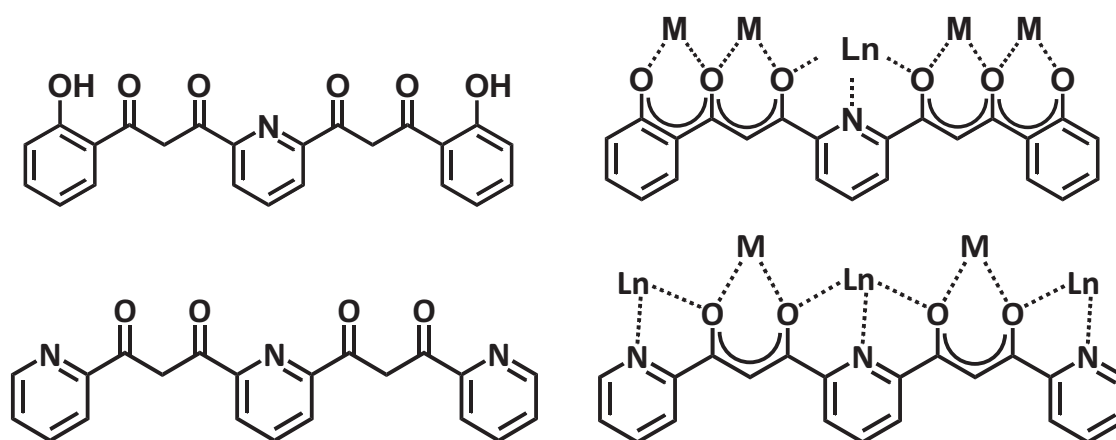


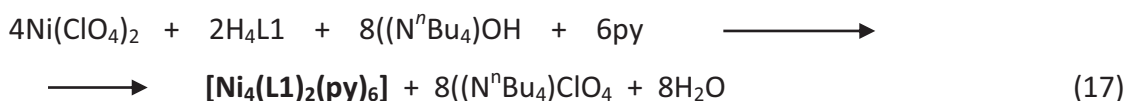
Figure IV.2. Schematic representation and possible coordination mode of ligands $\text{H}_4\text{L2}$ (top) and $\text{H}_2\text{L3}$ (bottom).

As it will be described in this chapter, H₂L3 facilitates the formation of molecular assemblies that can be used as building blocks for the assembly of architectures comprising two units (Section 3). This approach can be seen as a new strategy for the design of molecules featuring two weakly coupled clusters.

2. Homometallic tetranuclear [MM...MM] clusters

2.1. Synthesis and study of the crystal structures

One of the main goals when designing ligand H₄L1 was to induce the formation of linear tetranuclear clusters disposed as two pairs of interacting metals. This objective is targeted by disposing arrays of adjacent O-based chelating pockets, with a benzene group as spacer in the middle. As previously introduced, one special property of H₄L1 is the difference in acidity between the two different ionisable protons in the molecule. Since the acetate anion can only remove the β-diketone protons, a stronger base was chosen to deprotonate the phenol groups in both sides of the ligand and promote tetranuclear architectures. Following this strategy, the organic hydroxide (NⁿBu₄)OH was used to obtain the fully deprotonated ligand L1⁴⁻. Thus, the reaction in pyridine of two equivalents of Ni(ClO₄)₂ with H₄L1 and four equivalents of (NⁿBu₄)OH leads to a yellow solution that produces yellow crystals of the complex [Ni₄(L1)₂(py)₆] (**4**) after layering with MeOH:



The crystallographic structure of **4** belongs to the monoclinic P2₁/n space group (cell parameters are listed in Table IV.A1, Appendix). The structure reveals a neutral complex of four Ni^{II} ions coordinated equatorially by two fully deprotonated μ₄:η⁶-L1⁴⁻ ligands disposed in opposite sides of the complex. Each ligand coordinates four metals, accommodated by four pair-wise adjacent coordination pockets, using two β-diketonate and two phenolate groups. The metals are consequently distributed in two closed pairs (see Figure IV.3) in a nearly linear topology. The coordination polyhedra of the four Ni^{II} ions in the cluster are completed by six pyridine molecules occupying the

axial positions. Interestingly, the geometry of the nickel ions within the Ni₂ pair is dissimilar. The metal ions at both ends of the complex are five-coordinated, exhibiting a square-pyramidal geometry with only one molecule of pyridine as axial ligand, arranged in an opposite side comparing both ends.

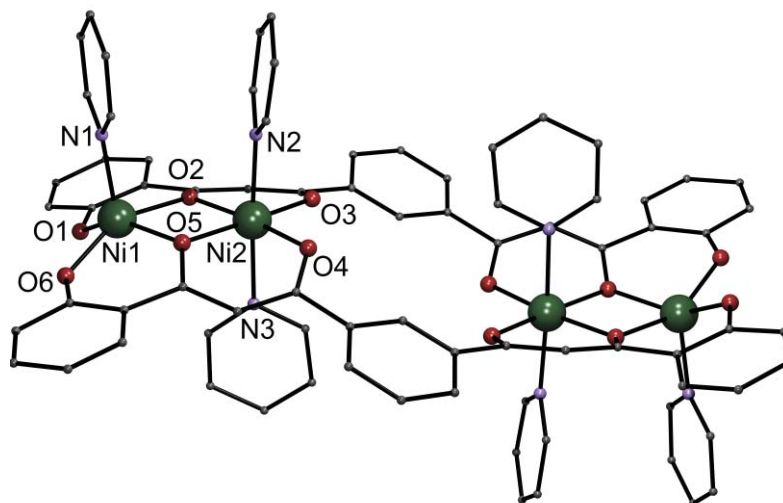


Figure IV.3. Representation of the molecular structure of the complex [Ni₄(L1)₂(py)₆] (**4**). Dark green, Ni; violet, N; red, O; rest, C. H atoms excluded.

The inner metals, by contrast, are six-coordinated, binding two molecules of pyridine and exhibiting a distorted octahedral geometry. The origin of this unusual feature could be caused by geometric constraints of the L1⁴⁻ ligand, which prevents the external Ni^{II} ions to accept the second pyridine molecule, avoiding its most common octahedral geometry. A detailed assessment of the geometric parameters in the complex reveals a difference between the C-C-C angles within both types of chelating rings (1,3-diketonate versus 2-hydroxybenzoyl), as depicted in Figure IV.4, left. The C atoms involved in the chelating moiety formally exhibit sp² hybridization, which represents angles of 120° when no restraints affect to the ligand. However, the process of coordination causes departures from this angle to accommodate the Ni^{II} ions. While 1,3-diketonate can adapt such departure, reaching an angle of 128°, the 2-hydroxybenzoyl frame forces an angle C-C-C of 122° that prevents the external nickel ions of complex **3** to be accommodated in the equatorial plane of the four oxygen atoms.

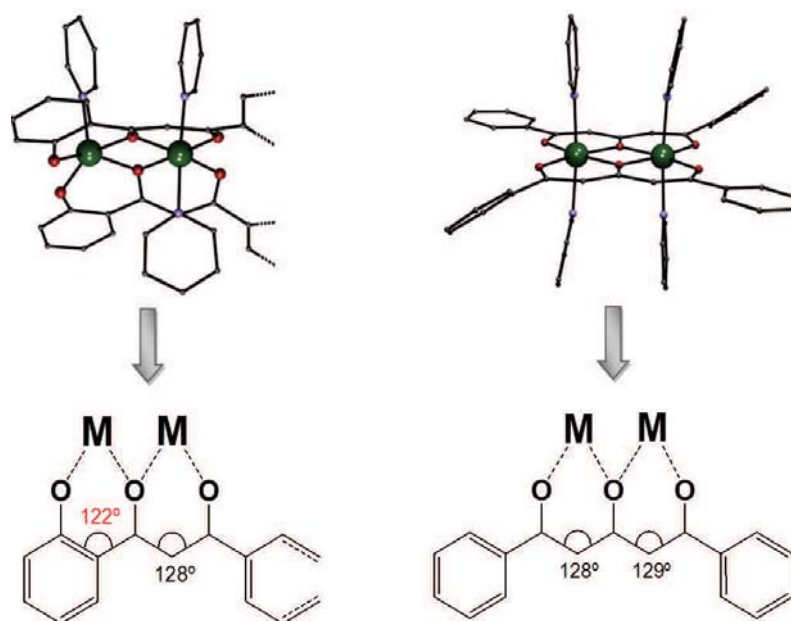


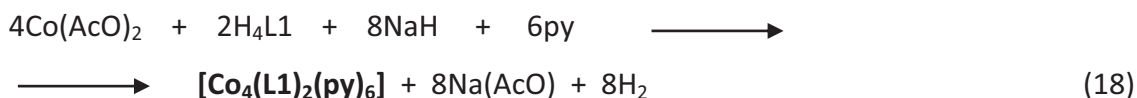
Figure IV.4. Representation of the molecular structure of the complex $[\text{Ni}_2(\text{DBA})_2(\text{py})_4]$ (right) and half molecule of complex **4** (left) with schematic representation of each ligand emphasizing C-C-C angles (1,3-diketonate and 2-hydroxybenzoyl). Colours as Figure IV.3.

Consequently, the two contiguous planes form a mutual angle of $5.1(5)^\circ$ that blocks the entry to one of the axial ligands, leading the five-coordination. This feature can be evaluated comparing complex **3** with reported dinuclear complexes of the type $[\text{Ni}_2(\text{L}')_2(\text{py})_4]$ ($\text{H}_2\text{L}' = 1,3,5\text{-triketone ligand}$).^[9, 10] For example, complex $[\text{Ni}_2(\text{DBA})_2(\text{py})_4]$ (Figure IV.4, right, $\text{DBA}^{2-} = \text{dibenzoylacetone}$) exhibits two Ni^{II} ions with a topology very close to that exhibited by each $[\text{Ni}_2]$ part of complex **4**. However, the triketonate ligand DBA is not restricted by a 2-hydroxybenzoyl group as it occurs in the ligand $\text{H}_4\text{L1}$, providing more flexibility to the complex at both chelate rings. This feature allows both ketonate groups to reach angles C-C-C of 128 and 129° and to accommodate each Ni^{II} ion within the plane of the four oxygen donor atoms. Thus, in this case, both metals have enough room to adopt the six-coordination.

Compound **4** displays a sinusoidal conformation, with a $\text{Ni}\cdots\text{Ni}$ distance within the $[\text{Ni}_2]$ pairs of $3.098(2) \text{ \AA}$. In between pairs, the intramolecular metal-metal distance is $7.279(3) \text{ \AA}$. A list of selected metric parameters is shown in Table IV.1.

Ni1-O1	1.920(6)	O5-Ni1-O6	87.6(2)
Ni1-O2	2.067(5)	O5-Ni1-N1	99.8(3)
Ni1-O5	2.073(5)	O6-Ni1-N1	113.6(3)
Ni1-O6	1.928(6)	O2-Ni2-O3	91.4(2)
Ni1-N1	2.027(8)	O2-Ni2-O4	172.4(2)
Ni2-O2	2.010(5)	O2-Ni2-O5	82.8(2)
Ni2-O3	1.989(6)	O2-Ni2-N2	90.9(2)
Ni2-O4	1.994(5)	O2-Ni2-N3	90.3(3)
Ni2-O5	2.045(5)	O3-Ni2-O4	96.0(2)
Ni2-N2	2.080(8)	O3-Ni2-O5	173.9(2)
Ni2-N3	2.119(8)	O3-Ni2-N2	89.0(3)
O1-Ni1-O2	86.6(2)	O3-Ni2-N3	87.4(3)
O1-Ni1-O5	148.9(2)	O4-Ni2-O5	89.7(2)
O1-Ni1-O6	90.5(3)	O4-Ni2-N2	90.7(3)
O1-Ni1-N1	109.3(3)	O4-Ni2-N3	88.6(3)
O2-Ni1-O5	80.8(2)	O5-Ni2-N2	93.1(3)
O2-Ni1-O6	151.7(2)	O5-Ni2-N3	90.7(3)
O2-Ni1-N1	93.8(3)	N2-Ni2-N3	176.1(3)

Following the same strategy, attempts to reproduce similar assemblies with other interesting divalent metals were carried out. In that sense, H₄L1 was made react with four equivalents of NaH for its full deprotonation and with two equivalents of Co(AcO)₂ in pyridine. After heating to reflux, and layering the resulting solution with ether, compound [Co₄(L1)(py)₆] (5) was obtained as orange crystals.



As in the former tetranuclear Ni^{II} analogue, the structure of this complex features four Co^{II} ions disposed in a linear fashion as two independent pairs, which demonstrates that both ligands have been completely deprotonated (Figure IV.5). Again, both deprotonated ligands coordinate the metals in a $\mu_4:\eta^6\text{-L1}^{4-}$ mode from two opposite sides of the complex, occupying all the equatorial positions. The remaining axial coordination sites of the Co^{II} ions are compensated by pyridine terminal ligands. As observed in compound **4**, the Co^{II} ions exhibit two different coordination numbers. Thus, while the external cobalt atoms are five-coordinated with an O₄N environment

(geometry halfway between square pyramidal and trigonal bipyramidal; $\tau = 0.53$),^[11] the central metals exhibit a distorted octahedral geometry (O_4N_2 environment). Again, the ligand's constraints induce the disparity in the coordination geometry between external and central metals, blocking the entrance of a second molecule of pyridine in the external Co^{II} ions. The distance between centres within the Co-Co dimers is 3.160(1) Å, whereas the shortest $Co \cdots Co$ distance between pairs is 6.962(1) Å.

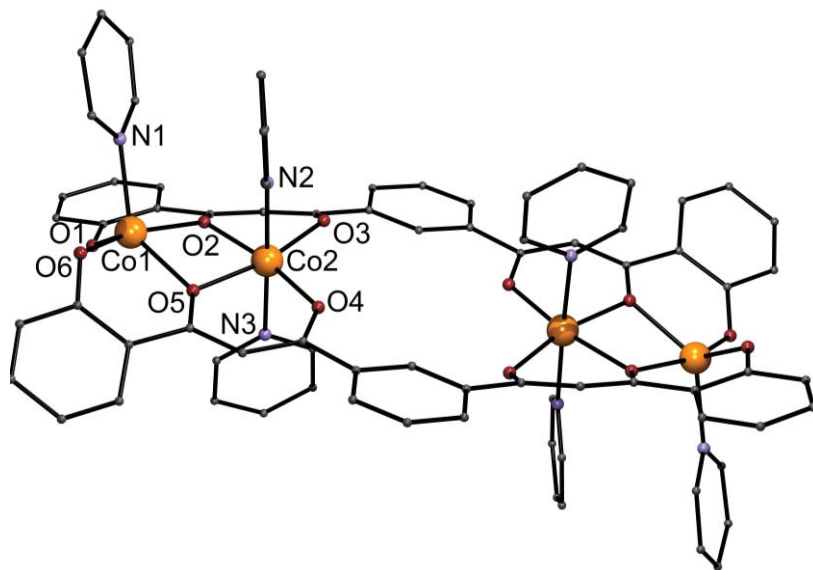


Figure IV.5. Representation of the molecular structure of the complex $[Co_4(L1)_2(py)_6]$ (**5**). Orange, Co; violet, N; red, O; rest, C. H atoms excluded.

The crystallographic structure of **5** belongs to the triclinic P-1 space group (cell parameters are listed in Table IV.A1, Appendix). Bond lengths and angles are listed in Table IV.2. The aromatic rings present in **5** are involved in the packing of its molecules through van der Waals and π -stacking interactions. Along the crystallographic a axis, interactions between the aromatic rings belonging to the $L1^{4-}$ ligand connect molecules featuring a chain, whereas in the b axis, the molecules pack with the help of π - π interactions between pyridine axial ligands (Figure IV.6).

This new tetranuclear complex is one of the few linear cobalt clusters in the literature. Although around two hundred $[Co_4]$ clusters have been reported, only very few examples have been found as linear strings of four cobalt ions,^[12-14] confirming the rarity of this kind of discrete linear clusters in coordination chemistry.

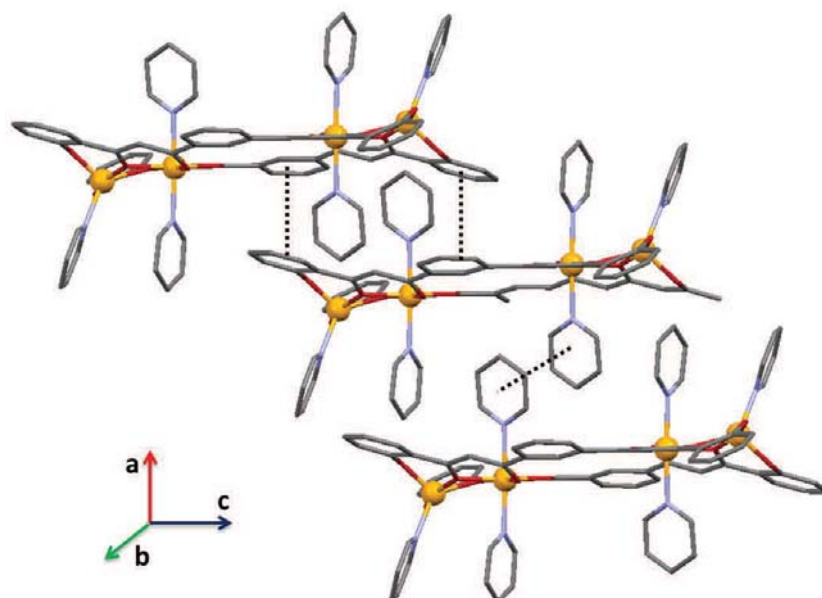


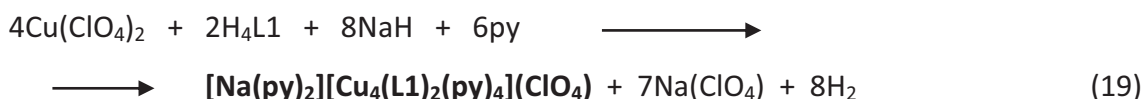
Figure IV.6. Representation of the crystal packing of the complex $[\text{Co}_4(\text{L1})_2(\text{py})_6]$ (**5**), featuring π - π stacking in the a and the b axis (dashed black lines). Orange, Co; violet, N; red, O; rest, C. H atoms excluded.

Table IV2. Selected interatomic distances [Å] and angles [°] for $[\text{Co}_4(\text{L1})(\text{py})_6]$ (**5**)

Co1-O6	1.925(3)	O1-Co1-O5	162.07(13)
Co1-O1	1.931(3)	O2-Co1-O5	78.65(12)
Co1-O2	2.109(3)	N1-Co1-O5	92.28(16)
Co1-N1	2.121(5)	O3-Co2-O4	103.67(13)
Co1-O5	2.137(3)	O3-Co2-O2	88.90(13)
Co2-O3	1.991(3)	O4-Co2-O2	167.13(13)
Co2-O4	1.992(3)	O3-Co2-O5	170.23(13)
Co2-O2	2.060(3)	O4-Co2-O5	85.99(12)
Co2-O5	2.061(3)	O2-Co2-O5	81.54(12)
Co2-N2	2.157(4)	O3-Co2-N2	92.74(14)
Co2-N3	2.204(4)	O4-Co2-N2	88.45(15)
O6-Co1-O1	112.40(15)	O2-Co2-N2	88.15(15)
O6-Co1-O2	125.37(15)	O5-Co2-N2	88.95(14)
O1-Co1-O2	84.06(13)	O3-Co2-N3	90.62(14)
O6-Co1-N1	101.10(17)	O4-Co2-N3	90.04(15)
O1-Co1-N1	95.26(17)	O2-Co2-N3	92.65(15)
O2-Co1-N1	130.03(17)	O5-Co2-N3	87.85(14)
O6-Co1-O5	81.90(13)	N2-Co2-N3	176.56(14)

An analogous reaction was explored using Cu^{II} , which is one of the most employed transition metals in molecular magnetism due to the simplicity of its magnetic

behavior (only one unpaired electron). Such behavior usually facilitates the modelization of the magnetic exchange in a molecular system. In this case, the reaction was performed with $\text{Cu}(\text{ClO}_4)_2$ in pyridine and using sodium hydride for the fully deprotonation of the $\text{H}_4\text{L1}$ ligand (2:6:1 molar ratio). The reaction, once layered with ethyl acetate, yields orange crystals of the related complex $[\text{Na}(\text{py})_2][\text{Cu}_4(\text{L1})_2(\text{py})_4](\text{ClO}_4)$ (**6**):



The structure of this compound belongs to the monoclinic $\text{C2}/c$ space group, and is described as a polymer of discrete and neutral entities formulated as $[\text{Cu}_4(\text{L1})_2(\text{py})_4]$ (Figure IV.7). These moieties are linked to each other by their external oxygen atoms through Na^+ ions, which in turn are coordinated to two pyridine molecules each, featuring an octahedral geometry (Figure IV.8). The extra positive charge of sodium in the complex is compensated with perchlorate anions.

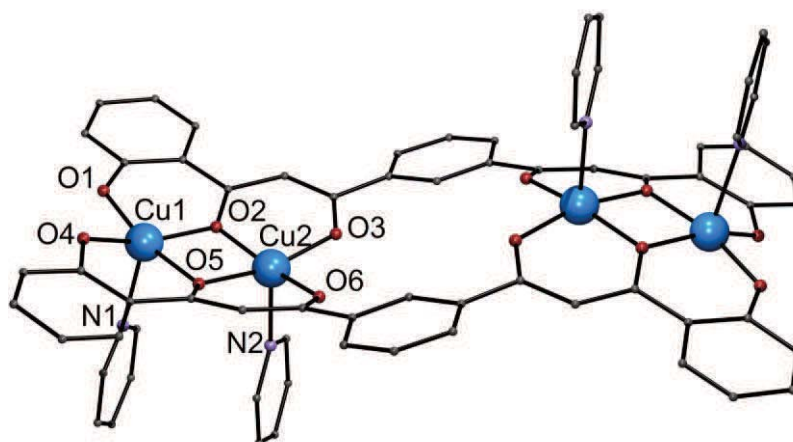


Figure IV.7. Representation of the molecular structure of the neutral moiety $[\text{Cu}_4(\text{L1})_2(\text{py})_6]$ of **6**. Blue, Cu; violet, N; red, O; rest, C. H atoms excluded.

The neutral moiety $[\text{Cu}_4(\text{L1})_2(\text{py})_4]$ exhibits four copper(II) ions that are coordinated by two L1^{4-} ligands in both sides of the metal array, as it occurs in compounds **4** and **5**. However, in this case the axial positions of all Cu^{II} ions are occupied by only one solvent pyridine ligand completing a square-pyramidal geometry, very common with

this metal. The inner metals exhibit a value of $\tau = 0.13$, while the Cu^{II} in both ends are described almost as perfect square-pyramids ($\tau = 0.01$). The distance within each metal pair is $3.075(2) \text{ \AA}$, and each dimer is separated by $7.563(2) \text{ \AA}$. The cationic $([\text{Na}(\text{py})_2]_n[\text{Cu}_4(\text{L1})_2(\text{py})_4]_n)^{n+}$ 1D chain grows along the crystallographic ac direction, as shown in Figure IV.8. Near such chains, ClO_4^- anions are located within the channels, which are disposed in the same direction. A complete list of selected metric parameters for compound **6** is in Table IV.3. Crystallographic parameters are shown in Table IV.A1 (Appendix).

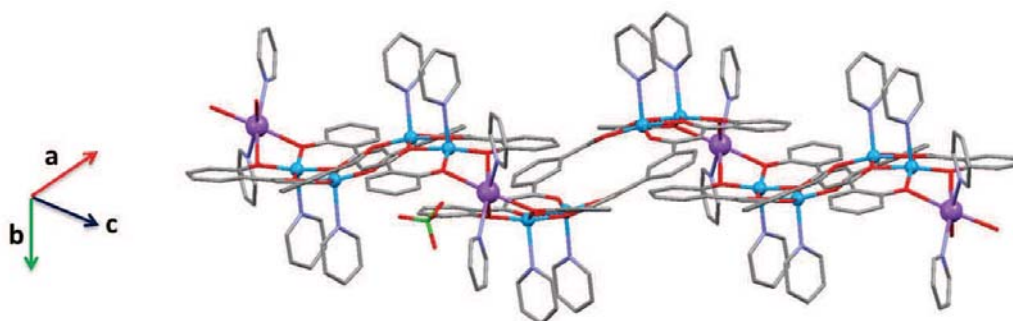


Figure IV.8. Representation of the molecular structure of $[\text{Na}(\text{py})_2][\text{Cu}_4(\text{L1})_2(\text{py})_6](\text{ClO}_4)$ (**6**) emphasizing the link between $[\text{Cu}_4(\text{L1})_2(\text{py})_4]$ neutral moieties by Na cations leading a 1D polymer. Blue, Cu; dark violet, Na; red, O; violet, N; green, Cl, rest, C. H atoms excluded.

Table IV.3. Selected interatomic distances [\AA] and angles [$^\circ$] for $[\text{Na}(\text{py})_2][\text{Cu}_4(\text{L1})_2(\text{py})_6](\text{ClO}_4)$ (**6**)

Cu1-O1	1.928(5)	O2-Cu1-N1	97.0(2)
Cu1-O2	2.005(5)	O5-Cu1-N1	90.79(18)
Cu1-O5	2.029(5)	O3-Cu2-O4	91.4(2)
Cu1-O6	1.944(5)	O3-Cu2-O5	165.2(2)
Cu1-N1	2.337(4)	O4-Cu2-O5	91.6(2)
Cu2-O2	2.022(5)	O3-Cu2-O2	93.2(2)
Cu2-O3	1.956(6)	O4-Cu2-O2	165.6(2)
Cu2-O4	1.965(5)	O5-Cu2-O2	80.7(2)
Cu2-O5	2.012(5)	O3-Cu2-N2	94.7(3)
Cu2-N2	2.303(5)	O4-Cu2-N2	100.3(3)
Na1-O1	2.513(6)	O5-Cu2-N2	98.9(2)
Na1-O6	2.444(5)	O2-Cu2-N2	92.9(2)
Na1-N3	2.627(5)	O6-Na1-O1	67.47(17)

Cu1-Na1	3.381(3)	O6-Na1-O6#	162.2(3)
O1-Cu1-O6	90.6(2)	O6-Na1-O1#	98.25(19)
O1-Cu1-O2	92.3(2)	O1-Na1-O1#	78.6(3)
O6-Cu1-O2	160.1(2)	O6-Na1-N3	87.86(16)
O1-Cu1-O5	168.1(2)	O6-Na1-N3#	104.21(17)
O6-Cu1-O5	92.8(2)	O1-Na1-N3	93.71(16)
O2-Cu1-O5	80.7(2)	O1-Na1-N3#	167.35(18)
O1-Cu1-N1	99.6(2)	Cu1-O2-Cu2	99.6(2)
O6-Cu1-N1	101.89(19)	Cu2-O5-Cu1	99.1(2)
Cu1-O6-Na1	100.2(2)	Cu1-O1-Na1	98.3(2)

(The suffix # denotes atoms generated by symmetry operation (-x, -y, -z))

2.2. Study of the redox activity

The electrochemical properties of tetranuclear compounds **4** and **5** ($[\text{Ni}_4]$ and $[\text{Co}_4]$, respectively) were evaluated by cyclic voltammetry and square-wave voltammetry. All measurements were carried out in DMF at ambient temperature using TBA.PF_6 as supporting electrolyte, in an air-free conditions, with a conventional three-electrode configuration consisting of one platinum wire as the auxiliary electrode, one silver wire as reference electrode, and a working glassy carbon (GC) electrode (1 mm diameter). The ferrocene/ferrocenium (Fc/Fc^+) couple was used as internal reference. All electrochemical measurements presented in this chapter were carried out within a three months stay in the Electrochemistry Group of Monash University (Melbourne, Australia) under the supervision of Prof. Alan Bond.

The cyclic voltammogram of compound **4** $[\text{Ni}_4(\text{L1})_2(\text{py})_6]$ (1 mM solution) shows four weak irreversible reduction processes, and an additional one with much higher intensity (Figure IV.9, left). This last peak, which appears at around -3 V vs Fc^+/Fc , can be assigned to the reduction of the pyridine ligands of the complex, since the study of pyridine in the same conditions reveals a reduction peak at similar potentials. A smaller potential window was then chosen to avoid this process, allowing a better study of the four peaks at lower potentials. The first two irreversible reduction processes appear very close to each other (Figure IV.9, left, inner). For a better resolution, this region was investigated through square-wave voltammetry, which

facilitates the characterization of the first two peaks at -1.810 V and at -2.085 V vs fc^+/fc respectively (Figure IV.9, right). When the first peak was studied independently, no further reversibility was observed, thus demonstrating that adding just one electron to the complex must involve important rearrangements in the molecular entity rendering the process irreversible. When going to positive potentials, no oxidation processes were observed.

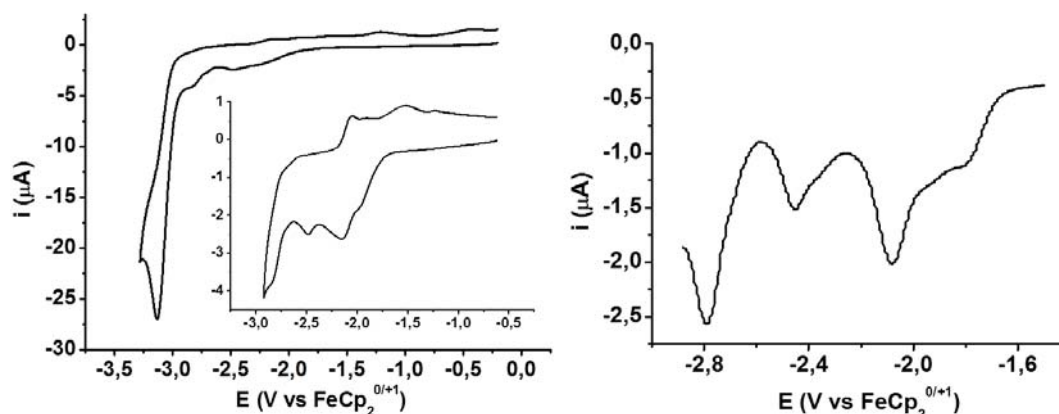


Figure IV.9. Study of the redox activity of $[Ni_4(L1)_2(py)_6]$ (**4**) Left: Cyclic Voltammetry in DMF at room temperature with a scan rate of 100 mVs^{-1} . Right: Squarewave Voltammetry in DMF at room temperature with a frequency of 15 mHz and a step of 4 mV.

The redox activity of compound **5** $[Co_4(L1)_2(py)_6]$ is similar to **4**. Cyclic voltammetry (1.7 mM solution) reflects again the intense reduction process related to the pyridine molecules at very negative potentials (around -3 V vs fc^+/fc , Figure IV.10, left). In addition, four more reduction peaks are observed, which can be characterized when the window is modified (Figure IV.10). In that case, the first peak reveals a reversible process, which demonstrates that this compound affords the introduction of an additional electron to the system. The formal potential $E^{0'}$ is centered at 1.961 V vs fc/fc^+ , while the $\Delta E_p = 0.097\text{ V}$ (see equations 20 and 21).

$$\Delta E_p = E_{pa} - E_{pc} \approx \frac{0.059}{n} \quad (20)$$

$$E^{0'} = \frac{E_{pa} + E_{pc}}{2} \quad (21)$$

For an electrochemically reversible reaction, the separation between E_{pa} and E_{pc} reaches values similar to $0.059/n$ V for a n electron transfer reaction (equation 20).^[15] Larger values of ΔE_p are characteristic of slow electron transfer kinetics, thus approaching irreversible processes. Before this, ΔE_p values up to 0.2 V are considered quasi-reversible processes. Thus, the first reduction process in complex **5** can be considered a quasi-reversible reaction. While showing also reversibility, the following reduction peaks cannot be evaluated due their low resolution. However, when the same window is evaluated using square-wave voltammetry, the second peak shows a two electron process, thus revealing a total of five reduction processes. No oxidation peaks were found when scanning positive potentials.

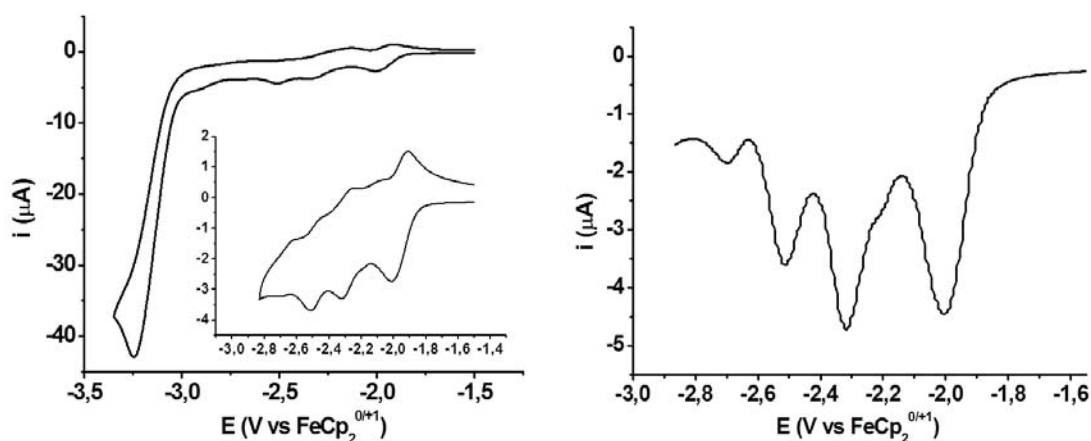


Figure IV.10. Study of the redox activity of $[\text{Co}_4(\text{L1})_2(\text{py})_6]$ (**5**) Left: Cyclic Voltammetry in DMF at room temperature with a scan rate of 100 mVs^{-1} . Right: Squarewave Voltammetry in DMF at room temperature with a frequency of 15 mHz and a step of 4 mV.

2.3. Study of the magnetic behavior

The main objective in the design of these systems is to facilitate the assembly of metallic spin carriers into two weakly coupled aggregates, and the study of each aggregate within the cluster for its application as a quantum bit. The electronic spin within each dimer of the $[\text{MM}\cdots\text{MM}]$ is intended to be a qubit, while in turn, a weak interaction between both dinuclear units is expected. Thus, the magnetic properties of complexes **4**, **5** and **6** were investigated. A first assessment was made through variable-

temperature bulk magnetization measurements on powdered microcrystalline samples.

The results for complex **4**, measured under a constant magnetic field of 1 T, are shown in Figure IV.11 in form of $\chi_M T$ vs T plot, where χ_M is the molar paramagnetic susceptibility. At high temperatures, the product reaches a value of $4.45 \text{ cm}^3 \text{ K mol}^{-1}$, which nearly corresponds to four independent Ni^{II} centers with $g = 2.08$. The values of $\chi_M T$ decrease steadily on cooling down to $0.3 \text{ cm}^3 \text{ K mol}^{-1}$ at 2 K, reflecting the presence of weak antiferromagnetic coupling between the Ni^{II} ions within the $[\text{Ni}_2]$ pairs. This exchange coupling, which occurs through the diketone O double bridge, can be quantified by fitting the susceptibility data with a theoretical $\chi_M = f(T)$ expression derived from the Van Vleck equation:

$$\chi_M = \frac{2Ng^2\beta^2}{kT} \frac{2\exp(J/kT) + 10\exp(3J/kT)}{1 + 3\exp(J/kT) + 5\exp(3J/kT)} \quad (22)$$

As mentioned in Chapter 1, this equation derives from the corresponding Hamiltonian, which in this case is $H = 2x[-2JS_{\text{Ni}1}S_{\text{Ni}2} + gH\beta S_{Tz}]$, where $S_{\text{Ni}1} = S_{\text{Ni}2} = 1$ and S_T is the total spin of one $[\text{Ni}_2]$ pair. No further coupling pathways such as potential $\text{Ni}\cdots\text{Ni}$ interactions *via* the $\text{L}1^{4-}$ ligand or single-ion zero field splitting parameters were included in the analysis, since they are considered to be masked by the main antiferromagnetic interaction. The best fit was obtained for $J = -5.04 \text{ cm}^{-1}$ and $g = 2.08$.

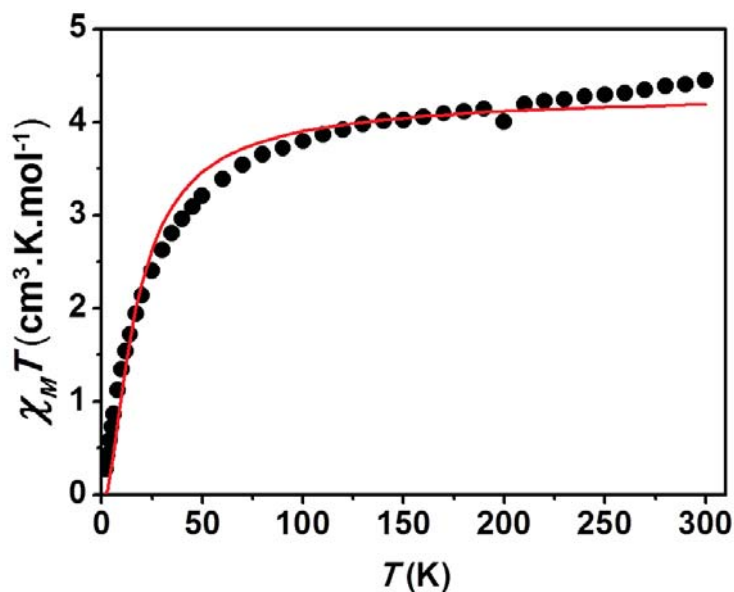


Figure IV.11. Plot of $\chi_M T$ vs T per mol of complex **4** at a constant field of 1 T. The solid red line is the fit to the experimental data (see the text).

The results obtained confirm that the magnetic exchange within the $[\text{Ni}_2]$ pairs is relatively weak. Magneto-structural correlations for alkoxido-bridged Ni^{II} ions indicate that Ni-O-Ni angles smaller than 99° favor ferromagnetic interactions.^[16, 17] The angles observed in **4** are 98° and 99° respectively, thus near the limiting value indicated by the correlations. This can explain the weak antiferromagnetic coupling observed between Ni^{II} ions. It must be pointed out that the correlations mentioned were conducted with all octahedral Ni^{II} centers, not one octahedral ion bridged to a five coordinate one.

A similar magnetic behavior was found when complex **5** ($[\text{Co}_2]_2$) was investigated (Figure IV.12). However, the curve for this complex clearly shows that the magnetic susceptibility is affected by spin-orbit coupling (SOC), since the $\chi_M T$ product reaches a value ($11.1 \text{ cm}^3 \text{ K mol}^{-1}$) higher than expected for a spin-only system (calculated as $7.5 \text{ cm}^3 \text{ K mol}^{-1}$ for four cobalt(II) centers with $S = 3/2$ and $g = 2$). The decline of the $\chi_M T$ values suggests the antiferromagnetic exchange coupling within the metal pairs, as indicated by the low temperature values of $\chi_M T$ ($1.6 \text{ cm}^3 \text{ K mol}^{-1}$ at 2 K). Unfortunately, the SOC hampers the analytical simulation of the data since it involves a Hamiltonian containing both the exchange coupling and parameters from the SOC. This prevents

the possibility of finding an analytical expression for the magnetic susceptibility. Thus, numerical procedures must be carried out involving the full diagonalization of the matrix obtained from such Hamiltonian containing both SOC and exchange coupling.^[18] The assumed antiferromagnetic interaction, which should lead to the vanishing of the total spin momentum for each [Co₂] dimer, would dissipate the possibility of considering each dimer as a qubit, and thus no further calculations have been done.

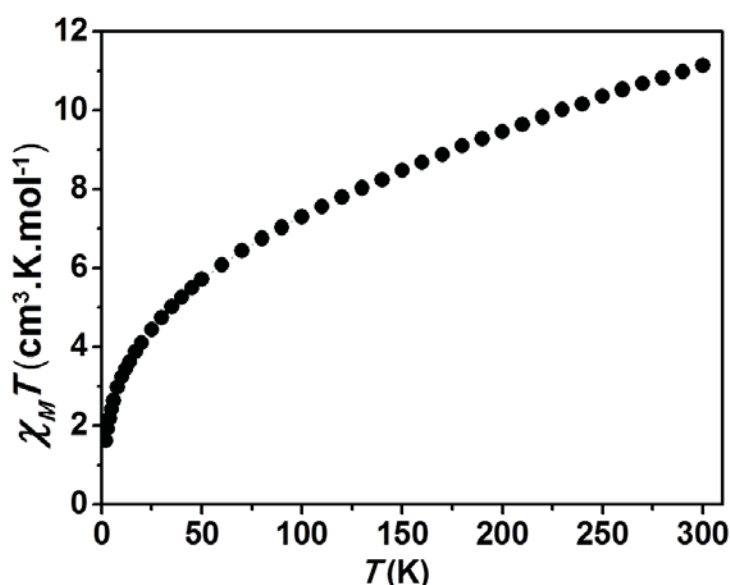


Figure IV.12. Plot of $\chi_M T$ vs T per mol of complex **5** at a constant field of 0.5 T.

The results obtained for **6** ([Cu₂]₂) clearly indicate that the Cu^{II} ions are pairwise strongly coupled (Figure IV.13). Variable temperature magnetization measurements under a constant magnetic field of 1 T reveals a $\chi_M T$ product of 0.67 cm³ K mol⁻¹ at 300 K, significantly lower than the expected for four non-interacting $S = \frac{1}{2}$ centres (1.5 cm³ K mol⁻¹ for $g = 2$). Below 100 K, the magnetic susceptibility falls to a plateau near zero.

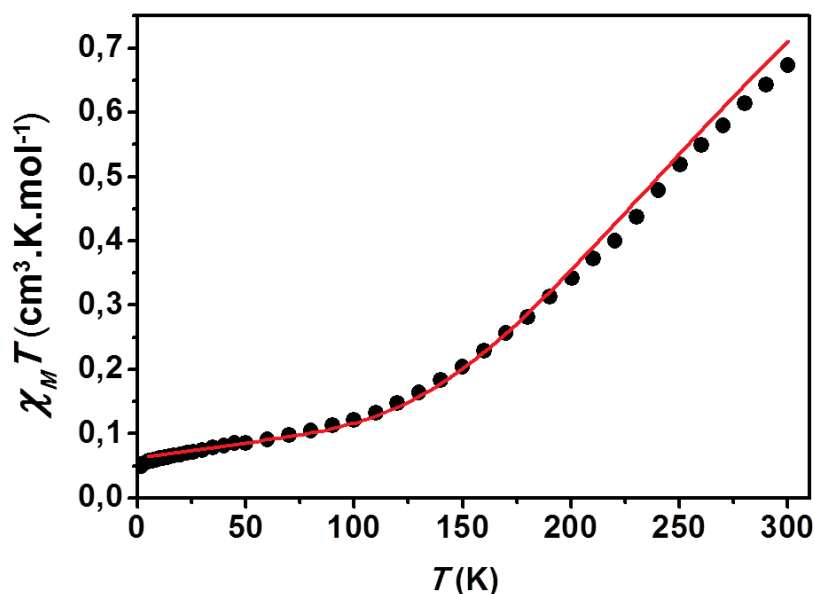


Figure IV.13. Plot of $\chi_M T$ vs T per mol of complex 6 at a constant field of 1 T. The solid red line is the fit to the experimental data (see the text).

The data was fit using the Bleaney-Bowers equation,^[19] defined as a simplification of the Van Vleck equation for two copper(II) ions, considering the spin Hamiltonian $H = 2\chi[-2JS_{Cu1}S_{Cu2} + gH\beta S_{Tz}]$, where $S_{Cu1} = S_{Cu2} = \frac{1}{2}$ and S_T is the total spin of one $[Cu_2]$ pair.

$$\chi_M = \frac{2Ng^2\beta^2}{kT [3 + \exp(-J/kT)]} \quad (23)$$

The best results were found with g fixed at 2.1, which provided $J = -238 \text{ cm}^{-1}$. Its magnitude is in line with the type of interaction expected between Cu^{II} ions bridged at the equatorial position by alkoxide-type moieties and Cu-O-Cu angles near 100° ($99,1^\circ$ and $99,6^\circ$).^[20, 21] The very strong coupling within each $[Cu_2]$ pair prevents the observation of any possible interaction between the central Cu^{II} ions. As in the other two homometallic Ni^{II} and Co^{II} related complexes, each copper pair loses its potential as a qubit prototype due to the vanishing of its spin momentum. Thus, different strategy must be followed to obtain a “pair of clusters” molecule where each dimer could retain an identity as a quantum bit.

3. Site-selective heterometallic [MM'...M'M] clusters

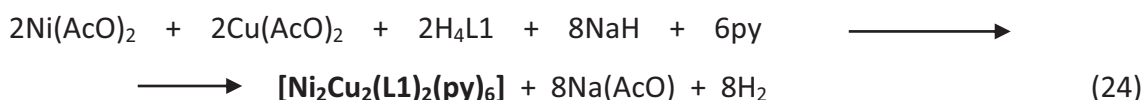
The magnetic characterization of complexes [NiNi...NiNi] (**4**), [CoCo...CoCo] (**5**) and [CuCu...CuCu] (**6**) reveals that these homometallic “pair-of-dimers” cannot fulfill the requirements of a quantum gate. The suppression of the total spin momentum of the system due to the antiferromagnetic interaction within each pair prevents them to embody the electronic spin necessary for their definition as a qubit. Moreover, this behavior impedes the evaluation of a possible entanglement between the spin wave functions of both parts of the molecule, and thus the study of this kind of system as a prototype of a double qubit quantum gate.

On the other side, the crystallographic study of these systems has confirmed the ability of H₄L1 to design dinuclear or tetranuclear species with a predetermined topology. While the linear conformation is induced by the structure of the ligand, the nuclearity may be controlled by using bases with the appropriate strength. In addition, this study has revealed the origin of a site-dependent coordination number. In complexes **4** and **5**, the geometric features of the ligand induce a difference in coordination geometry between neighboring metals, observing an octahedral coordination for the inner ions and a five-coordination for the centers at the ends. For Cu^{II} (complex **6**), the structural characteristics of L1⁴⁻ lead naturally to the formation of four square-pyramidal environments, a preferred geometry for this ion, which is not prevented by the constraints imposed by the ligand at any site of the complex. This phenomenon can thus be exploited for the design of heterometallic clusters with predetermined topology and a site-selective control on the location of the different types of metals within the array. The characteristics of the system suggest that if a metal M with a preference to form square pyramidal polyhedra is mixed in a coordinating solvent with a metal M' that favors the octahedral geometry, under thermodynamic conditions, a heterometallic analogous tetranuclear array with a MM'...M'M sequence should be obtained. Thus, following such strategy, two new [MM'...M'M] linear clusters have been synthesized and studied.

3.1. Synthesis and structural study of [CuNi...NiCu] and [CuCo...CoCu]

The strategy proposed was carried out taking into account the geometric preferences of Ni^{II}, Co^{II} and Cu^{II} ions shown in the corresponding homometallic complexes **4**, **5**, and **6**. Since Cu^{II} ions features a square-pyramidal environment in all the coordination sites, and Ni^{II} and Co^{II} centers adopts both octahedral and five-coordination geometries, with a preference for the former one, it is expected that a mixture of Cu^{II} with Ni^{II} or Co^{II} ions would lead pure [CuNi...NiCu] and [CoCu...CuCo] heterometallic entities.

The reaction of H₄L1 with NaH, Ni(AcO)₂ and Cu(AcO)₂ in pyridine heated at reflux (with a 1:4:1:2 molar ratio) led the formation of yellow crystals of the complex [Ni₂Cu₂(L1)₂(py)₆] (**7**) in pure form and good yield after layering the solution in ether:



Reactions using a stoichiometric amount of Cu(AcO)₂ were found by X-ray crystallography to lead a small percentage (< 10 %) of molecules in the crystal with a vacant Cu^{II} site. Thus, a small excess of this reagent was used to force the reaction to completion. The crystallographic structure of **7** belongs to the tetragonal P4/*ncc* space group (cell parameters are listed in Table IV.A2, Appendix). The structure was obtained using a synchrotron radiation source, which provided strong evidence for the location of each metal (Ni and Cu) in the cluster. Again, the complex exhibits two separated dimers, which in that case are [NiCu] heterometallic pairs, disposed in a linear array leading a tetranuclear entity. The metals lay in the expected [CuNi...NiCu] form, accommodated by two L1⁴⁻ ligands at both sides of the metallic chain that bridge and chelate the metals in the η⁶:μ₄-L1⁴⁻ coordination mode (Figure IV.14).

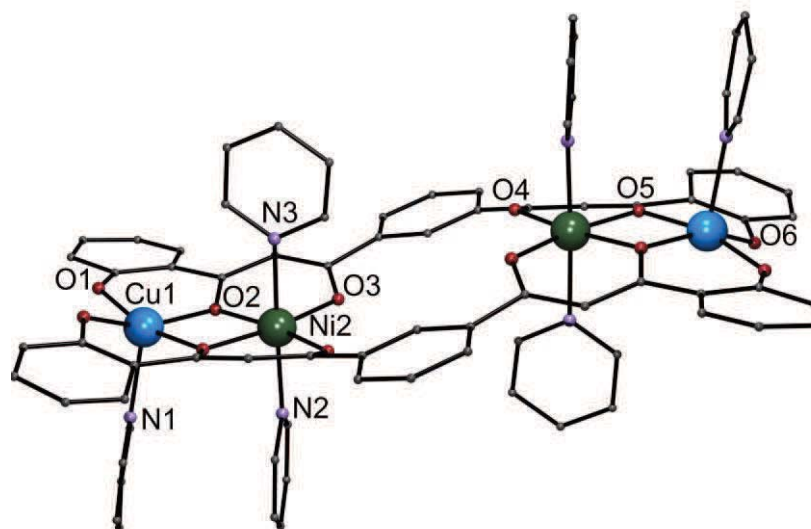


Figure IV.14. Representation of the molecular structure of the complex $[\text{Ni}_2\text{Cu}_2(\text{L1})_2(\text{py})_6]$ (**7**). Dark green, Ni; Blue, Cu; violet, N; red, O; rest, C. H atoms excluded.

The crystal structure reveals the nickel(II) ions at the inner position, with an octahedral coordination sphere due to two pyridine solvent ligands coordinated to the axial positions. The copper(II) centers are situated at the external sites featuring a square pyramidal geometry with only one pyridine molecule coordinated. The intermetallic distance within the dimer $[\text{NiCu}]$ is $3.043(4)$ Å, while both Ni^{II} ions are separated within the molecule by $7.062(6)$ Å. Other important metric parameters are listed in Table IV.4. X-ray diffraction is thus the first evidence that the distribution of the metal ions in **7** shown in Figure IV.14 is the expected one. The refining of the crystal structure has also been carried out distributing the metal centers in the other possible configurations, like $[\text{NiCu}\cdots\text{CuNi}]$, $[\text{NiCu}\cdots\text{NiCu}]$ or $[\text{NiNi}\cdots\text{CuCu}]$. However, these topologies always result in an increase of the $R1$ factor (0.2, 0.3 and 0.6 % respectively). In addition, the metal distribution was further proved by DFT calculations and magnetic measurements (see below), while conductively coupled plasma (ICP) measurements serve to proof a 1:1 composition of Ni and Cu in the bulk. The molecules are disposed in two perpendicular orientations within the crystallographic ab plane, which coincide with the crystallographic a and b directions, respectively (Figure IV.15).

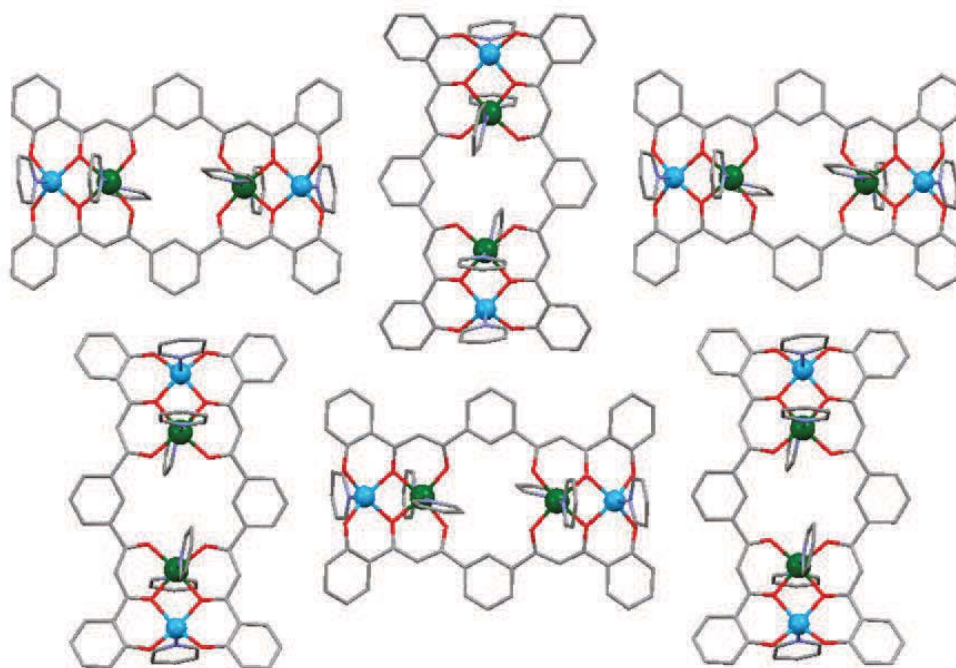


Figure IV.15. Representation of $[\text{Ni}_2\text{Cu}_2(\text{L1})_2(\text{py})_6]$ (**7**) down the c axis. Dark green, Ni; Blue, Cu; violet, N; red, O; rest, C. H atoms and lattice solvents are not shown.

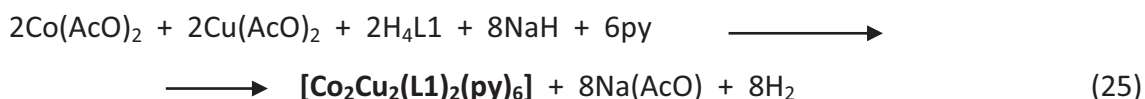
Table IV.4. Selected interatomic distances [\AA] and angles [$^\circ$] for $[\text{Ni}_2\text{Cu}_2(\text{L1})_2(\text{py})_6]$ (**7**)

Cu1-O1	1.887(4)	O2-Ni2-N3	93.29(17)
Cu1-O2	1.979(4)	O5#-Ni2-N3	90.06(18)
Cu1-O5#	1.984(4)	N2-Ni2-N3	176.1(2)
Cu1-O6#	1.894(4)	O1-Cu1-O2	90.72(17)
Cu1-N1	2.197(6)	O1-Cu1-O6#	91.84(19)
Ni2-O2	2.019(4)	O6#-Cu1-O2	156.92(19)
Ni2-O3	1.986(4)	O1-Cu1-O5#	165.5(2)
Ni2-O4#	1.980(4)	O2-Ni2-N2	90.53(19)
Ni2-O5#	2.019(4)	O5#-Ni2-N2	89.70(19)
Ni2-N2	2.100(5)	O4-Ni2-N3	87.72(17)
Ni2-N3	2.162(5)	O3-Ni2-N3	87.55(17)
O4#-Ni2-O3	99.25(15)	O6#-Cu1-O5#	90.26(17)
O4#-Ni2-O2	169.92(15)	O2-Cu1-O5#	81.84(15)
O3-Ni2-O2	90.82(15)	O1-Cu1-N1	99.3(3)
O4#-Ni2-O5#	89.97(15)	O6#-Cu1-N1	103.5(5)
O3#-Ni2-O5#	170.37(15)	O2-Cu1-N1	98.7(2)
O2-Ni2-O5#	80.01(15)	O5#-Cu1-N1	94.2(2)
O4#-Ni2-N2	88.36(19)	Cu1-O2-Ni2	99.11(16)
O3-Ni1-N2	93.33(18)	Cu1-O5#-Ni2	98.93(17)

(The suffix # denotes atoms generated by symmetry operation $(-x, -y, -z)$)

The scarcity of examples of clusters exhibiting a $[\text{Cu}_2\text{Ni}_2]$ composition reported to date reflects the originality of the crystal structure of complex **7**. Moreover, its topology is unprecedented. The closest examples are two $[\text{Ni-Cu-Cu-Ni}]$ linear complexes consisting of two oxamido-based NiCu pairs linked by N_3^- , NCS^- or Cl^- ligands.^[22-24]

Following the same strategy, the reaction between $\text{H}_4\text{L1}$ and NaH , $\text{Co}(\text{AcO})_2$ and $\text{Cu}(\text{AcO})_2$ in pyridine (1:4:1:1 molar ratio) produced orange crystals of complex $[\text{Co}_2\text{Cu}_2(\text{L1})_2(\text{py})_6]$ (**8**) after layering the solution in methanol:



Again, some percentage of vacancy in the Cu site was found by X-Ray crystallography, and the search for the ideal metal proportions is still subject of study. However, the specific location of Co^{II} and Cu^{II} within the cluster was again suggested by the crystal structure of **8** (Figure IV.16), which belongs in this case to the tetragonal $I4/cm$ space group (cell parameters are listed in Table IV.A2, Appendix). The complex exhibits two separated $[\text{CoCu}]$ dimers featuring a tetranuclear linear array, with both metals located in the expected positions $[\text{CuCo}\cdots\text{CoCu}]$. Similarly to complex **7**, the metallic chain is sustained by two ligands in the $\eta^6:\mu_4\text{-L1}^{4-}$ coordination mode. Six pyridine solvent ligands coordinate the axial positions of the complex, completing the preferred coordination sphere of each metal ion (i.e., octahedral for Co^{II} and square pyramidal for Cu^{II}). However, in that case the complex adopts a sinusoidal conformation, since unlike the analogous complexes **4**, **5**, **6** and **7**, both copper(II) ions exhibit their axial pyridine ligand in the same direction.

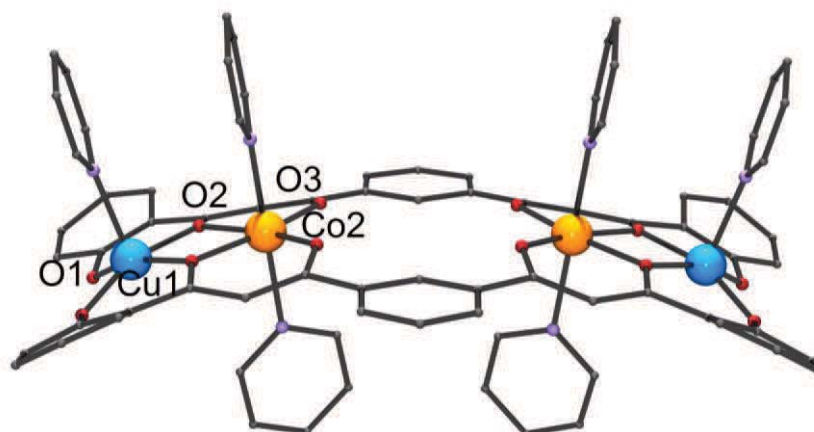


Figure IV.16. Representation of the molecular structure of the complex $[\text{Co}_2\text{Cu}_2(\text{L1})_2(\text{py})_6]$ (**8**). Orange, Co; Blue, Cu; violet, N; red, O; rest, C. H atoms excluded.

The $\text{Co}\cdots\text{Cu}$ distances are $3.0744(10)$ Å, whereas the Co^{II} ions are separated within the molecule by $6.8107(16)$ Å. A complete list with metric parameters is shown in Table IV.5. In the literature, no similar structures featuring $[\text{Cu}-\text{Co}\cdots\text{Co}-\text{Cu}]$ in the oxidation state +2 have been found, which demonstrates again the novelty of this kind of molecular architectures. As it has been observed in **7**, the crystal packing of **8** shows the complex disposed with the molecular plane parallel to the crystallographic ab plane, and the axis oriented in two perpendicular directions coinciding with the crystallographic a and b directions, respectively (Figure IV.17).

Table IV.5. Selected interatomic distances [Å] and angles [°] for $[\text{Co}_2\text{Cu}_2(\text{L1})_2(\text{py})_6]$ (**8**)

Cu1-O1	1.875(4)	O3-Co2-O2	87.89(12)
Cu1-O2	1.982(3)	O3-Co2-O2	166.78(13)
Cu1-N1	2.213(8)	O2-Co2-O2	78.90(17)
Co2-O3	1.964(3)	O3-Co2-N2	89.42(17)
Co2-O2	2.054(3)	O2-Co2-N2	90.98(18)
Co2-N2	2.165(8)	O3-Co2-N3	90.43(17)
Co2-N3	2.261(5)	O2-Co2-N3	89.20(18)
O1-Cu1-O1	90.6(3)	N2-Co2-N3	179.69(14)
O1-Cu1-O2	90.30(15)	Cu1-O2-Co2	99.23(12)
O1-Cu1-O2	160.29(19)	O1-Cu1-N1	104.2(2)
O2-Cu1-O2	82.40(17)	O2-Cu1-N1	94.64(18)
O3-Co2-O3	105.32(18)		

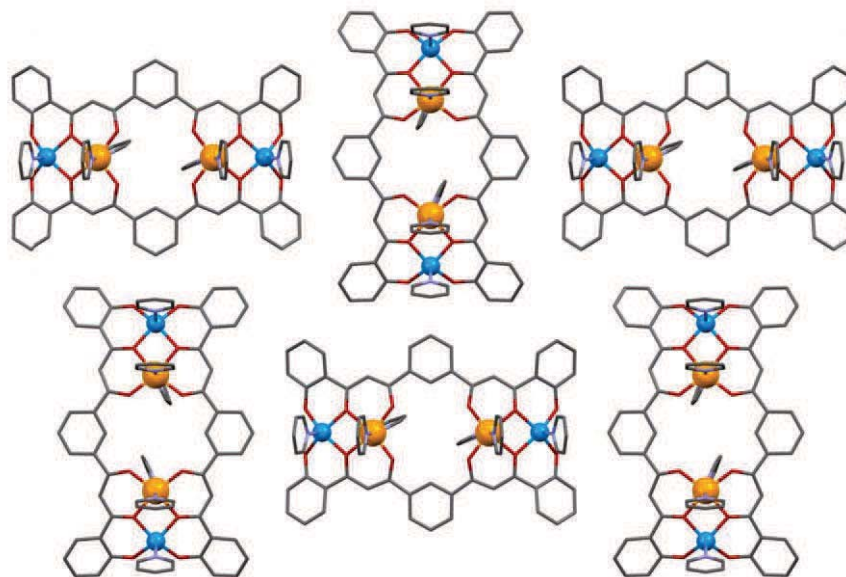
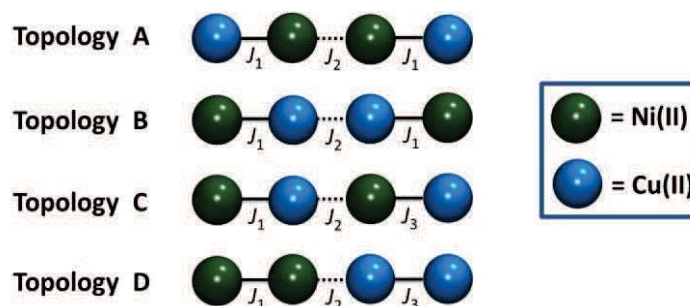


Figure IV.17. Representation of the crystal packing of $[\text{Co}_2\text{Cu}_2(\text{L1})_2(\text{py})_6]$ (**8**) down the c axis. Orange, Co; Blue, Cu; violet, N; red, O; rest, C. H atoms and lattice solvents are not shown.

3.2. Study of the metal composition of $[\text{CuNi}\cdots\text{NiCu}]$

The composition and distribution of the different metal ions within the array in complex **7** was examined in detail through inductively coupled plasma (ICP) measurements and Density functional theory (DFT) calculations. In spite that the structural refinement strongly indicates the predicted metallic distribution, the high similarity between the Ni^{II} and Cu^{II} ions forces a further examination of the site-selective organization of these centres within the molecule. First, the 1:1 molar ratio observed for single crystals of **7** was shown to remain in the bulk, since ICP measurements revealed a Ni/Cu molar ratio of 1.02. Once the metals were confirmed to be in the same ratio, different topologies for the structure of **7** were investigated through DFT calculations, considering the possible distributions $[\text{CuNi}\cdots\text{NiCu}]$, $[\text{NiNi}\cdots\text{CuCu}]$, $[\text{CuNi}\cdots\text{CuNi}]$ and $[\text{NiCu}\cdots\text{CuNi}]$ within the structure determined by single crystal X ray diffraction (see Scheme IV.17).



Scheme IV.17. Metal topologies used for DFT calculations with the structure of the complex $[\text{Ni}_2\text{Cu}_2(\text{L}1)_2(\text{py})_6]$ (**7**).

The calculations were conducted by Dr. Jordi Ribas-Ariño, from Universitat de Barcelona, with the Gaussian 03 program using the B3LYP functional. The energy of the spin ground states of each of the four topologies were evaluated in an indirect way by the difference in energy between the high-spin state (accessible through DFT calculations) and the spin ground state using the calculated magnetic coupling constants (J). The computed relative energies of the spin ground state for these topologies were 0 cm^{-1} (0 kcal mol^{-1}), 7696 cm^{-1} ($21.99 \text{ kcal mol}^{-1}$), 7194.5 cm^{-1} ($20.56 \text{ kcal mol}^{-1}$) and 14088.0 cm^{-1} ($40.26 \text{ kcal mol}^{-1}$) for topologies A, B, C and D respectively. Therefore, the stability of the topology observed by X-Ray diffraction (Topology A) is of the order of magnitude of a weak covalent bond over the one immediately above, demonstrating the stability of this metallic distribution over the rest. Table IV.6 contains the spin ground states and their relative energies, together with the coupling constants calculated for the four studied distributions (Scheme IV.17).

Table IV.6. Spin ground states, relative energies and coupling constants calculated for topologies A, B, C and D.

Topology	S ^[a]	E ^[b] [cm^{-1}] ([kcal mol^{-1}])	J_1 ^[c] [cm^{-1}]	J_2 ^[c] [cm^{-1}]	J_3 ^[c] [cm^{-1}]
A	0	0	-49.60	-0.04	-
B	0	14087.99 (40.26)	-72.90	-0.28	-
C	1	7194.54 (20.56)	-72.45	-0.10	-49.60
D	0	7696.65 (21.99)	-12.55	-0.10	-125.30

[a] Spin ground state. [b] Energy of the ground state. [c] The convention used for the spin-coupling Hamiltonian is $H = -2JS_iS_j$

The J values obtained for the topology assigned to complex **7** ([CuNi...NiCu], topology A) are in good agreement with the experimental magnetic data obtained (see below). Moreover, the magnetic exchange calculated within the pairs of closely spaced metals follows the gradation observed experimentally for compounds [NiNi...NiNi] (**4**), [CuCu...CuCu] (**6**) and [CuNi...NiCu] (**7**) ($0 > J_{\text{Ni...Ni}} > J_{\text{Cu...Ni}} > J_{\text{Cu...Cu}}$), as will be discussed in section 3.4.

3.3. Study of the redox activity of [CuNi...NiCu]

The tetranuclear compound **7** was studied by cyclic voltammetry and square-wave voltammetry. All measurements were carried out in the same conditions as the analogous complexes **4**, **5** and **6** (DMF at ambient temperature, TBA.PF₆ as supporting electrolyte, air-free conditions, and a conventional three-electrode configuration consisting of one platinum wire as the auxiliary electrode, one silver wire as reference electrode, and a working glassy carbon (GC) electrode (1 mm diameter)). Again, the ferrocene/ferrocenium (Fc/Fc⁺) couple was used as internal reference.

Cyclic Voltammetry of compound [Ni₂Cu₂(py)₆] **7** (1 mM solution) shows an intense reduction process from the pyridine ligands at very negative potentials (-3.2 V vs fc⁺/fc), as observed in previous complexes (Figure IV.18, left). In addition, several reduction processes occurs with a very low intensity, which can be studied in more detail when the window is reduced (Figure IV.18, left, inset).

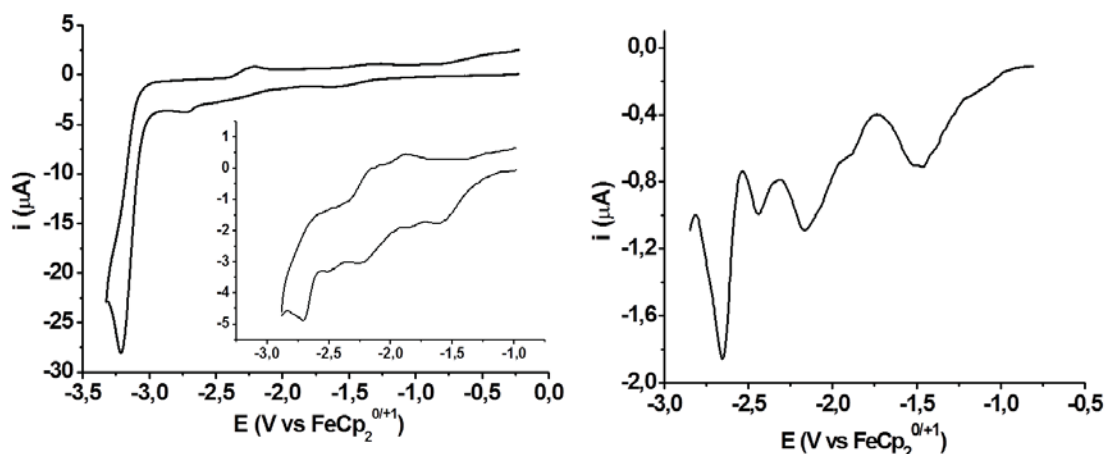


Figure IV.18. Study of the redox activity of $[\text{Ni}_2\text{Cu}_2(\text{L1})_2(\text{py})_6]$ (**7**) Left: Cyclic Voltammetry in DMF at room temperature with a scan rate of 100 mVs^{-1} . Right: Squarewave Voltammetry in DMF at room temperature with a frequency of 15 mHz and a step of 4 mV.

The first reduction process appears around $-1.3 \text{ V vs fc}^+/\text{fc}$ as an irreversible process, which demonstrates that this heterometallic cluster cannot support an additional electron in the system, and therefore must suffer a rearrangement of its architecture, or decompose into other species. This reduction occurs at lower potentials compared with the analogous $[\text{Ni}_4]$ compound, which demonstrates that it is probably a metal-based process. When the same window is evaluated using square-wave voltammetry, this first peak reveals a two electron process, thus unveiling a total number of six reduction processes before the reduction of the pyridine molecules. No significant oxidation processes were found when examining positive potentials.

3.4. Study of the magnetic properties of $[\text{CuNi}\cdots\text{NiCu}]$

After the evaluation of the crystal structure and the assignation of its topology, complex **7** seems to contain the ingredients needed to embody two qubits, since it shows to be a real semi-independent pair of heterometallic clusters. The interaction within the $[\text{NiCu}]$ pair gives rise to a spin doublet ($S = \frac{1}{2}$) and a spin quartet ($S = \frac{3}{2}$) from the interaction between the local spins $S_{\text{Cu}} = \frac{1}{2}$ and $S_{\text{Ni}} = 1$. Thus, the existence of two spin carriers ($[\text{NiCu}]$) with $S \neq 0$ is assured, and consequently the possibility of quantum entanglement between their spin wave functions. A first assessment of the

magnetic properties of compound **7** was carried out through variable-temperature bulk magnetization measurements on a powdered microcrystalline sample. The $\chi_M T$ versus T plot of **7** (Figure IV.19) exhibits a value of $2.8 \text{ cm}^3 \text{ K mol}^{-1}$ at 300 K, which is very close to the calculated value for two Cu^{II} and two Ni^{II} independent centers with an average $g = 2$ ($2.7 \text{ cm}^3 \text{ K mol}^{-1}$). $\chi_M T$ decreases upon lowering the temperature to a plateau near $1.2 \text{ cm}^3 \text{ K mol}^{-1}$ around 50 K, thus demonstrating the presence of NiCu pairs coupled antiferromagnetically to yield entities with $S = \frac{1}{2}$ ground states. Therefore, we can assure that the quartet excited state is totally depopulated below 50 K. This constitutes at the same time a proof that the Ni^{II} centers of the sample are all coupled to a Cu^{II} ion. Below 10 K, the $\chi_M T$ values begin to drop again, which can be ascribed to an antiferromagnetic interaction between the dimers within the complex or to intermolecular interactions.

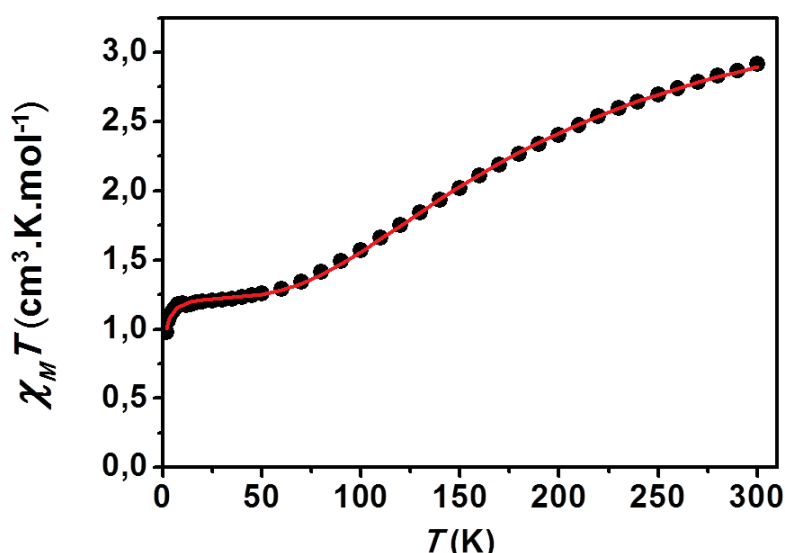


Figure IV.19. Plot of $\chi_M T$ vs T per mol of complex **7** at a constant field of 1 T. The solid red line is the fit to the experimental data (see the text).

The data was evaluated using a theoretical $\chi_M = f(T)$ expression derived from the spin Hamiltonian $H = 2x[-2JS_{\text{Ni}}S_{\text{Cu}} + gH\beta S_{\text{Tz}}]$:

$$\chi_M = \frac{2N\beta^2}{4k(T - \theta)} \frac{g_{1/2}^2 + 10g_{3/2}^2 \exp(3J/2kT)}{1 + 2 \exp(3J/2kT)} \quad (26)$$

In this Van Vleck equation, $g_{1/2}$ and $g_{3/2}$ are the average g factors associated with the doublet and quartet states, respectively, and it is assumed that zero-field splitting is very small with regard to the doublet-quartet splitting. The relationships between the $g_{1/2}$ and $g_{3/2}$ tensors and the local g_{Cu} and g_{Ni} tensors in the limit where the magnetic coupling within [NiCu] pair dominates the magnetic behavior are described as follows

$$g_{1/2} = \frac{1}{3} (4g_{\text{Ni}} - g_{\text{Cu}}) \quad (27)$$

$$g_{3/2} = \frac{1}{3} (2g_{\text{Ni}} + g_{\text{Cu}}) \quad (28)$$

The best fit was obtained with the following parameters: $J = -72.9 \text{ cm}^{-1}$, $g_{\text{Ni}} = 2.4$ and $g_{\text{Cu}} = 2.3$. A Curie-Weiss term (θ) was included in the formula to account for the drop of $\chi_{\text{M}}T$ at very low temperatures, with a best fit value of $\theta = -0.6 \text{ K}$. Similar NiCu pairs exhibiting phenoxido-type bridging moieties in the literature show a wide range of coupling constants (from $-11.8^{[26]}$ to $-161.5 \text{ cm}^{-1[27]}$). This extensive variety of values have been partly explained in term of the dihedral angle between equatorial coordination planes of Ni^{II} and Cu^{II} , respectively, although large disparities have been observed due to the nature of the axial ligands.^[28] The value of g_{Ni} , which is slightly higher than expected, is still not clear. Electron paramagnetic resonance (EPR) measurements, one of the most accurate tools to determine the value of g parameter, should be carried out to confirm such values.

The magnetic study of complex [CuNi...NiCu] (**7**) demonstrates that it fulfills some of the conditions required to embody two qubits, thus potentially constituting a 2-qubit quantum gate. Each [NiCu] pair has a ground state of $S = \frac{1}{2}$, which represents a real two level system ($m_s = \pm \frac{1}{2}$) that can be completely populated below 50 K. The possible weak interaction between both pairs opens the possibility of quantum entanglement, which should be explored through advanced physical and spectroscopic techniques. High-field EPR experiments, for example, could be used to evaluate the possibility of entanglement between the spin wave functions of both parts of the molecule. However, the two qubits within the complex cannot be discriminated due to the symmetry of the molecule, which becomes a serious drawback for its application as a logic gate since it precludes the possibility of addressing each qubit individually.

4. Linear metal chain assembly using bifunctional ligands

The previous sections describe how a ligand-based strategy can be followed to successfully design stable molecules that contain two-semi-independent and well defined magnetic clusters. In this section, efforts are directed at preparing complexes in a linear fashion exhibiting a chain of paramagnetic metal ions. This motif, which is quite uncommon in coordination chemistry, constitutes an interesting object for the study of the magnetic anisotropy or for its potential application in quantum electronics.^[29, 30] Moreover, such chains can be regarded as building blocks to design molecular pairs by linking them through other external ligands. In the group, several polynuclear complexes featuring a linear topology have been prepared, including trinuclear compounds with Mn^{II} or Co^{II} as asymmetric triple-stranded helicates,^[18, 31] tetranuclear or trinuclear strings of manganese in oxidation states +2 and +3,^[32] or a trinuclear Mn(II)/(III) cluster that exhibits superparamagnetic behavior at low temperatures.^[33] Following on from these efforts, H₄L2 and H₂L3 ligands have been used in order to access other molecular strings of aligned paramagnetic ions due to the disposition of their donor atoms. The possibilities of constructing extended architectures by binding such strings have been also explored.

4.1 Synthesis and structural study of a rhombohedral cobalt(II)/cobalt(III) cluster

The ligand H₄L2 was devised to enable the assembly of linear heterometallic complexes featuring 3d and 4f centers, in attempt to benefit from its different types and sizes of coordination pockets (see Figure IV.2). To achieve this goal, the ligand was reacted in pyridine with Co(NO₃)₂ and Ln(NO₃)₂ (Ln = Gd, Tb) using (NⁿBu₄)OH to ensure the deprotonation of the phenol groups (2:4:1:8 molar ratio). The resulting red solution was layered with ether, which for the case of Gd^{III} produced crystals that allowed the resolution of the molecular structure by use of synchrotron X-ray diffraction. The identity of the product did not show any Gd^{III} in the structure, and turned out to be a tetranuclear cobalt cluster [Co₄(L2)₂(py)₇(OH)](NO₃) (**9**) (Figure IV.20).

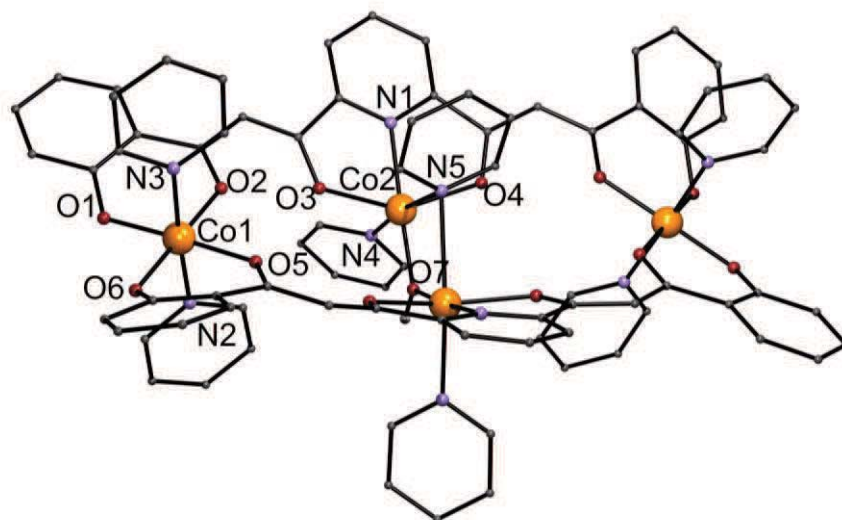


Figure IV.20. Representation of the molecular structure of the cationic complex $[\text{Co}_4(\text{L}2)_2(\text{py})_7(\text{OH})]^+$. Orange, Co; violet, N; red, O; rest, C. Only crystallographically found H atoms on O carriers are represented.

IR strongly suggested that complex **9** was also the outcome from the reaction with Tb^{III} , where the structure was not determined. Any attempts of a direct preparation of this compound from its components were unsatisfactory. The role of the lanthanide ion in the reaction is not yet clear, although its necessity for the formation of the system suggests that it is acting as a template. Another possibility is that it stays in solution as a complex together with $\text{H}_2\text{L}3$, since lanthanide ions have been shown to form stable species with pyridyl- β -diketonate related ligands.^[34] Although the structure of this compound is far from the objectives of this work, it exhibits very interesting features that should be highlighted. Compound **9** crystallizes in the monoclinic $\text{C}2/c$ space group, and consists of four cobalt ions accommodated by two ligands in the $\eta^7:\mu_3\text{-L}2^{4-}$ coordination mode. The distorted octahedral environment of each center is completed by a total of seven pyridine molecules in their axial positions. The equatorial plane of the metals located at both ends of the $[\text{Co}_4(\text{L}2)_2(\text{py})_7(\text{OH})]^+$ unit are formed by two "OO" units (one from each ligand) from adjacent oxygen atoms of phenolate and β -diketonate groups. The dipicolinate-like "ONO" central pockets of the ligands chelate two inner cobalt ions, which are also bridged through a shared axial pyridine ligand. This singularity turns out to be very uncommon, since very few examples of molecules exhibiting pyridine bridging ligands can be found in the

literature.^[35, 36] Additionally, both inner metals share one oxygen atom in the equatorial plane, provided by a bridging hydroxo group. The intermetallic distance between the inner cobalt ions is 3.2838(8) Å. These metals are separated by 6.2200(10) Å from the external ones. Other interatomic distances and angles for compound **9** are shown in Table IV.7, while crystallographic parameters are listed in Table IV.A2 in the Appendix. As shown in Figure IV.20, the metallic distribution within the system leads to an elongated rhombohedral conformation. The distances of the opposite vertex of the rhombus created by the four cobalt ions are 3.2838(8) and 11.8629(16) Å, respectively. The equatorial and axial Co-O distances range from 2.529 to 1.926 Å for the inner metals and from 1.945 to 1.866 Å for the external centers, suggesting the oxidation states of +2 and +3 for the central and the external ions, respectively. The oxidation of the external metals is consistent with the presence of a NO₃⁻ molecule in the crystal lattice, which ensures the charge balance of the compound.

Table IV.7. Selected interatomic distances [Å] and angles [°] for [Co₄(L2)₂(py)₇(OH)](NO₃) (9**)**

Co1-O1	1.866(2)	O1-Co1-O6	86.26(11)
Co1-O6	1.871(3)	O1-Co1-O5	177.82(11)
Co1-O5	1.889(2)	O6-Co1-O5	92.03(11)
Co1-O2	1.891(2)	O1-Co1-O2	93.22(11)
Co1-N3	1.945(3)	O6-Co1-O2	178.62(11)
Co1-N2	1.946(3)	O5-Co1-O2	88.46(11)
Co2-O7	1.9257(18)	O1-Co1-N3	90.21(12)
Co2-O3	2.073(2)	O6-Co1-N3	92.32(12)
Co2-N1	2.076(3)	O5-Co1-N3	91.22(12)
Co2-O4	2.089(2)	O2-Co1-N3	88.97(12)
Co2-N4	2.167(3)	O1-Co1-N2	91.56(12)
Co2-N5	2.529(4)	O7-Co2-O4	103.93(7)
O6-Co1-N2	91.68(12)	O3-Co2-O4	149.09(10)
O5-Co1-N2	87.12(12)	N1-Co2-O4	75.29(10)
O2-Co1-N2	87.05(12)	O7-Co2-N4	92.22(12)
N3-Co1-N2	175.72(13)	O3-Co2-N4	95.74(11)
O7-Co2-O3	104.66(7)	N1-Co2-N4	92.11(12)
O7-Co2-N1	175.65(12)	O4-Co2-N4	94.62(11)
O3 Co2 N1	75.30(10)	Co2 O7 Co2	116.99(18)

The tetranuclear entities are linked in the *b* axis through weak hydrogen bonds of the C-H...N and C-H...O type. These involve the axial pyridine ligands from the external metals, the hydroxo group, and both the nitrate anion and solvent pyridine molecules (Figure IV.21).

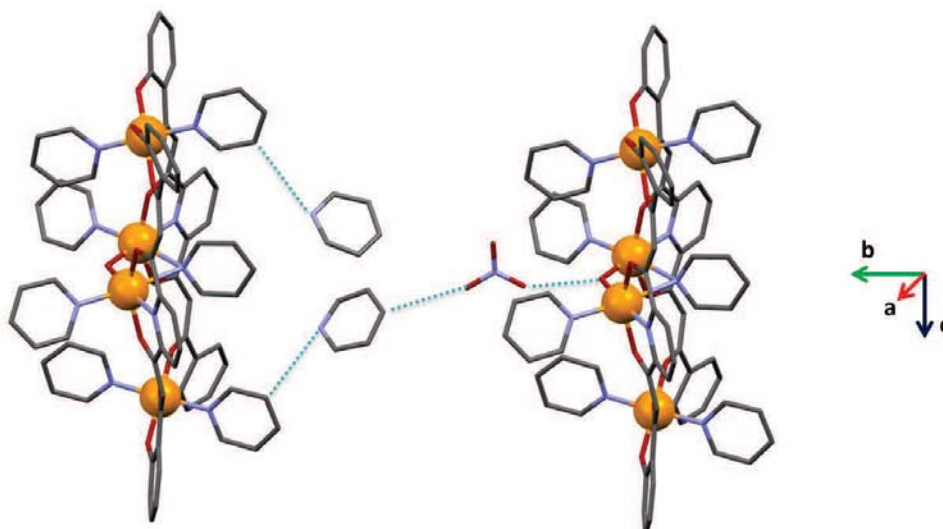


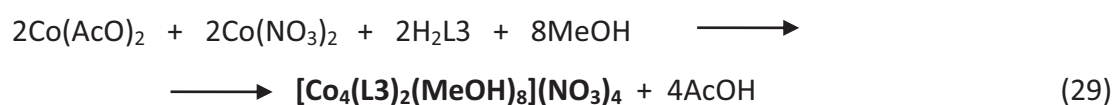
Figure IV.21. Representation of the crystal packing of the complex $[\text{Co}_4(\text{L}2)_2(\text{py})_7(\text{OH})]^+$ along the *b* crystallographic direction emphasizing the hydrogen bond interactions (dashed blue lines). Orange, Co; violet, N; red, O; rest, C, H atoms excluded.

4.2 Pair of clusters using a tetranuclear linear cobalt(II) complex

4.2.1. Synthesis and structural study

As previously introduced, initial reactions with the ligand $\text{H}_2\text{L}3$ were aimed at the preparation of heterometallic chain-like complexes involving 3d and 4f metal ions (see Figure IV.2). Therefore, several reactions were carried out combining the ligand with $\text{Co}(\text{AcO})_2$ and $\text{Ln}(\text{NO}_3)_3$ (2:2:3 molar ratio) in hot methanol ($\text{Ln} = \text{Tb}, \text{Gd}, \text{Dy}, \text{Er}$), producing orange solutions that were layered in ether. Small red crystals were obtained from all the reactions, some of them allowing the resolution of the molecular structure by use of synchrotron X-ray diffraction. For all of them, the same product was obtained, i.e., a tetranuclear compound $[\text{Co}_4(\text{L}3)_2(\text{MeOH})_8](\text{NO}_3)_4$ (**10**), with no lanthanide ion in the structure (Figure IV.22). The reasons why the 4f metals cannot be included in the molecular entity are still not clear. As previously exposed, one possibility

would be that these stay in solution in the form of soluble complexes, forming complexes with ligand H_2L3 .^[34] Nevertheless, the interesting structural properties of complex **10** prompted the direct preparation of this complex from its simplest components. Thus, a synthetic procedure was carried out through the reaction of the ligand with two sources of cobalt(II) in equivalent amounts: $Co(AcO)_2$ and $Co(NO_3)_2$. The former was employed as the source of base needed for removing the diketonate protons of H_2L3 , while the latter furnished the nitrate counter-ions of the cationic cluster **10**. In that way, the complex was readily obtained and characterized by IR spectroscopy and microanalysis, according to the following equation:



The crystal structure of compound **10** belongs to the monoclinic $P2_1/c$, and shows that the cation of the compound $[Co_4(L3)_2(MeOH)_8]^{4+}$ exhibits a centro-symmetric linear array of Co^{II} metal ions in a zig-zag form accommodated by two fully deprotonated ligands. The latter lie on opposite sides of the tetranuclear string, and are mutually shifted in the chain direction (Figure IV.22). Each ligand uses the two diketonate groups, the central pyridyl group and one of the external pyridyl rings to bind the four metals, while the other external pyridyl moieties remain uncoordinated.

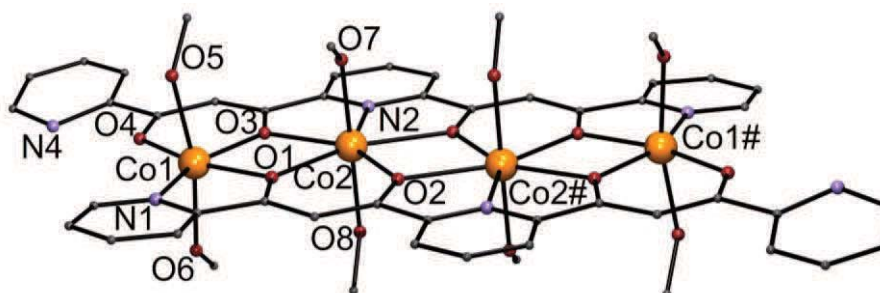


Figure IV.22. Representation of the molecular structure of the cationic complex $[Co_4(L3)_2(MeOH)_8]^{4+}$. Orange, Co; violet, N; red, O; rest, C. H atoms excluded.

The free pyridyl rings of the ligands lie on opposite ends of the molecule. The external Co^{II} ions are coordinated by one β -diketone group from one of the ligands and a picolinate-like moiety (N,O-donation) from the other ligand in the equatorial plane. On

the other hand, the central Co^{II} ions are encapsulated by one β -diketone group from one ligand and by one dipicolinate-like group from the other (O,N,O-donor). The resulting $[\text{Co}_4(\text{L3})_2]^{4+}$ ensemble reflects a remarkably flat entity, as depicted in Figure IV.23.



Figure IV.23. Side view representation of the cationic complex $[\text{Co}_4(\text{L3})_4(\text{MeOH})_8]^{4+}$, emphasizing its planarity. Orange, Co; violet, N; red, O; rest, C. H atoms excluded.

The four metal ions are coordinated to two MeOH ligands in the axial positions, which involve the external Co^{II} to exhibit very strongly distorted octahedral coordination geometry. The central Co^{II} ions are heptacoordinated, and display a rare pentagonal bipyramidal environment. The intermetallic distances between both kinds of cobalt ions are 3.550(2) Å, while the two central Co^{II} ions are separated by 3.692(2) Å. Selected interatomic distances and angles for compound **10** are shown in Table IV.8, and crystallographic parameters are listed in Table IV.A3 (Appendix). This cationic complex crystallizes together with four NO₃⁻ ions per [Co₄] unit, thus ensuring the electric neutrality of the compound. These anions are located between the clusters, linking them through a network of hydrogen bonds via the methanol ligands approximately within the *bc* crystallographic plane (Figure IV.24). As mentioned before, the literature contains hundreds of coordination clusters of Co^{II}, of which almost 200 are tetranuclear, but only very few exhibit a linear topology,^[12-14] thus demonstrating that the arrangement of complex **10** is difficult to achieve.

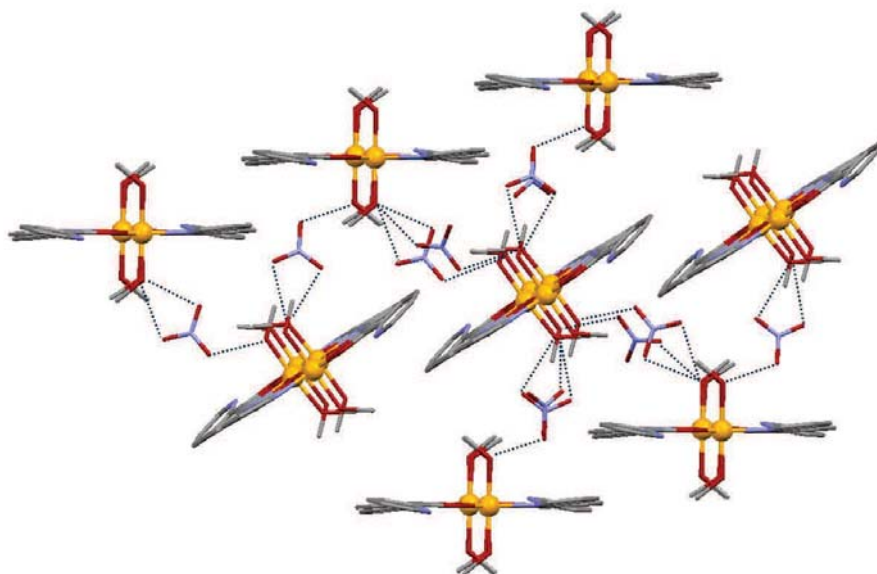


Figure IV.24. Representation of the crystal packing of $[\text{Co}_4(\text{L3})_2(\text{MeOH})_8](\text{NO}_3)_4$ (**10**) along the a crystallographic direction emphasizing the hydrogen bond interactions (dashed blue lines). Orange, Co; violet, N; red, O; rest, C. H atoms excluded.

Several experiments by elemental analysis revealed that upon exposure to moist air, compound **10** undergoes full replacement of its axial methanol ligands by water molecules, therefore transforming the entity into the octa-aqua species $[\text{Co}_4(\text{L3})_2(\text{H}_2\text{O})_8](\text{NO}_3)_4$ (**10a**).

Table IV.8. Selected interatomic distances [Å] and angles [°] for $[\text{Co}_4(\text{L3})_2(\text{MeOH})_8](\text{NO}_3)_4$ (**10**)

Co1-O3	2.054(3)	O4-Co1-N1	120.57(15)
Co1-O4	2.121(4)	O1-Co1-N1	76.77(13)
Co1-O1	2.141(3)	O5-Co1-N1	89.56(16)
Co1-O5	2.147(4)	O3-Co1-O6	95.11(14)
Co1-N1	2.156(4)	O4-Co1-O6	85.76(15)
Co1-O6	2.159(4)	O1-Co1-O6	95.36(13)
Co2-O7	2.117(3)	O5-Co1-O6	167.80(15)
Co2-O8	2.141(3)	N1-Co1-O6	85.23(16)
Co2-O2	2.204(3)	O7-Co2-O8	176.26(12)
Co2-O1	2.239(3)	O7-Co2-O2	87.99(11)
Co2-N2	2.257(3)	O8-Co2-O2	88.94(12)
Co2-O3	2.304(3)	O7-Co2-O1	89.60(12)
Co2-O2#	2.333(3)	O8-Co2-O1	87.77(12)

Co1-O1-Co2	108.27(12)	O2-Co2-O1	80.07(11)
Co2-O2-Co2	108.86(11)	O7-Co2-N2	90.63(12)
Co1-O3-Co2	108.95(14)	O8-Co2-N2	93.11(12)
O3-Co1-O4	87.97(14)	O2-Co2-N2	141.95(12)
O3-Co1-O1	74.66(12)	O1-Co2-N2	137.96(12)
O4-Co1-O1	162.63(13)	O7-Co2-O3	90.45(12)
O3-Co1-O5	94.75(14)	O8-Co2-O3	91.04(13)
O4-Co1-O5	87.41(16)	O2-Co2-O3	148.15(11)
O1-Co1-O5	94.17(13)	O1-Co2-O3	68.12(11)
O3-Co1-N1	151.34(15)	N2-Co2-O3	69.85(12)
O7-Co2-O2#	89.38(12)	O1-Co2-O2#	151.21(11)
O8-Co2-O2#	91.65(12)	N2-Co2-O2#	70.82(11)
O2-Co2-O2#	71.14(11)	O3-Co2-O2#	140.66(11)

(The suffix # denotes atoms generated by symmetry operation (-x, -y, -z))

4.2.2. Characterization of tetranuclear linear cobalt(II) complexes

The hydration phenomena observed in going from complex **10** to complex **10a** by exchange of methanol ligands by atmospheric water molecules is very common and has been observed before.^[37] The process of dehydration/re-hydration of **10a** was studied by thermogravimetric analysis (TGA) experiments, consisting in measuring the changes of weight in front of the temperature, and by differential thermal analysis (DTA), based on the comparison of temperature changes between the sample and an inert reference. Thus, if one sample of **10a** is brought to 200 °C, a loss of 17 % of the sample weight is found, which is related to eight water ligands of the molecule together with six molecules of hydration, as seen with microanalysis (Figure IV.25). On the other hand, if a sample is maintained at 50 °C for 2 hours under a 2×10^{-2} bar vacuum and then exposed to the atmosphere for half an hour, it shows that the amount of water necessary to saturate the eight axial coordination positions of complex **10a** is re-absorbed.

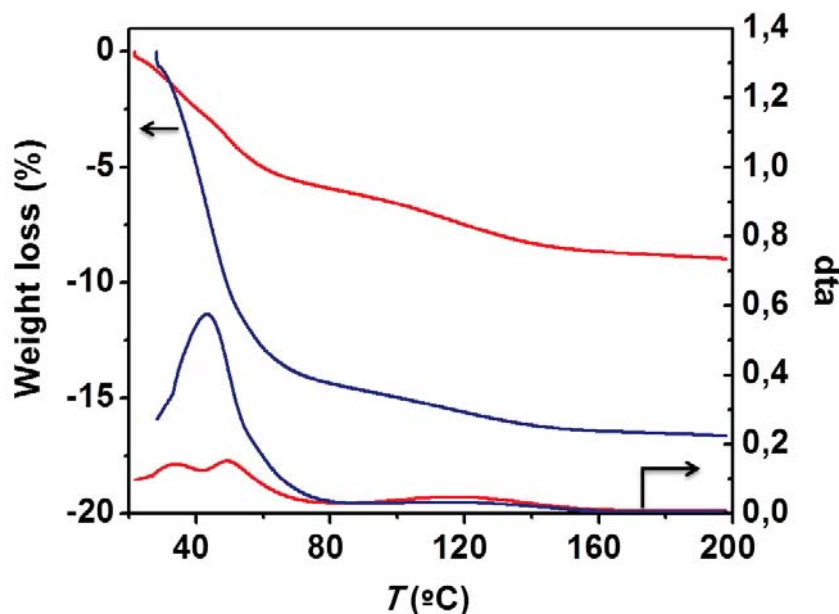


Figure IV.25. Red lines: TGA and DTA analysis of complex **10a**. Red lines: Obtained by atmospheric hydration from the amorphous precursor **7**. Blue lines: After treatment (50 °C, 2.10^{-2} bar, 2 hours) and brief exposure to the atmosphere.

The initial solid, as well as the sample treated at 50 °C and the one after the TGA experiment were evaluated by IR. The three spectra were found to be virtually identical, thus demonstrating that the *core* of the compound is maintained.

The stability of the moiety $[\text{Co}_4(\text{L3})_2]^{4+}$ from complex **10** upon ligand exchange was further evaluated by mass spectrometry. A sample of **10a** was dissolved in MeOH and examined by positive ion electrospray (ESI⁺) using a mixture of MeCN and H₂O as eluent. Different fragments involving the tetranuclear moiety $[\text{Co}_4(\text{L3})_2]$ were confirmed by exact mass, the fragment $[\text{Co}_4(\text{L3})_2]^{4+}$ being the strongest peak observed (m/z 244.4786 amu). The species corresponding to $[\text{Co}_4(\text{L3})_2]^{3+}$ and $[\text{Co}_4(\text{L3})_2]^{2+}$ were also obtained (Figure IV.26). In addition to these moieties, species of $[\text{Co}_4(\text{L3})_2]^{4+}$ together with H₂O, MeCN and/or NO₃³⁻ molecules, probably acting as ligands, were also identified (Figure IV.27 and IV.28), like $[\text{Co}_4(\text{L3})_2(\text{H}_2\text{O})]^{4+}$ (248.9812 amu), $[\text{Co}_4(\text{L3})_2(\text{MeCN})]^{4+}$ (254.7351 amu), $[\text{Co}_4(\text{L3})_2(\text{MeCN})_2]^{4+}$ (264.9918 amu), $[\text{Co}_4(\text{L3})_2(\text{MeCN})_3]^{4+}$ (275.2484 amu), $[\text{Co}_4(\text{L3})_2(\text{NO}_3)]^{3+}$ (346.6344 amu) and $[\text{Co}_4(\text{L3})_2(\text{NO}_3)(\text{MeCN})]^{3+}$ (360.3096 amu). At the same time, other peaks involving more than two ligands were also assigned, related to $[\text{Co}_4(\text{L3})_3]^{n+}$ ($n = 2, 3,$ and 4) and

$[\text{Co}_4(\text{L3})_4]^{2+}$ (Figure IV.26). The peaks that could not be assigned to any structure related to **10** or **10a** could arise from reduction processes that take place as an intrinsic effect of this technique. All these different fragments observed by mass spectrometry indicate that the exchange of MeOH ligands by H_2O molecules from the atmosphere in passing from **10** to **10a** occurs without alteration of the basic $[\text{Co}_4(\text{L3})_2]^{4+}$ framework of the cluster.

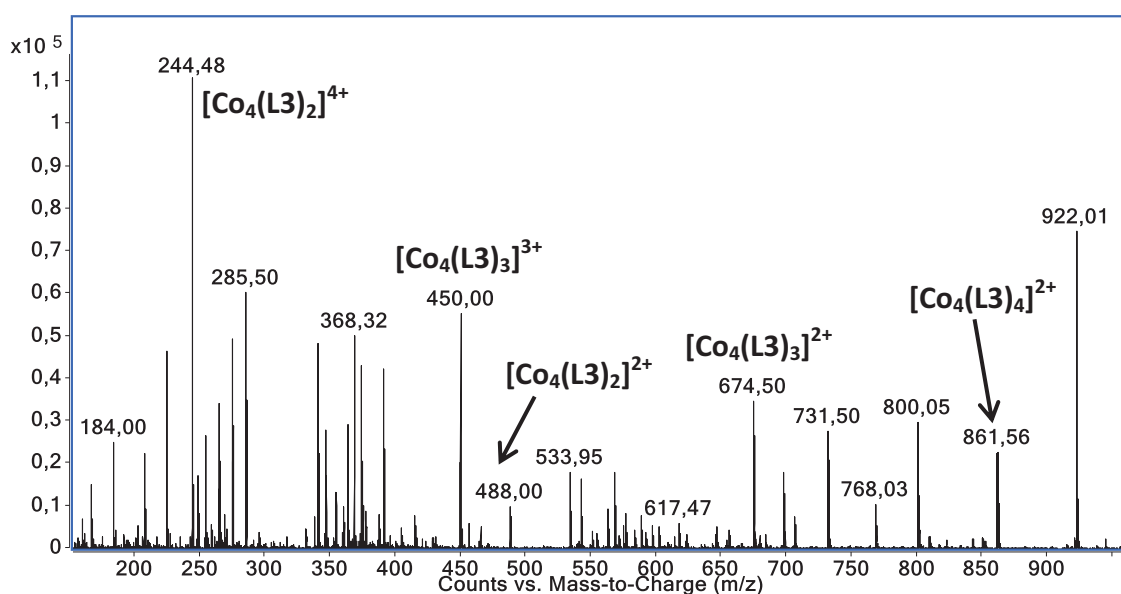


Figure IV.26. Positive ion ESI mass spectrum at 125 V of **10a** dissolved in MeOH

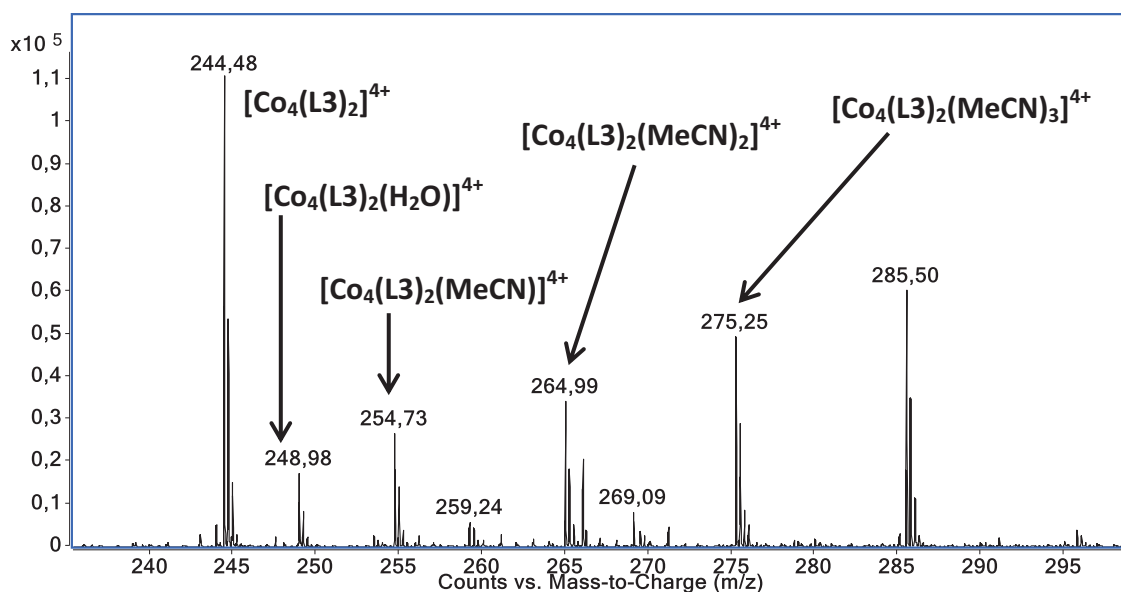


Figure IV.27. Positive ion ESI mass spectrum at 125 V of **10a** dissolved in MeOH (236-298 m/z range).

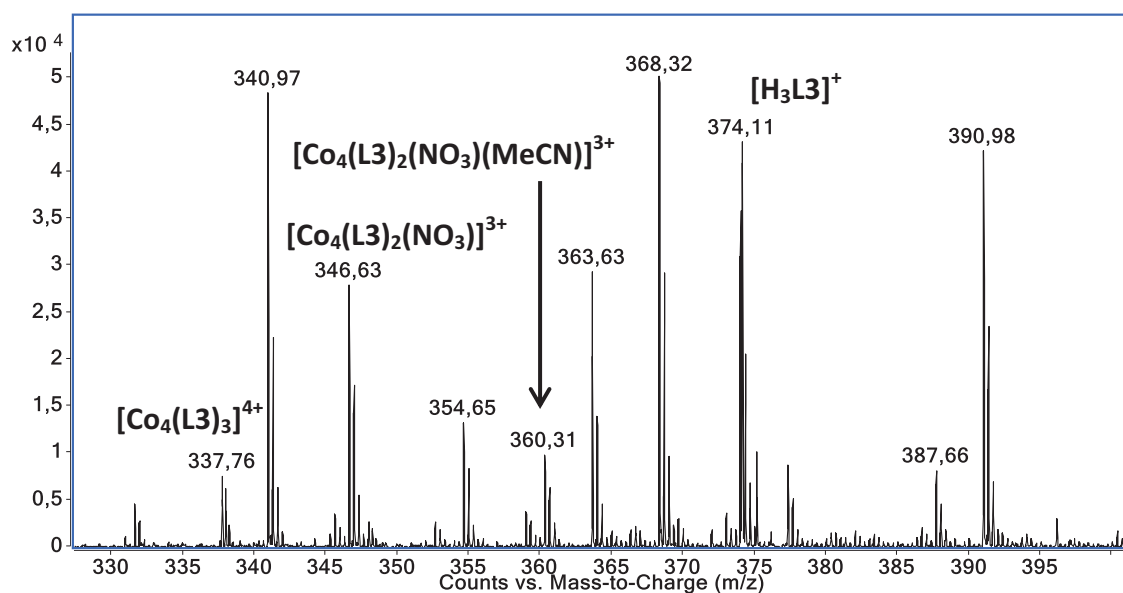


Figure IV.28. Positive ion ESI mass spectrum at 125 V of **10a** dissolved in MeOH, expanded in the 330-400 m/z range.

4.2.3. Electrochemical behavior of $[\text{Co}_4(\text{L}_3)_2(\text{H}_2\text{O})_8](\text{NO}_3)_4$

The electrochemical properties of $[\text{Co}_4(\text{L}_3)_2(\text{H}_2\text{O})_8](\text{NO}_3)_4$ (**10a**), as well as the redox activity of the ligand H_2L_3 , were investigated by cyclic voltammetry and square-wave voltammetry. Due to the hydration phenomena studied in the previous section, the evaluation of the redox properties of complex $[\text{Co}_4(\text{L}_3)_2(\text{MeOH})_8](\text{NO}_3)_4$ (**10**) appears to be inaccessible. However, since the main backbone is preserved after the exchange of the axial ligands, very similar behavior is expected for both compounds. All measurements were carried out in DMF at ambient temperature, using TBA.PF_6 as supporting electrolyte, air-free conditions, and a conventional three-electrode configuration consisting of one platinum wire as the auxiliary electrode, one silver wire as reference electrode, and a working glassy carbon (GC) electrode (1 mm diameter). The ferrocene/ferrocenium (Fc/Fc^+) couple was used as internal reference. The voltammograms obtained (1.3 mM solution) are depicted in Figure IV.29.

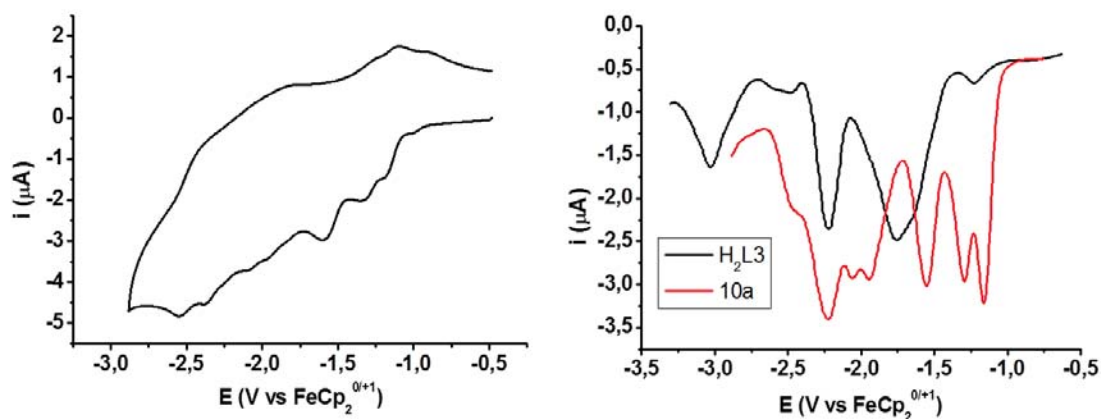


Figure IV.29. Study of the redox activity of $[\text{Co}_4(\text{L3})_2(\text{H}_2\text{O})_8](\text{NO}_3)_4$ (**10a**) Left: Cyclic Voltammetry in DMF at room temperature with a scan rate of 100 mVs^{-1} . Right: Squarewave Voltammetry in DMF, room temperature of **10a** and $\text{H}_2\text{L3}$, frequency of 15 mHz and a step of 4 mV.

Seven reduction processes can be extracted from the cyclic voltammogram, with some reversibility in the first two processes. However, the reversibility of the isolated first peak could not be evaluated due to its very low intensity. A deeper assessment was carried out evaluating the square-wave voltammogram, where the seven reduction processes are clearly identified. For more comprehensive results, the redox behavior of the isolated $\text{H}_2\text{L3}$ ligand was also studied in the same conditions. Five reduction processes were found, some of them suggesting multiple electron processes. The first reduction process for complex **10a** ($-1.16 \text{ V vs fc}^+/\text{fc}$ according to the square-wave voltammogram) and for the isolated ligand ($-1.24 \text{ V vs fc}^+/\text{fc}$) are considerably close. This suggests that the first reduction process within the cluster occurs through a ligand-based process. No redox activity was found when evaluating the oxidation window.

4.2.4. Magnetic behavior of $[\text{Co}_4(\text{L3})_2(\text{H}_2\text{O})_8](\text{NO}_3)_4$

As for the study of the redox behavior, the magnetic properties of complex **10** cannot be evaluated due to the fast replacement of the axial MeOH ligands by H_2O molecules to form the related aqua-complex **10a**. However, the behavior of the latter is expected to be very similar to that of the structurally characterized version, since the molecular backbone has been demonstrated to remain. Therefore, variable temperature

magnetization measurements under a constant magnetic field of 0.5 T were carried out in the 2 to 300 K range (Figure IV.30). The $\chi_M T$ versus T curve exhibits a value of $9.9 \text{ cm}^3 \text{ K mol}^{-1}$ near room temperature, which is higher than expected for four Co^{II} uncoupled ions with $S = 3/2$ and $g = 2$ ($7.5 \text{ cm}^3 \text{ K mol}^{-1}$). This phenomenon indicates that the orbital angular momentum contributes to the magnetic susceptibility of the system, since it is not quenched. The curve exhibits a decrease to almost zero when the temperature is lowered to 2 K, which confirms the presence of antiferromagnetic interactions between the metal ions in the cluster, leading to an $S = 0$ ground state. Due to the spin-orbit coupling effects, modeling the magnetic behavior of exchange-coupled Co^{II} clusters with more than two metals turns into a difficult and challenging task.^[38-40] However, the structural characteristics of complex **10** are expected to attenuate this effect since the metals exhibit a strong deviation from the ideal octahedral geometry. Thus, an estimate of the coupling constants was obtained using the isotropic Heisenberg spin Hamiltonian $H = -2J_1(S_1S_2 + S_1'S_2') - 2J_2S_2S_2'$, where S_1, S_2, S_1', S_2' are the spin operators for Co1, Co2, Co1# and Co2#, respectively (see Figure IV.22) and assumed to have values of $S = 3/2$. This model contemplates that part of the contribution by the spin-orbit coupling effect is included in the g parameter, which then adopts an unusually larger value. Another strategy that can be used when evaluating polynuclear complexes of Co^{II} exhibiting strong spin-orbit coupling is to assume that this interaction stabilizes the lowest Kramer doublet, the ions thus exhibiting effective spin values of $1/2$.^[41, 42] However, this theory deals with the situation when the cobalt ions present a perfect octahedral environment, which is not the case for complex **10** due to the severe distortion of the coordination geometry around the metals.

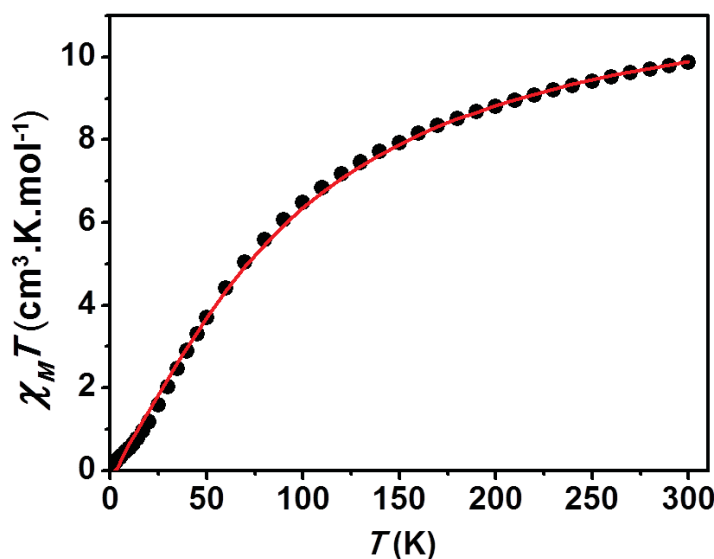


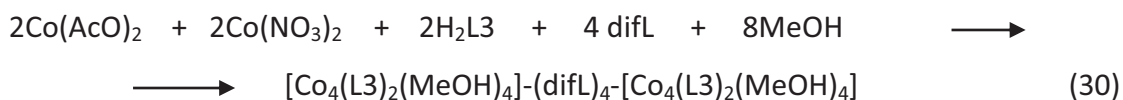
Figure IV.30. Plot of $\chi_M T$ vs T per mol of complex **10a** at a constant field of 0.5 T.

The fit was thus performed for the whole temperature range by full matrix diagonalization with the program *CLUMAG*.^[43] Several runs revealed that J_2 and g parameters were strongly correlated, thus causing the former to reach unrealistic high and positive values while leading to a very good fits. It was then found more appropriate to force the condition $J_1 = J_2$ to avoid the effects of this correlations, which seems reasonable after evaluating the crystal structure. Following such strategy, the best fit was obtained with $J_1 = J_2 = -12.2 \text{ cm}^{-1}$ and $g = 2.57$. The large value of the latter parameter confirms that the magnetic data is highly influenced by the spin-orbit coupling and thus that these results do not have a strict physical meaning but represent just an estimate solution.

4.2.5. Linking chemically $[\text{Co}^{\text{II}}_4]$ complexes: Synthesis and structural study of $[\text{Co}^{\text{II}}_4]$ - $(\text{bpy})_4$ - $[\text{Co}^{\text{II}}_4]$

The study carried out of complex **10** has demonstrated that it has all the requirements to be used as a building block. The high lability of the axial MeOH ligands, which can be easily replaced by water molecules, and the remarkable planarity of its crystal structure make complex **10** (**10a**) an ideal candidate to build up architectures based on

this moiety. To explore such possibility, different attempts to link two of these tetranuclear cobalt(II) chains involved the use of difunctional heterocyclic rings (difL) such as pyrazine, aminopyrazine or imidazole. The $[\text{Co}^{\text{II}}_4]$ units were generated in situ in the course of these reactions, according to the equation:



This synthetic methodology could afford good molecular candidates of two-qubit quantum gates, since it would lead to systems displaying two weakly coupled aggregates of spins. However, none of the different trials carried out furnished any indication that the assembly between $[\text{Co}_4]$ entities was occurring. On the contrary, a simple exchange of the axial ligands by other ligands was taking place. For one of the cases, the final product could be evaluated by X-ray diffraction since it was obtained as red crystals after layering the solution with ether. Thus, if the ligand $\text{H}_2\text{L3}$ is reacted with a mixture of $\text{Co}(\text{AcO})_2$, $\text{Co}(\text{NO}_3)_2$ and dimethyl terephthalate in MeOH (1:1:1:2 molar ratio), the complex found is a tetranuclear aggregate $[\text{Co}_4(\text{L3})_2(\text{H}_2\text{O})_6(\text{MeOH})_2](\text{NO}_3)_4$ (**10b**). This compound is a close derivative of **10**, with six methanol axial ligands replaced by molecules of water (Figure IV.31). The crystal structure belongs to the triclinic P-1 space group, and exhibits a complex cation of four Co^{II} ions linked together as a *zig-zag* chain. The two ligands L3^{2-} are located opposite to each other, sandwiching the string of metals and chelating them on all the equatorial positions. All the axial positions are saturated by water molecules except for the external cobalt ions, which exhibit one H_2O molecule and one MeOH ligand. As in complex **10**, the central Co^{II} ions are heptacoordinated, displaying a pentagonal bipyramidal environment. On the other hand, the external Co^{II} centers exhibit highly distorted octahedral coordination geometry.

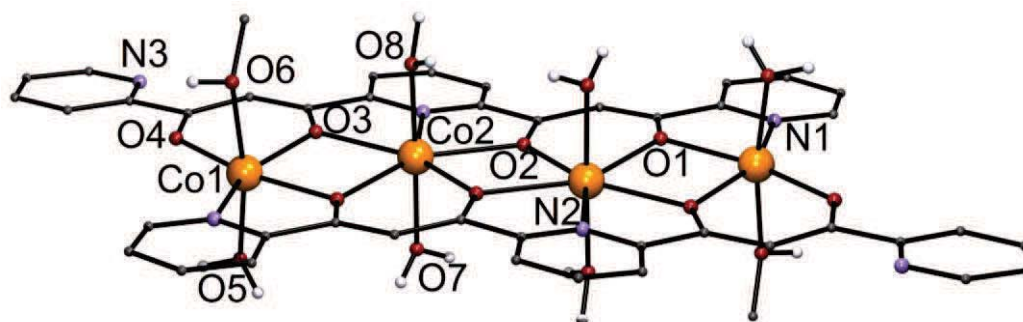


Figure IV.31. Representation of the molecular structure of the cationic complex $[\text{Co}_4(\text{L3})_4(\text{MeOH})_2(\text{H}_2\text{O})_6]^{4+}$ (**10b**). Orange, Co; violet, N; red, O; rest, C. Only hydrogen atoms bound to O are shown.

Again, this ensemble features a remarkable flat configuration. The distances between the external and the central metals are 3.4754(4) Å, while both central Co^{II} ions are separated by 3.6164(4) Å. Four NO_3^- counterions are located within the crystal lattice, which compensate the extra charge +4 of the $[\text{Co}_4]$ assembly and connect them through a network of hydrogen bonds (Figure IV.32, left). In addition, π - π stacking interactions between the pyridine rings of the ligand contribute to the crystal packing of the molecule (Figure IV.32, right).

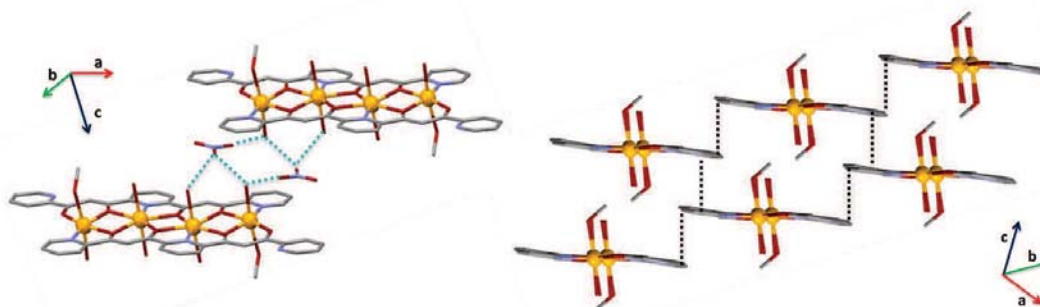


Figure IV.32. Representation of the crystal packing of $[\text{Co}_4(\text{L3})_2(\text{MeOH})_2(\text{H}_2\text{O})_6](\text{NO}_3)_4$ emphasizing the hydrogen bond (blue dashed lines) and π - π interactions (black dashed lines). Orange, Co; violet, N; red, O; rest, C. H atoms excluded.

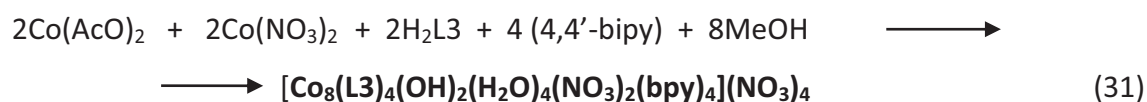
The structure of **10b** corroborates the hypothesis that the $[\text{Co}_4(\text{L3})_2]^{4+}$ unit is a robust moiety and it is maintained after substitution of their axial ligands, as exposed in the previous section. Selected structural parameters for **10b** can be found in Table IV.9, whereas crystallographic parameters are listed in Table IV.A3 (Appendix).

Table IV.9. Selected interatomic distances [Å] and angles [°] for [Co₄(L3)₂(H₂O)₆(MeOH)₈] (10b)

Co1-O3#	2.0179(11)	N1-Co1-O6	82.04(6)
Co1-O4#	2.0278(11)	O5-Co1-O6	170.87(5)
Co1-N1	2.0840(14)	O1-Co1-O6	94.23(5)
Co1-O5	2.0899(13)	O8-Co2-O7	178.29(5)
Co1-O1	2.1130(11)	O8-Co2-O2	88.09(5)
Co1-O6	2.1519(13)	O7-Co2-O2	91.99(4)
Co2-O8	2.0765(12)	O8-Co2-N2#	92.86(5)
Co2-O7	2.1051(12)	O7-Co2-N2#	88.13(5)
Co2-O2	2.1572(11)	O2-Co2-N2#	142.01(4)
Co2-N2#	2.1831(12)	O8-Co2-O1	92.54(5)
Co2-O1	2.1890(11)	O7-Co2-O1	85.80(5)
Co2-O3#	2.2250(11)	O2-Co2-O1	79.85(4)
Co2-O2#	2.2778(10)	N2#-Co2-O1	137.94(4)
O3#-Co1-O4#	89.41(5)	O8-Co2-O3#	85.49(5)
O3#-Co1-N1	149.66(5)	O7-Co2-O3#	93.52(4)
O4#-Co1-N1	120.07(5)	O2-Co2-O3#	147.29(4)
O3#-Co1-O5	93.80(5)	N2#-Co2-O3#	70.44(4)
O4#-Co1-O5	84.67(5)	O1-Co2-O3#	68.46(4)
N1-Co1-O5	95.85(5)	O8-Co2-O2#	92.74(4)
O3#-Co1-O1	73.86(4)	O7-Co2-O2#	88.90(4)
O4#-Co1-O1	163.10(5)	O2-Co2-O2#	70.77(4)
N1-Co1-O1	76.83(5)	N2#-Co2-O2#	71.24(4)
O5-Co1-O1	93.92(5)	O1-Co2-O2#	149.93(4)
O3-Co1-O6	92.41(5)	O3#-Co2-O2#	141.50(4)
O4-Co1-O6	88.71(5)	Co1-O1#-Co2	107.76(5)
N1-Co1-O6	82.04(6)	Co2-O2-Co2#	109.23(4)
Co1-O3-Co2	109.90(5)		

(The suffix # denotes atoms generated by symmetry operation (-x, -y, -z))

New attempts to find an assembly of [Co₄(L3)₂] moieties were carried out using longer difunctional auxiliary ligands. The addition of 4,4'-bipyridine (bpy) in the reaction mixture of Co(AcO)₂, Co(NO₃)₂, H₂L3 in MeOH using the 2 : 1 : 1: 1 molar ratio generated an orange precipitate and a deep red solution, which upon layering with toluene produced red crystals of the complex [Co₈(L3)₄(OH)₂(H₂O)₄(NO₃)₂(bpy)₄](NO₃)₄ (**11**) (hereafter, [Co₄(L3)₂]₂-(bpy)₄-[Co₄(L3)₂]):



The structure of **11** belongs to the triclinic P-1 space group, and reveals two $[\text{Co}_4(\text{L3})_2]$ units linked covalently, face-to-face by four difunctional 4,4'-bipyridine molecules in the axial positions of all the eight Co^{II} centres (Figure IV.33). Interestingly, the external apical sites are occupied by two OH^- ligands, two NO_3^- and six molecules of water (the hydrogen atoms of these ligands were found in difference Fourier maps). The metric parameters around the metals in the $[\text{Co}_4(\text{L3})_2]$ moieties are very similar to the ones exhibited in complexes **10** and **10b**. However, they reveal some deviation from the planarity exhibited in the previous complexes, probably due to steric repulsions with the 4,4'-bpy ligands. Thus, the external rings from the L3^{2-} ligand are pushed away from the molecular plane (Figure IV.34). This crystal structure opens the hypothesis that larger bridging ligands offer more flexibility for the establishment of the eight coordination bonds required to assemble two $[\text{Co}_4(\text{L3})_2]$ units into pair-of-clusters systems. In addition, the presence of six π - π stacking interactions within the four 4,4'-bipy ligands promotes a better stability of the assembly, with distances between aromatic rings in the range of 3.601 to 3.662 Å.

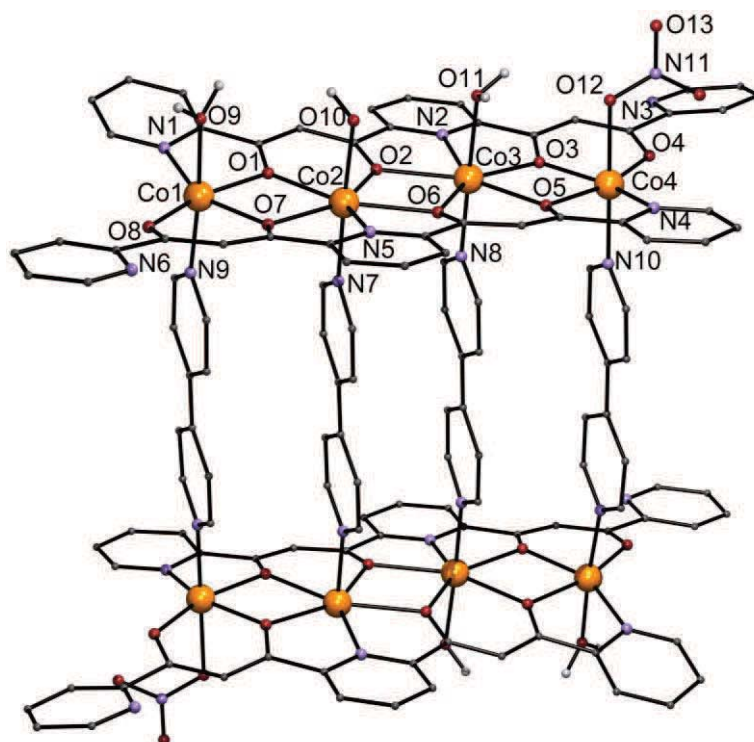


Figure IV.33. Representation of the molecular structure of the complex cation of $[\text{Co}_8(\text{L3})_4(\text{OH})_2(\text{H}_2\text{O})_4(\text{NO}_3)_2(\text{bpy})_4](\text{NO}_3)_4$ (**11**). Orange, Co; violet, N; red, O; rest, C. Only hydrogen atoms bound to O are shown.

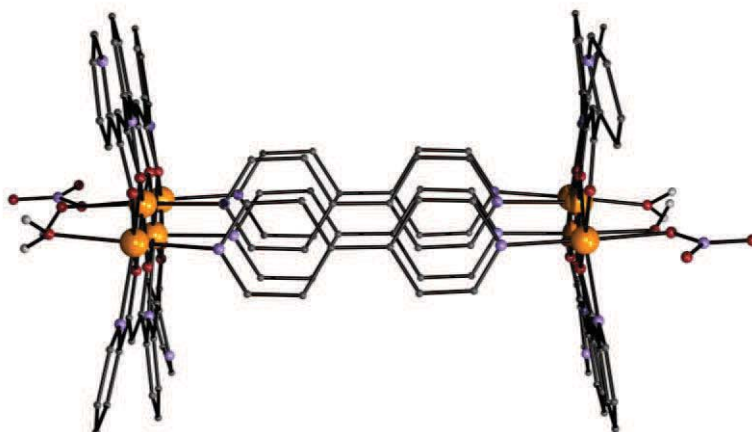


Figure IV.34. Representation of the molecular structure of the complex cation of $[\text{Co}_8(\text{L3})_4(\text{OH})_2(\text{H}_2\text{O})_4(\text{NO}_3)_2(\text{bpy})_4](\text{NO}_3)_4$ (**11**). Orange, Co; violet, N; red, O; rest, C. Only hydrogen atoms bound to O are shown.

The shortest intermetallic distances in **11** are 3.4666(14) and 3.4707(14) Å, spanning the external and the central Co^{II} ions, whereas 3.6139(13) Å is the separation between both central Co^{II} ions. A complete list of distances and angles can be found in Table IV.10, while crystallographic parameters are listed in Table IV.A3 (Appendix). In the literature, almost 3000 coordination complexes contain the difunctional 4,4'-bipyridil ligand, but only less than 15 % correspond to discrete compounds, of which many are coordination molecules featuring this ligand at the edges of the architecture.^[44] This illustrates the uniqueness of the crystal structure of complex **11** and the difficulty of finding discrete assemblies with this difunctional ligand acting as bridge. In addition, this opens the hypothesis that the orange solid that precipitates from the initial reaction corresponds to polymeric species, and thus that the crystals of **11** would originate from the species remaining in the solution. This would also explain the low yield obtained in the reaction.

Table IV.10. Selected interatomic distances [Å] and angles [°] for $[\text{Co}_8(\text{L3})_4(\text{OH})_2(\text{H}_2\text{O})_4(\text{NO}_3)_2(\text{bpy})_4](\text{NO}_3)_4$ (**11**)

Co1-O8	2.023(4)	O2-Co2-O1	79.04(14)
Co1-O7	2.032(4)	N7-Co2-O7	88.68(15)
Co1-N1	2.089(5)	O10-Co2-O7	95.33(14)
Co1-O1	2.099(4)	N5-Co2-O7	70.40(15)
Co1-N9	2.130(4)	O2-Co2-O7	147.38(14)
Co1-O9	2.154(4)	O1-Co2-O7	68.58(14)

Co2-N7	2.114(4)	N7-Co2-O6	88.62(15)
Co2-O10	2.117(4)	O10-Co2-O6	89.02(15)
Co2-N5	2.159(4)	N5-Co2-O6	71.73(15)
Co2-O2	2.177(4)	O2-Co2-O6	71.15(14)
Co2-O1	2.185(4)	O1-Co2-O6	150.15(13)
Co2-O7	2.219(4)	O7-Co2-O6	141.26(14)
Co2-O6	2.258(4)	N8-Co3-N2	93.77(16)
Co3-N8	2.127(4)	N8-Co3-O6	91.20(15)
Co3-N2	2.183(4)	N2-Co3-O6	142.05(15)
Co3-O6	2.186(4)	N8-Co3-O5	89.55(15)
Co3-O5	2.187(4)	N2-Co3-O5	138.52(16)
Co3-O3	2.225(4)	O6-Co3-O5	79.04(14)
Co3-O2	2.259(4)	N8-Co3-O3	88.29(15)
Co3-O11	2.340(4)	N2-Co3-O3	70.27(15)
Co4-O4	2.012(4)	O6-Co3-O3	147.56(14)
Co4-O3	2.019(4)	O5-Co3-O3	68.52(14)
Co4-N4	2.084(5)	N8-Co3-O2	91.08(15)
Co4-O5	2.102(4)	N2-Co3-O2	71.33(15)
Co4-N10	2.132(4)	O6-Co3-O2	70.98(13)
Co4-O12	2.201(4)	O5-Co3-O2	150.02(14)
O8-Co1-O7	88.97(16)	O3-Co3-O2	141.46(14)
O8-Co1-N1	119.83(17)	N8-Co3-O11	174.34(15)
O7-Co1-N1	150.25(16)	N2-Co3-O11	91.71(14)
O8-Co1-O1	162.71(16)	O6-Co3-O11	83.59(13)
O7-Co1-O1	73.79(15)	O5-Co3-O11	87.28(13)
N1-Co1-O1	77.11(16)	O3-Co3-O11	94.90(14)
O8-Co1-N9	90.03(16)	O2-Co3-O11	89.33(13)
O7-Co1-N9	92.24(16)	O4-Co4-O3	88.68(17)
N1-Co1-N9	94.84(17)	O4-Co4-N4	119.32(19)
O1-Co1-N9	91.98(15)	O3-Co4-N4	150.58(17)
O8-Co1-O9	85.08(16)	O4-Co4-O5	162.74(17)
O7-Co1-O9	89.59(16)	O3-Co4-O5	74.10(15)
N1-Co1-O9	85.96(17)	N4-Co4-O5	77.51(17)
O1-Co1-O9	93.26(15)	O4-Co4-N10	90.40(17)
N9-Co1-O9	174.75(16)	O3-Co4-N10	93.48(17)
N7-Co2-O10	175.80(16)	N4-Co4-N10	95.02(18)
N7-Co2-N5	97.87(16)	O5-Co4-N10	91.87(16)
O10-Co-N5	84.68(15)	O4-Co4-O12	88.39(16)
N7-Co2-O2	88.75(15)	O3-Co4-O12	85.57(16)
O10-Co2-O2	87.19(14)	N4-Co4-O12	86.38(18)
N5-Co2-O2	142.08(15)	O5-Co4-O12	89.01(14)
N7-Co2-O1	92.41(16)	N10-Co4-O12	178.48(18)
O10-Co2-O1	87.92(15)	N5-Co2-O1	137.36(15)

(The suffix # denotes atoms generated by symmetry operation (-x, -y, -z))

The molecular assembly is arranged as infinite chains through hydrogen bonds involving the axial ligands and some additional lattice water molecules. In addition, the chains are connected to each other by π - π interactions between the rings of $L3^{2-}$ (Figure IV.35).

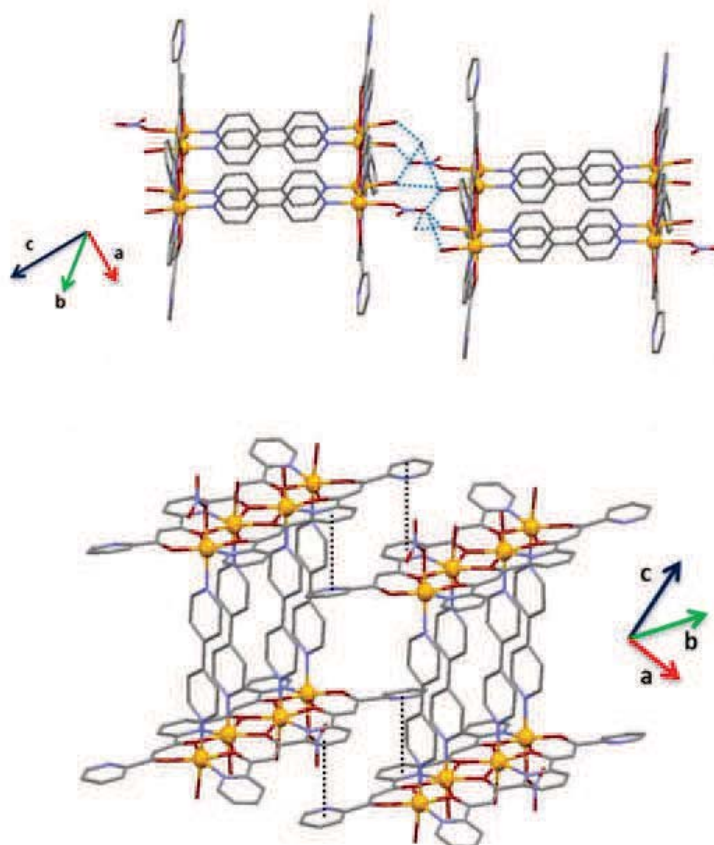


Figure IV.35. Representation of the crystal packing of the complex $[Co_8(L3)_4(OH)_2(H_2O)_4(NO_3)_2(bpy)_4](NO_3)_4$ (**11**) emphasizing the hydrogen bond (top, blue dashed lines) and π - π interactions (bottom, black dashed lines). Orange, Co; violet, N; red, O; rest, C. H atoms excluded.

4.2.6. Electrochemical behavior of $[Co_4(L3)_2]-(bpy)_4-[Co_4(L3)_2]$

The redox activity of **11** was evaluated by cyclic voltammetry and square-wave voltammetry. The measurements were carried out in DMF at ambient temperature, using TBA.PF₆ as supporting electrolyte, air-free conditions, and a conventional three-electrode configuration consisting of one platinum wire as the auxiliary electrode, one silver wire as reference electrode, and a working glassy carbon (GC) electrode (1 mm

diameter)). The cyclic voltammogram (2 mM solution) shows eight reduction processes that can be individually evaluated (Figure IV.36). In this case, all the peaks show chemical reversibility, thus indicating that compound **11** is restored after a total of eight reversible redox processes. For each process, the values of E_{pa} , E_{pc} , $E^{0'}$ and ΔE_p have been examined to assess their electrochemical reversibility (see equations 20, 21 and Figure IV.36).

$$\Delta E_p = E_{pa} - E_{pc} \approx \frac{0.059}{n} \quad (20)$$

$$E^{0'} = \frac{E_{pa} + E_{pc}}{2} \quad (21)$$

The first reduction peak appears at $E^{0'} = -1.080$ V vs fc^+/fc , with a difference of $\Delta E_p = 0.072$ V. According to the equation 20, which proposes this ΔE_p difference to be close to $0.059/n$ when the process is electrochemically reversible for an n electron transfer reaction, this first reduction peak belongs to a reversible electrochemical process.^[15] The second reduction process appears at -1.260 V, but with a $\Delta E_p = 0.126$ V vs fc^+/fc , therefore suggesting that is composed by two close one-electron reversible reduction processes (see below). The third peak is composed by multiple processes, and although they suggest also high reversibility, they are too close for their evaluation. On the other hand, fourth and fifth processes, at -1.858 and -2.043 V vs fc^+/fc respectively, have the characteristics of a reversible redox process, given the ΔE_p value of 0.068 V for the fourth peak and 0.088 V for the fifth one. The sixth peak appears slightly more spaced, featuring a $\Delta E_p = 0.102$ V at -2.311 V vs fc^+/fc . It may, however, still be considered a quasi-reversible process.^[15] The last two peaks, albeit featuring good reversibility, have not enough resolution to be evaluated.

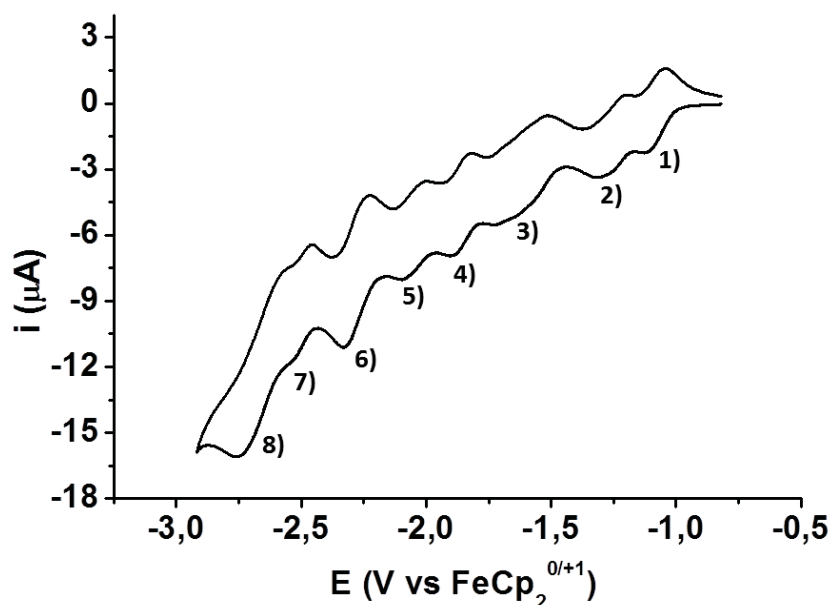


Figure IV.36. Cyclic voltammogram at 100 mVs^{-1} for complex **11** in DMF at room temperature

In addition, the compound exhibits a less resolved pair of irreversible oxidation processes. For a better resolution of the observed reduction peaks, the square-wave voltammetry of complex **11** was carried out and compared with the redox behavior of both ligands present in the molecular system ($\text{H}_2\text{L3}$ and 4,4'-bipyridine). The voltammogram shows the eight reduction processes for the complex, but the resolution is still not good enough to see the different possible processes involved in the third wide peak. Figure IV.37 shows the response of complex **11** compared with the square-wave voltammograms for $\text{H}_2\text{L3}$ and 4,4'-bipy ligands (left), and with the voltammogram corresponding to the precursor complex **10a** (right). The seven reduction processes observed in complex **10a** are shifted in the cyclic voltammogram of complex **11**, which exhibits an additional eighth peak at very negative potentials ($-2.672 \text{ V vs fc/fc}^+$). The square-wave voltammogram of 4,4'-bipyridine ligand shows two reduction processes, one of them at $-2.712 \text{ V vs fc/fc}^+$. This strongly suggests that the additional peak of complex **11** could be induced by this difunctional ligand. As in the precursor complex, the free $\text{H}_2\text{L3}$ ligand is active in the region where the first reduction process of the complex **11** takes place, indicating that it could belong to a ligand-based process.

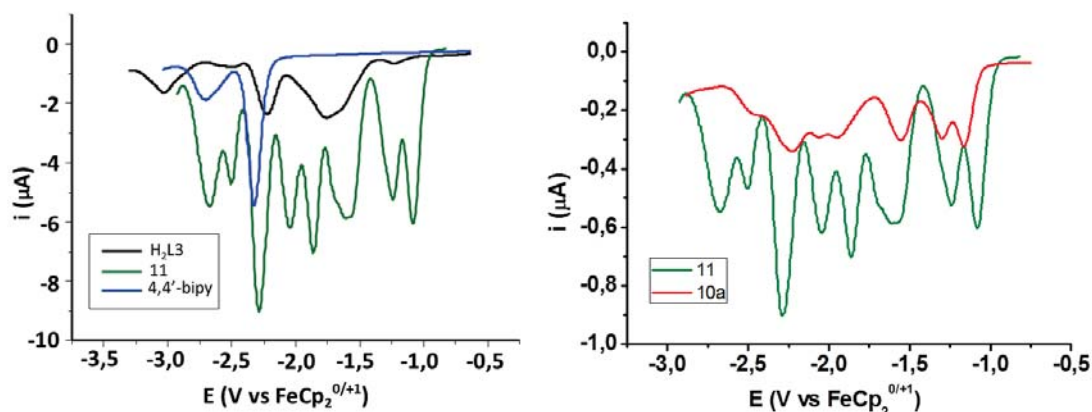


Figure IV.37. Square-wave voltammogram for complex **11** in DMF at room temperature with a frequency of 15 mHz and a step of 4 mV. Left: Comparison with the free ligands H_2L3 and 4,4'-bipy. Right: Comparison with the precursor **10a**.

4.2.7. Magnetic behavior of $[Co_4(L3)_2]-(bpy)_4-[Co_4(L3)_2]$

The magnetic study of the molecular assembly $[Co_8(L3)_4(OH)_2(H_2O)_4(NO_3)_2(bpy)_4](NO_3)_4$ has been investigated through variable temperature bulk magnetization measurements, working between 2 and 300 K with an applied magnetic field of 0.5 T. The $\chi_M T$ versus T curve (Figure IV.38) shows a value of $18.8 \text{ cm}^3 \text{ K mol}^{-1}$ at 300 K, which reveals that Co^{II} ions are high-spin ($S = 3/2$) and display a weak effect of spin-orbit coupling (the spin-only calculated value for $g = 2.2$ is $18.15 \text{ cm}^3 \text{ K mol}^{-1}$). The decrease of the influence of spin-orbit coupling when comparing complex **11** with complex **10a** is attributed to the larger distortion of the coordination geometry due to the replacement of some O-donors by the 4,4'-bipy N-donor ligands. When going to low temperatures, the values of $\chi_M T$ decrease down to almost zero at $T = 2 \text{ K}$, indicating that the curve is dominated by antiferromagnetic interactions possibly with a small contribution from single ion zero-field splitting (ZFS). Since the strongest interactions within the $[Co_4(L3)_2]-(bpy)_4-[Co_4(L3)_2]$ assembly are expected to occur between adjacent metals, the effects of the interaction between both $[Co_4(L3)_2]$ are masked by the former and thus cannot be detected. In addition, ZFS effect is expected to be correlated with the antiferromagnetic coupling, and probably only slightly modifies the values of the magnetic parameters. Thus, as an approximation, the data were modeled using the isotropic Heisenberg spin Hamiltonian $H = 2 \times [-2J_1(S_1S_2 + S_3S_4) - 2J_2S_2S_3]$

where S_1, S_2, S_3, S_4 are the spin operators for Co1, Co2, Co3 and Co4 (see Figure IV.33), and are all equal to $3/2$. As for its predecessor, the modeling was carried out by full matrix diagonalization using the program *CLUMAG*. The best fit parameters were $g = 2.44$, $J_1 = -10.87 \text{ cm}^{-1}$ and $J_2 = -6.44 \text{ cm}^{-1}$. The values of the exchange couplings are lower if compared with the ones obtained in complex **10a** ($J_1 = J_2 = -12.2 \text{ cm}^{-1}$), again explained by the increase of the distortion of the coordination geometry of the metal centers.

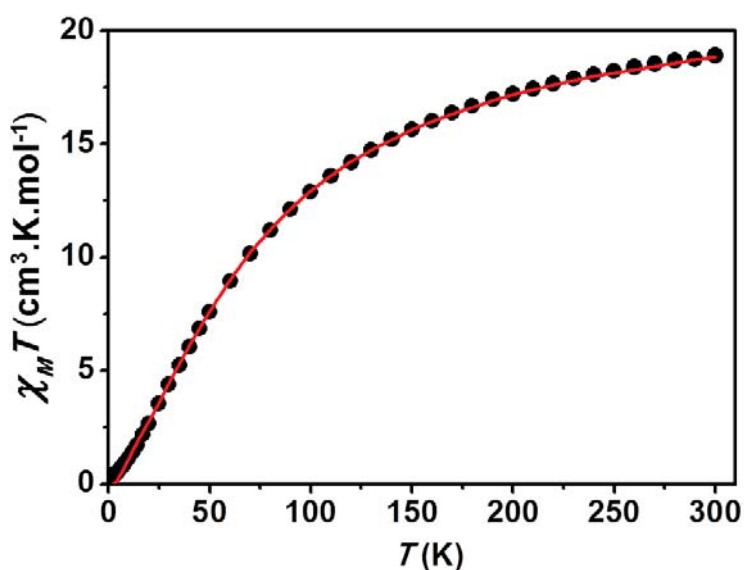


Figure IV.38. Plot of $\chi_M T$ vs T per mol of complex **11** at a constant field of 0.5 T. The solid curve is a fit to the experimental data using a spin-only Hamiltonian (see text)

This molecular architecture represents a good example of how ligand synthesis and coordination chemistry is a convenient strategy for the design of molecular assemblies with the appropriate structure for the exploitation of their functional properties. However, after evaluating the magnetic properties of **11**, one can realize that the suppression of the magnetic response due to the antiferromagnetic interactions leads the linkage of two species with a ground state $S = 0$. Thus, no possible qubit carriers can be defined in the system. Despite of that, this can serve as the basis for the preparation of other related assemblies exhibiting non-zero spin, enabling the possibility of exploring their potential as 2-qubit quantum gates.

5. Experimental

[Ni₄(L1)₂(py)₆] (4). A suspension of H₄L1 (50 mg, 0.12 mmol) and (NⁿBu₄)OH (0.6 ml, 0.6 mmol) in pyridine (30 ml) was added dropwise onto a solution of Ni(ClO₄)₂·6H₂O (90.9 mg, 0.25 mmol) in pyridine (10 ml). The resulting orange solution was stirred for 1 hour and filtrated. The filtrate was layered with MeOH, and yellow crystals formed after two days in 20 % yield. Anal Calcd (Found) for **4**·3.7MeOH·2H₂O: C 58.57 (59.09), H 4.66 (4.06), N 5.06 (5.06). IR (KBr pellet, cm⁻¹): 3052 wb, 1599 s, 1558 s, 1512 s, 1479 s, 1445 s, 1385 s, 1323 m, 1251 m, 1197 m, 1137 m, 1070 w, 1031 m, 859 w, 793 w, 752 m, 694 m, 649 w, 564 w.

[Co₄(L1)₂(py)₆] (5). A suspension of H₄L1 (50 mg, 0.12 mmol) and 60 % NaH (30 mg, 0.75 mmol) in pyridine (30 ml) was added dropwise onto a solution of Co(AcO)₂·4H₂O (62 mg, 0.25 mmol) in pyridine (10 ml). The resulting orange-red solution was stirred for 1 hour and filtrated. The filtrate was layered with MeOH, and orange crystals were formed after two days in 42 % yield. Anal Calcd (Found) for **5**: C 62.16 (62.15), H 3.88 (3.92), N 5.58 (5.40). IR (KBr pellet, cm⁻¹): 3430 wb, 1597 s, 1553 s, 1506 s, 1479 s, 1444 s, 1376 s, 1323 m, 1254 m, 1192 m, 1136 m, 1072 w, 1030 m, 859 w, 788 w, 749 m, 696 m, 643 w, 551 w.

[Na(py₂)] [Cu₄(L1)₂(py)₆] (ClO₄) (6). A suspension of H₄L1 (50 mg, 0.12 mmol) and 60 % NaH (30 mg, 0.75 mmol) in pyridine (30 ml) was added dropwise onto a solution of Cu(ClO₄)₂·6H₂O (92 mg, 0.24 mmol) in pyridine (10 ml). The resulting yellow solution was stirred for 1 hour and filtrated. The filtrate was layered with AcOEt, and greenish-yellow crystals were formed after two days in 30 % yield. Anal Calcd (Found) for **6**·4H₂O(-3py): C 51.03 (50.74), H 3.47 (3.26), N 3.30 (2.83). IR (KBr pellet, cm⁻¹): 3425 wb, 1604 m, 1554 m, 1506 s, 1481 s, 1436 s, 1359 m, 1258 m, 1228 m, 1198 m, 1137 m, 1103 w, 1033 m, 939 w, 861 w, 787 w, 753 w, 705 w, 675 w, 577 w.

[Ni₂Cu₂(L1)₂(py)₆] (7). A suspension of H₄L1 (50 mg, 0.12 mmol) and 60 % NaH (22 mg, 0.55 mmol) in pyridine (20 ml) was added dropwise onto a solution of Ni(AcO)₂·4H₂O (31 mg, 0.12 mmol) and Cu(AcO)₂·4H₂O (63 mg, 0.25 mmol) in pyridine (10 ml). The resulting mixture was stirred under reflux for 2 hour and then cooled down to room temperature. A brown solid was removed by filtration and the dark yellow filtrate was

layered with Et₂O. Green-yellow crystals formed in 24 hours in 27 % yield. Anal Calcd (Found) for 7·2.5H₂O: C 60.02 (60.12), H 4.07 (3.69), N 5.39 (5.00). IR (KBr pellet, cm⁻¹): 3451 wb, 1601 m, 1554 m, 1503 s, 1479 m, 1445 s, 1376 m, 1334 m, 1253 m, 1196 m, 1138 m, 1069 w, 1029 w, 793 w, 752 m, 701 m, 655 w, 575 w.

[Co₂Cu₂(L1)₂(py)₆] (8). A suspension of H₄L1 (50 mg, 0.12 mmol) and 60 % NaH (22 mg, 0.55 mmol) in pyridine (30 ml) was added dropwise onto a solution of Co(AcO)₂·4H₂O (31 mg, 0.12 mmol) and Cu(AcO)₂·4H₂O (31 mg, 0.12 mmol) in pyridine (10 ml). The resulting brown solution was stirred under reflux for 2 hours and then cooled down to room temperature. A brown solid was removed by filtration and the dark red filtrate was layered with MeOH. Red crystals formed after three days in 10 % yield. IR (KBr pellet, cm⁻¹): 3420 wb, 1598 s, 1536 s, 1521 s, 1481 s, 1451 s, 1375 m, 1336 m, 1271 m, 1244 m, 1213 m, 1143 m, 1098 w, 1065 m, 1035 w, 944 w, 878 w, 798 m, 720 m, 694 w, 574 w, 481 w.

[Co₄(L2)₂(py)₇(OH)](NO₃) (9). A suspension of H₄L2 (50 mg, 0.12 mmol) and (NⁿBu₄)OH (0.6 ml, 0.6 mmol) in pyridine (20 ml) was added dropwise onto a solution of Co(NO₃)₂·6H₂O (72 mg, 0.25 mmol) and Gd(NO₃)₃·6H₂O (36 mg, 0.08 mmol) in pyridine (10 ml). The resulting brown solution was stirred under reflux for 2 hours and then cooled down to room temperature. A dark red solid was removed by filtration and the dark red filtrate was layered with Et₂O. Green crystals were formed after two days in 30 % yield. IR (KBr pellet, cm⁻¹): 3447 wb, 1598 s, 1565 s, 1512 s, 1529 m, 1506 s, 1457 s, 1384 s, 1317 m, 1207 m, 1151 m, 1122 w, 1067 w, 1033 m, 864 w, 756 w, 696 m, 667 w, 648 w, 585 w, 493 w.

[Co₄(L3)₂(MeOH)₈](NO₃)₄ (10). (Method 1): A suspension of H₂L3 (30 mg, 0.08 mmol) in MeOH (20 ml) was added into a solution of Co(AcO)₂·4H₂O (20 mg, 0.08 mmol) and Tb(NO₃)₃·6H₂O (54 mg, 0.12 mmol) in MeOH (10 ml). The mixture was brought to reflux for 2 hours and then allowed to cool. The resulting orange solution was layered with Et₂O. After 10 days, orange crystals of **10** had deposited on the walls of the tube in 15 % yield. IR (KBr pellet, cm⁻¹): 3366 mb, 1609 m, 1579 m, 1564 m, 1546 m, 1521 m, 1457 m, 1384 s, 1320 w, 1293 w, 1170 w, 1079 w, 777 w, 707 w, 654 w, 517 w.

(Method 2): A mixture of $\text{Co}(\text{AcO})_2 \cdot 4\text{H}_2\text{O}$ (60 mg, 0.24 mmol), $\text{Co}(\text{NO}_3)_2 \cdot 6\text{H}_2\text{O}$ (69 mg, 0.24 mmol), and $\text{H}_2\text{L3}$ (90 mg, 0.24 mmol) in MeOH (90 ml) was heated to near 60 °C for 1 hour and then allowed to cool to room temperature. Upon addition of Et_2O , a fine orange precipitate started to form. After letting the powder deposit for a few hours it was collected by filtration, washed with Et_2O , and let dry in air. The yield was 60 %. Following the same procedure but layering the reaction mixture in Et_2O , microcrystalline form of **10** could be obtained after 10 days. Elemental analysis after **10** exchanged the methanol ligands with atmospheric water molecules, which led to the aqua species $[\text{Co}_4(\text{L3})_2(\text{H}_2\text{O})_8](\text{NO}_3)_4$ (**10a**): Anal Calcd (Found) C 36.81 (36.70), H 2.94 (3.09), N 10.22 (9.95). IR (KBr pellet, cm^{-1}): 3366 m, 1609 m, 1579 m, 1564 m, 1546 m, 1521 m, 1457 m, 1384 s, 1319 w, 1293 w, 1170 w, 1079 w, 777 w, 708 w, 659 w, 517 w.

$[\text{Co}_4(\text{L3})_2(\text{H}_2\text{O})_6(\text{MeOH})_2](\text{NO}_3)_4$ (10b**).** A grey suspension of $\text{H}_2\text{L3}$ (45 mg, 0.12 mmol) and dimethyl terephthalate (47 mg, 0.24 mmol) in MeOH (10 ml) was added to a pink solution of $\text{Co}(\text{AcO})_2 \cdot 4\text{H}_2\text{O}$ (30 mg, 0.12 mmol) and $\text{Co}(\text{NO}_3)_2 \cdot 6\text{H}_2\text{O}$ (35 mg, 0.12 mmol) in MeOH (15 ml). The mixture was brought to reflux for 45 minutes, cooled down to room temperature and filtrated. The resulting red solution was layered with Et_2O . After one month, red crystals of **10b** suitable for X-ray crystallography were obtained.

$[\text{Co}_8(\text{L3})_4(\text{OH})_2(\text{H}_2\text{O})_4(\text{NO}_3)_4(\text{bpy})_4](\text{NO}_3)_4$ (11**).** A grey suspension of $\text{H}_2\text{L3}$ (45 mg, 0.12 mmol) and 4,4'-bipyridine (38 mg, 0.24 mmol) in MeOH (10 ml) was added to a pink solution of $\text{Co}(\text{AcO})_2 \cdot 4\text{H}_2\text{O}$ (30 mg, 0.12 mmol) and $\text{Co}(\text{NO}_3)_2 \cdot 6\text{H}_2\text{O}$ (35 mg, 0.12 mmol) in MeOH (15 ml). The mixture was brought to reflux for 45 minutes and then cooled down to room temperature. An orange solid was removed by filtration and the red solution was layered with toluene. After one month, red crystals of **11** were obtained in 12 % yield. Anal Calcd (Found) for **11**·12 H_2O : C 45.46 (45.96), H 3.63 (3.32), N 11.12 (10.62). IR (KBr pellet, cm^{-1}): 1608 m, 1578 s, 1563 s, 1545 s, 1517 m, 1457 s, 1384 s, 1318 m, 1294 m, 1257 w, 1224 w, 1170 w, 1126 w, 1077 w, 1049 w, 1017 w, 944 w, 868 w, 810 w, 777 w, 748 w, 709 w, 684 w, 657 w, 634 w, 517 w.

- [1] T. Glaser, M. Heidemeier, J. B. H. Strautmann, H. Bögge, A. Stammler, E. Krickemeyer, R. Huenerbein, S. Grimme, E. Bothe, E. Bill, *Chemistry – A European Journal* **2007**, *13*, 9191.
- [2] S. K. Dey, T. S. M. Abedin, L. N. Dawe, S. S. Tandon, J. L. Collins, L. K. Thompson, A. V. Postnikov, M. S. Alam, P. Müller, *Inorganic Chemistry* **2007**, *46*, 7767.
- [3] A. R. Stefankiewicz, J.-M. Lehn, *Chemistry – A European Journal* **2009**, *15*, 2500.
- [4] G. A. Timco, T. B. Faust, F. Tuna, R. E. P. Winpenny, *Chemical Society Reviews* **2011**, *40*, 3067.
- [5] G. Aromí, C. Boldron, P. Gamez, O. Roubeau, H. Kooijman, A. L. Spek, H. Stoeckli-Evans, J. Ribas, J. Reedijk, *Dalton Transactions* **2004**, 3586.
- [6] T. Shiga, M. Ohba, H. Ökawa, *Inorganic Chemistry* **2004**, *43*, 4435.
- [7] R. W. Saalfrank, A. Dresel, V. Seitz, S. Trummer, F. Hampel, M. Teichert, D. Stalke, C. Stadler, J. Daub, V. Schünemann, A. X. Trautwein, *Chemistry – A European Journal* **1997**, *3*, 2058.
- [8] T. Shiga, T. Nakanishi, M. Ohba, H. Ökawa, *Polyhedron* **2005**, *24*, 2732.
- [9] R. L. Lintvedt, M. D. Glick, B. K. Tomlonovic, D. P. Gavel, J. M. Kuszaj, *Inorganic Chemistry* **1976**, *15*, 1633.
- [10] P. D. W. Boyd, K. S. Lee, M. Zvagulis, *Australian Journal of Chemistry* **1986**, *39*, 1249.
- [11] A. W. Addison, T. N. Rao, J. Reedijk, J. van Rijn, G. C. Verschoor, *Journal of the Chemical Society, Dalton Transactions* **1984**, 1349.
- [12] R. J. Irving, M. L. Post, R. W. Baker, *Journal of the Chemical Society, Dalton Transactions* **1975**, 1898.
- [13] F. A. Cotton, R. C. Elder, *Inorganic Chemistry* **1965**, *4*, 1145.
- [14] T. Konno, Y. Gotoh, K.-i. Okamoto, *Inorganic Chemistry* **1997**, *36*, 4992.
- [15] A. J. Bard, L. R. Faulkner, *Electrochemical Methods: Fundamentals and Applications*, Second Edition ed., John Wiley and Sons Publishers, New York, **2001**.
- [16] J. M. Clemente-Juan, B. Chansou, B. Donnadiou, J.-P. Tuchagues, *Inorganic Chemistry* **2000**, *39*, 5515.
- [17] M. A. Halcrow, J.-S. Sun, J. C. Huffman, G. Christou, *Inorganic Chemistry* **1995**, *34*, 4167.
- [18] G. Aromí, H. Stoeckli-Evans, S. J. Teat, J. Cano, J. Ribas, *Journal of Materials Chemistry* **2006**, *16*, 2635.
- [19] B. Bleaney, K. D. Bowers, *Proceedings of the Royal Society A*, **1952**, *214*, 451.
- [20] G. Aromí, J. Ribas, P. Gamez, O. Roubeau, H. Kooijman, A. L. Spek, S. Teat, E. MacLean, H. Stoeckli-Evans, J. Reedijk, *Chemistry – A European Journal* **2004**, *10*, 6476.
- [21] L. K. Thompson, S. K. Mandal, S. S. Tandon, J. N. Bridson, M. K. Park, *Inorganic Chemistry* **1996**, *35*, 3117.
- [22] C. Jing, S. Qiu, *Transition Metal Chemistry* **2007**, *32*, 528.
- [23] X.-Z. Li, L.-N. Zhu, C.-Q. Li, D.-Z. Liao, *Inorganic Chemistry Communications* **2006**, *9*, 1297.
- [24] X. Liu, Y. Sun, Y. Xu, D. Gao, *Russian Journal of Coordination Chemistry* **2011**, *37*, 362.
- [25] I. Morgenstern-Badarau, M. Rerat, O. Kahn, J. Jaud, J. Galy, *Inorganic Chemistry* **1982**, *21*, 3050.
- [26] Y. Journaux, O. Kahn, I. Morgenstern-Badarau, J. Galy, J. Jaud, A. Bencini, D. Gatteschi, *Journal of the American Chemical Society* **1985**, *107*, 6305.
- [27] C. Nazari Verani, T. Weyhermuller, E. Rentschler, E. Bill, P. Chaudhuri, *Chemical Communications* **1998**, 2475.
- [28] M. Yonemura, M. Ohba, K. Takahashi, H. Ökawa, D. E. Fenton, *Inorganica Chimica Acta* **1998**, *283*, 72.
- [29] S.-Y. Lai, T.-W. Lin, Y.-H. Chen, C.-C. Wang, G.-H. Lee, M.-h. Yang, M.-k. Leung, S.-M. Peng, *Journal of the American Chemical Society* **1998**, *121*, 250.

- [30] I. P.-C. Liu, M. Bénard, H. Hasanov, I. W. P. Chen, W.-H. Tseng, M.-D. Fu, M.-M. Rohmer, C.-h. Chen, G.-H. Lee, S.-M. Peng, *Chemistry – A European Journal* **2007**, *13*, 8667.
- [31] G. Aromí, P. Carrero Berzal, P. Gamez, O. Roubeau, H. Kooijman, A. L. Spek, W. L. Driessen, J. Reedijk, *Angewandte Chemie International Edition* **2001**, *40*, 3444.
- [32] G. Aromí, P. Gamez, J. Krzystek, H. Kooijman, A. L. Spek, E. J. MacLean, S. J. Teat, H. Nowell, *Inorganic Chemistry* **2007**, *46*, 2519.
- [33] L. A. Barrios, G. Aromí, J. Ribas, J. Salinas Uber, O. Roubeau, K. Sakai, S. Masaoka, P. Gamez, J. Reedijk, *European Journal of Inorganic Chemistry* **2008**, 3871.
- [34] P. C. Andrews, G. B. Deacon, R. Frank, B. H. Fraser, P. C. Junk, J. G. MacLellan, M. Massi, B. Moubaraki, K. S. Murray, M. Silberstein, *European Journal of Inorganic Chemistry* **2009**, *2009*, 744.
- [35] M. R. Bermejo, M. Fondo, A. M. Gonzalez, O. L. Hoyos, A. Sousa, C. A. McAuliffe, W. Hussain, R. Pritchard, V. M. Novotorsev, *Journal of the Chemical Society, Dalton Transactions* **1999**, 2211.
- [36] M. Akbar Ali, A. H. Mirza, R. J. Butcher, M. T. H. Tarafder, M. A. Ali, *Inorganica Chimica Acta* **2001**, *320*, 1.
- [37] G. Aromí, O. Roubeau, M. Helliwell, S. J. Teat, R. E. P. Winpenny, *Dalton Transactions* **2003**, 3436.
- [38] J. M. Clemente-Juan, E. Coronado, A. Gaita-Ariño, C. Giménez-Saiz, H.-U. Güdel, A. Sieber, R. Bircher, H. Mutka, *Inorganic Chemistry* **2005**, *44*, 3389.
- [39] A. V. Palii, B. S. Tsukerblat, E. Coronado, J. M. Clemente-Juan, J. J. Borrás-Almenar, *The Journal of Chemical Physics* **2003**, *118*, 5566.
- [40] F. Lloret, M. Julve, J. Cano, R. Ruiz-García, E. Pardo, *Inorganica Chimica Acta* **2008**, *361*, 3432.
- [41] N. Casan-Pastor, J. Bas-Serra, E. Coronado, G. Pourroy, L. C. W. Baker, *Journal of the American Chemical Society* **1992**, *114*, 10380.
- [42] J. C. Bonner, H. Kobayashi, I. Tsujikawa, S. A. Friedberg, *The journal of Chemical Physics* **1975**, *63*, 19.
- [43] D. Gatteschi, L. Pardi, *Gazzetta Chimica Italiana* **1993**, *123*, 10.
- [44] M. Fujita, O. Sasaki, T. Mitsuhashi, T. Fujita, J. Yazaki, K. Yamaguchi, K. Ogura, *Chemical Communications* **1996**, 1535.

CHAPTER V

**DINUCLEAR LANTHANIDE COMPLEXES AS PROTOTYPES
FOR 2-QUBIT QUANTUM GATES**

1. Introduction

In the previous chapters, the strategy followed for the design of molecular assemblies to embody quantum bits has involved clusters with transition metal ions. In this respect, the use of such metalloaggregates allows a versatile approach to define the spin carriers, since their magnetic properties can be modified in many ways by chemical methods. Compound **7** $[\text{Ni}_2\text{Cu}_2(\text{L1})_2(\text{py})_6]$, for example, is based on two weakly coupled cluster units ($[\text{NiCu}]$), each of them exhibiting two states in a certain regime (below 50 K) due to an isolated $S = 1/2$ ground-state on each side of the molecule.

On the other hand, 4f elements have a large unquenched orbital moment that makes them an interesting tool in molecular magnetism, and in particular, for their application in quantum computing.^[1] Their complex $4f^n$ configuration is split into different J states due to the effects of the electron repulsion and spin-orbit coupling. The interaction with the crystal field removes the $(2J + 1)$ -fold degeneracy of each state, leading to m_J substates known as Stark levels. This magnetic richness makes lanthanide single ions to be very promising candidates to embody a quantum bit. Thus, if the splitting of J leads to a ground state magnetic doublet $\pm m_J$, well separated from the excited sublevels due to high anisotropy, it can provide a well-defined two-level system, describing possible $|1\rangle$ and $|0\rangle$ states (Figure V.1). In addition, lanthanide-based complexes usually exhibit weak magnetic exchange couplings due to the inner nature of 4f orbitals, and can facilitate the weak interaction required for the entanglement between qubits. It is also important to emphasize that the robustness of a quantum state decreases with the system's number of degrees of freedom, since this provides larger stability against decoherence.^[2] Therefore, in comparison with larger 3d metalloaggregates, using a single lanthanide ion to embody a qubit should improve the coherence of the system. Another advantage is the large tunneling gap (Δ) that usually exhibits the ground state of mononuclear lanthanide-based magnetic molecules, which can reach values up to $\Delta = 0.1\text{-}1\text{ cm}^{-1}$ (much higher than usual gaps from 3d cluster-type magnetic complexes, in the range of $\Delta = 10^{-8}\text{-}10^{-4}\text{ cm}^{-1}$).^[2] Tunneling gap is considered to be critical for the manipulation of the quantum state, since large gaps facilitate the spin manipulation and the diminishing of the

decoherence of the system.^[3] All these different features make lanthanide ions to be regarded as an excellent tool for the rational design of molecular spin qubits.

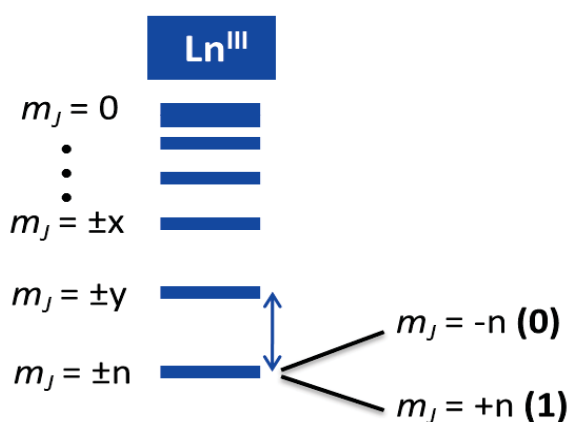


Figure V.1. Splitting of the J ground state leading to a ground-state magnetic doublet $\pm m_J$ due to high anisotropy.

The asymmetric topology of the ligand $\text{H}_3\text{L4}$ can be exploited to design dinuclear species with different environments within the molecular entity (Figure V.2). The ligand, which exhibits a β -diketone unit linked to a phenol group and a pyridine-2-carboxylic acid moiety, may coordinate two highly anisotropic metal ions, as lanthanides, perhaps integrating two inequivalent qubits in the same molecule. The characteristics of this system can thus represent an ideal model for a 2-qubit quantum gate. In this chapter, several homo and heterometallic dinuclear complexes using the ligand $\text{H}_3\text{L4}$ together with lanthanide ions are presented, and their properties as quantum gates are deeply discussed through enhanced magnetic and thermal studies.

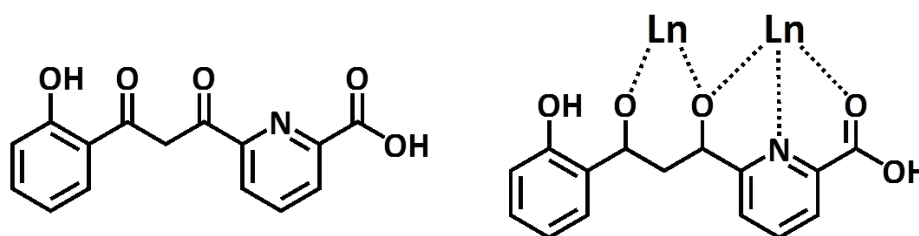
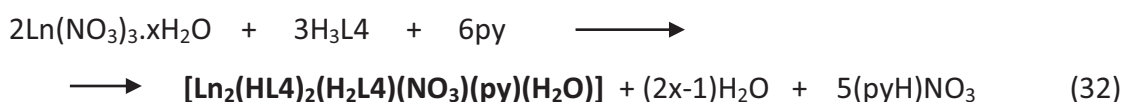


Figure V.2. Schematic representation of ligand $\text{H}_3\text{L4}$ (left) and possible coordination mode (right).

2. A comprehensive family of dinuclear homometallic lanthanide complexes

One of the more interesting strategies to build a universal quantum computer is through combination of single qubits and 2-qubit CNOT quantum gates.^[4] As detailed in Chapter I, this latter operation requires dissimilar qubits exhibiting weak interaction.^[5] Since it has been demonstrated that individual lanthanide ions are potential candidates for embodying the qubits of scalable quantum gates, a strategy to build up such molecular models is to design dinuclear asymmetric lanthanide systems. In that sense, the ligand H₃L4 has been synthesized in order to introduce the necessary inequivalence between both halves of the targeted assemblies. Following this proposition, the reaction of the ligand H₃L4 with Ln^{III} lanthanide (or yttrium) nitrate in the ratio H₃L4/Ln (or Y) = 3:2 in pyridine was carried out for each lanthanide ion of the series, producing dinuclear complexes with general formula, [Ln₂(HL4)₂(H₂L4)(NO₃)(py)(H₂O)], according to the following equation:



Single crystals suitable for X-ray analysis were obtained from the reactions with Ln = Ce (**13**), Pr (**14**), Nd (**15**), Sm (**16**), Eu (**17**), Gd (**18**), Tb (**19**), Dy (**20**), Ho (**21**), Er (**22**), Tm (**23**) and with Y (**26**), formed by the slow diffusion of the reaction solution with ether or toluene. Interestingly, when using the lightest and the heaviest metals of the series (La and Yb or Lu) in the above reaction, no crystals were obtained from layers. However, yellow crystals of [La₂(HL)₂(H₂L)(NO₃)(py)(H₂O)] (**12**) and [Yb₂(HL)₂(H₂L)(NO₃)(py)(H₂O)] (**24**) were obtained when one and three equivalents, respectively, of HNO₃ were added to the reaction. The presence of a small amount of nitric acid was used to affect the formation of crystallization, a process that coexists with a series of acid-base equilibria due to the presence of different deprotonated forms of H₃L4 in the system (see below). Similar attempts to obtain crystals of the analog with Lu (**25**) failed. Nevertheless, the formation of this complex as a solid was evidenced by IR spectroscopy, elemental analysis, and mass spectrometry (see below). To the best of our knowledge, no complete series of dinuclear lanthanide ions can be found in the literature, and only very few complete or almost complete series featuring

mononuclear rare earth complexes have been published.^[6-11] The high coordination number required when forming clusters, as well as the flexible coordination geometry of rare earth ions due to the absence of strong ligand field effects, makes lanthanide complexes very difficult to predict and control when prepared. In addition, the shrinking of the ionic radii through the series due to the phenomenon of lanthanide contraction favors the formation of different structures depending on the position of the rare earth in the series. In that sense, lanthanide ions exhibit big radii at the beginning of the period (i.e, La, Ce, Pr, Nd...) or a smaller size at the end of it (like Ho, Er, Tm, Yb, Lu) usually causing different coordination environments within the series.^[12-14] Therefore, the family of isostructural compounds $[\text{Ln}_2(\text{HL}_4)_2(\text{H}_2\text{L}_4)(\text{NO}_3)(\text{py})(\text{H}_2\text{O})]$ ($[\text{Ln}_2]$) represents a really exceptional system, since it constitutes the first comprehensive dinuclear lanthanide series, and provides an exquisite tool to investigate not only their physical properties but also the characteristics of the lanthanide contraction.

2.1. Study of the crystal structures

The crystal structure of each compound reveals a dinuclear asymmetric cluster where the two lanthanides are encapsulated by three molecules of the ligand, with a general formula $[\text{Ln}_2(\text{HL}_4)_2(\text{H}_2\text{L}_4)(\text{NO}_3)(\text{py})(\text{H}_2\text{O})]$. All the compounds in the series exhibit very similar molecular structure (Figure V.3, crystal structure of $[\text{Sm}_2(\text{HL}_4)_2(\text{H}_2\text{L}_4)(\text{NO}_3)(\text{py})(\text{H}_2\text{O})]$ as example), with one dinuclear asymmetric molecule per asymmetric unit, together with pyridine and water molecules in the lattice. The crystallographic structures for all clusters belong to the space group $P2_1/c$ and have similar cell parameters (see Tables V.A1 and V.A2, Appendix).

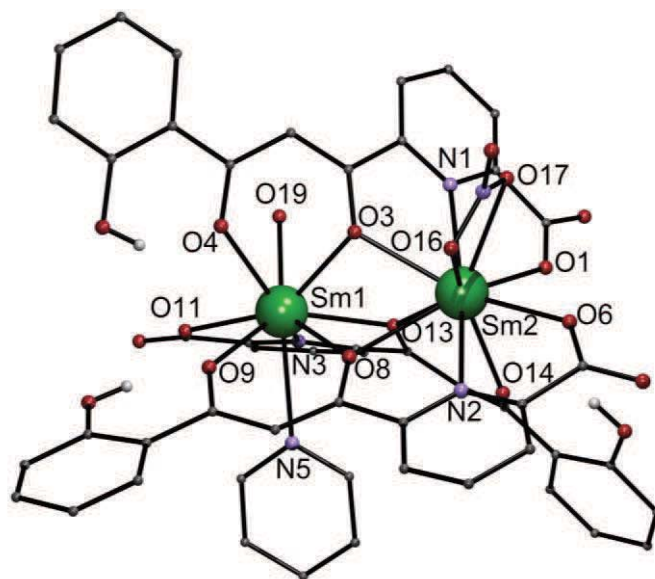


Figure V.3. Representation of the molecular structure of the complex $[\text{Sm}_2(\text{HL}_4)_2(\text{H}_2\text{L}_4)(\text{NO}_3)(\text{py})(\text{H}_2\text{O})]$ (**16**). Green, Sm; violet, N; red, O; rest, C. Only hydrogen atoms bound to O are shown.

The Ln^{III} ions are chelated and bridged by three partially deprotonated ligands. While HL_4^{2-} lacks both the carboxylic and β -diketonic protons, the third molecule of ligand maintains the carboxylic proton (H_2L_4^-), and the head-head-tail disposition leads, with the help of a NO_3^- ligand, to a neutral asymmetric entity. Although this carboxylic proton is not always found crystallographically, it can be confirmed due to the formation of a hydrogen bond with a pyridine molecule oriented accordingly (Figure V.4). The two metals are accommodated by the β -diketone and dipicolinate-like groups from the ligand, and bridged by common oxygen atoms from these pockets (Scheme V.5). For all the complexes in the series, the lanthanide ion placed in pocket 1 (henceforward called Ln1) does not vary the coordination number through the series, achieving for all cases coordination nine. Ln1 is coordinated to one dipicolinate-like group from one ligand, and two β -diketone groups from the other two. The nonacoordination is completed with one H_2O and one pyridine ligand. The protons of the water ligand were found to form hydrogen bonds with lattice pyridine molecules. The lanthanide ion located in pocket 2, hereafter called Ln2, is coordinated to one β -diketone group from one ligand and two dipicolinate-like groups from the other two ligands, and contains a NO_3^- ligand to reach either nona or decacoordination.

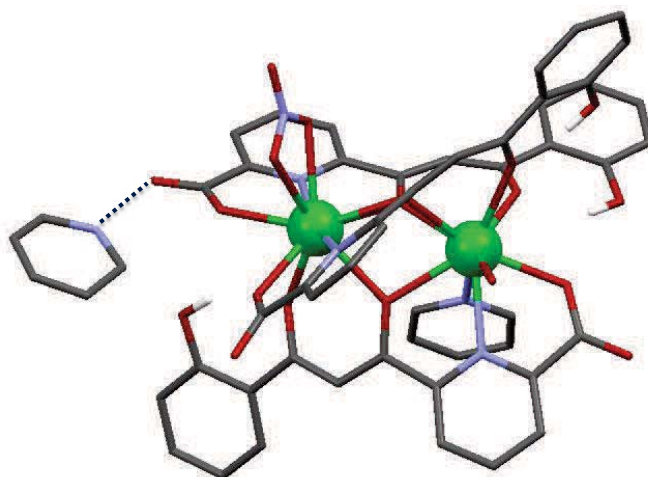
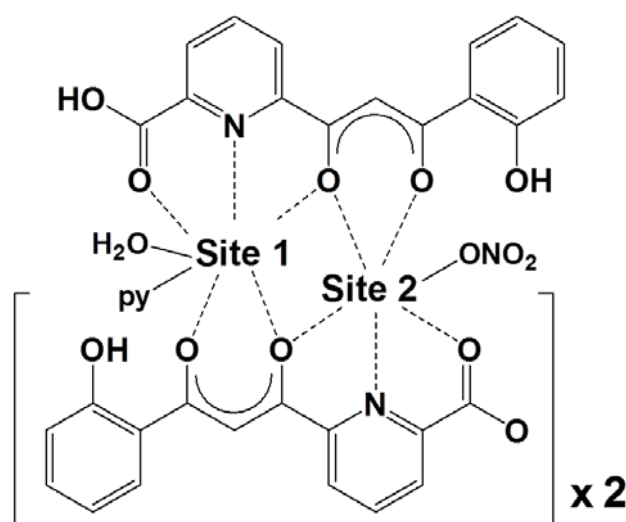


Figure V.4. Representation of the complex $[\text{Sm}_2(\text{HL4})_2(\text{H}_2\text{L4})(\text{NO}_3)(\text{py})(\text{H}_2\text{O})]$ (**16**) exhibiting hydrogen bonding interaction with a lattice molecule of pyridine through the proton of the carboxylic acid moiety. Green, Sm; violet, N; red, O; rest, C. Only hydrogen atoms bound to O are shown.



Scheme V.5. Schematic representation of the molecular system $[\text{Ln}_2(\text{HL4})_2(\text{H}_2\text{L4})(\text{NO}_3)(\text{py})(\text{H}_2\text{O})]$. Site 2 offers two dipicolinate-like groups and one diketone group, while site 1 contains one dipicolinate group and two diketone groups.

Thus, for bigger ionic radii Ln^{III} (La, Ce, Pr, Nd, Sm and Eu complexes **12-17**), bidentate coordination is preferred for the NO_3^- ligand in Ln_2 , leading to decacoordinated metals. In the literature there are several examples that demonstrate how the coordination number decreases through the lanthanide series.^[12-15] In this case, the system selects Eu^{III} (compound **17**) as the smallest ion that can afford coordination number of ten.

However, attempts to repeat complex **17** revealed also that the cluster can crystallize with NO_3^- ligand in a monodentate mode (complex **17a**). This sort of “bistability”, which has been observed already for other Ln series,^[16] demonstrates that this metal ion marks the border between deca- and nonacoordination in site 2. On the other part, Gd, Tb, Dy, Ho, Er, Tm, Yb and Y (complexes **18-24** and **26**) have their ionic radii not big enough to achieve this coordination number ten, and the NO_3^- ligand coordinates in a monodentate mode. The structure of $[\text{Ce}_2(\text{HL4})_2(\text{H}_2\text{L4})(\text{NO}_3)(\text{py})(\text{H}_2\text{O})]$ and $[\text{Tm}_2(\text{HL4})_2(\text{H}_2\text{L4})(\text{NO}_3)(\text{py})(\text{H}_2\text{O})]$ are shown in Figure V.6, representing the crystal structure of complexes with big and small ionic radii lanthanides, respectively. As expected, the only difference between both structures is the coordination mode of the NO_3^- ligand, obtaining therefore a practically isostructural series.

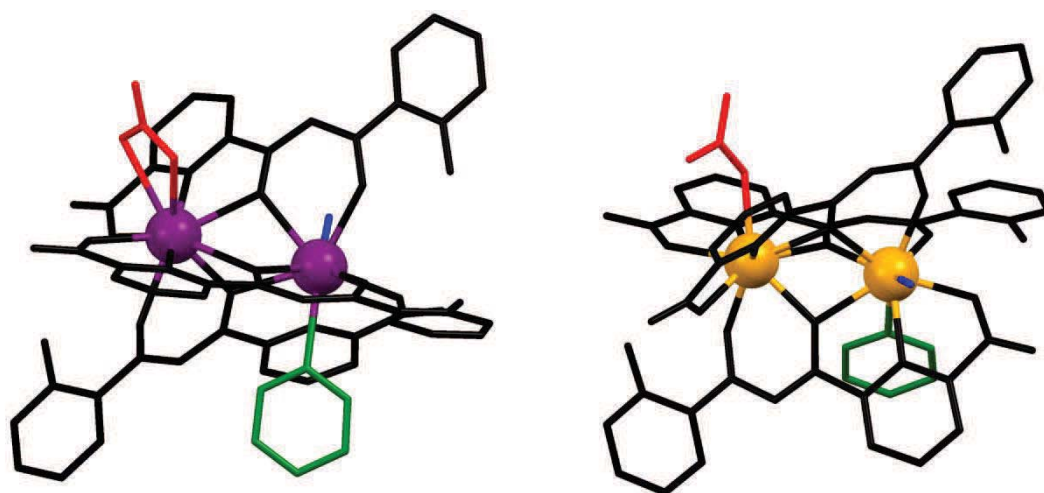


Figure V.6. Representation of complexes $[\text{Ce}_2(\text{HL4})_2(\text{H}_2\text{L4})(\text{NO}_3)(\text{py})(\text{H}_2\text{O})]$ (left) and $[\text{Tm}_2(\text{HL4})_2(\text{H}_2\text{L4})(\text{NO}_3)(\text{py})(\text{H}_2\text{O})]$ (right). Black, deprotonated forms of the ligand; Violet, Ce; Orange, Tm; Red, NO_3^- ; Blue, H_2O ; Green, pyridine. H atoms are excluded.

2.2. Analysis of the lanthanide contraction

One of the main characteristics of an isostructural series of Ln^{III} complexes is that no parameters other than the nature of the metal change along it. Recently, it has been demonstrated that X-ray structural studies on these kinds of series can be used as an experimental evaluation of the lanthanide contraction.^[17] When certain parameters such as the Ln-X bond distances are assessed versus the number of f electrons, it is shown that they can be best described by a second-order polynomial (equation 33),

$$d(\text{Ln} - \text{X}) = A_0 + A_1n + A_2n^2 \quad (33)$$

A_0 , A_1 and A_2 being the constant, linear and quadratic parameters of the polynomial respectively, and n the number of f electrons. Such study has been carried out using isostructural series of lanthanide complexes published in the literature, and also on some incomplete series including solid-state non-molecular materials.^[17] The system $[\text{Ln}_2(\text{HL4})_2(\text{H}_2\text{L4})(\text{NO}_3)(\text{py})(\text{H}_2\text{O})]$ exhibits two different lanthanide environments that can be evaluated, including new parameters like the distance between both centres ($\text{Ln}\cdots\text{Ln}$), due to the dinuclearity of the complexes. Thus, each Ln-O and Ln-N distance has been extracted from the crystallographic data of each compound, and compiled in Table V.1. The additional bond distances and angles for all the dinuclear complexes of the series can be found in the Appendix (Table V.A3 and V.A5).

Table V.1. Bond lengths Ln-X in the system [Ln₂(HL₄)₂(H₂L₄)(NO₃)(py)(H₂O)] for complexes 12 to 24 and 26

Bond	La (12)	Ce (13)	Pr (14)	Nd (15)	Sm (16)	Eu (17)	Gd (18)	Tb (19)	Dy (20)	Ho (21)	Er (22)	Tm (23)	Yb (24)	Y (26)
d _{Ln1-O3} (σ)	2.493(3)	2.467(4)	2.445(3)	2.422(9)	2.422(10)	2.406(5)	2.375(11)	2.374(12)	2.311(11)	2.319(5)	2.339(5)	2.295(5)	2.311(8)	2.269(17)
d _{Ln1-O4} (σ)	2.524(3)	2.513(4)	2.486(3)	2.485(9)	2.466(9)	2.447(5)	2.458(11)	2.445(11)	2.435(8)	2.407(5)	2.415(5)	2.386(4)	2.400(7)	2.402(15)
d _{Ln1-O8} (σ)	2.541(3)	2.511(3)	2.482(3)	2.484(9)	2.408(9)	2.409(5)	2.416(10)	2.383(11)	2.378(8)	2.369(5)	2.358(4)	2.349(4)	2.351(7)	2.346(14)
d _{Ln1-O9} (σ)	2.457(3)	2.444(3)	2.419(3)	2.394(9)	2.361(10)	2.352(5)	2.339(11)	2.336(11)	2.323(9)	2.304(6)	2.290(5)	2.296(4)	2.273(8)	2.282(14)
d _{Ln1-O11} (σ)	2.455(3)	2.428(4)	2.412(3)	2.415(9)	2.388(10)	2.383(5)	2.372(12)	2.355(12)	2.315(10)	2.328(5)	2.324(5)	2.307(5)	2.305(8)	2.329(15)
d _{Ln1-O13} (σ)	2.532(3)	2.520(3)	2.492(3)	2.500(8)	2.439(9)	2.430(4)	2.465(9)	2.463(9)	2.455(7)	2.431(4)	2.394(4)	2.414(4)	2.401(7)	2.433(13)
d _{Ln1-O19} (σ)	2.579(3)	2.548(4)	2.545(3)	2.487(9)	2.478(11)	2.453(5)	2.444(12)	2.416(12)	2.424(10)	2.394(6)	2.381(5)	2.371(5)	2.357(8)	2.383(16)
d _{Ln1-N3} (σ)	2.599(4)	2.581(4)	2.557(4)	2.537(11)	2.500(12)	2.500(6)	2.483(13)	2.482(13)	2.466(10)	2.447(6)	2.437(6)	2.423(5)	2.419(8)	2.434(18)
d _{Ln1-N5} (σ)	2.786(4)	2.767(5)	2.737(4)	2.729(13)	2.720(14)	2.699(7)	2.700(14)	2.648(16)	2.682(15)	2.665(7)	2.670(7)	2.664(6)	2.666(11)	2.680(20)
d _{Ln2-O1} (σ)	2.463(3)	2.438(4)	2.416(3)	2.418(9)	2.403(10)	2.390(5)	2.361(11)	2.375(11)	2.358(9)	2.348(5)	2.339(4)	2.344(5)	2.328(7)	2.313(14)
d _{Ln2-O3} (σ)	2.577(3)	2.548(3)	2.534(3)	2.558(9)	2.468(9)	2.473(4)	2.437(9)	2.459(10)	2.471(8)	2.451(5)	2.418(4)	2.450(4)	2.399(7)	2.441(14)
d _{Ln2-O6} (σ)	2.485(3)	2.461(4)	2.440(3)	2.439(9)	2.397(9)	2.391(5)	2.393(10)	2.367(10)	2.359(9)	2.354(5)	2.339(4)	2.342(4)	2.327(7)	2.317(14)
d _{Ln2-O8} (σ)	2.693(3)	2.694(4)	2.671(3)	2.685(9)	2.651(9)	2.637(5)	2.631(10)	2.630(10)	2.570(9)	2.562(5)	2.603(4)	2.545(4)	2.600(7)	2.618(13)
d _{Ln2-O13} (σ)	2.547(3)	2.517(4)	2.499(3)	2.495(9)	2.437(9)	2.430(5)	2.384(10)	2.359(10)	2.374(9)	2.365(5)	2.331(5)	2.352(4)	2.304(7)	2.291(15)
d _{Ln2-O14} (σ)	2.503(3)	2.483(4)	2.470(3)	2.425(9)	2.454(9)	2.431(5)	2.373(10)	2.371(10)	2.340(9)	2.337(5)	2.333(5)	2.323(5)	2.308(7)	2.292(14)
d _{Ln2-O16} (σ)	2.628(4)	2.588(5)	2.581(3)	2.545(11)	2.542(10)	2.519(6)	2.424(12)	2.399(12)	2.396(11)	2.375(5)	2.380(5)	2.359(5)	2.362(8)	2.392(16)
d _{Ln2-O17} (σ)	2.767(4)	2.869(5)	2.771(4)	2.891(17)	2.674(11)	2.687(6)	-	-	-	-	-	-	-	-
d _{Ln2-N1} (σ)	2.674(4)	2.635(5)	2.630(4)	2.589(12)	2.604(13)	2.581(6)	2.538(13)	2.492(14)	2.480(12)	2.474(7)	2.483(6)	2.467(6)	2.440(10)	2.460(20)
d _{Ln2-N2} (σ)	2.739(4)	2.736(4)	2.714(3)	2.694(11)	2.656(12)	2.664(6)	2.619(12)	2.610(13)	2.591(11)	2.581(7)	2.590(5)	2.562(5)	2.554(10)	2.568(18)
d _{Ln1...Ln2} (σ)	3.9590(4)	3.9286(5)	3.8941(6)	3.8814(5)	3.8197(13)	3.8173(8)	3.8038(11)	3.7854(13)	3.7709(9)	3.7570(5)	3.7405(5)	3.7354(4)	3.7245(7)	3.741(4)

As a general trend, it is shown how each individual bond decreases through the series. However, while the metal contraction leads to a shrinking of all the metal-ligand distances, the effect is more pronounced in some Ln-X bonds than other. This is reflexed in some irregularities when evaluating each individual bond distance, which harms their fit by a second-order polynomial as it was proposed.^[10]

Nevertheless, the fit can be carried out more satisfactorily when the sum of the bond distances in each environment is studied. For the series presented here, we considered that the metal size reduction would have a concerted effect on the overall distance to the metals from the donors of the $(H_{3-x}L_4)^{-x}$ ligands. Thus, for each of the two metals in the cluster, the sum of the bond lengths Ln-O from these ligands versus the number of f electrons was evaluated, excluding Ln-N bonds for a more homogeneous study. Figure V.7 shows the variation with n of the sums $\sum_m(Ln1-O)$ and $\sum_m(Ln2-O)$ ($m = 6$ in both sites), demonstrating that the expected quadratic trend is obtained. A weighted polynomial regression has been performed on each parameter (the weight of each datum being the reciprocal of the error associated with the sum of the bond distances) obtaining good results for both fits ($R^2 = 0.9946$ for site 1 and $R^2 = 0.9951$ for site 2).

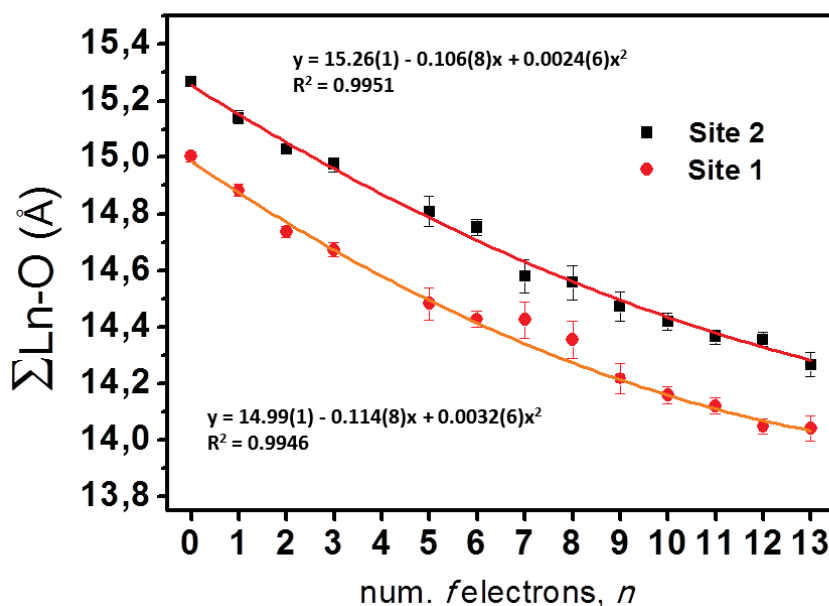


Figure V.7. Sum of the Ln-O bond distances against the number of f electrons for site 1 (red) and site 2 (black) and second order polynomial weighting fitting.

The dependence of the sum of the Ln-X bond lengths with the n number of f electrons, $S(n)$, has served to produce insights into the origin of the lanthanide contraction through an isostructural series.^[10] This phenomenon is caused by the poor shielding effect of $4f$ electrons (quantified by the screening constant of one f electron, k) that leads the ionic radii of lanthanide elements to decrease greater than expected. A theoretical model introduced first by Slater^[18] and later modified by Clementi et al.^[19, 20] has been used to treat this behavior, using a set of empirical rules for the shielding of the nuclear charge. Thus, the sum $S(n)$ of m Ln-X bond lengths for each lanthanide ion can be written as m times the corresponding ionic radius $r(n)$ and the sum of the radii $r_L(n)$ of all the coordinating atoms considered:

$$S(n) = \sum_{i=1}^m r_{L,i}(n) + mr(n) \quad (34)$$

In an isostructural series, the radii $\sum_{i=1}^m r_{L,i}(n)$ of the ligating atoms can be considered constant (S_L) for all the different complexes. In addition, the radius $r(n)$ of any lanthanide ion with n $4f$ electrons can be described as a function of the ionic radius (r_0) and the effective nuclear charge (Z^*_0) of La^{III} . Under these assumptions, the sum $S(n)$ can be rewritten as the following equation:

$$S(n) = S_L + mr_0 - \frac{mr_0(1-k)}{Z^*_0}n + \frac{mr_0(1-k)^2}{(Z^*_0)^2}n^2 = a + bn + cn^2 \quad (35)$$

From this polynomial equation, the different a , b and c parameters from the fit can be attributed to their respective parts,

$$a = S_L + mr_0; \quad b = \frac{mr_0(1-k)}{Z^*_0}n; \quad c = \frac{mr_0(1-k)^2}{(Z^*_0)^2}n^2 \quad (36)$$

Thus, taking into account the fit obtained for each environment, the screening constant k can be determined by means of b and c parameters using the following relations:

$$\frac{c}{b} = -\frac{(1-k)}{Z^*_0} \quad k = 1 + Z^*_0 \frac{c}{b} \quad (37)$$

The commonly accepted value for the screening constant of one f electron is $k = 0.69$.^[10] Slater's model was thus applied to assess the effects of the lanthanide contraction by calculating the k value from both lanthanide ions of the $[\text{Ln}_2(\text{HL4})_2(\text{H}_2\text{L4})(\text{NO}_3)(\text{py})(\text{H}_2\text{O})]$ dinuclear system. Using the fit for site 1 (Figure V.7), which produces values of $c = 0.0031(7)$ and $b = -0.114(8)$, and considering $Z_0^* = 15.42$, the screening constant acquires a value of $k = 0.58$. The same procedure for site 2 ($c = 0.0025(7)$ and $b = -0.107(8)$) generates a value of $k = 0.63$. These values are close to the expected value described above, and are also very similar to the screening constant observed in a mononuclear cluster series.^[10] Additionally, it demonstrates that the monotonic quadratic trend of the lanthanide contraction is followed similarly on both sites, and that the model can be applied for the selected bond lengths. The different value of k in each environment may indicate the effect of the crystal-field on the capacity of these electrons to shield the nuclear charge.

The study of the sum of Ln-O bonds for each site allows evaluating not only the phenomenon of lanthanide contraction but also the differences between both environments. These data reflect the remarkable difference in size between pockets 1 and 2, and how this difference is nearly maintained in the whole series. The bigger site 2 (Figure V.7, in black), which contains two dipicolinate-like groups and one diketone unit from the ligands, seems to have more room and flexibility compared with the smaller site 1 (Figure V.7, in red), in which the two smaller diketone units significantly contract the environment of Ln1, despite the presence of a dipicolinate group from the third ligand. Thus, this difference in "cavity size" between both sites is undoubtedly the result of the structural constraints imposed by the disposition of ligands within the assembly.

The quadratic decay of the lanthanide contraction can be extended to other structural parameters, such as the overall shrinkage of the coordination polyhedron. Representative parameters for this in the $[\text{Ln}_2(\text{HL4})_2(\text{H}_2\text{L4})(\text{NO}_3)(\text{py})(\text{H}_2\text{O})]$ system would be the length of the O...O edges. This was studied simultaneously for both sites, thus the three O...O vectors shared in both polyhedra from the three bridging oxygen atoms (O3, O8 and O13) were taken (Figure V.8, inset). Since the previous study demonstrates a quadratic decay in both environments, the study on these selected

O...O distances is expected to follow also the same decrease. To assess this behavior, the dependence of the distance between these three oxygen atoms was studied as the variation of their average versus the number of f electrons (Figure V.8).

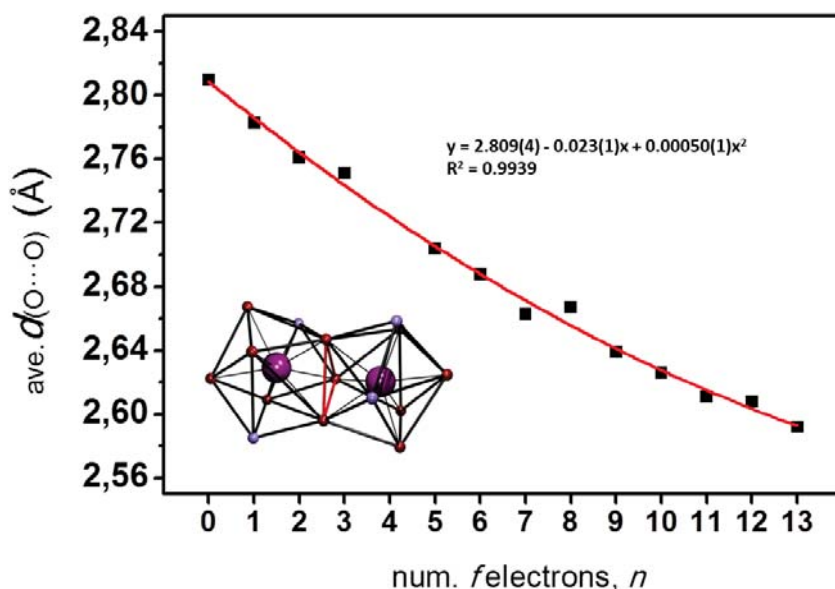


Figure V.8. Average of the O...O distances shared between both coordination polyhedra (highlighted in red, figure) against the number of f electrons and second order polynomial fitting.

The results of the fit show that the dependence follows a quadratic decay in a good agreement ($R^2 = 0.9939$). Despite the fact that the quadratic term entails quite large relative error, it is smaller than the term itself. As has been seen in the previous study, the quadratic nature of the lanthanide contraction is better followed studying the average of these three parameters rather than using any of the three distances individually.

The evaluation of the bridging oxygen donor atoms, together with the sum of the Ln-O distances, is strictly related to shrinkage involving the scaffold of the structure (the deprotonated forms of H_3L4). However, both sites complete their coordination sphere with additional molecules (water and pyridine for site 1, NO_3^- for site 2). The decrease of the Ln-X distances involving the H_2O and pyridine ligands in site 1 was evaluated to elucidate the possible quadratic decay and thus the influence of the lanthanide contraction on them. The dependence of Ln-O (water) and Ln-N (pyridine) bond

lengths in Ln1 versus the number of f electrons is shown in Figure V.9. Worse polynomial fits were obtained comparing the former parameters ($R^2 = 0.9682$ and 0.9797 for Ln-N_{py} and Ln-O_{water}, respectively). This behavior can be related to the greater freedom and flexibility of both solvent molecules to adapt themselves in the dinuclear system, accommodating and stabilizing the crystal structure and thus possibly moving away from the pure lanthanide contraction effect. In addition, this is consistent with the proposed fact that individual bonds may exhibit a more irregular behavior.^[10]

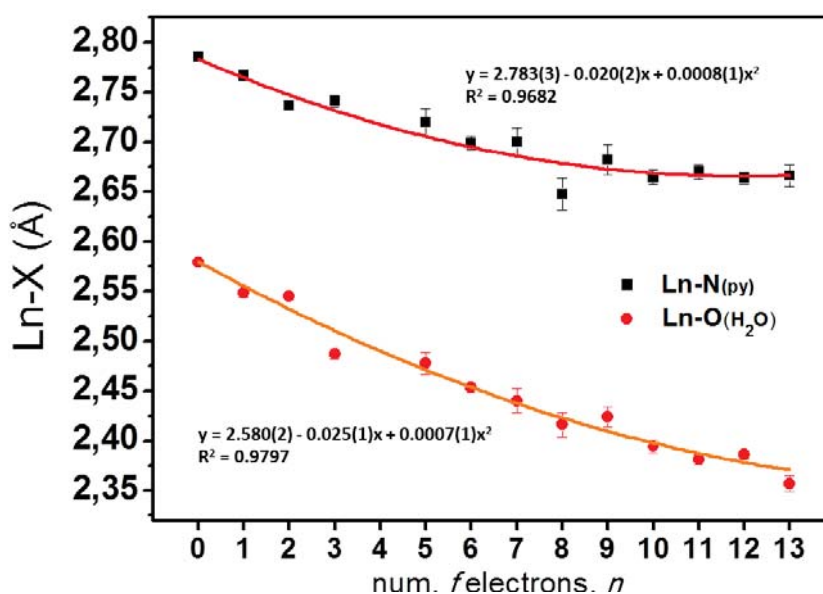


Figure V.9. Ln-O_{water} (red) and Ln-N_{py} (black) bond distances of site 1 versus the number of f electrons and second order polynomial weighting fitting.

The quadratic decay has been also studied with regard to the distance between both ions in the system. Thus, the parameter Ln...Ln was evaluated in front of the number of f electrons. As depicted in Figure V.10, this dependence follows satisfactorily a quadratic decrease through the whole series ($R^2 = 0.9978$). The evaluation of this parameter, as well as the average of O...O distances within the coordination polyhedra shared by both metals, show for the first time the manifestation of the lanthanide contraction on parameters that receive the contribution of two lanthanide ions simultaneously.

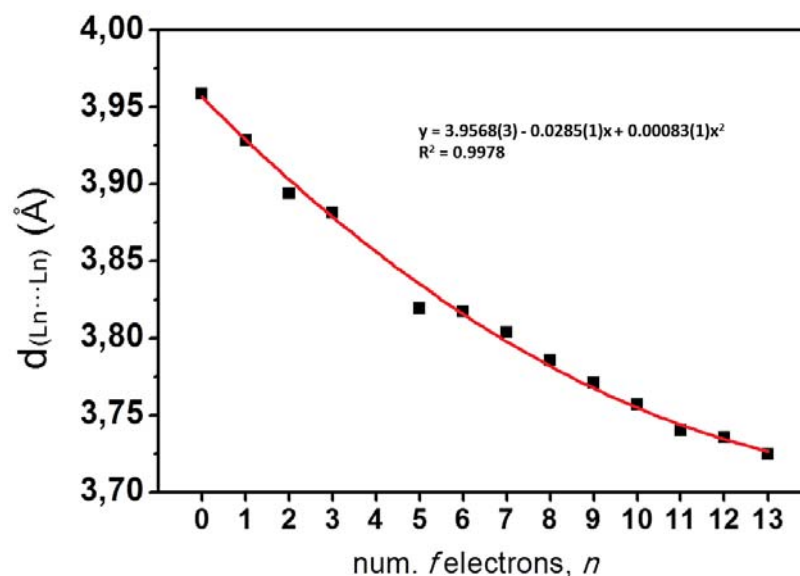


Figure V.10. Ln...Ln distances against the number of f electrons for $[\text{Ln}_2(\text{HL4})_2(\text{H}_2\text{L4})(\text{NO}_3)(\text{H}_2\text{O})(\text{py})]$ and second order polynomial weighting fitting.

2.3 Continuous-shape measures of the coordination polyhedra in $[\text{Ln}_2(\text{HL4})_2(\text{H}_2\text{L4})(\text{NO}_3)(\text{H}_2\text{O})(\text{py})]$

The stereochemical disparity between both metals within the $[\text{Ln}_2(\text{HL4})_2(\text{H}_2\text{L4})(\text{NO}_3)(\text{H}_2\text{O})(\text{py})]$ system has been quantified by means of continuous-shape measures (CShMs).^[21, 22] As introduced in Chapter 3, this measurement compares the coordination polyhedra of a metal ion with different ideal polyhedra existing for its respective coordination number. Thus, the environment in site 2 was compared with some reference ten-coordination polyhedra when studying complexes **12-17**, and with several ideal nine-coordination polyhedra for complexes **17'-24** and **26**. Since the environment in site 1 does not change throughout the series, the measurement was carried out regarding the ideal nine-coordination polyhedra in all complexes. The reference polyhedra proposed for each coordination number are detailed in Table V.2.

Table V.2. Reference coordination polyhedra for coordination number nine and ten.^[21, 22]

MFF-9	“muffin”	C_s
JCSAPR-9	Capped square antiprism	C_{4v}
JTCTPR-9	Tricapped trigonal prism	D_{3h}
JTDIC-9	Tridiminished icosahedron	C_{3v}
CSAPR-9	Capped square antiprism	C_{4v}
TCTPR-9	Tricapped trigonal prism	D_{3h}
CCU-9	Capped cube	C_{4v}
HH-9	Hula-hoop	C_{2v}
JBCSAPR-10	Biccapped square antiprism	D_{4d}
TD-10	Tetradecahedron	C_{2v}
HD10	Hexadecahedron	D_{4h}
SDD-10	Staggered dodecahedron	D_2
JSPC-10	Sphenocorona	C_{2v}
JMBIC-10	Metabidiminished icosahedron	C_{2v}
PPR-10	Pentagonal prism	D_{5h}
PAPR-10	Pentagonal antiprism	D_{5d}

The results of the measurement are showed in Table V.3 for complexes **12-17** and in Table V.4 for complexes **17'-24** and **26**. The study reflects the greater irregularity of site 2, since the distances of the coordination figures of this site to any ideal polyhedron are always more than four times larger than any of the best values observed for site 1. For compounds **12-17**, where decacoordination is accomplished in site 2 due to the chelating preference of nitrate ligand, the closest symmetry is C_{2v} , describing a sphenocorona geometry in **13-15** (Ce-Nd), and a tetradecahedron in **12** (La) and **17** (Eu). For compounds **17'-24** and **26** (Eu-Yb and Y), where site 2 belongs to coordination nine, the shape is best described as a “muffin” (C_1 symmetry).

Table V.3. Continuous Shape Measures (CSHMs) for the coordination geometry of Ln1 and Ln2 in compounds 12-17. Highlighted are the closest polyhedra for each metal

	MFF-9	JCSAPR-9	JTCTPR-9	JTDIC-9	CSAPR-9	TCTPR-9	CCU-9	HH-9
La1	1.023	1.934	3.010	12.744	0.897	1.158	9.396	11.567
Ce1	1.041	1.908	2.941	12.566	0.857	1.059	9.548	11.605
Pr1	1.015	1.839	2.897	12.581	0.767	0.984	9.410	11.617
Nd1	1.037	1.858	2.974	12.786	0.767	0.827	8.997	11.496
Sm1	1.013	1.839	2.853	13.138	0.715	1.114	8.630	10.937
Eu1	1.006	1.785	2.836	13.023	0.684	1.015	8.763	10.996
	JBCSAPR-10	TD-10	HD-10	SDD-10	JSPC-10	JMBIC-10	PPR-10	PAPR-10
La2	4.843	3.443	8.956	3.492	3.466	7.205	9.871	10.598
Ce2	5.324	3.973	8.949	3.809	3.210	7.528	9.699	10.558
Pr2	4.692	3.564	9.154	3.619	3.260	7.259	10.217	10.813
Nd2	6.284	4.468	8.162	3.804	3.575	8.037	9.693	9.524
Sm2	3.779	3.086	8.317	3.871	3.736	7.126	11.537	12.174
Eu2	3.873	3.169	8.623	3.782	3.559	7.165	11.291	11.944

Table V.4. Continuous Shape Measures (CSHMs) for the coordination geometry of Ln1 and Ln2 in compounds 17'-24 and 26. Highlighted are the closest polyhedra for each metal

	MFF-9	JCSAPR-9	JTCTPR-9	JTDIC-9	CSAPR-9	TCTPR-9	CCU-9	HH-9
Eu1	1.066	1.807	2.852	12.674	0.682	0.900	9.129	11.291
Eu2	3.139	5.232	5.904	9.890	4.238	5.280	6.285	3.982
Gd1	1.086	1.871	3.013	12.501	0.678	0.866	9.252	11.481
Gd2	2.945	5.002	6.146	10.016	4.094	4.979	6.647	4.233
Tb1	1.069	1.799	2.793	12.671	0.669	0.835	9.040	11.182
Tb2	2.933	5.008	5.708	10.079	4.033	5.091	6.393	4.186
Dy1	1.118	1.899	3.059	12.619	0.695	0.693	9.360	11.673
Dy2	2.799	4.815	4.851	9.389	3.748	4.341	5.849	4.438
Ho1	1.110	1.939	3.018	12.630	0.734	0.665	9.309	11.490
Ho2	2.735	4.779	4.725	9.020	3.721	4.209	6.076	4.648
Er1	1.158	1.865	2.887	12.565	0.662	0.791	9.282	11.422
Er2	2.659	4.675	5.593	10.400	3.637	4.543	6.633	4.571
Tm1	1.098	1.940	2.983	12.785	0.716	0.673	9.377	11.570
Tm2	2.528	4.404	4.332	9.175	3.439	3.858	6.250	5.006
Y1	1.192	1.937	3.124	12.622	0.662	0.782	9.409	11.839
Y2	2.835	4.902	5.861	10.094	3.943	4.841	6.756	4.309

On the other hand, site 1 shows a higher symmetric coordination geometry denoted by the better correspondence when comparing with the best ideal polyhedron. According to the CSHMs results, two geometries are suiting properly in this position. While for

compounds **12-19** (Ce-Tb), **22** (Er) and **26** (Y), the best approximation is the polyhedron described as spherical capped square antiprism (C_{4v} symmetry), compounds **20** (Dy), **21** (Ho) and **23** (Tm) are better defined in a D_{3h} symmetry as a spherical tricapped trigonal prism. Figure V.11 shows the ideal nine-vertex and ten-vertex polyhedra to which the nine and ten coordinated metals, respectively, have been compared.

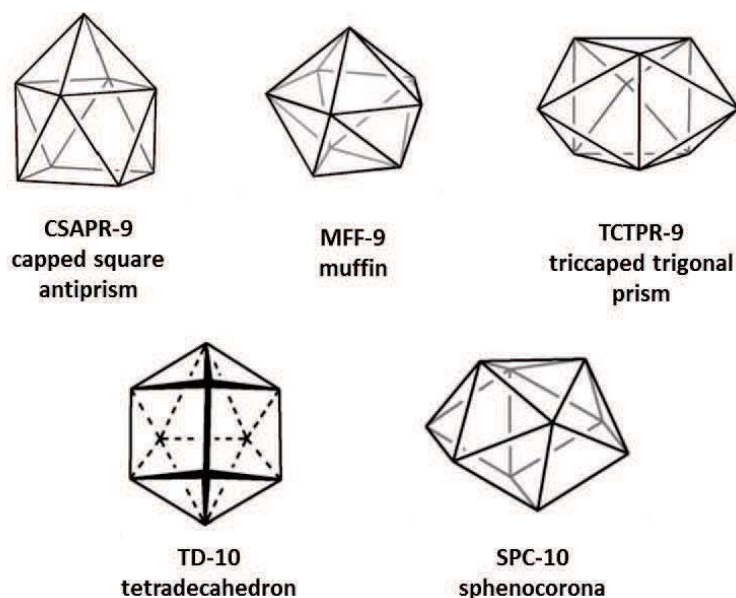


Figure V.11.^[21, 22] Ideal nine-vertex (capped square antiprism, muffin and tricapped trigonal prism) and ten-vertex polyhedra (tetradecahedron and sphenocorona) to which the coordination geometries of nine and ten coordinated metals, respectively, of complexes **1** to **13** have been compared.

2.4 Mass spectrometry of the $[\text{Ln}_2(\text{HL4})_2(\text{H}_2\text{L4})(\text{NO}_3)(\text{H}_2\text{O})(\text{py})]$ series

Electrospray mass spectrograms were recorded in methanol for all the compounds of the series, showing several important peaks for different species belonging to the free ligand and less intense signals for the complexes. The poor intensity of the coordination species in front of the ionization of the ligand was expected since unsaturated lanthanide complexes are known to possess weak ESMS responses because of the difficulty of solvated species to transfer to the gas phase.^[23] The ionization of the complexes was obtained after losing the pyridine and H_2O ligands as well as the NO_3^- group, leading to moieties with general formulae $[\text{Ln}_2(\text{HL4})_2(\text{H}_2\text{L4})]^+$. The mass spectrometric study also showed the addition of a second proton atom, $[\text{Ln}_2(\text{HL4})(\text{H}_2\text{L4})_2]^{2+}$, or the addition of a sodium ion substituting a proton ion, probably

from the diprotonated ligand: $[\text{Ln}_2(\text{HL}_4)_3+\text{Na}]^+$. The experimental isotope pattern for complex **17** (Eu) is depicted in Figure V.12 as a representative example, showing these different fragments, as well as the ones from the ligand. Selected fragments regarding $[\text{Er}_2(\text{HL}_4)_2(\text{H}_2\text{L}_4)]^+$ and $[\text{Er}_2(\text{HL}_4)(\text{H}_2\text{L}_4)_2]^{2+}$ species of complex **22** have been compared with the simulated signal considering the isotopic distribution (Figure V.13). Mass spectrograms for all the complexes in the series are shown in Figures V.A1 to V.A15 (Appendix), confirming the formulation of each system. Especially important is the case for compound **25** (Lu), where no crystal data could be obtained. The characteristic molecular peaks observed in this compound through the spectrometric study confirm the successful synthesis of this dimer, previously shown by infrared spectroscopy and chemical analysis.

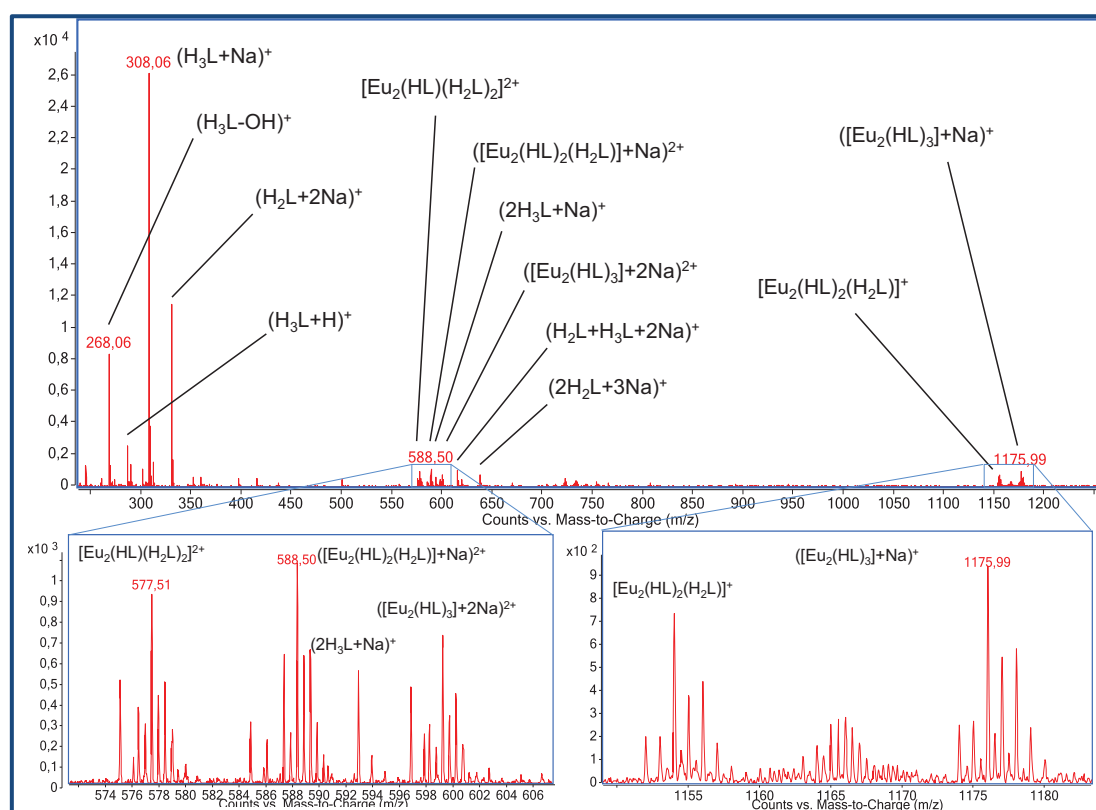


Figure V.12. Electrospray mass spectra recorded in methanol for $[\text{Eu}_2(\text{HL}_4)_2(\text{H}_2\text{L}_4)(\text{NO}_3)(\text{py})(\text{H}_2\text{O})]$ (**17**), featuring different related species (see text).

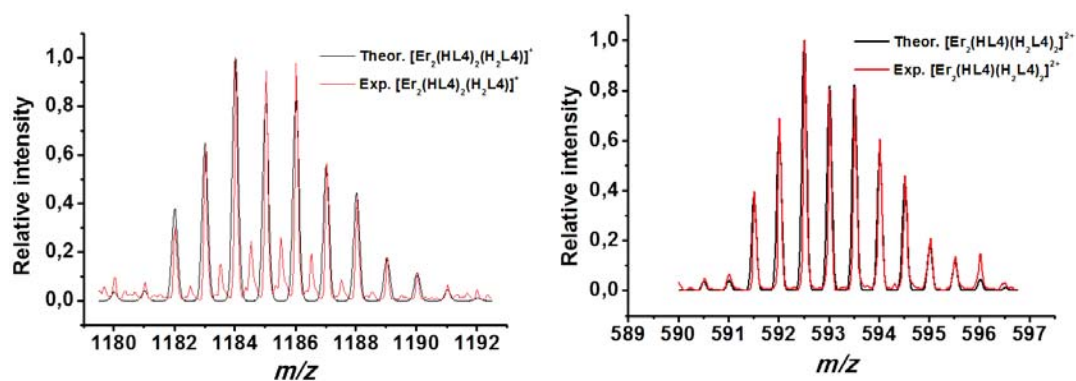


Figure V.13. Selected fragments of the mass spectrogram of $[\text{Er}_2(\text{HL4})_2(\text{H}_2\text{L4})(\text{NO}_3)(\text{py})(\text{H}_2\text{O})]$ (**22**). The simulated signals are also represented where the isotopic distribution has been taken into consideration. (left) Fragment $[\text{Ln}_2(\text{HL4})_2(\text{H}_2\text{L4})]^+$. (right) Fragment $[\text{Ln}_2(\text{HL4})(\text{H}_2\text{L4})_2]^{2+}$.

2.5. Magnetic behavior of complexes $[\text{Ln}_2(\text{HL4})_2(\text{H}_2\text{L4})(\text{NO}_3)(\text{H}_2\text{O})(\text{py})]$

As previously introduced, the large unquenched orbital moment of lanthanide ions makes them an exquisite tool in molecular magnetism. This is in spite that interpreting the magnetic properties of a $4f^n$ configuration ion turns to be much more complex because the spin-orbit coupling energy is usually larger than the crystal field effect. Indeed, this configuration is split into $^{2S+1}L_J$ states due to electron repulsions and the spin-orbit coupling. The crystal field removes the $(2J + 1)$ -fold degeneracy of these states leading to magnetic substates (m_J) known as Stark levels. At room temperature, all the Stark levels of the ground state are populated, but as temperature goes down, the excited m_J sublevels start depopulating, which translates into a variation of the χ_{MT} values. In a Ln^{III} dinuclear compound, the magnetic response depends not only on this effect but also on the possible magnetic exchange between both ions, except for La^{III} and Lu^{III} , which are diamagnetic. However, since the magnetic exchange constants are expected to be weak, masking the interaction by the effect of depopulating the Stark levels can occur. Another special case is Gd^{III} , that has no orbital momentum, thus exhibiting spin-only behavior in a $^8S_{7/2}$ configuration, which allows the investigation of the potential coupling between both lanthanide ions. For their application as quantum gates, the study of this coupling, as well as the evaluation of the magnetic energy levels of each ion in the complex must be carried out. As a first assessment of these physical properties, the magnetic behavior of the paramagnetic complexes in the

series has been investigated through variable-temperature bulk magnetization measurements on powdered microcrystalline samples (Figure V.14).

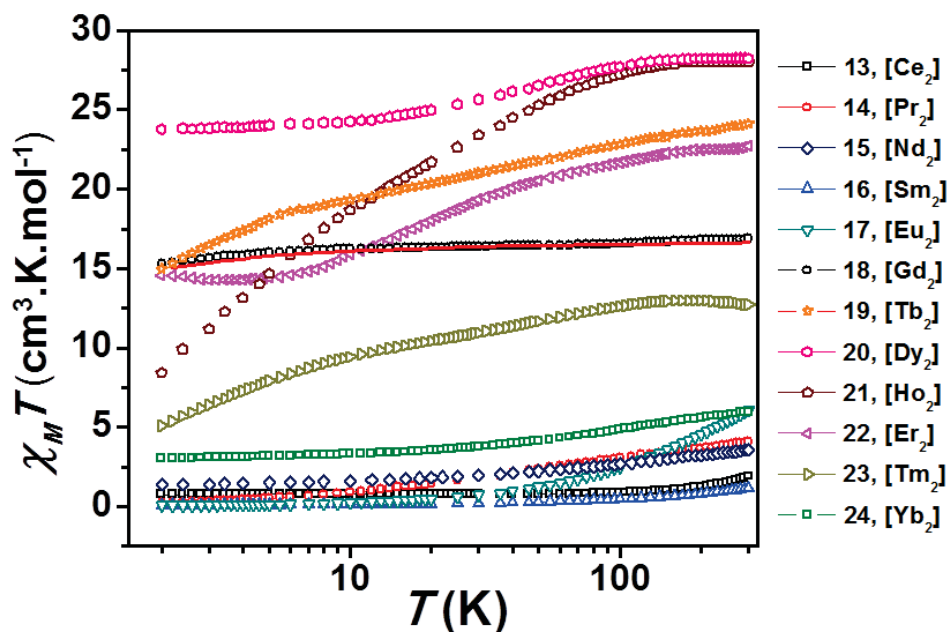


Figure V.14. $\chi_M T$ vs T curves for compounds **13** to **24**, χ_M being the molar paramagnetic susceptibility per $[\text{Ln}_2]$ unit. The full red line represents the best fit of the experimental data for **18** (see text for details).

Complex **18** ([Gd₂]) was used to evaluate the magnetic response of the system without the contribution of the spin-orbit coupling. The temperature dependence of $\chi_M T$ (with χ_M being the molar paramagnetic susceptibility per [Gd₂] unit) shows a stable $\chi_M T$ value of ca. 16.8 $\text{cm}^3 \text{K mol}^{-1}$ from room temperature down to 40 K, where a slight decrease occurs down to 15.28 $\text{cm}^3 \text{K mol}^{-1}$ at 2 K. Since no anisotropic effects can be invoked, this decline can only be ascribed to a weak antiferromagnetic interaction. The experimental $\chi_M T$ data at high temperature are close to the expected value for two uncoupled Gd^{III} ions with $g = 2$ (15.75 $\text{cm}^3 \text{K mol}^{-1}$). The $\chi_M T$ vs T curve was modeled using the isotropic spin Hamiltonian $H = -J(S_{\text{Gd1}} \cdot S_{\text{Gd2}})$, including a fixed temperature-independent paramagnetism (TIP) term.^[24] The parameters obtained were $J = -0.02(1)$ cm^{-1} and $g = 2.05(1)$, which are in correct agreement with the literature data.^[25] For the Ce^{III} complex **13**, the $\chi_M T$ value decreases continuously from 1.88 $\text{cm}^3 \text{K mol}^{-1}$ at 300 K, which is slightly higher than the expected value of 1.60 $\text{cm}^3 \text{K mol}^{-1}$ for two isolated Ce^{III} ions in the $^2F_{5/2}$ ground state and $g = 6/7$. This suggests that excited states

with higher J values are populated. The decline can be attributed to the depopulation of both excited levels and the Stark sublevels of the ground state. At 70 K, χ_{MT} remains stable at ca. $0.79 \text{ cm}^3 \text{ K mol}^{-1}$ down to 7 K, where a small decrease is observed, reaching a value of $0.74 \text{ cm}^3 \text{ K mol}^{-1}$. By analogy with **18**, this decrease is probably a consequence of a weak antiferromagnetic interaction between both Ce^{III} centres. The curve for complex **14** ($[\text{Pr}_2]$) shows a continuous decrease from $4.07 \text{ cm}^3 \text{ K mol}^{-1}$ at 300 K, a little above the calculated value of $3.20 \text{ cm}^3 \text{ K mol}^{-1}$ for two uncoupled Pr^{III} ions in the $^3\text{H}_4$ ground state with $g = 4/5$, down to $0.22 \text{ cm}^3 \text{ K mol}^{-1}$ at 2 K. This behavior can be ascribed both to the depopulation of the Stark levels and the weak antiferromagnetic interaction. The results for the Nd^{III} complex **15** show a similar response, in this case with a decrease of the value of χ_{MT} from $3.55 \text{ cm}^3 \text{ K mol}^{-1}$ at room temperature (very close to the expected value of $3.28 \text{ cm}^3 \text{ K mol}^{-1}$ for two isolated Nd^{III} ions in the $^4\text{I}_{9/2}$ ground state with $g = 8/11$) to $1.03 \text{ cm}^3 \text{ K mol}^{-1}$ at 2 K. Complex **16** ($[\text{Sm}_2]$) presents a χ_{MT} value of $1.17 \text{ cm}^3 \text{ K mol}^{-1}$ at 300 K, higher than the value expected for two magnetically insulated Sm^{III} ions in the $^6\text{H}_{5/2}$ ground state and $g = 2/7$ ($0.18 \text{ cm}^3 \text{ K mol}^{-1}$). This result confirms the low energy of the first and second excited multiplets ($J = 7/2$ and $J = 9/2$, respectively) of this particular lanthanide ion.^[26] χ_{MT} decreases continuously, reaching a value already close to zero at 15 K. The observed χ_{MT} vs T curve should be attributed to depopulation of the Stark levels of Sm^{III} ions, masking the possible weak interaction between them. For the Eu^{III} compound **17** (and, consequently, **17'**) χ_{MT} decreases from $3.45 \text{ cm}^3 \text{ K mol}^{-1}$ at room temperature, again far above the calculated value for two europium ions, that should be zero in the $^7\text{F}_0$ ground state. This behavior confirms also the influence of low-lying excited multiplets in this metal. At near 20 K, χ_{MT} is already close to zero, indicating that at this low temperatures, only the $J = 0$ ground state is populated. The magnetic behavior of the Tb^{III} complex **18** shows a continuous decrease from $\chi_{MT} = 24.11 \text{ cm}^3 \text{ K mol}^{-1}$ at room temperature down to 5 K, where the decline occurs faster until reaching a value of $\chi_{MT} = 14.98 \text{ cm}^3 \text{ K mol}^{-1}$ at 2 K. The high-temperature values are slightly above the expected ones for two uncoupled Tb^{III} ions in the $^7\text{F}_6$ ground state with $g = 3/2$ ($\chi_{MT} = 23.62 \text{ cm}^3 \text{ K mol}^{-1}$). The decrease at high temperatures can be attributed to the effects of the strong spin-orbit coupling of Tb^{III} , and reveals the strong magnetic anisotropy present in **17**. The decline at low temperatures is probably due to a weak

antiferromagnetic coupling between Tb^{III} ions. For the Dy^{III} complex **20**, χ_{MT} remains stable from 28.22 cm³ K mol⁻¹ at 300 K down to 150 K, when a gradual decrease begins, ending at 2 K with a value of 23.78 cm³ K mol⁻¹. The high-temperature values agree well with the expected value for two uncoupled Dy^{III} ions (⁶H_{15/2}, $g = 4/3$, $\chi_{MT} = 28.34$ cm³ K mol⁻¹). While the decline at low temperatures is probably caused by an antiferromagnetic coupling between both ions, the higher temperature behavior can be attributed to the effects of the strong spin-orbit coupling of Dy^{III}. For compound **21** ([Ho₂]), the value of χ_{MT} at 300 K (27.99 cm³ K mol⁻¹) is also very similar to the expected one for two Ho^{III} ions in the ⁵I₈ ground state and $g = 5/4$ (28.14 cm³ K mol⁻¹). Again, it remains stable until 150 K. In this case, χ_{MT} decreases more drastically down to low temperatures reaching a value of 8.43 cm³ K mol⁻¹. Complex **22** ([Er₂]) shows a value of χ_{MT} of 22.74 cm³ K mol⁻¹ at high temperatures, which agrees with the expected one for two independent Er^{III} ions in the ⁴I_{15/2} ground state with $g = 6/5$ ($\chi_{MT} = 22.96$ cm³ K mol⁻¹). As the temperature goes down, χ_{MT} reaches a minimum of 11.0 cm³ K mol⁻¹ at 3 K. When the temperature is lowered to 1.8 K, χ_{MT} reaches a plateau with a value of 11.4 cm³ K mol⁻¹. The decrease of the value of χ_{MT} from 300 K down to 3 K clearly belongs to the thermal depopulation of the excited magnetic sublevels, while the behavior at low temperatures indicates that there is almost no interaction between both ions within this complex. The thermal variation of the χ_{MT} product for the Tm^{III} complex **23** shows a decrease in two different phases. At high temperatures, the χ_{MT} value is 12.72 cm³ K mol⁻¹, lower than the expected value (14.3 cm³ K mol⁻¹) for two isolated Tm^{III} ions in a ³H₆ ground state with $g = 7/6$, and it drops to a value of 5.08 cm³ K mol⁻¹ at 2 K. Both declines at low and high temperatures can be again attributed to weak antiferromagnetic coupling and the depopulation of the excited Stark levels of this lanthanide ion, respectively. Complex **24** ([Yb₂]) shows a continuous decrease of the χ_{MT} product from 5.97 cm³ K mol⁻¹ at 300 K, slightly above the expected one for two uncoupled Yb^{III} ions (²F_{7/2}, $g = 8/7$, $\chi_{MT} = 5.14$ cm³ K mol⁻¹), down to 3.00 cm³ K mol⁻¹ at 2 K. Although two different slopes cannot be distinguished, both effects (spin-orbit and magnetic exchange coupling) may be also considered. The expected and observed (at 300 K) χ_{MT} values for all the complexes are summarized in Table V.3.

Table V.3. Calculated and experimental χ_{MT} values for complexes 13-24

	$(2s+1)L_J$	g_J	Calculated χ_{MT} ($\text{cm}^3 \text{ K mol}^{-1}$)	Experimental χ_{MT} ($\text{cm}^3 \text{ K mol}^{-1}$)
Ce(13)	$^2F_{5/2}$	6/7	1.60	1.88
Pr(14)	3H_4	4/5	3.20	4.07
Nd(15)	$^4I_{9/2}$	8/11	3.28	3.55
Sm(16)	$^6H_{5/2}$	2/7	0.18	1.17
Eu(17)	7F_0	-	0	3.45
Gd(18)	$^8S_{7/2}$	2	15.75	16.80
Tb(19)	7F_6	3/2	23.62	24.11
Dy(20)	$^6H_{15/2}$	4/3	28.34	28.22
Ho(21)	5I_8	5/4	28.14	27.99
Er(22)	$^4I_{15/2}$	6/5	22.96	22.74
Tm(23)	3H_6	7/6	14.30	12.72
Yb(24)	$^2F_{7/2}$	8/7	5.14	5.97

The magnetic study carried out in the series confirms that the $[\text{Ln}_2(\text{HL4})_2(\text{H}_2\text{L4})(\text{NO}_3)(\text{H}_2\text{O})(\text{py})]$ system can provide good candidates to embody a quantum gate, since practically all the species show a weak interaction between both lanthanide ions (the two possible quantum bits). In addition, the structural study of the series has demonstrated that these two lanthanide ions are encapsulated in two different cavities, conforming significantly different coordination polyhedra. These dissimilar coordination spheres are expected to provide a magnetic inequivalence between the two ions, which would allow the required differentiation of the two qubits within the quantum gate.

2.6. Photoluminescent properties of complexes $[\text{Ln}_2(\text{HL4})_2(\text{H}_2\text{L4})(\text{NO}_3)(\text{H}_2\text{O})(\text{py})]$

Lanthanide complexes are known to possess very attractive optical properties that make them of high interest for different applications, including optical amplification and wave guidance for telecommunications,^[27] solid state lasers,^[28] light emitting diodes^[29] or solar energy conversion cells.^[30] The series synthesized was thus a good opportunity to assess the different optical properties for each lanthanide ion within the same system. Thus, luminescence properties of all the complexes in the series were evaluated in collaboration with Dr. Núria Aliaga-Alcalde and Dr. Melita Menelaou at the Universitat de Barcelona. The absorption spectra of the complexes, as well as of

the free ligand H_3L_4 , were collected at room temperature in DMF using a concentration of 10^{-5} M. The suitability of this solvent was studied by performing absorption measurements of one of the complexes (**17**, $[Eu_2]$) at one hour intervals during 8 hours, and collecting the spectra 24 hours after (Figure A.16, Appendix). The absorption properties remain unaltered during the whole experiment, demonstrating the stability of these species in this solution. The values of the absorption maxima for all the complexes in the series are shown in Table V.4. The spectra of complex **18** ($[Gd_2]$), as well as the absorption measurement of the ligand H_3L_4 , are shown in Figure V.15 as representative UV-Vis spectra of the series.

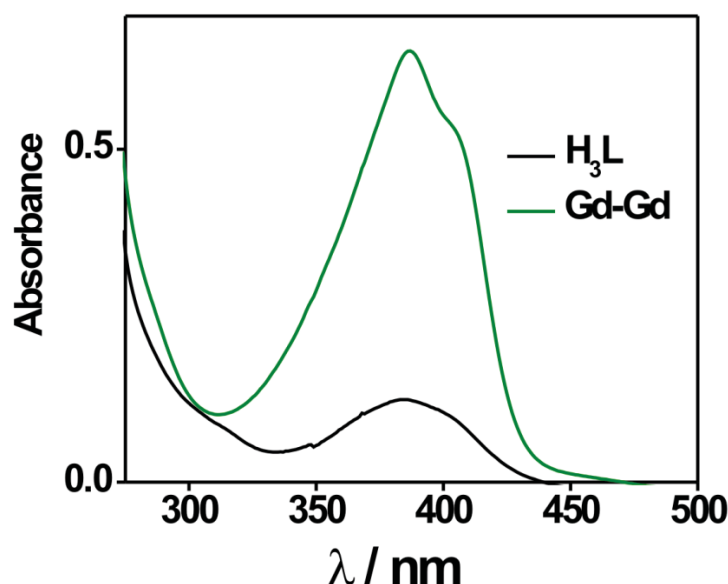


Figure V.15. Absorption spectra of the free ligand H_3L_4 10^{-5} M in DMF at room temperature (black line) and $[Gd_2(HL_4)_2(H_2L_4)(NO_3)py(H_2O)]$ (**18**) complex (green line) under the same conditions.

As shown in Table V.4, very similar values of the absorption maxima were found for all the complexes of the series. The results demonstrate that changing the lanthanide ions in the complex has a minor effect in the absorption properties, since only small differences on the intensity and shift of the bands have been found. The spectra exhibit a broad band above 300 nm, with a λ_{max} in the range from 385 to 387 nm, which is accompanied by a shoulder of lower intensity around 405-408 nm (Figure V.15). Both bands can be directly related to the ligand and are attributed to π - π^* transitions as it has been seen in other similar β -diketone ligand complexes.^[31, 32]

Compared with the free ligand, the bands appear slightly redshifted (higher wavenumbers), indicating the coordination between the ligands and the metal ions.

	Absorption spectra (DMF) λ_{max}, nm (ϵ, $10^3 \text{ M}^{-1} \text{ cm}^{-1}$)		
Ce(13)	222(416)	387(49.4)	408(38.5)
Pr(14)	225(410)	387(6.1)	408(5)
Nd(15)	222(411)	387(56.2)	407(40.8)
Sm(16)	222(429.5)	385(122)	409(82.1)
Eu(17)	222(415.6)	387(63.7)	406(52.2)
Gd(18)	223(412.7)	387(64.7)	407(51)
Tb(19)	226(435.4)	387(54.3)	408(40)
Dy(20)	222(404.2)	386(41.7)	407(30.3)
Ho(21)	222(419.2)	386(40.7)	406(33)
Er(22)	222(415.6)	387(63.7)	406(52.2)
Tm(23)	223(407)	388(53.1)	405(44)
Yb(24)	222(403.6)	385(25.6)	405(21.2)
H₃L₄	223(401)	385(12.4)	

The luminescence properties of the coordination compounds and H₃L₄ were evaluated in DMF using a concentration of 10^{-5} M. All the measurements were recorded in the visible and/or near-IR region. The spectra corresponding to the ligand exhibits a broad emission band at 388 nm, as shown in Figure V.16 (top, left). For all the complexes in the series, a single broad emission band in that region was found, while no sharp emission from the lanthanide ions was observed. This behavior suggests that, in this region, the luminescence of the complexes is exclusively due to the coordinated ligands (Figure V.16).

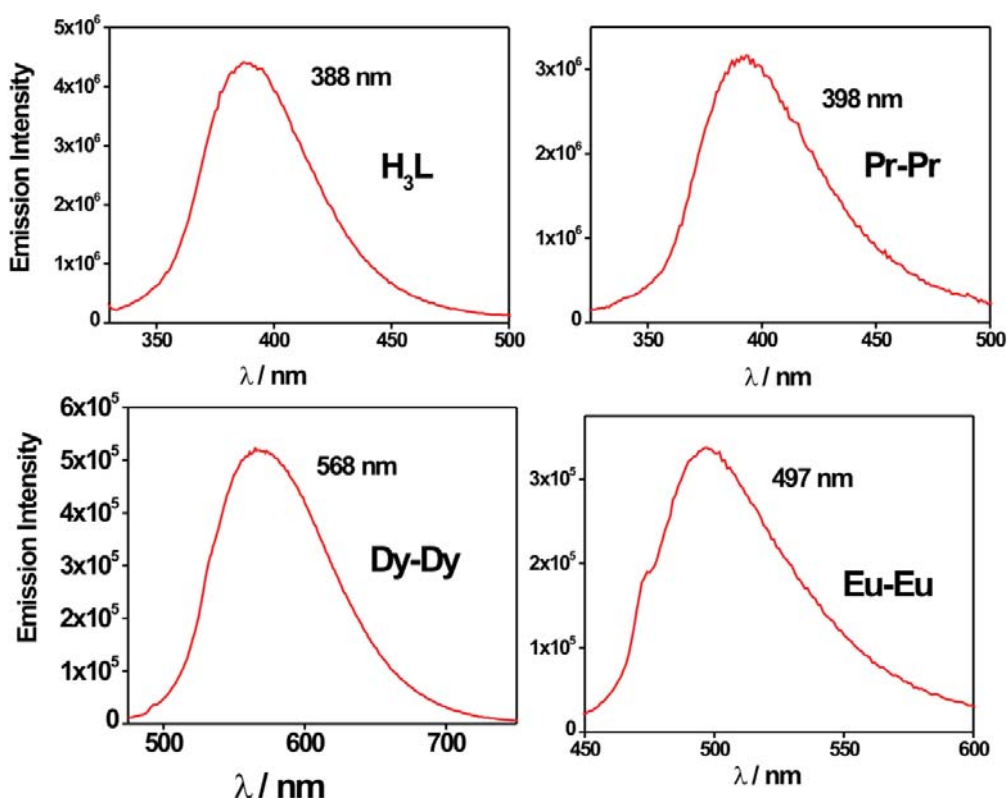


Figure V.16. Fluorescence emission spectra of H₃L₄ ligand and examples of some [Ln₂(HL₄)₂(H₂L₄)(NO₃)py(H₂O)] complexes (Pr (**14**), Dy (**20**) and Eu (**17**)) 10⁻⁵ M in DMF at room temperature.

When the near-IR region was studied, features corresponding to metal based transition were found for complexes **15** (Nd), **22** (Er) and **24** (Yb). The spectra of all the complexes were recorded from 800 nm to 1600 nm under each respective excitation of light ($\lambda = 385$ nm, 385 nm and 355 nm for Nd, Er and Yb complexes, respectively), and for all three cases, the corresponding transitions for each lanthanide ion were obtained (Figure V.17).^[33, 34] Thus, narrow emission bands at near 890, 1058 and 1331 nm appear in the spectrum for complex **15** (Nd), which can be assigned to the transitions $^4F_{3/2} \rightarrow ^4I_{9/2}$, $^4F_{3/2} \rightarrow ^4I_{11/2}$ (the most intense) and $^4F_{3/2} \rightarrow ^4I_{13/2}$, respectively. For complex **22** (Er), a band appears at 1523 nm (assigned to the transition $^4I_{13/2} \rightarrow ^4I_{15/2}$), while for complex **24** (Yb), one band occurs at 977 nm corresponding to the transition $^2F_{5/2} \rightarrow ^2F_{7/2}$. Similar behavior in other related β -diketonate systems has been described as an antenna effect, which suggests that effective intramolecular energy transference

from the coordinated H_3L4 ligands (in the $HL4^{2-}$ and H_2L4^- forms) to the central lanthanide ions would lead to the observed emitting processes.^[35]

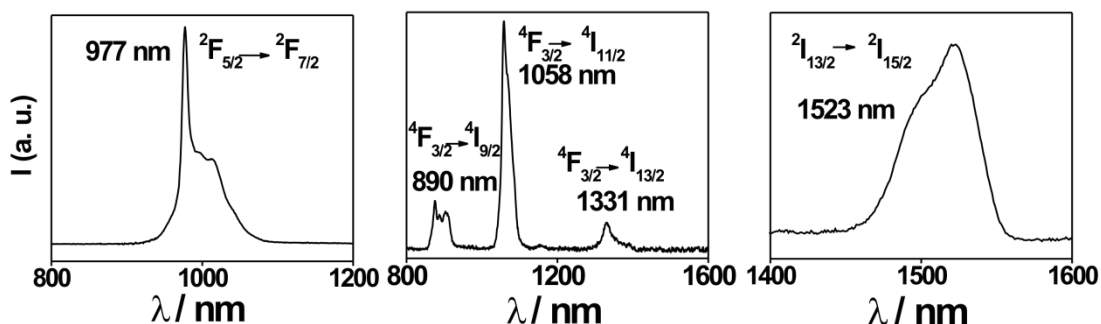
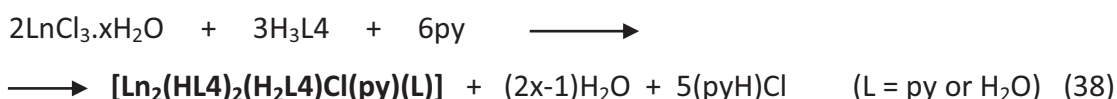


Figure V.17. Fluorescence emission spectra of $[Ln_2(HL4)_2(H_2L4)(NO_3)py(H_2O)]$ complexes (left: Yb (**24**), middle: Nd (**15**) and right: Er (**22**)) 10^{-5} M in DMF at room temperature. Intensities are normalized. Wavelengths and transitions are indicated for each compound.

3. Exchanging the anion in the series: $[Ln_2(HL4)_2(H_2L4)Cl(py)(L)]$ complexes

The study of the structural and physical properties of the $[Ln_2(HL4)_2(H_2L4)(NO_3)(H_2O)(py)]$ series demonstrates the ability of differentiating the two lanthanide ions within the system, which can be further modified by exchanging the nitrate ligand by other different anion. The magnetic energy levels of lanthanide ion in site 2 (where the anion is coordinated) may slightly differ depending of the nature of such anion ligand. With these possibilities in mind, reactions for obtaining the same system using different lanthanide salts were carried out. Different reactions with $Ln(AcO)_3$ did not succeed, providing powdered products that couldn't be evaluated. However, using the chloride anion, the same system where Cl^- is replacing the nitrate anion could be synthesized and characterized following the reaction:



Four different coordination complexes were obtained from this reaction using Nd^{III} (**27**), Gd^{III} (**28**), Tb^{III} (**29**) and Dy^{III} (**30**). Studies of the crystal structure as well as of the magnetic properties of these complexes are shown in the following sections.

3.1. Study of the crystal structures

The crystal structure of the four complexes $[\text{Nd}_2(\text{HL4})_2(\text{H}_2\text{L4})\text{Cl}(\text{py})(\text{H}_2\text{O})]$ (**27**), $[\text{Gd}_2(\text{HL4})_2(\text{H}_2\text{L4})\text{Cl}(\text{py})(\text{H}_2\text{O})]$ (**28**), $[\text{Tb}_2(\text{HL4})_2(\text{H}_2\text{L4})\text{Cl}(\text{py})_2]$ (**29**) and $[\text{Dy}_2(\text{HL4})_2(\text{H}_2\text{L4})\text{Cl}(\text{py})_2]$ (**30**) was obtained from X-ray diffraction using a synchrotron source. The crystals of the four complexes were formed in one week by layering the reaction solution (pyridine) with ether. Again, the four complexes crystallize in the monoclinic space group $P2_1/c$ and have similar cell parameters (see Table V.A4, Appendix). The compounds exhibit very similar structures, with one dinuclear molecule per asymmetric unit and pyridine and/or H_2O solvent molecules in the lattice (see crystal structure of complex **28** in Figure V.18 as an example). A complete list of bond distances and angles can be found in Table V.A6 in the Appendix. The two lanthanide ions are encapsulated and bridged by two HL4^{2-} ligands in a head-to-tail disposition and one $\text{H}_2\text{L4}^-$. Thus, as in the $[\text{Ln}_2(\text{HL4})_2(\text{H}_2\text{L4})(\text{NO}_3)(\text{py})(\text{H}_2\text{O})]$ series, the three ligands lose the β -diketonc proton, while only for two of them the carboxylic unit is deprotonated. The remaining carboxylic proton can be found crystallographically forming a strong hydrogen bond with a solvate pyridine molecule for complexes **27** and **28** (Nd and Gd, respectively). In contrast, for complexes **29** (Tb) and **30** (Dy), the proton is likely to be distributed over the two carboxylate units, forming a triangular hydrogen bond with a pyridine molecule oriented accordingly (Figure V.19, top).

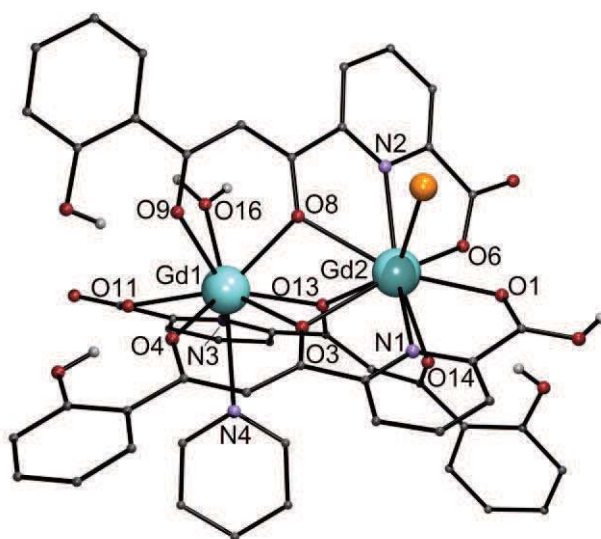


Figure V.18. Representation of the molecular structure of the complexes $[\text{Gd}_2(\text{HL4})_2(\text{H}_2\text{L4})\text{Cl}(\text{py})(\text{H}_2\text{O})]$ (**28**). Light blue, Gd; purple, N; red, O; rest, C. Only hydrogen atoms bound to O are shown.

The crystal structure demonstrates that the chloride anion can also afford an asymmetric dinuclear system. The three partially deprotonated $(\text{H}_{3-x}\text{L4})^{-x}$ ligands coordinate the two lanthanide ions through their β -diketonate and dipicolinate-like coordination pockets. Nonacoordination around the metal ion in site 1 (same assignment as in the previous series, see Scheme V.5) is completed by one pyridine molecule and one H_2O (in complexes **27** and **28**) or by two pyridine groups (in complexes **29** and **30**). In contrast, the environment of Ln2 is completed with the terminal Cl^- ligand. Since no bidentate mode can be achieved in this case, nonacoordination is reached in this site for all the synthesized complexes. Thus, coordination nine is observed in site 2 using Nd^{III} , in contrast to the results seen for the analogous complex $[\text{Nd}_2(\text{HL4})_2(\text{H}_2\text{L4})(\text{NO}_3)(\text{py})(\text{H}_2\text{O})]$ (**15**), where nitrate anion coordinates in a bidentate mode to complete a coordination environment with CN = 10. As for the series with the nitrate anion, the bond distances in both sites were studied, demonstrating that with the chloride anion, the system provides also two different environments with a remarkably different size. Bond distances within the coordination polyhedron defined in Ln1 and Ln2 are listed in Table V.5. Although no possible assessment through the complete series can be carried out, it is demonstrated how the change of the metal is followed by a decrease of the metal-ligand bond distances due to the lanthanide contraction. This effect is more pronounced in some individual parameters and less in others, as it happens within the previous series.

The dependence in each lanthanide environment of the sum of the bond lengths Ln-O related to the partially deprotonated ligands *versus* the number of f electrons was investigated. The six oxygen donor atoms belonging to $(\text{H}_{3-x}\text{L4})^{-x}$ (i.e., O4, O11, O9, O8, O13, O3 for Site 1, and O1, O6, O14, O13, O3, O8 for Site 2) were thus considered, comparing $\sum\text{Ln1-O}$ and $\sum\text{Ln2-O}$ for each of the four compounds (Figure V.19, bottom).

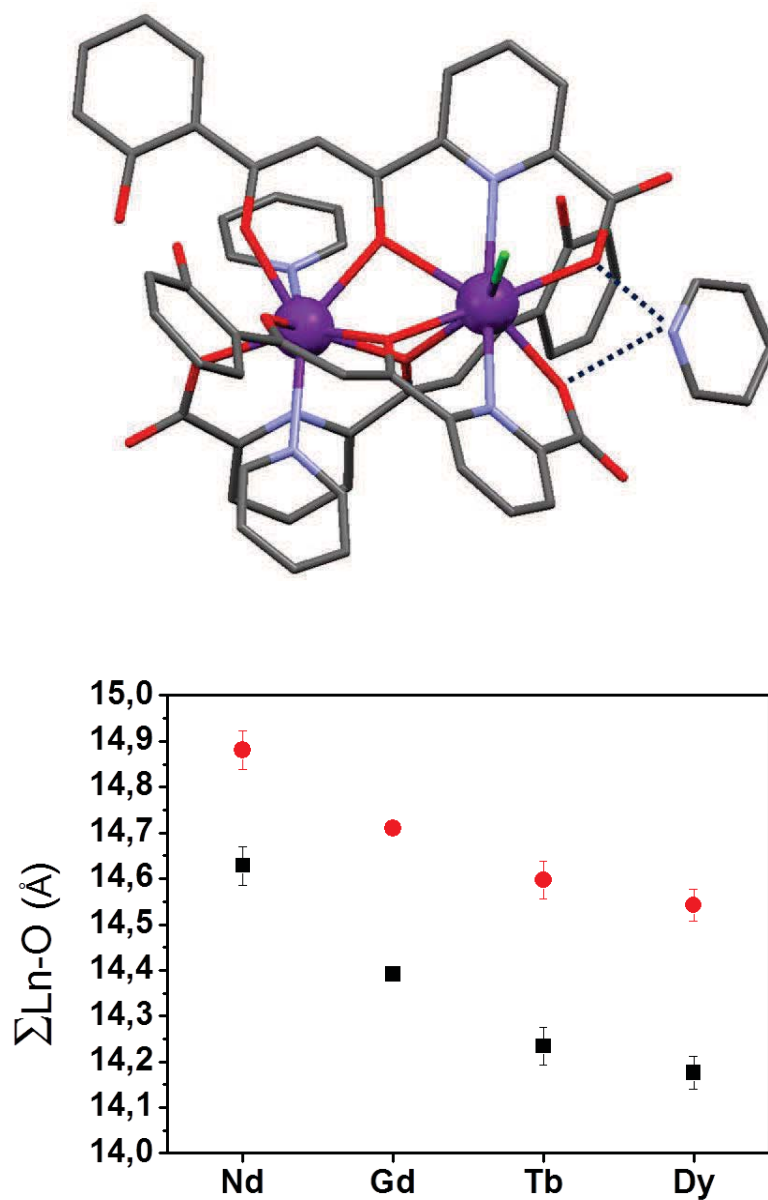


Figure V.19. (Top) Representation of the complex $[\text{Tb}_2(\text{HL}_4)_2(\text{H}_2\text{L}_4)\text{Cl}(\text{py})_2]$ (**29**) exhibiting the hydrogen bonding interaction with a lattice molecule of pyridine through the two carboxylic acid moieties. Dark purple, Tb; purple, N; red, O; rest, C. (Bottom) Sum of the Ln-O bond distances against the Ln^{III} ion in complexes **27-30** for site 1 (black) and site 2 (red).

Table V.5. Bond lengths Ln-X in the system $[\text{Ln}_2(\text{HL4})_2(\text{H}_2\text{L4})\text{Cl}(\text{py})(\text{X})]$ for complexes 27 to 30

Bond	Nd (27)	Gd (28)	Tb (29)	Dy (30)
Ln1-O4	2.385(8)	2.353(2)	2.409(6)	2.404(6)
Ln1-O8	2.395(7)	2.366(3)	2.406(8)	2.398(5)
Ln1-O11	2.401(7)	2.376(2)	2.320(8)	2.309(6)
Ln1-O3	2.465(8)	2.420(2)	2.320(6)	2.303(6)
Ln1-O9	2.470(6)	2.419(2)	2.347(8)	2.343(6)
Ln1-O16	2.472(9)	2.460(3)	-	-
Ln1-N5	-	-	2.644(9)	2.632(8)
Ln1-O13	2.512(6)	2.457(2)	2.432(6)	2.419(6)
Ln1-N3	2.517(8)	2.486(3)	2.505(10)	2.490(7)
Ln1-N4	2.715(10)	2.700(3)	2.652(10)	2.652(8)
Ln2-O6	2.394(8)	2.393(3)	2.377(8)	2.364(6)
Ln2-O1	2.415(7)	2.414(2)	2.373(7)	2.372(6)
Ln2-O14	2.431(7)	2.396(3)	2.423(7)	2.405(6)
Ln2-O13	2.468(6)	2.417(2)	2.394(7)	2.385(6)
Ln2-O8	2.538(6)	2.493(2)	2.537(6)	2.520(6)
Ln2-N2	2.611(11)	2.569(3)	2.547(9)	2.539(7)
Ln2-N1	2.625(10)	2.622(3)	2.540(10)	2.536(7)
Ln2-O3	2.635(8)	2.597(2)	2.493(6)	2.496(5)
Ln2-Cl1	2.810(3)	2.7758(9)	2.727(3)	2.725(2)
Ln1...Ln2	3.8770(9)	3.8127(3)	3.7853(10)	3.7748(6)

Far from pretending an exhaustive assessment of the lanthanide contraction in the series, the evolution of $\sum(\text{Ln-O})$ parameter for these four chloride complexes demonstrates how the decrease of the ionic radii ($r_{\text{Nd}} > r_{\text{Gd}} > r_{\text{Tb}} > r_{\text{Dy}}$)^[15] influences on the shrinking of the coordination polyhedron on each environment. In addition, these data show that the different pocket size between sites 1 and 2 is also present in the $[\text{Ln}_2(\text{HL4})_2(\text{H}_2\text{L4})\text{Cl}(\text{py})(\text{X})]$ system, and that it is maintained throughout the series.

The different environments within the chloride systems were examined by means of continuous-shape measures (CShMs), using the reference polyhedra proposed for coordination number 9 (Table V.2).^[21] As occurs with the nitrate compounds, the coordination geometry in site 2 is very irregular and does not follow any of the studied ideal polyhedra, the closest one being the so called “muffin” shape (MFF-9, C_1 symmetry) for complexes **29** and **30**, and the geometry known as “hula-hoop” (HH-9,

C_{2v} symmetry) for complexes **27** and **28**. By contrast, the calculations show that coordination polyhedra in site 1 are better described as a spherical capped square antiprism (CSAPR-9, C_{4v} symmetry) for complexes **27**, **29** and **30**, and as tricapped trigonal prism (TCTPR-9, D_{3h} symmetry) in compound **26**. The results are summarized in Table V.6.

Table V.6. Continuous Shape Measures (CSHMs) for coordination geometry of Ln1 and Ln2 in compounds 27-30. Highlighted are the closest polyhedra for each metal

	MFF-9	JCSAPR-9	JTCTPR-9	JTDIC-9	CSAPR-9	TCTPR-9	CCU-9	HH-9
Nd₁	1.094	2.129	3.130	12.724	0.989	0.926	9.195	10.987
Nd₂	4.431	6.631	7.923	8.625	5.771	6.803	6.376	2.826
Gd₁	1.048	1.989	3.040	12.524	0.791	0.823	9.142	11.133
Gd₂	3.829	5.933	7.081	9.505	4.960	5.971	6.220	3.237
Tb₁	0.967	2.083	3.185	13.032	0.871	1.088	9.761	11.486
Tb₂	2.972	4.801	5.184	9.864	3.766	4.334	6.245	4.042
Dy₁	0.952	2.053	3.193	12.998	0.821	1.053	9.863	11.525
Dy₂	2.802	4.572	4.950	9.865	3.545	4.100	6.330	4.239

The study evidences again the difference between both sites within the asymmetric system, which would enable the differentiation between each Ln^{III} if acting as qubits. The magnetic inequivalence between both ions, as well as the interaction between them, should be thus evaluated to ensure its application as a quantum gate (described in Section 4 for complex **29** [Tb₂]). A first assessment of the magnetic properties was carried out by studying variable-temperature bulk magnetization measurements on powdered microcrystalline samples.

3.2. Magnetic properties of complexes [Ln₂(HL4)₂(H₂L4)Cl(py)(L)]

For their relevance in quantum computing, the presence of weak interactions between both centers within complexes **27-30** was evaluated by studying the dependence of $\chi_M T$ vs T (Figure V.20). The behavior of these four complexes was expected to be very similar to each analogous compound from the series with NO₃⁻ anion previously studied. As for complex **18**, the lack of orbital momentum in [Gd₂(HL4)₂(H₂L4)Cl(py)(H₂O)] (**28**) was used to study the magnetic coupling between

both ions without the effects of the spin-orbit coupling. Complex **28** presents a stable $\chi_M T$ value of $15.50 \text{ cm}^3 \text{ K mol}^{-1}$ from 280 K down to near 30 K, where a small decrease is observed, reaching a value of $13.58 \text{ cm}^3 \text{ K mol}^{-1}$ at 1.8 K. The value at high temperatures agrees well with that expected from two isolated Gd^{III} ions with $g = 2$ ($15.75 \text{ cm}^3 \text{ K mol}^{-1}$), while the decrease at lower temperatures must belong to a weak antiferromagnetic interaction between both ions. The $\chi_M T$ vs T curve was reproduced satisfactorily with the isotropic spin Hamiltonian $H = -J(S_{\text{Gd1}} \cdot S_{\text{Gd2}})$, including a fixed temperature-independent paramagnetism (TIP) term.^[24] The best fit parameters were $J = -0.02(2) \text{ cm}^{-1}$ and $g = 1.95(2)$, which are very close to the ones obtained for **18** ($J = -0.02(1) \text{ cm}^{-1}$ and $g = 2.05(1)$). The results obtained for compound $[\text{Nd}_2(\text{HL4})_2(\text{H}_2\text{L4})\text{Cl}(\text{py})(\text{H}_2\text{O})]$ (**27**) show a continuous decrease of the $\chi_M T$ value from $2.60 \text{ cm}^3 \text{ K mol}^{-1}$ at 300 K down to $1.64 \text{ cm}^3 \text{ K mol}^{-1}$ at 1.8 K. The value at high temperatures is significantly lower than the one expected for two isolated Nd^{III} ions in the $^4I_{9/2}$ ground state and $g = 8/11$ ($3.28 \text{ cm}^3 \text{ K mol}^{-1}$). The continuous decline of the $\chi_M T$ vs T curve may be attributed to the effects of the depopulation of the Stark levels of Nd^{III} and a weak antiferromagnetic interaction between both ions. The curve for complex $[\text{Tb}_2(\text{HL4})_2(\text{H}_2\text{L4})\text{Cl}(\text{py})_2]$ (**29**) shows that the $\chi_M T$ value remains stable at $23.3 \text{ cm}^3 \text{ K mol}^{-1}$ from room temperature down to 150 K, when a gradual decrease begins. Around 5 K, a faster decline occurs, reaching a value of $17.46 \text{ cm}^3 \text{ K mol}^{-1}$ at 1.8 K. The high-temperature values are very close to the expected ones for two uncoupled Tb^{III} ions in the 7F_6 ground state and $g = 3/2$ ($\chi_M T = 23.62 \text{ cm}^3 \text{ K mol}^{-1}$). As occurs in the related compound **19**, the decrease at high temperatures may be attributed to the depopulation of the magnetic excited sublevels, demonstrating the strong spin-orbit coupling of Tb^{III} . On the other part, the decline at low temperatures should be attributed to a weak antiferromagnetic interaction within the complex. The results for complex **30** ($[\text{Dy}_2(\text{HL4})_2(\text{H}_2\text{L4})\text{Cl}(\text{py})_2]$) show that $\chi_M T$ stays stable around $28.6 \text{ cm}^3 \text{ K mol}^{-1}$ from high temperature until 190 K, when a gradual decrease starts down to around $23.32 \text{ cm}^3 \text{ K mol}^{-1}$ at 1.8 K. The value at room temperature agrees well with the expected value for two isolated Dy^{III} ions ($^6H_{15/2}$, $g = 4/3$, $\chi_M T = 28.34 \text{ cm}^3 \text{ K mol}^{-1}$). The decline of the $\chi_M T$ values can be again ascribed to the high spin-orbit coupling of this ion, perhaps with the contribution of a weak antiferromagnetic interaction.

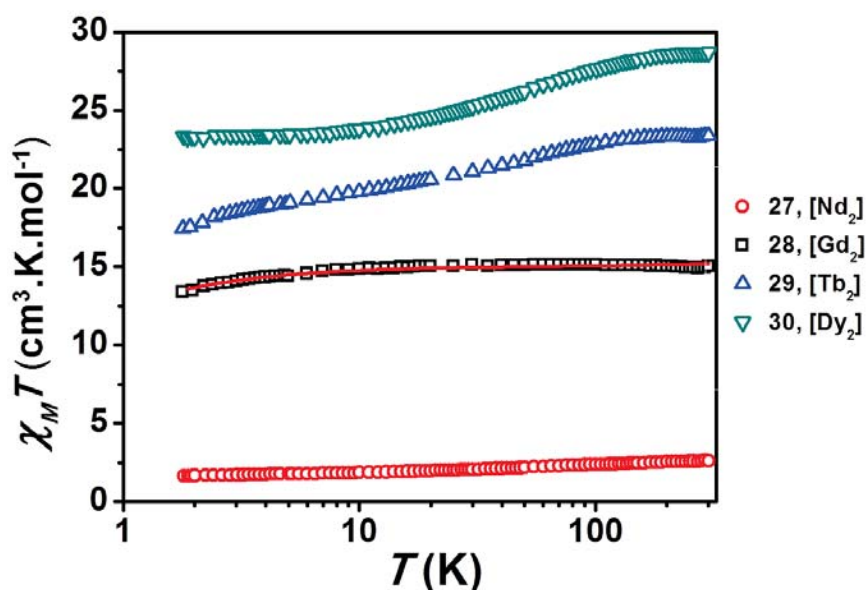


Figure V.20. $\chi_M T$ vs T curves for compounds **27** to **30**, χ_M being the molar paramagnetic susceptibility per $[\text{Ln}_2]$ unit. The full red line represents the best fit of the experimental data for **28** (see text for details).

Again, the results obtained show the successful synthetic strategy for locating two Ln^{III} ions weakly coupled, which again feature different environment that should provide the desired magnetic inequivalence. Ultralow-temperature magnetic studies presented in following chapter put into evidence that such dissymmetry is preserved at the magnetic level on the system with two terbium ions (**29**).

4. Dinuclear terbium(III) cluster as a molecular prototype for spin-based CNOT and $\sqrt{\text{SWAP}}$ quantum gates

Structural and magnetic properties of dinuclear lanthanide compounds described in the previous sections have demonstrated that these asymmetric molecules are excellent candidates to embody two inequivalent qubits. This asymmetry may allow each metal ion to respond inequivalently to some external stimulus, e.g., electric or magnetic fields, allowing operations as quantum gates. The universal controlled-NOT (CNOT) gate is the archetype of such a controlled operation (see Chapter I). Depending on the state of the control qubit, the targeted qubit can be flipped (if control qubit is in the 1 state) or not (if control qubit is in the 0 state). Another universal gate is the $\sqrt{\text{SWAP}}$ operation, which exchanges the states of two qubits only if they are in

opposite states (see Chapter I). The high magnetic anisotropy of the Tb^{III} ions in compound [Tb₂(HL4)₂(H₂L4)Cl(py)₂] (**29**), as well as their mutual coupling, provide this cluster with all the requirements to successfully be applied as a quantum gate. Dc and ac ultralow temperature magnetic susceptibility and heat capacity measurements, as well as continuous-wave electronic paramagnetic resonance (EPR) experiments, were carried out in collaboration with Dr. Olivier Roubeau and Dr. Fernando Luis at the Universidad de Zaragoza to demonstrate such hypothesis.

Ac magnetic susceptibility measurements in the ranges of 1.8 - 300 K (performed with a commercial SQUID magnetometer) and 13 mK - 1.5 K (measured with a μ SQUID susceptometer) were conducted to evaluate the magnetic anisotropy and the exchange coupling between the two Tb^{III} ions in the complex. The results for the in-phase component χ' as χT vs T and $(\mu_{eff}/\beta)^2$ vs T at different frequencies (15.8 mHz, 1.58 Hz, 158 Hz and 15.8 kHz) as well as for dc measurement at $H = 0.1$ T are shown in Figure V.21. At room temperature, the magnetic response agrees well with two uncoupled free terbium ions ($g_J = 3/2$ and $J = 6$), as the value of $\mu_{eff} = 13.7(1)\beta$ is very close to the expected one $\mu_{eff} = gJ\beta[2J(J+1)]^{1/2} = 13.74\beta$. The drop observed below 100 K is then ascribed to the thermal depopulation of the magnetic energy sublevels m_J split by the crystal field. Between 10 and 3 K, μ_{eff} reaches a value of $12.5(1)\beta$, near the expected one for two uncoupled Tb^{III} ions with their angular momenta J pointing up or down along the local anisotropy axes ($\mu_{eff} = gJ\beta 2^{1/2} J = 12.72\beta$). The magnetic behavior of this asymmetric system can be described considering a magnetic Hamiltonian of two coupled anisotropic spins interacting with their respective nuclear spins:

$$H = - \sum_{j=1}^2 D J_{z,j}^2 - g\beta \sum_{j=1}^2 J_j H - 2J_{ex} J_1 J_2 + A_j \sum_{j=1}^2 J_j I_j \quad (39)$$

The first term involves the uniaxial magnetic anisotropy of the angular momenta of both Tb1 and Tb2 ions (J_1 and J_2) with local anisotropy axes z_1 and z_2 . The second and third terms stand for the Zeeman effect (H referring to the magnetic field) and the exchange interaction (J_{ex} being the exchange coupling constant) respectively, while the last term accounts for the hyperfine interaction. For terbium, $g = 3/2$, $A_j/k_B = 0.025$ K, the total angular momentum is $J = 6$ and the nuclear spin $I = 3/2$.^[36]

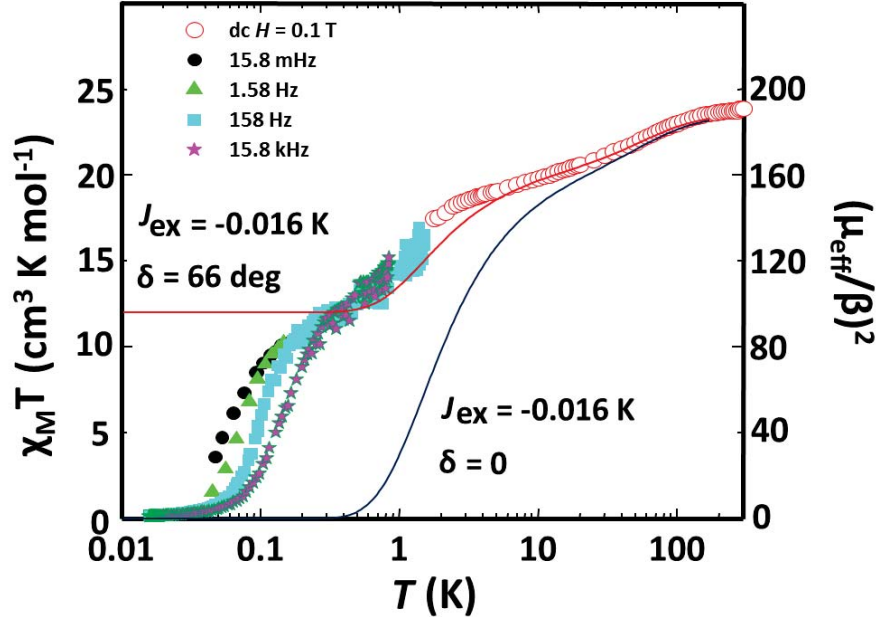


Figure V.21. Ac-susceptibility of polycrystalline $[\text{Tb}_2]$ at different frequencies. χT values (left axis) were used to determine μ_{eff} (right axis). Dc-susceptibility data measured at $H = 0.1$ T is also shown. Solid lines are least square fits for the ac susceptibility considering collinear ($\delta = 0^\circ$, in dark blue) and non-collinear ($\delta = 66^\circ$, in red) easy axes.

Between 3 and 300 K, the two spins behave as decoupled and the hyperfine coupling plays no role. Thus, the above Hamiltonian can be simplified as:

$$H = - \sum_{j=1}^2 D J_{z,j}^2 - g\beta \sum_{j=1}^2 J_j H \quad (40)$$

In this temperature range, the simplified Hamiltonian was used to describe the in-phase magnetic susceptibility by fitting the data with the following analytical formula:

$$\chi T = \frac{N_A g^2 \beta^2 J}{3k_B} \left(J + \frac{2}{\Omega} \frac{1 - e^{-\Omega}}{1 + e^{-\Omega}} \right) \quad ; \quad \Omega = \beta D (2J - 1) \quad (41)$$

The only free parameter in the above formula is the axial magnetic anisotropy constant, D , and the best fit was obtained with $D/k_B = 17$ K. Considering that the excited levels are separated by $(2J-1)D$, the first one lays more than 180 K above the ground state doublet $m_j = \pm 6$ (Figure V.22). This experimental demonstration of the isolated presence of these two substates at the ground state doublet, defined as $|\uparrow\rangle$

$= |J = 6, m_J = 6\rangle$ and $|\downarrow\rangle = |J = 6, m_J = -6\rangle$, confirms then each terbium ion as a potential qubit.

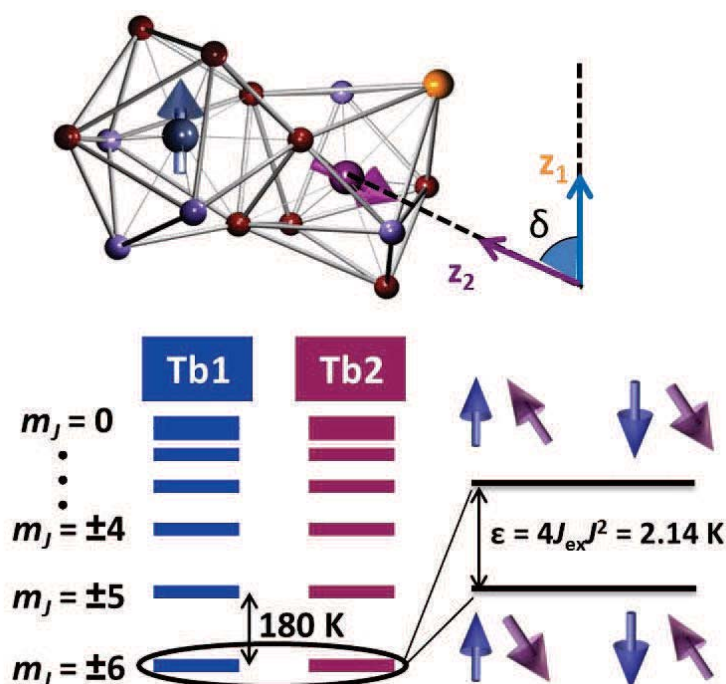


Figure V.22. (top) Resulting N_3O_6 (Tb1) and N_2O_6Cl (Tb2) coordination polyhedra around the two terbium ions exhibiting C_1 and C_{2v} symmetry, respectively, which allows it magnetically inequivalence due to a misalignment between their anisotropy axes. Purple, Tb2; Blue, Tb1; Yellow, Cl; Red, O; Light purple, N. (bottom) Zero-field energy level structure of [Tb2] derived from the fits on Figure V.21.

When decreasing the temperature below 3 K, a second drop in $\chi'T$ is observed, attributed to the antiferromagnetic coupling ($-2J_{ex}J_1J_2$) between the two terbium ions. Magnetic heat capacity measurements, $c_{m,p}$, were performed to corroborate this interpretation (Figure V.23). At zero field, $c_{m,p}$ shows a Schottky-type broad anomaly, which is centered at $T_{max} \approx 0.9$ K. Such anomaly arises from the energy splitting between the ferromagnetic ($|\uparrow_{>1}\rangle \times |\uparrow_{>2}\rangle$ and $|\downarrow_{>1}\rangle \times |\downarrow_{>2}\rangle$) and antiferromagnetic ($|\uparrow_{>1}\rangle \times |\downarrow_{>2}\rangle$ and $|\downarrow_{>1}\rangle \times |\uparrow_{>2}\rangle$) states (Figure V.22). This energy splitting ϵ can be quantified by using the condition $k_B T_{max} = 0.42\epsilon$, yielding a value of $\epsilon/k_B \approx 2.14$ K (see Figure V.22). From these equivalences, and considering $\epsilon = 4J_{ex}J^2$, the magnetic coupling constant can be calculated, $J_{ex}/k_B = -0.016(1)$ K.

Bearing in mind the antiferromagnetic ground state calculated above, the magnetic susceptibility χ' should be zero near 100 mK. However, the experimental net magnetic

moment observed at this temperature demonstrates that the magnetic moments of the two Tb^{III} ions within the complex do not compensate each other. Thus, the easy axes z_1 and z_2 of the two anisotropic ions, determined by the coordination sphere around them, must be not parallel. On the contrary, the two axes are defining an angle (δ), forcing the antiferromagnetic ($|\uparrow\rangle_1 \times |\downarrow\rangle_2$ and $|\downarrow\rangle_1 \times |\uparrow\rangle_2$) states to preserve a net magnetic moment (Figure V.22). As a consequence, the two ions will couple differently to an external magnetic field, since their gyromagnetic constants g_1 and g_2 will be different. Thus, if H is applied along one of the anisotropy axes, like for example in “qubit 1” (Tb1), then $g_1 = g_J$, while $g_2 = g_J \cos \delta$, making the two spins inequivalent.

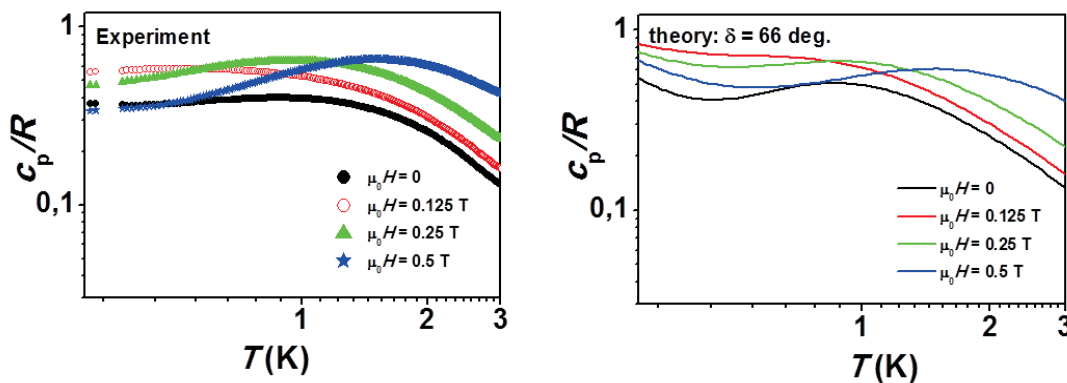


Figure V.23. (left) Magnetic heat capacity of a powdered sample of complex **29** [Tb₂]. (right) Theoretical prediction for non-collinear anisotropy axes.

An analytical expression for χ' has been used to fit the susceptibility curves considering the non-collinear angle $\delta \neq 0$.

$$k_B \chi T = \frac{2}{3} g^2 \beta^2 J^2 (1 + \cos(\delta) \tanh[2\beta' J_{ex} J^2]) \quad (42)$$

Since the exchange interaction J_{ex} has been already extracted from specific heat measurements, the angle δ can be obtained from fitting the data to the above equation, yielding best results for $\delta = 66^\circ$ (Figure V.21, solid red line). In contrast, the predicted $\chi'T$ curve for collinear anisotropy axes ($\delta = 0$, Figure V.21, solid dark blue line) does not follow the experimental $\chi'T$ curves, since below 10 K these show much larger values. Magnetic heat capacity measurements also confirm this magnetic

inequivalence ($g_1 \neq g_2$). The data measured under $H \neq 0$, shown in Figure V.23 (left), reflects the magnetic field dependence of the energy levels, which should at the same time exhibit a dependence on δ . Theoretical predictions of such heat capacity considering $\delta = 66^\circ$ (Figure V.23, right) are in good agreement with the experimental results.

The asymmetry within the magnetic complex **29** has been also assessed by magnetization isotherms measured at $T = 0.26$ and 2 K (Figure V.24). Starting already from $H = 0$, a finite paramagnetic response is observed, demonstrating that the molecular ground state possesses a net magnetic moment and consequently that $\delta \neq 0^\circ$. When the results were compared with calculations made for collinear ($\delta = 0^\circ$) and non-collinear ($\delta = 66^\circ$) anisotropy axes (dotted and solid blue lines in Figure V.24, respectively), a good agreement for the latter calculated isotherm was obtained.

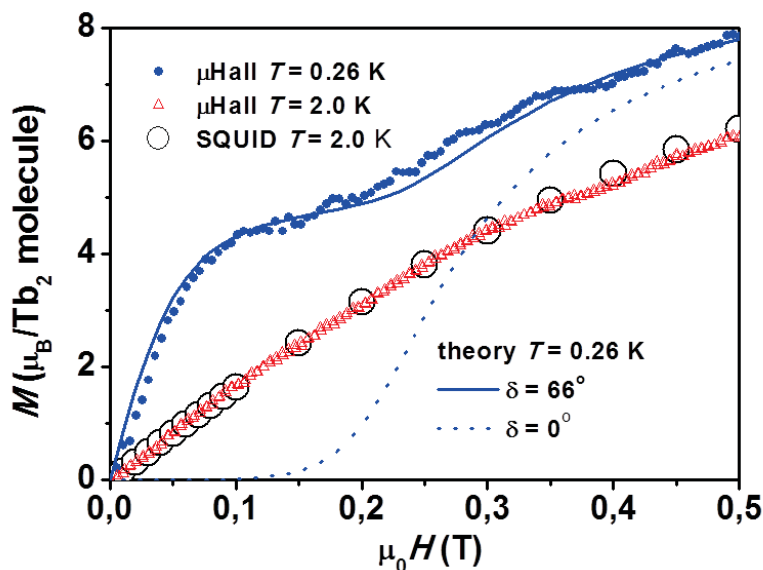


Figure V.24. Magnetization isotherms of complex **29** [Tb_2]. Data at $T = 0.26$ K are compared with calculations made for collinear ($\delta = 0^\circ$, dotted line) and non-collinear ($\delta = 66^\circ$, solid line) anisotropy axes.

To discuss the performance of complex **29** [Tb_2] as a two-qubit quantum gate, the magnetic energy level spectrum in the subspace where the two ions are defined by the two $m_j = \pm 6$ qubit states has been developed by a numerical diagonalization of the simplified Hamiltonian,

$$H = -2J_{ex}J_1J_2 - g_1\beta HJ_{1,z} - g_2\beta HJ_{2,z} + A_J(J_{1,z}I_{1,z} + J_{2,z}I_{2,z}) \quad (43)$$

using the experimental data obtained in magnetic heat capacity and susceptibility measurements. The resulting magnetic energy levels are represented in Figure V.25 for $\delta = 66^\circ$. Only the levels with nuclear spin projections $m_{I,1} = m_{I,2} = -3/2$ are shown for clarity. The magnetic disparity within the complex ($g_1 \neq g_2$) leads the two antiferromagnetic states to have different energy under an external magnetic field, thus enabling the desired transitions to perform CNOT and $\sqrt{\text{SWAP}}$ operations. For instance, at $\mu_0 H = 0.07$ T, only the transition between ($|\uparrow\rangle_1 \times |\downarrow\rangle_2$ and $|\downarrow\rangle_1 \times |\uparrow\rangle_2$) states would be resonant with the energy of $\nu = 9.8$ GHz photons (X-band EPR). This transition would directly produce the $\sqrt{\text{SWAP}}$ operation, since it implies the exchange of the states of both qubits when those are in a different state (Figure V.25 and Scheme V.26). Unlike other proposals,^[37] such $\sqrt{\text{SWAP}}$ gate operation does not require the need of turning on and off interactions between the two qubits. On the other hand, just by changing to $\mu_0 H = 0.28$ T, the only X-band EPR resonant transition would be that between the ($|\uparrow\rangle_1 \times |\downarrow\rangle_2$ and the $|\uparrow\rangle_1 \times |\uparrow\rangle_2$) states, allowing the desired CNOT quantum gate (Figure V.25 and Scheme V.26). Under this definite magnetic field, Tb1 control qubit (light blue) can change the state of the Tb2 target qubit (purple) only when the former is in the $|\uparrow\rangle_1$ state. For both such operations (CNOT and $\sqrt{\text{SWAP}}$), the ground state ($|\uparrow\rangle_1 \times |\downarrow\rangle_2$) can be easily initialized by cooling, since at the two selected fields and at $T = 0.1$ K, the ground state is 99.3 %, populated.

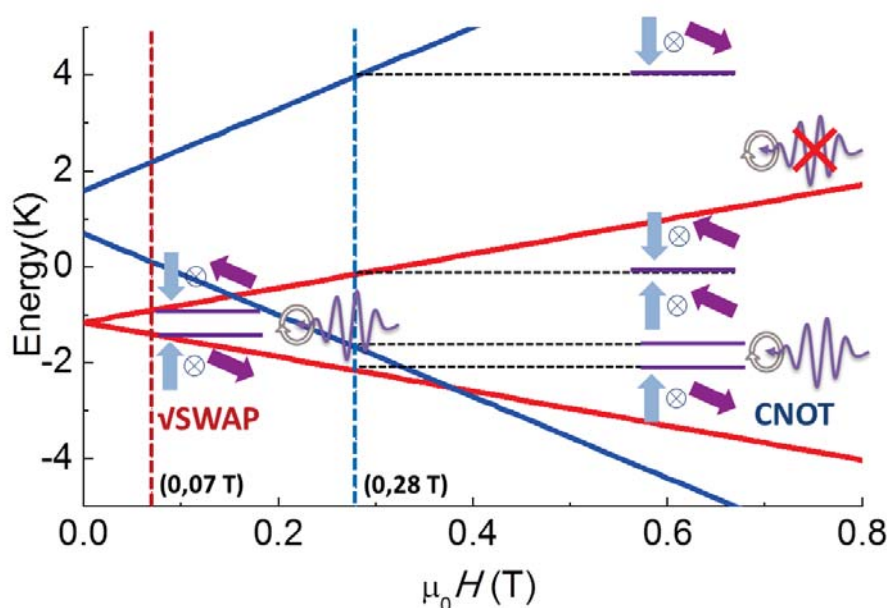
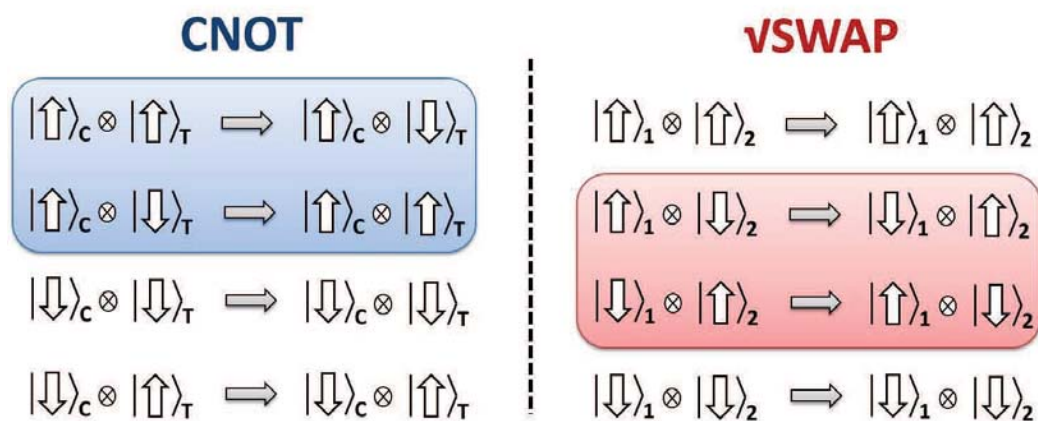


Figure V.25. Field-dependent magnetic energy levels of complex **29** [Tb₂] calculated by numerical diagonalization of the Hamiltonian (see text) for $\delta = 66^\circ$. Transitions in resonance with X-band EPR demonstrates both CNOT (in blue) and vSWAP operations.



Scheme V.26. CNOT and vSWAP operation schemes. For CNOT gate, the operation is allowed only when control (C) qubit is in the up-spin state (highlighted in blue). For vSWAP gate, only when the spin state of qubits 1 and 2 are different, the operation is allowed (highlighted in red).

By performing continuous-wave EPR measurements on a powdered sample of complex **29** [Tb₂], it has been demonstrated that the transitions describing both operations are allowed (Figure V.27). The absorption derivative measured at 6 K shows two broad absorption lines centered at $\mu_0 H$ next to 0.1 and 0.3 T, which can be associated with the vSWAP and CNOT transitions, respectively, corresponding to the expected

transitions in 0.07 and 0.28 T of the previously calculated energy level spectrum. The large widths observed in the spectrum are expected, due to the average in orientations (inherent to a powder measurement) and to the shift of the resonance fields depending on the nuclear spin state.

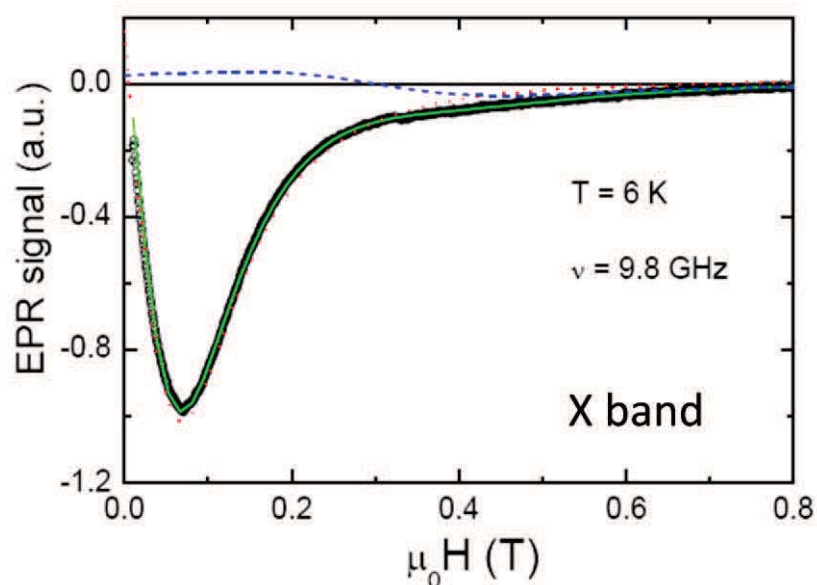


Figure V.27. X-band EPR spectrum of powdered sample of complex **29** [Tb₂]. Solid green line is a fit with two Lorentzian absorption contributions, showed by blue (centered at $\mu_0H \approx 0.3$ T) and red (centered at $\mu_0H \approx 0.1$ T) dashed lines.

The results obtained in magnetic susceptibility, magnetic heat capacity and X-band EPR show that this asymmetric [Tb₂] molecule meets the ingredients required to implement CNOT and $\sqrt{\text{SWAP}}$ gates due to its magnetic inequivalence. However, when the system was evaluated by X-band pulsed-EPR, no coherence was observed, probably due to enhance decoherence problems caused by the coupling between the electron and the nuclear spin ($I = 3/2$) carried by Tb^{III}. Therefore, although the magnetic energy levels of [Tb₂] (**29**) are in the desired disposition, such operations could not be performed since those levels are not maintained long enough to encode the information of the qubit.

5. Extending the family: Asymmetric heterometallic dinuclear lanthanide complexes

The structural study of the series $[\text{Ln}_2(\text{HL}_4)_2(\text{H}_2\text{L}_4)(\text{X})(\text{py})(\text{L})]$ ($\text{X} = \text{NO}_3^-$ or Cl^- , $\text{L} = \text{H}_2\text{O}$ or py) exposed in the previous sections has revealed that the two metal centers of the system exhibit significantly different environments due to the disposition of ligands HL_4^{2-} and H_2L_4^- in the assembly. This behavior causes a different “cavity size” of the two sites, as shown in the representation of Ln-O distances *versus* the number of f electrons of the lanthanide ion (Figure V.28). This demonstrates that in this system, the coordination bonds belonging to HL_4^{2-} and H_2L_4^- are consistently longer in one site (2) than in the other (1).

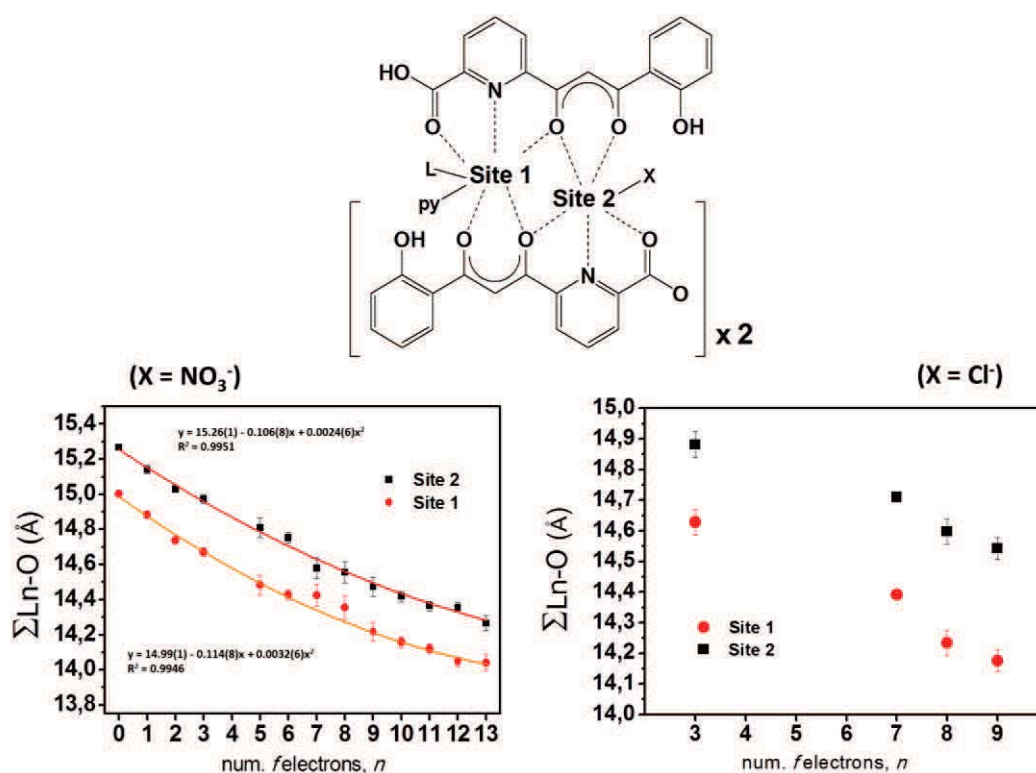


Figure V.28. (top) Schematic representation of the molecular system $[\text{Ln}_2(\text{HL}_4)_2(\text{H}_2\text{L}_4)(\text{X})(\text{py})(\text{L})]$ ($\text{X} = \text{NO}_3^-$ or Cl^- , $\text{L} = \text{H}_2\text{O}$ or py). (bottom): $\Sigma\text{Ln1-O}$ and $\Sigma\text{Ln2-O}$ parameters *versus* the number of f electrons for the series with nitrate (left) and chloride (right) ligand.

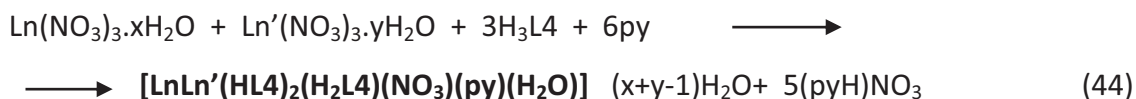
Thus, the scaffold around the metals of these asymmetric entities induces a bigger site 2 in front of the smaller size of site 1. The difference in average Ln-O when comparing one site with the other (termed ΔO) is given in Table V.7 for each complex of both

series, exhibiting the systematically dissimilar sizes between both environments. Only O-donors from partially deprotonated ligands have been considered.

$[\text{Ln}_2(\text{HL4})_2(\text{H}_2\text{L4})(\text{NO}_3)(\text{py})(\text{H}_2\text{O})]$	ΔO (Å)	$[\text{Ln}_2(\text{HL4})_2(\text{H}_2\text{L4})\text{Cl}(\text{py})(\text{L})]$	ΔO (Å)
La (12)	0,04	Nd (27)	0,04
Ce (13)	0,04	Gd (28)	0,05
Pr (14)	0,05	Tb (29)	0,06
Nd (15)	0,05	Dy (30)	0,06
Sm (16)	0,05		
Eu (17)	0,05		
Eu (17a)	0.03		
Gd (18)	0,03		
Tb (19)	0,03		
Dy (20)	0,04		
Ho (21)	0,04		
Er (22)	0,04		
Tm (23)	0,05		
Yb (24)	0,04		
Y (26)	0.04		

These peculiar structural characteristics suggest the possibility of exploiting the size difference between both environments to synthesize heterometallic $[\text{LnLn}'(\text{HL4})_2(\text{H}_2\text{L4})(\text{NO}_3)(\text{py})(\text{H}_2\text{O})]$ ($[\text{LnLn}']$) systems. To date, very few examples of crystal structures concerning 4f-4f' systems have been published, which demonstrates the difficulty of synthesizing these kind of heterometallic complexes.^[38-43] The few differences in chemical properties of lanthanide ions make their differentiation and recognition extremely difficult. However, their systematic size variation with the atomic number could be exploited to discriminate them. This has been attempted with use of “macrocyclic ligands”^[44], unsymmetrical ditopic ligands^[41] or by synthesizing monometallic complexes that are further reacted selectively with the second Ln^{III} .^[39, 40, 45] The dinuclear systems studied here, open the perspective of studying a large number of combinations through simple ligands and one pot reactions. Thus, if two Ln^{III} ions of different ionic radii are made react with three equivalents of $\text{H}_3\text{L4}$ in pyridine, a unique phase composed of complexes featuring the two different metals is expected. Selectively, the cation with larger ionic radius should occupy the bigger site

2, while the other one is expected to go to the position favoring smaller Ln-X bonds (site 1). Following such proposition, several reactions were carried out using different combinations of two lanthanide ions according to equation (44):



After layering the reaction mixture with ether or toluene, single crystals suitable for X-ray analysis were obtained from the reactions with the combinations highlighted in Table V.8 (compounds **31** to **72**). At the time of writing this document, most of the missing combinations had not been yet attempted. The results of the crystal structures suggested that the disposition of the two lanthanide ions within the dinuclear entity was the expected one.

	La	Ce	Pr	Nd	Sm	Eu	Gd	Tb	Dy	Ho	Er	Tm	Yb	Lu	Y
La	✓(12)														
Ce		✓(13)													
Pr	✓(31)	✓(37)	✓(14)												
Nd			✓(44)	✓(45)											
Sm			✓(45)	✓(56)	✓(16)										
Eu			✓(46)			✓(17)									
Gd			✓(47)	✓(57)	✓(63)		✓(18)								
Tb	✓(32)		✓(48)	✓(58)	✓(64)	✓(65)		✓(19)							
Dy	✓(33)	✓(38)	✓(49)						✓(20)						
Ho	✓(34)	✓(39)	✓(50)					✓(69)		✓(21)					
Er	✓(35)	✓(40)	✓(51)								✓(22)				
Tm		✓(41)	✓(52)	✓(59)						✓(72)		✓(23)			
Yb			✓(53)	✓(60)	✓(66)								✓(24)		
Lu		✓(42)	✓(54)	✓(61)	✓(67)		✓(70)	✓(71)							
Y	✓(36)	✓(43)	✓(55)	✓(62)	✓(68)										✓(26)

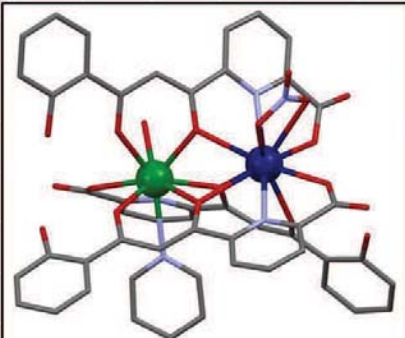


Table V.8. All possible combinations within the $[\text{LnLn}'(\text{HL4})_2(\text{H}_2\text{L4})(\text{NO}_3)(\text{py})(\text{H}_2\text{O})]$ system. Highlighted (red ticks) are the combinations where crystal structures could be obtained by single crystal X-ray diffraction, together with the corresponding compound number. Note that complexes in the diagonal belong to the series studied in section 2.

5.1. Crystal structure of [LnLn'(HL4)₂(H₂L4)(NO₃)(py)(H₂O)]

Like for their analogous homometallic compounds, complexes **31** to **72** crystalize in the monoclinic space group $P2_1/c$ exhibiting one [LnLn'] molecule in the asymmetric unit together with five or six molecules of pyridine. The unit cell contains four asymmetric units and display very similar cell parameters for all the compounds (see Tables V.A7 to V.A16 in the Appendix). Selected metric parameters of complexes **31** to **72** are shown in Tables V.A17 to V.A56 in the Appendix. The molecular structure of [CeEr(HL4)₂(H₂L4)(NO₃)(py)(H₂O)] (**40**) is represented in Figure V.29 as example. The molecule comprises a Ce^{III} ion and an Er^{III} center surrounded by three partially deprotonate H₃L4 ligands, one as H₂L4⁻ and two as HL4²⁻. Consistent with their relative ionic radii, Ce^{III} is encapsulated in the expected larger pocket (site 2), whereas the smaller cation Er^{III} occupies the more favored site 1. Both metals are chelated by the distinct coordination pockets of the ligands (β -diketonate unit and dipicolinate-like group), bridged by three common central O-donors. Ce^{III} is bound to two dipicolinate fragments and one β -diketonate group, and its coordination number ten is completed by a η^2 -NO₃⁻ ligand. In contrast, Er^{III} is encapsulated by one dipicolinate pocket and two β -diketonate units, in addition to one molecule of H₂O and one molecule of pyridine, completing a coordination number nine. The mutual head-to-head configuration of two ligands, together with a third one in the opposite direction, imposes the different environments around both ions. In this case, such difference is even more pronounced than with the analogous homometallic compounds. Thus, the difference between averages $\sum\text{Ce-O}$ and $\sum\text{Er-O}$ (considering only O-donors from the chelating ligands) reaches $\Delta\text{O} = 0.17$, being considerably higher than the differences observed in compounds **13** ([Ce₂]) and **22** ([Er₂]) (0.04 for both complexes, see Table V.7). Both metal ions within the complex are separated by 3.8505(6) Å.

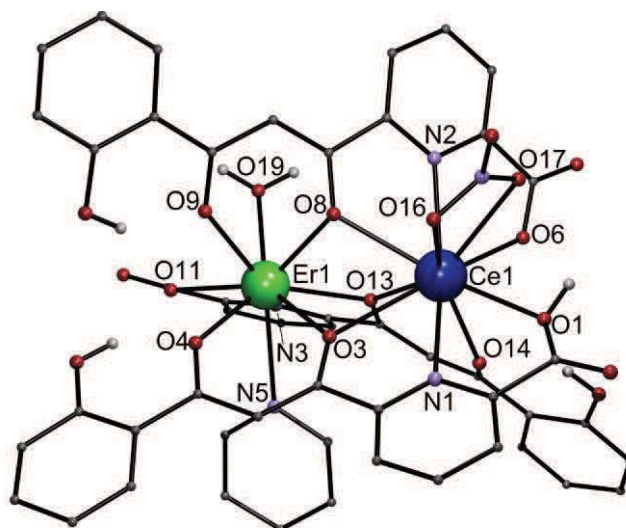


Figure V.29. Representation of the molecular structure of the complex $[\text{CeEr}(\text{HL4})_2(\text{H}_2\text{L4})(\text{NO}_3)(\text{py})(\text{H}_2\text{O})]$ (**40**). Dark blue, Ce; green, Er; purple, N; red, O; rest, C. Only hydrogen atoms bound to O are shown.

For most compounds, when the refining process of the crystal structure was performed exchanging the positions of Ln and Ln' or defining the two possible homometallic clusters ($[\text{LnLn}]$ or $[\text{Ln}'\text{Ln}']$), an increase of the *R1* factor was found. Crystal structures from combinations of lanthanides exhibiting highly different ionic radii, this is, relatively far from each other within the 4f series (like Ce^{III} and Er^{III} in compound **40**), are considered quite reliably since such factor is sufficiently lower compared with the other combinations. However, closer lanthanide ions cannot be differentiated by X-ray diffraction due to the high similarity between their electron scattering power. For these compounds, differences in *R1* values were found to be not significant or even nonexistent. Thus, further characterization by ICP-AES spectroscopy, mass spectrometry or magnetic susceptibility was necessary in order to establish the heterometallic nature of these compounds.

5.2. Study of the $[\text{LnPr}(\text{HL4})_2(\text{H}_2\text{L4})(\text{NO}_3)(\text{py})(\text{H}_2\text{O})]$ series

The interesting structural features of $[\text{LnLn}'(\text{HL4})_2(\text{H}_2\text{L4})(\text{NO}_3)(\text{py})(\text{H}_2\text{O})]$ allows the study of the selectivity of the system by combining one lanthanide ion with all the different metals of the 4f series. As previously exposed in Table V.8, praseodinium(III)

has been introduced in the asymmetric system together with the rest of the lanthanide ions, as well as with yttrium(III), producing all the possible complexes of the type $[\text{LnPr}(\text{HL4})_2(\text{H}_2\text{L4})(\text{NO}_3)(\text{py})(\text{H}_2\text{O})]$ ($\text{Ln} = \text{La}$ (**31**), Ce (**37**), Pr (**14**), Nd (**44**), Sm (**45**), Eu (**46**), Gd (**47**), Tb (**48**), Dy (**49**), Ho (**50**), Er (**51**), Tm (**52**), Yb (**53**), Lu (**54**), Y (**55**)). All the crystal structures are analogous to that of **40**. The specific location of Pr^{III} and Ln^{III} within the asymmetric entity was again suggested by the crystal structure. Thus, when Pr^{III} is combined with cations of larger size, like La^{III} or Ce^{III} , it occupies the expected position favoring smaller Ln-X bonds (site 1). In contrast, when it is accompanied by a smaller cation (Nd^{III} to Lu^{III} and Y^{III}), Pr^{III} goes to the larger site 2. This behavior can be assessed by studying the sum $\sum\text{Pr-O}$ and $\sum\text{Ln-O}$ within each complex, considering only O-donor atoms from partially deprotonated $\text{H}_3\text{L4}$ (Figure V.30). Structural parameters concerning complexes **47** and **51** ($[\text{PrGd}]$ and $[\text{PrEr}]$ respectively) have not been included due to the refinement status of the data.

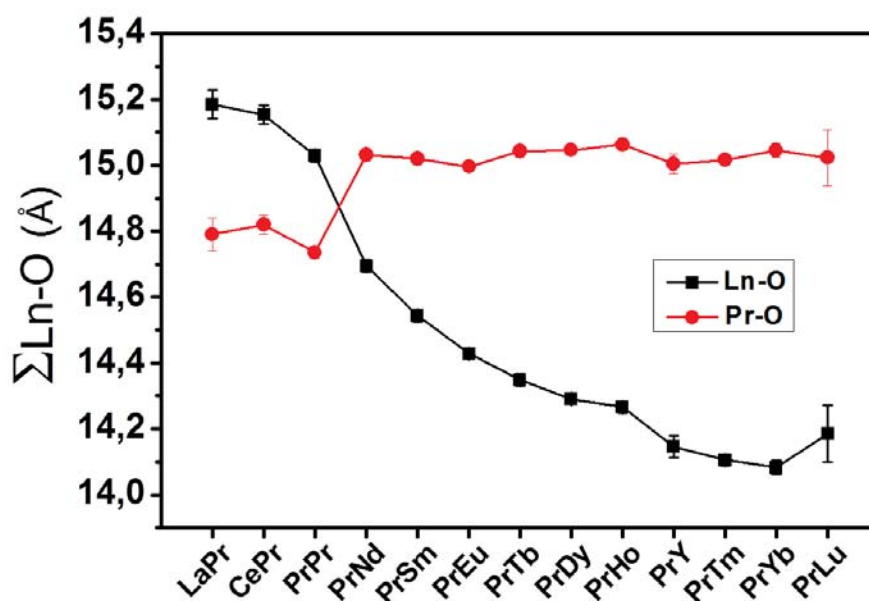


Figure V.30. $\sum\text{Pr-O}$ and $\sum\text{Ln-O}$ parameters for $[\text{LnPr}(\text{HL4})_2(\text{H}_2\text{L4})(\text{NO}_3)(\text{py})(\text{H}_2\text{O})]$ complexes.

Figure V.30 shows the parameter $\sum\text{Pr-O}$ in red and $\sum\text{Ln-O}$ and black. For complexes **31**, **37** and **14** ($\text{Ln} = \text{La}$, Ce and Pr respectively) the parameter $\sum\text{Ln-O}$ is larger than $\sum\text{Pr-O}$ since Ln^{III} occupies site 2. In addition, the values decrease in the order $\sum\text{La-O} > \sum\text{Ce-O} > \sum\text{Pr-O}$ (Pr being also Ln^{III} in the last case) due to the effects of the lanthanide

contraction. In contrast, as expected, the parameter $\sum\text{Pr-O}$ does not follow a specific trend, and the values are in good agreement with the one obtained in the homometallic $[\text{Pr}_2]$ complex for site 1 (14.736(18) Å). On the other part, for compounds **44**, **45**, **46**, **48**, **49**, **50**, **52**, **53**, **54** and **55** ($\text{Ln} = \text{Nd}, \text{Sm}, \text{Eu}, \text{Tb}, \text{Dy}, \text{Ho}, \text{Tm}, \text{Yb}, \text{Lu}$ and Y respectively), $\sum\text{Pr-O}$ reaches higher values than $\sum\text{Ln-O}$ since praseodinium(III) is encapsulated now in site 2. The smaller cations Ln^{III} occupy in these cases the expected location (site 1) favoring smaller values of $\sum\text{Ln-O}$, which in turn decreases through the series as the ionic radii of Ln^{III} shrinks. As expected, $\sum\text{Pr-O}$ (Pr^{III} being located in site 2) remains stable for all these complexes, reaching values very close to $\sum\text{Pr-O}$ for $[\text{Pr}_2]$ in site 2 (15.030(18) Å). In addition, similar $\sum\text{Ln-O}$ parameters were found when comparing the value in each heterometallic $[\text{LnPr}]$ compound with $\sum\text{Ln-O}$ from its respective homometallic $[\text{Ln}_2]$ complex and site (Table V.9).

Table V.9. Comparison of values $\sum\text{Pr-O}$ and $\sum\text{Ln-O}$ from heterometallic $[\text{LnPr}]$ complexes with $\sum\text{Ln-O}$ from the homometallic $[\text{Ln}_2]$ complexes

$[\text{LnPr}(\text{HL4})_2(\text{H}_2\text{L4})(\text{NO}_3)(\text{py})(\text{H}_2\text{O})]$	$\sum\text{Pr-O}$ (Å)	$\sum\text{Ln-O}$ (Å)	$\sum\text{Ln-O}$ $[\text{Ln}_2]^*$ (Å)
[LaPr] (31)	14.791(49)	15.185(44)	15.268(18)
[CePr] (37)	14.821(29)	15.154(29)	15.141(23)
$[\text{Pr}_2]$ (14)	14.736(18)	15.030(18)	-
[PrNd] (44)	15.032(18)	14.695(18)	14.672(25)
[PrSm] (45)	15.021(18)	14.544(18)	14.482(57)
[PrEu] (46)	14.9965(109)	14.4295(109)	14.427(29)
[PrTb] (48)	15.044(18)	14.349(18)	14.355(66)
[PrDy] (49)	15.0472(118)	14.2905(118)	14.217(53)
[PrHo] (50)	15.064(18)	14.266(18)	14.158(30)
[PrTm] (52)	15.017(18)	14.106(18)	14.047(26)
[PrYb] (53)	15.046(20)	14.083(20)	14.041(45)
[PrLu] (54)	15.023(83)	14.185(86)	-
[PrY] (55)	15.005(30)	14.146(33)	14.272(84)

* Values from site 2 (for complexes **31**, **37** and **14**) and from site 1 (for complexes **44** to **55**) of the respective homometallic compounds

For a further assessment, the difference between the average of the distances Ln-O and Pr-O (ΔO) for each $[\text{LnPr}(\text{HL4})_2(\text{H}_2\text{L4})(\text{NO}_3)(\text{py})(\text{H}_2\text{O})]$ compound has been calculated (Table V.10). The comparison with ΔO from the corresponding homometallic $[\text{Ln}_2(\text{HL4})_2(\text{H}_2\text{L4})(\text{NO}_3)(\text{py})(\text{H}_2\text{O})]$ compounds shows remarkably

differences for the cases were the ionic radii of both metal of the complex differ significantly (termed as Δr).^[15, 46] This strongly suggests the purity of the heterometallic moiety [PrLn] in complexes **45**, **46**, **48**, **49**, **50**, **52**, **53**, **54** and **55** (Ln = Sm, Eu, Tb, Dy, Ho, Tm, Yb, Lu and Y respectively). In contrast, similar ΔO values have been found for Ln = Ce (**37**) and Nd (**44**), where Δr is very small (0.02 and 0.03 Å respectively). Thus, for these two systems, the different [LnLn'], [LnLn] and [Ln'Ln'] possible compounds cannot be distinguished by X-ray diffraction.

Table V.10. ΔO parameters for [LnPr] complexes and [Ln₂] homometallic complexes

[LnPr(HL4) ₂ (H ₂ L4)(NO ₃)(py)(H ₂ O)]	ΔO (Å)	Δr (Å)	ΔO [LnLn] (Å)
[LaPr] (31)	0.07	0.05	0.04
[CePr] (37)	0.06	0.02	0.04
[PrPr] (14)	0.05	-	0.05
[PrNd] (44)	0.06	0.03	0.05
[PrSm] (45)	0.08	0.06	0.05
[PrEu] (46)	0.09	0.08	0.05
[PrTb] (48)	0.12	0.11	0.03
[PrDy] (49)	0.13	0.13	0.03
[PrHo] (50)	0.13	0.15	0.03
[PrTm] (52)	0.15	0.18	0.04
[PrYb] (53)	0.16	0.19	0.04
[PrLu] (54)	0.14	0.21	-
[PrY] (55)	0.14	0.13	0.05

The heterometallic nature of [CePr] (**37**) and [PrNd] (**44**) compounds was therefore examined by positive ion electrospray (ESI⁺) in MeOH/DMSO, using a mixture of MeCN and H₂O as eluent. For both complexes, the three possible combinations were found in solution. Selected fragments regarding [Ce₂(HL4)₂(H₂L4)]⁺, [Pr₂(HL4)₂(H₂L4)]⁺ and [CePr(HL4)₂(H₂L4)]⁺ species in complex **37** demonstrates that the system cannot discriminate these two metal ions (Figure V.31, left). Similarly, complex **44** shows the three possible [Pr₂(HL4)₂(H₂L4)]⁺, [Nd₂(HL4)₂(H₂L4)]⁺ and [PrNd(HL4)₂(H₂L4)]⁺ species (Figure V.31, right).

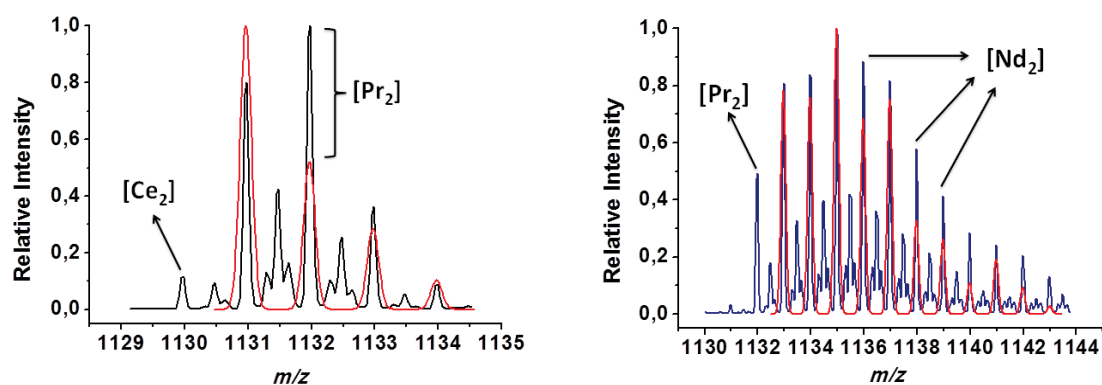


Figure V.31. Selected fragments of the mass spectrogram of $[\text{CePr}(\text{HL4})_2(\text{H}_2\text{L4})(\text{NO}_3)(\text{py})(\text{H}_2\text{O})]$ (**37**) (left, in black) and $[\text{PrNd}(\text{HL4})_2(\text{H}_2\text{L4})(\text{NO}_3)(\text{py})(\text{H}_2\text{O})]$ (**44**) (right, in blue). The simulated signals are also represented where the isotopic distribution has been taken into consideration (red). Both spectrograms show fragment $[\text{LnLn}'(\text{HL4})_2(\text{H}_2\text{L4})]^+$ as well as the peaks corresponding to the homometallic fragments.

Although the intensity of the peak from the heterometallic moiety is higher than the two possible homometallic analogous for both complexes, the results demonstrate that full selectivity is not achieved when Pr^{III} is combined with its two neighboring metal ions, Ce^{III} and Nd^{III} . The crystal structure of these two complexes should be then considered as a mixture of the three species, with some percentage of molecules in the crystal belonging to $[\text{Ln}_2]$ or $[\text{Ln}'_2]$, in addition to $[\text{LnLn}']$.

The selectivity for the rest of the complexes in the $[\text{LnPr}]$ series by mass spectrometry is still subject of study. Nonetheless, the greater difference of the ionic radii between Pr^{III} and Ln^{III} in these compounds strongly suggests that they correspond to pure heterometallic systems. This hypothesis could be verified for certain dinuclear compounds that present a special interest for the purposes of this thesis, where indeed, the ionic radii of Ln and Ln' differ significantly. The mass spectrometry of these systems shows only the peak from the heterometallic moiety thus demonstrating their heterometallic nature. This is the case of compounds **35** [LaEr], **36** [LaY], **40** [CeEr] and **43** [CeY] (see below). In addition, several complexes not included in this document, which are being studied in the group, reveal also only the heterometallic moiety $[\text{LnLn}']$ in the mass spectrogram (e.g., [LaLu], [LaHo], [LaTm], [LaYb], [LaTb], [CeLu], [CeYb], [CeSm] or [CeNd]).

In general terms, the results from the crystallographic study of the [LnPr] series and the mass spectrograms of the [LnLn'] systems obtained so far demonstrate that only when the two metal ions present very similar ionic radii, the selectivity is truncated. On the contrary, for all other combinations, the system can discriminate between two different lanthanides by their size and selectively distribute them over the two different locations, thus leading to pure heterometallic complexes. These results show therefore that for a majority of cases, the heterometallic system corresponds to the thermodynamically most stable product.

6. Study of [CeEr(HL4)₂(H₂L4)(NO₃)(py)(H₂O)] as a molecular 2-qubit quantum gate

Due to the structural constraints exhibited in the system [LnLn'(HL4)₂(H₂L4)(NO₃)(py)(H₂O)], it has been demonstrated how the preference of the two sites to encapsulate different lanthanides can be used to satisfactorily synthesize heterometallic dinuclear lanthanide complexes (Section 5). Such flexibility enables a vast choice of quantum gate designs, as well as the possibility of studying each lanthanide ion without the influence of the other magnetic center by combinations of paramagnetic and diamagnetic lanthanide ions. From all the different possible systems, the molecular dimer containing Ce^{III} and Er^{III} ([CeEr(HL4)₂(H₂L4)(NO₃)(py)(H₂O)], complex **40**) entails ideal properties for its application as a molecular quantum processor. First, these two lanthanide metals exhibit very different magnetic ground states as free ions. Thus, according to Hund's rules, Ce^{III} has a ground state multiplet with $J = 5/2$ and $g_J = 6/7$, while Er^{III} has $J = 15/2$ and $g_J = 6/5$. In addition, Ce^{III} has no nuclear spin, while for Er^{III}, only 23 % of the stable isotopes do. Taking into account that hyperfine interactions is a major source of decoherence for molecular-based quantum gates, the choice of these two lanthanide ions represents an important advantage for the present goal. For a detailed description of the magnet energy levels of **40**, it is required to study both metal centres in their respective environments, without the magnetic influence of the other. The goal can be achieved if the properly heterometallic system is designed. Complexes [CeY(HL4)₂(H₂L4)(NO₃)(py)(H₂O)] (**43**) and [LaEr(HL4)₂(H₂L4)(NO₃)(py)(H₂O)] (**35**) fulfill

such conditions, since Ce^{III} (in complex **43**) and Er^{III} (in complex **35**) occupy the same position they do in **40**, but are accompanied by a diamagnetic cation (Y^{III} and La^{III}, respectively). In addition, the design of a pure diamagnetic analogue is also important in order to determine experimentally the non-magnetic energy contributions to the specific heat capacity in this family of compounds (see below). These requirements are fulfilled by compound [LaY(HL4)₂(H₂L4)(NO₃)(py)(H₂O)] (**36**). Thus, as a first priority, the heterometallic nature of all these compounds was exhaustively assessed by single X-ray crystallography, as well as by metal analysis and mass spectrometry.

The crystal structure of compounds [CeY] (**43**), [LaEr] (**35**) and [LaY] (**36**) are analogous to that of [CeEr] (**40**). The difference in ionic radii (Δr), as well as the difference between the average of the distances Ln-O and Ln'-O (ΔO) are summarized in Table V.11. According to Δr , and considering $r_{\text{Ce}^{\text{III}}} > r_{\text{Y}^{\text{III}}}$ and $r_{\text{La}^{\text{III}}} > r_{\text{Er}^{\text{III}}} \approx r_{\text{Y}^{\text{III}}}$,^[15, 46] site 2 is occupied by Ce^{III} in complex **43**, and by La^{III} in complexes **35** and **36**. In contrast, Y^{III} (in complexes **43** and **36**) and Er^{III} (in complex **35**) are coordinated in site 1. Compounds **35** and **36** exhibit greater disparity in ionic radii of the two metal ions than complex **43**. Consequently, the difference ΔO (as previously defined) is slightly larger in the former complexes than in the latter. The Ln centre of site 1 (Ce^{III} and La^{III}) of the three complexes exhibits coordination number ten, with the nitrate ligand in the terminal η^2 -NO₃⁻ coordination mode. The metal-metal separations are 3.8515(13) Å (Ce...Y), 3.8572(8) Å (La...Er) and 3.8694(14) Å (La...Y).

Table V.11. ΔO and Δr values for complexes **43, **35** and **36****

[LnLn'(HL4) ₂ (H ₂ L4)(NO ₃)(py)(H ₂ O)]	ΔO (Å)	Δr (Å)
[CeY] (43)	0.15	0.15
[LaEr] (35)	0.18	0.21
[LaY] (36)	0.19	0.18

In addition, these compounds were exhaustively characterized with the techniques described above. The 1:1 metal composition obtained by ICP-AES spectroscopy for the four complexes strongly suggests that in the bulk, these compounds consist of 100 %

[LnLn'] species. As solid evidence, MS experiments revealed only heterometallic fragments of each system in solution, with no evidence of their corresponding [Ln₂] or [Ln'₂] homometallic complexes. Mass spectrograms of [CeEr] (**40**), [CeY] (**43**), [LaEr] (**35**) and [LaY] (**36**) featuring heterometallic fragments [LnLn'(HL4)₂(H₂L4)]⁺ and ([LnLn'(HL4)₃]+Na)⁺ are shown in the Appendix (Figures V.A17 to V.A20). The superposition of the mass spectra of complexes [CeEr] (**40**), [Ce₂] (**13**) and [Er₂] (**22**) is represented in Figure V.32, demonstrating that no signal from the corresponding homometallic complexes appears when the heterometallic entity is evaluated in the exact same conditions. The results from both techniques, as well as from the magnetic measurements (see below), therefore confirm that the pure heterometallic system has been successfully synthesized.

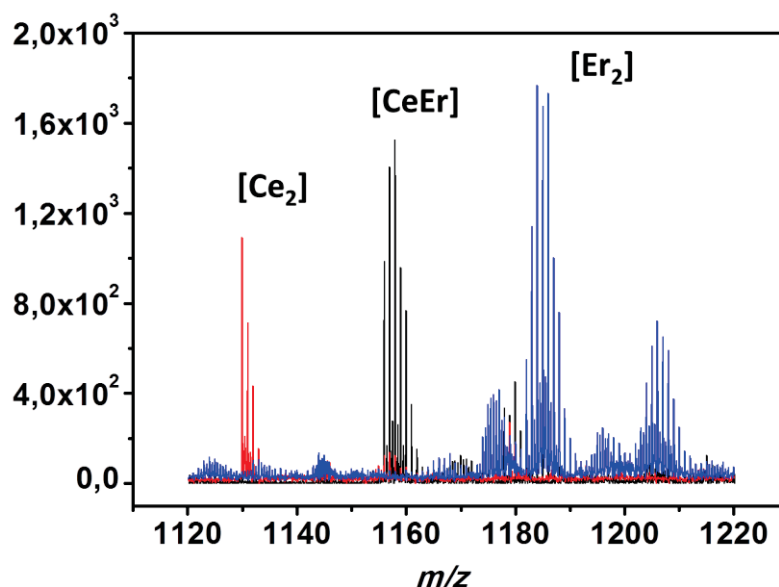


Figure V.32. Selected fragments of the mass spectrogram of [Ce₂(HL4)₂(H₂L4)(NO₃)(py)(H₂O)] (**13**), [Er₂(HL4)₂(H₂L4)(NO₃)(py)(H₂O)] (**22**) and [CeEr(HL4)₂(H₂L4)(NO₃)(py)(H₂O)] (**40**) in red, blue and black, respectively. Highest peak corresponds to the fragment [Ln₂(HL4)₂(H₂L4)]⁺ in each case.

The versatility of the system thus allows the characterization of each of the two lanthanide ions of [CeEr] (**40**) in their respective local coordination environments by studying complexes [CeY] (**43**) and [LaEr] (**35**) (Figure V.33). Physical characterization involving these three compounds, as well as the pure diamagnetic analog [LaY] (**36**), was carried out to show that complex **40** fulfills the conditions to be used as a 2-qubit molecular quantum gate, this is, that each lanthanide ion behaves as an effective spin

$\frac{1}{2}$ at sufficiently low temperatures and that both spins exhibit a weak magnetic interaction. This study has been done in collaboration with Dr. Olivier Roubeau and Dr. Fernando Luis at the Universidad de Zaragoza.

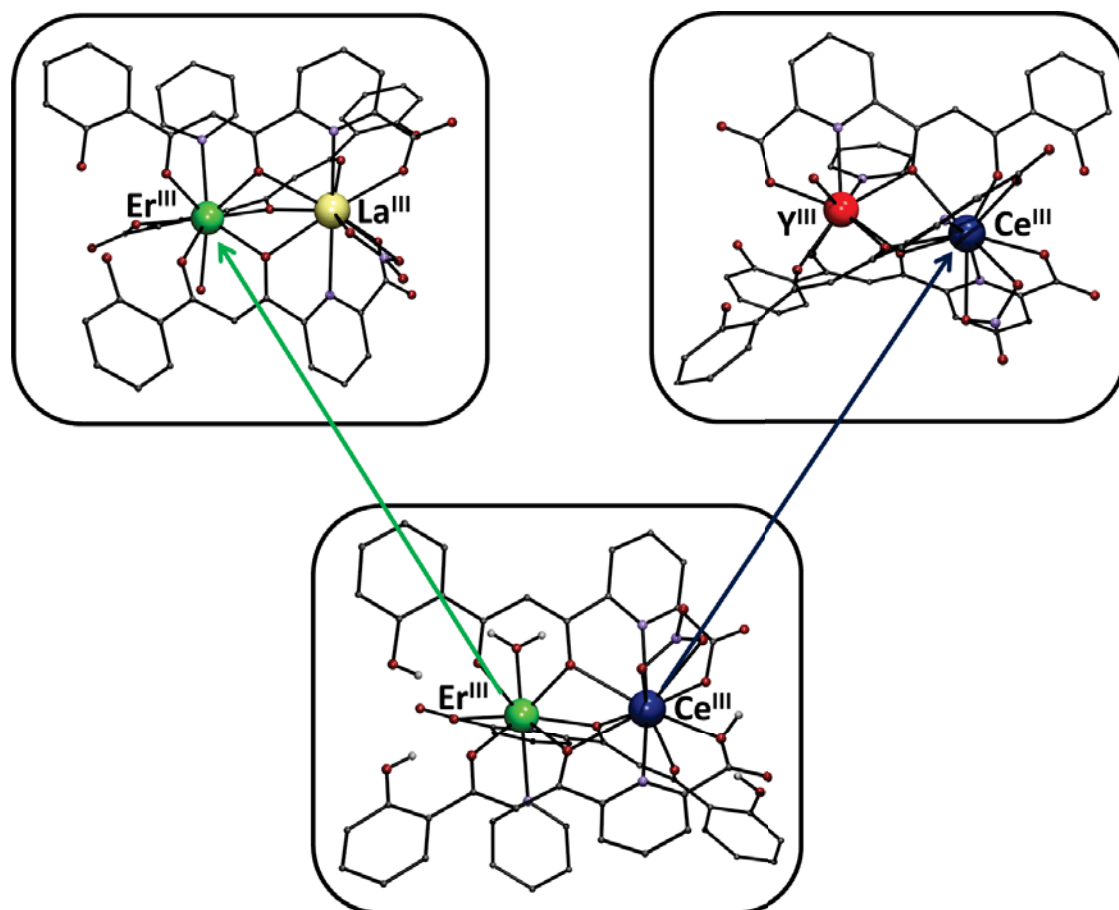


Figure V.33. Representation of the molecular structures of complexes $[\text{CeY}(\text{HL4})_2(\text{H}_2\text{L4})(\text{NO}_3)(\text{py})(\text{H}_2\text{O})]$ (**43**) (top, right), $[\text{LaEr}(\text{HL4})_2(\text{H}_2\text{L4})(\text{NO}_3)(\text{py})(\text{H}_2\text{O})]$ (**35**) (top, left) and $[\text{CeEr}(\text{HL4})_2(\text{H}_2\text{L4})(\text{NO}_3)(\text{py})(\text{H}_2\text{O})]$ (**40**) (bottom). Dark blue, Ce; green, Er; light yellow, La; light red, Y; purple, N; red, O; rest, C. Only hydrogen atoms bound to O are shown.

6.1. Defining Ce^{III} and Er^{III} as quantum bits

Magnetic susceptibility (χ), heat capacity (c_p) and EPR measurements were carried out in order to characterize both Ce^{III} and Er^{III} as qubits, as well as to establish the interaction between them within the $[\text{CeEr}]$ system. For the study of each ion as a qubit, measurements have been done on compounds $[\text{CeY}]$ and $[\text{LaEr}]$, each of them containing one magnetic lanthanide (Ce^{III} and Er^{III} , respectively) and a non-magnetic

one (Y^{III} and La^{III}). As previously introduced, the magnetic ions lie exactly at the same site as in the [CeEr] complex, thus having the same local coordination environment. Experiments were carried out by considering the local environment of each lanthanide ion, thus following the general spin Hamiltonian:

$$H = \sum_{n,m} B_n^m O_n^m - g_J \beta (H_x J_x + H_y J_y + H_z J_z) \quad (45)$$

where O_n^m are Steven's spin operators and B_n^m are anisotropy parameters. The magnitude and the number of terms involved in such Steven's spin operators are defined by the symmetry produced by the local environment of the lanthanide ion. However, the coordination spheres of the two ions within these dinuclear systems have a very low symmetry, and thus any term is allowed. As an approximation, in order to reduce the number of free parameters, the following simplified Hamiltonian is considered:

$$H = B_2^0 O_2^0 + B_2^1 (O_2^1 + O_2^{-1}) + B_2^2 O_2^2 + B_4^0 O_4^0 - g_J \beta (H_x J_x + H_y J_y + H_z J_z) \quad (46)$$

It includes the diagonal terms (those with $m = 0$) up to fourth order ($n = 4$), and the lowest order off-diagonal terms ($m = \pm 1, 2$). Figure V.34 shows $\chi_M T$ versus T data of a powdered sample of complex [LaEr(HL4)₂(H₂L4)(NO₃)(py)(H₂O)] (**35**). The value at room temperature ($11.44 \text{ cm}^3 \text{ K mol}^{-1}$) is very close to the one expected for a free Er^{III} ion ($11.5 \text{ cm}^3 \text{ K mol}^{-1}$). The decline observed when decreasing the temperature is ascribed to the depopulation of the excited magnetic levels (split by the crystal field). The curve reaches a plateau at 4 K with $\chi_M T \approx 5.9 \text{ cm}^3 \text{ K mol}^{-1}$, indicating that only the ground state doublet remains populated down to this temperature. The value is compatible with the expected susceptibility of a $m_J = \pm 1/2$ doublet ($\chi_M T = 5.81 \text{ cm}^3 \text{ K mol}^{-1}$) and also with that of a $m_J = \pm 11/2$ doublet ($\chi_M T = 5.50 \text{ cm}^3 \text{ K mol}^{-1}$). These values have been obtained from the equation of the magnetic susceptibility for the case where only the doublet ground state has significant population:

$$\chi = N_A \frac{\beta^2}{4k_B T} \frac{(g_x^2 + g_y^2 + g_z^2)}{3} \quad (47)$$

The drop of the ac data observed below 0.1 K is associated with slow relaxation processes, probably due to the energy barrier produced by the coupling between the electronic and the nuclear spin of Er^{III} .

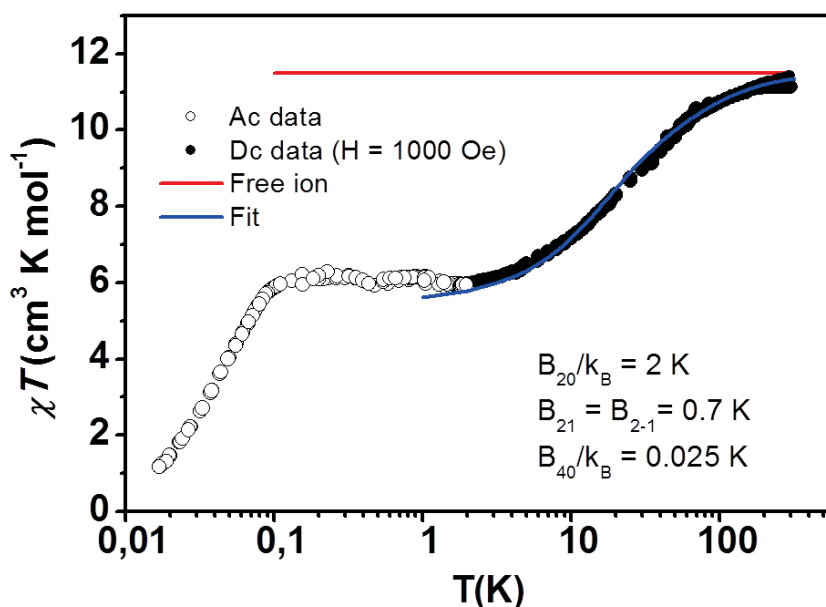


Figure V.34. $\chi_M T$ product from Ac data (open circles) and Dc data (black circles) of a powdered sample of [LaEr] (35). The red line gives the susceptibility of the free Er^{III} ion. Blue line is obtained from numerical calculations from the simplified Hamiltonian (see the text).

The data was fitted by full matrix diagonalization of the simplified Hamiltonian (Equation 46), leading to a reasonably good fit for $B_2^0/k_B = 2$ K, $B_2^1/k_B = 0.7$ K, $B_2^2/k_B = 0$ K and $B_4^0/k_B = 0.025$ K (Figure V.34, solid blue line). The fact that there is one off-diagonal term (B_2^1) different to zero indicates that the ground state is not defined by the pure states $m_j = \pm 11/2$ or $m_j = \pm 1/2$ but from a combination of them.

The results of the EPR measurement carried out on a powdered sample of [LaEr] are shown in Figure V.35. The broad lines observed are inherent to a powder experiment. The fit of these data suggests that the ground state doublet of Er^{III} can be characterized by $g_x = 3.70$, $g_y = 1.80$ and $g_z = 10.00$. It should be noticed that, for an erbium(III) ion, a set of one large g value and two small ones is characteristic of systems with a ground state like $m_j = \pm 11/2$ rather than $m_j = \pm 1/2$. Thus, since g_z is considerably higher than g_x and g_y , the ground state of compound [LaEr] is primarily $m_j = \pm 11/2$. Nevertheless, the fact that g_x/g_z and g_y/g_z are relatively large suggests that the off-diagonal term B_2^1 is

not zero (in agreement with the fit obtained from the magnetic measurements). This behavior thus corroborates that the doublet ground state of this Er^{III} ion is formed by a combination of the states $m_J = \pm 11/2$ and $m_J = \pm 1/2$, with a major contribution from the former.

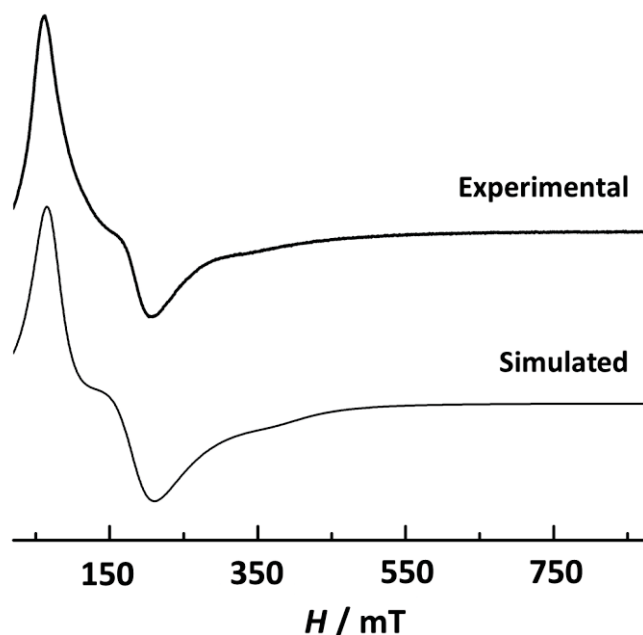


Figure V.35. Experimental X-band EPR spectrum of powdered [LaEr] (**35**) and theoretical simulation.

The existence of a well isolated ground state was also substantiated by heat capacity measurements, shown in Figure V.36. Above 10 K, the specific heat capacity is governed by the contribution from the lattice vibrations (C_{latt}). The non-magnetic compound [LaY] (**36**) was used to experimentally determine this contribution (Figure V.36, empty circles). These data were fitted (Figure V.36, dotted black line) with a Debye model, leading to a value of $\theta_D = 35$ K (which considers the specific heat of acoustic phonons) and two generalized Einstein contributions ($\theta_E = 39$ K and $\theta_E = 81$ K) involving molecular vibrational modes. For the compound [LaEr], a magnetic contribution, c_m , appears below 10 K as a Schottky anomaly that depends on the applied magnetic field. Such dependence agrees with that expected for a two-state magnetic system with strong anisotropy. On the other hand, the rise around 1 K of the magnetic heat capacity at zero field can be associated to dipolar interactions. In addition, Schottky anomalies are shifted from the ones observed when the heat

capacity is calculated using the anisotropy parameters from the fit of the magnetic susceptibility data (Figure V.36, solid lines). This behavior suggests that additional anisotropy terms, not included in the model, are required for the fit of the magnetic heat capacity data.

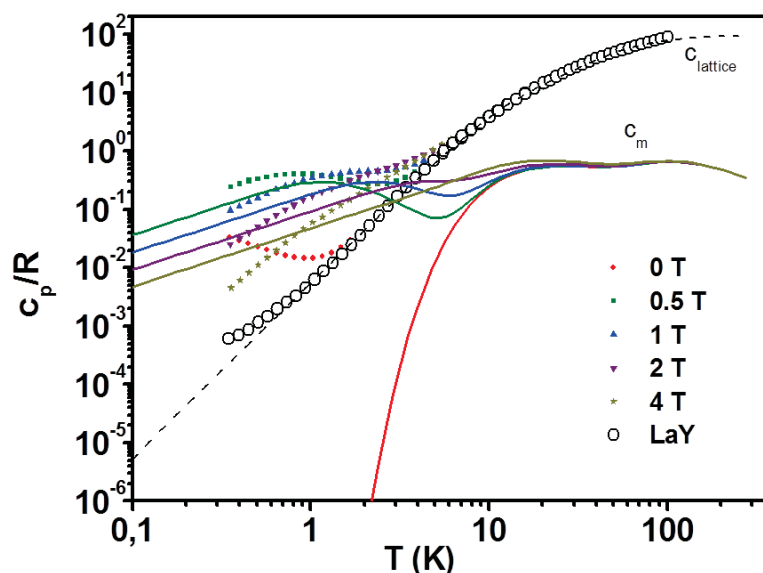


Figure V.36. Molar specific heat of [LaEr] (**35**) measured under varying magnetic fields. Solid lines are the calculated data considering the anisotropy parameters obtained in magnetic measurements. Empty circles and dotted line show the experimental and the fit of the specific heat of [LaY] (**36**).

The same procedure has been followed to characterize the Ce^{III} ion in this system as a quantum bit. This was done by studying the complex [CeY(HL4)₂(H₂L4)(NO₃)(py)(H₂O)] (**43**). Figure V.37 shows $\chi_M T$ versus T data from a powdered sample of the complex. The curve exhibits a decline from a value of 0.68 cm³ K mol⁻¹ at room temperature down to 20 K, where it reaches a plateau with $\chi_M T = 0.36$ cm³ K mol⁻¹, thus demonstrating that below this temperature only a ground state doublet is populated. However, this value does not correspond to any pure $\pm m_J$ ground state doublet of Ce^{III}, which indicates that also in this case, the ground state belongs to a combination of different states. Therefore, off-diagonal anisotropy terms (like B_2^1 or B_2^2) should have an important contribution to the magnetic behavior. The decrease of the $\chi_M T$ product can be associated to the depopulation of the excited Stark sublevels. In this case, the

value of $\chi_M T$ at room temperature does not reach completely the value of the susceptibility of a free Ce^{III} ion (Figure V.37, red solid line).

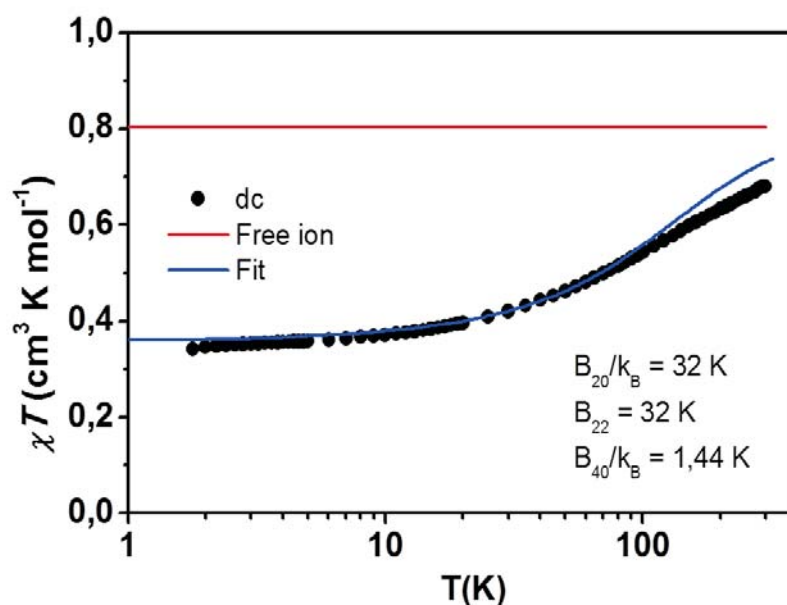


Figure V.37. $\chi_M T$ product from Dc data (black circles) of a powdered sample of $[\text{CeY}]$ (**43**). The red line gives the susceptibility of the free Ce^{III} ion. Blue line is obtained from numerical calculations from the Hamiltonian (see the text).

A reasonably good fit was obtained by full matrix diagonalization of the simplified Hamiltonian (Equation 46) with the following values for the anisotropic parameters: $B_2^0/k_B = B_2^2/k_B = 32$ K, $B_2^1/k_B = 0$ and $B_4^0/k_B = 1.44$ K (Figure V.37, solid blue line). On the other hand, EPR measurements were carried out on a powdered sample of $[\text{CeY}]$ between 9 and 20 K (Figure V.38). The data show that the signal does not increase with the temperature, which demonstrates that the two-level system ground state remains far from the first excited state.

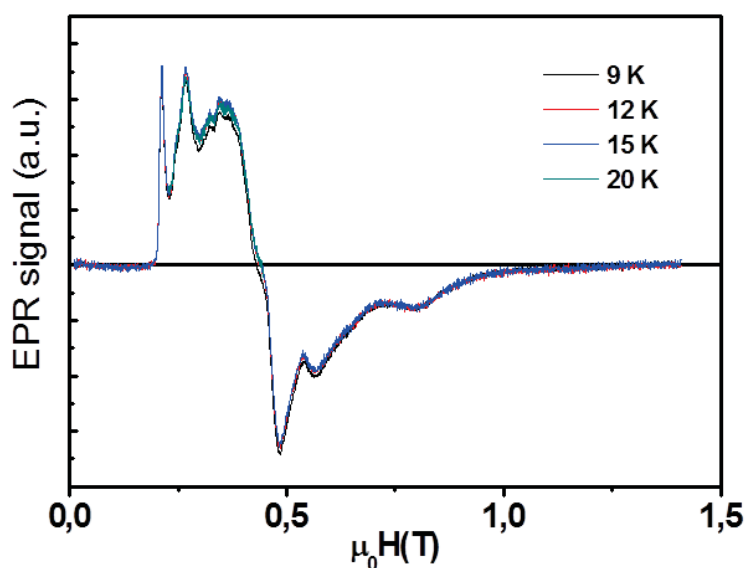


Figure V.38. Experimental EPR measurements on a powdered sample of [CeY] (43) between 9 and 20 K.

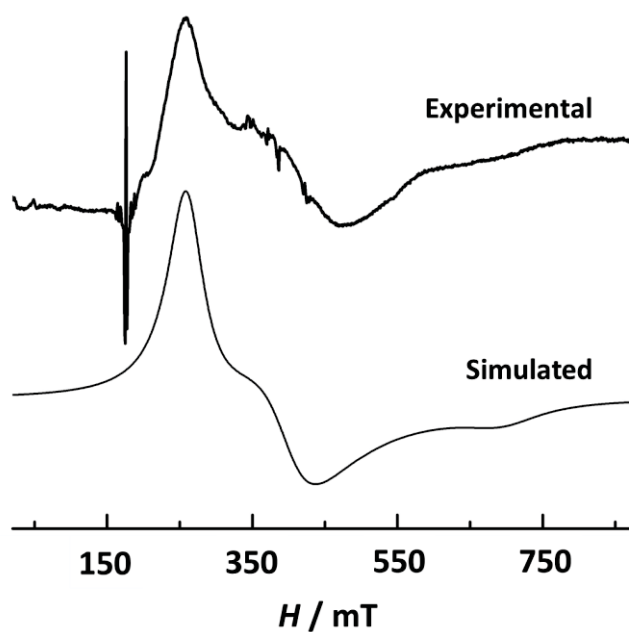


Figure V.39. Experimental X-band EPR spectrum of powdered [CeY] (43) and theoretical simulation.

The fit of the spectrum was obtained with the following g -factors: $g_x = 1.75$, $g_y = 1.00$ and $g_z = 2.67$ (Figure V.39). The values of the three g -factors suggest a ground state $m_J = \pm 3/2$ with a strong influence of other states by off-diagonal anisotropy terms.

Compound **43** was also studied by heat capacity measurements, shown in Figure V.40. Reasonably good fits were obtained with the same parameters previously handled ($B_2^0/k_B = B_2^2/k_B = 32$ K, $B_2^1/k_B = 0$ and $B_4^0/k_B = 1.14$ K).

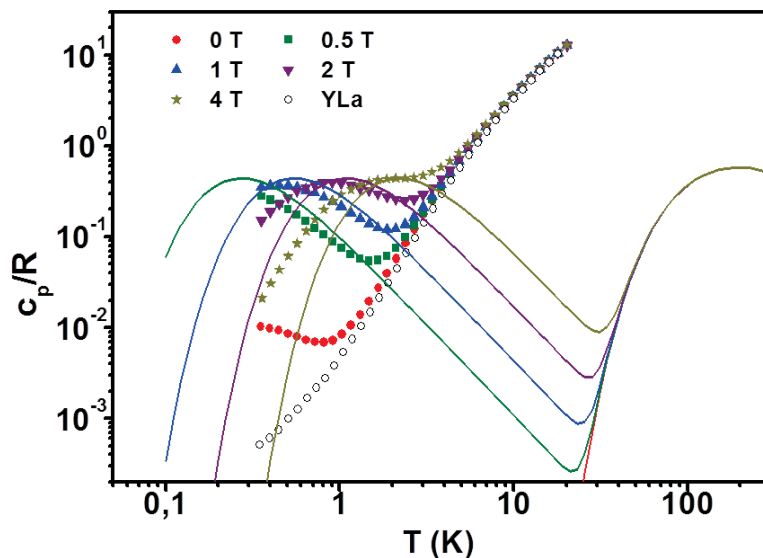
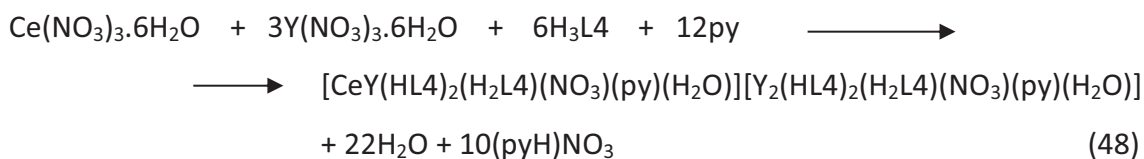


Figure V.40. Molar specific heat of [CeY] (**43**) measured under varying magnetic fields. Solid lines are the calculated data considering the anisotropy parameters described in the text. Empty circles are experimental data for specific heat of [LaY] (**36**).

As was seen when studying the [LaEr] compound, the zero-field heat capacity of [CeY] shows an increase below 1 K, associated to intermolecular interactions (Figure V.40, red circles). These interactions can be confirmed if the same experiment is carried out on a solid dilution of the complex within a diamagnetic matrix, increasing the distances between the paramagnetic [CeY] entities. To achieve such system, attempts to dilute [CeY] within an isostructural [Y₂] diamagnetic lattice were carried out by performing the reaction of the ligand H₃L4 with Ce(NO₃)₃ and Y(NO₃)₃ in a 6:1:3 molar ratio, devised to produce the mixture of complexes [CeY] + [Y₂] in equimolar amounts, as described by equation 48:



Such outcome could be expected if one assumes that the heterometallic complex forms preferentially and that both complexes cocrystallize in form of homogeneous solid mixtures. When the reaction solution was layered with ether, orange crystals suitable for X-ray diffraction were obtained. The crystal structure reveals that both [CeY] and [Y₂] complexes are present in the crystal within a homogeneous solid solution, randomly distributed in a 70:30 molar ratio: [CeY(HL4)₂(H₂L4)(NO₃)(py)(H₂O)]_{0.7}[Y₂(HL4)₂(H₂L4)(NO₃)(py)(H₂O)]_{0.3} (**73**) (Figure V.41). Crystallographic data and selected structural parameters are shown in Tables V.A16 and V.A57, respectively (Appendix). Thus, the compound consists of 70 % of the heterometallic complex [CeY(HL4)₂(H₂L4)(NO₃)(py)(H₂O)] (**43**) and 30 % of the diamagnetic complex [Y₂(HL4)₂(H₂L4)(NO₃)(py)(H₂O)] (**26**). Both molecules occupy the same space of the unit cell, and the composition of the solid solution is reflected by the occupancy ratios of the two of them. The positions of all the atoms for the two molecules of the dilution are exactly the same, with the exception of the metal in site 2 (Ce^{III} or Y^{III}) and three of the four atoms of the nitrate ligand. Each of these atoms is disordered over two locations with 0.7:0.3 occupancy ratios. Ce^{III} exhibits coordination number ten, with the nitrate ligand in a η^2 -NO₃⁻ mode (O16-N4-O17-O18). In contrast, when site 1 is occupied by Y^{III}, the nona-coordination around the metal is evidenced by the monodentate mode of the nitrate ligand (O16-N6-O27-O28). The only non-disordered atom of NO₃⁻ is the one featuring the shortest distance to the metal (O16). The two metal-metal distances Y...Y and Y...Ce are 3.70(4) and 3.880(11) Å, respectively. The common Y1 of site 1 exhibits the expected nona-coordination, completed by one molecule of pyridine and one of water. In addition, five molecules of pyridine appear in the unit cell.

The composition of the dilution of [CeY] molecules within the [Y₂] lattice was corroborated with ICP-AES metal analysis (0.7:0.3). In addition, MS experiments revealed fragments of both species in solution (Appendix, Figure V.A21), whereas as expected, no trace of [Ce₂] moieties could be observed.

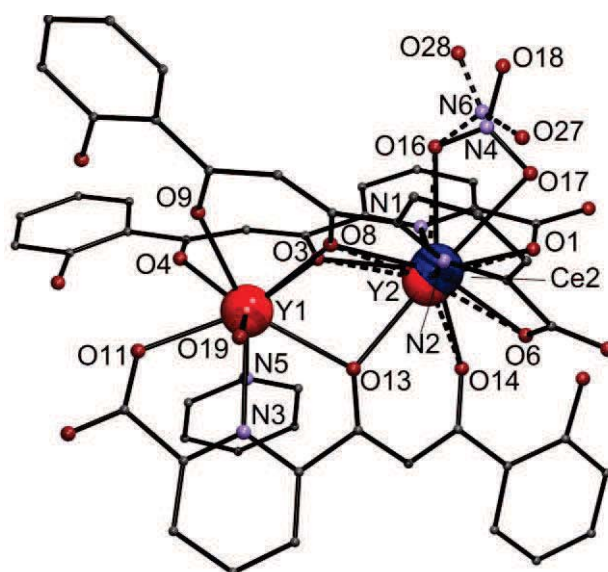


Figure V.41. Representation of the molecular structure of the complex (solid dilution) $[\text{CeY}(\text{HL4})_2(\text{H}_2\text{L4})(\text{NO}_3)(\text{py})(\text{H}_2\text{O})]_{0.7}[\text{Y}_2(\text{HL4})_2(\text{H}_2\text{L4})(\text{NO}_3)(\text{py})(\text{H}_2\text{O})]_{0.3}$ (**73**). Dark blue, Ce; light red, Y; purple, N; red, O; rest, C.

Compound $[\text{CeY}]_{0.7}[\text{Y}_2]_{0.3}$ (**73**) was thus used to experimentally evaluate the increase below 1 K of the zero-field heat capacity of complex $[\text{CeY}]$ (**43**). The decrease of such upturn for **73** as compared to **43** elegantly confirms that this contribution is related to dipolar interactions (Figure V.42). Such magnetic contribution diminishes with respect to that measured in complex **43** by a ratio 2/3, which corresponds approximately to the concentration of $[\text{CeY}]$ in complex **73**.

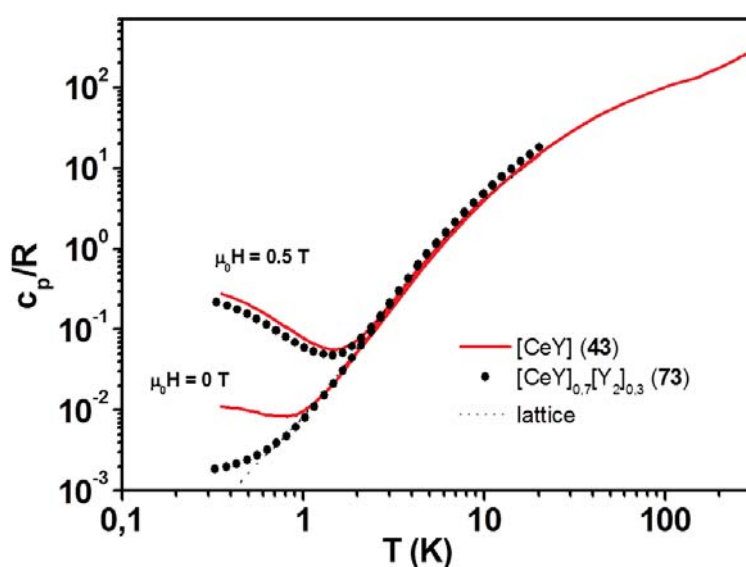


Figure V.42. Molar specific heat of $[\text{CeY}]_{0.7}[\text{Y}_2]_{0.3}$ (**73**) measured at $\mu_0 H = 0$ T and $\mu_0 H = 0.5$ T. The results for $[\text{CeY}]$ (**43**) under the same conditions are represented for comparison.

The results of the magnetic and thermal characterization of complexes [CeY] (**43**) and [LaEr] (**35**) show that both Ce^{III} and Er^{III} behave, at sufficiently low temperatures, as effective $S = 1/2$ (two state) qubits. However, these studies have also shown that the ground state of both ions does not belong to pure orientations of the angular momentum but to a combination of them, which can be associated to the low symmetry of their coordination environments. Despite this, the fact that the ground state of both ions is a well-separated two-level system should enable to encode the two basic states '0' and '1' of a quantum bit. The magnetic energy level structure of Ce^{III} and Er^{III} in complexes [CeY] and [LaEr], respectively, was calculated from the magnetic susceptibility and heat capacity data (Figure V.43). From these calculations, the energy difference between the ground state and the first excited state for Ce^{III} and Er^{III} was established as 350 K and 43 K, respectively.

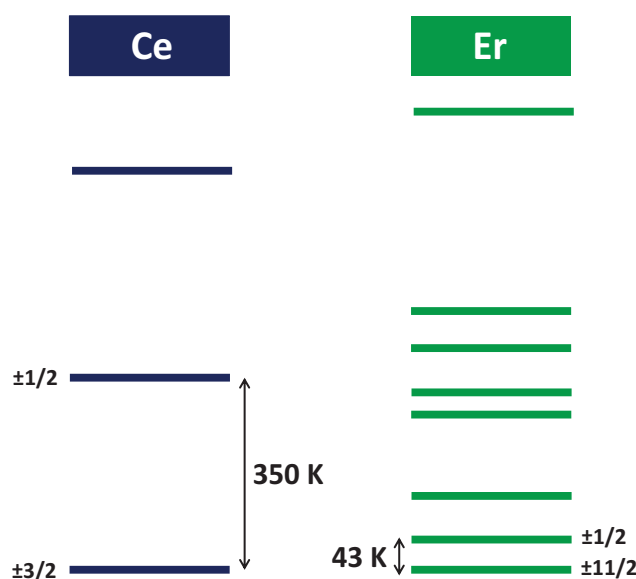


Figure V.43. Magnetic energy level structure of Ce^{III} and Er^{III} ions in their respective complexes **43** and **35**. The doublets are labeled by the m_j values considering no off-diagonal anisotropy terms (no combination of states).

6.2. Heterometallic [CeEr] complex as a molecular quantum processor

After the evaluation of the properties of each lanthanide ion as a quantum bit, complex **40** [CeEr] was studied to characterize the magnetic coupling between them

and to evaluate its potential as a quantum gate. Therefore, the magnetic and thermal properties of the three complexes [CeEr], [CeY] and [LaEr] were compared.

The magnetic susceptibility results are shown in Figure V.44. For $T > 2$ K, the $\chi_M T$ data of complex **40** [CeEr] is almost exactly equal to the sum of the $\chi_M T$ products of [CeY] and [LaEr], which reflects that the magnetic coupling must be very weak. Below this temperature, the $\chi_M T$ product of [CeEr] shows a decline that can be ascribed to an antiferromagnetic interaction between the two paramagnetic centres.

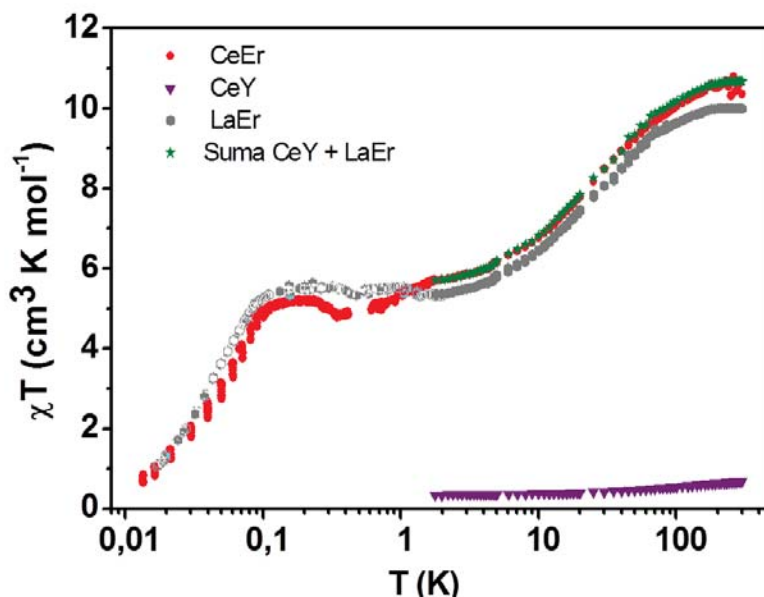


Figure V.44. $\chi_M T$ product (red circles) of a powdered sample of [CeEr] (**40**) Direct comparison with the $\chi_M T$ product of the complexes [CeY] (purple triangles) and [LaEr] (grey circles), and the sum of them (green stars).

Very similar results can be extracted from heat capacity measurements (Figure V.45). The response of [CeEr] significantly deviates from the sum of the heat capacity of compounds [CeY] and [LaEr] at very low temperatures. Thus, the onset of the Schottky anomaly shown at zero field heat capacity of [CeEr] can be associated to the splitting between the antiferromagnetic and the ferromagnetic configurations of both spins. Such anomaly, that appears at $T_{\max} < 0.35$ K, can be used to quantify the energy splitting of both configurations by using the relationship $k_B T_{\max} = 0.42\varepsilon$, which led to a value of $\varepsilon/k_B \approx 0.83$ K. From the equivalence $\varepsilon = 4J_{\text{ex}} m_{J_{\text{Ce}}} m_{J_{\text{Er}}}$ (where $m_{J_{\text{Ce}}}$ and $m_{J_{\text{Er}}}$ are considered $3/2$ and $11/2$, respectively), the magnetic coupling constant can be

calculated, $J_{ex}/k_B \approx -0.05$ K. On the other hand, the Hamiltonian in equation 49 was used to fit the magnetic heat capacity data (H_{Er} and H_{Ce} being the Hamiltonian of each isolated ion given by Equation 46). Numerical calculations produced a reasonably good fit (Figure V.45, solid blue line) with a value for the magnetic coupling of the same order ($J_{ex}/k_B \approx -0.1$ K).

$$H = H_{Er} + H_{Ce} - J_{ex}J_{Er}J_{Ce} \quad (49)$$

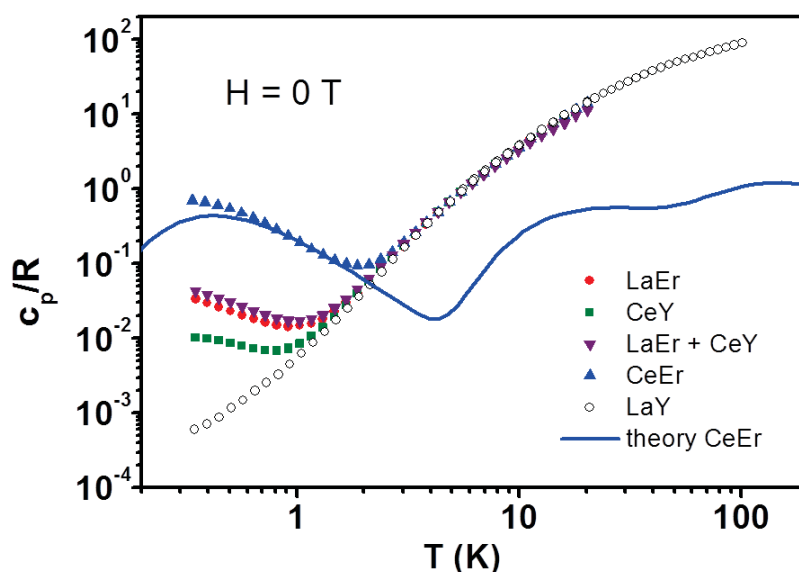


Figure V.45. Molar specific heat data measured, at zero field, on the [CeEr] (**40**) (blue triangles). The results are compared with the zero field heat capacity of [CeY] (green squares) and [LaEr] (red circles), as well as with the sum of both of them (purple triangles). Solid blue line is a theoretical calculation from the spin Hamiltonian of the coupled ions (see text).

In addition, EPR measurements were carried out on a powdered sample of [CeEr] (Figure V.46). The spectra has been compared with the measurements performed on [CeY] and [LaEr], showing that it cannot be decomposed into a weighed sum of the spectra recorded on each of these two compounds. This demonstrates that the magnetic coupling between Ce^{III} and Er^{III} determines the shape of the EPR spectra.

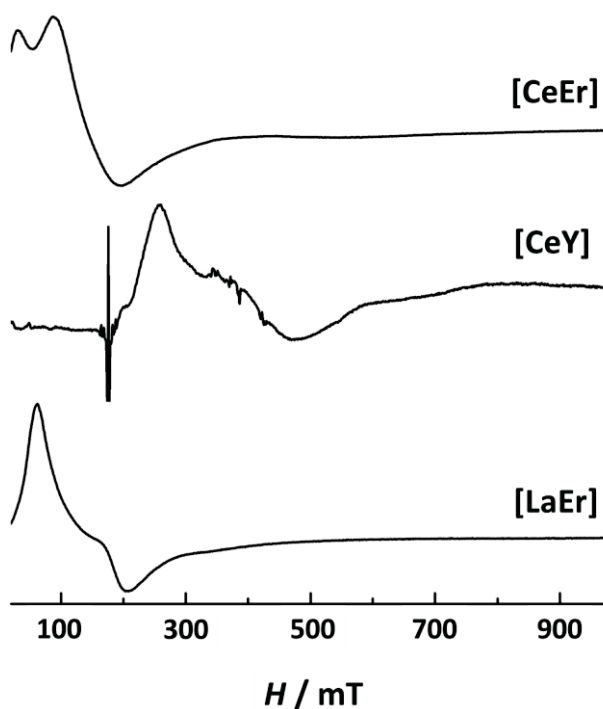


Figure V.46. EPR measured on powdered samples of [CeEr] (top), [CeY] (center) and [LaEr] (bottom)

All the measurements carried out for complexes [CeY], [LaEr] and [CeEr] have demonstrated that the latter fulfills all the requirements to be used as a 2-qubit quantum gate. The two Ce^{III} and Er^{III} qubits exhibit a two-level ground state at sufficient low temperatures, and are weakly interacting for their application in logical operations. This is illustrated by the structure of the magnetic energy levels of complex **40** [CeEr], calculated from the parameters obtained in magnetic susceptibility and heat capacity data (Figure V.47). The very different magnetic properties of Ce^{III} and Er^{III} ions lead to four levels unequally separated, which provides no degenerate transitions. Thus, these states can form the computational basis of this molecular quantum processor. Operations from such a processor might be performed by using the transitions between the different states, which can be induced by the application of radio-frequency magnetic field pulses. The energies shown in the scheme ensure that this quantum processor can operate at low fields and with relatively conventional technologies. The energy of an X-band (9.8 GHz) photon, for example, is approximately 0.5 K, and could be then used to selectively induce a desired transition.

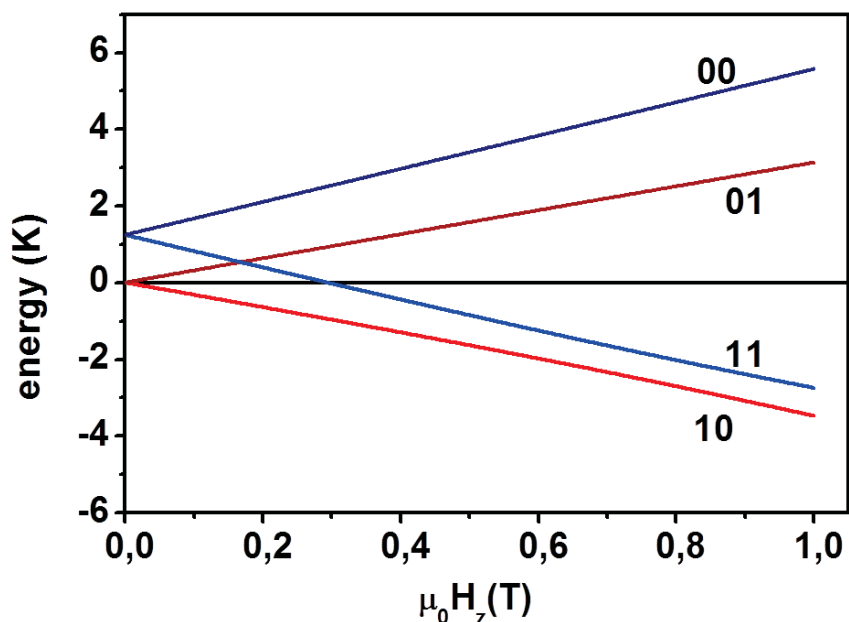


Figure V.47. Magnetic energy level scheme of the complex [CeEr] (**40**) for a magnetic field applied parallel to the easy axes z of both ions. Only the four lowest lying levels are shown.

Therefore, the antiferromagnetic (“10” and “01”) and ferromagnetic (“11” and “00”) states can be used to define the CNOT or the $\sqrt{\text{SWAP}}$ quantum logical operation. The resonant transition between “10” to “11” magnetic energy levels would correspond to the CNOT operation. On the other part, the $\sqrt{\text{SWAP}}$ gate would be performed if the resonant transition takes place from “10” to “01”.

The coherence of the [CeEr] complex as a molecular quantum processor was studied by X-band pulsed-EPR. Some preliminary experiments were carried out on a concentrated solution of the complex in a 1:1 mixture of methanol and ethanol. The pulsed-EPR spectrum is depicted in Figure V.48, showing the echo amplitude as a function of magnetic field for a constant time separation between pulses. The signal observed demonstrates that the radiation pulses generate some coherent spin dynamics, which ensures that the magnetic levels (“10”, “11”, “01” and “00”) are maintained during a determined time. To evaluate this time scale, T_2 has been identified by performing a Hahn echo sequence on the [CeEr] solution using a 16 ns $\pi/2$ pulse and a 32 ns π pulse (Figure V.48, inset). The measurement was carried out at $\mu_0 H_z = 0.47$ T, which approximately belongs to the transition from state “10” to “11”,

corresponding to the CNOT gate operation. T_2 has been calculated by fitting the decay with the exponential function (echo signal = $\exp(-2\tau/T_2)$), estimating a value of the order of 400 ns. The oscillations in the echo amplitude can be ascribed to the ESEEM effect, corresponding to the coupling of the electronic spins to the spin of the protons.

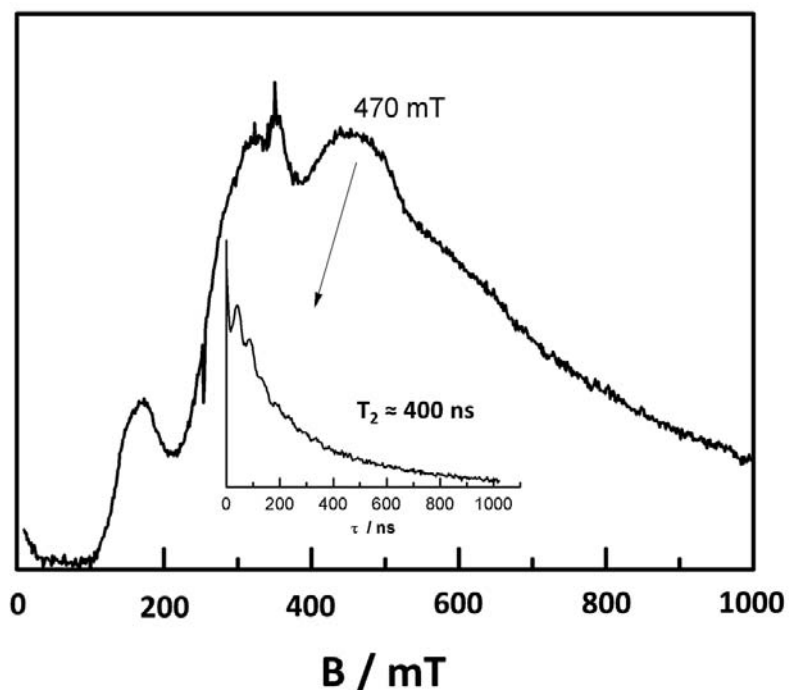


Figure V.48. Echo-detected absorption spectrum of a saturated solution of [CeEr] in a 1:1 mixture of methanol and ethanol (inset) Decay of the Hahn echo intensity in [CeEr] as function of delay time (16 ns $\pi/2$ pulse, 32 ns π pulse).

Bearing in mind that, to perform QC operations, the coherence of a system must be kept much longer than the gate time (τ_g), T_2 is still far from the desirable value to fulfill such requirement. The switching time of the electronic spin under experimental conditions is around 10 ns using a magnetic pulse of 10 Oe to an electronic spin $S = 1/2$ with g -factor $g = 2$.^[47] Thus, as an approximation, this value was used as τ_g to estimate the figure of merit, which in this system leads $Q = \tau_g/T_2 \approx 0.025$. For a fault-tolerant computation, Q must be $\tau_g/T_2 \leq 10^{-4}$, which demonstrates that T_2 is not long enough for a successful quantum information processing. However, the short coherence time observed should be further assessed by performing experiments in a diluted solution

of [CeEr], which could diminish the possible hyperfine interactions that may be influencing the measurement.

7. Experimental

[La₂(HL4)₂(H₂L4)(NO₃)(py)(H₂O)] (12). (*Method 1*) A yellow solution of H₃L4 (30.0 mg, 0.11 mmol) in pyridine (10 ml) was added into a colorless solution of La(NO₃)₃·6H₂O (30.3 mg, 0.07 mmol) in pyridine (10 ml). The mixture was stirred for 2 hours, and the resulting yellow solution was layered with Et₂O. After two weeks, the complex was obtained as yellow solid in 43 % yield. Anal Calcd (Found) for **12**·2.6py·4.8H₂O: C, 47.9 (47.31); H 3.67 (3.07), N 6.74 (7.32). ESI MS: $m/z = 1127.96$ [La₂(HL4)₂(H₂L4)]⁺. IR (KBr pellet, cm⁻¹): 3426 mb, 1618 s, 1583 s, 1558 m, 1527 s, 1462 m, 1400 s, 1384 s, 1322 m, 1298 m, 1240 w, 1205 w, 1148 w, 1120 w, 1058 w, 947 w, 889 w, 754 w, 705 w, 663 w, 633 w, 568 w.

(*Method 2*) A yellow solution of H₃L4 (30.0 mg, 0.11 mmol) in pyridine (10 ml) was added into a colourless solution of La(NO₃)₃·6H₂O (30.3 mg, 0.07 mmol) in pyridine (10 ml). The mixture was stirred for 30 minutes, when 270 µl of a colorless 0.13 M solution of HNO₃ in MeCN was added dropwise. The reaction was left stirring for 2 hours, and the resulting yellow solution was layered with Et₂O. After three weeks, small yellow crystals of **1** were collected in 40 % yield

[Ce₂(HL4)₂(H₂L4)(NO₃)(py)(H₂O)] (13). A yellow solution of H₃L4 (30.0 mg, 0.11 mmol) in pyridine (10 ml) was added into a colorless solution of Ce(NO₃)₃·6H₂O (30.4 mg, 0.07 mmol) in pyridine (10 ml). The mixture was stirred for 2 hours, and the resulting orange solution was layered with Et₂O. After two weeks, the complex was obtained as red crystals in 77 % yield. Anal Calcd (Found) for **13**·1.5py: C 49.02 (48.74), H 3.04 (3.28), N 6.46 (6.75). ESI MS: $m/z = 1130.98$ [Ce₂(HL4)₂(H₂L4)]⁺. IR (KBr pellet, cm⁻¹): 3417 mb, 1619 s, 1583 s, 1556 m, 1525 s, 1462 m, 1399 s, 1384 s, 1323 m, 1297 m, 1240 w, 1207 w, 1147 w, 1120 w, 1057 w, 947 w, 889 w, 756 w, 705 w, 663 w, 633 w, 567 w.

[Pr₂(HL4)₂(H₂L4)(NO₃)(py)(H₂O)] (14). The procedure is identical to the above one, with the use of Pr(NO₃)₃·6H₂O (30.5 mg, 0.07 mmol) in pyridine (10 ml) and layering the resulting yellow solution with Et₂O. The complex was obtained as yellow crystals after two weeks in 87 % yield. Anal Calcd (Found) for **14**·3.8py·1.2H₂O: C 51.40 (51.43), H 3.53 (3.53), N 7.65 (7.64). ESI MS: *m/z* = 1132.96 [Pr₂(HL4)₂(H₂L4)]⁺. IR (KBr pellet, cm⁻¹): 3407 mb, 1618 s, 1583 s, 1557 m, 1525 s, 1462 m, 1399 s, 1384 s, 1323 m, 1297 m, 1240 w, 1207 w, 1146 w, 1120 w, 1057 w, 947 w, 890 w, 754 w, 705 w, 663 w, 634 w, 567 w.

[Nd₂(HL4)₂(H₂L4)(NO₃)(py)(H₂O)] (15). The procedure is identical to the above one, with the use of Nd(NO₃)₃·6H₂O (30.7 mg, 0.07 mmol) in pyridine (10 ml) and layering the resulting yellow solution with toluene. The complex was obtained as yellow crystals after two weeks in 69 % yield. Anal Calcd (Found) for **15**·1.5H₂O: C 45.45 (45.76), H 2.90 (3.00), N 5.30 (5.44). ESI MS: *m/z* = 1133.99 [Nd₂(HL4)₂(H₂L4)]⁺. IR (KBr pellet, cm⁻¹): 3406 mb, 1619 s, 1584 s, 1558 m, 1526 s, 1462 m, 1384 s, 1324 m, 1297 m, 1239 w, 1208 w, 1147 w, 1121 w, 1058 w, 948 w, 891 w, 761 w, 706 w, 664 w, 634 w, 568 w.

[Sm₂(HL4)₂(H₂L4)(NO₃)(py)(H₂O)] (16). The procedure is identical to the above one, with the use of Sm(NO₃)₃·6H₂O (31.1 mg, 0.07 mmol) in pyridine (10 ml) and layering the resulting yellow solution with Et₂O. The complex was obtained as yellow crystals after two weeks in 81 % yield. Anal Calcd (Found) for **16**·0.5py·1.7H₂O: C 45.67 (45.67), H 2.99 (3.01), N 5.58 (5.60). ESI MS: *m/z* = 1153.97 [Sm₂(HL4)₂(H₂L4)]⁺. IR (KBr pellet, cm⁻¹): 3399 mb, 1619 s, 1584 s, 1559 m, 1526 s, 1462 m, 1399 s, 1384 s, 1324 m, 1297 m, 1240 w, 1207 w, 1146 w, 1121 w, 1057 w, 948 w, 890 w, 754 w, 706 w, 664 w, 635 w, 568 w.

[Eu₂(HL4)₂(H₂L4)(NO₃)(py)(H₂O)] (17). The procedure is identical to the above one, with the use of Eu(NO₃)₃·5H₂O (30.0 mg, 0.07 mmol) in pyridine (10 ml) and layering the resulting orange solution with Et₂O. The complex was obtained as yellow crystals after two weeks in 91 % yield. Anal Calcd (Found) for **17**·3.5py·H₂O: C 50.40 (50.07), H 3.41 (3.27), N 7.40 (7.75). ESI MS: *m/z* = 1155.99 [Eu₂(HL4)₂(H₂L4)]⁺. IR (KBr pellet, cm⁻¹): 3406 mb, 1619 s, 1585 s, 1559 m, 1526 s, 1464 m, 1396 s, 1384 s, 1324 m, 1298 m,

1239 w, 1209 w, 1147 w, 1121 w, 1058 w, 949 w, 891 w, 756 w, 707 w, 665 w, 636 w, 568 w.

[Gd₂(HL4)₂(H₂L4)(NO₃)(py)(H₂O)] (18). The procedure is identical to the above one, with the use of Gd(NO₃)₃·6H₂O (31.6 mg, 0.07 mmol) in pyridine (10 ml) and layering the resulting yellow solution with Et₂O. The complex was obtained as yellow crystals after two weeks in 90 % yield. Anal Calcd (Found) for **18**·1.9H₂O: C 44.20 (44.24), H 2.88 (2.99), N 5.15 (5.27). ESI MS: *m/z* = 1166.01 [Gd₂(HL4)₂(H₂L4)]⁺. IR (KBr pellet, cm⁻¹): 3398 mb, 1619 s, 1585 s, 1559 m, 1526 s, 1464 m, 1401 s, 1384 s, 1325 m, 1298 m, 1240 w, 1208 w, 1146 w, 1121 w, 1058 w, 949 w, 891 w, 756 w, 707 w, 665 w, 636 w, 568 w.

[Tb₂(HL4)₂(H₂L4)(NO₃)(py)(H₂O)] (19). The procedure is identical to the above one, with the use of Tb(NO₃)₃·5H₂O (30.5 mg, 0.07 mmol) in pyridine (10 ml) and layering the resulting yellow solution with Et₂O. The complex was obtained as yellow crystals after two weeks in 66 % yield. Anal Calcd (Found) for **19**·1.4py: C 47.60 (47.38), H 2.94 (3.11), N 6.23 (6.54). ESI MS: *m/z* = 1168.01 [Tb₂(HL4)₂(H₂L4)]⁺. IR (KBr pellet, cm⁻¹): 3392 mb, 1619 s, 1585 s, 1556 m, 1526 s, 1463 m, 1404 s, 1385 s, 1325 m, 1299 m, 1240 w, 1208 w, 1147 w, 1121 w, 1058 w, 951 w, 891 w, 756 w, 707 w, 665 w, 636 w, 569 w.

[Dy₂(HL4)₂(H₂L4)(NO₃)(py)(H₂O)] (20). The procedure is identical to the above one, with the use of Dy(NO₃)₃·6H₂O (32.0 mg, 0.07 mmol) in pyridine (10 ml) and layering the resulting orange solution with Et₂O. The complex was obtained as yellow crystals after two weeks in 71 % yield. Anal Calcd (Found) for **20**·1.5py·1.4H₂O: C 46.70 (46.72), H 3.09 (3.14), N 6.16 (6.19). ESI MS: *m/z* = 1178.01 [Dy₂(HL4)₂(H₂L4)]⁺. IR (KBr pellet, cm⁻¹): 3398 mb, 1619 s, 1585 s, 1560 m, 1526 s, 1464 m, 1401 s, 1384 s, 1325 m, 1298 m, 1240 w, 1208 w, 1147 w, 1121 w, 1058 w, 951 w, 891 w, 755 w, 707 w, 665 w, 636 w, 569 w.

[Ho₂(HL4)₂(H₂L4)(NO₃)(py)(H₂O)] (21). The procedure is identical to the above one, with the use of Ho(NO₃)₃·5H₂O (30.8 mg, 0.07 mmol) in pyridine (10 ml) and layering the resulting yellow solution with Et₂O. The complex was obtained as yellow crystals after two weeks in 75 % yield. Anal Calcd (Found) for **21**·0.6py·1.3H₂O: C 45.13 (44.99),

H 2.90 (3.08), N 5.56 (5.74). ESI MS: $m/z = 1180.02$ [$\text{Ho}_2(\text{HL4})_2(\text{H}_2\text{L4})$] $^+$. IR (KBr pellet, cm^{-1}): 3417 mb, 1619 s, 1586 s, 1560 m, 1527 s, 1464 m, 1402 s, 1384 s, 1325 m, 1299 m, 1240 w, 1208 w, 1147 w, 1121 w, 1059 w, 951 w, 892 w, 753 w, 707 w, 665 w, 637 w, 569 w.

[Er₂(HL4)₂(H₂L4)(NO₃)(py)(H₂O)] (22). The procedure is identical to the above one, with the use of Er(NO₃)₃·5H₂O (31.0 mg, 0.07 mmol) in pyridine (10 ml) and layering the resulting orange solution with toluene. The complex was obtained as yellow crystals after two weeks in 59 % yield. Anal Calcd (Found) for **22**·1.8py: C 47.66 (47.36), H 2.98 (3.21), N 6.41 (6.80). ESI MS: $m/z = 1184.03$ [$\text{Er}_2(\text{HL4})_2(\text{H}_2\text{L4})$] $^+$. IR (KBr pellet, cm^{-1}): 3416 mb, 1619 s, 1586 s, 1561 m, 1528 s, 1465 m, 1402 s, 1384 s, 1325 m, 1299 m, 1239 w, 1208 w, 1147 w, 1122 w, 1059 w, 951 w, 892 w, 757 w, 708 w, 665 w, 638 w, 569 w.

[Tm₂(HL4)₂(H₂L4)(NO₃)(py)(H₂O)] (23). The procedure is identical to the above one, with the use of Ho(NO₃)₃·5H₂O (31.2 mg, 0.07 mmol) in pyridine (10 ml) and layering the resulting yellow solution with Et₂O. The complex was obtained as yellow crystals after two weeks in 15 % yield. Anal Calcd (Found) for **23**·0.9py·7.2H₂O: C, 42.27 (41.78); H 3.51 (3.03); N 5.34 (5.85). ESI MS: $m/z = 1188.02$ [$\text{Tm}_2(\text{HL4})_2(\text{H}_2\text{L4})$] $^+$. IR (KBr pellet, cm^{-1}): 3401 mb, 1619 s, 1586 s, 1561 m, 1528 s, 1465 m, 1402 s, 1384 s, 1325 m, 1299 m, 1240 w, 1208 w, 1147 w, 1122 w, 1058 w, 952 w, 892 w, 754 w, 707 w, 665 w, 637 w, 569 w.

[Yb₂(HL4)₂(H₂L4)(NO₃)(py)(H₂O)] (24). (*Method 1*) A yellow solution of H₃L4 (30.0 mg, 0.11 mmol) in pyridine (10 ml) was added into a colorless solution of Yb(NO₃)₃·5H₂O (31.4 mg, 0.07 mmol) in pyridine (10 ml). The mixture was stirred for 2 hours, and the resulting orange solution was layered with Et₂O. After two weeks, the complex was obtained as yellow solid in 40 % yield. Anal Calcd (Found) for **24**·2.2py·9.3H₂O: C 43.16 (42.25); H 3.84 (2.94); N 5.94 (6.87). ESI MS: $m/z = 1198.04$ [$\text{Yb}_2(\text{HL4})_2(\text{H}_2\text{L4})$] $^+$. IR (KBr pellet, cm^{-1}): 3427 mb, 1619 s, 1587 s, 1561 m, 1528 s, 1466 m, 1401 s, 1384 s, 1327 m, 1301 m, 1239 w, 1204 w, 1147 w, 1119 w, 1058 w, 948 w, 893 w, 754 w, 708 w, 670 w, 639 w, 570 w. (*Method 2*) A yellow solution of H₃L4 (30.0 mg, 0.11 mmol) in pyridine (8 ml) was added into a colorless solution of Yb(NO₃)₃·5H₂O (31.1 mg, 0.07 mmol) in

pyridine (8 ml). After addition of 69% HNO₃ (6.81 μl, 0.11 mmol), the mixture was stirred for 1 h, and the resulting yellow solution was layered with hexane. After four weeks, small orange crystals of **24** were collected in 7 % yield.

[Lu₂(HL4)₂(H₂L4)(NO₃)(py)(H₂O)] (25). A yellow solution of H₃L4 (30.0 mg, 0.11 mmol) in pyridine (10 ml) was added into a colorless solution of Lu(NO₃)₃·H₂O (25.3 mg, 0.07 mmol) in pyridine (10 ml). The mixture was stirred for 2 hours, and the resulting orange solution was layered with Et₂O. After two weeks, the complex was obtained as orange solid in 23 % yield (10.9 mg). Anal Calcd (Found) for **25**·0.7py: C 45.41 (45.09), H 2.74 (2.94), N 5.64 (5.99). ESI MS: $m/z = 1200.04$ [Lu₂(HL4)₂(H₂L4)]⁺. IR (KBr pellet, cm⁻¹): 3419 mb, 1619 s, 1587 s, 1561 m, 1528 s, 1466 m, 1402 s, 1384 s, 1326 m, 1300 m, 1240 w, 1206 w, 1147 w, 1120 w, 1058 w, 950 w, 893 w, 754 w, 708 w, 668 w, 638 w, 569 w.

[Y₂(HL4)₂(H₂L4)(NO₃)(py)(H₂O)] (26). A yellow solution of H₃L4 (30.0 mg, 0.11 mmol) in pyridine (15 ml) was added into a colorless solution of Y(NO₃)₃·6H₂O (26.9 mg, 0.07 mmol) in pyridine (15 ml). The mixture was stirred under reflux for 2 hours, and then cooled down to room temperature. The resulting orange solution was layered with ether. After two weeks, the complex was obtained as orange crystals in 39 % yield. Anal Calcd (Found) for **26**·2.3py·4.5H₂O: C 50.92 (50.55); H 3.86 (3.47); N 7.05 (7.44). ESI MS: $m/z = 1027.96$ [Y₂(HL4)₂(H₂L4)]⁺. IR (KBr pellet, cm⁻¹): 3401 mb, 1619 s, 1586 s, 1561 m, 1528 s, 1465 m, 1402 s, 1384 s, 1325 m, 1299 m, 1240 w, 1208 w, 1147 w, 1122 w, 1058 w, 952 w, 892 w, 754 w, 707 w, 665 w, 637 w, 569 w.

[Nd₂(HL4)₂(H₂L4)Cl(py)(H₂O)] (27). A yellow solution of H₃L4 (30.0 mg, 0.11 mmol) in pyridine (10 ml) was added into a colorless solution of NdCl₃·6H₂O (30.4 mg, 0.07 mmol) in pyridine (10 ml). The mixture was stirred for 2 hours, and the resulting yellow solution was layered with Et₂O. After two weeks, the complex was obtained as yellow crystals. IR (KBr pellet, cm⁻¹): 3406 mb, 1619 s, 1584 s, 1558 m, 1525 s, 1462 m, 1399 s, 1323 m, 1297 m, 1239 w, 1208 w, 1147 w, 1120 w, 1057 w, 947 w, 890 w, 756 w, 706 w, 664 w, 634 w, 568 w.

[Gd₂(HL4)₂(H₂L4)Cl(py)(H₂O)] (28). The procedure is identical to the above one, with the use of GdCl₃·6H₂O (26.0 mg, 0.07 mmol) in pyridine (10 ml) and layering the

resulting orange solution with Et₂O. The complex was obtained as yellow crystals after one week in 87 % yield. Anal Calcd (Found) for **28**·H₂O·2,5py: C 49.60 (49.60), H 3.30 (3.27), N 6.02 (6.33). IR (KBr pellet, cm⁻¹): 3384 mb, 1619 s, 1585 s, 1559 m, 1526 s, 1464 m, 1401 s, 1324 m, 1298 m, 1239 w, 1209 w, 1147 w, 1121 w, 1058 w, 949 w, 892 w, 756 w, 707 w, 665 w, 636 w, 569 w.

[Tb₂(HL4)₂(H₂L4)Cl(py)₂] (29). The procedure is identical to the above one, with the use of TbCl₃·xH₂O (18.6 mg, 0.07 mmol) in pyridine (10 ml) and layering the resulting yellow solution with Et₂O. The complex was obtained as yellow crystals after one week in 72 % yield. Anal Calcd (Found) for **29**·2H₂O·1,5py: C 49.49 (49.33), H 3.29 (3.11), N 6.00 (6.13). IR (KBr pellet, cm⁻¹): 3402 mb, 1619 s, 1585 s, 1560 m, 1527 s, 1464 m, 1402 s, 1325 m, 1298 m, 1239 w, 1209 w, 1147 w, 1121 w, 1059 w, 950 w, 892 w, 760 w, 708 w, 665 w, 636 w, 569 w.

[Nd₂(HL4)₂(H₂L4)Cl(py)(H₂O)] (30). The procedure is identical to the above one, with the use of DyCl₃·6H₂O (26.4 mg, 0.07 mmol) in pyridine (10 ml) and layering the resulting orange solution with Et₂O. The complex was obtained as yellow crystals after one week. IR (KBr pellet, cm⁻¹): 3393 mb, 1618 s, 1585 s, 1560 m, 1526 s, 1464 m, 1401 s, 1325 m, 1298 m, 1239 w, 1208 w, 1147 w, 1121 w, 1058 w, 950 w, 891 w, 754 w, 707 w, 665 w, 636 w, 569 w.

[LaPr(HL4)₂(H₂L4)(NO₃)(py)(H₂O)] (31). A yellow solution of H₃L4 (30.0 mg, 0.105 mmol) in pyridine (10 ml) was added into a colourless solution of La(NO₃)₃·6H₂O (15.2 mg, 0.035 mmol) and Pr(NO₃)₃·6H₂O (15.2 mg, 0.035 mmol) in pyridine (10 ml). The mixture was stirred for 2 hours, and the resulting yellow solution was layered with Et₂O. After two weeks, the complex was obtained as yellow crystals.

[LaTb(HL4)₂(H₂L4)(NO₃)(py)(H₂O)] (32). The procedure is identical to the above one, with the use of La(NO₃)₃·6H₂O (15.2 mg, 0.035 mmol) and Tb(NO₃)₃·5H₂O (15.2 mg, 0.035 mmol) in pyridine (10 ml). The mixture was stirred for 2 hours, and the resulting yellow solution was layered with toluene. After two weeks, the complex was obtained as yellow crystals.

[LaDy(HL4)₂(H₂L4)(NO₃)(py)(H₂O)] (33). The procedure is identical to the above one, with the use of La(NO₃)₃·6H₂O (15.2 mg, 0.035 mmol) and Dy(NO₃)₃·xH₂O (12.2 mg, 0.035 mmol) in pyridine (10 ml). The mixture was stirred for 2 hours, and the resulting yellow solution was layered with Et₂O. After two weeks, the complex was obtained as yellow crystals.

[LaHo(HL4)₂(H₂L4)(NO₃)(py)(H₂O)] (34). The procedure is identical to the above one, with the use of La(NO₃)₃·6H₂O (15.2 mg, 0.035 mmol) and Ho(NO₃)₃·5H₂O (15.6 mg, 0.035 mmol) in pyridine (10 ml). The mixture was stirred for 2 hours, and the resulting yellow solution was layered with Et₂O. After two weeks, the complex was obtained as yellow crystals.

[LaEr(HL4)₂(H₂L4)(NO₃)(py)(H₂O)] (35). A yellow solution of H₃L4 (30.0 mg, 0.105 mmol) in pyridine (10 ml) was added into a colourless solution of La(NO₃)₃·6H₂O (15.2 mg, 0.035 mmol) and Er(NO₃)₃·5H₂O (15.5 mg, 0.035 mmol) in pyridine (10 ml). The mixture was stirred for 2 hours, and the resulting orange solution was layered with Et₂O. After two weeks, the complex was obtained as yellow crystals in 69 % yield. Anal Calcd (Found) for **35**·1.7H₂O·1.2py: C 46.66 (46.59), H 3.10 (2.98), N 6.02 (6.12). ESI MS: *m/z* = 1156.99 [LaEr(HL)₂(H₂L)]⁺. IR (KBr pellet, cm⁻¹): 3447 mb, 1617 s, 1584 s, 1559 m, 1533 s, 1464 m, 1399 s, 1384 s, 1323 m, 1298 m, 1239 w, 1198 w, 1148 w, 1120 w, 1060 w, 951 w, 890 w, 764 w, 706 w, 668 w, 635 w, 568 w.

[LaY(HL4)₂(H₂L4)(NO₃)(py)(H₂O)] (36). A yellow solution of H₃L4 (30.0 mg, 0.105 mmol) in pyridine (10 ml) was added into a colourless solution of La(NO₃)₃·6H₂O (15.2 mg, 0.035 mmol) and Y(NO₃)₃·6H₂O (13.4 mg, 0.035 mmol) in pyridine (10 ml). The mixture was stirred for 2 hours, and the resulting yellow solution was layered with Et₂O. After two weeks, the complex was obtained as yellow crystals in 40 % yield. Anal Calcd (Found) for **36**·3.9H₂O: C 45.92 (45.51), H 3.30 (2.87), N 5.35 (5.52). ESI MS: *m/z* = 1077.96 [LaY(HL)₂(H₂L)]⁺. IR (KBr pellet, cm⁻¹): 3445 mb, 1618 s, 1583 s, 1557 m, 1530 s, 1463 m, 1402 s, 1382 s, 1325 m, 1299 m, 1239 w, 1202 w, 1148 w, 1120 w, 1060 w, 951 w, 891 w, 762 w, 707 w, 664 w, 635 w, 569 w.

[CePr(HL4)₂(H₂L4)(NO₃)(py)(H₂O)] (37). A yellow solution of H₃L4 (30.0 mg, 0.105 mmol) in pyridine (10 ml) was added into a colourless solution of Ce(NO₃)₃·6H₂O (15.2

mg, 0.035 mmol) and $\text{Pr}(\text{NO}_3)_3 \cdot 6\text{H}_2\text{O}$ (15.2 mg, 0.035 mmol) in pyridine (10 ml). The mixture was stirred for 2 hours, and the resulting yellow solution was layered with toluene. After two weeks, the complex was obtained as orange crystals.

[CeDy(HL4)₂(H₂L4)(NO₃)(py)(H₂O)] (38). The procedure is identical to the above one, with the use of $\text{Ce}(\text{NO}_3)_3 \cdot 6\text{H}_2\text{O}$ (15.2 mg, 0.035 mmol) and $\text{Dy}(\text{NO}_3)_3 \cdot 5\text{H}_2\text{O}$ (15.4 mg, 0.035 mmol) in pyridine (10 ml) and layering the resulting orange solution with Et_2O . The complex was obtained as orange crystals after two weeks.

[CeHo(HL4)₂(H₂L4)(NO₃)(py)(H₂O)] (39). The procedure is identical to the above one, with the use of $\text{Ce}(\text{NO}_3)_3 \cdot 6\text{H}_2\text{O}$ (15.2 mg, 0.035 mmol) and $\text{Ho}(\text{NO}_3)_3 \cdot 5\text{H}_2\text{O}$ (15.4 mg, 0.035 mmol) in pyridine (10 ml) and layering the resulting orange solution with Et_2O . The complex was obtained as orange crystals after two weeks.

[CeEr(HL4)₂(H₂L4)(NO₃)(py)(H₂O)] (40). The procedure is identical to the above one, with the use of $\text{Ce}(\text{NO}_3)_3 \cdot 6\text{H}_2\text{O}$ (15.2 mg, 0.035 mmol) and $\text{Er}(\text{NO}_3)_3 \cdot 5\text{H}_2\text{O}$ (15.5 mg, 0.035 mmol) in pyridine (10 ml) and layering the resulting orange solution with Et_2O . After two weeks, the complex was obtained as orange crystals in 61 % yield. Anal Calcd (Found) for $\mathbf{40} \cdot 1.3\text{H}_2\text{O} \cdot 1.7\text{py}$: C 47.63 (47.58), H 3.15 (3.04), N 6.36 (6.46). ESI MS: $m/z = 1057.99$ $[\text{CeEr}(\text{HL4})_2(\text{H}_2\text{L4})]^+$. IR (KBr pellet, cm^{-1}): 3403 mb, 1618 s, 1584 s, 1558 m, 1528 s, 1463 m, 1401 s, 1384 s, 1324 m, 1299 m, 1240 w, 1201 w, 1147 w, 1120 w, 1060 w, 951 w, 890 w, 763 w, 706 w, 664 w, 635 w, 569 w.

[CeTm(HL4)₂(H₂L4)(NO₃)(py)(H₂O)] (41). The procedure is identical to the above one, with the use of $\text{Ce}(\text{NO}_3)_3 \cdot 6\text{H}_2\text{O}$ (15.2 mg, 0.035 mmol) and $\text{Tm}(\text{NO}_3)_3 \cdot 5\text{H}_2\text{O}$ (15.6 mg, 0.035 mmol) in pyridine (10 ml) and layering the resulting orange solution with Et_2O . After one week, the complex was obtained as orange crystals. IR (KBr pellet, cm^{-1}): 3397 mb, 1618 s, 1584 s, 1558 m, 1531 s, 1468 m, 1402 s, 1384 s, 1326 m, 1300 m, 1240 w, 1199 w, 1147 w, 1121 w, 1060 w, 951 w, 891 w, 764 w, 707 w, 664 w, 636 w, 569 w.

[CeLu(HL4)₂(H₂L4)(NO₃)(py)(H₂O)] (42). The procedure is identical to the above one, with the use of $\text{Ce}(\text{NO}_3)_3 \cdot 6\text{H}_2\text{O}$ (15.2 mg, 0.035 mmol) and $\text{Lu}(\text{NO}_3)_3 \cdot x\text{H}_2\text{O}$ (12.6 g, 0.035 mmol) in pyridine (10 ml) and layering the resulting orange solution with Et_2O . After

one week, the complex was obtained as orange crystals. IR (KBr pellet, cm^{-1}): 3419 mb, 1618 s, 1584 s, 1558 m, 1529 s, 1463 m, 1402 s, 1384 s, 1326 m, 1300 m, 1241 w, 1200 w, 1147 w, 1121 w, 1059 w, 952 w, 891 w, 762 w, 706 w, 664 w, 635 w, 569 w.

[CeY(HL4)₂(H₂L4)(NO₃)(py)(H₂O)] (43). The procedure is identical to the above one, with the use of Ce(NO₃)₃·6H₂O (15.2 mg, 0.035 mmol) and Y(NO₃)₃·6H₂O (13.4 mg, 0.035 mmol) in pyridine (10 ml) and layering the resulting orange solution with Et₂O. After two weeks, the complex was obtained as orange crystals in 70 % yield. Anal Calcd (Found) for **43**·1.8py: C 51.30 (51.13), H 3.21 (3.22), N 6.90 (7.09). ESI MS: m/z = 1078.97 [CeY(HL)₂(H₂L)]⁺. IR (KBr pellet, cm^{-1}): 3446 mb, 1617 s, 1584 s, 1559 m, 1533 s, 1464 m, 1399 s, 1384 s, 1323 m, 1298 m, 1239 w, 1200 w, 1147 w, 1120 w, 1060 w, 951 w, 891 w, 763 w, 706 w, 664 w, 635 w, 569 w.

[NdPr(HL4)₂(H₂L4)(NO₃)(py)(H₂O)] (44). A yellow solution of H₃L4 (30.0 mg, 0.105 mmol) in pyridine (10 ml) was added into a colourless solution of Nd(NO₃)₃·6H₂O (15.3 mg, 0.035 mmol) and Pr(NO₃)₃·6H₂O (15.2 mg, 0.035 mmol) in pyridine (10 ml). The mixture was stirred for 2 hours, and the resulting yellow solution was layered with Et₂O. After two weeks, the complex was obtained as yellow crystals.

[PrSm(HL4)₂(H₂L4)(NO₃)(py)(H₂O)] (45). The procedure is identical to the above one, with the use of Pr(NO₃)₃·6H₂O (15.2 mg, 0.035 mmol) and Sm(NO₃)₃·6H₂O (15.6 mg, 0.035 mmol) in pyridine (10 ml) and layering the resulting yellow solution with Et₂O. The complex was obtained as yellow crystals after one week.

[PrEu(HL4)₂(H₂L4)(NO₃)(py)(H₂O)] (46). The procedure is identical to the above one, with the use of Pr(NO₃)₃·6H₂O (15.2 mg, 0.035 mmol) and Eu(NO₃)₃·5H₂O (15.0 mg, 0.035 mmol) in pyridine (10 ml) and layering the resulting orange solution with toluene. The complex was obtained as yellow crystals after one week.

[PrGd(HL4)₂(H₂L4)(NO₃)(py)(H₂O)] (47). The procedure is identical to the above one, with the use of Pr(NO₃)₃·6H₂O (15.2 mg, 0.035 mmol) and Gd(NO₃)₃·6H₂O (15.8 mg, 0.035 mmol) in pyridine (10 ml) and layering the resulting yellow solution with Et₂O. The complex was obtained as yellow crystals after one week.

[PrTb(HL4)₂(H₂L4)(NO₃)(py)(H₂O)] (48). The procedure is identical to the above one, with the use of Pr(NO₃)₃·6H₂O (15.2 mg, 0.035 mmol) and Tb(NO₃)₃·5H₂O (15.2 mg, 0.035 mmol) in pyridine (10 ml) and layering the resulting yellow solution with Et₂O. The complex was obtained as yellow crystals after one week.

[PrDy(HL4)₂(H₂L4)(NO₃)(py)(H₂O)] (49). The procedure is identical to the above one, with the use of Pr(NO₃)₃·6H₂O (15.2 mg, 0.035 mmol) and Dy(NO₃)₃·5H₂O (15.4 mg, 0.035 mmol) in pyridine (10 ml) and layering the resulting yellow solution with Et₂O. The complex was obtained as yellow crystals after one week.

[PrHo(HL4)₂(H₂L4)(NO₃)(py)(H₂O)] (50). The procedure is identical to the above one, with the use of Pr(NO₃)₃·6H₂O (15.2 mg, 0.035 mmol) and Ho(NO₃)₃·5H₂O (15.4 mg, 0.035 mmol) in pyridine (10 ml) and layering the resulting yellow solution with Et₂O. The complex was obtained as yellow crystals after one week.

[PrEr(HL4)₂(H₂L4)(NO₃)(py)(H₂O)] (51). The procedure is identical to the above one, with the use of Pr(NO₃)₃·6H₂O (15.2 mg, 0.035 mmol) and Er(NO₃)₃·5H₂O (15.5 mg, 0.035 mmol) in pyridine (10 ml) and layering the resulting orange solution with Et₂O. The complex was obtained as yellow crystals after one week.

[PrTm(HL4)₂(H₂L4)(NO₃)(py)(H₂O)] (52). The procedure is identical to the above one, with the use of Pr(NO₃)₃·6H₂O (15.2 mg, 0.035 mmol) and Tm(NO₃)₃·5H₂O (15.6 mg, 0.035 mmol) in pyridine (10 ml) and layering the resulting yellow solution with Et₂O. The complex was obtained as yellow crystals after one week.

[PrYb(HL4)₂(H₂L4)(NO₃)(py)(H₂O)] (53). The procedure is identical to the above one, with the use of Pr(NO₃)₃·6H₂O (15.2 mg, 0.035 mmol) and Yb(NO₃)₃·5H₂O (15.7 mg, 0.035 mmol) in pyridine (10 ml) and layering the resulting orange solution with Et₂O. The complex was obtained as yellow crystals after one week.

[PrLu(HL4)₂(H₂L4)(NO₃)(py)(H₂O)] (54). The procedure is identical to the above one, with the use of Pr(NO₃)₃·6H₂O (15.2 mg, 0.035 mmol) and Lu(NO₃)₃·H₂O (12.6 mg, 0.035 mmol) in pyridine (10 ml) and layering the resulting orange solution with Et₂O. The complex was obtained as yellow crystals after one week.

[PrY(HL4)₂(H₂L4)(NO₃)(py)(H₂O)] (55). The procedure is identical to the above one, with the use of Pr(NO₃)₃·6H₂O (15.2 mg, 0.035 mmol) and Y(NO₃)₃·5H₂O (13.4 mg, 0.035 mmol) in pyridine (10 ml) and layering the resulting orange solution with Et₂O. The complex was obtained as yellow crystals after one week. IR (KBr pellet, cm⁻¹): 3397 mb, 1618 s, 1584 s, 1559 m, 1528 s, 1464 m, 1402 s, 1384 s, 1325 m, 1299 m, 1239 w, 1205 w, 1147 w, 1121 w, 1059 w, 951 w, 891 w, 757 w, 707 w, 664 w, 635 w, 569 w.

[NdSm(HL4)₂(H₂L4)(NO₃)(py)(H₂O)] (56). A yellow solution of H₃L4 (30.0 mg, 0.105 mmol) in pyridine (10 ml) was added into a colourless solution of Nd(NO₃)₃·6H₂O (15.3 mg, 0.035 mmol) and Sm(NO₃)₃·6H₂O (15.6 mg, 0.035 mmol) in pyridine (10 ml). The mixture was stirred for 2 hours, and the resulting orange solution was layered with toluene. After two weeks, the complex was obtained as yellow crystals. IR (KBr pellet, cm⁻¹): 3397 mb, 1618 s, 1584 s, 1558 m, 1526 s, 1462 m, 1399 s, 1384 s, 1323 m, 1297 m, 1239 w, 1207 w, 1147 w, 1121 w, 1058 w, 948 w, 890 w, 754 w, 706 w, 664 w, 635 w, 568 w.

[NdGd(HL4)₂(H₂L4)(NO₃)(py)(H₂O)] (57). The procedure is identical to the above one, with the use of Nd(NO₃)₃·6H₂O (15.3 mg, 0.035 mmol) and Gd(NO₃)₃·6H₂O (15.8 mg, 0.035 mmol) in pyridine (10 ml) and layering the resulting orange solution with Et₂O. The complex was obtained as yellow crystals after one week. IR (KBr pellet, cm⁻¹): 3397 mb, 1618 s, 1584 s, 1559 m, 1527 s, 1463 m, 1400 s, 1384 s, 1324 m, 1298 m, 1240 w, 1207 w, 1147 w, 1121 w, 1058 w, 949 w, 891 w, 754 w, 706 w, 664 w, 635 w, 568 w.

[NdTb(HL4)₂(H₂L4)(NO₃)(py)(H₂O)] (58). The procedure is identical to the above one, with the use of Nd(NO₃)₃·6H₂O (15.3 mg, 0.035 mmol) and Tb(NO₃)₃·5H₂O (15.2 mg, 0.035 mmol) in pyridine (10 ml) and layering the resulting orange solution with toluene. The complex was obtained as yellow crystals after one week. IR (KBr pellet, cm⁻¹): 3398 mb, 1618 s, 1584 s, 1559 m, 1527 s, 1463 m, 1400 s, 1384 s, 1324 m, 1298 m, 1239 w, 1207 w, 1147 w, 1120 w, 1058 w, 949 w, 891 w, 754 w, 707 w, 664 w, 635 w, 568 w.

[NdTm(HL4)₂(H₂L4)(NO₃)(py)(H₂O)] (59). The procedure is identical to the above one, with the use of Nd(NO₃)₃·6H₂O (15.3 mg, 0.035 mmol) and Tm(NO₃)₃·5H₂O (15.6 mg,

0.035 mmol) in pyridine (10 ml) and layering the resulting orange solution with Et₂O. The complex was obtained as yellow crystals after one week.

[NdYb(HL4)₂(H₂L4)(NO₃)(py)(H₂O)] (60). The procedure is identical to the above one, with the use of Nd(NO₃)₃·6H₂O (15.3 mg, 0.035 mmol) and Yb(NO₃)₃·5H₂O (15.7 mg, 0.035 mmol) in pyridine (10 ml) and layering the resulting orange solution with Et₂O. The complex was obtained as yellow crystals after one week.

[NdLu(HL4)₂(H₂L4)(NO₃)(py)(H₂O)] (61). The procedure is identical to the above one, with the use of Nd(NO₃)₃·6H₂O (15.3 mg, 0.035 mmol) and Lu(NO₃)₃·H₂O (12.6 mg, 0.035 mmol) in pyridine (10 ml) and layering the resulting orange solution with Et₂O. The complex was obtained as yellow crystals after one week.

[NdY(HL4)₂(H₂L4)(NO₃)(py)(H₂O)] (62). The procedure is identical to the above one, with the use of Nd(NO₃)₃·6H₂O (15.3 mg, 0.035 mmol) and Y(NO₃)₃·6H₂O (13.4 mg, 0.035 mmol) in pyridine (10 ml) and layering the resulting orange solution with Et₂O. The complex was obtained as yellow crystals after one week.

[SmGd(HL4)₂(H₂L4)(NO₃)(py)(H₂O)] (63). A yellow solution of H₃L4 (30.0 mg, 0.105 mmol) in pyridine (10 ml) was added into a colourless solution of Gd(NO₃)₃·6H₂O (15.8 mg, 0.035 mmol) and Sm(NO₃)₃·6H₂O (15.6 mg, 0.035 mmol) in pyridine (10 ml). The mixture was stirred for 2 hours, and the resulting orange solution was layered with toluene. After two weeks, the complex was obtained as yellow crystals.

[SmTb(HL4)₂(H₂L4)(NO₃)(py)(H₂O)] (64). The procedure is identical to the above one, with the use of Sm(NO₃)₃·6H₂O (15.6 mg, 0.035 mmol) and Tb(NO₃)₃·5H₂O (15.2 mg, 0.035 mmol) in pyridine (10 ml) and layering the resulting orange solution with Et₂O. The complex was obtained as yellow crystals after one week.

[EuTb(HL4)₂(H₂L4)(NO₃)(py)(H₂O)] (65). A yellow solution of H₃L4 (30.0 mg, 0.105 mmol) in pyridine (10 ml) was added into a colourless solution of Eu(NO₃)₃·5H₂O (15.0 mg, 0.035 mmol) and Tb(NO₃)₃·5H₂O (15.2 mg, 0.035 mmol) in pyridine (10 ml). The mixture was stirred for 2 hours, and the resulting orange solution was layered with Et₂O. After two weeks, the complex was obtained as yellow crystals. IR (KBr pellet, cm⁻¹): 3393 mb, 1619 s, 1585 s, 1560 m, 1527 s, 1464 m, 1400 s, 1384 s, 1325 m, 1298 m,

1239 w, 1208 w, 1147 w, 1121 w, 1058 w, 950 w, 891 w, 755 w, 707 w, 665 w, 636 w, 568 w.

[EuYb(HL4)₂(H₂L4)(NO₃)(py)(H₂O)] (66). The procedure is identical to the above one, with the use of Eu(NO₃)₃·5H₂O (15.0 mg, 0.035 mmol) and Yb(NO₃)₃·5H₂O (15.7 mg, 0.035 mmol) in pyridine (10 ml) and layering the resulting orange solution with Et₂O. The complex was obtained as orange crystals after two weeks. IR (KBr pellet, cm⁻¹): 1619 s, 1585 s, 1558 m, 1527 s, 1464 m, 1401 s, 1384 s, 1326 m, 1299 m, 1240 w, 1206 w, 1147 w, 1121 w, 1058 w, 950 w, 891 w, 761 w, 708 w, 664 w, 636 w, 569 w.

[EuLu(HL4)₂(H₂L4)(NO₃)(py)(H₂O)] (67). The procedure is identical to the above one, with the use of Eu(NO₃)₃·5H₂O (15.0 mg, 0.035 mmol) and Lu(NO₃)₃·xH₂O (12.6 mg, 0.035 mmol) in pyridine (10 ml) and layering the resulting yellow solution with Et₂O. The complex was obtained as yellow crystals after two weeks.

[EuY(HL4)₂(H₂L4)(NO₃)(py)(H₂O)] (68). The procedure is identical to the above one, with the use of Eu(NO₃)₃·5H₂O (15.0 mg, 0.035 mmol) and Y(NO₃)₃·H₂O (13.4 mg, 0.035 mmol) in pyridine (10 ml) and layering the resulting orange solution with Et₂O. The complex was obtained as yellow crystals after two weeks. IR (KBr pellet, cm⁻¹): 1619 s, 1585 s, 1558 m, 1527 s, 1464 m, 1401 s, 1384 s, 1325 m, 1298 m, 1240 w, 1209 w, 1147 w, 1121 w, 1058 w, 950 w, 891 w, 755 w, 707 w, 665 w, 636 w, 569 w.

[TbHo(HL4)₂(H₂L4)(NO₃)(py)(H₂O)] (69). A yellow solution of H₃L4 (30.0 mg, 0.105 mmol) in pyridine (10 ml) was added into a colourless solution of Tb(NO₃)₃·5H₂O (15.2 mg, 0.035 mmol) and Ho(NO₃)₃·5H₂O (15.4 mg, 0.035 mmol) in pyridine (10 ml). The mixture was stirred for 2 hours, and the resulting yellow solution was layered with toluene. After two weeks, the complex was obtained as yellow crystals. IR (KBr pellet, cm⁻¹): 3400 mb, 1619 s, 1586 s, 1558 m, 1528 s, 1464 m, 1401 s, 1384 s, 1325 m, 1298 m, 1240 w, 1208 w, 1147 w, 1121 w, 1058 w, 951 w, 891 w, 761 w, 707 w, 664 w, 636 w, 569 w.

[TbLu(HL4)₂(H₂L4)(NO₃)(py)(H₂O)] (70). The procedure is identical to the above one, with the use of Tb(NO₃)₃·5H₂O (15.2 mg, 0.035 mmol) and Lu(NO₃)₃·xH₂O (12.6 mg,

0.035 mmol) in pyridine (10 ml) and layering the resulting yellow solution with Et₂O. The complex was obtained as yellow crystals after one week.

[DyLu(HL4)₂(H₂L4)(NO₃)(py)(H₂O)] (71). A yellow solution of H₃L4 (30.0 mg, 0.105 mmol) in pyridine (10 ml) was added into a colourless solution of Dy(NO₃)₃·5H₂O (15.4 mg, 0.035 mmol) and Lu(NO₃)₃·xH₂O (12.6 mg, 0.035 mmol) in pyridine (10 ml). The mixture was stirred for 2 hours, and the resulting orange solution was layered with Et₂O. After two weeks, the complex was obtained as yellow crystals. IR (KBr pellet, cm⁻¹): 3417 mb, 1619 s, 1585 s, 1558 m, 1528 s, 1467 m, 1402 s, 1384 s, 1326 m, 1299 m, 1240 w, 1209 w, 1147 w, 1122 w, 1059 w, 951 w, 754 w, 708 w, 666 w, 637 w, 569 w.

[HoTm(HL4)₂(H₂L4)(NO₃)(py)(H₂O)] (72). A yellow solution of H₃L4 (30.0 mg, 0.105 mmol) in pyridine (10 ml) was added into a colourless solution of Ho(NO₃)₃·5H₂O (15.4 mg, 0.035 mmol) and Tm(NO₃)₃·5H₂O (15.6 mg, 0.035 mmol) in pyridine (10 ml). The mixture was stirred for 2 hours, and the resulting orange solution was layered with Et₂O. After two weeks, the complex was obtained as orange crystals. IR (KBr pellet, cm⁻¹): 3397 mb, 1619 s, 1585 s, 1561 m, 1529 s, 1465 m, 1402 s, 1384 s, 1325 m, 1298 m, 1240 w, 1208 w, 1147 w, 1122 w, 1059 w, 951 w, 891 w, 754 w, 707 w, 666 w, 637 w, 569 w.

[CeY(HL4)₂(H₂L4)(NO₃)(py)(H₂O)]_{0.7}[Y₂(HL4)₂(H₂L4)(NO₃)(py)(H₂O)]_{0.3} (73). A yellow solution of H₃L4 (30.0 mg, 0.105 mmol) in pyridine (10 ml) was added into a colourless solution of Ce(NO₃)₃·6H₂O (7.6 mg, 0.018 mmol) and Y(NO₃)₃·6H₂O (20.1 mg, 0.053 mmol) in pyridine (10 ml). The mixture was stirred for 2 hours, and the resulting orange solution was layered with Et₂O. After two weeks, orange crystals of **75** were obtained in 41 % yield. Anal Calcd (Found) for **75**·0.5H₂O·1.3py: C 50.81 (50.68), H 3.21 (3.33), N 6.61 (6.99). ESI MS: *m/z* = 1078.95 [CeY(HL4)₂(H₂L4)]⁺ and 1027.95 [Y₂(HL4)₂(H₂L4)]⁺. IR (KBr pellet, cm⁻¹): 3400 mb, 1618 s, 1584 s, 1558 m, 1529 s, 1464 m, 1404 s, 1384 s, 1325 m, 1299 m, 1240 w, 1206 w, 1148 w, 1121 w, 1059 w, 951 w, 891 w, 755 w, 707 w, 665 w, 636 w, 569 w.

- [1] S. Bertaina, S. Gambarelli, A. Tkachuk, I. N. Kurkin, B. Malkin, A. Stepanov, B. Barbara, *Nat Nano* **2007**, *2*, 39.
- [2] J. J. Baldoví, S. Cardona-Serra, J. M. Clemente-Juan, E. Coronado, A. Gaita-Ariño, A. Palií, *Inorganic Chemistry* **2012**, *51*, 12565
- [3] A. Palií, B. Tsukerblat, J. M. Clemente-Juan, A. Gaita-Ariño, E. Coronado, *Physical Review B* **2011**, *84*, 184426.
- [4] F. Luis, O. Roubeau, G. Aromí, *Artificial Molecular Nanomagnets as Spin-Based Quantum Logic Gates*, in *Architecture and Design of Molecule Logic Gates and Atom Circuits*, (Eds.: N. Lorente, C. Joachim), Springer Berlin Heidelberg, Berlin, **2013**
- [5] A. Ardavan, S. J. Blundell, *Journal of Materials Chemistry* **2009**, *19*, 1754.
- [6] A. Chatterjee, E. N. Maslen, K. J. Watson, *Acta Crystallographica Section B* **1988**, *44*, 381.
- [7] D. Parker, H. Puschmann, A. S. Batsanov, K. Senanayake, *Inorganic Chemistry* **2003**, *42*, 8646.
- [8] R. E. Gerkin, W. J. Reppart, in *Acta Crystallographica Section C* **1984**, *40*, 781.
- [9] K. Matsumoto, K. Suzuki, T. Tsukuda, T. Tsubomura, *Inorganic Chemistry* **2010**, *49*, 4717.
- [10] M. Seitz, A. G. Oliver, K. N. Raymond, *Journal of the American Chemical Society* **2007**, *129*, 11153.
- [11] S. A. Cotton, V. Franckevicius, M. F. Mahon, L. L. Ooi, P. R. Raithby, S. J. Teat, *Polyhedron* **2006**, *25*, 1057.
- [12] J. Cepeda, R. Balda, G. Beobide, O. Castillo, J. Fernández, A. Luque, S. Pérez-Yáñez, P. Román, D. Vallejo-Sánchez, *Inorganic Chemistry* **2011**, *50*, 8437.
- [13] L. Pan, X. Huang, J. Li, Y. Wu, N. Zheng, *Angewandte Chemie International Edition* **2000**, *39*, 527.
- [14] Z. He, E.-Q. Gao, Z.-M. Wang, C.-H. Yan, M. Kurmoo, *Inorganic Chemistry* **2005**, *44*, 862.
- [15] P. D'Angelo, A. Zitolo, V. Migliorati, G. Chillemi, M. Duvail, P. Vitorge, S. Abadie, R. Spezia, *Inorganic Chemistry* **2011**, *50*, 4572.
- [16] M. Estrader, J. Ribas, V. Tangoulis, X. Solans, M. Font-Bardía, M. Maestro, C. Diaz, *Inorganic Chemistry* **2006**, *45*, 8239.
- [17] E. A. Quadrelli, *Inorganic Chemistry* **2002**, *41*, 167.
- [18] J. C. Slater, *Physical Review* **1930**, *36*, 57.
- [19] E. Clementi, D. L. Raimondi, *The Journal of Chemical Physics* **1963**, *38*, 2686.
- [20] E. Clementi, D. L. Raimondi, W. P. Reinhardt, *The Journal of Chemical Physics* **1967**, *47*, 1300.
- [21] A. Ruiz-Martínez, D. Casanova, S. Alvarez, *Chemistry – A European Journal* **2008**, *14*, 1291.
- [22] A. Ruiz-Martínez, S. Alvarez, *Chemistry – A European Journal* **2009**, *15*, 7470.
- [23] C. Piguet, J.-C. G. Bünzli, G. r. Bernardinelli, G. r. Hopfgartner, S. p. Petoud, O. Schaad, *Journal of the American Chemical Society* **1996**, *118*, 6681.
- [24] A. Panagiotopoulos, T. F. Zafiropoulos, S. P. Perlepes, E. Bakalbassis, I. Masson-Ramade, O. Kahn, A. Terzis, C. P. Raptopoulou, *Inorganic Chemistry* **1995**, *34*, 4918.
- [25] L. E. Roy, T. Hughbanks, *Journal of the American Chemical Society* **2005**, *128*, 568.
- [26] G. H. Dieke, *Spectra and Energy Levels of Rare Earth Ions in Crystals*, John Wiley & Sons, USA, **1968**.
- [27] K. Kuriki, Y. Koike, Y. Okamoto, *Chemical Reviews* **2002**, *102*, 2347.
- [28] Y. Hasegawa, Y. Wada, S. Yanagida, H. Kawai, N. Yasuda, T. Nagamura, *Applied Physics Letters* **2003**, *83*, 3599.
- [29] A. de Bettencourt-Dias, *Dalton Transactions* **2007**, 2229.
- [30] B. S. Richards, *Solar Energy Materials and Solar Cells* **2006**, *90*, 1189.
- [31] Y. Luo, B. Chen, W. Wu, X. Yu, Q. Yan, Q. Zhang, *Journal of Luminescence* **2009**, *129*, 1309.

- [32] A. P. Bassett, S. W. Magennis, P. B. Glover, D. J. Lewis, N. Spencer, S. Parsons, R. M. Williams, L. De Cola, Z. Pikramenou, *Journal of the American Chemical Society* **2004**, *126*, 9413.
- [33] N. M. Shavaleev, G. Accorsi, D. Virgili, Z. R. Bell, T. Lazarides, G. Calogero, N. Armaroli, M. D. Ward, *Inorganic Chemistry* **2005**, *44*, 61.
- [34] N. M. Shavaleev, R. Scopelliti, F. Gummy, J.-C. G. Bünzli, *Inorganic Chemistry* **2009**, *48*, 2908.
- [35] K. Binnemans, J.-C. G. Bünzli, V. K. Pecharsky, K. A. Gschneidner, *Rear-Earth beta-diketonates*, in *Handbook on the Physics and Chemistry of Rare Earths* (Eds.: J.-C. G. Bünzli, V. K. Pecharsky), Elsevier, **2005**, *35*, 107.
- [36] A. Abraham, B. Bleaney, *Electron paramagnetic resonance of transition ions*, Oxford Clarendon Press, Oxford, **1970**.
- [37] J. Lehmann, A. Gaita-Ariño, E. Coronado, D. Loss, *Nat Nano* **2007**, *2*, 312.
- [38] N. André, T. B. Jensen, R. Scopelliti, D. Imbert, M. Elhabiri, G. Hopfgartner, C. Piguet, J.-C. G. Bünzli, *Inorganic Chemistry* **2004**, *43*, 515.
- [39] J. P. Costes, F. Dahan, A. Dupuis, S. Lagrave, J. P. Laurent, *Inorganic Chemistry* **1998**, *37*, 153.
- [40] D. Chabach, A. De Cian, J. Fischer, R. Weiss, M. E. M. Bibout, *Angewandte Chemie International Edition in English* **1996**, *35*, 898.
- [41] N. André, R. Scopelliti, G. Hopfgartner, C. Piguet, J.-C. G. Bünzli, *Chemical Communications* **2002**, 214.
- [42] T. B. Jensen, R. Scopelliti, J.-C. G. Bünzli, *Inorganic Chemistry* **2006**, *45*, 7806.
- [43] P. Zhu, N. Pan, R. Li, J. Dou, Y. Zhang, D. Y. Y. Cheng, D. Wang, D. K. P. Ng, J. Jiang, *Chemistry – A European Journal* **2005**, *11*, 1425.
- [44] P. Guerriero, P. A. Vigato, J.-C. G. Bünzli, E. Moret, *Journal of the Chemical Society, Dalton Transactions* **1990**, 647.
- [45] N. Ishikawa, T. Iino, Y. Kaizu, *Journal of the American Chemical Society* **2002**, *124*, 11440.
- [46] R. D. Shannon, *Acta Crystallographica Section A* **1976**, *32*, 751.
- [47] M. Affronte, *Journal of Materials Chemistry* **2009**, *19*, 1731.

CHAPTER VI

CONCLUSIONS AND FUTURE PERSPECTIVES

The results obtained along this thesis demonstrate the potential of coordination chemistry for the design of molecules able to carry out qubits and embody quantum gates. Three different approaches proposed for such goal have been assessed using synthetic strategies based on different β -diketone ligands. The study of the physical properties of the resulting molecular systems has been pursued to demonstrate their potential in quantum computation.

H₄L1 has been designed to achieve the assembly of transition metal ions in a linear topology featuring two separated and weakly coupled groups of metals. The possibility of exploiting this topology to wrap metals into helicoidal structures has been also explored. The structural characteristics of three dinuclear helicates have been assessed (complexes **1-3**, Chapter III). One may think about the possibility of using these helicoidal motifs as an electron spin-qubit version of a Lloyd model, as proposed by Takui and coworkers (see Chapter I). This approach is based on the non-equivalent g -tensors of the metals, which arise from the twisted helical structure within a crystal lattice. However, the low twist angle values observed in the three different structures demonstrate the low flexibility of the ligand, thus diminishing the possibilities of using the open-shell metals of such complexes as electron-spin qubits.

On the other hand, the first approach proposed here has been carried out satisfactorily in this thesis, since H₄L1 has demonstrated the ability of encapsulating two separate groups of paramagnetic metals into the same molecular system. The topology of the ligand, as well as the different acidity of its ionisable protons, allows the control of the topology and the nuclearity of such systems. Three tetranuclear homometallic examples with Ni^{II}, Co^{II} and Cu^{II} (complexes **4**, **5** and **6**, respectively, Chapter IV) have been isolated and studied, exhibiting the expected [MM \cdots MM] topology. However, the strong antiferromagnetic coupling observed within each [M₂] pair overrides any possible interaction between the central metal ions. In addition, each metal pair loses its potential as a qubit prototype due to the vanishing of their spin momenta. This drawback could be solved by exploiting the structural features of the system for the design of heterometallic [MM' \cdots M'M] complexes. The geometric features of the ligand induce a difference in coordination environment between neighboring metals of the system (octahedral coordination for the inner ions and a five-coordination for the

centers at the ends). This site-dependent coordination number has been therefore used to synthesize heterometallic clusters with predetermined topology and a site-selective control on the location of the metals within the array (complexes **7** and **8**, Chapter IV). DFT calculations and magnetic susceptibility measurements have confirmed the desired [CuNi...NiCu] topology of complex **7**. This study has demonstrated that this molecular system fulfills some of the conditions required to embody two qubits and thus to behave as a 2-qubit quantum gate. Each [NiCu] pair has a ground state of $S = 1/2$, which represents a real two level system. In addition, the possible weak interaction between the two pairs of the system would enable the study of a possible quantum entanglement between their respective spin wave functions. Nonetheless, the symmetry of the molecule wouldn't allow the discrimination of the two qubits, thus precluding the possibility of addressing them individually. This represents a considerable disadvantage for the application of such molecular systems as a logic CNOT quantum gate. For its application as a $\sqrt{\text{SWAP}}$ gate, the switch of the interaction between both pairs of the system should be feasible. As a future perspective, the modification of the central part of the ligand by a photoswitchable moiety could be explored. The versatility in the design of β -diketone ligands allows the addition of different functional groups. In that respect, replacing the benzene group of H₄L1 by a dithienylcyclopentene moiety, for example, may allow the desired switchable interaction due to the photochromism of the latter. Likewise, the possibility of accessing other heterometallic compounds with predetermined topology using H₄L1 can be further investigated.

The second approach for the design of molecular 2-qubit QGs is based on the preparation of poly- β -diketones for the aggregation of linear arrays of metal ions, to be then linked as molecular pairs by auxiliary ligands. H₄L2 and H₂L3 have been designed for the former purpose, with the aim of preparing heterometallic Ln/M linear clusters. However, all different attempts to synthesize these kinds of complexes failed. In contrast, two homometallic [Co₄] (complexes **9** and **10**, Chapter IV) have been obtained using H₄L2 and H₂L3, respectively. Nevertheless, the structural characteristics of **10** lead this complex to be to a potentially building block for the desired molecular pairs systems. The high lability of its axial MeOH ligands and the remarkable planarity

of its crystal structure have been used to build up a new architecture based on this moiety (complex **11**). This new molecular system, which shows two $[\text{Co}_4]$ units linked covalently by four difunctional 4,4'-bipyridine molecules, turns to be the prototype of a molecular pair. However, the magnetic properties of **11** demonstrates a strong antiferromagnetic interactions within each $[\text{Co}_4]$ moiety, thus leading to two species with ground state $S = 0$. Despite that, this complex can be considered as a basis for the preparation of similar assemblies exhibiting non-zero spin. This may be accomplished if the different functional groups of H_4L_2 and H_2L_3 can be used to enable heterometallic moieties. Furthermore, using again photoswitchable ligands for the linkage of the complexes could be explored. In that sense, binding such units by difunctional ligands like 4,4'-azopyridine, for example, may allow the possibility of turning on and off the interaction between the molecular systems just by changing the conformation of the linker.

The construction of molecular prototypes of CNOT and $\sqrt{\text{SWAP}}$ gates by using dinuclear complexes of lanthanide ions has become the most promising of the three approaches proposed. The non-symmetric ligand strategy has been successfully carried out to design asymmetric $[\text{Ln}_2]$ compounds. The structural features of this system have allowed the synthesis of the first structurally characterized quasi-complete series of dinuclear lanthanide complexes (complexes **13-26** and **27-30**, Chapter V). This has been employed to study the quadratic nature of the decay of several structural parameters related to the lanthanide contraction. The results have demonstrated also the successful synthetic strategy for locating two Ln^{III} ions within a molecule, exhibiting different environments and a weak antiferromagnetic interaction. These properties, together with the strong magnetic anisotropy of terbium(III), have demonstrated to provide complex **29** with the ingredients required to implement the CNOT quantum gate. The definition of both control and target qubits is based on the magnetic inequivalence of each Tb^{III} ion. The magnetic energy levels of this molecular system have been studied using the experimental data obtained in magnetic heat capacity and susceptibility measurements at ultra-low temperatures. The results have revealed that not only the CNOT but also the $\sqrt{\text{SWAP}}$ operation can be induced with radiation of a constant frequency by modifying the external magnetic field. EPR measurements have

confirmed the transitions related to both operations. However, when the system was assessed by X-band pulsed EPR, no coherence was observed. The most likely cause is the coupling between the electron and the nuclear spin carried by Tb^{III}, which would prevent the magnetic levels to be maintained long enough to encode the information of the qubit.

The study of these dinuclear molecular entities has also shown that the scaffold around the metals induces one site significantly bigger than the other. This dissimilar size between both environments is systematically maintained in the whole series, and has been exploited to synthesize heterometallic [LnLn'] systems (complexes **31-72**, Chapter V). The structural study, as well as mass spectrometry experiments, has revealed that only when Ln and Ln' present very similar ionic radii, the system cannot selectively distribute them over two different positions within a heterometallic moiety, leading also to the homometallic analogues. On the contrary, when the two lanthanide ions have significantly different ionic radii (the great majority of combinations), the pure heterometallic compound is always observed, corresponding to the thermodynamically most stable product. This stability has been used to obtain the diluted compound **73**, which contains heterometallic [CeY] molecules within an isostructural [Y₂] diamagnetic lattice.

The versatile [LnLn'] system enables a vast choice of quantum gate designs. In that sense, complex **40** ([CeEr]) has been chosen due to the very different magnetic ground states of its ions, as well as the low nuclear spin of them. Ce^{III} and Er^{III} have been studied individually using compounds **43** ([CeY]) and **35** ([LaEr]), respectively. Magnetic susceptibility, heat capacity and EPR measurements have shown that both ions behave, at sufficiently low temperatures, as effective $S = 1/2$ (two state) qubits. The study has also revealed that their ground states do not belong to pure orientations of the angular momentum but a combination of them due to the low symmetry of their coordination polyhedra. The calculated magnetic energy level structure of Ce^{III} and Er^{III} confirms that the ground state of both ions is a well-separated two-level system that enable the encodement of the two basic states '0' and '1' of a quantum bit. In addition, the metal ions in [CeEr] exhibit the weak interaction required for a quantum gate. The possible $\sqrt{\text{SWAP}}$ and CNOT operations have been studied by calculating the

structure of the magnetic energy levels using the magnetic susceptibility and heat capacity data. This study demonstrates that both operations could be carried out with this molecular quantum gate at low fields and conventional technologies.

The coherence of [CeEr] as a molecular quantum processor has been studied by pulsed-EPR. The observed signal of the echo amplitude as a function of the magnetic field confirmed that the radiation pulses generate coherent spin dynamics. A Hahn echo sequence on a [CeEr] solution has been carried out to evaluate the decoherence time of the system. The low value obtained would not enable successful quantum information processes since is still far to allow fault-tolerant computation. Nevertheless, the value is expected to increase employing a diluted solution of this compound, thus diminishing the possible hyperfine interactions that could be influencing the measurement

The possibility of using coordination magnetic molecules as hardware for quantum computation is therefore still a promising project. Indeed, the significant progress that has been made towards this goal and the results obtained along this thesis show that there are different feasible ways to address this attractive challenge. The ligand-based strategy that has been followed to satisfactorily generate pairs of magnetic moieties within molecules, the possibility of generating an energy scheme that potentially can produce CNOT or $\sqrt{\text{SWAP}}$ logical operations, or the experimental demonstration of encouraging decoherence times are examples that demonstrate such progress. However, for coordination magnetic complexes to be considered more than an utopic goal in QIP, considerably efforts towards the implementation of these functional materials in technological devices must be carried out. This involves not only the capacity of organizing the molecules into devices, but also to introduce the mechanisms to address and read out the information codified in the qubits. In that sense, the stability in solution of the studied dinuclear lanthanide complexes may allow the possibility of organizing these molecular processors by depositing them on surfaces. Despite the fact that their physical properties may be altered upon deposition, this new research line would open a promising approach towards the integration of molecular quantum bits into nanodevices and thus the realization of scalable quantum computing architectures.

APPENDIX

APPENDIX - CHAPTER II. DESIGN, SYNTHESIS AND CHARACTERIZATION OF β -DIKETONE LIGANDS TO ACCESS FUNCTIONAL COORDINATION COMPLEXES

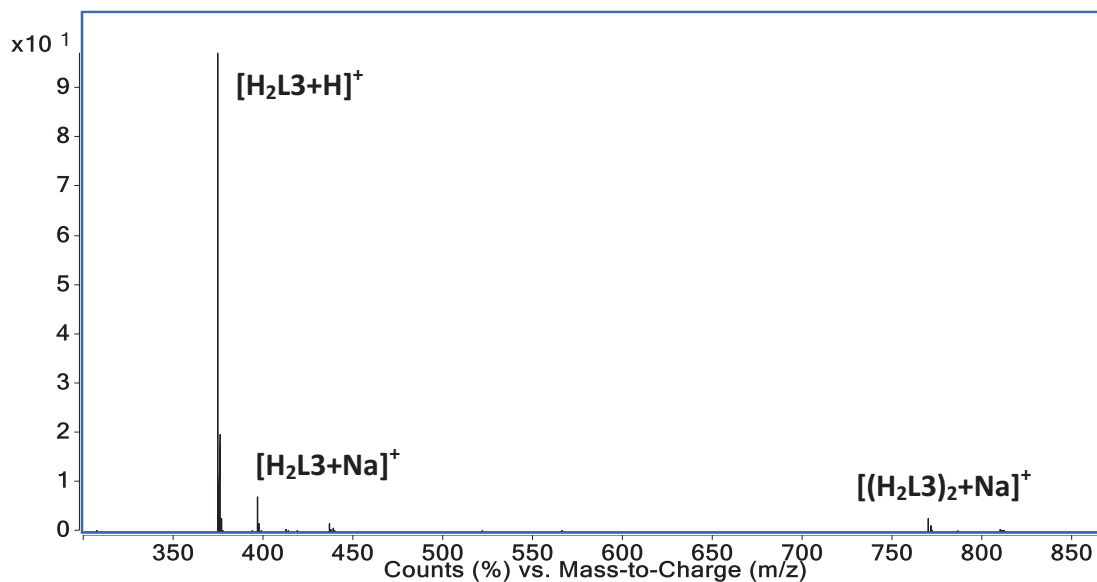


Figure II.A1. Positive ion ESI mass spectrum at 125 V of H₂L3 dissolved in CHCl₃.

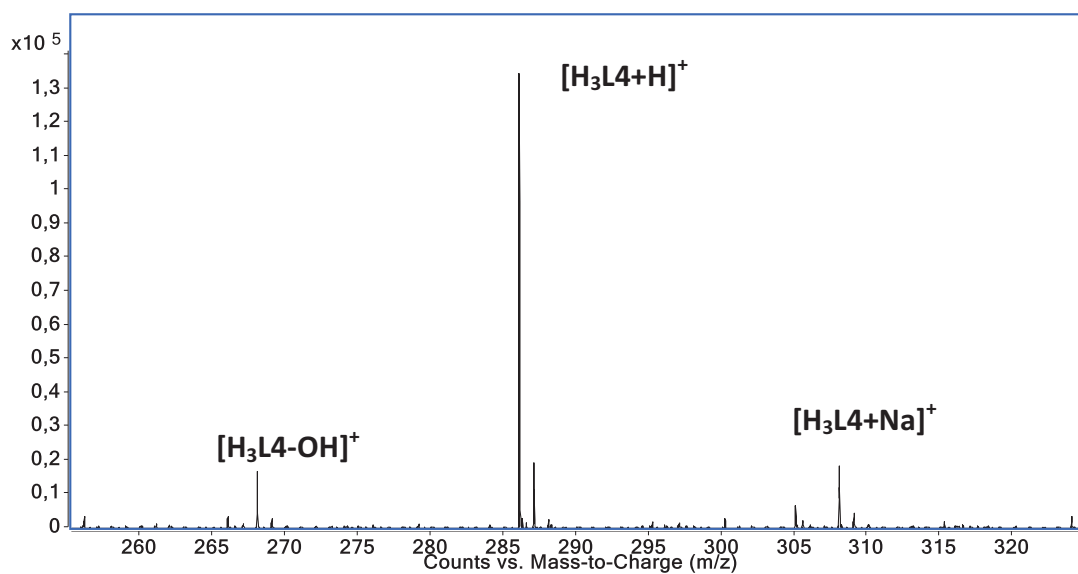


Figure II.A2. Positive ion ESI mass spectrum at 125 V of H₃L4 dissolved in MeOH.

APPENDIX - CHAPTER III. TRIPLE- AND QUADRUPLE-STRANDED HELICATES

Table III.A1. Crystal data and structure refinement for compounds 1-3

	Complex 1	Complex 2	Complex 3
Formula	C ₈₅ H _{74.33} Fe ₂ O _{21.25}	C ₃₅₂ O ₈₈ Ga ₈	C ₁₄₄ H ₉₆ O ₃₆ N ₄ U ₄
<i>M_r</i>	1547.47	6182,96	3408,78
Crystal system	monoclinic	monoclinic	triclinic
Space group	P2 ₁ / <i>n</i>	P2 ₁ / <i>c</i>	P-1
λ (Å)	0.7749	0.71073	0.71073
<i>a</i> (Å)	23.4757(17)	16.3989(4)	14.3818
<i>b</i> (Å)	34.645(2)	23.6742(7)	14.3818
<i>c</i> (Å)	30.737(2)	19.9154(6)	19.5655
α (°)	90	90	90.000
β (°)	105.815(2)	94.534(2)	90.000
γ (°)	90	90	90.000
<i>V</i> (Å ³)	24053(3)	7707.58	4046.85
<i>T</i> [K]	190	-	130
<i>Z</i>	12	4	2
ρ (g/cm ³)	1.282	-	-
Shape and colour	red needle	yellow needle	red needle
Crystal size (mm ³)	0.40x0.04x0.02	-	0.102x0.134x0.16
Reflections	38358	-	-
Parameters	3134	-	1117
Restraints	1209	-	0
<i>R</i> _{int}	0.0647	-	-
<i>R</i> ₁ ^[a]	0.0693	-	0.0679
<i>wR</i> ₂ ^[b]	0.2381	-	0.1330
<i>S</i>	1.067	-	-

[a] $R_1 = \sum ||F_o| - |F_c| | / \sum |F_o|$, for $l > 2\sigma(l)$. [b] $wR_2 = \{\sum [w(F_o^2 - F_c^2)^2] / \sum [w(F_o^2)^2]\}^{1/2}$, for all data

Table III.A2. Continuous Shape Measures (CShMs) for the coordination geometry of the metals in 3, with respect to the reference polyhedra. Highlighted are the closest polyhedra for each metal. Below is the symmetry and description of each polyhedron.

	MFF-9	JCSAPR-9	JTCTPR-9	JTDIC-9	CSAPR-9	TCTPR-9	CCU-9	HH-9
U1	2.180	1.015	3.202	13.135	1.298	2.559	5.207	11.425
U2	2.163	0.962	3.174	13.204	1.286	2.530	5.339	11,570

MFF-9	“muffin”	C _s
JCSAPR-9	Capped square antiprism	C _{4v}
JTCTPR-9	Tricapped trigonal prism	D _{3h}
JTDIC-9	Tridiminished icosahedron	C _{3v}
CSAPR-9	Capped square antiprism	C _{4v}
TCTPR-9	Tricapped trigonal prism	D _{3h}
CCU-9	Capped cube	C _{4v}
HH-9	Hula-hoop	C _{2v}

APPENDIX - CHAPTER IV. TRIPLE- AND QUADRUPLE-STRANDED HELICATES

Table IV.A1. Crystal data and structure refinement for compounds 4-6

	Complex 4	Complex 5	Complex 6
Formula	C _{82.50} H ₇₆ N ₆ Ni ₄ O _{16.50}	Co ₄ C ₇₈ H ₅₈ N ₆ O ₁₂	Cu ₈ C ₁₉₆ H ₁₅₆ Cl ₂ N ₂₀ Na ₂ O ₃₂
<i>M_r</i>	1650.33	1507.02	3928.61
Crystal system	monoclinic	triclinic	monoclinic
Space group	P2 ₁ /n	P-1	C2/c
λ (Å)	0.77490	0.71073	0.81290
<i>a</i> (Å)	11.664(4)	8.9561(5)	27.157(4)
<i>b</i> (Å)	18.406(7)	10.8718(4)	26.899(7)
<i>c</i> (Å)	18.854(7)	17.5215(6)	19.952(3)
α (°)	90	80.016(3)	90.000
β (°)	103.706(7)	89.121(2)	125.494(9)
γ (°)	90	75.481(3)	90.000
<i>V</i> (Å ³)	3932(2)	1625.85(14)	11866(4)
<i>T</i> [K]	150	150	150
<i>Z</i>	2	1	2
ρ (g/cm ³)	1.394	1.539	1.100
Shape and colour	yellow needle	orange plate	green rod
Crystal size (mm ³)	0.20x0.04x0.04	0.30x0.25x0.02	0.30x0.05x0.05
Reflections	5614	7308	7250
Parameters	503	451	549
Restraints	387	0	352
<i>R</i> _{int}	0.0605	0.0466	0.0582
<i>R</i> ₁ ^[a]	0.0719	0.0664	0.0840
<i>wR</i> ₂ ^[b]	0.1715	0.2021	0.2790
<i>S</i>	1.081	1.028	1.030

[a] $R_1 = \sum ||F_o| - |F_c| | / \sum |F_o|$, for $l > 2\sigma(l)$. [b] $wR_2 = \{ \sum [w(F_o^2 - F_c^2)^2] / \sum [w(F_o^2)] \}^{1/2}$, for all data

Table IV.A2. Crystal data and structure refinement for compounds 7-9

	Complex 7	Complex 8	Complex 9
Formula	Cu ₂ Ni ₂ C ₉₈ H ₇₈ N ₁₀ O ₁₂	C ₁₀₀ H ₈₀ Co ₂ Cu ₂ N ₁₀ O ₁₂	C ₄₃₄ H ₃₅₆ Co ₁₆ N ₆₂ O ₆₅
<i>M_r</i>	1832.20	1858.68	8420.67
Crystal system	tetragonal	Tetragonal	Monoclinic
Space group	P4/ncc	I4/cm	C2/c
λ (Å)	0.77490	0.71073	0.77490
<i>a</i> (Å)	32.2551(8)	22.874(5)	16.674(2)
<i>b</i> (Å)	32.2551(8)	22.874(5)	19.154(2)
<i>c</i> (Å)	16.5692(8)	16.751(3)	30.873(3)
α (°)	90	90	90
β (°)	90	90	101.397(2)
γ (°)	90	90	90
<i>V</i> (Å ³)	17238.5(10)	8764(3)	9665.6(18)
<i>T</i> [K]	150	150	150
<i>Z</i>	8	4	1
ρ (g/cm ³)	1.412	1.409	1.447
Shape and colour	orange block	orange block	red block
Crystal size (mm ³)	0.35x0.11x0.11	0.35x0.12x0.10	0.20x0.14x0.09
Reflections	8490	4829	8982
Parameters	549	291	688

Restraints	334	190	126
R_{int}	0.0585	0.0275	0.0829
R_1 ^[a]	0.0848	0.0569	0.0554
wR_2 ^[b]	0.2270	0.1662	0.1569
S	1.112	1.079	1.052

[a] $R_1 = \Sigma ||F_o| - |F_c| | / \Sigma |F_o|$, for $l > 2\sigma(l)$. [b] $wR_2 = \{\Sigma [w(F_o^2 - F_c^2)^2] / \Sigma [w(F_o^2)^2]\}^{1/2}$, for all data

Table IV.A3. Crystal data and structure refinement for compounds 10-11

	Complex 10	Complex 10b	Complex 11
Formula	Co ₄ C ₅₀ H ₅₈ N ₁₀ O ₂₈	C ₄₈ H ₆₆ Co ₄ N ₁₀ O ₃₄	C ₁₃₈ H ₁₁₀ Co ₈ N ₂₆ O ₄₆
M_r	1482.78	1562.83	3339.96
Crystal system	monoclinic	triclinic	triclinic
Space group	$P2_1/c$	P-1	P-1
λ (Å)	0.81290	0.77490	0.75150
a (Å)	20.511(5)	10.5822(7)	12.775(3)
b (Å)	11.122(4)	12.3023(8)	16.956(3)
c (Å)	16.630(2)	13.8898(10)	18.838(4)
α (°)	90	64.4450(10)	65.59(3)
β (°)	106.95(2)	89.4460(10)	70.26(3)
γ (°)	90	72.1670(10)	87.57(3)
V (Å³)	3629(2)	1537.11(18)	3474.9(17)
T [K]	150	100	150
Z	2	1	1
ρ (g/cm³)	1.357	1.688	1.596
Shape and colour	orange plate	red block	red plate
Crystal size (mm³)	0.30x0.20x0.05	0.04x0.04x0.03	0.18x0.15x0.02
Reflections	6145	9091	13157
Parameters	419	460	1066
Restraints	96	4	324
R_{int}	0.0339	0.0267	-
R_1 ^[a]	0.0623	0.0342	0.0792
wR_2 ^[b]	0.1967	0.0977	0.2403
S	1.067	1.019	1.041

[a] $R_1 = \Sigma ||F_o| - |F_c| | / \Sigma |F_o|$, for $l > 2\sigma(l)$. [b] $wR_2 = \{\Sigma [w(F_o^2 - F_c^2)^2] / \Sigma [w(F_o^2)^2]\}^{1/2}$, for all data

APPENDIX - CHAPTER V. DINUCLEAR LANTHANIDE COMPLEXES AS PROTOTYPES FOR 2-QUBIT QUANTUM GATES

Table V.A1. Crystal data and structure refinement for compounds 12-17a							
	Complex 12	Complex 13	Complex 14	Complex 15	Complex 16	Complex 17	Complex 17a
T (K)	100	100	100	100	150	100	150
Formula	C ₇₅ H ₆₀ La ₂ N ₁₀ O ₁₉	C ₈₀ H ₆₅ Ce ₂ N ₁₁ O ₁₉	C ₈₀ H ₆₅ N ₁₁ O ₁₉ Pr ₂	C ₈₀ H ₆₅ N ₁₁ Nd ₂ O ₁₉	C ₇₅ H ₆₂ N ₁₀ O ₂₀ Sm ₂	C ₇₅ H ₆₂ Eu ₂ N ₁₀ O ₂₀	Eu ₂ C ₇₅ H ₆₀ N ₁₀ O ₁₉
FW	1683.15	1764.67	1766.25	1772.91	1724.05	1727.27	1709.25
λ (Å)	0.71073	0.7749	0.7749	0.71073	0.7749	0.7749	0.7749
Crystal syst.				Monoclinic			
Space group				<i>P</i> 2 ₁ / <i>c</i>			
a (Å)	14.9646(7)	14.867(2)	14.907(3)	14.514(1)	14.894(5)	14.813(3)	14.405(2)
b (Å)	15.6293(7)	15.560(2)	15.574(3)	15.772(1)	15.586(5)	15.637(4)	15.464(2)
c (Å)	33.8889(14)	34.323(3)	34.009(6)	35.797(3)	32.554(8)	32.594(6)	34.519(3)
β (°)	110.799(2)	110.830(4)	111.316(8)	113.692(4)	111.183(11)	110.806(8)	110.050(4)
V (Å³)	7409.6(6)	7421.0(15)	7355(2)	7503.8(9)	7046(4)	7057(3)	7223.4(16)
Z				4			
ρ (g/cm³)	1.509	1.579	1.595	1.569	1.625	1.626	1.572
Shape and colour	yellow lath	yellow lath	yellow needle	yellow block	yellow rod	yellow lath	yellow plate
Crystal size (mm³)	0.25x0.09x0.08	0.25x0.05x0.05	0.60x0.06x0.04	0.34x0.14x0.12	0.60x0.10x0.06	0.18x0.05x0.05	0.13x0.07x0.04
Reflections	15134	18408	22491	16524	11763	19770	14735
Parameters	1010	1077	1063	955	964	970	969
Restraints	302	234	454	242	272	182	233
R_{int}	0.0832	0.0586	0.0479	0.0687	0.0561	0.0508	0.0621
R₁^[a]	0.0518	0.0605	0.0536	0.0657	0.0907	0.0729	0.0973
wR₂^[b]	0.1295	0.1480	0.1364	0.1607	0.2535	0.1642	0.2518
S	1.029	1.134	1.160	1.079	1.216	1.257	1.135

[a] $R_1 = \sum |F_o| - |F_c| / \sum |F_o|$, for $I > 2\sigma(I)$. [b] $wR_2 = \{ \sum [w(F_o^2 - F_c^2)]^2 / \sum [w(F_o^2)]^2 \}^{1/2}$, for all data

Table V.A2. Crystal data and structure refinement for compounds 18-26

	Complex 18	Complex 19	Complex 20	Complex 21	Complex 22	Complex 23	Complex 24	Complex 26
T (K)	150	100	150	150	100	150	100	100
Formula	C ₇₅ H ₆₀ Gd ₂ N ₁₀ O ₁₉	C ₇₅ H ₆₀ N ₁₀ O ₁₉ Tb ₂	C ₇₅ H ₆₀ Dy ₂ N ₁₀ O ₁₉	C ₇₅ H ₆₀ Ho ₂ N ₁₀ O ₁₉	C ₇₅ H ₆₀ Er ₂ N ₁₀ O ₁₉	C ₇₉ H ₇₀ N ₁₀ O ₂₀ Tm ₂	C ₈₀ H ₆₅ N ₁₁ O ₁₉ Yb ₂	C ₇₀ H ₅₅ N ₉ O ₁₉ Y ₂
FW	1719.83	1723.17	1730.33	1735.19	1739.85	1817.31	1830.51	1504.05
λ (Å)	0.71073	0.7749	0.71073	0.71073	0.7749	0.71073	0.71073	0.7749
Crystal syst.				monoclinic				
Space group				P2 ₁ /c				
a (Å)	14.2665(11)	14.255(4)	14.3307(10)	14.3450(5)	14.123(2)	14.3231(2)	14.1022(8)	14.108(7)
b (Å)	15.4250(8)	15.513(4)	15.6882(7)	15.6609(3)	15.400(2)	15.6838(2)	15.3860(8)	15.367(8)
c (Å)	35.006(3)	34.078(8)	35.637(2)	35.6109(9)	34.488(3)	35.5024(7)	35.172(2)	34.70(2)
β (°)	109.791(7)	110.416(10)	110.910(5)	110.211(2)	110.659(4)	109.857(2)	110.131(4)	110.79(2)
V (Å³)	7248.4(9)	7063(3)	7484.4(7)	7507.6(4)	7018.6(15)	7501.1(2)	7165.3(7)	7033(6)
Z				4				
ρ (g/cm³)	1.576	1.621	1.536	1.535	1.647	1.609	1.697	1.420
Shape and colour	yellow lath	yellow lath	yellow lath	yellow needle	yellow block	yellow lath	yellow block	yellow block
Crystal size (mm³)	0.40x0.09x0.05	0.12x0.04x0.03	0.54x0.09x0.08	0.49x0.11x0.04	0.11x0.08x0.05	0.30x0.12x0.04	0.41x0.17x0.14	0.15x0.09x0.07
Reflections	12317	9440	10619	10634	17299	15325	14547	5953
Parameters	985	974	955	937	964	1006	1009	901
Restraints	430	359	437	169	116	229	162	561
R_{int}	0.1501	0.0949	0.1656	0.0955	0.0524	0.1090	0.0907	0.1410
R₁^[b]	0.1172	0.0912	0.0819	0.0453	0.0608	0.0540	0.0767	0.1376
wR₂^[c]	0.2290	0.2059	0.1646	0.0938	0.1472	0.1135	0.2076	0.3382
S	1.172	1.090	0.960	0.902	1.067	0.982	1.058	1.086

[a] $R_1 = \sum ||F_o| - |F_c|| / \sum |F_o|$, for $I > 2\sigma(I)$. [b] $wR_2 = \{ \sum [w(F_o^2 - F_c^2)]^2 / \sum [w(F_o^2)]^2 \}^{1/2}$, for all data

Table V.A3 Selected interatomic distances (Å) and angles for complexes 12 to 24 and 26.

	La (12)	Ce (13)	Pr (14)	Nd (15)	Sm (16)	Eu (17)	Gd (18)	Tb (19)	Dy (20)	Ho (21)	Er (22)	Tm (23)	Yb (24)	Y (26)
Ln1-O3	2.493(3)	2.467(4)	2.445(3)	2.420(5)	2.422(10)	2.406(5)	2.375(11)	2.374(12)	2.311(11)	2.319(5)	2.339(5)	2.295(5)	2.311(8)	2.269(17)
Ln1-O4	2.524(3)	2.513(4)	2.486(3)	2.483(4)	2.466(9)	2.447(5)	2.458(11)	2.445(11)	2.435(8)	2.407(5)	2.415(5)	2.386(4)	2.400(7)	2.402(15)
Ln1-O8	2.541(3)	2.511(3)	2.482(3)	2.469(4)	2.408(9)	2.409(5)	2.416(10)	2.383(11)	2.378(8)	2.369(5)	2.358(4)	2.349(4)	2.351(7)	2.346(14)
Ln1-O9	2.457(3)	2.444(3)	2.419(3)	2.405(4)	2.361(10)	2.352(5)	2.339(11)	2.336(11)	2.323(9)	2.304(6)	2.290(5)	2.296(4)	2.273(8)	2.282(14)
Ln1-O11	2.455(3)	2.428(4)	2.412(3)	2.407(4)	2.388(10)	2.383(5)	2.372(12)	2.355(12)	2.315(10)	2.328(5)	2.324(5)	2.307(5)	2.305(8)	2.329(15)
Ln1-O13	2.532(3)	2.520(3)	2.492(3)	2.488(4)	2.439(9)	2.430(4)	2.465(9)	2.463(12)	2.455(7)	2.431(4)	2.394(4)	2.414(4)	2.401(7)	2.433(13)
Ln1-O19	2.579(3)	2.548(4)	2.545(3)	2.487(5)	2.478(11)	2.453(5)	2.444(12)	2.416(12)	2.424(10)	2.394(6)	2.381(5)	2.371(5)	2.357(8)	2.383(16)
Ln1-N3	2.599(4)	2.581(4)	2.557(4)	2.534(5)	2.500(12)	2.500(6)	2.483(13)	2.482(13)	2.466(10)	2.447(6)	2.437(6)	2.423(5)	2.419(8)	2.434(18)
Ln1-N5	2.786(4)	2.767(5)	2.737(4)	2.741(6)	2.720(14)	2.699(7)	2.700(14)	2.648(16)	2.682(15)	2.665(7)	2.670(7)	2.664(6)	2.666(11)	2.680(20)
Ln2-O1	2.463(3)	2.438(4)	2.416(3)	2.419(5)	2.403(10)	2.390(5)	2.361(11)	2.375(11)	2.358(9)	2.348(5)	2.339(4)	2.344(5)	2.328(7)	2.313(14)
Ln2-O3	2.577(3)	2.548(3)	2.534(3)	2.546(4)	2.468(9)	2.473(4)	2.437(9)	2.459(10)	2.471(8)	2.451(5)	2.418(4)	2.450(4)	2.399(7)	2.441(14)
Ln2-O6	2.485(3)	2.461(4)	2.440(3)	2.435(4)	2.397(9)	2.391(5)	2.393(10)	2.367(10)	2.359(9)	2.354(5)	2.339(4)	2.342(4)	2.327(7)	2.317(14)
Ln2-O8	2.693(3)	2.694(4)	2.671(3)	2.661(4)	2.651(9)	2.637(5)	2.631(10)	2.630(10)	2.570(9)	2.562(5)	2.603(4)	2.545(4)	2.600(7)	2.618(13)
Ln2-O13	2.547(3)	2.517(4)	2.499(3)	2.486(4)	2.437(9)	2.430(5)	2.384(10)	2.359(10)	2.374(9)	2.365(5)	2.331(5)	2.352(4)	2.304(7)	2.291(15)
Ln2-O14	2.503(3)	2.483(4)	2.470(3)	2.427(4)	2.454(9)	2.431(5)	2.373(10)	2.371(10)	2.340(9)	2.337(5)	2.333(5)	2.323(5)	2.308(7)	2.292(14)
Ln2-O16	2.628(4)	2.588(5)	2.581(3)	2.544(5)	2.542(10)	2.519(6)	2.424(12)	2.399(12)	2.396(11)	2.375(5)	2.380(5)	2.359(5)	2.362(8)	2.392(16)
Ln2-O17	2.767(4)	2.869(5)	2.771(4)	2.933(8)	2.674(11)	2.687(6)	-	-	-	-	-	-	-	-
Ln2-N1	2.674(4)	2.635(5)	2.630(4)	2.595(6)	2.604(13)	2.581(6)	2.538(13)	2.492(14)	2.480(12)	2.474(7)	2.483(6)	2.467(6)	2.440(10)	2.460(20)
Ln2-N2	2.739(4)	2.736(4)	2.714(3)	2.691(5)	2.656(12)	2.664(6)	2.619(12)	2.610(13)	2.591(11)	2.581(7)	2.590(5)	2.562(5)	2.554(10)	2.568(18)
Ln1...Ln2	3.9590(4)	3.9286(5)	3.8941(6)	3.8814(5)	3.8197(13)	3.8173(8)	3.8038(11)	3.7854(13)	3.7709(9)	3.7570(5)	3.7405(5)	3.7354(4)	3.7245(7)	3.741(4)
O11-Ln1-O9	82.00(11)	81.40(13)	80.01(10)	78.15(15)	75.1(3)	75.22(17)	76.8(4)	75.5(4)	75.4(3)	74.75(19)	74.23(18)	74.03(16)	74.4(3)	75.5(5)
O11-Ln1-O3	146.37(11)	145.50(14)	145.38(11)	145.87(16)	148.4(3)	147.63(17)	145.9(4)	146.1(4)	144.4(3)	144.2(2)	145.09(18)	143.88(17)	143.7(3)	144.4(5)
O9-Ln1-O3	111.30(11)	111.62(13)	112.24(10)	112.28(16)	112.4(3)	112.46(17)	112.1(4)	112.8(4)	113.4(3)	114.44(18)	113.52(17)	115.13(16)	113.4(3)	112.7(5)
O11-Ln1-O4	91.40(12)	89.85(14)	88.64(11)	87.23(15)	89.1(3)	87.92(17)	85.3(4)	86.3(4)	83.0(3)	82.90(17)	84.14(18)	82.31(16)	81.8(3)	83.4(5)
O9-Ln1-O4	72.71(11)	71.98(13)	72.23(10)	72.04(15)	71.4(3)	70.76(17)	70.9(4)	70.6(4)	70.4(3)	70.5(2)	70.53(17)	70.60(16)	70.4(3)	71.1(5)
O3-Ln1-O4	65.45(11)	66.17(13)	66.56(10)	67.15(15)	66.4(3)	67.03(16)	68.3(3)	67.6(4)	69.3(3)	69.47(17)	68.32(16)	69.75(15)	69.2(3)	68.4(5)
O11-Ln1-O13	124.37(11)	125.17(12)	125.93(10)	127.26(14)	128.1(3)	128.46(16)	129.2(4)	129.4(4)	131.1(3)	131.45(16)	131.03(16)	131.81(15)	132.1(3)	131.1(5)
O9-Ln1-O13	132.30(11)	132.73(11)	133.53(9)	133.73(15)	135.5(3)	135.55(16)	134.8(4)	135.2(4)	134.0(3)	134.56(19)	135.58(16)	135.05(15)	135.5(3)	134.7(5)
O3-Ln1-O13	70.14(11)	70.12(12)	69.94(10)	70.02(15)	69.2(3)	69.25(16)	68.9(3)	69.0(3)	68.9(3)	68.30(16)	68.64(15)	68.07(16)	68.4(2)	68.9(5)
O4-Ln1-O13	135.08(10)	135.81(13)	135.88(10)	136.47(15)	134.9(3)	135.63(17)	136.4(3)	136.1(4)	137.7(3)	137.32(18)	136.36(17)	137.35(16)	136.9(3)	136.6(5)
O11-Ln1-O8	146.68(10)	147.33(14)	146.57(11)	144.98(16)	142.0(3)	142.85(17)	145.9(4)	144.5(4)	144.6(3)	144.6(2)	144.65(18)	144.39(17)	145.5(3)	145.9(5)
O9-Ln1-O8	70.01(11)	70.51(12)	70.96(9)	70.96(14)	71.8(3)	72.34(16)	72.6(4)	72.6(4)	72.3(3)	72.83(18)	73.34(16)	73.08(15)	73.6(3)	73.1(5)
O3-Ln1-O8	64.28(10)	63.98(12)	64.45(9)	64.60(15)	64.6(3)	64.48(16)	62.7(3)	63.8(4)	64.6(3)	65.0(2)	63.61(16)	65.28(16)	63.7(3)	63.0(5)
O4-Ln1-O8	96.95(10)	96.76(12)	97.70(9)	98.29(14)	97.5(3)	97.96(16)	98.2(4)	97.4(4)	99.1(3)	99.11(17)	97.91(16)	99.19(15)	99.3(3)	98.6(5)
O13-Ln1-O8	68.80(10)	68.96(10)	69.23(8)	69.42(13)	69.7(3)	69.23(15)	68.7(3)	69.0(3)	68.2(3)	68.17(17)	68.82(14)	68.52(14)	68.2(3)	68.2(5)
O11-Ln1-O19	76.14(11)	75.85(15)	76.38(13)	75.44(16)	78.8(4)	77.99(19)	76.6(4)	77.2(4)	75.0(3)	74.0(2)	77.6(2)	74.33(18)	76.5(3)	75.9(5)
O9-Ln1-O19	140.63(12)	140.28(12)	139.65(10)	137.50(15)	138.3(3)	137.48(17)	138.2(4)	136.9(4)	135.6(3)	134.60(18)	137.48(16)	134.55(16)	137.3(3)	137.4(5)

	La (12)	Ce (13)	Pr (14)	Nd (15)	Sm (16)	Eu (17)	Gd (18)	Tb (19)	Dy (20)	Ho (21)	Er (22)	Tm (23)	Yb (24)	Y (26)
O3-Ln1-O19	74.62(11)	74.44(14)	74.10(12)	75.99(16)	76.3(3)	76.27(18)	76.0(4)	75.5(4)	76.1(3)	76.5(2)	75.07(18)	76.07(18)	75.3(3)	76.1(5)
O4-Ln1-O19	75.50(11)	75.81(13)	74.94(10)	73.98(15)	76.2(3)	75.90(17)	75.3(4)	75.0(4)	73.8(3)	73.60(19)	75.51(17)	73.57(16)	75.0(3)	74.8(5)
O13-Ln1-O19	86.90(11)	86.84(12)	86.69(10)	88.72(15)	86.2(3)	86.93(16)	86.9(4)	87.9(3)	90.3(3)	90.82(18)	86.89(16)	90.39(16)	87.2(3)	87.9(5)
O8-Ln1-O19	137.18(11)	136.79(14)	136.98(12)	139.37(16)	139.1(3)	139.06(18)	137.2(4)	138.0(4)	139.8(3)	140.64(19)	137.24(18)	140.52(17)	137.4(3)	137.7(5)
O11-Ln1-N3	63.07(12)	63.69(13)	63.98(10)	64.87(16)	65.1(3)	65.35(17)	65.9(4)	65.5(4)	66.5(3)	67.02(18)	66.61(18)	67.40(16)	67.4(3)	65.6(6)
O9-Ln1-N3	128.41(11)	127.76(15)	127.20(12)	125.97(17)	125.4(4)	125.97(19)	125.4(4)	125.3(5)	124.1(4)	124.1(2)	123.7(2)	123.94(18)	124.2(3)	123.7(6)
O3-Ln1-N3	118.88(11)	119.25(13)	119.44(11)	120.58(16)	121.2(3)	120.80(18)	121.3(4)	121.1(4)	121.5(3)	120.6(2)	121.88(19)	120.15(18)	121.6(3)	122.8(6)
O4-Ln1-N3	139.24(11)	139.55(13)	138.38(10)	138.41(16)	139.0(3)	138.52(17)	138.6(4)	138.4(4)	137.9(3)	138.0(2)	138.58(18)	137.56(17)	137.3(3)	137.1(6)
O13-Ln1-N3	61.42(11)	61.54(12)	62.01(10)	62.45(15)	63.2(3)	63.27(17)	63.3(4)	63.9(4)	64.7(3)	64.45(18)	64.43(17)	64.42(16)	64.7(3)	65.6(6)
O8-Ln1-N3	122.11(11)	122.27(12)	122.65(9)	122.45(15)	122.6(3)	122.70(16)	122.4(4)	123.5(4)	122.7(3)	122.47(19)	123.03(17)	122.83(16)	122.9(3)	123.9(5)
O19-Ln1-N3	68.06(12)	68.61(14)	68.72(12)	69.63(17)	68.3(4)	68.15(19)	69.6(4)	69.4(5)	70.8(3)	70.5(2)	70.2(2)	70.15(19)	69.7(3)	69.5(6)
O11-Ln1-N5	82.89(12)	83.93(15)	83.85(12)	84.16(17)	80.4(4)	81.42(19)	85.1(4)	83.5(5)	85.1(4)	85.0(2)	85.1(2)	84.37(18)	86.1(3)	85.5(6)
O9-Ln1-N5	69.95(12)	69.75(13)	70.01(11)	70.38(17)	70.5(4)	70.73(18)	70.0(4)	70.4(4)	70.2(3)	70.0(2)	69.85(18)	69.90(17)	69.7(3)	70.0(5)
O3-Ln1-N5	130.40(11)	130.32(13)	130.57(10)	129.89(16)	131.1(4)	130.94(18)	129.1(4)	130.4(4)	130.5(3)	130.8(2)	129.79(17)	131.73(17)	130.1(3)	130.1(6)
O4-Ln1-N5	142.65(12)	141.72(13)	142.22(10)	142.41(16)	141.9(3)	141.48(17)	140.9(4)	140.9(4)	140.5(3)	140.5(2)	140.38(18)	140.40(17)	140.1(3)	141.0(5)
O13-Ln1-N5	74.74(12)	74.95(13)	75.17(11)	74.58(16)	76.7(4)	76.39(18)	75.9(4)	76.1(4)	75.5(3)	75.9(2)	76.34(17)	76.58(17)	76.8(3)	76.1(5)
O8-Ln1-N5	70.99(11)	71.14(13)	71.08(11)	70.41(16)	71.4(4)	71.22(18)	70.8(4)	71.4(4)	70.9(4)	71.0(2)	70.84(18)	71.86(16)	70.8(3)	71.6(5)
O19-Ln1-N5	137.13(12)	137.61(14)	137.63(12)	137.57(17)	135.7(4)	136.20(19)	138.0(4)	137.9(4)	138.0(3)	137.6(2)	138.27(19)	137.09(17)	138.2(3)	137.5(5)
N3-Ln1-N5	69.13(12)	69.05(14)	68.95(11)	68.04(17)	67.5(4)	68.16(19)	68.4(4)	68.5(5)	67.4(4)	67.5(2)	68.1(2)	67.33(18)	68.6(3)	68.0(6)
O11-Ln1-Ln2	163.07(8)	163.44(9)	164.38(7)	165.84(11)	166.5(2)	166.68(11)	166.3(3)	166.5(3)	168.8(2)	169.00(13)	167.72(12)	169.45(11)	168.00(18)	166.7(4)
O9-Ln1-Ln2	111.61(8)	112.61(10)	113.04(7)	113.03(11)	114.4(2)	114.62(12)	115.2(3)	115.4(3)	113.8(2)	114.45(12)	116.33(12)	114.67(11)	116.67(19)	116.5(4)
O3-Ln1-Ln2	39.42(8)	39.18(8)	39.37(6)	39.76(10)	39.1(2)	39.15(10)	38.3(2)	39.3(3)	39.5(2)	39.31(12)	38.91(10)	39.58(11)	38.59(18)	39.0(4)
O4-Ln1-Ln2	102.08(8)	102.65(10)	103.25(7)	104.22(10)	102.9(2)	103.60(12)	104.6(3)	104.4(3)	105.7(2)	105.51(12)	104.92(12)	105.87(11)	105.70(18)	105.6(4)
O13-Ln1-Ln2	38.92(7)	38.71(8)	38.78(7)	38.70(10)	38.4(2)	38.23(11)	37.6(2)	37.3(2)	37.9(2)	37.80(11)	37.07(11)	37.81(11)	36.77(18)	36.3(3)
O8-Ln1-Ln2	42.32(7)	42.77(8)	42.77(6)	42.72(10)	43.4(2)	43.15(11)	43.3(2)	43.5(2)	42.3(2)	42.32(13)	43.60(11)	42.23(11)	43.80(18)	43.9(3)
O19-Ln1-Ln2	97.18(8)	96.50(10)	96.72(9)	99.43(11)	97.8(3)	98.12(13)	96.5(3)	97.5(3)	100.4(2)	101.20(13)	96.40(13)	101.26(13)	96.14(18)	96.7(4)
N5-Ln1-Ln2	100.03(9)	99.93(9)	100.52(8)	101.00(12)	101.5(3)	101.34(13)	100.6(3)	101.0(3)	102.4(2)	102.13(14)	101.35(13)	102.14(13)	101.2(2)	101.6(4)
O1-Ln2-O6	92.23(9)	92.56(10)	92.48(8)	91.39(12)	93.5(3)	93.19(14)	92.6(3)	92.7(3)	92.1(3)	92.48(15)	92.65(14)	92.98(13)	93.4(2)	93.1(4)
O1-Ln2-O14	75.74(11)	75.58(12)	74.60(10)	74.65(16)	72.9(3)	72.65(17)	72.7(4)	72.5(4)	70.5(3)	70.80(19)	71.83(16)	70.66(16)	71.4(3)	72.5(5)
O1-Ln2-O14	70.76(11)	70.68(13)	70.45(10)	69.99(16)	68.6(3)	68.64(17)	70.8(4)	69.9(4)	69.1(3)	69.7(2)	70.03(17)	69.59(17)	70.2(3)	69.9(5)
O6-Ln2-O14	71.65(11)	71.74(13)	72.20(10)	71.82(15)	72.6(3)	72.62(17)	73.5(4)	73.8(4)	75.4(3)	74.80(18)	73.74(17)	75.21(16)	73.7(3)	72.8(5)
O1-Ln2-O13	87.68(11)	87.69(12)	87.71(10)	88.89(15)	87.4(3)	87.85(17)	88.5(4)	87.5(4)	89.2(3)	89.58(17)	88.15(16)	88.55(15)	88.3(3)	88.3(5)
O6-Ln2-O13	137.35(11)	138.27(12)	138.78(10)	139.62(15)	139.8(3)	140.27(16)	142.4(4)	142.2(3)	144.1(3)	144.14(17)	143.97(16)	144.90(16)	143.8(3)	142.9(5)
O14-Ln2-O13	65.79(10)	66.66(11)	66.81(9)	67.90(14)	67.6(3)	68.05(15)	69.5(3)	69.2(3)	69.7(3)	70.24(17)	71.31(15)	71.04(15)	71.2(3)	70.7(5)
O1-Ln2-O3	117.35(11)	118.45(12)	118.88(10)	118.60(15)	120.5(3)	120.80(16)	122.3(4)	121.2(4)	120.3(3)	119.3(2)	122.93(16)	119.13(16)	123.8(3)	123.2(5)
O6-Ln2-O3	153.51(11)	152.28(13)	152.41(11)	151.90(15)	151.6(3)	151.42(17)	148.2(4)	148.4(4)	148.2(4)	148.56(17)	147.64(17)	148.30(16)	147.6(3)	148.5(5)
O14-Ln2-O3	133.25(10)	34.10(13)	133.73(10)	134.82(14)	134.5(3)	134.58(17)	136.1(4)	136.3(4)	135.9(3)	136.19(17)	136.65(16)	136.11(16)	136.4(3)	136.2(5)
O13-Ln2-O3	68.60(10)	68.88(12)	68.43(10)	68.06(14)	68.5(3)	68.16(15)	69.3(3)	69.3(3)	67.7(3)	67.24(16)	68.36(16)	66.59(15)	68.6(3)	68.4(5)
O1-Ln2-O16	121.92(11)	19.30(14)	122.52(11)	116.27(17)	127.6(4)	127.15(19)	110.3(4)	112.5(4)	115.7(4)	117.2(2)	111.85(17)	119.19(17)	111.0(3)	110.8(5)

	La (12)	Ce (13)	Pr (14)	Nd (15)	Sm (16)	Eu (17)	Gd (18)	Tb (19)	Dy (20)	Ho (21)	Er (22)	Tm (23)	Yb (24)	Y (26)
O6-Ln2-O16	77.61(12)	77.08(14)	77.31(11)	78.99(16)	76.1(3)	76.50(17)	75.6(4)	75.8(4)	75.4(3)	76.74(18)	74.93(17)	76.88(17)	74.7(3)	75.3(5)
O14-Ln2-O16	142.35(11)	143.46(13)	141.82(10)	147.31(15)	137.2(3)	137.93(17)	147.0(4)	146.9(4)	146.1(3)	146.0(2)	145.99(16)	145.23(16)	145.9(3)	146.2(5)
O13-Ln2-O16	141.87(12)	142.59(12)	141.21(10)	140.38(15)	140.2(3)	139.59(16)	142.1(4)	142.0(4)	140.4(3)	138.88(17)	141.08(15)	138.07(16)	141.5(3)	141.8(5)
O3-Ln2-O16	75.98(11)	75.21(14)	75.23(11)	72.91(15)	76.3(3)	75.66(17)	72.9(4)	72.7(4)	73.1(3)	72.31(18)	72.78(16)	72.26(16)	73.0(3)	73.5(5)
O1-Ln2-N1	61.70(12)	62.18(14)	62.32(11)	62.74(17)	62.2(3)	62.66(17)	63.7(4)	63.3(4)	64.0(3)	64.0(2)	64.39(17)	64.45(17)	64.7(3)	63.7(6)
O6-Ln2-N1	121.34(11)	120.45(14)	119.90(11)	117.44(17)	119.8(4)	119.44(18)	113.8(4)	113.3(4)	106.8(4)	106.1(2)	111.76(18)	104.59(17)	111.0(3)	112.5(6)
O14-Ln2-N1	122.49(11)	123.59(14)	123.01(11)	125.21(17)	119.7(3)	120.41(18)	127.6(4)	126.3(4)	128.5(3)	129.85(19)	128.37(17)	130.65(17)	129.2(3)	127.7(6)
O13-Ln2-N1	81.32(11)	81.79(14)	80.87(11)	84.65(16)	77.2(4)	77.71(18)	84.3(4)	83.5(4)	89.0(3)	90.62(19)	84.04(18)	90.45(16)	85.0(3)	84.9(6)
O3-Ln2-N1	57.99(11)	58.72(13)	58.89(10)	59.18(15)	59.8(3)	59.75(16)	61.7(3)	60.9(4)	61.5(3)	61.2(2)	62.07(17)	61.43(16)	62.8(3)	63.2(6)
O16-Ln2-N1	91.89(12)	88.56(16)	91.97(12)	81.30(18)	101.0(4)	99.43(19)	76.0(4)	78.1(4)	76.7(4)	76.1(2)	76.12(18)	76.54(17)	74.8(3)	75.6(6)
O1-Ln2-O8	152.98(10)	152.82(13)	152.57(10)	154.26(15)	151.3(3)	151.46(17)	153.3(4)	152.7(4)	154.1(3)	154.25(17)	151.63(16)	153.31(16)	151.3(2)	152.6(5)
O6-Ln2-O8	118.33(10)	118.78(12)	119.40(9)	119.29(14)	121.1(3)	121.25(15)	121.7(3)	123.0(4)	124.8(3)	124.5(2)	123.33(15)	125.56(15)	123.4(2)	123.0(5)
O14-Ln2-O8	91.08(10)	91.21(11)	90.66(9)	92.92(14)	90.8(3)	90.82(16)	90.9(3)	91.8(3)	93.3(3)	93.10(17)	90.35(15)	92.82(15)	89.6(2)	92.2(5)
O13-Ln2-O8	66.26(10)	66.16(11)	66.17(8)	66.41(13)	65.8(3)	65.55(15)	66.4(3)	66.6(3)	66.3(3)	66.05(16)	65.68(15)	86.81(15)	65.5(2)	65.8(4)
O3-Ln2-O8	61.05(10)	60.34(11)	60.57(9)	60.20(14)	60.4(3)	60.24(15)	58.8(3)	59.1(4)	59.6(3)	60.28(19)	58.95(15)	60.17(15)	58.8(3)	56.9(5)
O16-Ln2-O8	84.72(11)	87.39(12)	84.66(10)	88.61(15)	81.1(3)	81.38(16)	95.7(4)	94.0(4)	89.6(3)	87.89(18)	95.93(15)	86.81(15)	97.1(3)	95.6(5)
N1-Ln2-O8	117.80(11)	117.82(12)	118.06(9)	118.86(15)	117.6(3)	117.50(16)	119.6(3)	119.0(4)	121.0(3)	121.50(18)	120.03(16)	121.59(16)	120.7(3)	119.3(5)
O1-Ln2-N2	132.46(12)	132.86(13)	131.52(10)	132.67(16)	129.1(3)	129.12(17)	133.3(4)	132.8(4)	129.6(3)	130.2(2)	132.34(16)	130.10(16)	132.4(3)	132.9(5)
O6-Ln2-N2	61.07(11)	61.50(13)	61.81(10)	61.73(16)	63.0(3)	62.95(17)	63.8(4)	64.2(4)	64.6(3)	64.5(2)	64.60(17)	65.04(17)	64.7(3)	63.7(5)
O14-Ln2-N2	77.30(11)	77.84(12)	76.68(9)	79.34(15)	74.9(3)	75.25(16)	81.3(4)	80.6(4)	78.3(3)	78.18(19)	79.91(16)	77.80(16)	80.5(3)	81.0(5)
O13-Ln2-N2	110.32(10)	111.08(13)	110.98(10)	112.19(15)	110.3(4)	112.19(17)	116.1(4)	115.8(4)	114.6(3)	114.4(2)	116.51(17)	115.53(17)	117.1(3)	116.4(5)
O3-Ln2-N2	110.19(11)	108.68(12)	109.60(9)	108.65(15)	110.4(3)	110.06(16)	103.8(3)	105.6(4)	110.0(3)	110.3(2)	104.40(16)	110.62(16)	103.4(3)	103.5(5)
O16-Ln2-N2	68.97(11)	70.73(14)	68.83(11)	73.98(16)	65.1(3)	65.46(18)	63.8(4)	74.7(4)	74.0(4)	73.0(2)	74.95(17)	71.83(17)	74.6(3)	74.9(5)
N1-Ln2-N2	160.20(12)	158.54(15)	160.28(11)	154.99(17)	165.4(4)	164.34(18)	150.4(4)	152.4(4)	150.7(3)	148.98(19)	150.70(18)	148.18(17)	149.1(3)	150.1(6)
O8-Ln2-N2	57.41(11)	57.46(12)	57.70(9)	57.71(14)	58.1(3)	58.33(16)	58.4(3)	59.1(4)	60.3(3)	59.94(19)	59.11(16)	60.52(16)	59.2(2)	59.6(5)
O1-Ln2-O17	75.98(13)	74.14(14)	76.42(12)	71.0(2)	82.7(3)	81.56(19)	-	-	-	-	-	-	-	-
O6-Ln2-O17	70.40(13)	68.14(15)	69.48(13)	64.4(2)	74.2(3)	72.75(18)	-	-	-	-	-	-	-	-
O14-Ln2-O17	134.28(14)	131.66(14)	134.48(12)	127.1(2)	141.1(3)	139.54(18)	-	-	-	-	-	-	-	-
O13-Ln2-O17	143.19(11)	131.66(14)	142.32(11)	144.01(17)	138.7(3)	139.37(17)	-	-	-	-	-	-	-	-
O3-Ln2-O17	89.79(13)	91.78(15)	89.53(12)	95.2(2)	82.5(3)	83.98(18)	-	-	-	-	-	-	-	-
O16-Ln2-O17	46.54(12)	45.43(14)	46.83(11)	45.3(2)	48.4(3)	48.42(18)	-	-	-	-	-	-	-	-
N1-Ln2-O17	61.87(11)	61.50(15)	61.48(12)	59.76(18)	62.7(4)	62.54(19)	-	-	-	-	-	-	-	-
O8-Ln2-O17	129.37(13)	131.56(13)	129.52(11)	133.7(2)	124.0(3)	125.20(17)	-	-	-	-	-	-	-	-
N2-Ln2-O17	104.93(11)	104.57(13)	105.00(11)	103.21(18)	107.0(3)	106.32(18)	-	-	-	-	-	-	-	-
O1-Ln2-Ln1	120.79(8)	121.01(9)	121.42(7)	122.36(11)	121.7(2)	121.96(13)	122.9(3)	122.2(3)	123.8(2)	123.69(13)	122.51(12)	123.09(11)	122.89(18)	122.6(4)
O6-Ln2-Ln1	156.15(8)	156.74(10)	157.25(8)	157.20(12)	158.5(2)	158.85(12)	160.3(3)	161.1(3)	163.2(2)	162.82(15)	161.69(12)	163.78(12)	161.9(2)	161.1(4)
O14-Ln2-Ln1	96.50(7)	97.24(8)	96.87(7)	98.50(10)	97.1(2)	97.46(12)	99.1(3)	99.0(2)	100.4(2)	100.49(12)	99.39(11)	100.54(11)	99.58(17)	100.5(4)
O13-Ln2-Ln1	38.65(7)	38.76(7)	38.66(6)	38.73(9)	38.4(2)	38.23(10)	39.1(2)	39.3(2)	39.44(17)	39.05(10)	38.25(10)	38.99(10)	38.58(17)	39.0(3)
O3-Ln2-Ln1	37.90(7)	37.70(10)	37.74(7)	37.45(10)	38.2(2)	37.89(12)	37.2(3)	37.7(3)	36.5(3)	36.81(13)	37.42(12)	36.64(11)	36.93(19)	35.8(4)

	La (12)	Ce (13)	Pr (14)	Nd (15)	Sm (16)	Eu (17)	Gd (18)	Tb (19)	Dy (20)	Ho (21)	Er (22)	Tm (23)	Yb (24)	Y (26)
O16-Ln2-Ln1	103.38(9)	104.32(10)	102.79(8)	157.20(12)	101.7(2)	101.37(13)	106.3(3)	105.7(3)	102.6(3)	101.22(13)	106.31(11)	100.47(12)	106.53(19)	106.0(4)
N1-Ln2-Ln1	82.51(8)	82.78(10)	82.84(8)	85.14(11)	81.7(3)	81.71(13)	85.3(3)	85.1(3)	88.7(2)	89.72(13)	85.94(13)	90.11(12)	86.4(2)	85.7(5)
O8-Ln2-Ln1	39.44(6)	39.27(7)	39.13(6)	39.02(9)	38.63(19)	38.66(10)	39.0(2)	38.6(2)	38.49(19)	38.51(13)	38.67(10)	38.34(10)	38.75(16)	38.4(3)
N2-Ln2-Ln1	96.63(8)	96.61(10)	96.65(7)	96.63(11)	96.5(3)	96.76(13)	97.3(3)	97.6(3)	98.7(2)	98.41(14)	97.74(12)	98.83(12)	97.87(19)	98.0(4)
O17-Ln2-Ln1	127.69(11)	129.44(11)	127.27(10)	132.58(17)	120.7(2)	121.87(14)	-	-	-	-	-	-	-	-
Ln1-O3-Ln2	102.68(11)	103.13(14)	102.89(11)	102.79(16)	102.7(3)	102.96(17)	104.4(4)	103.1(4)	104.1(4)	103.9(2)	103.67(18)	103.78(18)	104.5(3)	105.1(6)
Ln1-O8-Ln2	98.24(10)	97.95(11)	98.10(9)	98.26(14)	98.0(3)	98.19(15)	97.7(3)	98.0(4)	99.2(3)	99.2(2)	97.73(15)	99.43(16)	97.5(3)	97.7(5)
Ln1-O13-Ln2	102.43(11)	102.53(12)	102.56(9)	102.57(15)	103.1(3)	103.54(16)	103.3(4)	103.4(4)	102.7(3)	103.16(17)	104.68(16)	103.19(16)	104.7(3)	104.7(5)

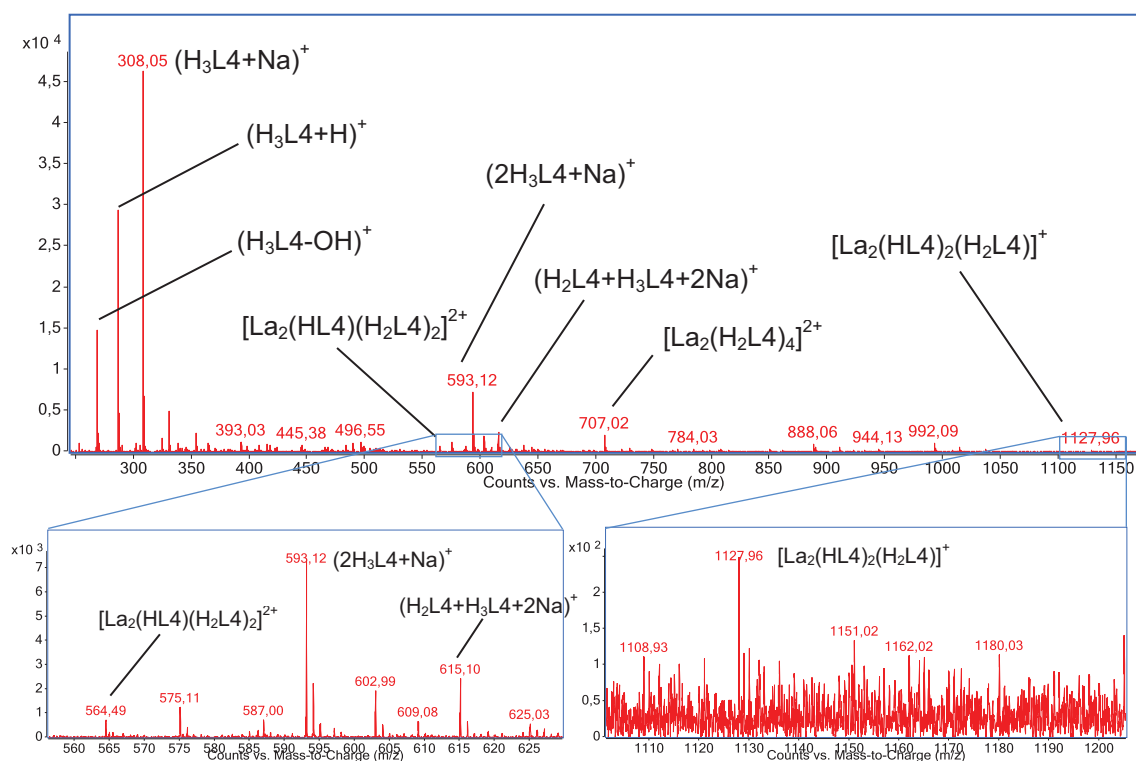


Figure V.A1. Electrospray mass spectrogram of complex $[La_2]$ (12) displaying the peaks of the free ligand and complex species.

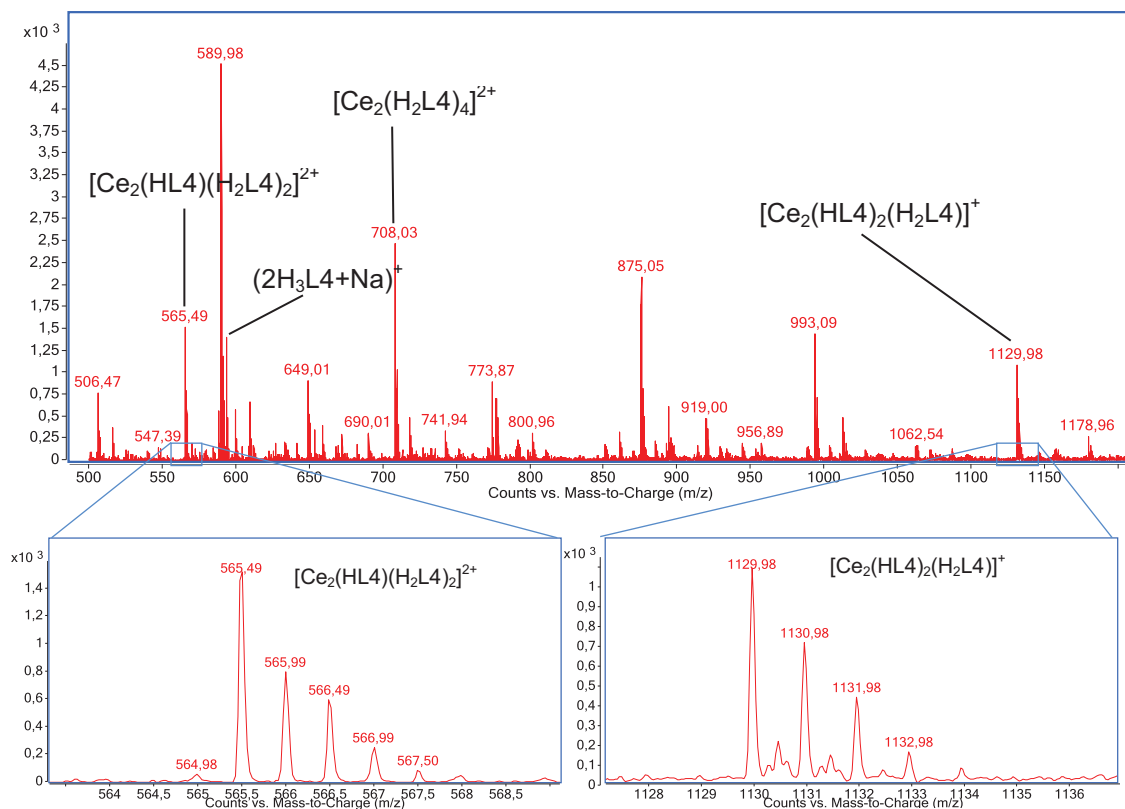


Figure V.A2. Electrospray mass spectrogram of complex $[Ce_2]$ (13) displaying the peaks of the free ligand and complex species.

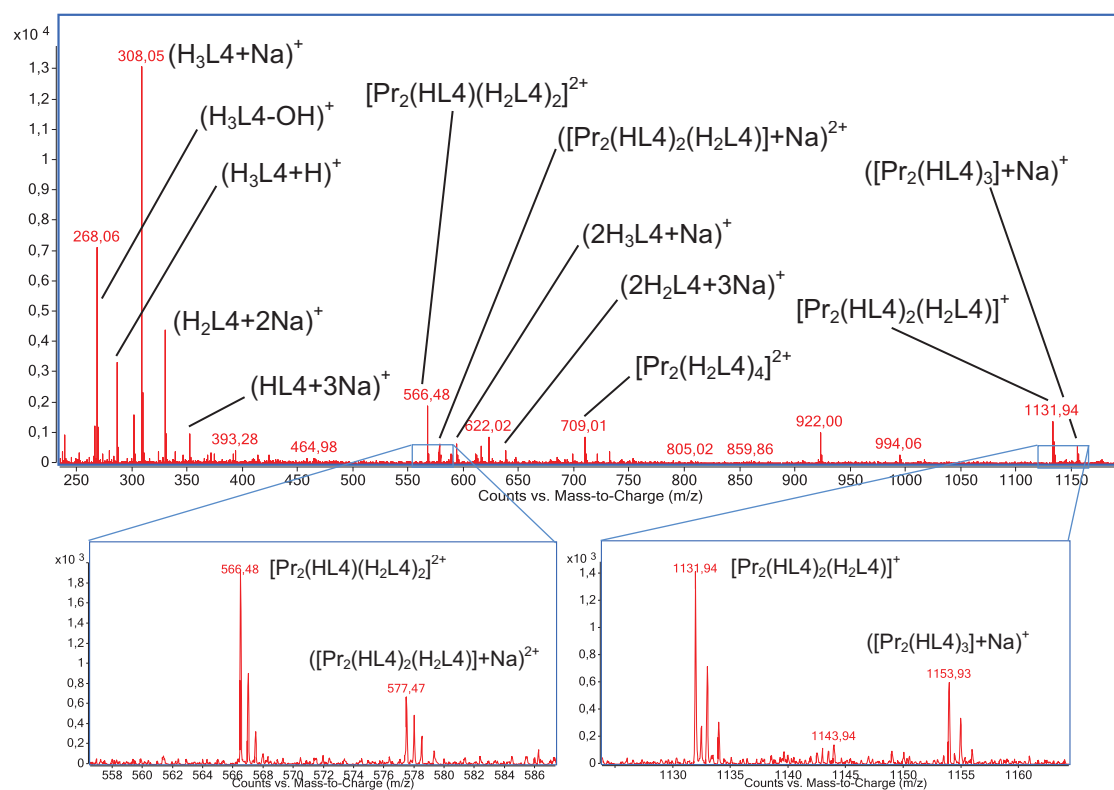


Figure V.A3. Electrospray mass spectrogram of complex $[\text{Pr}_2]$ (14) displaying the peaks of the free ligand and complex species.

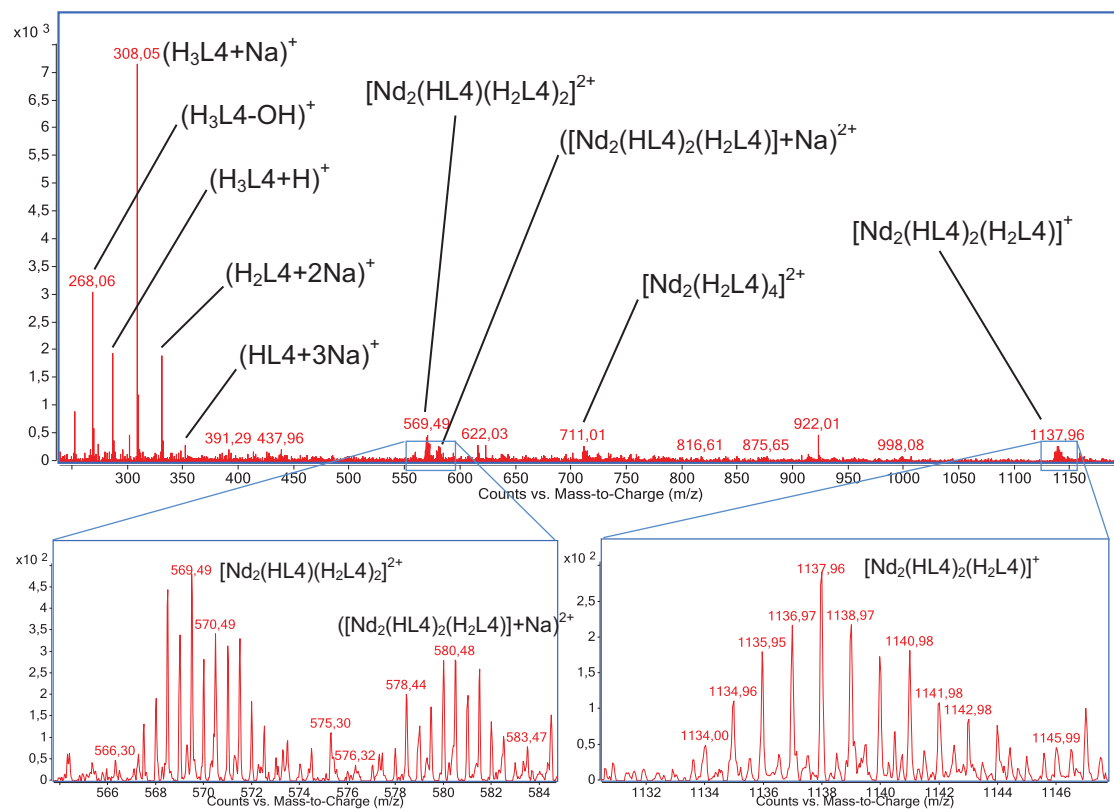


Figure V.A4. Electrospray mass spectrogram of complex $[\text{Nd}_2]$ (15) displaying the peaks of the free ligand and complex species.

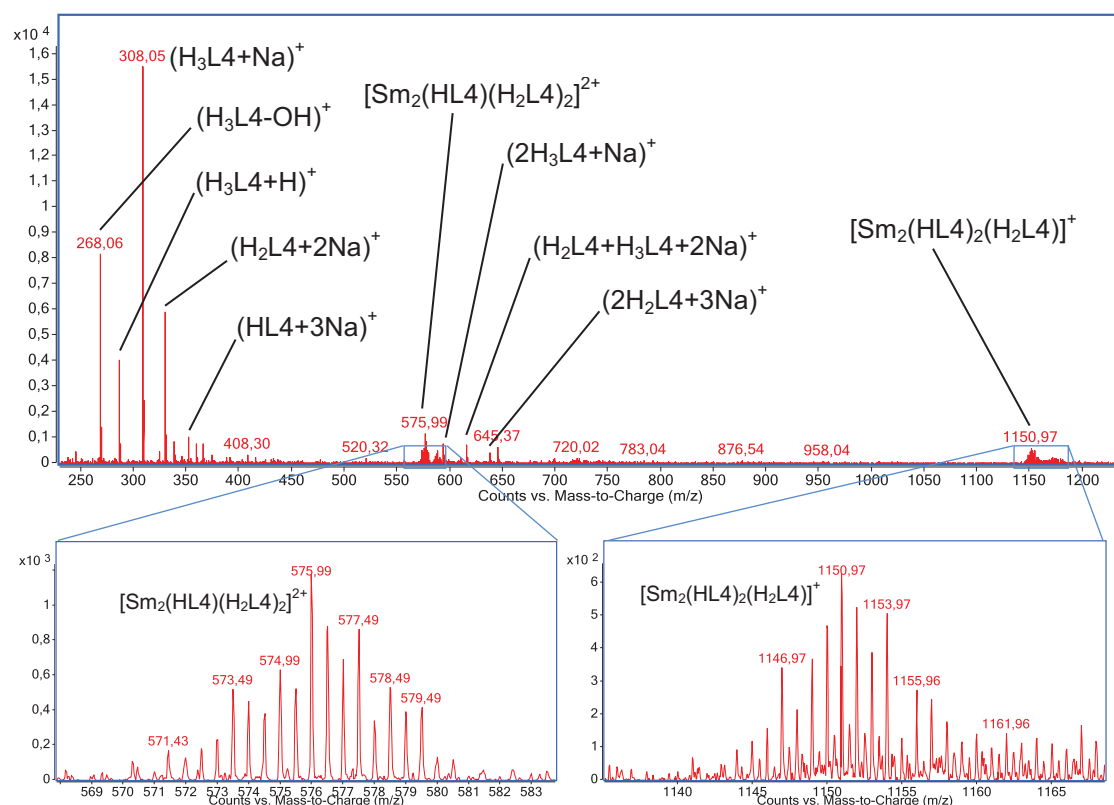


Figure V.A5. Electrospray mass spectrometry (ESI-MS) spectra of complex $[\text{Sm}_2]$ (**16**) displaying the peaks of the free ligand and complex species.

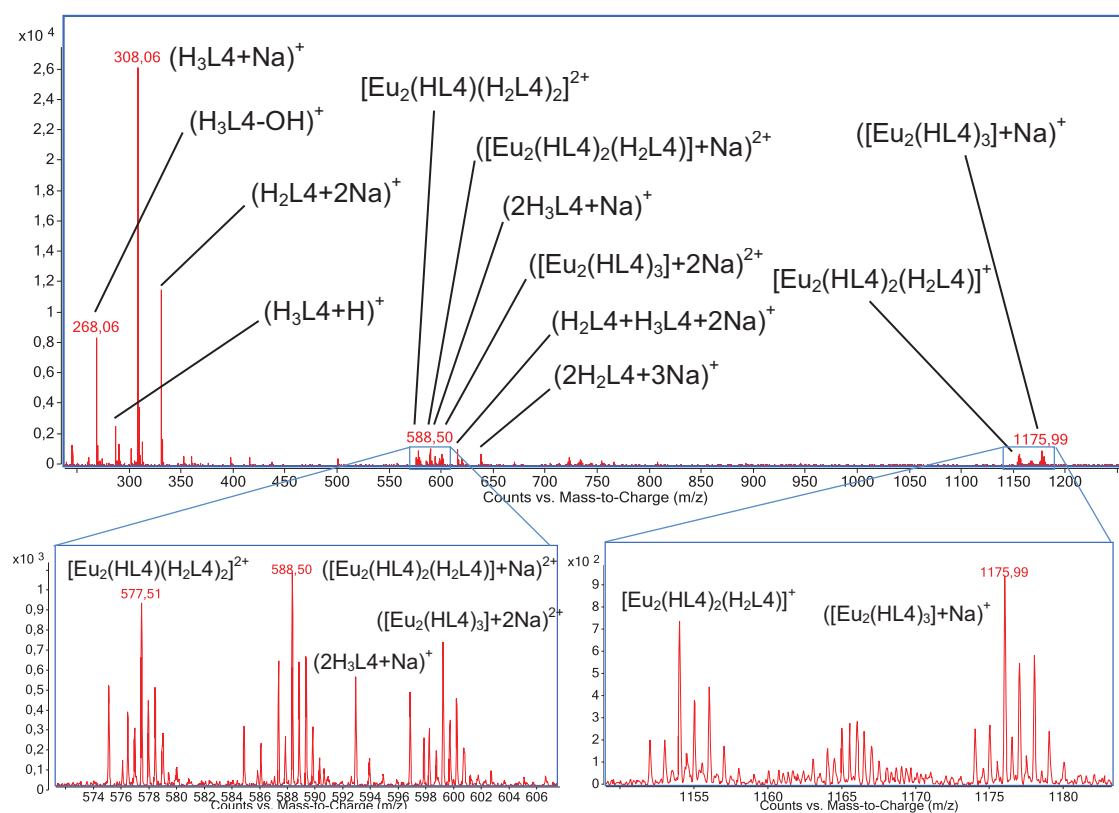


Figure V.A6. Electrospray mass spectrometry (ESI-MS) spectra of complex $[\text{Eu}_2]$ (**17**) displaying the peaks of the free ligand and complex species.

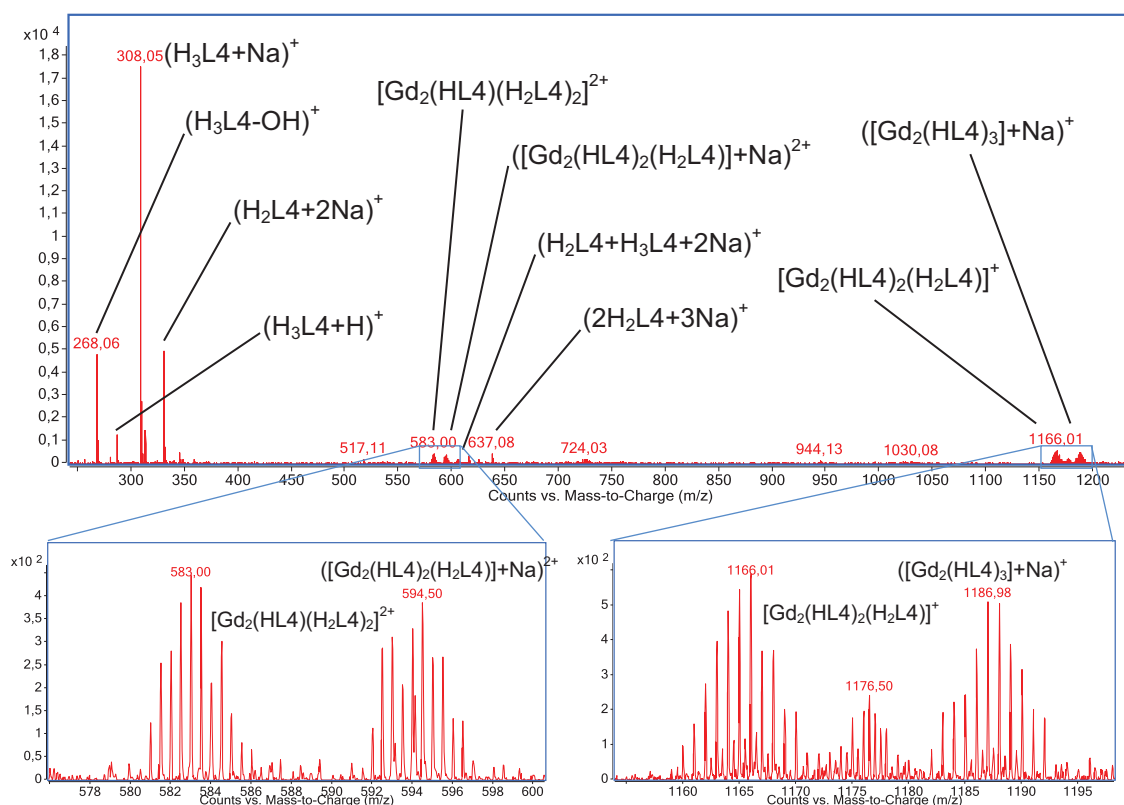


Figure V.A7. Electrospray mass spectrometry of complex $[Gd_2]$ (**18**) displaying the peaks of the free ligand and complex species.

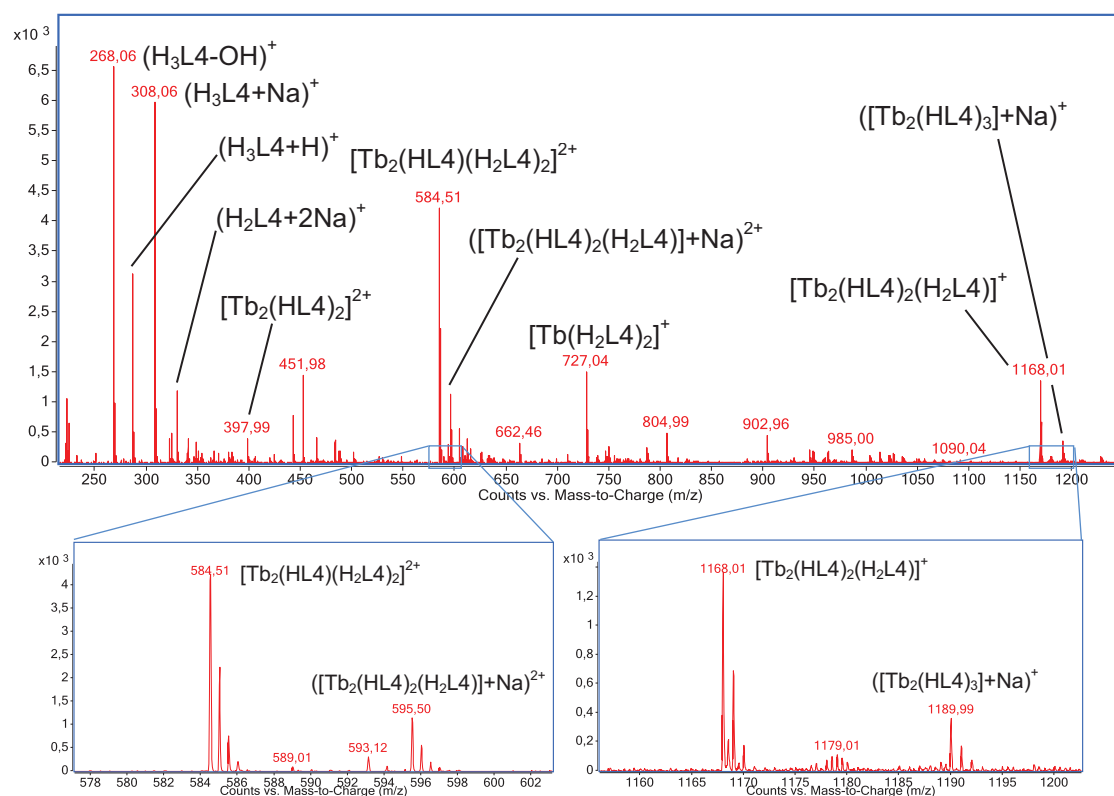


Figure V.A8. Electrospray mass spectrometry of complex $[Tb_2]$ (**19**) displaying the peaks of the free ligand and complex species.

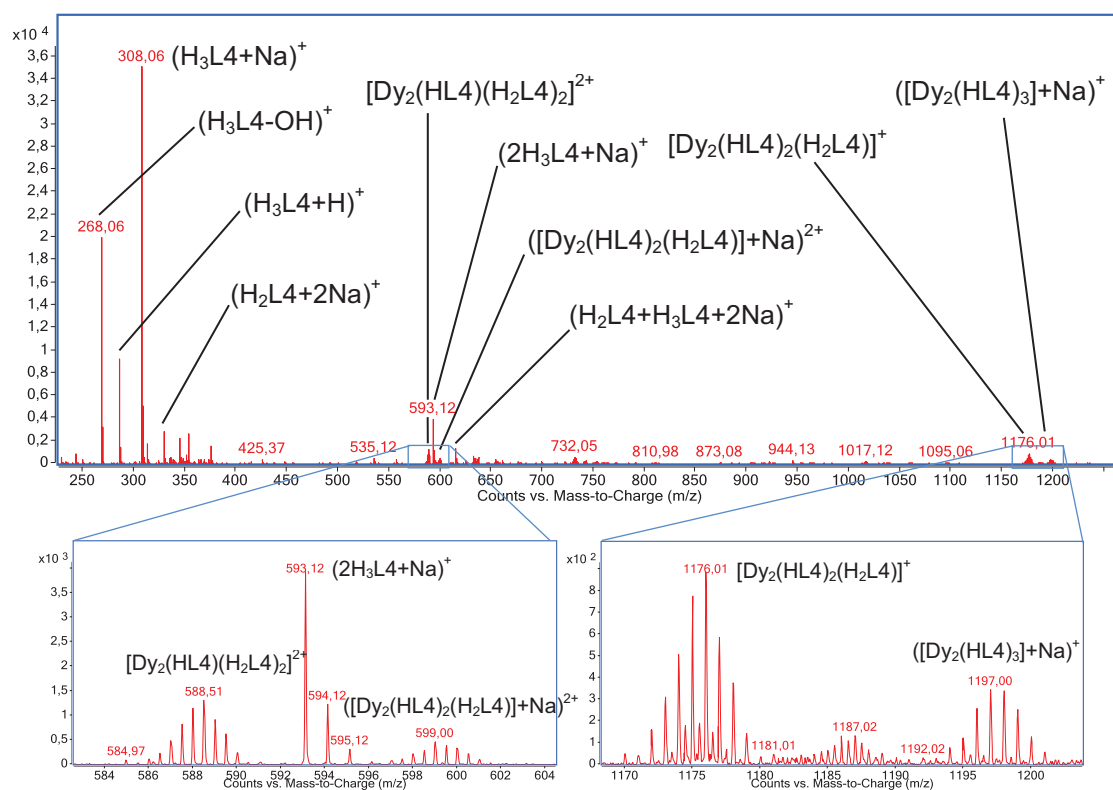


Figure V.A9. Electrospray mass spectrogram of complex $[Dy_2]$ (20) displaying the peaks of the free ligand and complex species.

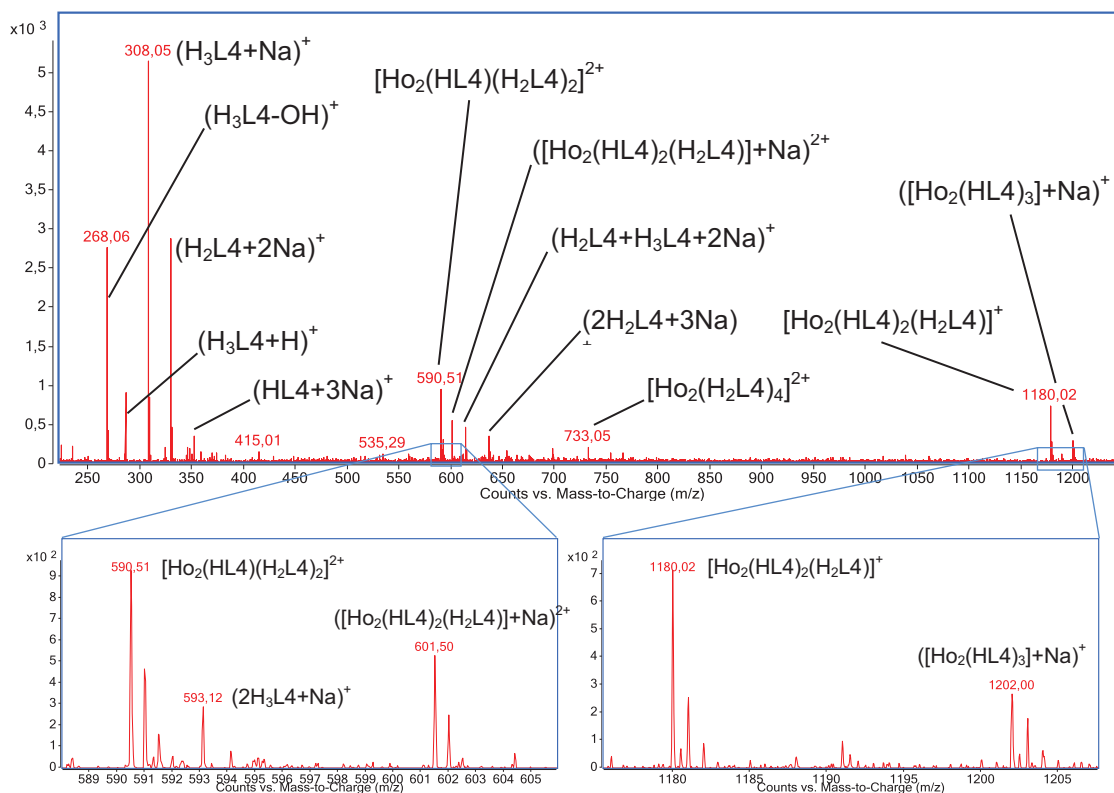


Figure V.A10. Electrospray mass spectrogram of complex $[Ho_2]$ (21) displaying the peaks of the free ligand and complex species.

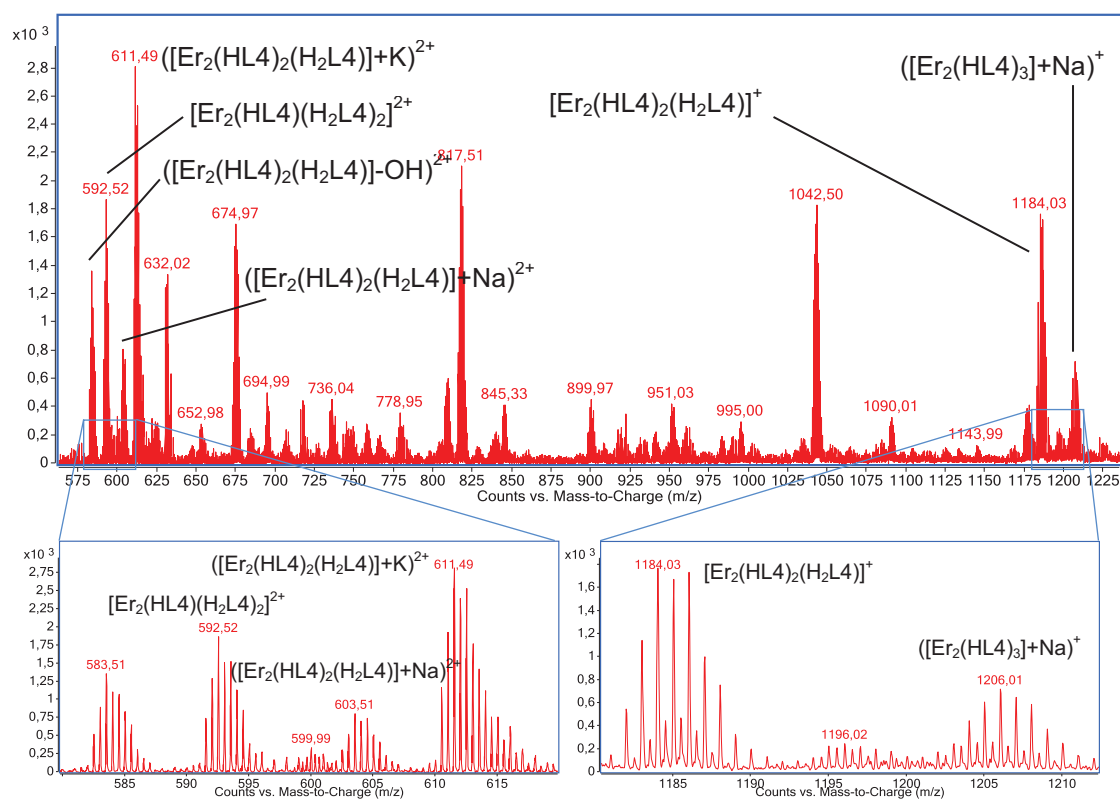


Figure V.A11. Electrospray mass spectrogram of complex $[Er_2]$ (**22**) displaying the peaks of the free ligand and complex species.

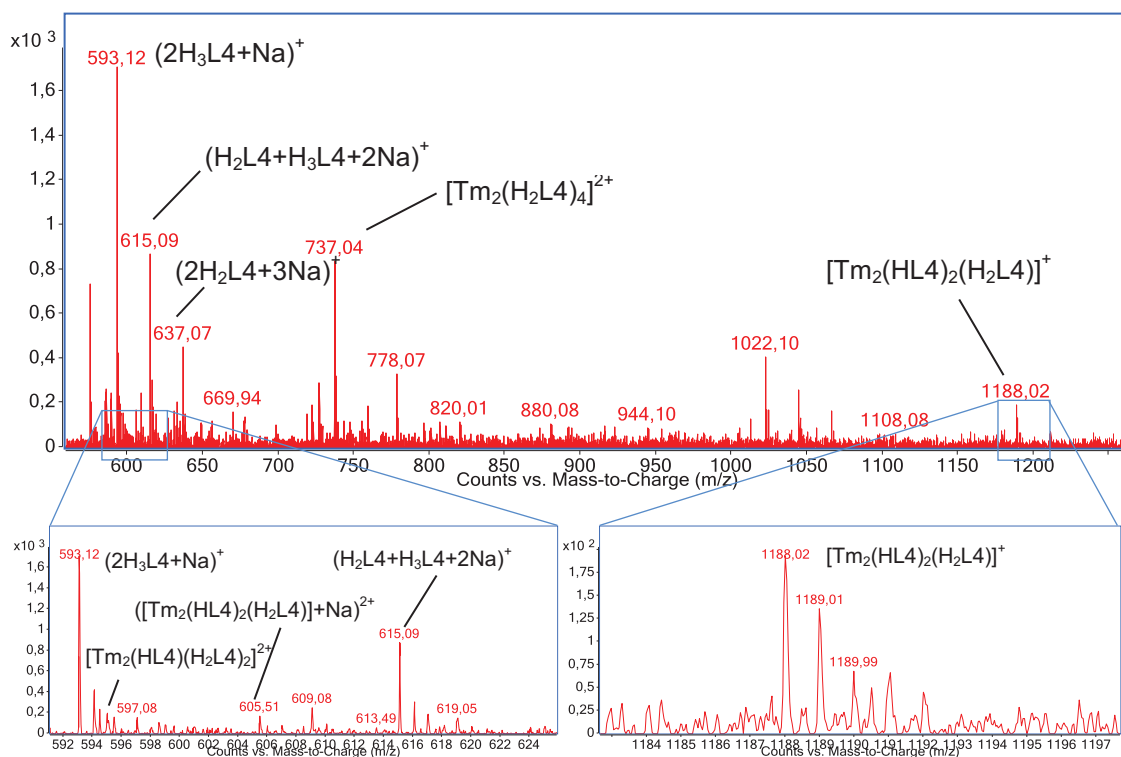


Figure V.A12. Electrospray mass spectrogram of complex $[Tm_2]$ (**23**) displaying the peaks of the free ligand and complex species.

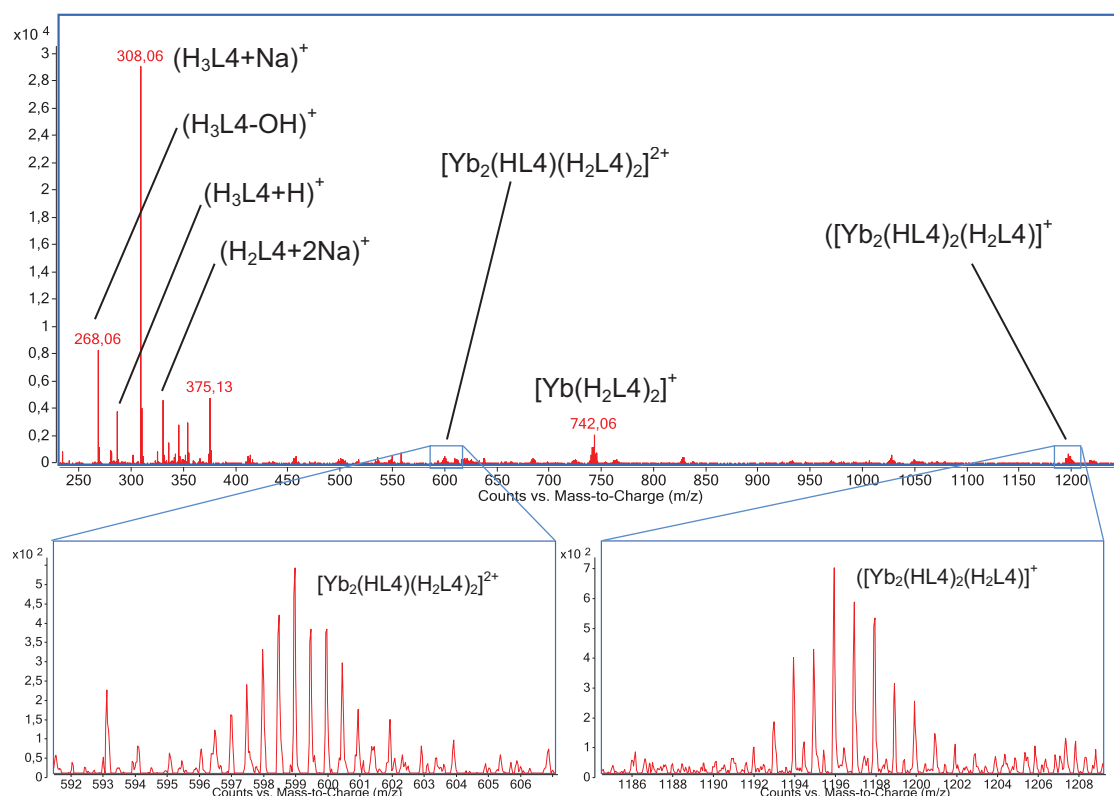


Figure V.A13. Electrospray mass spectrogram of complex $[Yb_2]$ (24) displaying the peaks of the free ligand and complex species.

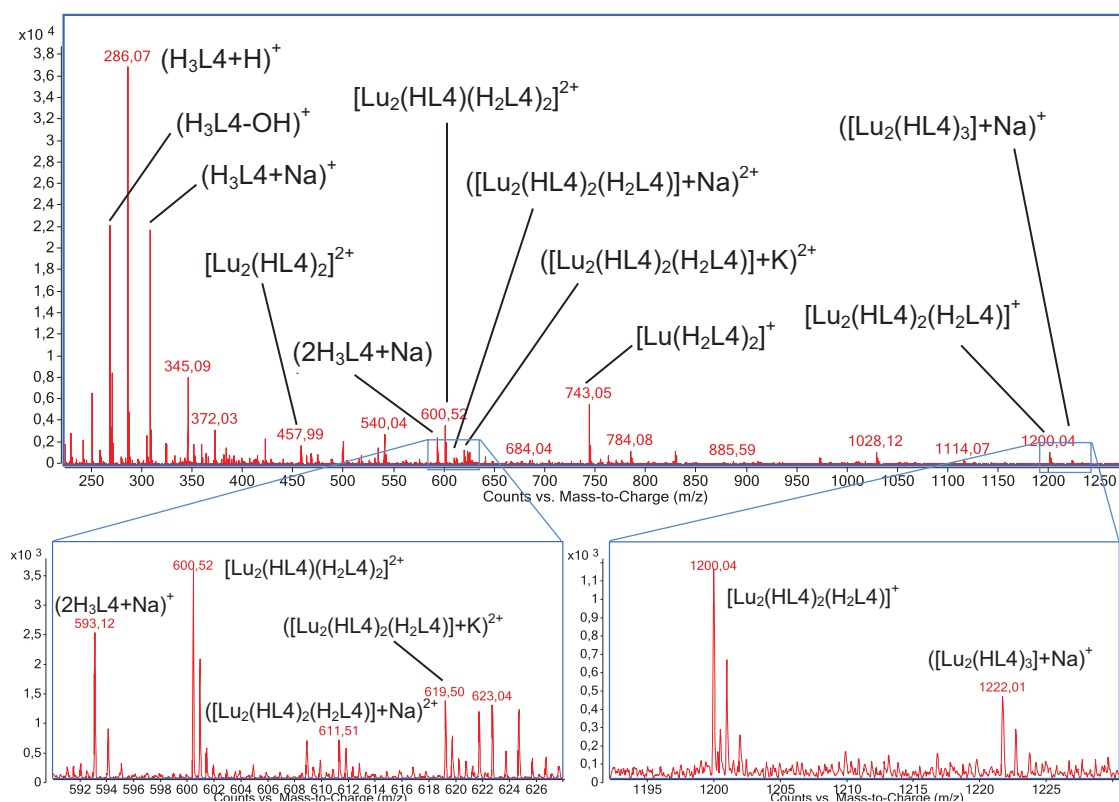


Figure S17. Electrospray mass spectrogram of complex $[Lu_2]$ (25) displaying the peaks of the free ligand and complex species.

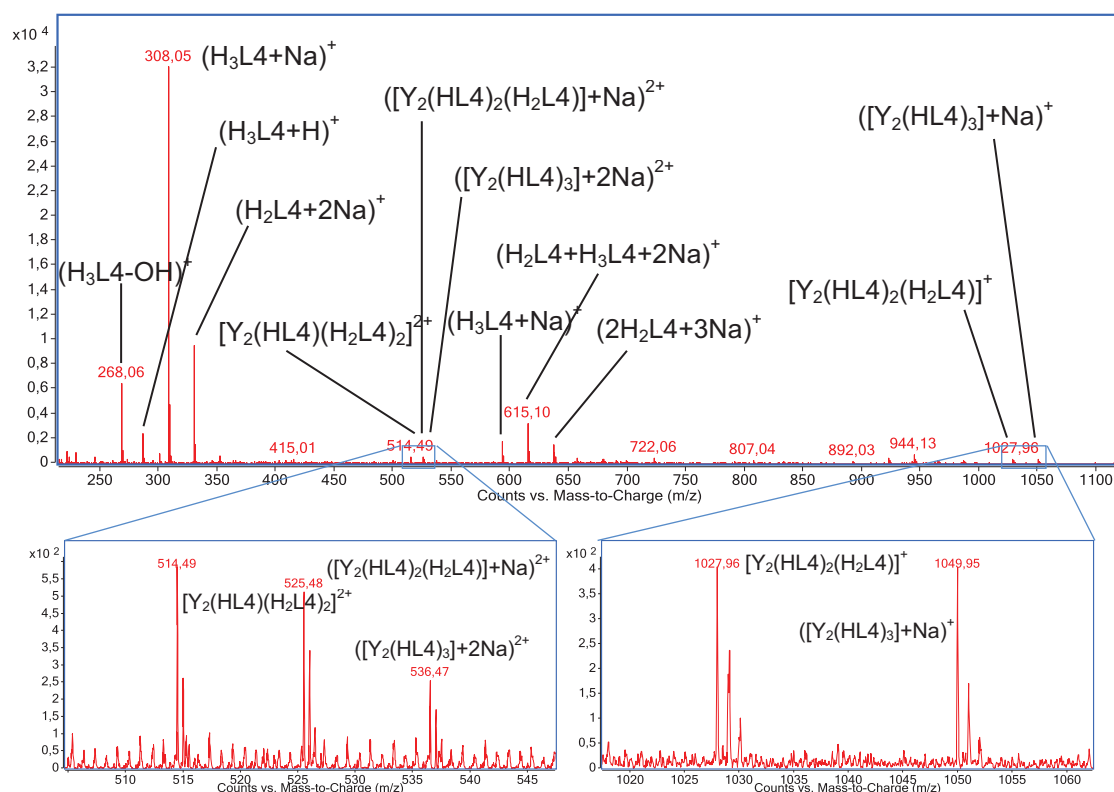


Figure V.A15. Electrospray mass spectrogram of complex $[Y_2]$ (**26**) displaying the peaks of the free ligand and complex species.

Table V.A4. Crystal data and structure refinement for compounds **27-30**

	Complex 27	Complex 28	Complex 29	Complex 30
Formula	$C_{80}H_{67}ClN_{10}Nd_2O_{17}$	$Gd_2C_{80}H_{67}ClN_{10}O_{17}$	$Tb_2C_{75}H_{58}ClN_9O_{15}$	$C_{75}H_{58}ClDy_2N_9O_{15}$
M_r	1764.37	1790.39	1678.59	1685.75
Crystal system			monoclinic	
Space group			$P2_1/c$	
λ (Å)	0.71073	0.7749	0.71073	0.71073
a (Å)	14.4880(11)	14.4830(10)	12.844(3)	12.7916(4)
b (Å)	15.5910(6)	15.5050(10)	16.584(4)	16.6444(4)
c (Å)	36.162(2)	35.862(3)	33.449(9)	33.4639(11)
β (°)	112.441(5)	112.539(3)	105.16(3)	105.187(3)
V (Å ³)	7549.8(8)	7438.0(9)	6877(3)	6875.9(4)
T [K]	150	100	150	150
Z			4	
ρ (g/cm ³)	1.552	1.599	1.621	1.628
Shape and colour	yellow plate	yellow plate	yellow block	yellow prism
Crystal size (mm ³)	0.23x0.07x0.02	0.24x0.06x0.04	0.25x0.20x0.17	0.12x0.10x0.09
Reflections	10833	18465	8589	11680
Parameters	1012	999	919	919
Restraints	658	64	270	144
R_{int}	0.1829	0.0676	0.1218	0.1399
R_1 [a]	0.0567	0.0359	0.0630	0.0655
wR_2 [b]	0.0868	0.0913	0.1296	0.1271
S	0.622	1.015	0.995	1.019

[a] $R_1 = \sum ||F_o| - |F_c|| / \sum |F_o|$, for $I > 2\sigma(I)$. [b] $wR_2 = \{\sum [w(F_o^2 - F_c^2)^2] / \sum [w(F_o^2)^2]\}^{1/2}$, for all data

Eu2-O1	2.392(8)	O3-Eu2-N2	106.1(3)
Eu2-O14	2.395(8)	N1-Eu2-N2	153.1(3)
Eu2-O6	2.397(8)	O8-Eu2-N2	58.3(3)
Eu2-O13	2.400(8)	O1-Eu2-Eu1	122.6(2)
Eu2-O16	2.458(9)	O14-Eu2-Eu1	98.9(2)
Eu2-O3	2.466(8)	O6-Eu2-Eu1	159.8(2)
Eu2-N1	2.535(11)	O13-Eu2-Eu1	38.75(1)
Eu2-O8	2.647(8)	O16-Eu2-Eu1	105.7(2)
Eu2-N2	2.652(10)	O3-Eu2-Eu1	37.7(2)
Eu1...Eu2	3.8190(9)	N1-Eu1-Eu2	85.2(2)
Eu1-O9	2.368(8)	O8-Eu1-Eu2	39.15(17)
Eu1-O11	2.385(10)	N2-Eu1-Eu2	97.5(2)
Eu1-O3	2.399(9)	O9-Eu1-O11	76.6(3)
Eu1-O8	2.432(8)	O9-Eu1-O3	112.7(3)
Eu1-O13	2.459(7)	O11-Eu1-O3	146.6(3)
Eu1-O4	2.461(9)	O9-Eu1-O8	72.0(3)
Eu1-O19	2.462(9)	O11-Eu1-O8	144.7(3)
Eu1-N3	2.511(11)	O3-Eu1-O8	63.8(3)
Eu1-N5	2.703(12)	O9-Eu1-O13	134.5(3)
O1-Eu2-O14	69.8(3)	O11-Eu1-O13	128.4(3)
O1-Eu2-O6	72.8(3)	O3-Eu1-O13	69.0(3)
O14-Eu2-O6	73.1(3)	O8-Eu1-O13	69.0(3)
O1-Eu2-O13	88.5(3)	O9-Eu1-O4	71.2(3)
O14-Eu2-O13	69.2(3)	O11-Eu1-O4	87.0(3)
O6-Eu2-O13	141.8(3)	O3-Eu1-O4	67.7(3)
O1-Eu2-O16	112.9(3)	O8-Eu1-O4	97.8(3)
O14-Eu2-O16	146.6(3)	O13-Eu1-O4	136.1(3)
O6-Eu2-O16	76.1(3)	O9-Eu1-O19	138.4(3)
O13-Eu2-O16	142.0(3)	O11-Eu1-O19	77.6(4)
O1-Eu2-O3	121.3(3)	O3-Eu1-O19	75.2(3)
O14-Eu2-O3	136.1(3)	O8-Eu1-O19	137.5(3)
O6-Eu2-O3	149.1(3)	O13-Eu1-O19	87.0(3)
O13-Eu2-O3	68.9(3)	O4-Eu1-O19	75.4(3)
O16-Eu2-O3	73.1(3)	O9-Eu1-N3	125.1(4)
O1-Eu2-N1	63.4(3)	O11-Eu1-N3	65.0(3)
O14-Eu2-N1	125.9(3)	O3-Eu1-N3	121.1(3)
O6-Eu2-N1	114.7(3)	O8-Eu1-N3	122.8(3)
O13-Eu2-N1	83.7(3)	O13-Eu1-N3	63.6(3)
O16-Eu2-N1	79.1(4)	O4-Eu1-N3	138.7(3)
O3-Eu2-N1	60.8(3)	O19-Eu1-N3	69.6(4)
O1-Eu2-O8	153.1(3)	O9-Eu1-N5	69.8(3)
O14-Eu2-O8	91.5(3)	O11-Eu1-N5	83.6(4)
O6-Eu2-O8	121.3(3)	O3-Eu1-N5	129.8(3)
O13-Eu2-O8	66.4(2)	O8-Eu1-N5	70.7(3)
O16-Eu2-O8	93.5(3)	O13-Eu1-N5	75.9(3)
O3-Eu2-O8	59.8(3)	O4-Eu1-N5	141.0(3)
N1-Eu2-O8	119.7(3)	O19-Eu1-N5	138.0(3)
O1-Eu2-N2	132.3(3)	N3-Eu1-N5	68.5(3)
O14-Eu2-N2	80.3(3)	O13-Eu2-N2	114.9(3)
O6-Eu2-N2	63.3(3)	O16-Eu2-N2	74.5(3)

Table V.A6 Selected interatomic distances (Å) and angles for complexes 27 to 30.

	Nd (27)	Gd (28)	Tb (29)	Dy (30)
Ln1-O4	2.385(8)	2.353(2)	2.409(6)	2.404(6)
Ln1-O8	2.395(7)	2.366(3)	2.406(8)	2.398(5)
Ln1-O11	2.401(7)	2.376(2)	2.320(8)	2.309(6)
Ln1-O3	2.465(8)	2.420(2)	2.320(6)	2.303(6)
Ln1-O9	2.470(6)	2.419(2)	2.347(8)	2.343(6)
Ln1-O16	2.472(9)	2.460(3)	-	-
Ln1-N5	-	-	2.644(9)	2.632(8)
Ln1-O13	2.512(6)	2.457(2)	2.432(6)	2.419(6)
Ln1-N3	2.517(8)	2.486(3)	2.505(10)	2.490(7)
Ln1-N4	2.715(10)	2.700(3)	2.652(10)	2.652(8)
Ln2-O6	2.394(8)	2.393(3)	2.377(8)	2.364(6)
Ln2-O1	2.415(7)	2.414(2)	2.373(7)	2.372(6)
Ln2-O14	2.431(7)	2.396(3)	2.423(7)	2.405(6)
Ln2-O13	2.468(6)	2.417(2)	2.394(7)	2.385(6)
Ln2-O8	2.538(6)	2.493(2)	2.537(6)	2.520(6)
Ln2-N2	2.611(11)	2.569(3)	2.547(9)	2.539(7)
Ln2-N1	2.625(10)	2.622(3)	2.540(10)	2.536(7)
Ln2-O3	2.635(8)	2.597(2)	2.493(6)	2.496(5)
Ln2-Cl1	2.810(3)	2.7758(9)	2.727(3)	2.725(2)
Ln1...Ln2	3.8770(9)	3.8127(3)	3.7853(10)	3.7748(6)
O4-Ln1-O8	113.2(2)	113.36(9)	98.4(2)	99.0(2)
O4-Ln1-O11	78.7(3)	76.18(8)	86.7(2)	85.2(2)
O8-Ln1-O11	146.1(3)	145.71(9)	147.2(3)	147.7(2)
O4-Ln1-O3	71.0(2)	72.12(8)	68.0(2)	68.4(2)
O8-Ln1-O3	65.2(3)	64.64(9)	65.6(2)	65.5(2)
O11-Ln1-O3	145.0(3)	144.54(9)	143.6(3)	142.8(2)
O4-Ln1-O9	70.6(3)	70.31(9)	71.0(2)	70.9(2)
O8-Ln1-O9	67.8(2)	68.91(9)	71.5(2)	72.3(2)
O11-Ln1-O9	88.7(2)	85.34(9)	79.8(3)	79.0(2)
O3-Ln1-O9	97.0(2)	98.40(8)	113.5(3)	113.8(2)
O4-Ln1-O16	134.4(2)	134.26(9)	-	-
O8-Ln1-O16	76.7(3)	76.86(9)	-	-
O11-Ln1-O16	73.3(3)	74.18(9)	-	-
O3-Ln1-O16	141.3(3)	140.76(9)	-	-
O9-Ln1-O16	73.5(3)	73.26(9)	-	-
O4-Ln1-O13	132.9(3)	134.62(8)	135.1(2)	135.2(2)
O8-Ln1-O13	69.1(2)	68.77(8)	68.1(3)	68.17(19)
O11-Ln1-O13	127.2(2)	129.20(8)	128.3(3)	129.0(2)
O3-Ln1-O13	68.4(2)	68.85(8)	67.5(2)	67.4(2)
O9-Ln1-O13	136.6(2)	137.17(9)	134.2(3)	135.1(2)
O16-Ln1-O13	92.7(2)	91.07(9)	-	-
O4-Ln1-N3	126.8(3)	126.32(10)	136.4(3)	136.3(2)
O8-Ln1-N3	118.9(3)	119.51(9)	123.7(3)	123.2(2)
O11-Ln1-N3	64.5(2)	65.88(9)	64.9(3)	65.7(2)
O3-Ln1-N3	122.4(3)	123.25(9)	116.5(3)	116.8(2)
O9-Ln1-N3	139.8(3)	137.61(9)	129.4(3)	128.8(2)
O16-Ln1-N3	70.4(3)	69.42(10)	-	-
O13-Ln1-N3	62.8(2)	63.43(8)	63.5(3)	63.3(2)
O4-Ln1-N4	70.0(3)	69.67(9)	74.2(3)	73.9(2)
O8-Ln1-N4	131.0(3)	130.91(9)	138.7(3)	138.1(2)
O11-Ln1-N4	82.6(3)	83.35(9)	74.0(3)	74.0(2)
O3-Ln1-N4	71.1(3)	71.13(9)	74.2(3)	73.8(2)
O9-Ln1-N4	140.5(3)	139.93(9)	137.2(3)	136.9(2)
O16-Ln1-N4	138.2(3)	138.37(9)	-	-
O13-Ln1-N4	75.2(3)	76.48(9)	88.3(3)	87.7(2)

	Nd (27)	Gd (28)	Tb (29)	Dy (30)
O13-Ln1-N4	75.2(3)	76.48(9)	88.3(3)	87.7(2)
O13-Ln1-N4	75.2(3)	76.48(9)	88.3(3)	87.7(2)
N3-Ln1-N4	68.5(3)	69.49(9)	66.7(3)	67.4(2)
O4-Ln1-Ln2	112.43(17)	113.75(6)	103.88(17)	104.53(14)
O8-Ln1-Ln2	39.51(16)	39.50(6)	41.32(16)	41.08(14)
O11-Ln1-Ln2	165.56(17)	167.28(6)	166.06(19)	166.60(15)
O3-Ln1-Ln2	42.17(19)	42.30(6)	39.79(15)	39.97(14)
O9-Ln1-Ln2	103.49(15)	105.21(6)	111.97(19)	112.62(14)
O16-Ln1-Ln2	102.48(18)	101.70(7)	-	-
O13-Ln1-Ln2	38.46(15)	38.15(5)	37.97(18)	37.90(14)
N3-Ln1-Ln2	101.06(19)	101.40(7)	101.3(2)	101.09(17)
N4-Ln1-Ln2	92.37(19)	92.59(7)	99.9(2)	99.53(18)
O6-Ln2-O1	69.7(3)	69.60(9)	69.3(3)	68.9(2)
O6-Ln2-O14	71.7(3)	71.05(9)	74.2(2)	74.5(2)
O1-Ln2-O14	69.9(2)	71.13(9)	73.7(2)	73.3(2)
O6-Ln2-O13	93.2(2)	91.19(8)	139.2(2)	139.9(2)
O1-Ln2-O13	136.8(2)	139.47(9)	86.5(2)	86.3(2)
O14-Ln2-O13	67.0(2)	68.89(8)	67.6(2)	68.3(2)
O6-Ln2-O8	117.8(3)	119.31(9)	125.6(3)	126.27(19)
O1-Ln2-O8	155.6(2)	153.11(9)	151.5(3)	151.2(2)
O14-Ln2-O8	134.0(2)	135.11(8)	86.8(2)	86.9(2)
O13-Ln2-O8	67.6(2)	67.41(8)	66.6(2)	66.72(19)
O6-Ln2-N2	62.2(3)	63.32(10)	64.6(3)	65.1(2)
O1-Ln2-N2	114.0(3)	112.37(10)	128.8(3)	128.8(2)
O14-Ln2-N2	126.5(3)	127.78(9)	73.5(3)	73.9(2)
O13-Ln2-N2	89.3(3)	87.55(9)	115.0(2)	116.0(2)
O8-Ln2-N2	59.3(3)	59.85(9)	61.2(3)	61.4(2)
O6-Ln2-N1	130.7(3)	129.70(9)	110.1(3)	108.7(2)
O1-Ln2-N1	63.0(3)	63.20(9)	63.3(3)	63.5(2)
O14-Ln2-N1	79.7(3)	78.09(9)	130.4(3)	130.6(2)
O13-Ln2-N1	111.6(3)	113.60(9)	85.5(3)	85.6(2)
O8-Ln2-N1	111.0(2)	110.67(8)	120.6(3)	121.1(2)
N2-Ln2-N1	152.4(2)	152.51(9)	154.9(3)	153.8(2)
O6-Ln2-O3	158.8(2)	156.62(8)	155.0(2)	154.6(2)
O1-Ln2-O3	121.1(3)	122.46(8)	117.1(3)	117.51(19)
O14-Ln2-O3	94.2(2)	93.08(8)	130.5(2)	130.6(2)
O13-Ln2-O3	66.4(2)	66.62(8)	65.4(2)	64.9(2)
O8-Ln2-O3	60.8(3)	60.32(8)	61.2(2)	60.92(19)
N2-Ln2-O3	120.1(3)	120.05(9)	114.1(3)	113.7(2)
N1-Ln2-O3	58.4(2)	59.42(8)	59.5(2)	60.3(2)
O6-Ln2-Cl1	102.0(2)	104.46(7)	80.92(19)	80.74(16)
O1-Ln2-Cl1	77.07(17)	75.49(7)	116.81(19)	117.37(16)
O14-Ln2-Cl1	146.53(17)	145.71(6)	147.2(2)	147.08(14)
O13-Ln2-Cl1	146.17(16)	145.01(6)	139.86(16)	139.32(15)
O8-Ln2-Cl1	78.63(16)	77.66(6)	90.81(17)	90.61(14)
N2-Ln2-Cl1	71.99(19)	72.68(7)	76.79(19)	76.12(17)
N1-Ln2-Cl1	80.86(18)	80.14(7)	78.1(2)	77.77(16)
O3-Ln2-Cl1	98.37(15)	98.28(6)	74.76(18)	74.65(15)
O6-Ln2-Nd2	125.93(18)	124.88(6)	162.73(19)	163.45(15)
O1-Ln2-Nd2	67.6(2)	160.02(7)	121.1(2)	121.08(14)
O14-Ln2-Nd2	62.2(3)	99.19(6)	94.86(16)	95.08(14)
O13-Ln2-Nd2	114.0(3)	38.92(6)	38.70(15)	38.54(14)
O8-Ln2-Nd2	126.5(3)	37.14(6)	38.77(19)	38.70(12)
N2-Ln2-Nd2	89.3(3)	87.46(7)	99.81(19)	100.00(16)
N1-Ln2-Nd2	59.3(3)	98.15(6)	87.2(2)	87.89(16)
O3-Ln2-Nd2	130.7(3)	38.84(5)	36.55(15)	36.35(14)

	Nd (27)	Gd (28)	Tb (29)	Dy (30)
O11-Ln1-N5	-	-	82.0(3)	82.5(2)
O3-Ln1-N5	-	-	134.0(3)	134.5(2)
O9-Ln1-N5	-	-	69.6(3)	69.6(2)
O8-Ln1-N5	-	-	73.4(3)	73.8(2)
O4-Ln1-N5	-	-	140.3(3)	140.2(2)
O13-Ln1-N5	-	-	78.9(2)	79.5(2)
N3-Ln1-N5	-	-	70.6(3)	70.0(2)
N5-Ln1-N4	-	-	136.8(3)	136.8(2)
N5-Ln1-Tb1	-	-	94.9(2)	95.20(18)

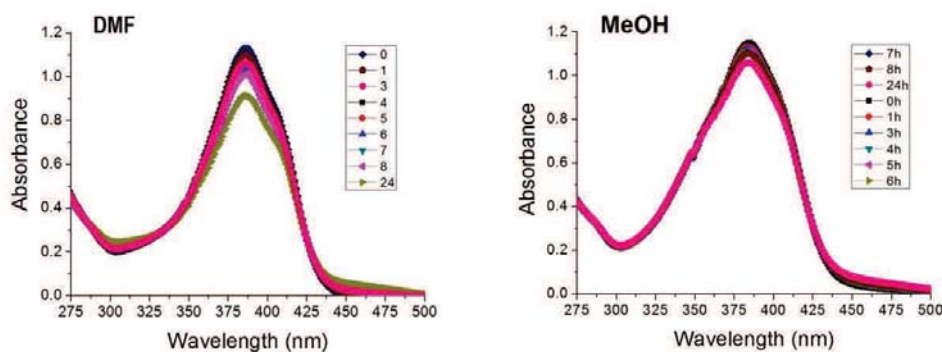


Figure V.A16. Absorption spectra of 10^{-5} M solutions of $[\text{Eu}_2(\text{HL4})_2(\text{H}_2\text{L4})(\text{NO}_3)(\text{py})(\text{H}_2\text{O})]$ (17) in DMF and MeOH, taken after several time intervals.

Table V.A7. Crystal data and structure refinement for compounds 31-34

	Complex 31	Complex 32	Complex 33	Complex 34
Formula	$\text{C}_{75}\text{H}_{62}\text{LaN}_{10}\text{O}_{20}\text{Pr}$	$\text{C}_{75}\text{H}_{60}\text{LaN}_{10}\text{O}_{19}\text{Tb}$	$\text{C}_{75}\text{H}_{60}\text{DyLaN}_{10}\text{O}_{19}$	$\text{C}_{75}\text{H}_{60}\text{HoLaN}_{10}\text{O}_{19}$
M_r	1703.17	1703.16	1706.74	1709.17
Crystal system			monoclinic	
Space group			$P2_1/c$	
λ (Å)	0.77490	0.77490	0.71073	0.71073
a (Å)	14.944(2)	14.484(2)	14.533(4)	14.4964(6)
b (Å)	15.583(2)	15.894(2)	15.8767(13)	15.8937(5)
c (Å)	33.435(3)	35.528(5)	35.750(5)	35.5286(12)
β (°)	110.735(4)	112.889(5)	112.898(14)	112.106(3)
V (Å ³)	7281.8(15)	7534.8(18)	7599(2)	7584.1(5)
T [K]	100	100	150	150
Z			4	
ρ (g/cm ³)	1.554	1.501	1.492	1.497
Shape and colour	yellow needle	yellow rod	yellow lath	yellow lath
Crystal size (mm ³)	0.48x0.07x0.02	0.15x0.10x0.03	0.23x0.05x0.02	0.44x0.15x0.14
Reflections	9829	22899	9272	12643
Parameters	967	955	955	1002
Restraints	299	236	315	533
R_{int}	0.0882	0.0642	0.1648	0.0695
R_1 [a]	0.0787	0.0506	0.0732	0.1107
wR_2 [b]	0.1875	0.1374	0.1674	0.2541
S	1.102	1.042	0.979	1.179

[a] $R_1 = \sum ||F_o| - |F_c|| / \sum |F_o|$, for $l > 2\sigma(l)$. [b] $wR_2 = \{\sum [w(F_o^2 - F_c^2)^2] / \sum [w(F_o^2)]\}^{1/2}$, for all data

Table V.A8. Crystal data and structure refinement for compounds 35-38

	Complex 35	Complex 36	Complex 37	Complex 38
Formula	C ₁₅₅ H ₁₂₅ Er ₂ La ₂ N ₂₁ O ₃₈	C ₆₅ H ₅₀ LaN ₈ O ₁₉ Y	C ₇₅ H ₆₄ CeN ₁₀ O ₂₀ Pr	C ₇₅ H ₆₀ CeDyN ₁₀ O ₁₉
M_r	3502.09	1474.95	1706.40	1707.95
Crystal system			monoclinic	
Space group			<i>P</i> 2 ₁ / <i>c</i>	
λ (Å)	0.77490	0.71073	0.77490	0.77490
a (Å)	14.5226(11)	14.465(2)	15.061(6)	14.454(2)
b (Å)	15.8712(11)	15.9220(10)	15.636(6)	15.833(2)
c (Å)	35.345(2)	35.520(3)	32.925(11)	35.482(3)
β (°)	112.646(2)	111.570(10)	110.636(14)	112.513(3)
V (Å³)	7518.6(9)	7607.8(13)	7256(5)	7501.3(15)
T [K]	100(2)	150	100	100
Z			4	
ρ (g/cm³)	1.546	1.288	1.562	1.512
Shape and colour	yellow needle	yellow parallelepiped	orange lath	orange rod
Crystal size (mm³)	0.50x0.10x0.10	0.28x0.05x0.05	0.30x0.02x0.02	0.25x0.01x0.01
Reflections	14111	9231	9141	13077
Parameters	1006	923	958	925
Restraints	371	559	192	288
R_{int}	0.0543	0.1465	0.0934	0.0607
R₁^[a]	0.0838	0.0593	0.0455	0.0704
wR₂^[b]	0.2003	0.1322	0.1163	0.1641
S	1.185	0.731	1.041	1.167

[a] $R_1 = \sum ||F_o| - |F_c|| / \sum |F_o|$, for $l > 2\sigma(l)$. [b] $wR_2 = \{\sum [w(F_o^2 - F_c^2)^2] / \sum [w(F_o^2)^2]\}^{1/2}$, for all data

Table V.A9. Crystal data and structure refinement for compounds 39-42

	Complex 39	Complex 40	Complex 41	Complex 42
Formula	C ₈₀ H ₆₅ CeHoN ₁₁ O ₁₉	C ₇₅ H ₆₀ CeErN ₁₀ O ₁₉	C ₆₅ H ₄₇ CeN ₈ O ₁₉ Tm	C ₇₅ H ₆₀ CeLuN ₁₀ O ₁₉
M_r	1789.48	1712.71	1553.16	1720.42
Crystal system			monoclinic	
Space group			<i>P</i> 2 ₁ / <i>c</i>	
λ (Å)	0.77490	0.71073	0.71073	0.73780
a (Å)	14.5077(13)	14.5502(3)	14.552(2)	14.502(3)
b (Å)	15.8645(14)	15.8974(3)	15.8950(10)	15.852(3)
c (Å)	35.520(3)	35.5552(9)	35.336(3)	35.312(9)
β (°)	112.729(3)	112.521(2)	111.699(7)	112.76(3)
V (Å³)	7540.3(11)	7597.1(3)	7594.2(13)	7486(3)
T [K]	100	150	150	100
Z			4	
ρ (g/cm³)	1.576	1.497	1.358	1.527
Shape and colour	yellow rod	yellow lath	orange plate	orange lath
Crystal size (mm³)	0,20x0.11x0.09	0.31x0.06x0.05	0.22x0.09x0.03	0.35x0.09x0.05
Reflections	22965	12933	6854	16452
Parameters	1106	940	835	932
Restraints	440	206	213	218
R_{int}	0.0533	0.1115	0.1456	-
R₁^[a]	0.0369	0.0569	0.0700	0.0535
wR₂^[b]	0.0933	0.1208	0.1604	0.1525
S	1.073	0.921	0.803	1.079

[a] $R_1 = \sum ||F_o| - |F_c|| / \sum |F_o|$, for $l > 2\sigma(l)$. [b] $wR_2 = \{\sum [w(F_o^2 - F_c^2)^2] / \sum [w(F_o^2)^2]\}^{1/2}$, for all data

Table V.A10. Crystal data and structure refinement for compounds 43-46

	Complex 43	Complex 44	Complex 45	Complex 46
Formula	C ₇₅ H ₆₀ CeN ₁₀ O ₁₉ Y	C ₇₅ H ₆₂ N ₁₀ NdO ₂₀ Pr	C ₇₅ H ₆₂ N ₁₀ O ₂₀ PrSm	C ₇₅ H ₆₂ EuN ₁₀ O ₂₀ Pr
M_r	1634.36	1708.50	1714.61	1716.22
Crystal system			monoclinic	
Space group			<i>P</i> 2 ₁ / <i>c</i>	
λ (Å)	0.77490	0.77490	0.77490	0.77490
a (Å)	14.450(3)	14.9637(11)	14.944(2)	14.923(2)
b (Å)	15.827(3)	15.6214(11)	15.664(2)	15.6485(8)
c (Å)	35.468(6)	32.655(2)	32.606(4)	32.395(7)
β (°)	112.707(6)	110.769(3)	110.857(5)	110.979(15)
V (Å³)	7483(2)	7137.2(8)	7132.4(16)	7063.5(18)
T [K]	100	150	150	100
Z			4	
ρ (g/cm³)	1.451	1.590	1.597	1.614
Shape and colour	orange needle	yellow needle	yellow needle	yellow rod
Crystal size (mm³)	0.40x0.09x0.03	0.21x0.01x0.01	0.18x0.02x0.02	0.50x0.10x0.05
Reflections	8403	18613	10885	19850
Parameters	1097	1006	1006	1007
Restraints	697	235	236	233
R_{int}	0.0926	0.0457	0.0390	0.0538
R₁^[a]	0.0583	0.0480	0.0341	0.0309
wR₂^[b]	0.1650	0.1176	0.0872	0.0768
S	1.041	1.203	1.177	1.017

[a] $R_1 = \sum ||F_o| - |F_c|| / \sum |F_o|$, for $I > 2\sigma(I)$. [b] $wR_2 = \{\sum [w(F_o^2 - F_c^2)^2] / \sum [w(F_o^2)^2]\}^{1/2}$, for all data

Table V.A11. Crystal data and structure refinement for compounds 48-52

	Complex 48	Complex 49	Complex 50	Complex 52
Formula	C ₈₀ H ₆₅ N ₁₁ O ₁₉ PrTb	C ₈₀ H ₆₅ DyN ₁₁ O ₁₉ Pr	C ₈₀ H ₆₅ HoN ₁₁ O ₁₉ Pr	C ₈₀ H ₆₅ N ₁₁ O ₁₉ PrTm
M_r	1784.26	1787.84	1790.27	1794.27
Crystal system			monoclinic	
Space group			<i>P</i> 2 ₁ / <i>c</i>	
λ (Å)	0.77490	0.77490	0.77490	0.77490
a (Å)	14.4957(10)	14.514(3)	14.552(7)	14.526(2)
b (Å)	15.8090(11)	15.799(3)	15.853(8)	15.823(2)
c (Å)	35.6637(19)	35.629(6)	35.858(15)	35.410(3)
β (°)	113.270(2)	113.034(6)	113.943(15)	112.544(3)
V (Å³)	7508.0(8)	7519(2)	7560(6)	7516.9(15)
T [K]	150	150	100	150
Z			4	
ρ (g/cm³)	1.579	1.579	1.573	1.585
Shape and colour	yellow rod	yellow rod	yellow rod	yellow plate
Crystal size (mm³)	0.35x0.10x0.08	0.70x0.20x0.20	0.30x0.02x0.02	0.16x0.02x0.02
Reflections	22891	22901	22973	18623
Parameters	991	1119	1095	1111
Restraints	140	581	329	666
R_{int}	0.0737	0.0746	0.0704	0.0864
R₁^[a]	0.0506	0.0366	0.0439	0.0474
wR₂^[b]	0.1355	0.0913	0.1116	0.1213
S	1.039	1.058	1.022	1.029

[a] $R_1 = \sum ||F_o| - |F_c|| / \sum |F_o|$, for $I > 2\sigma(I)$. [b] $wR_2 = \{\sum [w(F_o^2 - F_c^2)^2] / \sum [w(F_o^2)^2]\}^{1/2}$, for all data

Table V.A12. Crystal data and structure refinement for compounds 53-56

	Complex 53	Complex 54	Complex 55	Complex 56
Formula	C ₇₅ H ₆₀ N ₁₀ O ₁₉ PrYb	C ₇₅ H ₆₀ N ₁₀ O ₁₉ PrLu	C ₇₅ H ₆₂ N ₁₀ O ₂₀ PrY	C ₇₅ H ₆₀ N ₁₀ O ₁₉ NdSm
<i>M_r</i>	1719.28	1721.21	1653.17	1699.92
Crystal system			monoclinic	
Space group			<i>P</i> 2 ₁ / <i>c</i>	
λ (Å)	0.77490	0.77749	0.77749	0.77749
<i>a</i> (Å)	14.5212(9)	14.584(2)	14.890(3)	14.457(2)
<i>b</i> (Å)	15.8174(10)	15.815(2)	15.735(3)	15.691(3)
<i>c</i> (Å)	35.3296(19)	35.395(5)	32.224(7)	35.954(5)
β (°)	112.064(2)	112.736(5)	111.172(9)	112.634(5)
<i>V</i> (Å ³)	7520.5(8)	7529.4(18)	7040(2)	7528(2)
<i>T</i> [K]	100	100	100	100
<i>Z</i>			4	
ρ (g/cm ³)	1.518	1.518	1.560	1.500
Shape and colour	yellow rod	yellow rod	yellow block	yellow lath
Crystal size (mm ³)	0.80x0.10x0.10	0.34x0.12x0.10	0.30x0.20x0.10	0.32x0.10x0.07
Reflections	22829	9516	7386	18079
Parameters	1028	993	970	987
Restraints	158	627	70	480
<i>R</i> _{int}	0.0611	0.0735	0.0953	0.0856
<i>R</i> ₁ ^[a]	0.0605	0.1257	0.0463	0.1058
<i>wR</i> ₂ ^[b]	0.1502	0.2922	0.1207	0.2776
<i>S</i>	1.128	1.179	1.041	1.116

[a] $R_1 = \sum ||F_o| - |F_c|| / \sum |F_o|$, for $I > 2\sigma(I)$. [b] $wR_2 = \{\sum [w(F_o^2 - F_c^2)^2] / \sum [w(F_o^2)^2]\}^{1/2}$, for all data

Table V.A13. Crystal data and structure refinement for compounds 57-60

	Complex 57	Complex 58	Complex 59	Complex 60
Formula	C ₇₅ H ₆₀ GdN ₁₀ NdO ₁₉	C ₇₅ H ₆₀ N ₁₀ NdO ₁₉ Tb	C ₇₅ H ₆₀ N ₁₀ NdO ₁₉ Tm	C ₇₅ H ₆₀ N ₁₀ NdO ₁₉ Yb
<i>M_r</i>	1706.82	1708.49	1718.50	1722.61
Crystal system			monoclinic	
Space group			<i>P</i> 2 ₁ / <i>c</i>	
λ (Å)	0.77490	0.77490	0.77490	0.77490
<i>a</i> (Å)	14.880(2)	14.467(2)	14.536(2)	14.496(2)
<i>b</i> (Å)	15.646(2)	15.802(3)	15.811(2)	15.787(2)
<i>c</i> (Å)	32.827(4)	35.562(5)	35.427(4)	35.510(4)
β (°)	110.916(5)	112.366(5)	112.985(4)	112.678(4)
<i>V</i> (Å ³)	7138.9(16)	7518(2)	7495.7(16)	7498.1(16)
<i>T</i> [K]	100	100	100	100
<i>Z</i>			4	
ρ (g/cm ³)	1.588	1.509	1.523	1.526
Shape and colour	yellow lath	yellow needle	yellow lath	yellow needle
Crystal size (mm ³)	0.32x0.08x0.07	0.42x0.06x0.06	0.14x0.03x0.02	0.60x0.05x0.04
Reflections	17584	17078	8052	19262
Parameters	1016	1059	932	1040
Restraints	267	708	604	458
<i>R</i> _{int}	0.0598	0.0666	0.0847	0.0552
<i>R</i> ₁ ^[a]	0.0707	0.0553	0.1232	0.0707
<i>wR</i> ₂ ^[b]	0.1826	0.1334	0.2932	0.1924
<i>S</i>	1.093	1.199	1.178	1.134

[a] $R_1 = \sum ||F_o| - |F_c|| / \sum |F_o|$, for $I > 2\sigma(I)$. [b] $wR_2 = \{\sum [w(F_o^2 - F_c^2)^2] / \sum [w(F_o^2)^2]\}^{1/2}$, for all data

Table V.A14. Crystal data and structure refinement for compounds 61-64

	Complex 61	Complex 62	Complex 63	Complex 64
Formula	C ₈₀ H ₆₅ LuN ₁₁ NdO ₁₉	C ₇₅ H ₆₀ NdN ₁₀ O ₁₉ Y	C ₇₀ H ₅₅ GdN ₉ O ₁₉ Sm	C ₇₀ H ₆₀ N ₁₀ O ₁₉ SmTb
M_r	1803.64	1638.48	1633.83	1714.60
Crystal system			monoclinic	
Space group			<i>P2₁/c</i>	
λ (Å)	0.77490	0.77490	0.77490	0.77490
a (Å)	14.4930(10)	14.493(5)	14.365(3)	14.818(2)
b (Å)	15.7398(11)	15.819(5)	15.368(4)	15.674(2)
c (Å)	35.523(2)	35.570(10)	34.471(7)	32.990(4)
β (°)	112.656(2)	112.667(12)	110.370(8)	110.956(5)
V (Å³)	7478.1(8)	7525(4)	7134(3)	7155.4(16)
T [K]	100	100	100	100
Z			4	
ρ (g/cm³)	1.602	1.446	1.521	1.592
Shape and colour	yellow needle	yellow needle	yellow lath	yellow plate
Crystal size (mm³)	0.33x0.02x0.02	0.30x0.04x0.03	0.09x0.06x0.04	0.08x0.08x0.04
Reflections	8829	14332	7519	6437
Parameters	1056	1065	901	949
Restraints	570	693	198	166
R_{int}	0.0788	0.0947	0.0930	0.0679
R₁^[a]	0.0564	0.0641	0.0754	0.0560
wR₂^[b]	0.1437	0.1800	0.1531	0.1634
S	1.074	1.047	1.096	1.044

[a] $R_1 = \sum ||F_o| - |F_c|| / \sum |F_o|$, for $I > 2\sigma(I)$. [b] $wR_2 = \{\sum [w(F_o^2 - F_c^2)^2] / \sum [w(F_o^2)^2]\}^{1/2}$, for all data

Table V.A15. Crystal data and structure refinement for compounds 65-68

	Complex 65	Complex 66	Complex 67	Complex 68
Formula	C ₈₀ H ₆₅ N ₁₁ O ₁₉ EuTb	C ₇₅ H ₆₀ EuN ₁₀ O ₁₉ Yb	C ₇₅ H ₆₀ EuN ₁₀ O ₁₉ Lu	C ₇₅ H ₆₀ EuN ₁₀ O ₁₉ Y
M_r	1795.31	1730.33	1732.26	1646.20
Crystal system			monoclinic	
Space group			<i>P2₁/c</i>	
λ (Å)	0.71073	0.73800	0.73800	0.73800
a (Å)	14.2902(8)	14.287(3)	14.181(3)	14.241(3)
b (Å)	15.4525(8)	15.502(3)	15.387(3)	15.415(3)
c (Å)	35.339(2)	34.032(9)	34.748(9)	34.478(9)
β (°)	109.735(5)	110.45(3)	110.54(3)	110.33(3)
V (Å³)	7345.2(7)	7062(3)	7100(3)	7097(3)
T [K]	150	100	100	100
Z			4	
ρ (g/cm³)	1.623	1.627	1.621	1.541
Shape and colour	yellow lath	yellow rod	yellow lath	yellow rod
Crystal size (mm³)	0.19x0.05x0.03	0.20x0.08x0.05	0.28x0.07x0.05	0.40x0.07x0.05
Reflections	7666	9858	13810	10158
Parameters	961	941	1004	1004
Restraints	411	251	345	373
R_{int}	0.1918	-	-	-
R₁^[a]	0.0895	0.0605	0.0480	0.1140
wR₂^[b]	0.2252	0.1843	0.1456	0.3413
S	1.089	1.033	1.051	1.095

[a] $R_1 = \sum ||F_o| - |F_c|| / \sum |F_o|$, for $I > 2\sigma(I)$. [b] $wR_2 = \{\sum [w(F_o^2 - F_c^2)^2] / \sum [w(F_o^2)^2]\}^{1/2}$, for all data

Table V.A16. Crystal data and structure refinement for compounds 69-73

	Complex 69	Complex 71	Complex 72	Complex 73
Formula	C ₇₅ H ₆₀ HoN ₁₀ O ₁₉ Tb	C ₈₀ H ₆₅ DyLuN ₁₁ O ₁₉	C ₇₅ H ₆₀ HoN ₁₀ O ₁₉ Tm	C ₇₅ H ₅₇ Ce _{0.70} N ₁₀ O ₁₉ Y _{1.30}
<i>M_r</i>	1729.18	1821.90	1739.19	1615.97
Crystal system			monoclinic	
Space group			<i>P</i> 2 ₁ / <i>c</i>	
λ (Å)	0.77490	0.71073	0.77490	0.71073
<i>a</i> (Å)	14.221(5)	14.0266(7)	14.211(3)	14.4500(10)
<i>b</i> (Å)	15.407(5)	15.5088(8)	15.441(3)	15.867(2)
<i>c</i> (Å)	33.780(10)	35.285(2)	34.343(6)	35.483(3)
β (°)	110.325(12)	109.151(3)	110.650(7)	110.535(7)
<i>V</i> (Å ³)	6940(4)	7251.0(7)	7052(2)	7618.5(13)
<i>T</i> [K]	100	100	100	150
<i>Z</i>			4	
ρ (g/cm ³)	1.655	1.669	1.638	1.409
Shape and colour	yellow lath	yellow lath	yellow rod	orange plate
Crystal size (mm ³)	0.10x0.06x0.02	0.20x0.06x0.08	0.25x0.05x0.05	0.16x0.06x0.02
Reflections	7357	14679	12009	7964
Parameters	964	920	964	932
Restraints	359	404	227	347
<i>R</i> _{int}	0.0475	0.1510	0.0742	0.2088
<i>R</i> ₁ ^[a]	0.0842	0.0986	0.0871	0.0973
<i>wR</i> ₂ ^[b]	0.1932	0.2488	0.1911	0.2721
<i>S</i>	1.127	1.028	1.203	1.022

[a] $R_1 = \sum (|F_o| - |F_c|) / \sum |F_o|$, for $I > 2\sigma(I)$. [b] $wR_2 = \{\sum [w(F_o^2 - F_c^2)^2] / \sum [w(F_o^2)^2]\}^{1/2}$, for all data

Table V.A17 Selected interatomic distances (Å) and angles for complex 31

La1-O1	2.465(8)	O14-La1-N1	76.7(2)
La1-O6	2.466(7)	O13-La1-N1	109.8(3)
La1-O14	2.497(7)	O8-La1-N1	109.8(2)
La1-O13	2.514(8)	O16-La1-N1	67.0(3)
La1-O8	2.548(7)	N2-La1-N1	162.6(3)
La1-O16	2.610(9)	O3-La1-N1	57.3(3)
La1-N2	2.653(8)	O1-La1-O17	73.2(3)
La1-O3	2.695(7)	O6-La1-O17	78.5(3)
La1-N1	2.724(8)	O14-La1-O17	137.5(3)
La1-O17	2.749(11)	O13-La1-O17	141.7(3)
La1...Pr1	3.9071(10)	O8-La1-O17	86.8(3)
Pr1-O4	2.419(7)	O16-La1-O17	46.8(3)
Pr1-O11	2.430(10)	N2-La1-O17	62.6(3)
Pr1-O8	2.453(9)	O3-La1-O17	126.6(3)
Pr1-O3	2.486(8)	N1-La1-O17	105.9(3)
Pr1-O9	2.499(8)	O1-La1-Pr1	156.01(19)
Pr1-O13	2.504(7)	O6-La1-Pr1	121.52(19)
Pr1-O19	2.534(8)	O14-La1-Pr1	196.58(18)
Pr1-N3	2.567(10)	O13-La1-Pr1	138.78(16)
Pr1-N5	2.749(11)	O8-La1-Pr1	37.77(19)
O1-La1-O6	74.9(2)	O16-La1-Pr1	103.5(2)
O1-La1-O14	71.4(3)	N2-La1-Pr1	81.8(2)
O6-La1-O14	70.1(3)	O3-La1-Pr1	39.07(16)
O1-La1-O13	137.3(3)	N1-La1-Pr1	96.1(2)
O6-La1-O13	87.9(3)	O17-La1-Pr1	124.6(2)

O14-La1-O13	13 65.9(2)	O4-Pr1-O11	78.7(3)
O1-La1-O8	153.5(3)	O4-Pr1-O8	111.8(3)
O6-La1-O8	118.7(2)	O11-Pr1-O8	147.5(3)
O14-La1-O8	133.3(3)	O4-Pr1-O3	70.5(2)
O13-La1-O8	68.6(2)	O11-Pr1-O3	144.1(3)
O1-La1-O16	76.4(3)	O8-Pr1-O3	64.7(2)
O6-La1-O16	123.5(3)	O4-Pr1-O9	71.9(3)
O14-La1-O16	139.8(3)	O11-Pr1-O9	90.4(3)
O13-La1-O16	142.2(3)	O8-Pr1-O9	65.9(3)
O8-La1-O16	77.2(3)	O3-Pr1-O9	97.0(3)
O1-La1-N2	122.2(3)	O4-Pr1-O13	133.7(2)
O6-La1-N2	61.8(3)	O11-Pr1-O13	125.7(3)
O14-La1-N2	120.8(3)	O8-Pr1-O13	70.3(2)
O13-La1-N2	79.4(3)	O3-Pr1-O13	69.6(2)
O8-La1-N2	58.6(3)	O9-Pr1-O13	135.6(3)
O16-La1-N2	96.6(3)	O4-Pr1-O19	139.2(3)
O1-La1-O3	118.6(2)	O11-Pr1-O19	77.4(3)
O6-La1-O3	153.0(3)	O8-Pr1-O19	75.4(3)
O14-La1-O3	91.2(2)	O3-Pr1-O19	138.4(3)
O13-La1-O3	66.2(2)	O9-Pr1-O19	75.7(3)
O8-La1-O3	60.4(2)	O13-Pr1-O19	87.1(3)
O16-La1-O3	83.4(3)	O4-Pr1-N3	126.7(3)
N2-La1-O3	117.3(3)	O11-Pr1-N3	63.5(3)
O1-La1-N1	61.4(3)	O8-Pr1-N3	120.4(3)
O3-Pr1-N3	122.9(3)	N3-Pr1-N5	68.3(3)
O9-Pr1-N3	139.0(3)	O4-Pr1-La1	112.9(2)
O13-Pr1-N3	62.4(3)	O11-Pr1-La1	164.6(2)
O19-Pr1-N3	68.4(3)	O8-Pr1-La1	139.51(16)
O4-Pr1-N5	70.5(3)	O3-Pr1-La1	143.10(16)
O11-Pr1-N5	81.9(4)	O9-Pr1-La1	102.7(2)
O8-Pr1-N5	130.5(3)	O13-Pr1-La1	38.96(18)
O3-Pr1-N5	70.9(3)	O19-Pr1-La1	97.7(2)
O9-Pr1-N5	142.4(3)	N3-Pr1-La1	101.1(2)
O13-Pr1-N5	74.8(3)	N5-Pr1-La1	92.3(3)
O19-Pr1-N5	136.7(3)		

Table V.A18 Selected interatomic distances (Å) and angles for complex 32

Tb1-O4	2.344(3)	O9-Tb1-La2	105.37(7)
Tb1-O11	2.344(3)	O19-Tb1-La2	100.53(8)
Tb1-O8	2.367(3)	O13-Tb1-La2	40.14(6)
Tb1-O3	2.424(3)	N3-Tb1-La2	103.36(7)
Tb1-O9	2.428(3)	N5-Tb1-La2	92.23(8)
Tb1-O19	2.431(3)	O6-La2-O14	70.07(10)
Tb1-O13	2.438(3)	O6-La2-O1	76.83(10)
Tb1-N3	2.475(3)	O14-La2-O1	71.18(10)
Tb1-N5	2.687(4)	O6-La2-O13	89.96(10)
Tb1...La2	3.8799(4)	O14-La2-O13	66.18(9)
La2-O6	2.468(3)	O1-La2-O13	137.34(10)
La2-O14	2.481(3)	O6-La2-O8	116.47(10)
La2-O1	2.493(3)	O14-La2-O8	131.72(9)
La2-O13	2.556(3)	O1-La2-O8	155.40(10)
La2-O8	2.581(3)	O13-La2-O8	66.07(9)
La2-N2	2.650(4)	O6-La2-N2	61.99(10)
La2-O16	2.650(3)	O14-La2-N2	123.46(10)

La2-O3	2.697(3)	O1-La2-N2	121.11(11)
La2-N1	2.753(3)	O13-La2-N2	85.06(10)
La2-O17	2.783(4)	O8-La2-N2	58.22(10)
O4-Tb1-O11	73.83(9)	O6-La2-O16	116.55(11)
O4-Tb1-O8	114.43(10)	O14-La2-O16	149.66(10)
O11-Tb1-O8	143.51(10)	O1-La2-O16	81.38(11)
O4-Tb1-O3	72.03(9)	O13-La2-O16	139.18(9)
O11-Tb1-O3	143.18(10)	O8-La2-O16	74.15(10)
O8-Tb1-O3	66.10(10)	N2-La2-O16	81.68(11)
O4-Tb1-O9	70.38(10)	O6-La2-O3	154.65(10)
O11-Tb1-O9	83.05(10)	O14-La2-O3	94.07(9)
O8-Tb1-O9	68.37(9)	O1-La2-O3	117.71(9)
O3-Tb1-O9	98.03(9)	O13-La2-O3	65.16(8)
O4-Tb1-O19	135.19(10)	O8-La2-O3	59.31(9)
O11-Tb1-O19	75.09(11)	N2-La2-O3	117.25(9)
O8-Tb1-O19	75.73(11)	O16-La2-O3	87.26(9)
O3-Tb1-O19	140.91(10)	O6-La2-N1	134.02(10)
O9-Tb1-O19	74.54(10)	O14-La2-N1	79.93(9)
O4-Tb1-O13	135.49(9)	O1-La2-N1	60.60(10)
O11-Tb1-O13	129.37(9)	O13-La2-N1	109.14(9)
O8-Tb1-O13	71.29(10)	O8-La2-N1	109.52(9)
O3-Tb1-O13	71.23(8)	N2-La2-N1	156.50(10)
O9-Tb1-O13	139.08(10)	O16-La2-N1	75.38(10)
O19-Tb1-O13	89.30(10)	O3-La2-N1	57.25(9)
O4-Tb1-N3	123.41(11)	O6-La2-O17	70.02(12)
O11-Tb1-N3	66.04(10)	O14-La2-O17	125.73(11)
O8-Tb1-N3	121.69(11)	O1-La2-O17	65.09(12)
O3-Tb1-N3	124.72(10)	O13-La2-O17	146.82(10)
O9-Tb1-N3	136.99(10)	O8-La2-O17	98.71(11)
O19-Tb1-N3	69.25(11)	N2-La2-O17	62.36(11)
O13-Tb1-N3	63.39(9)	O16-La2-O17	46.81(11)
O4-Tb1-N5	70.78(10)	O3-La2-O17	134.02(10)
O11-Tb1-N5	84.83(11)	N1-La2-O17	103.70(10)
O8-Tb1-N5	131.65(10)	O6-La2-Tb1	121.98(7)
O3-Tb1-N5	71.31(10)	O14-La2-Tb1	97.25(6)
O9-Tb1-N5	141.12(10)	O1-La2-Tb1	154.11(8)
O19-Tb1-N5	136.64(11)	O13-La2-Tb1	37.93(6)
O13-Tb1-N5	74.31(10)	O8-La2-Tb1	36.43(6)
N3-Tb1-N5	67.51(11)	N2-La2-Tb1	84.70(7)
O4-Tb1-La2	114.88(7)	O16-La2-Tb1	102.22(7)
O11-Tb1-La2	169.33(7)	O3-La2-Tb1	38.19(5)
O8-Tb1-La2	40.36(7)	N1-La2-Tb1	95.14(7)
O3-Tb1-La2	43.45(6)	O17-La2-Tb1	

Table V.A19 Selected interatomic distances (Å) and angles for complex 33

Dy1-O11	2.359(8)	O14-La1-N1	76.7(2)
Dy1-O9	2.362(9)	O13-La1-N1	109.8(3)
Dy1-O3	2.363(9)	O8-La1-N1	109.8(2)
Dy1-O8	2.434(8)	O16-La1-N1	67.0(3)
Dy1-O4	2.435(8)	N2-La1-N1	162.6(3)
Dy1-O13	2.448(7)	O3-La1-N1	57.3(3)
Dy1-O19	2.452(9)	O1-La1-O17	73.2(3)
Dy1-N3	2.478(10)	O6-La1-O17	78.5(3)
Dy1-N5	2.701(11)	O14-La1-O17	137.5(3)
Dy1...La2	3.8833(10)	O13-La1-O17	141.7(3)

La2-O14	2.478(9)	O13-Dy1-La2	39.78(19)
La2-O1	2.485(9)	O19-Dy1-La2	100.7(2)
La2-O6	2.500(8)	N3-Dy1-La2	103.7(2)
La2-O13	2.542(8)	N5-Dy1-La2	92.3(2)
La2-O3	2.585(8)	O14-La2-O1	70.9(3)
La2-N1	2.640(11)	O14-La2-O6	70.7(3)
La2-O16	2.648(9)	O1-La2-O6	76.6(3)
La2-O8	2.685(8)	O14-La2-O13	66.0(3)
La2-N2	2.739(11)	O1-La2-O13	90.8(3)
La2-O17	2.810(12)	O6-La2-O13	136.7(3)
O11-Dy1-O9	74.1(3)	O14-La2-O3	131.8(3)
O11-Dy1-O3	143.3(3)	O1-La2-O3	116.2(3)
O9-Dy1-O3	114.5(3)	O6-La2-O3	155.9(3)
O11-Dy1-O8	143.8(3)	O13-La2-O3	66.2(3)
O9-Dy1-O8	72.3(3)	O14-La2-N1	123.6(3)
O3-Dy1-O8	65.9(3)	O1-La2-N1	61.4(3)
O11-Dy1-O4	83.2(3)	O6-La2-N1	121.1(3)
O9-Dy1-O4	70.4(3)	O13-La2-N1	85.6(3)
O3-Dy1-O4	68.3(3)	O3-La2-N1	58.3(3)
O8-Dy1-O4	97.8(3)	O14-La2-O16	149.8(3)
O11-Dy1-O13	129.6(3)	O1-La2-O16	115.5(3)
O9-Dy1-O13	134.9(3)	O6-La2-O16	82.0(3)
O3-Dy1-O13	71.2(3)	O13-La2-O16	139.2(3)
O8-Dy1-O13	70.5(3)	O3-La2-O16	74.1(3)
O4-Dy1-O13	139.1(3)	N1-La2-O16	81.2(3)
O11-Dy1-O19	74.8(3)	O14-La2-O8	94.3(3)
O9-Dy1-O19	134.7(3)	O1-La2-O8	155.6(3)
O3-Dy1-O19	75.4(3)	O6-La2-O8	117.6(3)
O8-Dy1-O19	140.5(3)	O13-La2-O8	65.1(2)
O4-Dy1-O19	73.9(3)	O3-La2-O8	59.3(3)
O13-Dy1-O19	90.4(3)	N1-La2-O8	117.4(3)
O11-Dy1-N3	65.5(3)	O16-La2-O8	87.3(3)
O9-Dy1-N3	123.5(3)	O14-La2-N2	79.7(3)
O3-Dy1-N3	121.6(3)	O1-La2-N2	133.9(3)
O8-Dy1-N3	125.3(3)	O6-La2-N2	60.3(3)
O4-Dy1-N3	136.5(3)	O13-La2-N2	108.9(3)
O13-Dy1-N3	64.2(3)	O3-La2-N2	109.9(3)
O19-Dy1-N3	69.4(3)	N1-La2-N2	156.6(3)
O11-Dy1-N5	84.9(3)	O16-La2-N2	75.8(3)
O9-Dy1-N5	70.5(3)	O8-La2-N2	57.4(3)
O3-Dy1-N5	131.8(3)	O14-La2-O17	126.1(3)
O8-Dy1-N5	71.5(3)	O1-La2-O17	69.7(3)
O4-Dy1-N5	140.8(3)	O6-La2-O17	65.6(3)
O13-Dy1-N5	74.3(3)	O13-La2-O17	147.4(3)
O19-Dy1-N5	137.4(3)	O3-La2-O17	98.5(3)
N3-Dy1-N5	68.2(3)	N1-La2-O17	62.3(3)
O9-Dy1-La2	114.8(2)	O16-La2-O17	46.1(3)
O3-Dy1-La2	40.4(2)	O8-La2-O17	133.3(3)
O8-Dy1-La2	43.1(2)	N2-La2-O17	103.4(3)
O4-Dy1-La2	105.3(2)	O14-La2-Dy1	97.43(19)
O1-La2-Dy1	122.4(2)	O16-La2-Dy1	102.1(2)
O6-La2-Dy1	154.0(2)	O8-La2-Dy1	38.29(18)
O13-La2-Dy1	38.03(16)	N2-La2-Dy1	95.4(2)
O3-La2-Dy1	36.3(2)	O17-La2-Dy1	134.8(2)
N1-La2-Dy1	84.8(2)		

Ho1-O11	2.326(9)	O6-La2-O14	70.4(3)
Ho1-O4	2.336(9)	O6-La2-O1	75.9(3)
Ho1-O8	2.344(9)	O14-La2-O1	71.3(3)
Ho1-O9	2.388(9)	O6-La2-O13	91.7(3)
Ho1-O3	2.413(8)	O1-La2-O13	66.0(3)
Ho1-O13	2.416(10)	O1-La2-O13	137.2(3)
Ho1-O19	2.429(10)	O6-La2-O8	116.3(3)
Ho1-N3	2.444(10)	O14-La2-O8	130.9(3)
Ho1-N5	2.683(13)	O1-La2-O8	156.3(3)
Ho1...La2	3.8645(10)	O13-La2-O8	65.3(3)
La2-O6	2.460(10)	O6-La2-N2	61.7(4)
La2-O14	2.472(10)	O14-La2-N2	123.1(4)
La2-O1	2.496(9)	O1-La2-N2	120.6(4)
La2-O13	2.565(9)	O13-La2-N2	85.9(3)
La2-O8	2.566(9)	O8-La2-N2	58.3(4)
La2-N2	2.634(14)	O6-La2-O16	115.7(4)
La2-O16	2.666(11)	O14-La2-O16	150.6(3)
La2-O3	2.692(9)	O1-La2-O16	82.1(4)
La2-N1	2.756(11)	O13-La2-O16	138.3(3)
La2-O17	2.799(12)	O8-La2-O16	74.3(3)
O11-Ho1-O4	73.2(3)	N2-La2-O16	81.2(4)
O11-Ho1-O8	143.0(4)	O6-La2-O3	156.4(3)
O4-Ho1-O8	115.3(4)	O14-La2-O3	94.7(3)
O11-Ho1-O9	81.8(3)	O1-La2-O3	117.7(3)
O4-Ho1-O9	70.9(4)	O13-La2-O3	65.1(3)
O8-Ho1-O9	69.0(3)	O8-La2-O3	59.4(3)
O11-Ho1-O3	142.9(3)	N2-La2-O3	117.6(3)
O4-Ho1-O3	71.9(3)	O16-La2-O3	86.4(3)
O8-Ho1-O3	66.4(3)	O6-La2-N1	133.7(3)
O9-Ho1-O3	98.4(3)	O14-La2-N1	80.3(3)
O11-Ho1-O13	129.9(3)	O1-La2-N1	60.8(3)
O4-Ho1-O13	135.6(3)	O13-La2-N1	108.4(3)
O8-Ho1-O13	71.1(3)	O8-La2-N1	110.0(3)
O9-Ho1-O13	139.4(3)	N2-La2-N1	156.5(4)
O3-Ho1-O13	71.8(3)	O16-La2-N1	75.8(4)
O11-Ho1-O19	75.0(4)	O3-La2-N1	57.0(3)
O4-Ho1-O19	135.0(3)	O6-La2-O17	70.5(4)
O8-Ho1-O19	75.3(4)	O14-La2-O17	127.2(4)
O9-Ho1-O19	73.7(3)	O1-La2-O17	65.8(4)
O3-Ho1-O19	141.0(3)	O13-La2-O17	147.7(4)
O13-Ho1-O19	89.4(3)	O8-La2-O17	97.9(4)
O11-Ho1-N3	66.5(3)	N2-La2-O17	62.0(4)
O4-Ho1-N3	123.1(4)	O16-La2-O17	45.5(4)
O8-Ho1-N3	121.1(4)	O3-La2-O17	131.8(4)
O9-Ho1-N3	135.8(4)	N1-La2-O17	103.2(4)
O3-Ho1-N3	125.5(4)	O6-La2-Ho1	123.3(2)
O13-Ho1-N3	63.5(3)	O14-La2-Ho1	97.2(2)
O19-Ho1-N3	69.0(4)	O1-La2-Ho1	154.0(2)
O11-Ho1-N5	85.1(4)	O13-La2-Ho1	37.8(2)
O4-Ho1-N5	70.4(4)	O8-La2-Ho1	36.1(2)
O8-Ho1-N5	132.0(3)	N2-La2-Ho1	85.4(3)
O9-Ho1-N5	141.2(3)	O16-La2-Ho1	101.5(3)
O3-Ho1-N5	71.6(3)	O3-La2-Ho1	38.17(18)
O13-Ho1-N5	74.5(3)	N1-La2-Ho1	94.7(2)
O19-Ho1-N5	136.8(4)	O17-La2-Ho1	133.9(3)
N3-Ho1-N5	67.9(4)	O1-La2-Ho1	154.0(2)

O11 Ho1 La2	170.2(2)	O13-La2-Ho1	37.8(2)
O4 Ho1 La2	115.0(2)	O8-La2-Ho1	36.1(2)
O8 Ho1 La2	40.2(2)	N2-La2-Ho1	85.4(3)
O9 Ho1 La2	105.7(2)	O16-La2-Ho1	101.5(3)
O3 Ho1 La2	43.6(2)	O3-La2-Ho1	38.17(18)
O13 Ho1 La2	40.5(2)	N1-La2-Ho1	94.7(2)
O19 Ho1 La2	100.7(2)	O17-La2-Ho1	133.9(3)
N3 Ho1 La2	103.9(2)	Ho1-O3-La2	98.2(3)
N5 Ho1 La2	92.6(3)	Ho1-O8-La2	103.7(4)
Ho1 O13 La2	101.7(3)		

Table V.A21 Selected interatomic distances (Å) and angles for complex 35

Er1-O4	2.313(7)	O6-La2-O1	76.5(2)
Er1-O11	2.314(7)	O14-La2-O1	71.0(3)
Er1-O8	2.339(7)	O6-La2-O13	90.7(2)
Er1-O3	2.395(7)	O14-La2-O13	66.1(2)
Er1-O9	2.396(7)	O1-La2-O13	137.0(2)
Er1-O19	2.405(8)	O6-La2-O8	116.4(2)
Er1-O13	2.412(6)	O14-La2-O8	131.0(2)
Er1-N3	2.439(8)	O1-La2-O8	156.3(2)
Er1-N4	2.665(9)	O13-La2-O8	65.4(2)
Er1...La2	3.8572(7)	O6-La2-N2	61.8(3)
La2-O6	2.469(7)	O14-La2-N2	122.9(3)
La2-O14	2.474(7)	O1-La2-N2	121.4(3)
La2-O1	2.503(7)	O13-La2-N2	85.0(3)
La2-O13	2.551(7)	O8-La2-N2	58.2(2)
La2-O8	2.574(7)	O6-La2-O16	117.1(3)
La2-N2	2.639(9)	O14-La2-O16	149.0(2)
La2-O16	2.642(8)	O1-La2-O16	81.2(3)
La2-O3	2.687(7)	O13-La2-O16	139.2(2)
La2-N1	2.745(9)	O8-La2-O16	75.2(2)
La2-O17	2.774(10)	N2-La2-O16	83.2(3)
O4-Er1-O11	72.2(2)	O6-La2-O3	154.7(3)
O4-Er1-O8	115.7(3)	O14-La2-O3	93.7(2)
O11-Er1-O8	142.2(3)	O1-La2-O3	117.7(2)
O4-Er1-O3	72.9(2)	O13-La2-O3	64.5(2)
O11-Er1-O3	142.8(2)	O8-La2-O3	59.5(2)
O8-Er1-O3	66.9(2)	N2-La2-O3	117.4(2)
O4-Er1-O9	70.4(2)	O16-La2-O3	87.0(2)
O11-Er1-O9	81.2(2)	O6-La2-N1	133.6(3)
O8-Er1-O9	68.8(2)	O14-La2-N1	79.5(2)
O3-Er1-O9	98.7(2)	O1-La2-N1	60.6(2)
O4-Er1-O19	135.0(3)	O13-La2-N1	108.4(2)
O11-Er1-O19	75.4(3)	O8-La2-N1	110.0(2)
O8-Er1-O19	74.8(3)	N2-La2-N1	157.5(3)
O3-Er1-O19	140.7(3)	O16-La2-N1	74.8(3)
O9-Er1-O19	74.5(3)	O3-La2-N1	57.2(2)
O4-Er1-O13	136.1(2)	O6-La2-O17	70.1(3)
O11-Er1-O13	130.7(2)	O14-La2-O17	126.5(3)
O8-Er1-O13	71.2(2)	O1-La2-O17	66.2(3)
O3-Er1-O13	71.2(2)	O13-La2-O17	146.7(3)
O9-Er1-O13	139.4(2)	O8-La2-O17	98.3(3)
O19-Er1-O13	88.9(3)	N2-La2-O17	62.1(3)
O4-Er1-N3	122.0(3)	O16-La2-O17	47.1(3)
O11-Er1-N3	66.6(3)	O3-La2-O17	133.9(3)

O8-Er1-N3	122.0(3)	N1-La2-O17	104.5(3)
O3-Er1-N3	125.0(3)	O6-La2-Er1	122.48(19)
O9-Er1-N3	136.2(3)	O14-La2-Er1	97.06(16)
O19-Er1-N3	69.4(3)	O1-La2-Er1	153.72(19)
O13-Er1-N3	64.2(2)	O13-La2-Er1	37.70(14)
O4-Er1-N4	70.8(3)	O8-La2-Er1	36.15(16)
O11-Er1-N4	85.4(3)	N2-La2-Er1	84.81(18)
O8-Er1-N4	132.5(3)	O16-La2-Er1	102.19(19)
O3-Er1-N4	71.5(3)	O3-La2-Er1	37.88(14)
O9-Er1-N4	141.1(3)	N1-La2-Er1	94.80(18)
O19-Er1-N4	136.3(3)	O17-La2-Er1	134.5(2)
O13-Er1-N4	74.5(3)	Er1-O3-La2	98.6(2)
N3-Er1-N4	67.0(3)	Er1-O8-La2	103.4(3)
O4-Er1-La2	115.75(17)	Er1-O13-La2	102.0(2)
O11-Er1-La2	170.73(17)	O13-Er1-La2	40.30(16)
O8-Er1-La2	40.47(17)	N3-Er1-La2	104.36(19)
O3-Er1-La2	43.53(16)	N4-Er1-La2	92.7(2)
O9-Er1-La2	105.66(17)	O6-La2-O14	70.1(3)
O19-Er1-La2	100.07(19)		

Table V.A22 Selected interatomic distances (Å) and angles for complex 36

La1-O6	2.459(8)	O17-La1-O16	45.4(3)
La1-O1	2.473(8)	O3-La1-O16	132.2(3)
La1-O14	2.507(7)	N1-La1-O16	102.7(3)
La1-O13	2.551(8)	O6-La1-Y2	23.9(2)
La1-O8	2.584(7)	O1-La1-Y2	54.8(2)
La1-N2	2.618(11)	O14-La1-Y2	97.63(16)
La1-O17	2.667(9)	O13-La1-Y2	37.77(15)
La1-O3	2.707(7)	O8-La1-Y2	35.62(15)
La1-N1	2.739(11)	N2-La1-Y2	85.7(2)
La1-O16	2.816(9)	O17-La1-Y2	101.69(19)
La1...Y2	3.8692(14)	O3-La1-Y2	38.18(19)
Y2-O11	2.303(7)	N1-La1-Y2	94.6(2)
Y2-O8	2.322(7)	O16-La1-Y2	134.4(2)
Y2-O4	2.326(8)	O11-Y2-O8	142.4(3)
Y2-O3	2.415(9)	O11-Y2-O4	72.4(3)
Y2-O9	2.416(7)	O8-Y2-O4	15.7(3)
Y2-O13	2.424(6)	O11-Y2-O3	142.2(3)
Y2-O19	2.431(8)	O8-Y2-O3	7.4(3)
Y2-N3	2.464(10)	O4-Y2-O3	2.1(3)
Y2-N5	2.666(10)	O11-Y2-O9	81.1(3)
O6-La1-O1	74.6(3)	O8-Y2-O9	9.0(2)
O6-La1-O14	69.8(3)	O4-Y2-O9	70.9(2)
O1-La1-O14	71.3(3)	O3-Y2-O9	99.2(3)
O6-La1-O13	92.7(3)	O11-Y2-O13	131.0(3)
O1-La1-O13	136.8(2)	O8-Y2-O13	71.1(2)
O14-La1-O13	65.6(2)	O4-Y2-O13	135.1(3)
O6-La1-O8	116.5(3)	O3-Y2-O13	70.9(3)
O1-La1-O8	157.1(2)	O9-Y2-O13	139.6(2)
O14-La1-O8	130.5(2)	O11-Y2-O19	75.9(3)
O13-La1-O8	65.1(2)	O8-Y2-O19	74.2(3)
O6-La1-N2	62.0(3)	O4-Y2-O19	135.0(3)
O1-La1-N2	119.5(3)	O3-Y2-O19	140.8(2)
O14-La1-N2	122.8(3)	O9-Y2-O19	73.4(3)
O13-La1-N2	87.2(3)	O13-Y2-O19	89.8(3)

O8-La1-N2	58.5(3)	O11-Y2-N3	66.3(3)
O6-La1-O17	115.2(3)	O8-Y2-N3	122.5(3)
O1-La1-O17	82.1(3)	O4-Y2-N3	121.4(3)
O14-La1-O17	150.7(3)	O3-Y2-N3	124.6(3)
O13-La1-O17	138.8(2)	O9-Y2-N3	136.1(3)
O8-La1-O17	75.1(3)	O13-Y2-N3	64.7(3)
N2-La1-O17	80.8(3)	O19-Y2-N3	70.8(3)
O6-La1-O3	156.7(3)	O11-Y2-N5	85.4(3)
O1-La1-O3	118.4(3)	O8-Y2-N5	132.2(3)
O14-La1-O3	95.1(2)	O4-Y2-N5	70.2(3)
O13-La1-O3	64.4(2)	O3-Y2-N5	70.7(3)
O8-La1-O3	59.5(2)	O9-Y2-N5	141.1(3)
N2-La1-O3	117.9(3)	O13-Y2-N5	74.2(3)
O17-La1-O3	86.8(2)	O19-Y2-N5	137.6(3)
O6-La1-N1	133.6(3)	N3-Y2-N5	66.8(3)
O1-La1-N1	61.9(3)	O11-Y2-La1	170.8(2)
O14-La1-N1	81.4(3)	O8-Y2-La1	40.38(17)
O13-La1-N1	107.8(3)	O4-Y2-La1	115.3(2).
O8-La1-N1	109.9(3)	O3-Y2-La1	43.86(18)
N2-La1-N1	155.7(3)	O9-Y2-La1	105.79(18)
O17-La1-N1	75.3(3)	O13-Y2-La1	40.14(19)
O3-La1-N1	56.7(3)	O19-Y2-La1	100.02(17)
O6-La1-O16	70.0(3)	N3-Y2-La1	104.7(2)
O1-La1-O16	64.9(3)	N5-Y2-La1	92.6(3)
O14-La1-O16	126.3(3)	Y2-O3-La1	98.0(3)
O13-La1-O16	148.9(3)	Y2-O8-La1	104.0(3)
O8-La1-O16	98.9(3)	Y2-O13-La1	102.1(3)
N2-La1-O16	62.0(3)		

Table V.A23 Selected interatomic distances (Å) and angles for complex 37

Pr1-O9	2.411(5)	O19-Pr1-Ce2	98.13(13)
Pr1-O11	2.435(5)	N3-Pr1-Ce2	101.04(13)
Pr1-O3	2.473(5)	N5-Pr1 Ce2	92.74(14)
Pr1-O8	2.494(5)	O6-Ce2-O1	74.48(16)
Pr1-O13	2.503(4)	O6-Ce2-O14	71.95(16)
Pr1-O4	2.504(5)	O1-Ce2-O14	69.52(16)
Pr1-O19	2.537(6)	O6-Ce2-O13	137.90(15)
Pr1-N3	2.576(6)	O1-Ce2-O13	87.20(16)
Pr1-N5	2.779(7)	O14-Ce2-O13	66.14(15)
Pr1...Ce2	3.9100(1)	O6-Ce2-O3	153.09(16)
Ce2-O6	2.461(5)	O1-Ce2-O3	118.92(15)
Ce2-O1	2.464(5)	O14-Ce2-O3	133.41(16)
Ce2-O14	2.497(5)	O13-Ce2-O3	68.62(15)
Ce2-O13	2.511(5)	O6-Ce2-O16	75.18(16)
Ce2-O3	2.529(4)	O1-Ce2-O16	125.76(17)
Ce2-O16	2.615(5)	O14-Ce2-O16	137.36(16)
Ce2-N1	2.664(6)	O13-Ce2-O16	142.27(15)
Ce2-O8	2.692(5)	O3-Ce2-O16	78.33(16)
Ce2-O17	2.731(6)	O6-Ce2-N1	122.02(17)
Ce2-N2	2.736(6)	O1-Ce2-N1	61.55(16)
O9-Pr1-O11	77.79(17)	O14-Ce2-N1	119.37(16)
O9-Pr1-O3	112.04(16)	O13-Ce2-N1	77.59(17)
O11-Pr1-O3	148.95(16)	O3-Ce2-N1	58.86(16)
O9-Pr1-O8	70.81(16)	O16-Ce2-N1	100.85(18)
O11-Pr1-O8	143.00(17)	O6-Ce2-O8	119.10(16)

O3-Pr1-O8	64.51(16)	O1-Ce2-O8	152.00(16)
O9-Pr1-O13	133.96(15)	O14-Ce2-O8	90.65(14)
O11-Pr1-O13	125.74(16)	O13-Ce2-O8	66.27(14)
O3-Pr1-O13	69.64(15)	O3-Ce2-O8	60.93(15)
O8-Pr1-O13	69.50(14)	O16-Ce2-O8	82.23(16)
O9-Pr1-O4	72.15(16)	N1-Ce2-O8	117.41(15)
O11Pr1-O4	91.86(16)	O6-Ce2-O17	75.01(17)
O3-Pr1-O4	65.50(15)	O1-Ce2-O17	81.57(16)
O8-Pr1-O4	96.58(15)	O14-Ce2-O17	140.64(16)
O13-Pr1-O4	134.59(16)	O13-Ce2-O17	140.13(16)
O9-Pr1-O19	139.25(17)	O3-Ce2-O17	83.72(16)
O11-Pr1-O19	78.00(18)	O16-Ce2-O17	47.50(16)
O3-Pr1-O19	76.20(18)	N1-Ce2-O17	63.39(17)
O8-Pr1-O19	138.99(18)	O8-Ce2-O17	124.41(15)
O13-Pr1-O19	86.75(17)	O6-Ce2-N2	61.62(17)
O4-Pr1-O19	76.41(17)	O1-Ce2-N2	130.44(16)
O9-Pr1-N3	126.47(19)	O14-Ce2-N2	75.71(16)
O11-Pr1-N3	63.59(17)	O13-Ce2-N2	109.86(17)
O3-Pr1-N3	120.30(17)	O3-Ce2-N2	110.60(15)
O8-Pr1-N3	122.43(16)	O16-Ce2-N2	65.01(17)
O13-Pr1-N3	62.40(17)	N1-Ce2-N2	164.85(16)
O4-Pr1-N3	139.82(17)	O8-Ce2-N2	57.54(16)
O19-Pr1-N3	67.96(19)	O17-Ce2-N2	106.45(17)
O9-Pr1-N5	70.22(17)	O6-Ce2-Pr1	156.75(12)
O11-Pr1-N5	80.38(19)	O1-Ce2-Pr1	121.14(12)
O3-Pr1-N5	130.55(18)	O14-Ce2-Pr1	96.37(11)
O8-Pr1-N5	71.04(18)	O13-Ce2-Pr1	38.67(10)
O13-Pr1-N5	75.57(17)	O3-Ce2-Pr1	38.06(11)
O4-Pr1-N5	142.36(17)	O16-Ce2-Pr1	103.60(12)
O19-Pr1-N5	135.94(18)	N1-Ce2-Pr1	81.19(12)
N3-Pr1-N5	68.06(18)	O8-Ce2-Pr1	39.19(10)
O9-Pr1-Ce2	113.04(12)	O17-Ce2-Pr1	121.78(12)
O11-Pr1-Ce2	164.56(11)	N2-Ce2-Pr1	96.42(12)
O3-Pr1-Ce2	39.09(10)	Pr1-O3-Ce2	102.84(17)
O8-Pr1-Ce2	43.00(11)	Pr1-O8-Ce2	97.81(16)
O13-Pr1-Ce2	38.82(11)	Pr1-O13-Ce2	102.51(16)
O4-Pr1-Ce2	101.82(12)		

Table V.A24 Selected interatomic distances (Å) and angles for complex 38

Dy1-O4	2.330(6)	O13-Dy1-Ce2	139.95(13)
Dy1-O11	2.335(5)	N3-Dy1-Ce2	103.48(16)
Dy1-O8	2.347(6)	N5-Dy1-Ce2	92.52(16)
Dy1-O3	2.406(5)	O6-Ce2-O14	70.0(2)
Dy1-O19	2.407(7)	O6-Ce2-O1	75.8(2)
Dy1-O9	2.417(6)	O14-Ce2-O1	71.1(2)
Dy1-O13	2.424(5)	O6-Ce2-O13	90.37(19)
Dy1-N3	2.457(7)	O14-Ce2-O13	66.70(18)
Dy1-N5	2.675(8)	O1-Ce2-O13	137.8(2)
Dy1...Ce2	3.8543(6)	O6-Ce2-O8	117.2(2)
Ce2-O6	2.449(6)	O14-Ce2-O8	132.08(18)
Ce2-O14	2.454(6)	O1-Ce2-O8	55.2(2)
Ce2-O1	2.467(6)	O13-Ce2-O8	65.97(18)
Ce2-O13	2.531(5)	O6-Ce2-O17	116.5(2)
Ce2-O8	2.559(6)	O14-Ce2-O17	149.1(2)
Ce2-O17	2.605(6)	O1-Ce2-O17	81.2(2)

Ce2-N2	2.622(8)	O13-Ce2-O17	139.12(19)
Ce2-O3	2.682(5)	O8-Ce2 O17	74.2(2)
Ce2-N1	2.733(7)	O6-Ce2 N2	62.2(2)
Ce2-O16	2.330(6)	O14-Ce2 N2	123.9(2)
O4-Dy1-O11	73.2(2)	O1-Ce2 N2	120.1(2)
O4-Dy1-O8	114.5(2)	O13-Ce2 N2	85.4(2)
O11-Dy1-O8	143.5(2)	O8-Ce2 N2	58.7(2)
O4-Dy1-O3	72.26(19)	O17-Ce2 N2	81.6(2)
O11-Dy1-O3	142.8(2)	O6-Ce2 O3	154.87(19)
O8-Dy1-O3	66.1(2)	O14-Ce2 O3	93.97(18)
O4-Dy1-O19	135.2(2)	O1-Ce2 O3	118.23(19)
O11-Dy1-O19	75.5(2)	O13-Ce2 O3	65.09(17)
O8-Dy1-O19	75.7(2)	O8-Ce2 O3	59.27(18)
O3-Dy1-O19	140.9(2)	O17-Ce2-O3	87.30(19)
O4-Dy1-O9	70.6(2)	N2-Ce2-O3	117.70(19)
O11-Dy1-O9	82.4(2)	O6-Ce2-N1	133.4(2)
O8-Dy1-O9	68.56(19)	O14-Ce2-N1	79.7(2)
O3-Dy1-O9	98.60(19)	O1-Ce2-N1	61.0(2)
O19-Dy1-O9	74.3(2)	O13-Ce2-N1	109.4(2)
O4-Dy1-O13	135.7(2)	O8-Ce2-N1	109.44(19)
O11-Dy1-O13	130.00(19)	O17-Ce2-N1	75.1(2)
O8-Dy1-O13	71.01(19)	N2-Ce2-N1	156.2(2)
O3-Dy1-O13	71.07(18)	O3-Ce2-N1	57.39(18)
O19-Dy1-O13	89.0(2)	O6-Ce2-O16	69.8(2)
O9-Dy1-O13	138.9(2)	O14-Ce2-O16	125.6(2)
O4-Dy1-N3	123.4(2)	O1-Ce2-O16	64.8(2)
O11-Dy1-N3	66.4(2)	O13-Ce2-O16	146.5(2)
O8-Dy1-N3	121.6(2)	O8-Ce2-O16	98.6(2)
O3-Dy1-N3	124.8(2)	O17-Ce2-O16	46.9(2)
O19-Dy1-N3	68.9(2)	N2-Ce2-O16	61.7(2)
O9-Dy1-N3	136.3(2)	O3-Ce2-O16	134.2(2)
O13-Dy1-N3	63.7(2)	N1-Ce2-O16	103.7(2)
O4-Dy1-N5	70.7(2)	O6-Ce2-Dy1	122.58(14)
O11-Dy1-N5	84.7(2)	O14-Ce2-Dy1	97.61(13)
O8-Dy1-N5	131.8(2)	O1-Ce2-Dy1	154.69(15)
O3-Dy1-N5	71.3(2)	O13-Ce2-Dy1	37.95(12)
O19-Dy1-N5	136.5(2)	O8-Ce2-Dy1	36.32(13)
O9-Dy1-N5	141.2(2)	O17-Ce2-Dy1	102.15(15)
O13-Dy1-N5	74.7(2)	N2-Ce2-Dy1	85.16(15)
N3-Dy1-N5	67.7(2)	O3-Ce2-Dy1	38.14(11)
O4-Dy1-Ce2	115.12(14)	N1-Ce2-Dy1	95.27(14)
O11-Dy1-Ce2	169.79(14)	O16-Ce2-Dy1	134.91(17)
O8-Dy1-Ce2	40.23(14)	Dy1-O3-Ce2	98.36(19)
O3-Dy1-Ce2	43.50(13)	Dy1-O8-Ce2	103.4(2)
O19-Dy1-Ce2	100.30(16)	Dy1-O13-Ce2	102.1(2)
O9-Dy1-Ce2	105.57(13)		

Table V.A25 Selected interatomic distances (Å) and angles for complex 39

Ho1-O4	2.322(2)	O13-Ho1-Ce2	39.85(5)
Ho1-O11	2.333(2)	N3-Ho1-Ce2	103.54(5)
Ho1-O8	2.348(2)	N5-Ho1-Ce2	92.39(6)
Ho1-O3	2.4025(19)	O6-Ce2-O14	69.98(8)
Ho1-O19	2.404(2)	O6-Ce2-O1	75.8(2)
Ho1-O9	2.408(2)	O14-Ce2-O1	71.1(2)
Ho1-O13	2.4142(19)	O6-Ce2-O13	90.37(19)

Ho1-N3	2.454(2)	O14-Ce2-O13	66.70(18)
Ho1-N5	2.675(3)	O1-Ce2-O13	75.91(7)
Ho1...Ce2	3.8551(3)	O6-Ce2-O8	71.38(7)
Ce2-O6	2.448(2)	O14-Ce2-O8	90.07(7)
Ce2-O14	2.463(2)	O1-Ce2-O8	66.84(6)
Ce2-O1	2.468(2)	O13-Ce2-O8	138.22(7)
Ce2-O13	2.530(2)	O6-Ce2-O16	117.16(7)
Ce2-O8	2.554(2)	O14-Ce2-O16	131.93(7)
Ce2-O16	2.610(2)	O1-Ce2-O16	155.08(7)
Ce2-N2	2.628(3)	O13-Ce2-O16	65.74(7)
Ce2-O3	2.6743(19)	O8-Ce2-O16	117.05(8)
Ce2-N1	2.735(2)	O6-Ce2-N2	148.99(7)
Ce2-O17	2.811(3)	O14-Ce2-N2	80.97(8)
O4-Ho1-O11	73.00(7)	O1-Ce2-N2	138.88(7)
O4-Ho1-O8	114.88(7)	O13-Ce2-N2	74.18(7)
O11-Ho1-O8	143.27(7)	O8-Ce2-N2	62.30(8)
O4-Ho1-O3	72.58(7)	O16-Ce2-N2	123.81(8)
O11-Ho1-O3	143.16(7)	O6-Ce2-O3	120.06(8)
O8-Ho1-O3	65.91(7)	O14-Ce2-O3	84.83(7)
O4-Ho1-O19	134.74(7)	O1-Ce2-O3	58.65(7)
O11-Ho1-O19	75.02(8)	O13-Ce2-O3	82.08(8)
O8-Ho1-O19	75.82(8)	O8-Ce2-O3	154.21(7)
O3-Ho1-O19	140.85(7)	O16-Ce2-O3	93.53(7)
O4-Ho1-O9	70.49(7)	N2-Ce2-O3	118.58(7)
O11-Ho1-O9	81.92(7)	O6-Ce2-N1	64.78(6)
O8-Ho1-O9	68.91(7)	O14-Ce2-N1	59.19(6)
O3-Ho1-O9	98.57(7)	O1-Ce2-N1	87.43(7)
O19-Ho1-O9	74.04(8)	O13-Ce2-N1	117.51(7)
O4-Ho1-O13	135.62(7)	O8-Ce2-N1	133.29(7)
O11-Ho1-O13	130.43(7)	O16-Ce2-N1	79.34(7)
O8-Ho1-O13	70.81(7)	N2-Ce2-N1	61.07(7)
O3-Ho1-O13	70.80(6)	O3-Ce2-N1	109.51(7)
O19-Ho1-O13	89.63(7)	O6-Ce2-O17	109.55(7)
O9-Ho1-O13	139.09(7)	O14-Ce2-O17	75.07(8)
O4-Ho1-N3	122.86(8)	O1-Ce2-O17	156.69(8)
O11-Ho1-N3	66.62(7)	O13-Ce2-O17	57.65(6)
O8-Ho1-N3	121.79(8)	O8-Ce2-O17	70.38(8)
O3-Ho1-N3	124.62(7)	O16-Ce2-O17	126.20(8)
O19-Ho1-N3	69.55(8)	N2-Ce2-O17	64.79(8)
O9-Ho1-N3	136.58(7)	O3-Ce2-O17	146.24(7)
O13-Ho1-N3	63.85(7)	N1-Ce2-O17	98.29(8)
O4-Ho1-N5	70.60(7)	O6-Ce2-Ho1	46.83(8)
O11-Ho1-N5	85.17(8)	O14-Ce2-Ho1	61.88(8)
O8-Ho1-N5	131.56(7)	O1-Ce2-Ho1	134.17(7)
O3-Ho1-N5	71.37(7)	O13-Ce2-Ho1	103.81(7)
O19-Ho1-N5	136.84(8)	O8-Ce2-Ho1	122.19(5)
O9-Ho1-N5	141.05(7)	O16-Ce2-Ho1	97.39(5)
O13-Ho1-N5	74.57(7)	N2-Ce2-Ho1	155.01(5)
N3-Ho1-N5	67.41(8)	O3-Ce2-Ho1	37.70(4)
O4-Ho1-Ce2	115.27(5)	N1-Ce2-Ho1	36.30(5)
O11-Ho1-Ce2	170.06(5)	O17-Ce2-Ho1	102.16(5)
O8-Ho1-Ce2	40.09(5)	Ho1-O3-Ce2	98.67(7)
O3-Ho1-Ce2	43.30(5)	Ho1-O8-Ce2	103.61(8)
O19-Ho1-Ce2	100.64(6)	Ho1-O13-Ce2	102.45(7)
O9-Ho1-Ce2	105.71(5)		

Table V.A26 Selected interatomic distances (Å) and angles for complex 40

Er1-O4	2.312(5)	O13-Er- Ce1	40.08(13)
Er1-O11	2.317(5)	N3-Er1-Ce1	103.80(15)
Er1-O8	2.329(6)	N5-Er1-Ce1	92.73(16)
Er1-O19	2.392(6)	O6-Ce1-O14	70.01(19)
Er1-O9	2.400(5)	O6-Ce1-O1	76.12(18)
Er1-O3	2.401(5)	O14-Ce1-O1	71.1(2)
Er1-O13	2.425(5)	O6-Ce1-O13	90.41(18)
Er1-N3	2.447(6)	O14-Ce1-O13	66.51(17)
Er1-N5	2.652(7)	O1-Ce1-O13	137.56(19)
Er1...Ce1	3.8505(6)	O6-Ce1-O8	116.88(18)
Ce1-O6	2.458(5)	O14-Ce1-O8	131.65(18)
Ce1-O14	2.460(5)	O1-Ce1-O8	155.64(19)
Ce1-O1	2.480(5)	O13-Ce1-O8	65.68(17)
Ce1-O13	2.534(5)	O6-Ce1-O16	117.2(2)
Ce1-O8	2.568(5)	O14-Ce1-O16	148.77(19)
Ce1-O16	2.597(6)	O1-Ce1-O16	81.1(2)
Ce1-N2	2.609(7)	O13-Ce1-O16	139.03(18)
Ce1-O3	2.679(5)	O8-Ce1-O16	74.63(19)
Ce1-N1	2.722(6)	O6-Ce1-N2	62.0(2)
Ce1-O17	2.843(7)	O14-Ce1-N2	123.5(2)
O4-Er1-O11	72.96(19)	O1-Ce1-N2	120.3(2)
O4-Er1-O8	115.29(19)	O13-Ce1-N2	85.38(19)
O11-Er1-O8	142.19(19)	O8-Ce1-N2	58.78(19)
O4-Er1-O19	134.68(18)	O16-Ce1-N2	82.6(2)
O11-Er1-O1	74.7(2)	O6-Ce1-O3	154.72(19)
O8-Er1-O19	75.2(2)	O14-Ce1-O3	93.79(17)
O4-Er1-O9	70.58(18)	O1-Ce1-O3	117.92(17)
O11-Er1-O9	81.06(19)	O13-Ce1-O3	64.91(16)
O8-Er1-O9	68.92(18)	O8-Ce1-O3	59.41(17)
O19-Er1-O9	73.77(18)	O16-Ce1-O3	86.80(19)
O4-Er1-O3	72.46(18)	N2-Ce1-O3	117.92(19)
O11-Er1-O3	143.18(19)	O6-Ce1-N1	133.18(19)
O8-Er1-O3	66.72(18)	O14-Ce1-N1	79.12(18)
O19-Er1-O3	141.1(2)	O1-Ce1-N1	60.73(19)
O9-Er1-O3	98.96(18)	O13-Ce1-N1	108.80(19)
O4-Er1-O13	135.52(18)	O8-Ce1-N1	109.93(18)
O11-Er1-O1	130.68(18)	O16-Ce1-N1	75.0(2)
O8-Er1-O13	71.15(18)	N2-Ce1-N1	157.2(2)
O19-Er1-O1	89.78(18)	O3-Ce1-N1	57.30(18)
O9-Er1-O13	139.47(19)	O6-Ce1-O17	71.0(2)
O3-Er1-O13	70.92(17)	O14-Ce1-O17	127.0(2)
O4-Er1N3	122.8(2)	O1-Ce1-O17	65.8(2)
O11-Er1-N3	66.8(2)	O13-Ce1-O17	146.78(18)
O8-Er1-N3	121.6(2)	O8-Ce1-O17	97.7(2)
O19-Er1-N3	69.4(2)	O16-Ce1-O17	46.3(2)
O9-Er1-N3	136.0(2)	N2-Ce1-O17	61.7(2)
O3-Er1-N3	124.8(2)	O3-Ce1-O17	132.99(19)
O13-Er1-N3	63.9(2)	N1-Ce1-O17	103.9(2)
O4-Er1-N5	70.5(2)	O6-Ce1-Er1	122.61(13)
O11-Er1-N5	85.5(2)	O14-Ce1-Er1	97.62(13)
O8-Er1-N5	132.3(2)	O1-Ce1-Er1	154.40(13)
O19-Er1-N5	136.8(2)	O13-Ce1-Er1	38.05(11)
O9-Er1-N5	141.0(2)	O8-Ce1-Er1	36.02(13)
O3-Er1-N5	71.4(2)	O16-Ce1-Er1	101.78(15)
O13-Er1-N5	74.6(2)	N2-Ce1-Er1	85.19(15)
N3-Er1-N5	67.5(2)	O3-Ce1-Er1	38.08(11)

O4-Er1-Ce1	115.30(14)	N1-Ce1-Er1	95.10(14)
O11-Er1-Ce1	170.41(13)	O17-Ce1-Er1	133.74(15)
O8-Er1-Ce1	40.42(13)	Er1-O3-Ce1	98.43(18)
O19-Er1-Ce1	100.62(14)	Er1-O8-Ce1	103.6(2)
O9-Er1-Ce1	105.90(13)	Er1-O13-Ce1	101.9(2)
O3-Er1-Ce1	43.49(12)		

Table V.A27 Selected interatomic distances (Å) and angles for complex 41

Tm1-O11	2.262(12)	N3-Tm1-Ce2	105.3(4)
Tm1-O9	2.314(14)	O13-Tm1-Ce2	40.2(3)
Tm1-O3	2.330(13)	N5-Tm1-Ce2	93.8(3)
Tm1-O8	2.358(13)	O6-Ce2-O14	71.7(4)
Tm1-O4	2.390(13)	O6-Ce2-O17	75.4(5)
Tm1-O19	2.396(13)	O14-Ce2-O1	71.0(5)
Tm1-N3	2.424(15)	O6-Ce2-O13	137.2(4)
Tm1-O13	2.425(11)	O14-Ce2-O13	65.5(4)
Tm1-N5	2.655(10)	O1-Ce2-O13	92.1(4)
Tm1...Ce2	3.8382(15)	O6-Ce2-O31	156.2(4)
Ce2-O6	2.439(13)	O14-Ce2-O3	131.1(4)
Ce2-O14	2.444(12)	O1-Ce2-O31	115.2(4)
Ce2-O1	2.473(14)	O13-Ce2-O3	65.8(4)
Ce2-O13	2.529(12)	O6-Ce2-O16	80.6(4)
Ce2-O3	2.575(12)	O14-Ce2-O16	148.1(5)
Ce2-O16	2.615(13)	O1-Ce2-O16	117.4(5)
Ce2-N1	2.615(18)	O13-Ce2-O16	139.0(4)
Ce2-O8	2.653(13)	O3-Ce2-O16	75.6(4)
Ce2-N2	2.690(17)	O6-Ce2-N11	117.9(5)
Ce2-O17	2.798(13)	O14-Ce2-N1	122.3(5)
O11-Tm1-O9	72.3(5)	O1-Ce2-N15	59.5(5)
O11-Tm1-O3	141.1(5)	O13-Ce2-N1	87.5(5)
O9-Tm1-O3	116.9(4)	O3-Ce2-N15	59.4(5)
O11-Tm1-O8	143.7(5)	O16-Ce2-N1	84.5(5)
O9-Tm1-O8	73.5(4)	O6-Ce2-O81	119.3(5)
O3-Tm1-O8	67.4(5)	O14-Ce2-O8	94.5(4)
O11-Tm1-O4	81.3(4)	O1-Ce2-O81	155.9(4)
O9-Tm1-O4	70.6(5)	O13-Ce2-O8	64.0(4)
O3-Tm1-O4	68.6(4)	O3-Ce2-O85	59.7(4)
O8-Tm1-O4	98.2(4)	O16-Ce2-O8	85.2(4)
O11-Tm1-O19	75.4(5)	N1-Ce2-O81	118.9(5)
O9-Tm1-O19	135.6(4)	O6-Ce2-N26	61.8(5)
O3-Tm1-O19	73.7(4)	O14-Ce2-N2	80.1(4)
O8-Tm1-O19	140.0(4)	O1-Ce2-N21	134.1(5)
O4-Tm1-O19	75.3(4)	O13-Ce2-N2	107.7(5)
O11-Tm1-N3	65.9(5)	O3-Ce2-N21	110.7(4)
O9-Tm1-N3	119.8(5)	O16-Ce2-N2	72.9(5)
O3-Tm1-N3	123.0(5)	N1-Ce2-N21	157.2(5)
O8-Tm1-N3	124.3(5)	O8-Ce2-N25	57.7(4)
O4-Tm1-N3	137.4(5)	O6-Ce2-O17	66.1(5)
O19-Tm1-N3	70.8(5)	O14-Ce2-O17	128.5(4)
O11-Tm1-O13	131.1(4)	O1-Ce2-O17	70.9(5)
O9-Tm1-O13	135.0(5)	O13-Ce2-O17	147.8(5)
O3-Tm1-O13	71.4(4)	O3-Ce2-O17	96.2(4)
O8-Tm1-O13	70.1(4)	O16-Ce2-O17	46.5(5)
O4-Tm1-O13	139.6(4)	N1-Ce2-O17	60.4(5)
O19-Tm1-O13	89.2(4)	O8-Ce2-O17	131.4(4)

N3-Tm1-O13	65.2(4)	N2-Ce2-O17	103.6(5)
O11-Tm1-N5	84.8(5)	O6-Ce2-Tm1	155.0(4)
O9-Tm1-N5	69.3(4)	O14-Ce2-Tm1	97.6(3)
O3-Tm1-N5	134.0(4)	O1-Ce2-Tm1	123.4(3)
O8-Tm1-N5	72.2(4)	O13-Ce2-Tm1	38.2(3)
O4-Tm1-N5	139.8(4)	O3-Ce2-Tm1	36.3(3)
O19-Tm1-N5	136.4(4)	O16-Ce2-Tm1	101.1(3)
N3-Tm1-N5	65.7(5)	N1-Ce2-Tm1	87.0(3)
O13-Tm1-N5	75.1(4)	O8-Ce2-Tm1	37.2(3)
O11-Tm1-Ce2	170.8(3)	N2-Ce2-Tm1	94.6(3)
O9-Tm1-Ce2	115.8(3)	O17-Ce2-Tm1	132.4(3)
O3-Tm1-Ce2	40.9(3)	Tm1-O3-Ce2	102.9(5)
O8-Tm1-Ce2	42.9(3)	Tm1-O8-Ce2	99.8(5)
O4-Tm1-Ce2	105.2(3)	Tm1-O13-Ce2	101.6(4)
O19-Tm1-Ce2	99.8(3)		

Table V.A28 Selected interatomic distances (Å) and angles for complex 42

Lu1-O4	2.294(3)	O13-Lu1-Ce2	39.97(8)
Lu1-O11	2.301(3)	N3-Lu1-Ce2	104.32(10)
Lu1-O8	2.309(4)	N5-Lu1-Ce2	92.65(10)
Lu1-O3	2.369(3)	O6-Ce2-O17	5.59(13)
Lu1-O19	2.375(4)	O6-Ce2-O14	70.18(14)
Lu1-O9	2.378(4)	O1-Ce2-O14	71.53(13)
Lu1-O13	2.380(3)	O6-Ce2-O13	90.75(13)
Lu1-N3	2.424(4)	O1-Ce2-O13	138.49(13)
Lu1-N5	2.654(5)	O14-Ce2-O13	66.97(12)
Lu1...Ce2	3.8327(9)	O6-Ce2-O8	117.24(13)
Ce2-O6	2.448(4)	O1-Ce2-O8	55.68(13)
Ce2-O1	2.461(4)	O14-Ce2-O8	131.17(12)
Ce2-O14	2.461(4)	O13-Ce2-O8	64.82(12)
Ce2-O13	2.524(4)	O6-Ce2-O16	117.88(14)
Ce2-O8	2.546(4)	O1-Ce2-O16	80.61(14)
Ce2-O16	2.607(4)	O14-Ce2-O16	148.13(13)
Ce2-N2	2.620(5)	O13-Ce2-O16	138.53(12)
Ce2-O3	2.668(3)	O8-Ce2-O16	75.11(13)
Ce2-N1	2.720(5)	O6-Ce2-N2	62.25(14)
Ce2-O17	2.807(5)	O1-Ce2-N2	120.08(14)
O4-Lu1-O11	72.19(13)	O14-Ce2-N2	123.63(13)
O4-Lu1-O8 1	115.56(13)	O13-Ce2-N2	84.69(13)
O11-Lu1-O8	142.04(13)	O8-Ce2-N2	58.83(13)
O4-Lu1-O3 7	72.83(12)	O16-Ce2-N2	83.60(15)
O11-Lu1-O3	143.11(13)	O6-Ce2-O3	154.14(12)
O8-Lu1-O3 6	66.28(13)	O1-Ce2-O3	119.08(12)
O4-Lu1-O19	134.68(13)	O14-Ce2-O3	93.37(12)
O11-Lu1-O19	74.87(14)	O13-Ce2-O3	64.00(11)
O8-Lu1-O19	75.36(14)	O8-Ce2-O3	58.69(11)
O3-Lu1-O19	140.79(13)	O16-Ce2-O3	86.75(12)
O4-Lu1-O9 7	70.15(13)	N2-Ce2-O3	117.18(12)
O11-Lu1-O9	80.20(12)	O6-Ce2-N1	132.81(13)
O8-Lu1-O9 6	69.44(13)	O1-Ce2-N1	61.08(13)
O3-Lu1-O9 9	98.64(12)	O14-Ce2-N1	78.74(12)
O19-Lu1-O9	74.32(13)	O13-Ce2-N1	108.95(13)
O4-Lu1-O13	135.73(12)	O8-Ce2-N1	109.95(12)
O11-Lu1-O13	131.52(12)	O16-Ce2-N1	74.34(14)
O8-Lu1-O13	70.84(13)	N2-Ce2-N1	157.51(14)

O3-Lu1-O13	70.90(11)	O3-Ce2-N1	58.10(11)
O19-Lu1-O13	89.56(13)	O6-Ce2-O17	71.27(15)
O9-Lu1-O13	139.72(13)	O1-Ce2-O17	65.33(16)
O4-Lu1-N3	121.96(14)	O14-Ce2-O17	127.48(15)
O11-Lu1-N3	67.02(13)	O13-Ce2-O17	146.55(13)
O8-Lu1-N3	122.13(14)	O8-Ce2-O17	97.94(15)
O3-Lu1-N3	125.17(13)	O16-Ce2-O17	46.67(14)
O19-Lu1-N3	69.57(15)	N2-Ce2-O17	62.07(14)
O9-Lu1-N3	136.07(13)	O3-Ce2-O17	133.20(13)
O13-Lu1-N3	64.52(12)	N1-Ce2-O17	103.82(14)
O4-Lu1-N5	70.60(13)	O6-Ce2-Lu1	122.44(9)
O11-Lu1-N5	86.02(14)	O1-Ce2-Lu1	155.12(10)
O8-Lu1-N5	131.94(13)	O14-Ce2-Lu1	97.24(9)
O3-Lu1-N5	71.59(13)	O13-Ce2-Lu1	37.28(8)
O19-Lu1-N5	136.63(14)	O8-Ce2-Lu1	35.73(8)
O9-Lu1-N5	140.69(13)	O16-Ce2-Lu1	101.96(9)
O13-Lu1-N5	74.48(13)	N2-Ce2-Lu1	84.72(10)
N3-Lu1-N5	67.15(15)	O3-Ce2-Lu1	37.63(7)
O4-Lu1-Ce2	115.68(9)	N1-Ce2-Lu1	95.44(9)
O11-Lu1-Ce2	171.06(8)	O17-Ce2-Lu1	133.66(12)
O8-Lu1-Ce2	40.11(9)	Lu1-O3-Ce2	98.92(12)
O3-Lu1-Ce2	43.45(8)	Lu1-O8-Ce2	104.16(14)
O19-Lu1-Ce2	100.40(10)	Lu1-O13-Ce2	102.75(12)
O9-Lu1-Ce2	106.07(9)		

Table V.A29 Selected interatomic distances (Å) and angles for complex 43

Ce1-O6	2.448(6)	N2-Ce1-O16	62.0(2)
Ce1-O14	2.453(6)	O3-Ce1-O16	134.2(2)
Ce1-O1	2.456(6)	N1-Ce1-O16	103.7(2)
Ce1-O13	2.518(6)	O6-Ce1-Y2	122.43(14)
Ce1-O8	2.550(6)	O14-Ce1-Y2	97.67(14)
Ce1-O17	2.608(6)	O1-Ce1-Y2	154.60(14)
Ce1-N2	2.621(7)	O13-Ce1-Y2	37.92(13)
Ce1-O3	2.677(5)	O8-Ce1-Y2	35.96(13)
Ce1-N1	2.732(6)	O17-Ce1-Y2	102.52(15)
Ce1-O16	2.812(7)	N2-Ce1-Y2	84.83(15)
Ce1...Y2	3.8516(11)	O3-Ce1-Y2	37.96(11)
Y2-O4	2.319(6)	N1-Ce1-Y2	95.49(14)
Y2-O11	2.323(6)	O16-Ce1-Y2	134.81(17)
Y2-O8	2.332(6)	O4-Y2-O11	73.0(2)
Y2-O3	2.396(5)	O4-Y2-O8	115.0(2)
Y2-O9	2.397(6)	O11-Y2-O8	143.6(2)
Y2-O19	2.401(6)	O4-Y2-O3	72.59(19)
Y2-O13	2.423(6)	O11-Y2-O3	143.10(19)
Y2-N3	2.443(7)	O8-Y2-O3	65.81(19)
Y2-N5	2.674(8)	O4-Y2-O9	70.6(2)
O6-Ce1-O14	69.8(2)	O11-Y2-O9	82.1(2)
O6-Ce1-O1	75.9(2)	O8-Y2-O9	69.0(2)
O14-Ce1-O1	70.9(2)	O3-Y2-O9	98.58(19)
O6-Ce1-O13	90.18(19)	O4-Y2-O19	135.2(2)
O14-Ce1-O13	66.82(18)	O11-Y2-O19	75.6(2)
O1-Ce1-O13	137.7(2)	O8-Y2-O19	75.5(2)
O6-Ce1-O8	117.32(19)	O3-Y2-O19	140.4(2)
O14-Ce1-O8	131.83(18)	O9-Y2-O19	74.1(2)
O1-Ce1-O8	155.5(2)	O4-Y2-O13	135.65(19)

O13-Ce1-O8	65.65(18)	O11-Y2-O13	130.4(2)
O6-Ce1-O17	116.3(2)	O8-Y2-O13	70.6(2)
O14-Ce1-O17	148.95(19)	O3-Y2-O13	70.83(18)
O1-Ce1-O17	81.0(2)	O9-Y2-O13	139.0(2)
O13-Ce1-O17	139.41(19)	O19-Y2-O13	89.1(2)
O8-Ce1-O17	74.68(19)	O4-Y2-N3	123.0(2)
O6-Ce1-N2	62.4(2)	O11-Y2-N3	66.6(2)
O14-Ce1-N2	123.8(2)	O8-Y2-N3	121.5(2)
O1-Ce1-N2	120.5(2)	O3-Y2-N3	124.7(2)
O13-Ce1-N2	85.0(2)	O9-Y2-N3	136.4(2)
O8-Ce1-N2	58.8(2)	O19-Y2-N3	69.4(2)
O17-Ce1-N2	81.7(2)	O13-Y2-N3	63.8(2)
O6-Ce1-O3	154.55(19)	O4-Y2-N5	70.6(2)
O14-Ce1-O3	94.02(18)	O11-Y2-N5	85.0(2)
O1-Ce1-O3	118.35(18)	O8-Y2-N5	131.4(2)
O13-Ce1-O3	64.95(17)	O3-Y2-N5	71.4(2)
O8-Ce1-O3	58.81(17)	O9-Y2-N5	141.2(2)
O17-Ce1-O3	87.78(19)	O19-Y2 N5	136.9(2)
N2-Ce1-O3	117.29(19)	O13-Y2-N5	74.6(2)
O6-Ce1-N1	133.1(2)	N3-Y2-N5	67.6(2)
O14-Ce1-N1	79.44(19)	O4-Y2-Ce1	115.42(14)
O1-Ce1-N1	60.7(2)	O11-Y2-Ce1	169.84(15)
O13-Ce1-N1	109.54(19)	O8-Y2-Ce1	39.95(14)
O8-Ce1-N1	109.56(19)	O3-Y2-Ce1	43.42(13)
O17-Ce1-N1	75.4(2)	O9-Y2-Ce1	105.77(14)
N2-Ce1-N1	156.6(2)	O19-Y2-Ce1	100.02(16)
O3-Ce1-N1	57.81(18)	O13-Y2-Ce1	39.69(13)
O6-Ce1-O16	70.0(2)	N3-Y2-Ce1	103.31(16)
O14-Ce1-O16	125.7(2)	N5-Y2-Ce1	92.39(16)
O1-Ce1-O16	65.0(2)	Y2-O3-Ce1	98.63(18)
O13-Ce1-O16	146.41(19)	Y2-O8-Ce1	104.1(2)
O8-Ce1-O16	98.9(2)	Y2-O13-Ce1	102.4(2)
O17-Ce1-O16	46.5(2)		

Table V.A30 Selected interatomic distances (Å) and angles for complex 44

Nd1-O9	2.399(3)	O19-Nd1-Pr1	97.84(8)
Nd1-O11	2.414(3)	N3-Nd1-Pr1	101.08(8)
Nd1-O3	2.458(3)	N5-Nd1-Pr1	93.05(9)
Nd1-O8	2.464(3)	O6-Pr1-O1	73.56(10)
Nd1-O13	2.474(3)	O6-Pr1-O14	71.91(10)
Nd1-O4	2.486(3)	O1-Pr1-O14	69.22(10)
Nd1-O19	2.510(3)	O6-Pr1-O13	138.44(10)
Nd1-N3	2.551(4)	O1-Pr1-O13	87.63(10)
Nd1-N5	2.754(4)	O14-Pr1-O13	66.78(9)
Nd1...Pr1	3.8806(4)	O6-Pr1-O3	152.74(10)
Pr1-O6	2.438(3)	O1-Pr1-O3	119.59(9)
Pr1-O1	2.440(3)	O14-Pr1-O3	133.92(10)
Pr1-O14	2.481(3)	O13-Pr1-O3	68.54(9)
Pr1-O13	2.489(3)	O6-Pr1-O16	75.82(11)
Pr1-O3	2.513(3)	O1-Pr1-O16	126.17(11)
Pr1-O16	2.589(3)	O14-Pr1-O16	137.43(10)
Pr1-N1	2.633(3)	O13-Pr1-O16	141.33(10)
Pr1-O8	2.671(3)	O3-Pr1-O16	77.46(10)
Pr1-O17	2.703(4)	O6-Pr1-N1	121.26(10)
Pr1-N2	2.707(3)	O1-Pr1-N1	61.88(10)

O9-Nd1-O11	77.21(10)	O14-Pr1-N1	119.48(10)
O9-Nd1-O3	112.00(10)	O13-Pr1-N1	77.48(11)
O11-Nd1-O3	148.45(10)	O3-Pr1-N1	59.12(10)
O9-Nd1-O8	71.22(10)	O16-Pr1-N1	100.76(11)
O11-Nd1-O8	143.11(10)	O6-Pr1-O8	119.91(9)
O3-Nd1-O8	64.47(9)	O1-Pr1-O8	151.93(10)
O9-Nd1-O13	134.39(9)	O14-Pr1-O8	90.75(9)
O11-Nd1-O13	126.51(10)	O13-Pr1-O8	65.92(9)
O3-Nd1-O13	69.64(9)	O3-Pr1-O8	60.77(9)
O8-Nd1-O13	69.40(9)	O16-Pr1-O8	81.89(10)
O9-Nd1-O4	71.88(10)	N1-Pr1-O8	117.37(9)
O11-Nd1-O4	90.58(10)	O6-Pr1-O17	74.74(11)
O3-Nd1-O4	65.87(10)	O1-Pr1-O17	81.66(11)
O8-Nd1-O4	97.17(10)	O14-Pr1-O17	140.54(11)
O13-Nd1-O4	134.89(10)	O13-Pr1-O17	139.72(10)
O9-Nd1-O19	139.06(10)	O3-Pr1-O17	83.39(11)
O11-Nd1-O19	78.19(11)	O16-Pr1-O17	47.84(10)
O3-Nd1-O19	76.00(11)	N1-Pr1-O17	63.20(11)
O8-Nd1-O19	138.68(11)	O8-Pr1-O17	124.45(10)
O13-Nd1-O19	86.50(10)	O6-Pr1-N2	62.30(10)
O4-Nd1-O19	76.18(10)	O1-Pr1-N2	129.89(10)
O9-Nd1-N3	126.41(11)	O14-Pr1-N2	75.34(9)
O11-Nd1-N3	64.16(10)	O13-Pr1-N2	109.74(10)
O3-Nd1-N3	120.49(10)	O3-Pr1-N2	110.48(9)
O8-Nd1-N3	122.42(10)	O16-Pr1-N2	65.31(10)
O13-Nd1-N3	62.55(10)	N1-Pr1-N2	165.13(10)
O4-Nd1-N3	139.32(10)	O8-Pr1-N2	57.66(9)
O19-Nd1-N3	68.05(11)	O17-Pr1-N2	106.83(10)
O9-Nd1-N5	70.27(11)	O6-Pr1-Nd1	157.38(7)
O11-Nd1-N5	80.60(12)	O1-Pr1-Nd1	121.55(7)
O3-Nd1-N5	130.89(11)	O14-Pr1-Nd1	96.69(7)
O8-Nd1-N5	71.24(11)	O13-Pr1-Nd1	38.42(6)
O13-Nd1-N5	76.00(11)	O3-Pr1-Nd1	38.18(7)
O4-Nd1-N5	142.15(10)	O16-Pr1-Nd1	102.91(8)
O19-Nd1-N5	136.03(11)	N1-Pr1-Nd1	81.31(8)
N3-Nd1-N5	68.07(11)	O8-Pr1-Nd1	38.96(6)
O9-Nd1-Pr1	113.38(7)	O17-Pr1-Nd1	121.57(8)
O11-Nd1-Pr1	165.20(7)	N2-Pr1-Nd1	96.31(8)
O3-Nd1-Pr1	39.19(6)	Nd1-O3-Pr1	102.62(10)
O8-Nd1-Pr1	42.96(6)	Nd1-O8-Pr1	98.08(9)
O13-Nd1-Pr1	38.69(7)	Nd1-O13-Pr1	102.88(10)
O4-Nd1-Pr1	102.41(7)		

Table V.A31. Selected interatomic distances (Å) and angles for complex 45

Sm1-O4	2.369(3)	O19-Sm1-Pr1	98.13(9)
Sm1-O11	2.393(3)	N3-Sm1-Pr1	101.81(8)
Sm1-O8	2.429(3)	N5-Sm1-Pr1	93.16(9)
Sm1-O3	2.435(3)	O1-Pr1-O6	73.52(10)
Sm1-O13	2.451(3)	O1-Pr1-O14	71.94(10)
Sm1-O9	2.467(3)	O6-Pr1-O14	69.10(10)
Sm1-O19	2.477(3)	O1-Pr1-O13	138.50(10)
Sm1-N3	2.524(4)	O6-Pr1-O13	87.85(10)
Sm1-N5	2.735(4)	O14-Pr1-O13	66.78(9)
Sm1...Pr1	3.8567(5)	O1-Pr1-O8	153.17(10)
Pr1-O1	2.435(3)	O6-Pr1-O8	119.38(10)

Pr1-O6	2.445(3)	O14-Pr1-O8	133.54(10)
Pr1-O14	2.481(3)	O13-Pr1-O8	68.04(10)
Pr1-O13	2.485(3)	O1-Pr1-O17	75.89(11)
Pr1-O8	2.508(3)	O6-Pr1-O17	126.24(11)
Pr1-O17	2.590(3)	O14-Pr1-O17	137.54(11)
Pr1-N2	2.633(4)	O13-Pr1-O17	141.09(10)
Pr1-O3	2.667(3)	O8-Pr1-O17	77.84(11)
Pr1-N1	2.703(4)	O1-Pr1-N2	121.20(11)
Pr1-O16	2.705(4)	O6-Pr1-N2	61.72(11)
O4-Sm1-O11	75.58(11)	O14-Pr1-N2	119.15(11)
O4-Sm1-O8	112.50(10)	O13-Pr1-N2	77.52(11)
O11-Sm1-O8	147.60(10)	O8-Pr1-N2	59.14(10)
O4-Sm1-O3	71.69(10)	O17-Pr1-N2	100.97(12)
O11-Sm1-O3	142.57(10)	O1-Pr1-O3	120.16(10)
O8-Sm1-O3	64.86(10)	O6-Pr1-O3	152.06(10)
O4-Sm1-O13	135.27(10)	O14-Pr1-O3	91.13(9)
O11-Sm1-O13	127.69(10)	O13-Pr1-O3	65.71(9)
O8-Sm1-O13	69.84(10)	O8-Pr1-O3	60.44(9)
O3-Sm1-O13	69.90(9)	O17-Pr1-O3	81.68(10)
O4-Sm1-O9	71.19(10)	N2-Pr1-O3	117.19(10)
O11-Sm1-O9	88.69(10)	O1-Pr1-N1	62.37(11)
O8-Sm1-O9	66.42(10)	O6-Pr1-N1	129.94(10)
O3-Sm1-O9	97.39(10)	O14-Pr1-N1	75.49(10)
O13-Sm1-O9	135.62(10)	O13-Pr1-N1	109.53(10)
O4-Sm1-O19	138.12(12)	O8-Pr1-N1	110.63(10)
O11-Sm1-O19	78.21(12)	O17-Pr1-N1	65.27(11)
O8-Sm1-O19	75.94(11)	N2-Pr1-N1	165.30(11)
O3-Sm1-O19	139.12(11)	O3-Pr1-N1	57.83(10)
O13-Sm1-O19	86.59(11)	O1-Pr1-O16	75.31(11)
O9-Sm1-O19	76.15(11)	O6-Pr1-O16	81.99(11)
O4-Sm1-N3	125.75(12)	O14-Pr1-O16	141.09(11)
O11-Sm1-N3	64.85(11)	O13-Pr1-O16	139.41(10)
O8-Sm1-N3	120.95(11)	O8-Pr1-O16	83.10(11)
O3-Sm1-N3	123.14(10)	O17-Pr1-O16	47.76(11)
O13-Sm1-N3	63.03(11)	N2-Pr1-O16	63.04(11)
O9-Sm1-N3	138.66(11)	O3-Pr1-O16	123.78(10)
O19-Sm1-N3	68.00(12)	N1-Pr1-O16	107.00(11)
O4-Sm1-N5	70.62(11)	O1-Pr1-Sm1	157.31(7)
O11-Sm1-N5	81.13(12)	O6-Pr1-Sm1	121.66(8)
O8-Sm1-N5	131.26(11)	O14-Pr1-Sm1	96.70(7)
O3-Sm1-N5	71.35(11)	O13-Pr1-Sm1	38.31(6)
O13-Sm1-N5	76.05(11)	O8-Pr1-Sm1	37.91(7)
O9-Sm1-N5	141.80(11)	O17-Pr1-Sm1	102.78(8)
O19-Sm1-N5	135.91(12)	N2-Pr1-Sm1	81.44(8)
N3-Sm1-N5	67.99(12)	O3-Pr1-Sm1	38.68(6)
O4-Sm1-Pr1	114.07(8)	N1-Pr1-Sm1	96.16(8)
O11-Sm1-Pr1	166.62(7)	O16-Pr1-Sm1	120.99(8)
O8-Sm1-Pr1	39.38(7)	Sm1-O3-Pr1	98.13(10)
O3-Sm1-Pr1	43.19(7)	Sm1-O8-Pr1	102.71(11)
O13-Sm1-Pr1	38.93(7)	Sm1-O13-Pr1	102.76(10)
O9-Sm1-Pr1	103.03(7)		

Table V.A32 Selected interatomic distances (Å) and angles for complex 46

Eu1-O9	2.3462(18)	O13 Pr2 N1	77.36(6)
Eu1-O11	2.3754(19)	O3 Pr2 N1	59.10(6)

Eu1-O3	2.4175(19)	O13-Eu1-Pr2	39.25(4)
Eu1-O8	2.4177(18)	O4-Eu1-Pr2	103.31(5)
Eu1-O13	2.4296(17)	O19-Eu1-Pr2	98.12(5)
Eu1-O4	2.4431(18)	N3-Eu1-Pr2	102.36(5)
Eu1-O19	2.462(2)	N5-Eu1-Pr2	93.48(5)
Eu1-N3	2.508(2)	C7-Eu1-Pr2	56.86(5)
Eu1-N5	2.715(2)	O6-Pr2-O1	73.56(6)
Eu1...Pr2	3.8421(6)	O6-Pr2-O14	72.22(6)
Pr2-O6	2.4328(18)	O1-Pr2-O14	68.91(6)
Pr2-O1	2.4373(19)	O6-Pr2-O13	138.63(6)
Pr2-O14	2.4773(18)	O1-Pr2-O13	88.14(6)
Pr2-O13	2.4914(19)	O14-Pr2-O13	66.58(6)
Pr2-O3	2.5005(17)	O6-Pr2-O3	153.20(6)
Pr2-O16	2.593(2)	O1-Pr2-O3	119.53(6)
Pr2-N1	2.629(2)	O14-Pr2-O3	133.21(6)
Pr2-O8	2.6572(18)	O13-Pr2-O3	67.84(6)
Pr2-O17	2.693(2)	O6-Pr2-O16	75.59(7)
Pr2-N2	2.696(2)	O1-Pr2-O16	126.95(7)
O9-Eu1-O11	74.88(7)	O14-Pr2-O16	137.02(6)
O9-Eu1-O3	112.56(6)	O13-Pr2-O16	140.67(6)
O11-Eu1-O3	147.15(6)	O3-Pr2-O16	78.22(6)
O9-Eu1-O8	72.14(6)	O6-Pr2-N1	121.54(6)
O11-Eu1-O8	142.50(6)	O1-Pr2-N1	61.86(6)
O3-Eu1-O8	64.96(6)	O14-Pr2-N1	118.72(6)
O9-Eu1-O13	135.81(6)	O16-Pr2-N1	102.17(7)
O11-Eu1-O13	128.04(6)	O6-Pr2-O8	120.11(6)
O3-Eu1-O13	70.15(6)	O1-Pr2-O8	151.92(6)
O8-Eu1-O13	70.05(6)	O14-Pr2-O8	91.04(6)
O9-Eu1-O4	70.86(6)	O13-Pr2-O8	65.32(6)
O11-Eu1-O4	87.74(6)	O3-Pr2-O8	60.36(6)
O3-Eu1-O4	66.64(6)	O16-Pr2-O8	81.13(6)
O8-Eu1-O4	97.80(6)	N1-Pr2-O8	116.96(6)
O13-Eu1-O4	136.09(6)	O6-Pr2-O17	75.69(7)
O9-Eu1-O19	137.75(7)	O1-Pr2-O17	82.97(7)
O3-Eu1-O19	76.00(7)	O14-Pr2-O17	142.00(6)
O8-Eu1-O19	139.20(7)	O13-Pr2-O17	139.57(6)
O13-Eu1-O1	86.43(6)	O3-Pr2-O17	82.61(6)
O4-Eu1-O19	76.17(6)	O16-Pr2-O17	47.89(6)
O9-Eu1-N3	125.46(7)	N1-Pr2-O17	63.66(7)
O11-Eu1-N3	64.95(7)	O8-Pr2-O17	122.96(6)
O3-Eu1-N3	121.33(7)	O6-Pr2-N2	62.24(6)
O8-Eu1-N3	123.49(6)	O1-Pr2-N2	129.53(6)
O13-Eu1-N3	63.27(6)	O14-Pr2-N2	75.20(6)
O4-Eu1-N3	138.00(6)	O13-Pr2-N2	108.96(6)
O19-Eu1-N3	67.72(7)	O3-Pr2-N2	110.86(6)
O9-Eu1-N5	70.91(7)	O16-Pr2-N2	64.83(6)
O11-Eu1-N5	81.22(7)	N1-Pr2-N2	165.98(7)
O3-Eu1-N5	131.62(7)	O8-Pr2-N2	57.90(6)
O8-Eu1-N5	71.56(7)	O17-Pr2-N2	107.00(6)
O13-Eu1-N5	76.09(7)	O6-Pr2-Eu1	157.13(4)
O4-Eu1-N5	141.75(7)	O1-Pr2-Eu1	121.76(5)
O19-Eu1-N5	135.58(7)	O14-Pr2-Eu1	96.46(4)
N3-Eu1-N5	67.93(7)	O13-Pr2-Eu1	38.10(4)
O9-Eu1-Pr2	114.44(5)	O3-Pr2-Eu1	37.86(4)
O11-Eu1-Pr2	167.28(4)	O16-Pr2-Eu1	102.58(5)
O3-Eu1-Pr2	39.41(4)	N1-Pr2-Eu1	81.28(5)
O8-Eu1-Pr2	43.18(4)	O8-Pr2-Eu1	38.51(4)

N2-Pr2-Eu1	96.02(5)	O17-Pr2-Eu1	120.43(5)
Eu1-O3-Pr2	102.73(6)	Eu1-O13-Pr2	102.65(6)
Eu1-O8-Pr2	98.30(6)		

Table V.A33 Selected interatomic distances (Å) and angles for complex 48

Tb1-O4	2.345(3)	O13-Tb1-Pr2	39.36(6)
Tb1-O11	2.350(3)	N3-Tb1-Pr2	102.65(8)
Tb1-O8	2.369(3)	N5-Tb1-Pr2	92.22(8)
Tb1-O3	2.417(3)	O6-Pr2-O14	69.87(10)
Tb1-O19	2.423(3)	O6-Pr2-O1	75.78(10)
Tb1-O9	2.433(3)	O14-Pr2-O1	71.65(10)
Tb1-O13	2.435(3)	O6-Pr2-O13	88.93(10)
Tb1-N3	2.474(3)	O14-Pr2-O13	67.45(9)
Tb1-N5	2.689(4)	O1-Pr2-O13	139.08(10)
Tb1...Pr2	3.8577(3)	O6-Pr2-O8	117.94(10)
Pr2-O6	2.427(3)	O14-Pr2-O8	132.99(9)
Pr2-O14	2.446(3)	O1-Pr2-O8	153.64(10)
Pr2-O1	2.448(3)	O13-Pr2-O8	66.53(9)
Pr2-O13	2.507(3)	O6-Pr2-O16	117.13(11)
Pr2-O8	2.547(3)	O14-Pr2-O16	148.16(10)
Pr2-O16	2.590(3)	O1-Pr2-O16	79.97(11)
Pr2-N2	2.611(4)	O13-Pr2-O16	139.52(10)
Pr2-O3	2.669(3)	O8-Pr2-O16	73.73(10)
Pr2-N1	2.715(3)	O6-Pr2-N2	62.66(11)
Pr2-O17	2.818(4)	O14-Pr2-N2	124.41(11)
O4-Tb1-O11	74.35(10)	O1-Pr2-N2	119.41(11)
O4-Tb1-O8	113.84(10)	O13-Pr2-N2	84.01(10)
O11-Tb1-O8	144.45(10)	O8-Pr2-N2	58.92(10)
O4-Tb1-O3	72.28(9)	O16-Pr2-N2	82.05(11)
O11-Tb1-O3	143.63(10)	O6-Pr2-O3	153.54(10)
O8-Tb1-O3	65.24(10)	O14-Pr2-O3	93.03(9)
O4-Tb1-O19	135.08(10)	O1-Pr2-O3	118.96(9)
O11-Tb1-O19	75.17(11)	O13-Pr2-O3	65.43(8)
O8-Tb1-O19	76.19(11)	O8-Pr2-O3	59.24(9)
O3-Tb1-O19	140.50(11)	O16-Pr2-O3	88.17(10)
O4-Tb1-O9	70.62(10)	N2-Pr2-O3	117.67(10)
O11-Tb1-O9	83.77(10)	O6-Pr2-N1	133.21(10)
O8-Tb1-O9	68.34(10)	O14-Pr2-N1	79.11(10)
O3-Tb1-O9	98.33(9)	O1-Pr2-N1	61.39(10)
O19-Tb1-O9	73.97(10)	O13-Pr2-N1	110.77(10)
O4-Tb1-O13	135.55(10)	O8-Pr2-N1	108.85(10)
O11-Tb1-O13	129.39(9)	O16-Pr2-N1	74.73(11)
O8-Tb1-O13	70.47(10)	N2-Pr2-N1	156.31(11)
O3-Tb1-O13	70.52(9)	O3-Pr2-N1	57.72(9)
O19-Tb1-O13	89.37(10)	O6-Pr2-O17	70.41(12)
O9-Tb1-O13	138.12(10)	O14-Pr2-O17	126.04(12)
O4-Tb1-N3	123.94(11)	O1-Pr2-O17	64.29(12)
O11-Tb1-N3	66.02(10)	O13-Pr2-O17	144.82(10)
O8-Tb1-N3	121.60(11)	O8-Pr2-O17	97.70(12)
O3-Tb1-N3	124.00(10)	O16-Pr2-O17	46.82(11)
O19-Tb1-N3	69.69(12)	N2-Pr2-O17	61.40(11)
O9-Tb1-N3	137.30(10)	O3-Pr2-O17	134.86(11)
O13-Tb1-N3	63.42(10)	N1-Pr2-O17	104.02(11)
O4-Tb1-N5	70.76(11)	O6-Pr2-Tb1	121.78(8)
O11-Tb1-N5	84.45(11)	O14-Pr2-Tb1	97.65(7)

O8-Tb1-N5	131.10(10)	O1-Pr2-Tb1	155.86(7)
O3-Tb1-N5	71.30(10)	O13-Pr2-Tb1	38.03(6)
O19-Tb1-N5	137.05(11)	O8-Pr2-Tb1	36.69(7)
O9-Tb1-N5	141.35(10)	O16-Pr2-Tb1	102.72(7)
O13-Tb1-N5	74.92(10)	N2-Pr2-Tb1	84.60(8)
N3-Tb1-N5	67.52(11)	O3-Pr2-Tb1	38.28(6)
O4-Tb1-Pr2	114.83(7)	N1-Pr2-Tb1	95.81(7)
O11-Tb1-Pr2	168.62(7)	O17-Pr2-Tb1	134.37(10)
O8-Tb1-Pr2	39.96(7)	Tb1-O3-Pr2	98.54(9)
O3-Tb1-Pr2	43.17(6)	Tb1-O8-Pr2	103.34(11)
O19-Tb1-Pr2	100.42(8)	Tb1-O13-Pr2	102.61(10)
O9-Tb1-Pr2	105.30(7)		

Table V.A34 Selected interatomic distances (Å) and angles for complex 49

Pr1-O6	2.431(2)	N2-Pr1-O16	61.29(8)
Pr1-O14	2.449(2)	O3-Pr1-O16	134.71(8)
Pr1-O1	2.451(2)	N1-Pr1-O16	104.08(8)
Pr1-O13	2.5067(19)	O6-Pr1-Dy1	121.79(5)
Pr1-O8	2.546(2)	O14-Pr1-Dy1	97.53(5)
Pr1-O17	2.591(2)	O1-Pr1-Dy1	155.73(5)
Pr1-N2	2.612(3)	O13-Pr1-Dy1	37.87(4)
Pr1-O3	2.6635(19)	O8-Pr1-Dy1	36.51(5)
Pr1-N1	2.715(2)	O17-Pr1-Dy1	102.54(5)
Pr1-O16	2.817(3)	N2-Pr1-Dy1	84.68(5)
Pr1...Dy1	3.8509(5)	O3-Pr1-Dy1	38.12(4)
Dy1-O4	2.333(2)	N1-Pr1-Dy1	95.80(5)
Dy1-O11	2.343(2)	O16-Pr1-Dy1	134.19(7)
Dy1-O8	2.356(2)	O4-Dy1-O11	73.84(7)
Dy1-O3	2.4053(19)	O4-Dy1-O8	114.24(7)
Dy1-O19	2.411(2)	O11-Dy1-O8	143.91(7)
Dy1-O13	2.4232(19)	O4-Dy1-O3	72.49(7)
Dy1-O9	2.424(2)	O11-Dy1-O3	143.61(7)
Dy1-N3	2.461(2)	O8-Dy1-O3	65.39(7)
Dy1-N5	2.678(3)	O4-Dy1-O19	134.98(8)
O6-Pr1-O14	69.89(7)	O11-Dy1-O19	74.91(8)
O6-Pr1-O1	75.78(7)	O8-Dy1-O19	76.25(8)
O14-Pr1-O1	71.59(7)	O3-Dy1-O19	140.70(7)
O6-Pr1-O13	89.13(7)	O4-Dy1-O13	135.52(7)
O14-Pr1-O13	67.39(6)	O11-Dy1-O13	129.97(7)
O1-Pr1-O13	138.97(7)	O8-Dy1-O13	70.51(7)
O6-Pr1-O8	117.83(7)	O3-Dy1-O13	70.46(6)
O14-Pr1-O8	132.64(6)	O19-Dy1-O13	89.50(7)
O1-Pr1-O8	154.05(7)	O4-Dy1-O9	70.74(7)
O13-Pr1-O8	66.19(6)	O11-Dy1-O9	82.89(7)
O6-Pr1-O17	117.40(8)	O8-Dy1-O9	68.57(7)
O14-Pr1-O17	148.22(7)	O3-Dy1-O9	98.59(7)
O1-Pr1-O17	80.22(8)	O19-Dy1-O9	73.95(8)
O13-Pr1-O17	139.26(7)	O13-Dy1-O9	138.39(7)
O8-Pr1-O17	73.89(7)	O4-Dy1-N3	123.48(8)
O6-Pr1-N2	62.63(8)	O11-Dy1-N3	66.26(7)
O14-Pr1-N2	124.37(7)	O8-Dy1-N3	121.73(8)
O1-Pr1-N2	119.48(7)	O3-Dy1-N3	124.27(7)
O13-Pr1-N2	84.17(7)	O19-Dy1-N3	69.45(8)
O8-Pr1-N2	58.95(7)	O13-Dy1-N3	63.74(7)
O17-Pr1-N2	82.18(8)	O9-Dy1-N3	136.82(7)

O6-Pr1-O3	153.44(7)	O4-Dy1-N5	70.65(8)
O14-Pr1-O3	92.98(7)	O11-Dy1-N5	84.79(8)
O1-Pr1-O3	119.03(7)	O8-Dy1-N5	131.30(7)
O13-Pr1-O3	65.12(6)	O3-Dy1-N5	71.41(7)
O8-Pr1-O3	59.11(6)	O19-Dy1-N5	136.78(8)
O17-Pr1-O3	87.98(7)	O13-Dy1-N5	74.86(7)
N2-Pr1-O3	117.61(7)	O9-Dy1-N5	141.33(7)
O6-Pr1-N1	133.11(7)	N3-Dy1-N5	67.48(8)
O14-Pr1-N1	79.00(7)	O4-Dy1-Pr1	115.01(5)
O1-Pr1-N1	61.30(7)	O11-Dy1-Pr1	169.20(5)
O13-Pr1-N1	110.53(7)	O8-Dy1-Pr1	40.02(5)
O8-Pr1-N1	109.06(7)	O3-Dy1-Pr1	43.13(5)
O17-Pr1-N1	74.70(8)	O19-Dy1-Pr1	100.61(6)
N2-Pr1-N1	156.44(8)	O13-Dy1-Pr1	39.42(4)
O3-Pr1-N1	57.88(6)	O9-Dy1-Pr1	105.54(5)
O6-Pr1-O16	70.61(8)	N3-Dy1-Pr1	103.02(5)
O14-Pr1-O16	126.36(8)	N5-Dy1-Pr1	92.31(5)
O1-Pr1-O16	64.61(8)	Dy1-O3-Pr1	98.75(7)
O13-Pr1-O16	144.95(7)	Dy1-O8-Pr1	103.47(7)
O8-Pr1-O16	97.69(8)	Dy1-O13-Pr1	102.72(7)
O17-Pr1-O16	46.89(8)		

Table V.A35 Selected interatomic distances (Å) and angles for complex 50

Ho1-O8	2.334(3)	O3-Ho1-Pr2	43.09(6)
Ho1-O4	2.335(3)	N3-Ho1-Pr2	103.48(7)
Ho1-O11	2.341(3)	N5-Ho1-Pr2	91.64(7)
Ho1-O9	2.412(3)	O6-Pr2-O14	69.68(10)
Ho1-O13	2.416(3)	O6-Pr2-O1	76.05(9)
Ho1-O19	2.421(3)	O14-Pr2-O1	71.30(9)
Ho1-O3	2.428(3)	O6-Pr2-O13	88.93(9)
Ho1-N3	2.469(3)	O14-Pr2-O13	67.92(8)
Ho1-N5	2.659(3)	O1-Pr2-O13	139.21(9)
Ho1...Pr2	3.8468(13)	O6-Pr2-O8	117.32(10)
Pr2-O6	2.435(3)	O14-Pr2-O8	132.60(9)
Pr2-O14	2.442(3)	O1-Pr2-O8	154.49(9)
Pr2-O1	2.467(3)	O13-Pr2-O8	65.55(8)
Pr2-O13	2.512(3)	O6-Pr2-O16	118.32(10)
Pr2-O8	2.552(3)	O14-Pr2-O16	147.70(9)
Pr2-O16	2.590(3)	O1-Pr2-O16	80.26(10)
Pr2-N2	2.620(4)	O13-Pr2-O16	138.81(9)
Pr2-O3	2.656(3)	O8-Pr2-O16	74.25(9)
Pr2-N1	2.738(3)	O6-Pr2-N2	62.52(10)
Pr2-O17	2.800(4)	O14-Pr2-N2	123.93(10)
O8-Ho1-O4	113.98(10)	O1-Pr2-N2	120.09(9)
O8-Ho1-O11	143.41(9)	O13-Pr2-N2	83.23(10)
O4-Ho1-O11	74.14(9)	O8-Pr2-N2	58.50(9)
O8-Ho1-O9	69.15(9)	O16-Pr2-N2	83.45(10)
O4-Ho1-O9	70.34(10)	O6-Pr2-O3	153.80(9)
O11-Ho1-O9	81.86(9)	O14-Pr2-O3	93.56(9)
O8-Ho1-O13	70.48(8)	O1-Pr2-O3	118.64(9)
O4-Ho1-O13	135.39(9)	O13-Pr2-O3	65.68(8)
O11-Ho1-O13	130.33(8)	O8-Pr2-O3	59.32(9)
O9-Ho1-O13	138.94(9)	O16-Pr2-O3	86.73(9)
O8-Ho1-O19	76.75(10)	N2-Pr2-O3	117.40(9)
O4-Ho1-O19	135.17(9)	O6-Pr2-N1	132.89(9)

O11-Ho1-O19	74.24(10)	O14-Pr2-N1	79.10(9)
O9-Ho1-O19	74.42(9)	O1-Pr2-N1	60.68(9)
O13-Ho1-O19	89.43(9)	O13-Pr2-N1	111.27(9)
O8-Ho1-O3	65.54(10)	O8-Pr2-N1	109.79(9)
O4-Ho1-O3	71.90(9)	O16-Pr2-N1	73.72(10)
O11-Ho1-O3	143.55(9)	N2-Pr2-N1	156.78(10)
O9-Ho1-O3	98.70(9)	O3-Pr2-N1	58.09(8)
O13-Ho1-O3	70.78(8)	O6-Pr2-O17	71.15(10)
O19-Ho1-O3	141.35(9)	O1-Pr2-O17	126.38(10)
O8-Ho1-N3	121.70(10)	O13-Pr2-O17	144.89(10)
O4-Ho1-N3	123.80(10)	O8-Pr2-O17	97.65(10)
O11-Ho1-N3	66.34(9)	O16-Pr2-O17	47.26(10)
O9-Ho1-N3	136.16(9)	N2-Pr2-O17	62.07(11)
O13-Ho1-N3	64.02(9)	O3-Pr2-O17	133.82(9)
O19-Ho1-N3	68.57(10)	N1-Pr2-O17	103.34(10)
O3-Ho1-N3	124.88(9)	O6-Pr2-Ho1	121.52(7)
O8-Ho1-N5	130.73(9)	O14-Pr2-Ho1	98.02(7)
O4-Ho1-N5	70.62(10)	O1-Pr2-Ho1	155.84(7)
O11-Ho1-N5	85.85(10)	O13-Pr2-Ho1	37.80(5)
O9-Ho1-N5	140.91(9)	O8-Pr2-Ho1	36.11(6)
O13-Ho1-N5	74.67(9)	O16-Pr2-Ho1	102.04(7)
O19-Ho1-N5	136.74(10)	N2-Pr2-Ho1	83.96(7)
O3-Ho1-N5	70.77(10)	O3-Pr2-Ho1	38.65(6)
N3-Ho1-N5	68.29(10)	N1-Pr2-Ho1	96.52(6)
O8-Ho1-Pr2	40.11(6)	O17-Pr2-Ho1	133.75(8)
O4-Ho1-Pr2	114.39(7)	Ho1-O3-Pr2	98.26(9)
O11-Ho1-Pr2	169.73(6)	Ho1-O8-Pr2	103.78(10)
O9-Ho1-Pr2	106.06(7)	Ho1-O13-Pr2	102.60(8)
O13-Ho1-Pr2	39.59(6)		
O19-Ho1-Pr2	101.23(7)		

Table V.A36 Selected interatomic distances (Å) and angles for complex 52

Tm1-O4	2.301(3)	O13-Tm1-Pr2	39.68(7)
Tm1-O11	2.310(3)	N3-Tm1-Pr2	103.93(8)
Tm1-O8	2.322(3)	N5-Tm1-Pr2	92.49(8)
Tm1-O3	2.379(3)	O6-Pr2-O14	70.00(12)
Tm1-O19	2.384(4)	O6-Pr2-O1	74.89(11)
Tm1-O9	2.394(3)	O14-Pr2-O1	71.65(11)
Tm1-O13	2.400(3)	O6-Pr2-O13	90.31(11)
Tm1-N3	2.434(4)	O14-Pr2-O1	67.42(10)
Tm1-N5	2.668(4)	O1-Pr2-O13	139.06(11)
Tm1...Pr2	3.8303(4)	O6-Pr2-O8	118.11(11)
Pr2-O6	2.426(3)	O14-Pr2-O8	132.08(10)
Pr2-O14	2.443(3)	O1-Pr2-O8	154.66(11)
Pr2-O1	2.451(3)	O13-Pr2-O8	65.49(10)
Pr2-O13	2.506(3)	O6-Pr2-O16	118.00(12)
Pr2-O8	2.536(3)	O14-Pr2-O1	147.63(11)
Pr2-O16	2.586(4)	O1-Pr2-O16	80.21(12)
Pr2-N2	2.600(4)	O13-Pr2-O1	138.76(10)
Pr2-O3	2.655(3)	O8-Pr2-O16	74.47(11)
Pr2-N1	2.705(4)	O6-Pr2-N2	62.64(12)
Pr2-O17	2.828(5)	O14-Pr2-N2	124.29(12)
O4-Tm1-O11	72.53(11)	O1-Pr2-N2	118.90(12)
O4-Tm1-O8	115.07(11)	O13-Pr2-N2	84.77(12)
O11-Tm1-O8	142.85(11)	O8-Pr2-N2	59.29(11)

O4-Tm1-O3	73.01(10)	O16-Pr2-N2	83.19(13)
O11-Tm1-O3	143.32(11)	O6-Pr2-O3	154.16(11)
O8-Tm1-O3	65.77(11)	O14-Pr2-O3	93.14(10)
O4-Tm1-O19	135.05(12)	O1-Pr2-O3	119.37(10)
O11-Tm1-O19	75.26(12)	O13-Pr2-O3	64.66(10)
O8-Tm1-O19	75.67(12)	O8-Pr2-O3	58.88(10)
O3-Tm1-O19	140.44(12)	O16-Pr2-O3	86.83(11)
O4-Tm1-O9	70.25(11)	N2-Pr2-O3	117.81(11)
O11-Tm1-O9	80.95(11)	O6-Pr2-N1	132.34(11)
O8-Tm1-O9	69.32(11)	O14-Pr2-N1	78.53(11)
O3-Tm1-O9	98.87(10)	O1-Pr2-N1	61.48(11)
O19-Tm1-O9	74.45(12)	O13-Pr2-N1	109.80(11)
O4-Tm1-O13	135.94(11)	O8-Pr2-N1	109.54(11)
O11-Tm1-O13	131.14(10)	O16-Pr2-N1	74.08(12)
O8-Tm1-O13	70.52(11)	N2-Pr2-N1	156.95(12)
O3-Tm1-O13	70.62(10)	O3-Pr2-N1	58.00(10)
O19-Tm1-O13	88.99(12)	O6-Pr2-O17	71.46(13)
O9-Tm1-O13	139.19(11)	O14-Pr2-O17	127.64(13)
O4-Tm1-N3	122.12(12)	O1-Pr2-O17	65.05(13)
O11-Tm1-N3	66.78(11)	O13-Pr2-O17	145.68(12)
O8-Tm1-N3	122.36(12)	O8-Pr2-O17	97.14(13)
O3-Tm1-N3	124.53(11)	O16-Pr2-O17	46.58(13)
O19-Tm1-N3	69.73(13)	N2-Pr2-O17	61.13(13)
O9-Tm1-N3	136.45(12)	O3-Pr2-O17	133.16(12)
O13-Tm1-N3	64.38(11)	N1-Pr2-O17	103.82(12)
O4-Tm1-N5	70.49(11)	O6-Pr2-Tm1	122.74(8)
O11-Tm1-N5	85.65(12)	O14-Pr2-Tm1	97.60(7)
O8-Tm1-N5	131.50(11)	O1-Pr2-Tm1	155.82(8)
O3-Tm1-N5	71.32(11)	O13-Pr2-Tm1	37.70(7)
O19-Tm1-N5	136.79(12)	O8-Pr2-Tm1	36.04(7)
O9-Tm1-N5	140.69(12)	O16-Pr2-Tm1	101.90(8)
O13-Tm1-N5	74.92(11)	N2-Pr2-Tm1	85.16(8)
N3-Tm1-N5	67.14(13)	O3-Pr2-Tm1	37.85(7)
O4-Tm1-Pr2	115.60(8)	N1-Pr2-Tm1	95.61(8)
O11-Tm1-Pr2	170.52(7)	O17-Pr2-Tm1	133.18(11)
O8-Tm1-Pr2	39.97(7)	Tm1-O3-Pr2	98.94(11)
O3-Tm1-Pr2	43.21(7)	Tm1-O8-Pr2	103.99(12)
O19-Tm1-Pr2	100.14(9)	Tm1-O13-Pr2	102.62(11)
O9-Tm1-Pr2	106.04(7)		

Table V.A37 Selected interatomic distances (Å) and angles for complex 53

Yb1-O9	2.299(4)	O13-Yb1-Pr2	39.87(8)
Yb1-O11	2.305(4)	N3-Yb1-Pr2	104.30(9)
Yb1-O3	2.319(4)	N5-Yb1-Pr2	92.87(10)
Yb1-O8	2.377(3)	C31-Yb1-Pr2	151.37(9)
Yb1-O19	2.386(4)	O1-Pr2-O14	70.35(14)
Yb1-O4	2.387(4)	O1-Pr2-O6	74.48(12)
Yb1-O13	2.396(3)	O1--Pr2-O6	71.73(13)
Yb1-N3	2.431(4)	O1-Pr2-O13	91.03(12)
Yb1-N5	2.666(5)	O14-Pr2-O13	67.04(11)
Yb1...Pr2	3.8272(3)	O6-Pr2-O13	138.76(13)
Pr2-O1	2.432(4)	O1-Pr2-O3	117.79(13)
Pr2-O14	2.446(4)	O14-Pr2-O3	131.74(12)
Pr2-O6	2.454(3)	O6-Pr2-O3	155.10(13)
Pr2-O13	2.512(3)	O13-Pr2-O3	65.40(12)

Pr2-O3	2.542(3)	O1-Pr2-O16	117.94(15)
Pr2-O16	2.585(4)	O14-Pr2-O16	148.07(13)
Pr2-N1	2.591(5)	O6-Pr2-O16	80.81(14)
Pr2-O8	2.660(3)	O13-Pr2-O16	138.28(12)
Pr2-N2	2.713(4)	O3-Pr2-O16	74.30(13)
Pr2-O17	2.822(6)	O1-Pr2-N1	62.56(14)
O9-Yb1-O11	72.47(13)	O14-Pr2-N1	124.32(14)
O9-Yb1-O3	115.30(14)	O6-Pr2-N1	18.74(14)
O11-Yb1-O3	142.41(13)	O13-Pr2-N1	85.32(13)
O9-Yb1-O8	72.76(12)	O3-Pr2-N1	59.01(13)
O11-Yb1-O8	143.11(13)	O16-Pr2-N1	83.03(15)
O3-Yb1-O8	66.23(13)	O1-Pr2-O8	154.94(13)
O9-Yb1-O19	135.34(13)	O14-Pr2-O8	93.33(12)
O11-Yb1-O19	75.48(14)	O6-Pr2-O8	119.42(12)
O3-Yb1-O19	75.13(14)	O13-Pr2-O8	64.63(10)
O8-Yb1-O19	140.36(13)	O3-Pr2-O8	59.06(11)
O9-Yb1-O4	70.32(13)	O16-Pr2-O8	86.07(13)
O11-Yb1-O4	80.67(13)	N1-Pr2-O8	117.80(12)
O3-Yb1-O4	69.27(13)	O1-Pr2-N2	132.11(12)
O8-Yb1-O4	98.85(12)	O14-Pr2-N2	78.35(12)
O19-Yb1-O4	74.51(13)	O6-Pr2-N2	61.55(13)
O9-Yb1-O13	135.83(12)	O13-Pr2-N2	109.23(13)
O11-Yb1-O13	131.19(12)	O3-Pr2-N2	110.10(12)
O3-Yb1-O13	70.77(13)	O16-Pr2-N2	74.35(14)
O8-Yb1-O13	70.88(11)	N1-Pr2-N2	157.10(14)
O19-Yb1-O13	88.81(12)	O8-Pr2-N2	57.95(11)
O4-Yb1-O13	139.42(13)	O1-Pr2-O17	71.57(16)
O9-Yb1-N3	121.78(14)	O14-Pr2-O17	128.07(16)
O11-Yb1-N3	66.65(13)	O6-Pr2-O17	64.97(17)
O3-Yb1-N3	122.52(14)	O13-Pr2-O17	146.54(14)
O8-Yb1-N3	124.81(13)	O3-Pr2-O17	97.07(16)
O19-Yb1-N3	69.82(14)	O16-Pr2-O17	46.42(16)
O4-Yb1-N3	136.24(13)	N1-Pr2-O17	61.38(15)
O13-Yb1-N3	64.55(12)	O8-Pr2-O17	132.30(15)
O9-Yb1-N5	70.33(13)	N2-Pr2-O17	103.48(14)
O11-Yb1-N5	85.42(14)	O1-Pr2-Yb1	123.21(9)
O3-Yb1-N5	132.17(13)	O14-Pr2-Yb1	97.44(8)
O8-Yb1-N5	71.62(13)	O6-Pr2-Yb1	155.81(10)
O19-Yb1-N5	136.63(14)	O13-Pr2-Yb1	37.69(7)
O4-Yb1-N5	140.58(13)	O3-Pr2-Yb1	36.05(9)
O13-Yb1-N5	75.02(13)	O16-Pr2-Yb1	101.33(10)
N3-Yb1-N5	66.87(14)	N1-Pr2-Yb1	85.34(10)
O9-Yb1-Pr2	115.54(9)	O8-Pr2-Yb1	37.87(7)
O11-Yb1-Pr2	170.72(9)	N2-Pr2-Yb1	95.52(9)
O3-Yb1-Pr2	40.18(9)	O17-Pr2-Yb1	133.09(14)
O8-Yb1-Pr2	43.39(8)	Yb1-O3-Pr2	103.77(14)
O19-Yb1-Pr2	99.89(10)	Yb1-O8-Pr2	98.74(12)
O4-Yb1-Pr2	106.08(9)	Yb1-O13-Pr2	102.44(12)

Table V.A38. Selected interatomic distances (Å) and angles for complex 54

Lu1-O8	2.306(14)	O13-Lu1-Pr2	39.1(4)
Lu1-O11	2.324(15)	N3-Lu1-Pr2	104.9(4)
Lu1-O4	2.328(15)	N5-Lu1-Pr2	93.5(4)
Lu1-O3	2.394(13)	O6-Pr2-O14	69.4(5)
Lu1-O19	2.400(16)	O6-Pr2-O1	74.7(5)

Lu1-O9	2.410(15)	O14-Pr2-O1	71.1(5)
Lu1-O13	2.423(14)	O6-Pr2-O13	90.2(5)
Lu1-N3	2.423(17)	O14-Pr2-O13	66.5(4)
Lu1-N5	2.65(2)	O1-Pr2-O13	137.6(5)
Lu1...Pr2	3.8240(15)	O6-Pr2-O8	118.0(5)
Pr2-O6	2.430(14)	O14-Pr2-O8	131.6(4)
Pr2-O14	2.440(14)	O1-Pr2-O8	155.8(5)
Pr2-O1	2.461(14)	O13-Pr2-O8	65.8(4)
Pr2-O13	2.471(15)	O6-Pr2-N2	62.1(5)
Pr2-O8	2.556(13)	O14-Pr2-N2	122.7(5)
Pr2-N2	2.59(2)	O1-Pr2-N2	119.6(5)
Pr2-O16	2.603(17)	O13-Pr2-N2	84.6(5)
Pr2-O3	2.655(13)	O8-Pr2-N2	59.5(5)
Pr2-N1	2.704(18)	O6-Pr2-O16	118.7(6)
Pr2-O17	2.76(2)	O14-Pr2-O16	147.4(5)
O8-Lu1-O11	142.3(5)	O1-Pr2-O16	80.6(5)
O8-Lu1-O4	115.6(5)	O13-Pr2-O16	139.5(5)
O11-Lu1-O4	72.9(5)	O8-Pr2-O16	75.2(5)
O8-Lu1-O3	66.5(5)	N2-Pr2-O16	85.1(6)
O11-Lu1-O3	143.6(5)	O6-Pr2-O3	154.5(5)
O4-Lu1-O3	73.0(5)	O14-Pr2-O3	93.4(4)
O8-Lu1-O19	74.6(5)	O1-Pr2-O3	118.7(4)
O11-Lu1-O19	75.4(5)	O13-Pr2-O3	65.2(4)
O4-Lu1-O19	135.4(5)	O8-Pr2-O3	59.3(4)
O3-Lu1-O19	140.1(5)	N2-Pr2-O3	118.4(5)
O8-Lu1-O9	68.8(5)	O16-Pr2-O3	86.0(5)
O11-Lu1-O9	81.3(5)	O6-Pr2-N1	132.3(5)
O4-Lu1-O9	70.8(5)	O14-Pr2-N1	78.8(5)
O3-Lu1-O9	99.0(5)	O1-Pr2-N1	61.6(5)
O19-Lu1-O9	74.1(5)	O13-Pr2-N1	109.0(5)
O8-Lu1-O13	70.5(5)	O8-Pr2-N1	109.7(5)
O11-Lu1-O13	131.3(5)	N2-Pr2-N1	158.3(6)
O4-Lu1-O13	135.4(5)	O16-Pr2-N1	73.6(6)
O3-Lu1-O13	70.0(5)	O3-Pr2-N1	57.2(5)
O19-Lu1-O13	89.2(5)	O6-Pr2-O17	72.4(6)
O9-Lu1-O13	138.8(5)	O14-Pr2-O17	128.5(6)
O8-Lu1-N3	123.0(5)	O1-Pr2-O17	66.4(6)
O11-Lu1-N3	65.3(5)	O13-Pr2-O17	146.2(5)
O4-Lu1-N3	121.1(6)	O8-Pr2-O17	96.6(6)
O3-Lu1-N3	125.3(6)	N2-Pr2-O17	61.7(6)
O19-Lu1-N3	69.9(6)	O16-Pr2-O17	46.3(6)
O9-Lu1-N3	135.6(6)	O3-Pr2-O17	132.0(6)
O13-Lu1-N3	66.0(5)	N1-Pr2-O17	104.1(6)
O8-Lu1-N5	133.0(5)	O6-Pr2-Lu1	122.9(4)
O11-Lu1-N5	84.7(6)	O14-Pr2-Lu1	97.5(3)
O4-Lu1-N5	69.7(6)	O1-Pr2-Lu1	155.3(4)
O3-Lu1-N5	71.9(5)	O13-Pr2-Lu1	38.2(3)
O19-Lu1-N5	136.9(6)	O8-Pr2-Lu1	35.9(3)
O9-Lu1-N5	140.4(6)	N2-Pr2-Lu1	85.1(4)
O13-Lu1-N5	75.7(6)	O16-Pr2-Lu1	101.9(4)
N3-Lu1-N5	67.1(6)	O3-Pr2-Lu1	38.3(3)
O8-Lu1-Pr2	40.5(3)	N1-Pr2-Lu1	95.2(4)
O11-Lu1-Pr2	170.0(4)	O17-Pr2-Lu1	132.4(5)
O4-Lu1-Pr2	115.8(4)	Lu1-O3-Pr2	98.3(4)
O3-Lu1-Pr2	43.4(3)	Lu1-O8-Pr2	103.6(5)
O19-Lu1-Pr2	99.7(4)	Lu1-O13-Pr2	102.8(5)
O9-Lu1-Pr2	106.0(4)		

Pr1-O6	2.437(5)	N1-Pr1-O17	63.79(19)
Pr1-O1	2.454(5)	O8-Pr1-O17	122.75(17)
Pr1-O13	2.478(5)	N2-Pr1-O17	107.41(19)
Pr1-O14	2.484(5)	O6-Pr1-Y2	157.04(13)
Pr1-O3	2.496(5)	O1-Pr1-Y2	122.21(13)
Pr1-O16	2.590(6)	O13-Pr1-Y2	37.82(12)
Pr1-N1	2.628(6)	O14-Pr1-Y2	96.31(12)
Pr1-O8	2.656(5)	O3-Pr1-Y2	37.15(13)
Pr1-N2	2.695(6)	O16-Pr1-Y2	102.06(13)
Pr1-O17	2.696(6)	N1-Pr1-Y2	81.29(14)
Pr1...Y2	3.8185(11)	O8-Pr1-Y2	37.93(11)
Y2-O9	2.292(5)	N2-Pr1-Y2	95.59(14)
Y2-O11	2.320(6)	O17-Pr1-Y2	120.19(13)
Y2-O3	2.370(6)	O9-Y2-O11	73.32(19)
Y2-O8	2.374(5)	O9-Y2-O3	113.35(18)
Y2-O4	2.388(6)	O11-Y2-O3	145.6(2)
Y2-O13	2.402(5)	O9-Y2-O8	72.74(18)
Y2-O19	2.405(6)	O11-Y2-O8	142.14(19)
Y2-N3	2.460(7)	O3-Y2-O8	65.80(19)
Y2-N5	2.663(7)	O9-Y2-O4	70.09(19)
O6-Pr1-O1	73.29(18)	O11-Y2-O4	85.00(19)
O6-Pr1-O13	138.75(18)	O3-Y2-O4	67.64(18)
O1-Pr1-O13	88.96(18)	O8-Y2-O4	98.71(18)
O6-Pr1-O14	72.48(18)	O9-Y2-O13	136.63(18)
O1-Pr1-O14	68.95(18)	O11-Y2-O13	129.82(18)
O13-Pr1-O14	66.39(17)	O3-Y2-O13	69.92(18)
O6-Pr1-O3	154.18(18)	O8-Y2-O13	70.09(17)
O1-Pr1-O3	119.21(17)	O4-Y2-O13	136.86(19)
O13-Pr1-O3	66.70(17)	O9-Y2-O19	136.76(19)
O14-Pr1-O3	132.09(18)	O11-Y2-O19	78.1(2)
O6-Pr1-O16	76.12(18)	O3-Y2-O19	75.4(2)
O1-Pr1-O16	126.8(2)	O8-Y2-O19	139.5(2)
O13-Pr1-O16	139.86(17)	O4-Y2-O19	75.81(19)
O14-Pr1-O16	137.80(18)	O13-Y2-O19	86.59(19)
O3-Pr1-O16	78.66(17)	O9-Y2-N3	125.1(2)
O6-Pr1-N1	121.63(19)	O11-Y2-N3	66.0(2)
O1-Pr1-N1	61.92(19)	O3-Y2-N3	121.2(2)
O13-Pr1-N1	77.55(19)	O8-Y2-N3	123.9(2)
O14-Pr1-N1	118.35(19)	O4-Y2-N3	136.8(2)
O3-Pr1-N1	58.84(18)	O13-Y2-N3	63.9(2)
O16-Pr1-N1	101.9(2)	O19-Y2-N3	67.7(2)
O6-Pr1-O8	120.57(17)	O9-Y2-N5	71.58(19)
O1-Pr1-O8	152.01(18)	O11-Y2-N5	82.3(2)
O13-Pr1-O8	64.47(16)	O3-Y2-N5	132.1(2)
O14-Pr1-O8	91.16(17)	O8-Y2-N5	71.5(2)
O3-Pr1-O8	59.92(17)	O4-Y2-N5	141.6(2)
O16-Pr1-O8	81.18(19)	O13-Y2-N5	76.1(2)
N1-Pr1-O8	116.46(18)	O19-Y2-N5	135.4(2)
O6-Pr1-N2	62.51(19)	N3-Y2-N5	67.8(2)
O1-Pr1-N2	129.44(19)	O9-Y2-Pr1	115.18(14)
O13-Pr1-N2	108.12(18)	O11-Y2-Pr1	169.01(14)
O14-Pr1-N2	75.16(18)	O3-Y2-Pr1	39.50(13)
O3-Pr1-N2	111.21(18)	O8-Y2-Pr1	43.45(13)
O16-Pr1-N2	65.55(19)	O4-Y2-Pr1	104.22(13)

N1-Pr1-N2	166.31(19)	O13-Y2-Pr1	39.22(12)
O8-Pr1-N2	58.08(18)	O19-Y2-Pr1	98.16(15)
O6-Pr1-O17	75.89(18)	N3-Y2-Pr1	102.98(16)
O1-Pr1-O17	82.93(19)	N5-Y2-Pr1	93.67(16)
O13-Pr1-O17	139.69(17)	Y2-O3-Pr1	103.4(2)
O14-Pr1-O17	142.38(18)	Y2-O8-Pr1	98.62(19)
O3-Pr1-O17	83.13(18)	Y2-O13-Pr1	102.96(19)
O16-Pr1-O17	47.65(19)		

Table V.A40 Selected interatomic distances (Å) and angles for complex 56

Sm2-O4	2.384(8)	N3-Sm2-Nd1	101.6(2)
Sm2-O11	2.386(8)	N5-Sm2-Nd1	91.7(2)
Sm2-O8	2.412(9)	O14-Nd1-O6	70.2(3)
Sm2-O3	2.445(7)	O14-Nd1-O1	72.5(3)
Sm2-O9	2.463(7)	O6-Nd1-O1	73.5(3)
Sm2-O13	2.470(7)	O14-Nd1-O13	68.4(2)
Sm2-O19	2.479(9)	O6-Nd1-O13	90.1(3)
Sm2-N3	2.503(9)	O1-Nd1-O13	140.7(3)
Sm2-N5	2.723(11)	O14-Nd1-O8	135.1(3)
Sm2...Nd1	3.8602(9)	O6-Nd1-O8	118.7(3)
Nd1-O14	2.404(8)	O1-Nd1-O8	151.4(3)
Nd1-O6	2.410(7)	O13-Nd1-O8	67.7(2)
Nd1-O1	2.439(7)	O14-Nd1-N2	125.8(3)
Nd1-O13	2.469(7)	O6-Nd1-N2	62.8(3)
Nd1-O8	2.530(8)	O1-Nd1-N2	115.4(3)
Nd1-N2	2.584(10)	O13-Nd1-N2	85.8(3)
Nd1-O16	2.589(9)	O8-Nd1-N2	59.4(3)
Nd1-O3	2.652(7)	O14-Nd1-O16	148.1(2)
Nd1-N1	2.682(9)	O6-Nd1-O16	112.8(3)
O4-Sm2-O11	77.0(3)	O1-Nd1-O16	78.1(3)
O4-Sm2-O8	113.0(3)	O13-Nd1-O16	140.7(2)
O11-Sm2-O8	145.5(3)	O8-Nd1-O16	73.3(3)
O4-Sm2-O3	71.5(2)	N2-Nd1-O16	78.0(3)
O11-Sm2-O3	144.7(3)	O14-Nd1-O3	93.7(2)
O8-Sm2-O3	64.7(3)	O6-Nd1-O3	155.6(3)
O4-Sm2-O9	71.5(3)	O1-Nd1-O3	120.1(2)
O11-Sm2-O9	86.7(3)	O13-Nd1-O3	66.5(2)
O8-Sm2-O9	67.3(3)	O8-Nd1-O3	60.1(2)
O3-Sm2-O9	97.7(2)	N2-Nd1-O3	119.2(3)
O4-Sm2-O13	134.6(3)	O16-Nd1-O3	90.6(2)
O11-Sm2-O13	128.1(2)	O14-Nd1-N1	79.8(3)
O8-Sm2-O13	69.5(3)	O6-Nd1-N1	132.1(3)
O3-Sm2-O13	69.8(2)	O1-Nd1-N1	62.1(3)
O9-Sm2-O13	136.3(3)	O13-Nd1-N1	112.8(3)
O4-Sm2-O19	136.5(3)	O8-Nd1-N1	109.0(3)
O11-Sm2-O19	75.6(3)	N2-Nd1-N1	153.6(3)
O8-Sm2-O19	75.6(3)	O16-Nd1-N1	75.8(3)
O3-Sm2-O19	139.3(3)	O3-Nd1-N1	58.1(2)
O9-Sm2-O19	73.8(3)	O14-Nd1-Sm2	98.80(17)
O13-Sm2-O19	88.8(3)	O6-Nd1-Sm2	23.5(2)
O4-Sm2-N3	124.8(3)	O1-Nd1-Sm2	157.9(2)
O11-Sm2-N3	65.0(3)	O13-Nd1-Sm2	38.60(15)
O8-Sm2-N3	121.2(3)	O8-Nd1-Sm2	37.5(2)
O3-Sm2-N3	122.8(3)	N2-Nd1-Sm2	86.3(2)
O9-Sm2-N3	138.9(3)	O16-Nd1-Sm2	104.14(17)

O13-Sm2-N3	63.1(3)	O3-Nd1-Sm2	38.81(14)
O19-Sm2-N3	70.7(3)	N1-Nd1-Sm2	96.8(2)
O4-Sm2-N5	70.3(3)	Sm2-O3-Nd1	98.4(2)
O11-Sm2-N5	84.1(3)	Sm2-O8-Nd1	102.7(3)
O8-Sm2-N5	130.3(3)	Nd1-O13-Sm2	102.8(2)
O3-Sm2-N5	70.9(3)	O11-Sm2-Nd1	166.55(19)
O9-Sm2-N5	141.8(3)	O8-Sm2-Nd1	39.75(19)
O13-Sm2-N5	75.3(3)	O3-Sm2-Nd1	42.83(17)
O19-Sm2-N5	138.1(3)	O9-Sm2-Nd1	104.20(18)
N3-Sm2-N5	67.5(3)	O13-Sm2-Nd1	38.57(17)
O4-Sm2-Nd1	113.69(19)	O19-Sm2-Nd1	99.6(2)

Table V.A41. Selected interatomic distances (Å) and angles for complex 57

Gd2-O4	2.350(5)	O19-Gd2-Nd1	97.90(15)
Gd2-O11	2.378(6)	N3-Gd2-Nd1	102.26(14)
Gd2-O8	2.407(6)	N5-Gd2-Nd1	93.41(16)
Gd2-O3	2.411(5)	O1-Nd1-O6	73.29(18)
Gd2-O13	2.430(5)	O1-Nd1-O14	72.26(19)
Gd2-O9	2.439(5)	O6-Nd1-O14	69.02(18)
Gd2-O19	2.448(5)	O1-Nd1-O13	139.23(18)
Gd2-N3	2.503(7)	O6-Nd1-O13	88.29(18)
Gd2-N5	2.711(7)	O14-Nd1-O1	67.19(17)
Gd2...Nd1	3.8358(7)	O1-Nd1-O8	152.61(19)
Nd1-O1	2.427(5)	O6-Nd1-O8	119.92(17)
Nd1-O6	2.427(5)	O14-Nd1-O8	133.71(19)
Nd1-O14	2.459(5)	O13-Nd1-O8	67.86(17)
Nd1-O13	2.471(6)	O1-Nd1-O16	76.16(19)
Nd1-O8	2.496(5)	O6-Nd1-O16	126.4(2)
Nd1-O16	2.565(6)	O14-Nd1-O1	137.97(18)
Nd1-N2	2.616(6)	O13-Nd1-O1	140.25(18)
Nd1-O3	2.658(5)	O8-Nd1-O16	77.01(19)
Nd1-N1	2.695(6)	O1-Nd1-N2	120.34(19)
Nd1-O17	2.707(7)	O6-Nd1-N2	62.16(18)
O4-Gd2-O11	74.26(19)	O14-Nd1-N2	120.06(19)
O4-Gd2-O8	113.07(19)	O13-Nd1-N2	78.5(2)
O11-Gd2-O8	146.77(18)	O8-Nd1-N2	59.45(17)
O4-Gd2-O3	72.58(18)	O16-Nd1-N2	99.6(2)
O11-Gd2-O3	142.57(18)	O1-Nd1-O3	120.55(16)
O8-Gd2-O3	65.01(17)	O6-Nd1-O3	151.81(19)
O4-Gd2-O13	135.77(17)	O14-Nd1-O3	90.95(16)
O11-Gd2-O13	128.75(18)	O13-Nd1-O3	65.13(16)
O8-Gd2-O13	69.94(17)	O8-Nd1-O3	60.22(15)
O3-Gd2-O13	69.67(17)	O16-Nd1-O3	81.81(17)
O4-Gd2-O9	71.11(17)	N2-Nd1-O3	117.41(17)
O11-Gd2-O9	86.82(19)	O1-Nd1-N1	62.52(19)
O8-Gd2-O9	67.00(18)	O6-Nd1-N1	129.70(18)
O3-Gd2-O9	98.36(18)	O14-Nd1-N1	75.45(17)
O13-Gd2-O9	136.23(19)	O13-Nd1-N1	109.57(19)
O4-Gd2-O19	137.51(19)	O8-Nd1-N1	110.34(17)
O11-Gd2-O19	78.2(2)	O16-Nd1-N1	65.59(18)
O8-Gd2-O19	75.8(2)	N2-Nd1-N1	164.48(19)
O3-Gd2-O19	139.1(2)	O3-Nd1-N1	58.07(18)
O13-Gd2-O19	86.71(18)	O1-Nd1-O17	73.6(2)
O9-Gd2-O19	75.68(18)	O6-Nd1-O17	81.4(2)
O4-Gd2-N3	124.8(2)		

O11-Gd2-N3	65.35(19)	O14-Nd1-O17	139.78(19)
O8-Gd2-N3	121.46(19)	O13-Nd1-O17	140.27(18)
O3-Gd2-N3	123.21(18)	O8-Nd1-O17	84.4(2)
O13-Gd2-N3	63.55(19)	O16-Nd1-O17	47.90(18)
O9-Gd2-N3	137.78(19)	N2-Nd1-O17	62.8(2)
O19-Gd2-N3	68.2(2)	O3-Nd1-O17	124.92(18)
O4-Gd2-N5	70.62(19)	N1-Nd1-O17	106.44(19)
O11-Gd2-N5	81.8(2)	O1-Nd1-Gd2	157.74(13)
O8-Gd2-N5	131.4(2)	O6-Nd1-Gd2	121.93(14)
O3-Gd2-N5	71.3(2)	O14-Nd1-Gd2	96.99(13)
O13-Gd2-N5	76.07(19)	O13-Nd1-Gd2	38.12(11)
O9-Gd2-N5	141.71(18)	O8-Nd1-Gd2	37.70(13)
O19-Gd2-N5	136.0(2)	O16-Nd1-Gd2	102.13(14)
N3-Gd2-N5	67.9(2)	N2-Nd1-Gd2	81.92(14)
O4-Gd2-Nd1	115.02(14)	O3-Nd1-Gd2	38.47(11)
O11-Gd2-Nd1	167.61(13)	N1-Nd1-Gd2	96.26(15)
O8-Gd2-Nd1	39.35(11)	O17-Nd1-Gd2	122.10(15)
O3-Gd2-Nd1	43.30(12)	Gd2-O3-Nd1	98.22(15)
O13-Gd2-Nd1	38.88(13)	Gd2-O8-Nd1	102.95(19)
O9-Gd2-Nd1	103.74(14)	Gd2-O13-Nd1	103.00(19)

Table V.A42. Selected interatomic distances (Å) and angles for complex 58

Tb2-O4	2.344(4)	O13-Tb2-Nd1	39.19(9)
Tb2-O11	2.349(4)	N3-Tb2-Nd1	102.63(10)
Tb2-O8	2.363(4)	N5-Tb2-Nd1	92.19(11)
Tb2-O3	2.410(4)	O6-Nd1-O14	69.79(14)
Tb2-O9	2.426(4)	O6-Nd1-O1	73.87(13)
Tb2-O19	2.427(4)	O14-Nd1-O1	71.90(14)
Tb2-O13	2.442(3)	O6-Nd1-O13	90.15(13)
Tb2-N3	2.469(5)	O14-Nd1-O13	67.91(12)
Tb2-N5	2.693(5)	O1-Nd1-O13	139.75(13)
Tb2...Nd1	3.8391(6)	O6-Nd1-O8	118.65(13)
Nd1-O6	2.413(4)	O14-Nd1-O8	133.94(13)
Nd1-O14	2.422(4)	O1-Nd1-O8	152.89(14)
Nd1-O1	2.431(4)	O13-Nd1-O8	66.94(13)
Nd1-O13	2.484(4)	O6-Nd1-O16	115.87(15)
Nd1-O8	2.531(4)	O14-Nd1-O16	147.88(13)
Nd1-O16	2.558(5)	O1-Nd1-O16	79.39(14)
Nd1-N2	2.580(5)	O13-Nd1-O16	139.74(13)
Nd1-O3	2.647(4)	O8-Nd1-O16	73.50(13)
Nd1-N1	2.690(4)	O6-Nd1-N2	63.13(15)
Nd1-O17	2.934(7)	O14-Nd1-N2	125.44(14)
O4-Tb2-O11	74.75(13)	O1-Nd1-N2	116.76(15)
O4-Tb2-O8	113.75(14)	O13-Nd1-N2	85.82(14)
O11-Tb2-O8	144.29(14)	O8-Nd1-N2	59.28(14)
O4-Tb2-O3	72.27(13)	O16-Nd1-N2	80.30(15)
O11-Tb2-O3	144.04(13)	O6-Nd1-O3	154.99(14)
O8-Tb2-O3	65.12(13)	O14-Nd1-O3	93.77(12)
O4-Tb2-O9	70.61(13)	O1-Nd1-O3	119.98(12)
O11-Tb2-O9	83.52(14)	O13-Nd1-O3	65.74(11)
O8-Tb2-O9	68.57(13)	O8-Nd1-O3	59.44(12)
O3-Tb2-O9	98.54(13)	O16-Nd1-O3	88.20(13)
O4-Tb2-O19	135.69(14)	N2-Nd1-O3	118.43(13)
O11-Tb2-O19	75.24(14)	O6-Nd1-N1	132.00(13)

O8-Tb2-O19	76.02(14)	O14-Nd1-N1	79.08(13)
O3-Tb2-O19	140.09(14)	O1-Nd1-N1	61.99(13)
O9-Tb2-O19	74.28(13)	O13-Nd1-N1	111.17(13)
O4-Tb2-O13	135.27(13)	O8-Nd1-N1	109.30(13)
O11-Tb2-O13	129.55(13)	O16-Nd1-N1	74.86(14)
O8-Tb2-O13	70.28(13)	N2-Nd1-N1	154.93(15)
O3-Tb2-O13	70.15(12)	O3-Nd1-N1	58.08(12)
O9-Tb2-O13	138.18(14)	O6-Nd1-O17	71.06(18)
O19-Tb2-O13	89.04(13)	O14-Nd1-O17	127.01(18)
O4-Tb2-N3	123.93(15)	O1-Nd1-O17	63.88(17)
O11-Tb2-N3	66.02(14)	O13-Nd1-O17	145.18(15)
O8-Tb2-N3	121.63(15)	O8-Nd1-O17	96.06(18)
O3-Tb2-N3	123.76(14)	O16-Nd1-O17	44.85(17)
O9-Tb2-N3	137.34(14)	N2-Nd1-O17	59.68(17)
O19-Tb2-N3	69.68(15)	O3-Nd1-O17	132.88(17)
O13-Tb2-N3	63.56(14)	N1-Nd1-O17	103.02(15)
O4-Tb2-N5	70.58(14)	O6-Nd1-Tb2	123.24(10)
O11-Tb2-N5	84.72(15)	O14-Nd1-Tb2	98.56(9)
O8-Tb2-N5	130.99(14)	O1-Nd1-Tb2	157.18(10)
O3-Tb2-N5	71.20(14)	O13-Nd1-Tb2	38.40(8)
O9-Tb2-N5	141.14(14)	O8-Nd1-Tb2	36.79(9)
O19-Tb2-N5	137.07(15)	O16-Nd1-Tb2	102.60(10)
O13-Tb2-N5	75.00(14)	N2-Nd1-Tb2	85.80(11)
N3-Tb2-N5	67.51(15)	O3-Nd1-Tb2	38.36(8)
O4-Tb2-Nd1	114.61(9)	N1-Nd1-Tb2	96.26(10)
O11-Tb2-Nd1	168.56(9)	O17-Nd1-Tb2	132.85(15)
O8-Tb2-Nd1	39.91(9)	Tb2-O3-Nd1	98.66(12)
O3-Tb2-Nd1	42.98(9)	Tb2-O8-Nd1	103.30(15)
O9-Tb2-Nd1	105.47(10)	Tb2-O13-Nd1	102.42(13)
O19-Tb2-Nd1	100.06(10)		

Table V.A43. Selected interatomic distances (Å) and angles for complex 59

Tm1-O8	2.324(16)	N3-Tm1-Nd2	103.8(5)
Tm1-O4	2.326(16)	O13-Tm1-Nd2	38.8(4)
Tm1-O11	2.328(16)	N5-Tm1-Nd2	92.9(5)
Tm1-O19	2.398(18)	O14-Nd2-O6	69.1(6)
Tm1-O3	2.397(14)	O14-Nd2-O1	71.6(5)
Tm1-O9	2.404(16)	O6-Nd2-O17	74.2(5)
Tm1-N3	2.417(19)	O14-Nd2-O13	67.4(5)
Tm1-O13	2.427(15)	O6-Nd2-O13	89.9(6)
Tm1-N5	2.67(2)	O1-Nd2-O13	139.0(5)
Tm1...Nd2	3.8160(17)	O14-Nd2-O8	132.9(5)
Nd2-O14	2.407(16)	O6-Nd2-O8	118.1(5)
Nd2-O6	2.430(16)	O1-Nd2-O8	154.2(5)
Nd2-O1	2.448(16)	O13-Nd2-O8	66.2(5)
Nd2-O13	2.454(15)	O14-Nd2-N2	123.3(6)
Nd2-O8	2.542(15)	O6-Nd2-N2	62.4(6)
Nd2-N2	2.55(2)	O1-Nd2-N2	118.1(6)
Nd2-O16	2.586(18)	O13-Nd2-N2	84.5(6)
Nd2-O3	2.644(15)	O8-Nd2-N2	59.2(6)
Nd2-N1	2.69(2)	O14-Nd2-O16	148.0(5)
Nd2-O17	2.82(3)	O6-Nd2-O16	117.8(6)
O8-Tm1-O4	115.4(6)	O1-Nd2-O16	80.2(5)
O8-Tm1-O11	142.6(5)	O13-Nd2-O16	139.1(5)

O4-Tm1-O11	73.3(6)	O8-Nd2-O16	74.0(5)
O8-Tm1-O19	75.3(6)	N2-Nd2-O16	83.3(6)
O4-Tm1-O19	135.5(6)	O14-Nd2-O3	93.7(5)
O11-Tm1-O19	74.9(6)	O6-Nd2-O3	154.4(6)
O8-Tm1-O3	66.4(5)	O1-Nd2-O3	119.5(5)
O4-Tm1-O3	72.9(5)	O13-Nd2-O3	65.5(5)
O11-Tm1-O3	143.7(5)	O8-Nd2-O3	59.8(5)
O19-Tm1-O3	140.6(6)	N2-Nd2-O3	118.6(5)
O8-Tm1-O9	68.6(5)	O16-Nd2-O3	86.9(5)
O4-Tm1-O9	71.1(6)	O14-Nd2-N1	78.9(6)
O11-Tm1-O9	81.9(6)	O6-Nd2-N1	132.5(6)
O19-Tm1-O9	74.3(6)	O1-Nd2-N1	62.6(6)
O3-Tm1-O9	99.1(5)	O13-Nd2-N1	109.5(6)
O8-Tm1-N3	122.2(6)	O8-Nd2-N1	109.4(6)
O4-Tm1-N3	121.9(6)	N2-Nd2-N1	157.6(6)
O11-Tm1-N3	65.9(6)	O16-Nd2-N1	74.7(6)
O19-Tm1-N3	69.5(6)	O3-Nd2-N15	56.9(5)
O3-Tm1-N3	124.3(6)	O14-Nd2-O17	128.1(7)
O9-Tm1-N3	136.3(6)	O6-Nd2-O17	72.1(7)
O8-Tm1-O13	70.1(5)	O1-Nd2-O17	65.5(6)
O4-Tm1-O13	135.4(5)	O13-Nd2-O17	145.0(6)
O11-Tm1-O13	131.0(5)	O8-Nd2-O17	95.5(6)
O19-Tm1-O13	89.1(6)	N2-Nd2-O17	60.6(7)
O3-Tm1-O13	69.9(5)	O16-Nd2-O17	45.7(7)
O9-Tm1-O13	138.2(6)	O3-Nd2-O17	132.4(7)
N3-Tm1-O13	65.1(6)	N1-Nd2-O17	104.7(7)
O8-Tm1-N5	132.4(6)	O14-Nd2-Tm1	98.3(4)
O4-Tm1-N5	69.8(6)	O6-Nd2-Tm1	122.9(4)
O11-Tm1-N5	85.0(6)	O1-Nd2-Tm1	156.6(4)
O19-Tm1-N5	136.6(6)	O13-Nd2-Tm1	38.3(4)
O3-Tm1-N5	71.4(6)	O8-Nd2-Tm1	36.4(4)
O9-Tm1-N5	140.8(6)	N2-Nd2-Tm1	85.2(5)
N3-Tm1-N5	67.2(6)	O16-Nd2-Tm1	101.8(4)
O13-Tm1-N5	75.7(6)	O3-Nd2-Tm1	38.4(3)
O8-Tm1-Nd2	40.4(4)	N1-Nd2-Tm1	95.1(4)
O4-Tm1-Nd2	115.6(4)	O17-Nd2-Tm1	131.9(5)
O11-Tm1-Nd2	169.6(4)	Tm1-O3-Nd2	98.3(5)
O19-Tm1-Nd2	100.1(5)	Tm1-O8-Nd2	103.2(5)
O3-Tm1-Nd2	43.3(3)	Tm1-O13-Nd2	102.8(6)
O9-Tm1-Nd2	105.8(4)		

Table V.A44. Selected interatomic distances (Å) and angles for complex 60

Yb1-O9	2.311(5)	O13-Yb1-Nd2	39.45(12)
Yb1-O11	2.321(5)	N3-Yb1-Nd2	103.60(14)
Yb1-O3	2.324(5)	N5-Yb1-Nd2	92.66(14)
Yb1-O8	2.383(5)	C31-Yb1-Nd2	150.61(14)
Yb1-O19	2.394(6)	O1-Nd2-O14	69.95(19)
Yb1-O4	2.403(5)	O1-Nd2-O6	74.10(18)
Yb1-O13	2.405(5)	O14-Nd2-O6	71.90(18)
Yb1-N3	2.443(6)	O1-Nd2-O13	90.51(18)
Yb1-N5	2.672(7)	O14-Nd2-O13	67.72(16)
Yb1...Nd2	3.8229(6)	O6-Nd2-O13	139.59(18)
Nd2-O1	2.418(5)	O1-Nd2-O3	118.47(18)
Nd2-O14	2.428(5)	O14-Nd2-O3	132.71(17)

Nd2-O6	2.438(5)	O6-Nd2-O3	154.00(18)
Nd2-O13	2.490(5)	O13-Nd2-O3	65.85(17)
Nd2-O3	2.534(5)	O1-Nd2-N1	62.9(2)
Nd2-N1	2.581(7)	O14-Nd2-N1	124.79(19)
Nd2-O16	2.582(6)	O6-Nd2-N1	117.69(19)
Nd2-O8	2.645(5)	O13-Nd2-N1	85.22(19)
Nd2-N2	2.688(6)	O3-Nd2-N1	59.37(18)
Nd2-O17	2.865(9)	O1-Nd2-O16	116.3(2)
O9-Yb1-O11	73.21(18)	O14-Nd2-O16	147.96(18)
O9-Yb1-O3	114.80(19)	O6-Nd2-O16	79.69(18)
O11-Yb1-O3	142.95(19)	O13-Nd2-O16	139.33(16)
O9-Yb1-O8	72.91(17)	O3-Nd2-O16	74.32(17)
O11-Yb1-O8	143.72(18)	N1-Nd2-O16	81.5(2)
O3-Yb1-O8	65.74(18)	O1-Nd2-O8	154.49(18)
O9-Yb1-O19	135.01(19)	O14-Nd2-O8	93.25(16)
O11-Yb1-O1	74.9(2)	O6-Nd2-O8	119.94(16)
O3-Yb1-O19	75.7(2)	O13-Nd2-O8	64.87(15)
O8-Yb1-O19	140.47(19)	O3-Nd2-O8	59.09(16)
O9-Yb1-O4	70.48(18)	N1-Nd2-O8	118.13(17)
O11-Yb1-O4	81.66(18)	O16-Nd2-O8	88.20(17)
O3-Yb1-O4	68.91(18)	O1-Nd2-N2	132.01(18)
O8-Yb1-O4	98.85(17)	O14-Nd2-N2	78.64(18)
O19-Yb1-O4	74.20(19)	O6-Nd2-N2	61.94(18)
O9-Yb1-O13	135.67(18)	O13-Nd2-N2	110.27(18)
O11-Yb1-O1	130.78(17)	O3-Nd2-N2	109.51(17)
O3-Yb1-O13	70.52(18)	N1-Nd2-N2	156.2(2)
O8-Yb1-O13	70.30(16)	O16-Nd2-N2	75.07(19)
O19-Yb1-O1	89.31(18)	O8-Nd2-N2 5	58.09(16)
O4-Yb1-O13	138.80(18)	O1-Nd2-O17	71.1(2)
O9-Yb1-N3	122.7(2)	O14-Nd2-O17	127.5(2)
O11-Yb1-N3	66.50(18)	O6-Nd2-O17	64.5(2)
O3-Yb1-N3	122.0(2)	O13-Nd2-O17	145.2(2)
O8-Yb1-N3	124.43(18)	O3-Nd2-O17	96.7(2)
O19-Yb1-N3	69.5(2)	N1-Nd2-O17	60.3(2)
O4-Yb1-N3	136.50(19)	O16-Nd2-O17	45.3(2)
O13-Yb1-N3	64.30(18)	O8-Nd2-O17	133.3(2)
O9-Yb1-N5	70.46(19)	N2-Nd2-O17	103.8(2)
O11-Yb1-N5	85.3(2)	O1-Nd2-Yb1	123.10(13)
O3-Yb1-N5	131.76(19)	O14-Nd2-Yb1	98.01(12)
O8-Yb1-N5	71.48(18)	O6-Nd2-Yb1	156.71(13)
O19-Yb1-N5	136.8(2)	O13-Nd2-Yb1	37.86(11)
O4-Yb1-N5	140.88(18)	O3-Nd2-Yb1	36.19(12)
O13-Yb1-N5	75.04(19)	N1-Nd2-Yb1	85.42(14)
N3-Yb1-N5	67.3(2)	O16-Nd2-Yb1	102.57(12)
O9-Yb1-Nd2	115.40(13)	O8-Nd2-Yb1	38.03(10)
O11-Yb1-Nd2	169.92(12)	N2-Nd2-Yb1	95.92(13)
O3-Yb1-Nd2	40.09(13)	O17-Nd2-Yb1	132.9(2)
O8-Yb1-Nd2	43.12(11)	Yb1-O3-Nd2	103.7(2)
O19-Yb1-Nd2	100.27(14)	Yb1-O8-Nd2	98.85(17)
O4-Yb1-Nd2	105.80(12)	Yb1-O13-Nd2	102.69(17)

Table V.A45. Selected interatomic distances (Å) and angles for complex 61

Lu1-O9	2.313(7)	O4-Lu1-Nd2	105.69(16)
Lu1-O11	2.324(7)	N3-Lu1-Nd2	103.58(18)
Lu1-O3	2.329(7)	N5-Lu1-Nd2	92.51(19)

Lu1-O8	2.386(6)	O14-Nd2-O1	69.9(2)
Lu1-O19	2.394(7)	O14-Nd2-O6	72.0(2)
Lu1-O13	2.400(6)	O1-Nd2-O6	74.1(2)
Lu1-O4	2.407(7)	O14-Nd2-O13	67.7(2)
Lu1-N3	2.444(8)	O1-Nd2-O13	90.6(2)
Lu1-N5	2.664(9)	O6-Nd2-O13	139.6(2)
Lu1...Nd2	3.8197(7)	O14-Nd2-O3	132.9(2)
Nd2-O14	2.422(7)	O1-Nd2-O3	118.4(2)
Nd2-O1	2.425(7)	O6-Nd2-O3	153.8(2)
Nd2-O6	2.443(6)	O13-Nd2-O3	66.0(2)
Nd2-O13	2.487(6)	O14-Nd2-O16	147.9(2)
Nd2-O3	2.530(6)	O1-Nd2-O16	116.2(2)
Nd2-O16	2.576(7)	O6-Nd2-O16	79.5(2)
Nd2-N1	2.580(8)	O13-Nd2-O16	139.4(2)
Nd2-O8	2.644(6)	O3-Nd2-O16	74.3(2)
Nd2-N2	2.686(8)	O14-Nd2-N1	124.9(2)
Nd2-O17	2.902(10)	O1-Nd2-N1	62.9(3)
O9-Lu1-O11	73.4(2)	O6-Nd2-N1	117.4(2)
O9-Lu1-O3	114.9(2)	O13-Nd2-N1	85.5(2)
O11-Lu1-O3	142.8(2)	O3-Nd2-N1	59.3(2)
O9-Lu1-O8	72.7(2)	O16-Nd2-N1	81.2(2)
O11-Lu1-O8	143.8(2)	O14-Nd2-O8	93.3(2)
O3-Lu1-O8	65.7(2)	O1-Nd2-O8	154.5(2)
O9-Lu1-O19	135.5(2)	O6-Nd2-O8	120.0(2)
O11-Lu1-O19	75.1(2)	O13-Nd2-O8	64.8(2)
O3-Lu1-O19	75.5(2)	O3-Nd2-O8	59.2(2)
O8-Lu1-O19	140.2(2)	O16-Nd2-O8	88.3(2)
O9-Lu1-O13	135.2(2)	N1-Nd2-O8	118.2(2)
O11-Lu1-O13	130.9(2)	O14-Nd2-N2	78.7(2)
O3-Lu1-O13	70.6(2)	O1-Nd2-N2	132.0(2)
O8-Lu1-O13	70.2(2)	O6-Nd2-N2	62.0(2)
O19-Lu1-O13	89.3(2)	O13-Nd2-N2	110.2(2)
O9-Lu1-O4	70.7(2)	O3-Nd2-N2	109.6(2)
O11-Lu1-O4	81.7(2)	O16-Nd2-N2	75.1(2)
O3-Lu1-O4	68.8(2)	N1-Nd2-N2	156.0(3)
O8-Lu1-O4	98.6(2)	O8-Nd2-N2	58.1(2)
O19-Lu1-O4	74.4(2)	O14-Nd2-O17	127.1(3)
O13-Lu1-O4	138.8(2)	O1-Nd2-O17	71.2(3)
O9-Lu1-N3	122.5(3)	O6-Nd2-O17	63.9(3)
O11-Lu1-N3	66.6(2)	O13-Nd2-O17	145.8(2)
O3-Lu1-N3	122.1(3)	O3-Nd2-O17	96.9(3)
O8-Lu1-N3	124.4(2)	O16-Nd2-O17	45.1(3)
O19-Lu1-N3	69.7(3)	N1-Nd2-O17	60.6(2)
O13-Lu1-N3	64.3(2)	O8-Nd2-O17	133.2(2)
O4-Lu1-N3	136.7(2)	N2-Nd2-O17	103.3(2)
O9-Lu1-N5	70.0(2)	O14-Nd2-Lu1	98.05(15)
O11-Lu1-N5	85.6(3)	O1-Nd2-Lu1	122.99(16)
O3-Lu1-N5	131.6(2)	O6-Nd2-Lu1	156.91(17)
O8-Lu1-N5	71.2(2)	O13-Nd2-Lu1	37.79(14)
O19-Lu1-N5	137.2(2)	O3-Nd2-Lu1	36.34(15)
O13-Lu1-N5	74.9(2)	O16-Nd2-Lu1	102.73(16)
O4-Lu1-N5	140.6(2)	N1-Nd2-Lu1	85.49(18)
N3-Lu1-N5	67.5(3)	O8-Nd2-Lu1	38.14(13)
O9-Lu1-Nd2	115.29(16)	N2-Nd2-Lu1	96.04(17)
O11-Lu1-Nd2	169.94(16)	O17-Nd2-Lu1	133.3(2)
O3-Lu1-Nd2	40.08(16)	Lu1-O3-Nd2	103.6(3)
O8-Lu1-Nd2	43.17(15)	Lu1-O8-Nd2	98.7(2)

O19-Lu1-Nd2	99.98(17)	Lu1-O13-Nd2	102.8(2)
O13-Lu1-Nd2	39.41(15)		

Table V.A46. Selected interatomic distances (Å) and angles for complex 62

Nd1-O6	2.417(4)	O16-Nd1-O17	45.38(18)
Nd1-O1	2.431(5)	O3-Nd1-O17	133.79(17)
Nd1-O14	2.432(4)	N1-Nd1-O17	103.39(18)
Nd1-O13	2.494(5)	O6-Nd1-Y2	123.14(12)
Nd1-O8	2.530(4)	O1-Nd1-Y2	156.83(11)
Nd1-N2	2.592(6)	O14-Nd1-Y2	98.13(11)
Nd1-O16	2.597(5)	O13-Nd1-Y2	38.31(9)
Nd1-O3	2.644(4)	O8-Nd1-Y2	36.52(11)
Nd1-N1	2.698(5)	N2-Nd1-Y2	85.35(12)
Nd1-O17	2.885(8)	O16-Nd1-Y2	102.54(11)
Nd1...Y2	3.8448(11)	O3-Nd1-Y2	38.19(9)
Y2-O11	2.326(5)	N1-Nd1-Y2	96.12(11)
Y2-O4	2.329(4)	O17-Nd1-Y2	133.41(15)
Y2-O8	2.356(5)	O11-Y2-O4	73.96(16)
Y2-O9	2.406(4)	O11-Y2-O8	144.36(16)
Y2-O3	2.407(4)	O4-Y2-O8	114.33(17)
Y2-O19	2.415(5)	O11-Y2-O9	83.03(16)
Y2-O13	2.440(4)	O4-Y2-O9	70.81(15)
Y2-N3	2.461(6)	O8-Y2-O9	68.91(15)
Y2-N5	2.692(6)	O11-Y2-O3	143.84(16)
O6-Nd1-O1	73.92(16)	O4-Y2-O3	72.82(15)
O6-Nd1-O14	69.85(16)	O8-Y2-O3	65.19(16)
O1-Nd1-O14	71.77(16)	O9-Y2-O3	99.09(15)
O6-Nd1-O13	90.22(15)	O11-Y2-O19	75.71(17)
O1-Nd1-O13	139.14(15)	O4-Y2-O19	135.72(16)
O14-Nd1-O13	67.41(14)	O8-Y2-O19	75.77(17)
O6-Nd1-O8	118.53(15)	O9-Y2-O19	74.16(16)
O1-Nd1-O8	153.72(16)	O3-Y2-O19	139.85(16)
O14-Nd1-O8	133.18(15)	O11-Y2-O13	129.90(15)
O13-Nd1-O8	66.64(14)	O4-Y2-O13	135.21(15)
O6-Nd1-N2	63.05(16)	O8-Y2-O13	70.24(15)
O1-Nd1-N2	117.65(17)	O9-Y2-O13	138.49(16)
O14-Nd1-N2	124.87(17)	O3-Y2-O13	69.77(14)
O13-Nd1-N2	85.36(17)	O19-Y2-O13	89.07(15)
O8-Nd1-N2	59.14(15)	O11-Y2-N3	66.54(16)
O6-Nd1-O16	115.93(17)	O4-Y2-N3	123.71(18)
O1-Nd1-O16	80.01(16)	O8-Y2-N3	121.29(17)
O14-Nd1-O16	148.39(15)	O9-Y2-N3	137.12(17)
O13-Nd1-O16	139.64(14)	O3-Y2-N3	123.41(16)
O8-Nd1-O16	73.72(15)	O19-Y2-N3	69.65(18)
N2-Nd1-O16	80.78(18)	O13-Y2-N3	63.41(16)
O6-Nd1-O3	154.55(16)	O11-Y2-N5	84.71(17)
O1-Nd1-O3	119.89(14)	O4-Y2-N5	70.49(16)
O14-Nd1-O3	93.25(14)	O8-Y2-N5	130.92(16)
O13-Nd1-O3	65.25(13)	O9-Y2-N5	141.25(16)
O8-Nd1-O3	59.42(14)	O3-Y2-N5	71.08(17)
N2-Nd1-O3	118.21(15)	O19-Y2-N5	137.07(17)
O16-Nd1-O3	88.54(15)	O13-Y2-N5	74.74(16)
O6-Nd1-N1	132.00(15)	N3-Y2-N5	67.53(18)
O1-Nd1-N1	61.91(15)	O11-Y2-Nd1	169.04(11)

O14-Nd1-N1	78.98(15)	O4-Y2-Nd1	114.93(12)
O13-Nd1-N1	110.67(16)	O8-Y2-Nd1	39.73(10)
O8-Nd1-N1	109.45(15)	O9-Y2-Nd1	105.61(11)
N2-Nd1-N1	155.77(18)	O3-Y2-Nd1	42.77(10)
O16-Nd1-N1	75.28(16)	O19-Y2-Nd1	99.86(12)
O3-Nd1-N1	58.10(14)	O13-Y2-Nd1	39.31(11)
O6-Nd1-O17	70.62(19)	N3-Y2-Nd1	102.57(12)
O1-Nd1-O17	64.01(19)	N5-Y2-Nd1	92.22(12)
O14-Nd1-O17	126.76(18)	Y2-O3-Nd1	99.04(15)
O13-Nd1-O17	145.43(17)	Y2-O8-Nd1	103.74(16)
O8-Nd1-O17	96.89(19)	Y2-O13-Nd1	102.38(15)
N2-Nd1-O17	60.47(19)		

Table V.A47. Selected interatomic distances (Å) and angles for complex 63

Gd1-O4	2.345(11)	N3-Gd1-Sm2	100.5(3)
Gd1-O11	2.368(10)	N5-Gd1-Sm2	93.0(3)
Gd1-O8	2.369(11)	O6-Sm2-O14	70.3(4)
Gd1-O3	2.415(10)	O6-Sm2-O1	72.8(3)
Gd1-O9	2.434(12)	O14-Sm2-O1	72.8(3)
Gd1-O19	2.453(10)	O6-Sm2-O13	88.8(3)
Gd1-O13	2.455(9)	O14-Sm2-O13	68.5(3)
Gd1-N3	2.485(12)	O1-Sm2-O13	140.9(3)
Gd1-N5	2.721(14)	O6-Sm2-O16	113.0(4)
Gd1...Sm2	3.7976(13)	O14-Sm2-O16	146.6(3)
Sm2-O6	2.368(11)	O1-Sm2-O16	76.7(4)
Sm2-O14	2.386(10)	O13-Sm2-O16	142.2(3)
Sm2-O1	2.389(9)	O6-Sm2-O8	121.0(3)
Sm2-O13	2.396(9)	O14-Sm2-O8	135.5(3)
Sm2-O16	2.411(12)	O1-Sm2-O8	150.0(3)
Sm2-O8	2.456(10)	O13-Sm2-O8	68.9(3)
Sm2-N2	2.508(14)	O16-Sm2-O8	73.3(4)
Sm2-N1	2.630(12)	O6-Sm2-N2	63.4(4)
Sm2-O3	2.636(10)	O14-Sm2-N2	126.0(4)
O4-Gd1-O11	76.4(3)	O1-Sm2-N2	115.5(4)
O4-Gd1-O8	113.0(3)	O13-Sm2-N2	83.9(4)
O11-Gd1-O8	145.5(4)	O16-Sm2-N2	79.6(4)
O4-Gd1-O3	72.2(3)	O8-Sm2-N2	60.6(4)
O11-Gd1-O3	145.0(4)	O6-Sm2-N1	132.1(4)
O8-Gd1-O3	64.1(4)	O14-Sm2-N1	80.0(3)
O4-Gd1-O9	70.7(4)	O1-Sm2-N1	62.8(4)
O11-Gd1-O9	85.7(4)	O13-Sm2-N1	114.5(4)
O8-Gd1-O9	68.2(4)	O16-Sm2-N1	74.2(4)
O3-Gd1-O9	97.9(3)	O8-Sm2-N1	106.6(3)
O4-Gd1-O19	138.1(3)	N2-Sm2-N1	153.4(4)
O11-Gd1-O19	77.2(4)	O6-Sm2-O3	153.5(3)
O8-Gd1-O19	74.8(3)	O14-Sm2-O3	91.3(3)
O3-Gd1-O19	137.5(4)	O1-Sm2-O3	121.0(3)
O9-Gd1-O19	75.5(3)	O13-Sm2-O3	66.3(3)
O4-Gd1-O13	134.5(3)	O16-Sm2-O3	92.9(4)
O11-Gd1-O13	128.9(3)	O8-Sm2-O3	59.7(3)
O8-Gd1-O13	69.4(3)	N2-Sm2-O3	119.3(4)
O3-Gd1-O13	69.0(3)	N1-Sm2-O3	58.5(4)
O9-Gd1-O13	137.0(4)	O6-Sm2-Gd1	122.9(2)
O19-Gd1-O13	87.3(3)	O14-Sm2-Gd1	98.7(2)

O4-Gd1-N3	125.7(4)	O1-Sm2-Gd1	159.4(3)
O11-Gd1-N3	66.1(4)	O13-Sm2-Gd1	39.0(2)
O8-Gd1-N3	120.3(4)	O16-Sm2-Gd1	105.3(3)
O3-Gd1-N3	122.7(4)	O8-Sm2-Gd1	37.3(3)
O9-Gd1-N3	138.7(4)	N2-Sm2-Gd1	84.8(3)
O19-Gd1-N3	69.4(4)	N1-Sm2-Gd1	97.6(3)
O13-Gd1-N3	62.9(4)	O3-Sm2-Gd1	39.1(2)
O4-Gd1-N5	70.3(3)	Gd1-O3-Sm2	97.4(4)
O11-Gd1-N5	84.0(4)	Gd1-O8-Sm2	103.8(4)
O8-Gd1-N5	130.4(4)	Sm2-O13-Gd1	103.0(3)
O3-Gd1-N5	71.3(4)	O11-Gd1-Sm2	166.5(2)
O9-Gd1-N5	140.9(4)	O8-Gd1-Sm2	38.9(2)
O19-Gd1-N5	137.5(3)	O3-Gd1-Sm2	43.5(3)
O13-Gd1-N5	75.5(4)	O9-Gd1-Sm2	104.6(3)
N3-Gd1-N5	68.1(4)	O19-Gd1-Sm2	96.6(2)
O4-Gd1-Sm2	115.0(2)	O13-Gd1-Sm2	37.9(2)

Table V.A48. Selected interatomic distances (Å) and angles for complex 64

Tb1-O9	2.332(9)	O19-Tb1-Sm	98.0(2)
Tb1-O11	2.362(10)	N3-Tb1-Sm2	102.1(3)
Tb1-O8	2.393(9)	N5-Tb1-Sm2	92.9(3)
Tb1-O3	2.394(10)	O1-Sm2-O6	72.4(3)
Tb1-O13	2.426(9)	O1-Sm2-O13	87.9(3)
Tb1-O4	2.435(10)	O6-Sm2-O13	140.1(3)
Tb1-O19	2.457(10)	O1-Sm2-O14	68.8(3)
Tb1-N3	2.480(11)	O6-Sm2-O14	72.7(3)
Tb1-N5	2.707(13)	O13-Sm2-O1	67.9(3)
Tb1...Sm2	3.8102(11)	O1-Sm2-O3	120.6(3)
Sm2-O1	2.399(9)	O6-Sm2-O3	151.9(3)
Sm2-O6	2.400(9)	O13-Sm2-O3	67.9(3)
Sm2-O13	2.438(10)	O14-Sm2-O3	134.2(3)
Sm2-O14	2.438(9)	O1-Sm2-O16	126.2(3)
Sm2-O3	2.463(9)	O6-Sm2-O16	76.5(3)
Sm2-O16	2.525(10)	O13-Sm2-O1	140.1(3)
Sm2-N1	2.597(11)	O14-Sm2-O1	138.5(3)
Sm2-O8	2.648(9)	O3-Sm2-O16	76.1(3)
Sm2-N2	2.659(11)	O1-Sm2-N1	62.6(3)
Sm2-O17	2.750(11)	O6-Sm2-N1	118.6(3)
O9-Tb1-O11	74.3(3)	O13-Sm2-N1	78.6(3)
O9-Tb1-O8	72.5(3)	O14-Sm2-N1	121.0(3)
O11-Tb1-O8	142.4(3)	O3-Sm2-N1	59.8(3)
O9-Tb1-O3	112.9(3)	O16-Sm2-N1	98.0(4)
O11-Tb1-O3	147.3(3)	O1-Sm2-O8	151.7(3)
O8-Tb1-O3	64.7(3)	O6-Sm2-O8	121.6(3)
O9-Tb1-O13	136.3(3)	O13-Sm2-O8	65.6(3)
O11-Tb1-O13	128.9(3)	O14-Sm2-O8	90.9(3)
O8-Tb1-O13	69.9(3)	O3-Sm2-O8	60.0(3)
O3-Tb1-O13	69.2(3)	O16-Sm2-O8	82.1(3)
O9-Tb1-O4	70.1(3)	N1-Sm2-O8	117.8(3)
O11-Tb1-O4	86.7(3)	O1-Sm2-N2	129.4(3)
O8-Tb1-O4	98.0(3)	O6-Sm2-N2	63.3(4)
O3-Tb1-O4	67.8(3)	O13-Sm2-N2	110.7(3)
O13-Tb1-O4	136.3(3)	O14-Sm2-N2	75.5(3)
O9-Tb1-O19	136.8(3)	O3-Sm2-N2	110.0(3)
O11-Tb1-O19	78.3(3)	O16-Sm2-N2	66.0(3)

O8-Tb1-O19	139.1(3)	N1-Sm2-N2	163.5(3)
O3-Tb1-O19	75.8(3)	O8-Sm2-N2	58.4(3)
O13-Tb1-O19	86.9(3)	O1-Sm2-O17	81.3(3)
O4-Tb1-O19	75.6(3)	O6-Sm2-O17	72.2(3)
O9-Tb1-N3	125.2(4)	O13-Sm2-O17	139.8(3)
O11-Tb1-N3	65.4(4)	O14-Sm2-O17	139.2(3)
O8-Tb1-N3	123.3(3)	O3-Sm2-O17	84.7(3)
O3-Tb1-N3	121.3(3)	O16-Sm2-O17	47.5(3)
O13-Tb1-N3	63.7(4)	N1-Sm2-O17	62.0(3)
O4-Tb1-N3	138.1(3)	O8-Sm2-O17	125.3(3)
O19-Tb1-N3	68.8(3)	N2-Sm2-O17	105.9(3)
O9-Tb1-N5	71.1(3)	O1-Sm2-Tb1	122.1(2)
O11-Tb1-N5	82.1(4)	O6-Sm2-Tb1	159.0(2)
O8-Tb1-N5	71.0(4)	O13-Sm2-Tb1	38.3(2)
O3-Tb1-N5	130.6(4)	O14-Sm2-Tb1	97.3(2)
O13-Tb1-N5	76.2(4)	O3-Sm2-Tb1	37.7(2)
O4-Tb1-N5	141.2(3)	O16-Sm2-Tb1	101.8(2)
O19-Tb1-N5	136.8(3)	N1-Sm2-Tb1	82.4(3)
N3-Tb1-N5	68.0(3)	O8-Sm2-Tb1	38.5(2)
O9-Tb1-Sm2	115.1(2)	N2-Sm2-Tb1	96.6(3)
O11-Tb1-Sm2	167.5(2)	O17-Sm2-Tb1	122.4(3)
O8-Tb1-Sm2	43.5(2)	Tb1-O3-Sm2	103.3(4)
O3-Tb1-Sm2	39.0(2)	Tb1-O8-Sm2	98.1(3)
O13-Tb1-Sm2	38.5(2)	Tb1-O13-Sm2	103.1(3)
O4-Tb1-Sm2	104.1(2)		

Table V.A49 Selected interatomic distances (Å) and angles for complex 65

Tb1-O4	2.354(13)	N3-Tb1-Eu1	100.9(4)
Tb1-O11	2.358(14)	N5-Tb1-Eu1	93.2(4)
Tb1-O8	2.384(14)	O1-Eu1-O13	141.3(4)
Tb1-O3	2.429(14)	O1-Eu1-O6	72.4(5)
Tb1-O9	2.455(15)	O13-Eu1-O6	89.2(5)
Tb1-O13	2.469(13)	O1-Eu1-O14	73.1(4)
Tb1-O19	2.472(12)	O13-Eu1-O14	68.7(4)
Tb1-N3	2.481(16)	O6-Eu1-O14	71.0(4)
Tb1-N5	2.720(17)	O1-Eu1-O16	75.4(5)
Tb1...Eu1	3.8006(15)	O13-Eu1-O16	143.3(5)
Eu1-O1	2.380(13)	O6-Eu1-O16	108.5(5)
Eu1-O13	2.389(13)	O14-Eu1-O16	146.9(5)
Eu1-O6	2.397(14)	O1-Eu1-O8	148.8(4)
Eu1-O14	2.406(13)	O13-Eu1-O8	69.8(4)
Eu1-O16	2.446(14)	O6-Eu1-O8	121.2(5)
Eu1-O8	2.468(13)	O14-Eu1-O8	136.4(4)
Eu1-N2	2.550(16)	O16-Eu1-O8	73.6(5)
Eu1-O3	2.618(13)	O1-Eu1-N2	114.0(5)
Eu1-N1	2.622(16)	O13-Eu1-N2	85.1(5)
O4-Tb1-O11	76.9(5)	O6-Eu1-N2	63.1(5)
O4-Tb1-O8	112.9(5)	O14-Eu1-N2	127.0(5)
O11-Tb1-O8	144.3(5)	O16-Eu1-N2	75.6(5)
O4-Tb1-O3	72.6(5)	O8-Eu1-N2	61.0(5)
O11-Tb1-O3	146.5(5)	O1-Eu1-O3	121.2(4)
O8-Tb1-O3	63.6(5)	O13-Eu1-O3	66.6(4)
O4-Tb1-O9	71.5(4)	O6-Eu1-O3	154.4(4)
O11-Tb1-O9	85.2(5)	O14-Eu1-O3	91.5(4)
O8-Tb1-O9	67.5(4)	O16-Eu1-O3	96.4(5)

O3-Tb1-O9 9	97.9(4)	O8-Eu1-O3	59.7(4)
O4-Tb1-O13	134.0(4)	N2-Eu1-O3	119.9(5)
O11-Tb1-O13	129.2(5)	O1-Eu1-N1	63.2(5)
O8-Tb1-O13	69.8(4)	O13-Eu1-N1	115.7(5)
O3-Tb1-O13	68.4(4)	O6-Eu1-N1	132.9(5)
O9-Tb1-O13	136.8(4)	O14-Eu1-N1	81.5(5)
O4-Tb1-O19	138.2(4)	O16-Eu1-N1	75.5(5)
O11-Tb1-O19	76.1(5)	O8-Eu1-N1	105.1(5)
O8-Tb1-O19	74.9(5)	N2-Eu1-N1	150.6(5)
O3-Tb1-O19	137.0(4)	O3-Eu1-N1	58.5(5)
O9-Tb1-O19	74.9(4)	O1-Eu1-Tb1	160.0(3)
O13-Tb1-O19	87.8(4)	O13-Eu1-Tb1	39.3(3)
O4-Tb1-N3	125.3(5)	O6-Eu1-Tb1	123.3(3)
O11-Tb1-N3	65.8(5)	O14-Eu1-Tb1	99.1(3)
O8-Tb1-N3	120.9(5)	O16-Eu1-Tb1	107.3(4)
O3-Tb1-N3	123.1(5)	O8-Eu1-Tb1	37.6(3)
O9-Tb1-N3	138.1(5)	N2-Eu1-Tb1	85.6(4)
O13-Tb1-N3	63.4(5)	O3-Eu1-Tb1	39.3(3)
O19-Tb1-N3	69.4(5)	N1-Eu1-Tb1	97.8(4)
O4-Tb1-N5	69.4(5)	Tb1-O3-Eu1	97.6(5)
O11-Tb1-N5	84.9(6)	Tb1-O8-Eu1	103.1(5)
O8-Tb1-N5	130.7(5)	Eu1-O13-Tb1	102.9(5)
O3-Tb1-N5	71.7(5)	O11-Tb1-Eu1	166.3(4)
O9-Tb1-N5	140.9(5)	O8-Tb1-Eu1	39.2(3)
O13-Tb1-N5	75.7(5)	O3-Tb1-Eu1	43.1(3)
O19-Tb1-N5	138.0(5)	O9-Tb1-Eu1	104.4(3)
N3-Tb1-N5	68.7(5)	O13-Tb1-Eu1	37.8(3)
O4-Tb1-Eu1	115.1(3)	O19-Tb1-Eu1	96.7(3)

Table V.A50. Selected interatomic distances (Å) and angles for complex 66

Yb1-O9	2.293(6)	N3-Yb1-Eu2	101.89(15)
Yb1-O11	2.320(6)	N5-Yb1-Eu2	92.51(16)
Yb1-O3	2.349(6)	C31-Yb1-Eu2	148.96(19)
Yb1-O8	2.355(6)	O1-Eu2-O13	89.3(2)
Yb1-O13	2.394(5)	O1-Eu2-O6	72.5(2)
Yb1-O19	2.397(7)	O13-Eu2-O6	141.86(19)
Yb1-O4	2.412(6)	O1-Eu2-O14	69.9(2)
Yb1-N3	2.439(7)	O13-Eu2-O14	69.44(18)
Yb1-N5	2.679(8)	O6-Eu2-O14	72.9(2)
Yb1...Eu2	3.7656(9)	O1-Eu2-O16	113.7(2)
Eu2-O1	2.375(6)	O13-Eu2-O16	140.9(2)
Eu2-O13	2.382(5)	O6-Eu2-O16	77.0(2)
Eu2-O6	2.383(6)	O14-Eu2-O16	146.8(2)
Eu2-O14	2.398(6)	O1-Eu2-O3	121.1(2)
Eu2-O16	2.429(7)	O13-Eu2-O3	67.87(19)
Eu2-O3	2.460(5)	O6-Eu2-O3	150.1(2)
Eu2-N1	2.539(7)	O14-Eu2-O3	135.5(2)
Eu2-O8	2.621(6)	O16-Eu2-O3	73.1(2)
Eu2-N2	2.628(7)	O1-Eu2-N1	63.4(2)
O9-Yb1-O11	73.1(2)	O13-Eu2-N1	83.3(2)
O9-Yb1-O3	114.2(2)	O6-Eu2-N1	115.3(2)
O11-Yb1-O3	144.6(2)	O14-Eu2-N1	125.6(2)
O9-Yb1-O8	73.6(2)	O16-Eu2-N1	80.1(3)
O11-Yb1-O8	143.9(2)	O3-Eu2-N1	60.6(2)

O3-Yb1-O8	64.4(2)	O1-Eu2-O8	153.1(2)
O9-Yb1-O13	136.0(2)	O13-Eu2-O8	65.29(18)
O11-Yb1-O13	130.9(2)	O6-Eu2-O8	122.0(2)
O3-Yb1-O13	69.50(19)	O14-Eu2-O8	91.80(18)
O8-Yb1-O13	69.47(18)	O16-Eu2-O8	92.5(2)
O9-Yb1-O19	136.8(2)	O3-Eu2-O8	59.01(19)
O11-Yb1-O19	77.6(2)	N1-Eu2-O8	118.6(2)
O3-Yb1-O19	74.9(2)	O1-Eu2-N2	132.5(2)
O8-Yb1-O19	137.9(2)	O13-Eu2-N2	113.9(2)
O13-Yb1-O19	87.2(2)	O6-Eu2-N2	63.8(2)
O9-Yb1-O4	70.2(2)	O14-Eu2-N2	80.1(2)
O11-Yb1-O4	84.1(2)	O16-Eu2-N2	74.2(2)
O3-Yb1-O4	68.0(2)	O3-Eu2-N2	106.1(2)
O8-Yb1-O4	97.5(2)	N1-Eu2-N2	153.8(2)
O13-Yb1-O4	137.0(2)	O8-Eu2-N2	58.6(2)
O19-Yb1-O4	75.8(2)	O1-Eu2-Yb1	122.88(15)
O9-Yb1-N3	124.0(2)	O13-Eu2-Yb1	38.08(12)
O11-Yb1-N3	66.7(2)	O6-Eu2-Yb1	159.52(16)
O3-Yb1-N3	121.3(2)	O14-Eu2-Yb1	98.61(13)
O8-Yb1-N3	124.2(2)	O16-Eu2-Yb1	104.96(16)
O13-Yb1-N3	64.3(2)	O3-Eu2-Yb1	37.41(15)
O19-Yb1-N3	68.9(2)	N1-Eu2-Yb1	84.94(16)
O4-Yb1-N3	137.8(2)	O8-Eu2-Yb1	38.24(12)
O9-Yb1-N5	70.5(2)	N2-Eu2-Yb1	96.80(16)
O11-Yb1-N5	84.8(2)	Yb1-O3-Eu2	103.1(2)
O3-Yb1-N5	130.6(2)	Yb1-O8-Eu2	98.2(2)
O8-Yb1-N5	71.3(2)	Eu2-O13-Yb1	104.06(19)
O13-Yb1-N5	75.6(2)	O3-Yb1-Eu2	39.52(14)
O19-Yb1-N5	137.4(2)	O8-Yb1-Eu2	43.54(14)
O4-Yb1-N5	140.7(2)	O13-Yb1-Eu2	37.85(13)
N3-Yb1-N5	68.6(2)	O19-Yb1-Eu2	97.15(16)
O9-Yb1-Eu2	116.57(16)	O4-Yb1-Eu2	104.81(15)
O11-Yb1-Eu2	168.46(15)		

Table V.A51. Selected interatomic distances (Å) and angles for complex 67

Lu1-O9	2.278(3)	O3-Lu1-Eu2	39.24(7)
Lu1-O11	2.301(3)	O8-Lu1-Eu2	43.92(7)
Lu1-O3	2.338(3)	O19-Lu1-Eu2	96.52(9)
Lu1-O8	2.350(3)	O13-Lu1-Eu2	37.89(7)
Lu1-O19	2.365(3)	O4-Lu1-Eu2	105.14(8)
Lu1-O13	2.379(3)	N3-Lu1-Eu2	102.10(9)
Lu1-O4	2.396(3)	N5-Lu1-Eu2	92.56(9)
Lu1-N3	2.426(4)	O1-Eu2-O13	89.93(11)
Lu1-N5	2.673(4)	O1-Eu2-O6	72.95(11)
Lu1...Eu2	3.7557(8)	O13-Eu2-O6	142.79(11)
Eu2-O1	2.371(3)	O1-Eu2-O14	70.28(11)
Eu2-O13	2.380(3)	O13-Eu2-O14	69.91(10)
Eu2-O6	2.381(3)	O6-Eu2-O14	73.22(11)
Eu2-O14	2.385(3)	O1-Eu2-O16	110.84(11)
Eu2-O16	2.431(3)	O13-Eu2-O16	141.12(11)
Eu2-O3	2.443(3)	O6-Eu2-O16	75.99(12)
Eu2-N1	2.531(4)	O14-Eu2-O16	147.22(11)
Eu2-O8	2.629(3)	O1-Eu2-O3	121.61(11)
Eu2-N2	2.634(4)	O13-Eu2-O3	68.00(10)

O9-Lu1-O11	73.28(12)	O6-Eu2-O3	148.94(11)
O9-Lu1-O3	114.66(12)	O14-Eu2-O3	135.92(11)
O11-Lu1-O3	143.29(12)	O16-Eu2-O3	73.12(11)
O9-Lu1-O8	73.44(11)	O1-Eu2-N1	63.85(11)
O11-Lu1-O8	144.63(12)	O13-Eu2-N1	84.54(12)
O3-Lu1-O8	64.26(11)	O6-Eu2-N1	114.68(12)
O9-Lu1-O19	137.39(12)	O14-Eu2-N1	126.97(12)
O11-Lu1-O1	77.01(13)	O16-Eu2-N1	76.60(13)
O3-Lu1-O19	74.61(13)	O3-Eu2-N1	60.86(11)
O8-Lu1-O19	137.54(12)	O1-Eu2-O8	153.25(11)
O9-Lu1-O13	135.18(11)	O13-Eu2-O8	64.82(10)
O11-Lu1-O13	131.60(11)	O6-Eu2-O8	121.75(10)
O3-Lu1-O13	69.75(10)	O14-Eu2-O8	91.68(10)
O8-Lu1-O13	69.41(10)	O16-Eu2-O8	95.07(10)
O19-Lu1-O13	87.42(11)	O3-Eu2-O8	58.76(10)
O9-Lu1-O4	70.47(11)	N1-Eu2-O8	118.76(11)
O11-Lu1-O4	82.42(12)	O1-Eu2-N2	133.08(11)
O3-Lu1-O4	68.52(11)	O13-Eu2-N2	114.39(12)
O8-Lu1-O4	97.43(11)	O6-Eu2-N2	63.47(11)
O19-Lu1-O4	75.98(12)	O14-Eu2-N2	80.98(11)
O13-Lu1-O4	137.81(11)	O16-Eu2-N2	75.44(12)
O9-Lu1-N3	122.72(13)	O3-Eu2-N2	104.93(11)
O11-Lu1-N3	67.15(12)	N1-Eu2-N2	151.43(12)
O3-Lu1-N3	121.97(12)	O8-Eu2-N2	58.63(11)
O8-Lu1-N3	124.15(11)	O1-Eu2-Lu1	123.08(8)
O19-Lu1-N3	69.75(13)	O13-Eu2-Lu1	37.88(6)
O13-Lu1-N3	64.47(11)	O6-Eu2-Lu1	159.56(8)
O4-Lu1-N3	138.08(12)	O14-Eu2-Lu1	99.09(7)
O9-Lu1-N5	69.80(12)	O16-Eu2-Lu1	106.02(8)
O11-Lu1-N5	86.44(13)	O3-Eu2-Lu1	37.25(8)
O3-Lu1-N5	130.26(12)	N1-Eu2-Lu1	85.22(9)
O8-Lu1-N5	71.11(12)	O8-Eu2-Lu1	38.33(7)
O19-Lu1-N5	137.83(13)	N2-Eu2-Lu1	96.95(9)
O13-Lu1-N5	75.07(11)	Lu1-O3-Eu2	103.51(12)
O4-Lu1-N5	140.27(11)	Lu1-O8-Eu2	97.75(10)
N3-Lu1-N5	68.09(13)	Lu1-O13-Eu2	104.23(11)
O9-Lu1-Eu2	116.85(9)		
O11-Lu1-Eu2	168.76(8)		

Table V.A52. Selected interatomic distances (Å) and angles for complex 68

Eu1-O6	2.365(10)	O14-Eu1-Y2	99.1(2)
Eu1-O1	2.375(10)	O13-Eu1-Y2	38.7(2)
Eu1-O14	2.381(10)	O16-Eu1-Y2	105.7(3)
Eu1-O13	2.387(10)	O3-Eu1-Y2	37.0(3)
Eu1-O16	2.435(12)	N1-Eu1-Y2	85.3(3)
Eu1-O3	2.440(10)	O8-Eu1-Y2	38.4(2)
Eu1-N1	2.506(14)	N2-Eu1-Y2	97.0(3)
Eu1-O8	2.621(10)	O9-Y2-O11	74.7(4)
Eu1-N2	2.630(13)	O9-Y2-O3	114.6(4)
Eu1...Y2	3.7815(18)	O11-Y2-O3	145.0(4)
Y2-O9	2.297(11)	O9-Y2-O8	73.2(4)
Y2-O11	2.319(11)	O11-Y2-O8	145.0(4)
Y2-O3	2.349(12)	O3-Y2-O8 6	64.1(4)
Y2-O8	2.372(10)	O9-Y2-O19	138.2(4)

Y2-O19	2.404(11)	O11-Y2-O19	77.2(4)
Y2-O42	2.414(12)	O3-Y2-O19	74.8(4)
Y2-O13	2.430(9)	O8-Y2-O19	137.4(4)
Y2-N3	2.457(13)	O9-Y2-O4	71.6(4)
Y2-N5	2.685(15)	O11-Y2-O4	84.5(4)
O6-Eu1-O1	72.2(4)	O3-Y2-O4	68.5(4)
O6-Eu1-O14	73.2(4)	O8-Y2-O4	98.2(3)
O1-Eu1-O14	69.7(4)	O19-Y2-O4	75.5(4)
O6-Eu1-O13	141.4(3)	O9-Y2-O13	134.0(3)
O1-Eu1-O13	89.5(4)	O11-Y2-O13	130.2(4)
O14-Eu1-O13	68.7(3)	O3-Y2-O13	69.3(4)
O6-Eu1-O16	76.1(4)	O8-Y2-O13	68.3(3)
O1-Eu1-O16	112.1(4)	O19-Y2-O13	87.8(3)
O14-Eu1-O16	146.8(4)	O4-Y2-O13	137.4(4)
O13-Eu1-O16	142.3(4)	O9-Y2-N3	123.9(5)
O6-Eu1-O3	149.9(4)	O11-Y2-N3	66.4(4)
O1-Eu1-O3	121.2(4)	O3-Y2-N3	120.6(4)
O14-Eu1-O3	135.5(4)	O8-Y2-N3	123.2(4)
O13-Eu1-O3	68.5(3)	O19-Y2-N3	69.1(5)
O16-Eu1-O3	73.8(4)	O4-Y2-N3	137.9(4)
O6-Eu1-N1	114.2(4)	O13-Y2-N3	63.9(4)
O1-Eu1-N1	63.9(4)	O9-Y2-N5	69.9(4)
O14-Eu1-N1	126.5(4)	O11-Y2-N5	85.1(4)
O13-Eu1-N1	85.3(4)	O3-Y2-N5	129.9(4)
O16-Eu1-N1	77.9(4)	O8-Y2-N5	71.1(4)
O3-Eu1-N1	60.6(4)	O19-Y2-N5	137.2(4)
O6-Eu1-O8	122.3(3)	O4-Y2-N5	141.5(4)
O1-Eu1-O8	152.9(4)	O13-Y2-N5	74.4(4)
O14-Eu1-O8	91.7(3)	N3-Y2-N5	68.2(4)
O13-Eu1-O8	64.9(3)	O9-Y2-Eu1	116.0(3)
O16-Eu1-O8	94.3(4)	O11-Y2-Eu1	167.6(3)
O3-Eu1-O8	59.2(4)	O3-Y2-Eu1	38.7(3)
N1-Eu1-O8	119.0(4)	O8-Y2-Eu1	43.3(2)
O6-Eu1-N2	63.9(4)	O19-Y2-Eu1	96.6(3)
O1-Eu1-N2	132.3(4)	O4-Y2-Eu1	104.6(3)
O14-Eu1-N2	80.2(4)	O13-Y2-Eu1	37.9(2)
O13-Eu1-N2	113.3(4)	N3-Y2-Eu1	101.4(3)
O16-Eu1-N2	75.3(4)	N5-Y2-Eu1	92.5(3)
O3-Eu1-N2	106.2(4)	Y2-O3-Eu1	104.3(5)
N1-Eu1-N2	152.7(4)	Y2-O8-Eu1	98.3(3)
O8-Eu1-N2	58.6(4)	Eu1-O13-Y2	103.4(4)
O6-Eu1-Y2	160.1(3)		
O1-Eu1-Y2	123.1(3)		

Table V.A53. Selected interatomic distances (Å) and angles for complex 69

Tb1-O6	2.330(14)	O1-Tb1-Ho2	160.7(3)
Tb1-O13	2.348(12)	O14-Tb1-Ho2	99.0(3)
Tb1-O1	2.361(12)	O16-Tb1-Ho2	105.3(3)
Tb1-O14	2.362(13)	O8-Tb1-Ho2	37.7(4)
Tb1-O16	2.386(14)	N2-Tb1-Ho2	85.2(3)
Tb1-O8	2.424(13)	N1-Tb1-Ho2	97.8(3)
Tb1-N2	2.448(16)	O3-Tb1-Ho2	38.8(3)
Tb1-N1	2.584(15)	O4-Ho2-O11	73.4(5)
Tb1-O3	2.618(13)	O4-Ho2-O8	113.4(4)
Tb1...Ho2	3.7553(15)	O11-Ho2-O8	147.6(5)

Ho2-O4	2.295(14)	O4-Ho2-O3	73.1(4)
Ho2-O11	2.349(12)	O11-Ho2-O3	142.4(5)
Ho2-O8	2.359(14)	O8-Ho2-O3	64.1(5)
Ho2-O3	2.374(12)	O4-Ho2-O19	137.1(4)
Ho2-O19	2.388(14)	O11-Ho2-O19	79.0(5)
Ho2-O13	2.421(11)	O8-Ho2-O19	75.7(5)
Ho2-O9	2.432(14)	O3-Ho2-O19	138.4(5)
Ho2-N3	2.443(15)	O4-Ho2-O13	134.8(5)
Ho2-N5	2.65(2)	O11-Ho2-O13	130.0(4)
O6-Tb1-O13	88.4(4)	O8-Ho2-O13	69.2(4)
O6-Tb1-O1	72.0(4)	O3-Ho2-O13	68.4(4)
O13-Tb1-O1	142.3(4)	O19-Ho2-O13	88.0(4)
O6-Tb1-O14	68.9(5)	O4-Ho2-O9	70.9(5)
O13-Tb1-O14	69.2(4)	O11-Ho2-O9	86.9(4)
O1-Tb1-O14	73.8(4)	O8-Ho2-O9	67.5(4)
O6-Tb1-O16	114.2(5)	O3-Ho2-O9	97.8(4)
O13-Tb1-O16	141.9(4)	O19-Ho2-O9	75.5(4)
O1-Tb1-O16	75.7(4)	O13-Ho2-O9	136.1(4)
O14-Tb1-O16	146.3(4)	O4-Ho2-N3	124.1(5)
O6-Tb1-O8	122.7(5)	O11-Ho2-N3	66.0(5)
O13-Tb1-O8	69.3(4)	O8-Ho2-N3	121.7(5)
O1-Tb1-O8	148.3(4)	O3-Ho2-N3	122.6(5)
O14-Tb1-O8	136.3(4)	O19-Ho2-N3	69.8(5)
O16-Tb1-O8	72.6(4)	O13-Ho2-N3	64.2(4)
O6-Tb1-N2	64.4(5)	O9-Ho2-N3	139.0(5)
O13-Tb1-N2	84.0(5)	O4-Ho2-N5	70.1(5)
O1-Tb1-N2	113.6(5)	O11-Ho2-N5	82.8(5)
O14-Tb1-N2	126.2(5)	O8-Ho2-N5	129.5(5)
O16-Tb1-N2	79.5(5)	O3-Ho2-N5	70.1(5)
O8-Tb1-N2	61.3(5)	O19-Ho2-N5	138.0(5)
O6-Tb1-N1	131.4(5)	O13-Ho2-N5	75.3(5)
O13-Tb1-N1	115.0(5)	O9-Ho2-N5	141.0(5)
O1-Tb1-N1	63.7(4)	N3-Ho2-N5	68.2(5)
O14-Tb1-N1	80.3(4)	O4-Ho2-Tb1	116.1(3)
O16-Tb1-N1	73.6(5)	O11-Ho2-Tb1	167.3(3)
O8-Tb1-N1	105.7(4)	O8-Ho2-Tb1	38.9(3)
N2-Tb1-N1	152.7(5)	O3-Ho2-Tb1	43.7(3)
O6-Tb1-O3	151.8(5)	O19-Ho2-Tb1	97.2(3)
O13-Tb1-O3	65.5(4)	O13-Ho2-Tb1	37.4(3)
O1-Tb1-O3	122.3(4)	O9-Ho2-Tb1	104.0(3)
O14-Tb1-O3	90.8(4)	N3-Ho2-Tb1	101.3(4)
O16-Tb1-O3	93.6(4)	N5-Ho2-Tb1	92.4(4)
O8-Tb1-O3	59.6(5)	Ho2-O3-Tb1	97.5(5)
N2-Tb1-O3	119.7(4)	Ho2-O8-Tb1	103.5(6)
N1-Tb1-O3	59.0(4)	Tb1-O13-Ho2	103.9(4)
O6-Tb1-Ho2	122.8(3)		
O13-Tb1-Ho2	38.8(3)		

Table V.A55. Selected interatomic distances (Å) and angles for complex 71

Lu1-O4	2.281(8)	O11-Lu1-Dy2	168.1(2)
Lu1-O8	2.307(8)	O3-Lu1-Dy2	43.5(2)
Lu1-O11	2.319(9)	O19-Lu1-Dy2	97.1(2)
Lu1-O3	2.337(8)	O9-Lu1-Dy2	105.52(19)
Lu1-O19	2.365(10)	O13-Lu1-Dy2	37.28(18)

Lu1-O9	2.397(8)	N3-Lu1-Dy2	101.8(2)
Lu1-O13	2.407(7)	N5-Lu1-Dy2	92.5(2)
Lu1-N3	2.430(10)	O13-Dy2-O6	88.7(3)
Lu1-N5	2.652(12)	O13-Dy2-O14	70.3(3)
Lu1...Dy2	3.7342(7)	O6-Dy2-O14	70.2(3)
Dy2-O13	2.331(8)	O13-Dy2-O1	142.4(3)
Dy2-O6	2.341(8)	O6-Dy2-O1	71.9(3)
Dy2-O14	2.345(8)	O14-Dy2-O1	72.9(3)
Dy2-O1	2.353(8)	O13-Dy2-O16	142.3(3)
Dy2-O16	2.391(8)	O6-Dy2-O16	109.7(3)
Dy2-O8	2.440(8)	O14-Dy2-O16	146.3(3)
Dy2-N2	2.477(12)	O1-Dy2-O16	75.2(3)
Dy2-N1	2.554(11)	O13-Dy2-O8	69.3(3)
Dy2-O3	2.596(8)	O6-Dy2-O8	124.0(3)
O4-Lu1-O8	112.5(3)	O14-Dy2-O8	136.4(3)
O4-Lu1-O11	73.9(3)	O1-Dy2-O8	148.1(3)
O8-Lu1-O11	144.0(3)	O16-Dy2-O8	73.2(3)
O4-Lu1-O3	73.8(3)	O13-Dy2-N2	85.6(3)
O8-Lu1-O3	62.8(3)	O6-Dy2-N2	64.9(3)
O11-Lu1-O3	145.3(3)	O14-Dy2-N2	129.0(3)
O4-Lu1-O19	136.0(3)	O1-Dy2-N2	112.6(3)
O8-Lu1-O19	75.9(3)	O16-Dy2-N2	74.1(3)
O11-Lu1-O19	76.5(3)	O8-Dy2-N2	62.7(3)
O3-Lu1-O19	137.4(3)	O13-Dy2-N1	116.6(3)
O4-Lu1-O9	70.0(3)	O6-Dy2-N1	133.5(3)
O8-Lu1-O9	68.1(3)	O14-Dy2-N1	82.2(3)
O11-Lu1-O9	82.7(3)	O1-Dy2-N1	64.5(3)
O3-Lu1-O9	97.9(3)	O16-Dy2-N1	74.4(3)
O19-Lu1-O9	74.6(3)	O8-Dy2-N1	101.9(3)
O4-Lu1-O13	135.1(3)	N2-Dy2-N1	147.8(4)
O8-Lu1-O13	70.2(3)	O13-Dy2-O3	65.4(3)
O11-Lu1-O13	131.5(3)	O6-Dy2-O3	152.4(3)
O3-Lu1-O13	68.5(3)	O14-Dy2-O3	91.1(3)
O19-Lu1-O13	88.9(3)	O1-Dy2-O3	123.0(3)
O9-Lu1-O13	137.7(3)	O16-Dy2-O3	97.2(3)
O4-Lu1-N3	123.6(3)	O8-Dy2-O3	57.3(3)
O8-Lu1-N3	123.2(3)	N2-Dy2-O3	119.2(3)
O11-Lu1-N3	66.7(3)	N1-Dy2-O3	59.2(3)
O3-Lu1-N3	124.0(3)	O13-Dy2-Lu1	38.72(18)
O19-Lu1-N3	70.4(3)	O6-Dy2-Lu1	123.0(2)
O9-Lu1-N3	137.7(3)	O14-Dy2-Lu1	99.61(19)
O13-Lu1-N3	64.8(3)	O1-Dy2-Lu1	160.9(2)
O4-Lu1-N5	70.4(3)	O16-Dy2-Lu1	107.1(2)
O8-Lu1-N5	129.7(3)	O8-Dy2-Lu1	36.89(19)
O11-Lu1-N5	86.2(3)	N2-Dy2-Lu1	85.9(2)
O3-Lu1-N5	71.3(3)	N1-Dy2-Lu1	97.4(2)
O19-Lu1-N5	138.8(3)	O3-Dy2-Lu1	38.27(17)
O9-Lu1-N5	140.3(3)	Lu1-O3-Dy2	98.3(3)
O13-Lu1-N5	75.0(3)	Lu1-O8-Dy2	103.7(3)
N3-Lu1-N5	68.4(4)	Dy2-O13-Lu1	104.0(3)
O4-Lu1-Dy2	116.7(2)		
O8-Lu1-Dy2	39.41(19)		

Tm1-O4	2.287(9)	O8-Tm1-Ho2	39.0(2)
Tm1-O11	2.312(10)	O3-Tm1-Ho2	43.9(2)
Tm1-O8	2.332(10)	O19-Tm1-Ho2	96.4(3)
Tm1-O3	2.349(9)	O13-Tm1-Ho2	37.1(2)
Tm1-O19	2.366(10)	O9-Tm1-Ho2	105.0(2)
Tm1-O13	2.403(8)	N3-Tm1-Ho2	101.1(3)
Tm1-O9	2.425(9)	N5-Tm1-Ho2	92.9(3)
Tm1-N3	2.427(12)	O13-Ho2-O1	143.4(3)
Tm1-N5	2.659(14)	O13-Ho2-O14	70.8(3)
Tm1...Ho2	3.7387(10)	O1-Ho2-O14	73.5(3)
Ho2-O13	2.327(9)	O13-Ho2-O6	87.9(3)
Ho2-O1	2.331(9)	O1-Ho2-O6	72.3(3)
Ho2-O14	2.335(8)	O14-Ho2-O6	69.6(3)
Ho2-O6	2.360(9)	O13-Ho2-O16	140.9(3)
Ho2-O16	2.373(10)	O1-Ho2-O16	75.7(3)
Ho2-O8	2.421(8)	O14-Ho2-O16	146.5(3)
Ho2-N2	2.463(13)	O6-Ho2-O16	112.7(3)
Ho2-N1	2.576(10)	O13-Ho2-O8	68.4(3)
Ho2-O3	2.617(8)	O1-Ho2-O8	148.1(3)
O4-Tm1-O11	74.2(3)	O14-Ho2-O8	136.6(3)
O4-Tm1-O8	113.4(3)	O6-Ho2-O8	122.2(3)
O11-Tm1-O8	145.1(4)	O16-Ho2-O8	72.5(3)
O4-Tm1-O3	72.9(3)	O13-Ho2-N2	84.1(4)
O11-Tm1-O3	144.0(3)	O1-Ho2-N2	112.2(4)
O8-Tm1-O3	64.2(3)	O14-Ho2-N2	127.5(3)
O4-Tm1-O19	137.7(3)	O6-Ho2-N2	64.0(3)
O11-Tm1-O19	77.8(4)	O16-Ho2-N2	76.8(4)
O8-Tm1-O19	75.1(4)	O8-Ho2-N2	61.8(3)
O3-Tm1-O19	137.8(3)	O13-Ho2-N1	116.0(3)
O4-Tm1-O13	135.5(3)	O1-Ho2-N1	64.5(3)
O11-Tm1-O13	131.1(3)	O14-Ho2-N1	80.3(3)
O8-Tm1-O13	68.6(3)	O6-Ho2-N1	132.8(3)
O3-Tm1-O13	68.9(3)	O16-Ho2-N1	74.8(3)
O19-Tm1-O13	86.8(3)	O8-Ho2-N1	104.8(3)
O4-Tm1-O9	70.5(3)	N2-Ho2-N1	151.2(4)
O11-Tm1-O9	84.0(4)	O13-Ho2-O3	65.6(3)
O8-Tm1-O9	68.3(3)	O1-Ho2-O3	123.2(3)
O3-Tm1-O9	98.3(3)	O14-Ho2-O3	91.0(3)
O19-Tm1-O9	75.6(3)	O6-Ho2-O3	151.6(3)
O13-Tm1-O9	136.4(3)	O16-Ho2-O3	95.0(3)
O4-Tm1-N3	124.3(4)	O8-Ho2-O3	59.0(3)
O11-Tm1-N3	66.9(3)	N2-Ho2-O3	119.8(3)
O8-Tm1-N3	121.5(4)	N1-Ho2-O3	59.0(3)
O3-Tm1-N3	122.8(3)	O13-Ho2-Tm1	38.48(19)
O19-Tm1-N3	69.7(4)	O1-Ho2-Tm1	161.4(2)
O13-Tm1-N3	64.2(3)	O14-Ho2-Tm1	99.5(2)
O9-Tm1-N3	138.4(4)	O6-Ho2-Tm1	122.3(2)
O4-Tm1-N5	70.2(3)	O16-Ho2-Tm1	105.6(2)
O11-Tm1-N5	84.6(4)	O8-Ho2-Tm1	37.3(2)
O8-Tm1-N5	130.2(4)	N2-Ho2-Tm1	85.8(3)
O3-Tm1-N5	70.9(4)	N1-Ho2-Tm1	97.5(2)
O19-Tm1-N5	137.5(4)	O3-Ho2-Tm1	38.53(19)
O13-Tm1-N5	76.3(3)	Tm1-O3-Ho2	97.5(3)
O9-Tm1-N5	140.7(3)	Tm1-O8-Ho2	103.7(3)
N3-Tm1-N5	67.8(4)	Ho2-O13-Tm1	104.5(3)
O4-Tm1-Ho2	116.2(2)	O11-Tm1-Ho2	167.9(2)

Table V.A57. Selected interatomic distances (Å) and angles for complex 73

Ce1-O1	2.380(18)	O13-Y1-O16	140(2)
Ce1-O6	2.406(17)	O6-Y1-O16	110.2(13)
Ce1-O14	2.461(16)	O8-Y1-O16	72.9(14)
Ce1-O16	2.474(17)	O1-Y1-O16	76.2(12)
Ce1-O8	2.545(16)	O3-Y1-O16	85.7(16)
Ce1-N2	2.560(19)	N2-Y1-O16	75.9(12)
Ce1-O13	2.576(15)	O14-Y1-N1	80.2(16)
Ce1-O3	2.688(15)	O13-Y1-N1	115.1(16)
Ce1-N1	2.711(17)	O6-Y1-N1	130(2)
Ce1-O17	2.87(2)	O8-Y1-N1	112(2)
Ce1...Y2	3.879(10)	O1-Y1-N1	61.0(13)
Y1-O14	2.33(5)	O3-Y1-N1	59.3(12)
Y1-O13	2.34(4)	N2-Y1-N1	148.1(18)
Y1-O6	2.47(5)	O16-Y1-N1	72.3(14)
Y1-O8	2.49(5)	O14-Y1-Y2	104.2(11)
Y1-O1	2.53(5)	O13-Y1-Y2	39.9(8)
Y1-O3	2.53(5)	O6-Y1-Y2	127.2(18)
Y1-N2	2.65(5)	O8-Y1-Y2	37.8(6)
Y1-O16	2.66(5)	O1-Y1-Y2	160.0(19)
Y1-N1	2.70(6)	O3-Y1-Y2	40.1(7)
Y1-Y2	3.69(4)	N2-Y1-Y2	88.6(14)
Y2-O11	2.301(11)	O16-Y1-Y2	101.7(15)
Y2-O8	2.302(12)	N1-Y1-Y2	99.2(13)
Y2-O4	2.306(10)	O11-Y2-O8	143.8(4)
Y2-O9	2.355(11)	O11-Y2-O4	71.7(4)
Y2-O3	2.393(11)	O8-Y2-O4	115.9(4)
Y2-N3	2.413(14)	O11-Y2-O9	81.8(4)
Y2-O13	2.416(12)	O8-Y2-O9	69.6(4)
Y2-O19	2.444(10)	O4-Y2-O9	69.9(4)
Y2-N5	2.675(14)	O11-Y2-O3	142.2(4)
O1-Ce1-O6	74.5(5)	O8-Y2-O3	66.5(4)
O1-Ce1-O14	71.6(5)	O4-Y2-O3	73.1(3)
O6-Ce1-O14	70.4(5)	O9-Y2-O3	98.7(3)
O1-Ce1-O16	82.6(5)	O11-Y2-N3	67.6(4)
O6-Ce1-O16	119.5(5)	O8-Y2-N3	121.2(4)
O14-Ce1-O16	149.0(7)	O4-Y2-N3	122.3(4)
O1-Ce1-O8	157.8(6)	O9-Y2-N3	137.8(4)
O6-Ce1-O8	116.9(6)	O3-Y2-N3	123.3(4)
O14-Ce1-O8	129.3(5)	O11-Y2-O13	131.2(4)
O16-Ce1-O8	75.2(5)	O8-Y2-O13	70.2(4)
O1-Ce1-N2	118.1(5)	O4-Y2-O13	135.6(4)
O6-Ce1-N2	63.6(5)	O9-Y2-O13	139.4(4)
O14-Ce1-N2	126.3(7)	O3-Y2-O13	70.2(4)
O16-Ce1-N2	80.9(5)	N3-Y2-O13	63.6(4)
O8-Ce1-N2	59.0(5)	O11-Y2-O19	76.6(4)
O1-Ce1-O13	137.4(6)	O8-Y2-O19	74.9(4)
O6-Ce1-O13	90.4(5)	O4-Y2-O19	135.1(4)
O14-Ce1-O13	65.8(4)	O9-Y2-O19	74.9(3)
O16-Ce1-O13	137.6(6)	O3-Y2-O19	140.5(4)
O8-Ce1-O13	64.0(4)	N3-Y2-O19	70.3(4)
N2-Ce1-O13	87.7(5)	O13-Y2-O19	89.3(4)
O1-Ce1-O3	120.0(6)	O11-Y2-N5	85.1(4)
O6-Ce1-O3	153.0(5)	O8-Y2-N5	131.1(4)
O14-Ce1-O3	91.8(4)	O4-Y2-N5	70.8(4)

O16-Ce1-O3	86.3(5)	O9-Y2-N5	140.7(4)
O8-Ce1-O3	58.9(4)	O3-Y2-N5	70.6(4)
N2-Ce1-O3	117.9(6)	N3-Y2-N5	66.8(4)
O13-Ce1-O3	63.3(4)	O13-Y2-N5	74.1(4)
O1-Ce1-N1	62.7(5)	O19-Y2-N5	137.0(4)
O6-Ce1-N1	132.8(6)	O11-Y2-Y1	169.6(8)
O14-Ce1-N1	77.8(5)	O8-Y2-Y1	41.5(8)
O16-Ce1-N1	75.1(5)	O4-Y2-Y1	115.6(9)
O8-Ce1-N1	110.2(6)	O9-Y2-Y1	107.4(8)
N2-Ce1-N1	155.7(6)	O3-Y2-Y1	42.9(9)
O13-Ce1-N1	107.5(5)	N3-Y2-Y1	102.0(9)
O3-Ce1-N1	57.5(5)	O13-Y2-Y1	38.4(8)
O1-Ce1-O17	63.8(5)	O19-Y2-Y1	100.7(9)
O6-Ce1-O17	73.2(5)	N5-Y2-Y1	90.4(8)
O14-Ce1-O17	128.1(7)	O11-Y2-Ce1	171.5(3)
O16-Ce1-O17	46.5(5)	O8-Y2-Ce1	39.0(3)
O8-Ce1-O17	99.9(6)	O4-Y2-Ce1	115.3(3)
N2-Ce1-O17	61.8(5)	O9-Y2-Ce1	104.8(3)
O13-Ce1-O17	149.3(7)	O3-Y2-Ce1	43.1(3)
O3-Ce1-O17	132.8(7)	N3-Y2-Ce1	104.0(4)
N1-Ce1-O17	102.5(6)	O13-Y2-Ce1	40.5(3)
O1-Ce1-Y2	155.8(5)	O19-Y2-Ce1	99.8(3)
O6-Ce1-Y2	122.2(5)	N5-Y2-Ce1	92.7(4)
O14-Ce1-Y2	96.5(3)	Y1-Y2-Ce1	2.6(9)
O16-Ce1-Y2	100.6(5)	Y2-O3-Y1	97.0(12)
O8-Ce1-Y2	34.8(3)	Y2-O3-Ce1	99.4(5)
N2-Ce1-Y2	86.0(4)	Y2-O8-Y1	100.7(9)
O13-Ce1-Y2	37.5(3)	Y2-O8-Ce1	106.2(5)
O3-Ce1-Y2	37.5(3)	Y1-O13-Y2	101.7(14)
N1-Ce1-Y2	94.7(4)	Y2-O13-Ce1	101.9(5)
O17-Ce1-Y2	134.5(6)	N6-O16-Ce1	124(2)
O14-Y1-O13	71.8(12)	N4-O16-Ce1	108.6(12)
O14-Y1-O6	71.4(15)	N6-O16-Y1	127(3)
O13-Y1-O6	94.5(19)	N4-O16-Y1	112.2(15)
O14-Y1-O8	139.8(17)	N4-O17-Ce1	89.5(15)
O13-Y1-O8	68.3(13)	O8-Y1-O3	61.7(12)
O6-Y1-O8	116(2)	O1-Y1-O3	120(2)
O14-Y1-O1	71.3(15)	O14-Y1-N2	128(2)
O13-Y1-O1	143(2)	O13-Y1-N2	90.6(18)
O6-Y1-O1	70.8(13)	O6-Y1-N2	61.3(12)
O8-Y1-O1	148.7(19)	O8-Y1-N2	58.4(12)
O14-Y1-O3	99.1(15)	O1-Y1-N2	109.7(14)
O13-Y1-O3	68.9(11)	O3-Y1-N2	120(2)
O6-Y1-O3	163.1(19)	O14-Y1-O16	145(2)

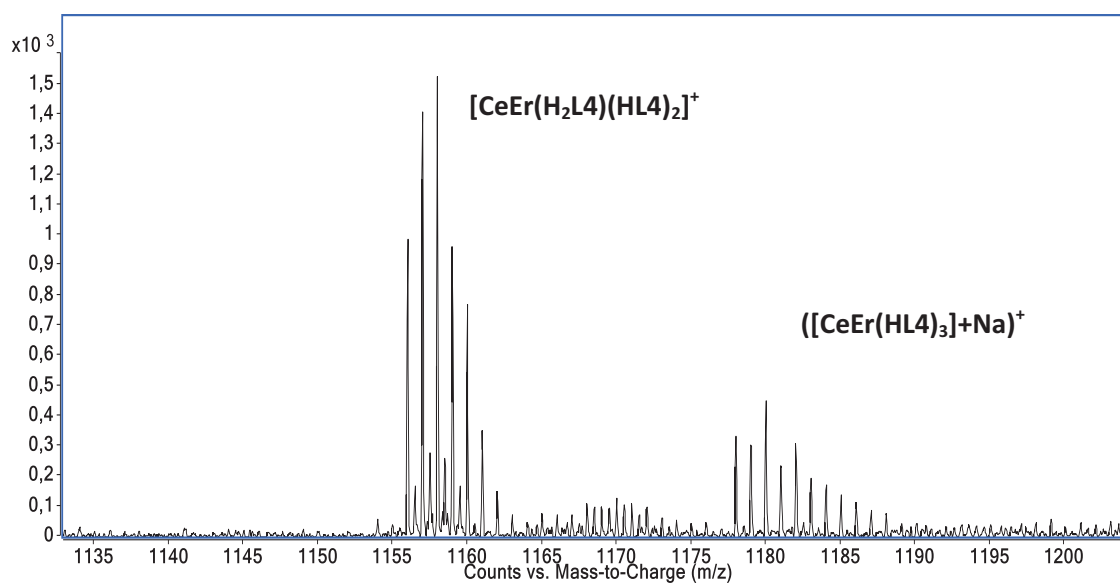


Figure V.A17. Electrospray mass spectrogram of complex [CeEr] (40) featuring heterometallic fragments $[\text{CeEr}(\text{HL4})_2(\text{H}_2\text{L4})]^+$ and $([\text{CeEr}(\text{HL4})_3]+\text{Na})^+$.

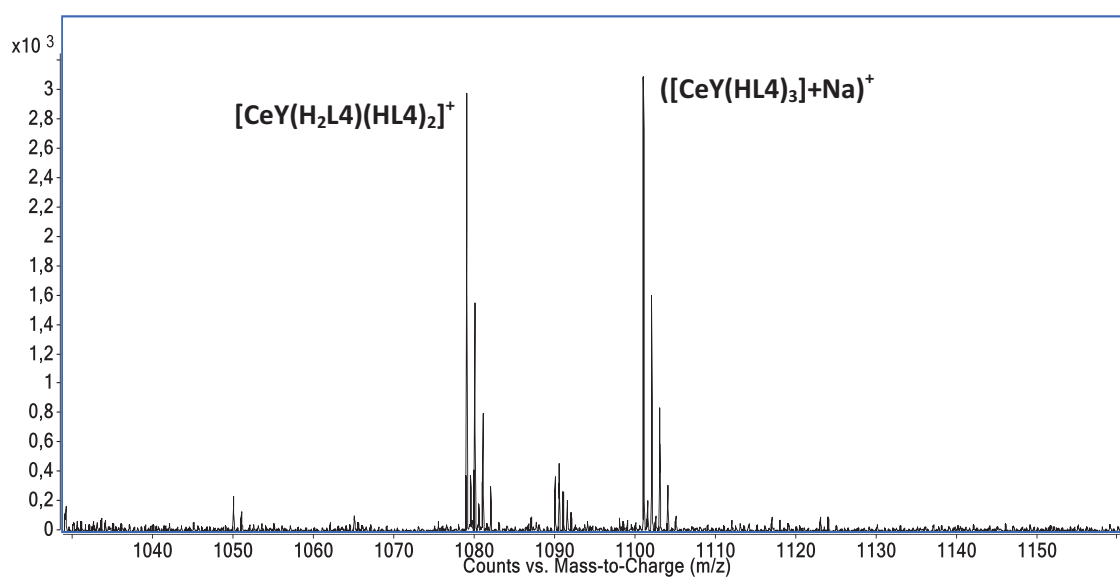


Figure V.A18. Electrospray mass spectrogram of complex [CeY] (43) featuring heterometallic fragments $[\text{CeY}(\text{HL4})_2(\text{H}_2\text{L4})]^+$ and $([\text{CeY}(\text{HL4})_3]+\text{Na})^+$.

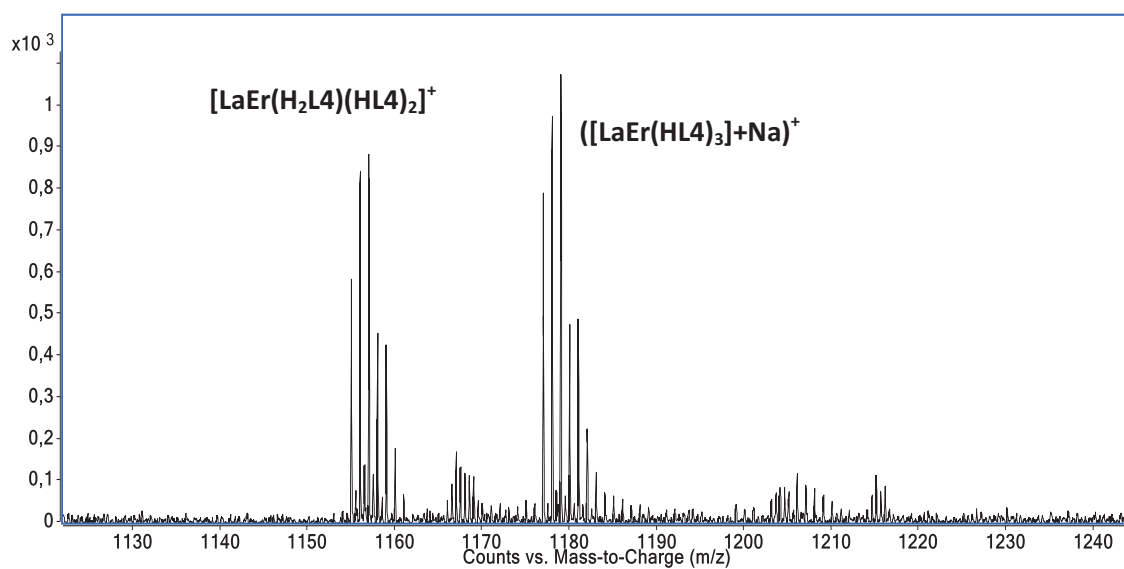


Figure V.A19. Electrospray mass spectrogram of complex [LaEr] (35) featuring heterometallic fragments $[\text{LaEr}(\text{HL4})_2(\text{H}_2\text{L4})]^+$ and $([\text{LaEr}(\text{HL4})_3]+\text{Na})^+$.

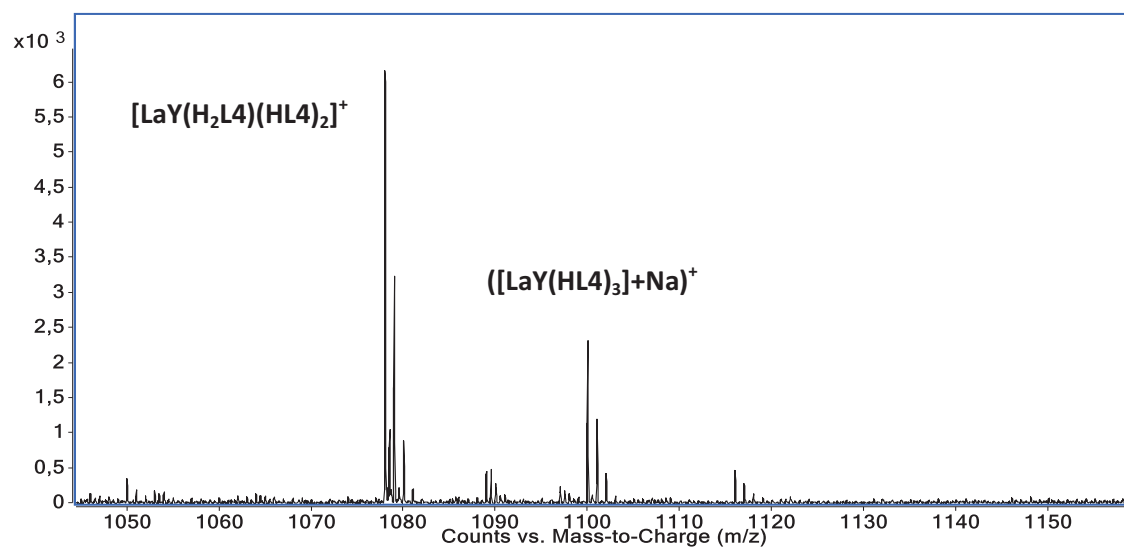


Figure V.A20. Electrospray mass spectrogram of complex [LaY] (36) featuring heterometallic fragments $[\text{LaY}(\text{HL4})_2(\text{H}_2\text{L4})]^+$ and $([\text{LaY}(\text{HL4})_3]+\text{Na})^+$.

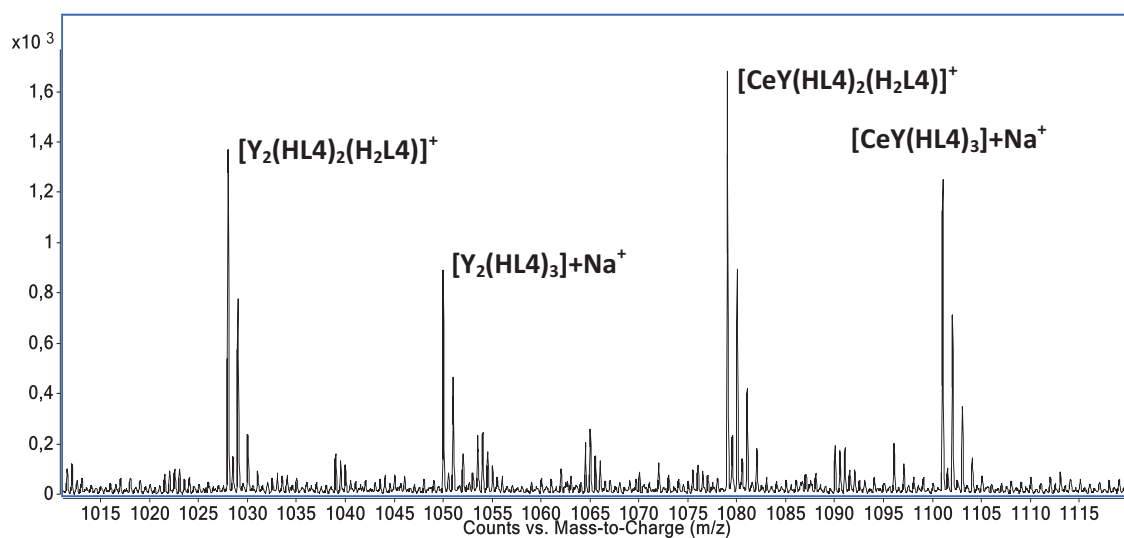


Figure V.A21. Electrospray mass spectrogram of complex $[CeY]_{0.7}[Y_2]_{0.3}$ (**73**) featuring heterometallic fragments corresponding to $[CeY]$ ($[CeY(HL4)_2(H_2L4)]^+$, $[CeY(HL4)_3]+Na^+$) and $[Y_2]$ ($[Y_2(HL4)_2(H_2L4)]^+$, $[Y_2(HL4)_3]+Na^+$).

PHYSICAL TECHNIQUES

Elemental Analysis (C, H, N) were performed on a Perkin-Elmer II Series CHNS/O Analyzer 2400, at the “Servei de Microanàlisi” of CSIC, Barcelona, Spain or at the Campbell Microanalytical Laboratory, University of Otago, Dunedin, New Zealand.

NMR spectra were recorded on Varian Gemini-300 spectrometer (300 MHz), on an Avance VRX 400 instrument (400 MHz) or on a Bruker AVQ 400 spectrometer (400 MHz).

Voltammetry experiments were performed on an SP-150 (BioLogic) potentiostat modulated by EC-Lab V10.02 software, or with an Autolab PGSTAT100 (ECO Chemie) workstation.

IR spectra were obtained as KBr pellet samples on a Nicolet 5700 FTIR spectrometer.

Magnetic measurements were performed using a Quantum Design MPMS-XL SQUID magnetometer either at the “Unitat de Mesures Magnètiques” of the Universitat de Barcelona or at the SAI Physical Measurements of the Universidad de Zaragoza.

Ultra-low magnetic measurements were conducted by Dr. Olivier Roubeau, Dr. Fernando Luis and Ana Repollés using an integrated μ SQUID susceptometer (*Rev. Sci. Instrum.* 81, 016108 (2010)), operating from 13 mK up to 3 K and for frequencies from 0.01 Hz up to 200 kHz for ac susceptibility data. Dc-magnetization measurements were performed using a Hall microprobe installed in a dilution refrigerator.

Electronic absorption spectra were recorded with 1 nm resolutions using a Varian Cary 100 UV/Vis spectrophotometer.

Fluorescence emission spectra were carried out by Dr. Núria Aliaga-Alcalde and Dr. Melita Menelaou, using Horiba Jobin-Yvon SPEX Nanolog-TM and Cary Eclipse spectrofluorimeters.

Positive-ion ESI mass spectrometry experiments were performed using a LC/MSD-TOF (Agilent Technologies) with a dual source equipped with a lock spray for internal reference introduction at the “Unitat d’Espectrometria de Masses” (SSR) of the Universitat de Barcelona.

Analysis of metals were performed by inductively coupled plasma (ICP) spectrometry using a Varian Vista-MPX instrument by Jos van Brussel, in Leiden Institute of Chemistry, or by ICP-AES using a iCap6500 spectrometer at the Mikroanalytisches Labor Pascher.

EPR experiments were carried out by Dr. P. J. Alonso with a Bruker Elexys ESP580E spectrophotometer working in the X frequency band (9.8 GHz) and under magnetic fields $\mu_0 H \leq 1.4$ T. CW-EPR and TD-EPR measurements were performed with an Oxford ESR900 and ESR980 cryostat, respectively.

X-ray data were collected with,

- Bruker APEX II QUAZAR diffractometer with $\text{Mo}_{K\alpha}$ radiation ($\lambda = 0.71073$ Å) and equipped with a microfocus multilayer monochromator.
- Bruker APEX II CCD diffractometer on the Advanced Light Source beamline 11.3.1 at Lawrence Berkeley National Laboratory, from a silicon 111 monochromator ($\lambda = 0.7749$ Å).
- Oxford Diffraction Excalibur diffractometer with enhanced $\text{Mo}_{K\alpha}$ radiation ($\lambda = 0.71073$ Å) at the X-ray diffraction and Fluorescence Analysis Service of the University of Zaragoza).
- Bruker APPEX II CCD diffractometer on station 16.2 of the Synchrotron Radiation Source at CCLRC Daresbury Laboratory ($\lambda = 0.8129$ Å).
- HUBER diffractometer on station BM16 of the European Synchrotron Radiation Facility ($\lambda = 0.7383$ Å).

TGA-DTA experiments were performed by Dr. Olivier Roubeau on a Q50000IR thermo-analyzer from TA instruments under N_2 .

Heat capacity measurements were performed in a Quantum Design PPMS (Physical Property Measurement System) using the relaxation method down to 0.35 K of the heat capacity option, in magnetic fields up to 14 T.

LIST OF PUBLICATIONS

- 1) Lanthanide contraction within a series of asymmetric dinuclear [Ln₂] complexes
D. Aguilà, L. A. Barrios, V. Velasco, L. Arnedo, N. Aliaga-Alcalde, M. Menelaou, S. J. Teat, O. Roubeau, F. Luis, G. Aromí
Chem. Eur. J. (DOI: 10.1002/chem.201204451)
- 2) Design of magnetic coordination complexes for quantum computing
G. Aromí, D. Aguilà, P. Gamez, F. Luis, O. Roubeau
Chem. Soc. Rev. 2012, 41, 537
- 3) Molecular prototypes for spin-based CNOT and SWAP quantum gates
F. Luis, A. Repollés, M. J. Martínez-Pérez, D. Aguilà, O. Roubeau, D. Zueco, P. J. Alonso, M. Evangelisti, A. Camón, J. Sesé, L. A. Barrios, G. Aromí
Phys. Rev. Lett. 2011, 107, 117203
- 4) Molecular [Co(III)Co(II)]₂ assemblies of a new bis-phenol/pyrazolyl ligand
G. A. Craig, J. Sánchez Costa, D. Aguilà, L. A. Barrios, O. Roubeau, S. J. Teat, G. Aromí
New J. Chem. 2010, 35, 1202
- 5) Molecular assembly of two [Co(II)₄] arrays
D. Aguilà, L. A. Barrios, O. Roubeau, S. J. Teat, G. Aromí
Chem. Commun. 2010, 47, 707
- 6) Synthesis and properties of a family of unsymmetric dinuclear complexes of Ln(III) (Ln = Eu, Gd, Tb)
D. Aguilà, L. A. Barrios, F. Luis, A. Repollés, O. Roubeau, S. J. Teat, G. Aromí
Inorg. Chem. 2010, 49, 6784
- 7) Calibrating the coordination chemistry tool chest: Metrics of bi- and tridentate ligands
D. Aguilà, E. Escribano, S. Speed, D. Talancón, L. Yermán, S. Alvarez
Dalton Trans. 2009, 6610
- 8) A molecular chain of four Co(II) ions stabilized by a tris-pyridil/bis-β-diketonate ligand
L. A. Barrios, D. Aguilà, O. Roubeau, K. S. Murray, G. Aromí
Aust. J. Chem. 2009, 62, 1130
- 9) Designed topology and site-selective metal composition in tetranuclear [MM'...M'M] linear complexes
L. A. Barrios, D. Aguilà, O. Roubeau, P. Gamez, J. Ribas-Ariño, S. J. Teat, G. Aromí
Chem. Eur. J. 2009, 15, 11235
- 10) Synthesis and properties of a novel linear [Ni₄L₂(py)₆] cluster: Designed ligand-controlled topology of the metals
L. A. Barrios, D. Aguilà, S. Méllat, O. Roubeau, S. J. Teat, P. Gamez, G. Aromí
C. R. Chimie, 2008, 11, 10, 1117

AGRAÏMENTS (ACKNOWLEDGEMENTS)

No voldria acabar aquest treball sense expressar tota la meva gratitud a les persones que m'han acompanyat durant aquests anys de tesi, i que han compartit tota aquesta aventura amb mi. Per ells, i per què aquestes emocions parlen la meua llengua, escric aquestes paraules en català.

En primer lloc, m'agradaria agrair l'estima i la dedicació del Guillem. Des de que ens vam conèixer, la relació d'estudiant i director s'ha anat encaminant cap a una amistat que sé que durarà per sempre. Gràcies per la confiança que has dipositat en mi des de el principi, per tot el coneixement i recolzament que m'has sabut donar, per totes les nostres converses, científiques, socials, i humanes. Gràcies, en resum, per fer-me una persona millor. D'igual manera, m'agradaria donar les gràcies de tot cor a la Leo. Ara fa sis anys que vaig arribar al laboratori, i em vas acollir amb els braços oberts. Des de llavors no hi hagut cap dia que no m'hagis fet sentir estimat, feliç. Gràcies per tot el que m'has ensenyat, totes les bones estones en el laboratori, en les festes, per portar sempre un somriure, i per cuidar-me i mimar-me.

Agrair molt sincerament a totes les persones que estan i han passat pel GMMF, Núria, Caro, Vero, Stephan, Mike, Matthieu, Marta, Raul "colchonero", Albert, Dani, Leti, Alba, Santi, Victor, MJ (merci per les cançonetes que t'han m'ajuden), i al Jorge per aportar tant de somriure al grup. Agrair molt especialment a la Ivana, per estar sempre al meu costat, per ser una persona tant i tant maca, i de qui m'emportaré una estima allà on vagi. Vull donar les gràcies de manera molt efusiva als meu germà escocès i "a mi hermano murciano". *Tengo TRES cosas que decir...* Gràcies Gavin i Jose per la vostra amistat, pels concerts de Vetusta, per les molt bones estones tant a la universitat com durant les sortides nocturnes, i per totes les aventures viscudes durant aquests anys... com veieu, necessito dir-vos moltíssimes més que tres coses per fer-vos saber que us portaré dintre allà on vagi. Agrair també a las "niñas" del Jose, la Ire i la Sofi, que em fan tant i tant feliç.

També vull donar les gràcies a tota la gent del departament que ha compartit les vivències d'aquesta tesi, en especial a la Saskia, qui m'ha cuidat i ajudat sempre des de el principi. Agrair a *los compadres* el Abuelo Luis i el pinche Dani, a l'Esther, al Jordi, la

Bea, la Vero, la Silvia, el Lluís, la Maria, la Fatima, el Ferran, la Rosinha, la Cris, el Tommy, i en general tots els que em responeu amb un somriure quan ens creuem pel passadís. Agrair molt especialment a la Bel, per ser com ets i per fer-me sentir tant i tant bé. També m'agradaria donar les gràcies a tots els amics i amigues tant de Melbourne com de Berkeley. Gràcies per fer-me veure que el món està ple de llocs bonics i persones maques. En especial, agrair al Professor Jeffrey Long i al Professor Alan Bond per donar-me l'oportunitat de treballar en els seus grups de recerca.

M'agradaria agrair molt especialment a l'Olivier per les mesures magnètiques, les estructures cristal·lines, i sobretot per totes les bones estones viscudes. Agrair al Dr. Fernando Luis per la gran col·laboració que hem creat entre els dos grups, al Dr. Pablo J. Alonso per les mesures d'EPR, al Dr. Simon Teat per les estructures cristal·lines, a la Dra. Núria Clos per les mesures magnètiques, a la Laura Ortiz i la Dra. Irene Fernández pel temps emprat i les discussions sobre els espectres de masses, i al Dr. Patrick Gamez per les seves constructives opinions. Agrair també de forma especial al Professor Joan Ribas per intorduir-me en el món de la Química de Coordinació.

A tots els meus amics de fora del departament, als "unis", als "ipsis", als "de Terrassa", als "sanses", que em feu sentir estimat, us vull donar les gràcies per formar part de la meva vida. Agrair especialment a l'Arnau, per ser-hi sempre, i a la Adri, per fer la portada d'aquesta tesi i per cuidar-me cada dia com un germanet. També vull donar les gràcies a tota la meva gran família, a mi *abuela* Júlia, tiets i cosins de Barcelona i Palau. Voldria donar les gràcies especialment al meu cosí Christian, pels seus suggeriments i les converses tant interessants sobre el món de la quàntica. També vull donar les gràcies amb un record molt especial al meu *abuelo* Herminio, i la meva àvia Carme.

Finalment, vull agrair de tot cor als meus pares, Josep i Maribel, i al meu germà Dani. Per què sou l'alegria que fa que cada dia sigui especial, la meva força i el meu suport. Per què sou les ales que em permeten volar i somiar.

David Aguilà Avilés

